frontiers | Research Topics

Functional tissue engineering for regenerative medical research and new drug development

Edited by
Junxi Wu, Fengxuan Han and Christopher Mccormick

Published in
Frontiers in Bioengineering and Biotechnology

ISSN 1664-8714
ISBN 978-2-8325-6472-1
DOI 10.3389/978-2-8325-6472-1

About Frontiers

Frontiers is more than just an open access publisher of scholarly articles: it is a pioneering approach to the world of academia, radically improving the way scholarly research is managed. The grand vision of Frontiers is a world where all people have an equal opportunity to seek, share and generate knowledge. Frontiers provides immediate and permanent online open access to all its publications, but this alone is not enough to realize our grand goals.

Frontiers journal series

The Frontiers journal series is a multi-tier and interdisciplinary set of open-access, online journals, promising a paradigm shift from the current review, selection and dissemination processes in academic publishing. All Frontiers journals are driven by researchers for researchers; therefore, they constitute a service to the scholarly community. At the same time, the *Frontiers journal series* operates on a revolutionary invention, the tiered publishing system, initially addressing specific communities of scholars, and gradually climbing up to broader public understanding, thus serving the interests of the lay society, too.

Dedication to quality

Each Frontiers article is a landmark of the highest quality, thanks to genuinely collaborative interactions between authors and review editors, who include some of the world's best academicians. Research must be certified by peers before entering a stream of knowledge that may eventually reach the public - and shape society; therefore, Frontiers only applies the most rigorous and unbiased reviews. Frontiers revolutionizes research publishing by freely delivering the most outstanding research, evaluated with no bias from both the academic and social point of view. By applying the most advanced information technologies, Frontiers is catapulting scholarly publishing into a new generation.

What are Frontiers Research Topics?

Frontiers Research Topics are very popular trademarks of the *Frontiers journals series*: they are collections of at least ten articles, all centered on a particular subject. With their unique mix of varied contributions from Original Research to Review Articles, Frontiers Research Topics unify the most influential researchers, the latest key findings and historical advances in a hot research area.

Find out more on how to host your own Frontiers Research Topic or contribute to one as an author by contacting the Frontiers editorial office: frontiersin.org/about/contact

Functional tissue engineering for regenerative medical research and new drug development

Topic editors
Junxi Wu — University of Strathclyde, United Kingdom
Fengxuan Han — Soochow University, China
Christopher Mccormick — University of Strathclyde, United Kingdom

Citation
Wu, J., Han, F., Mccormick, C., eds. (2025). *Functional tissue engineering for regenerative medical research and new drug development*.
Lausanne: Frontiers Media SA. doi: 10.3389/978-2-8325-6472-1

Table of contents

frontiers | Frontiers in Bioengineering and Biotechnology

TYPE Original Research
PUBLISHED 04 January 2023
DOI 10.3389/fbioe.2022.1109074

OPEN ACCESS

EDITED BY
Fengxuan Han,
Soochow University, China

REVIEWED BY
Qian Feng,
Chongqing University, China
Qin Zhang,
Shanghai University, China

*CORRESPONDENCE
Lin Liu,
✉ johnaskyou@sina.com

†These authors have contributed equally to this work

SPECIALTY SECTION
This article was submitted to Tissue Engineering and Regenerative Medicine, a section of the journal Frontiers in Bioengineering and Biotechnology

RECEIVED 27 November 2022
ACCEPTED 19 December 2022
PUBLISHED 04 January 2023

CITATION
Li H, Xiang D, Gong C, Wang X and Liu L (2023), Naturally derived injectable hydrogels with ROS-scavenging property to protect transplanted stem cell bioactivity for osteoarthritic cartilage repair.
Front. Bioeng. Biotechnol. 10:1109074.
doi: 10.3389/fbioe.2022.1109074

Naturally derived injectable hydrogels with ROS-scavenging property to protect transplanted stem cell bioactivity for osteoarthritic cartilage repair

Haobo Li[1,2†], Dong Xiang[2†], Chongcheng Gong[1†], Xiaomin Wang[1] and Lin Liu[1*]

[1]Department of Orthopaedics and Traumatology, Shanghai East Hospital, School of Medicine, Tongji University, Shanghai, China, [2]Department of Orthopaedics, Shanghai Changzheng Hospital, Naval Medical University, Shanghai, China

Intra-articular injection of adipose mesenchymal stem cells (ADSCs) is a potential alternative to the treatment of osteoarthritis (OA) and has aroused great interest of clinical researchers. However, the hostile microenvironment in the joint cavity, characterized by reactive oxygen species (ROS) accumulation and excessive inflammation, disturbs the bioactivity of the transplanted stem cells. The (-)-epigallocatechin-3-O-gallate (EGCG), a green tea catechin, has attracted the researchers' attention owing to its powerful ROS-scavenging and antioxidant properties. In this study, to avoid rapid degradation and/or depletion of EGCG, we prepare a long-lasting injectable hydrogel by EGCG and hyaluronic acid (HA). The naturally derived hydrogels with excellent biocompatibility and durable retention time can capture the redundant ROS continuously and efficiently, thus protecting ADSCs from ROS-mediated death and bioactivity inhibition, including cell survival, proliferation and chondrogenic differentiation. Intra-articular injection of this ADSCs loaded hydrogel significantly induced synovial macrophages polarization to M2 phenotype, decreased pro-inflammatory cytokines (e.g., IL-1β, MMP-13, and TNF-α) expression, promoted cartilage matrix formation, and repaired cartilage destruction in OA. This stem cell-protected hydrogel delivery strategy showed superior efficacy than ADSCs delivering or EGCG-HA injection singly, which providing a potential alternative strategy for OA management.

KEYWORDS

hydrogel, anti-oxidant, stem cell, cartilage repair, osteoarthritis

Introduction

Osteoarthritis (OA) is the most common chronic joint disease in orthopedics, characterized by articular cartilage degeneration, reactive hyperplasia of articular border and subchondral bone. OA has a complex disease process associated with synovium, articular cartilage, subchondral bone, ligament, joint capsule and muscles around joints (Huang et al., 2022). With the accelerating of population aging, the population suffering from OA has reached 200 million, which results in huge living obstacles and heavy economic burden to the society (Li Y. et al., 2022; Zhao et al., 2022). Over the past decades, intra-articular injection of various stem cells has emerged as an advanced therapy to delay the pathological progress of OA. Among them, some mesenchymal stem cells (MSCs), including adipose mesenchymal stem cells (ADSCs) and bone marrow mesenchymal stem cells (BMSCs), have become the most preferred therapeutic cells for treating OA owing to their extensive sources, accessibility, multi-directional differentiation, and the enviable paracrine effects (Molnar et al., 2022; Shoukrie et al., 2022; Zeng et al., 2022). Intra-articular injection of MSCs is well-proven as an alternative treatment to repair damaged cartilage, delay the pathological progress of OA, as well as relieve pain (Csaki et al., 2008; Maumus et al., 2011; Yin B. et al., 2022; Lin et al., 2022). However, the stem cells delivered to the articular cavity are seriously affected by the harsh microenvironment of OA. As a result, the stem cells are difficult to give full play to their multiple functions, thus limiting the wide application of this strategy.

The pathological microenvironment of OA is multifaceted and involves the whole joint (Kang et al., 2022). Recently, growing evidences suggested that accumulated reactive oxygen species (ROS) and oxidative stress show an increasingly important role in OA microenvironment (Ahmad et al., 2020). ROS participate in various biological processes and are closely associated with the aggravation of OA. The accumulated ROS will activate a series of signal pathways, subsequent lead to chondrocytes catabolism and apoptosis, matrix metalloproteases (MMPs) overexpression, extracellular matrix (ECM) degradation, and excessive inflammation, thus causing various pathological changes of OA (Li et al., 2017; Khan et al., 2018; Stocco et al., 2019). The balances of ROS production and deletion are greatly related to the occurrence, development, and progress of OA. Previously, Kim et al. (2019) developed manganese ferrite and ceria co-decorated nanoparticles that can scavenge ROS and produce O_2 synergistically. The functional nanoparticles alleviated hypoxia and excessive inflammation, induced inflammatory M1 macrophages polarization toward anti-inflammatory M2 phenotype, thus remodeling the pathological features of the arthritic joint. Therefore, removing excessive ROS to reshape the pathological microenvironment of OA to enable transplanted stem cells to give full play to their functions, may be an alternative therapy for OA treatment.

The hydrogels composed of hydrophilic three-dimensional (3D) network structure are widely used to deliver bioactive substances and stem cells to promote tissue repair and regeneration due to their fascinating properties (Li et al., 2021; Li et al., 2022b). In this study, we prepared a functional hydrogel, synthesized by thiolated hyaluronic acid (HA) and (-)-epigallocatechin-3-O-gallate (EGCG) quinone, as a protective carrier of stem cells for intra-articular injection to treat OA. As the main ingredient of green tea catechins, EGCG has attracted much interest in the field of biomedicine due to its enviable ROS-scavenging capacity, anti-oxidation, and anti-inflammatory performances (Yang et al., 2022; Zhu et al., 2022). By nucleophilic addition reaction of thiolated HA and EGCG quinone, the HA-EGCG hydrogel was synthesized and showed excellent ROS-scavenging ability and hyaluronidase (HAase)-inhibitory activity (Liu et al., 2017). Herein, we investigated the degradation resistance, ROS-scavenging ability, and protective effect on ADSCs chondrogenic differentiation of HA-EGCG hydrogel under oxidative stress state, to demonstrate its potential as a cytoprotective carrier in the management of OA.

Materials and methods

Materials

EGCG, HAase, xanthine, 2′, 7′-dichlorodihydrofluorescein diacetate (DCFH-DA), and streptomycin–penicillin were supplied by Sigma-Aldrich (St. Louis, MO, United States). Xanthine oxidase from buttermilk was provided by Oriental Yeast Co. (Osaka, Japan). Thiolated HA was provided by Qiyue Biotechnology Co., Ltd (Xi’an, China). Commercial HA was supplied by Boshilun Furida Pharmaceutical Co., Ltd (Shandong, China). Hydrogen peroxide (H_2O_2) and hematoxylin eosin (H&E) stain, Alcian blue stain, and Safranin O stain were purchased from Thermo Fisher Scientific (Waltham, MA, United States). Horseradish peroxidase (HRP) and fetal bovine serum (FBS) were provided by Yuanye Biotechnology Co., Ltd (Shanghai, China). Low glucose Dulbecco modified Eagle medium (DMEM) and 0.25% trypsin EDTA were obtained from HyClone (Logan, Utah, United States). Mice ADSCs and chondrogenic differentiation induction medium of ADSCs were supplied by Procell (Wuhan, China). Cell Counting Kit-8 (CCK-8) assay was purchased from Dojindo (Japan) and Calcein-AM/Propidium Iodide (PI) was supplied by Beyotime Biotechnology (Shanghai, China). Phosphate buffer saline (PBS) and 4% paraformaldehyde were obtained from Solarbio (Beijing, China). The enzyme-linked immunosorbent assay (ELISA) kits of interleukin-1 beta (IL-1β), matrix metalloproteinase-13 (MMP-13), tumor necrosis factor-alpha (TNF-α) were supplied by Hengyuan Biotechnology Co., Ltd (Shanghai, China). Eastep Super Total RNA Extraction Kit was supplied by Promega (Shanghai, China) and Perfect Real Time RT reagent kit was obtained from Takara Bio (Dalian, China). Primary antibodies were provided by Abcam (Cambridge, United Kingdom), and secondaries antibodies were supplied by Jackson ImmunoResearch Laboratories (West Grove, PA, United States). All other chemicals and reagents were of analytical grade.

HA-EGCG hydrogel preparation and characterization

The HA-EGCG conjugate was synthesized by coupling EGCG to thiolated HA derivatives as described previously (Liu et al., 2017). In brief, we dissolved thiolated HA (1 g) in the 140 ml PBS (pH = 7.4) under nitrogen atmosphere, then added drop by drop to 60 ml PBS (pH = 7.4) containing excess EGCG, and stirred continuously. Adjust the pH of the solution to 7.4 by dropping NaOH, and react at 25°C for 3 h, then adjust the pH to 6. The obtained solution was dialyzed under nitrogen atmosphere, and then the purified solution was freeze-dried to acquire HA-EGCG conjugate.

HA-EGCG conjugate was dissolved in deionized water at 25 °C to acquire the HA-EGCG solution (11.5 mg/ml) firstly. To obtain the HA-EGCG hydrogels, 7.8 ml HA-EGCG solution was merged with 150 μL of HRP solution, 150 μL of H_2O_2 solution, and 900 μL PBS (pH = 7.4) in a tube for 24 h. Rheological measurements were performed with a RH-20 rheometer (Bosin Tech, China) at room temperature. The viscosity of the hydrogels was tested by a viscometer (NDJ-5S, Shanghai, China).

Degradation of HA-EGCG hydrogel

To evaluate the degradation of hydrogel, 1 g HA-EGCG hydrogel was placed in glass bottles and immersed with 5 ml PBS or HAase (15 units/ml) contained PBS at 37°C. During the whole degradation process, HAase was supplemented every day. At the predetermined time intervals, the residual hydrogels were collected and weighed. The residual ratio of hydrogels was determined by following formula: residual hydrogel ratio (%) = $W_t/W_0 \times 100\%$. The Wt is the hydrated mass at the measured time point and W_0 is the initial weight of the hydrogel. Commercialized HA for intra-articular injection clinically was used as the control agent.

Biocompatibility of HA-EGCG hydrogel

ADSCs were seeded in a 48-well plate with density of 1×10^4/well. The plates pre-coated with 100 μL HA-EGCG hydrogel was used to investigate the biocompatibility of the material. The cells were incubated in the incubator for 2 days, and Calcein-AM/PI was performed according to the manufacturer's protocols. Briefly, 5 μM Calcein-AM solution was added into the samples for 15 min, subsequent 5 μM PI solution was transferred to the wells for 5 min, which conducted at room temperature and away from light. The pictures were observed by a confocal microscope (Olympus Fluoview FV1000, Japan). In addition, the proliferation of ADSCs cultured in different substrates were detected by CCK-8 test at predetermined time points. Briefly, the culture medium was removed and 10% CCK-8 solution was added to each well. The samples were incubated at 37 °C for 2 h and then transferred to a 96-well plate for absorbance detection by a microplate reader (Varioskan LUX, Thermo Fisher Scientific, MA, United States) at 450 nm.

ROS-scavenging capacity

The H_2O_2 depletion ability of the HA-EGCG hydrogel was monitored by mixing H_2O_2 (1 mM, 1 ml) and hydrogel (1 ml) in PBS at 37 °C as described previously (Li et al., 2022a). After designated times, the supernatant (100 μL) was collected and added 200 μL of $Ti(SO_4)_2$ solution. After incubation for 30 min, the H_2O_2 concentration was determined by testing the absorbance of samples at 405 nm by a microplate reader.

Intracellular ROS (H_2O_2) depletion and cell viability protection

The intracellular H_2O_2 scavenge capacity of HA-EGCG hydrogel was evaluated by a H_2O_2 probe DCFH-DA. Specifically, ADSCs were seeded in 48-well plates pre-coated with 100 μL HA or 100 μL HA-EGCG hydrogel at the density of 1×10^4/well under the oxidative environment (100 μM H_2O_2 in the culture medium). For comparison, ADSCs were also incubated with 100 μL PBS in the presence or absence of H_2O_2, respectively. After incubating for 2 days, DCFH-DA agent was transferred to various groups for 20 min at room temperature. The fluorescence intensity indicating the intracellular ROS level of the cells was observed by the confocal microscope. Furthermore, under the oxidative stress and the protection of HA-EGCG hydrogel, the cell viability was evaluated by a Calcein-AM/PI kit and observed with the confocal microscope.

TABLE 1 Primer sequences of genes.

Gene	Oligonucleotide primers (5′-3′)
GAPDH	F: 5′- TCA GCT GCT GGG GAG TCA CA-3′
	R: 5′- CCT AAG CCC CTC CCC TTC TT-3′
IL-1β	F: 5′- TCT CTG GAC CCA AAG GAG GG-3′
	R: 5′- ACG GCT GCT TTC ACG GGT GA-3′
MMP-13	F: 5′- CCT GTG CTC CTG CCA TTT GG-3′
	R: 5′- GAA TGG GCA GCT CCA TGG CT-3′
TNF-a	F: 5′- AGC TGG TGG TGC CGA CAG AT-3′
	R: 5′- TGC GAT GCG GCT GAT GGT GT-3′
ACAN	F: 5′- CTG CCC CGA AAC ATC ACC GA-3′
	R: 5′-GTA AAG GGC TCC TCA GGC TC-3′
COL-2	F: 5′-TAG AGA GGT TTC CTG GGC CG-3′
	R: 5′-AGG AGG ACG CTG GAA CAG AG-3′
SOX-9	F: 5′-CAG TCC CAG CGA ACG CAC AT-3′
	R: 5′-TGC TGC TGC TGC TCG CTG TA-3′

Real-time PCR analysis

ADSCs were seeded in 48-well plates pre-coated with 100 μL HA or 100 μL HA-EGCG hydrogel at the density of 1×10^4/well under the oxidative environment as described above. After incubation with chondrogenic induction medium for 14 days, cell samples were collected for real-time PCR analysis. In brief, the samples were ground within TRIzol reagent to extract total mRNA. The concentration of acquired RNA was determined by Infinite 200 PRO NanoQuant Microplate Readers (TECAN). Then the RNA (1 μg) was used for cDNA synthesis. Real-time PCR was performed using 2× Fast SYBR Green Master Mix (Roche Diagnostics, Basel, Switzerland) and ABI StepOnePlus™ Real-Time RCR system (Applied Biosystems). The relative mRNAs expression was calculated by the $2^{-\Delta\Delta Ct}$ formula. The primer sequences of GAPDH, IL-1β, MMP-13, TNF-α, aggrecan (ACAN), type II collagen (COL-2), and Sex determining region Y box 9 (SOX-9), were listed in Table 1.

Alcian blue and safranine O staining

The chondrogenic differentiation potential of ADSCs under the oxidative environment with the protection of HA-EGCG hydrogel was evaluated by staining the samples with Alcian blue and Safranin O dyes according the manufacturer's instructions. In brief, after culture in chondrogenic induction medium for 14 days, the cells were fixed by 4% paraformaldehyde for 5 min, followed by being stained with Alcian blue for 30 min at room temperature, and the remaining samples were incubated with Safranin O for 5 min according to the manufacturer's instructions. Finally, the stained pictures were observed and photographed with a DSX 500 optical microscope (Olympus, Japan).

OA model preparation and intra-articular administration

Sprague-Dawley rats (male, eight-week-old, ~250 g) were used to prepared OA model according to classic surgical destabilization of the medial meniscus (DMM) as described previously (Shao et al., 2021). Briefly, the rats were anesthetized by 3% pentobarbital injected intraperitoneally at the dose of 0.2ml/100g, and then the joint cavity was opened layer by layer and the medial collateral ligament was transacted. Four weeks after molding, intra-articular injection of different therapeutic agents was implemented once. Specifically, therapeutic agents included 100 μl PBS as negative control, 100 μl PBS containing 2×10^6 ADSCs, 100 μl HA-EGCG hydrogel, and 100 μl HA-EGCG hydrogel containing 2×10^6 ADSCs, abbreviated as PBS, ADSCs, Gel, and ADSCs/Gel, respectively. At the sixth week, the animals in each group received another intra-articular injection of therapeutic agents. Twelve weeks after the first injection, the experimental animals were euthanized and the articular cartilages and surrounding synovial tissues were collected for subsequent investigations.

Evaluation of inflammatory cytokines in synovium

Some inflammatory cytokines, including IL-1β, MMP-13, and TNF-α in the synovium tissues were evaluated by corresponding ELISA kits based on the manufacturer's protocols. In brief, 500 mg synovium tissues were collected, uniformly cut, and transferred to protease inhibitor contained PBS (5 ml). The synovium samples were placed in a glass homogenizer and grinded fully on ice. Subsequently, the absorbance of various samples was determined by the microplate reader at 450 nm. The concentrations of IL-1β, MMP-13, and TNF-α were determined according to the standard curve.

Histological sections preparation and staining

After the rats were sacrificed, the synovium and cartilage tissues were preserved and then fixed by 4% paraformaldehyde. The synovium tissues were embedded in paraffin for subsequent conventional histological processing and ~5 μm thickness slices were prepared. For cartilage tissues, the samples were decalcified with 0.5 M EDTA solution for 1 month first, and then prepared ~5 μm thickness slices. And then, the sections were incubated with H&E dye according to the instructions for subsequent histological observation.

Immunofluorescence staining

To study macrophages polarization, the sections of synovium tissues were stained with CD68 plus iNOS and CD68 plus CD163. The cartilage tissues were marked by ACAN, COL-2, and SOX-9. In brief, the sections were blocked with 3% BSA, and 0.2% Triton X-100 for 1 h. The synovium samples were incubated with primary antibodies, anti-CD68 antibody (1:100) plus anti-iNOS antibody (1:200), and anti-CD68 antibody (1:100) plus anti-CD163 antibody (1:150) at 4°C overnight. The sections of cartilage tissues were incubated with primary antibodies, anti-COL-2 antibody (1:200) plus anti-SOX-9 antibody (1:150), and anti-ACAN antibody (1:150). After washing by PBS for three times, the sections were incubated with secondary antibodies Cy3-conjugated goat anti-rabbit (1:500) and goat anti-mouse IgG DyLight 488-conjugated (1:600) for 1 h at room temperature. At last, the nucleus was stained with DAPI for 3 min, the images were observed and photographed by a confocal microscope. The relative fluorescence intensity of images was quantitatively analyzed with ImageJ software.

Statistical analysis

All results were presented as mean ± standard deviation. Statistical analysis was performed by SPSS (version 22.0, Chicago, IL, United States) and the difference between values was analyzed using Student's unpaired *t*-test. All experiments repeated at least 3 times independently.

Results and discussions

HA-EGCG hydrogel preparation and characterization

EGCG can undergo an autoxidation reaction to form an ortho-quinone in the pyrogallol part (B ring) at pH = 7.4. When excess EGCG mixed with thiolated HA, the nucleophilic addition of the thiol groups to the ortho-quinone and subsequent re-arrangement result in the conjugation of thiolated HA, specifically at the B ring in the EGCG (Cao et al., 2009). The preparation of HA-EGCG hydrogel is based on the previous well-established strategy (Lee et al., 2015; Liu et al., 2017). As illustrated in Figure 1A, the synthesis strategy of HA-EGCG conjugate was composed by multiple EGCG molecules grafted onto the HA backbone. The produced HA-EGCG conjugate was simple purification by dialysis against deionized water under nitrogen atmosphere. As shown in Figure 1B, the injectable hydrogel was prepared by using HA-EGCG conjugate *via* peroxidase catalyzed oxidative coupling reaction between EGCG moieties. After mixed by HRP and H_2O_2, the transparent HA-EGCG conjugate solution gradually formed yellow brown hydrogel within 1–2 min (Figure 1C). Previous studies have indicated that the catalytic oxidation of EGCG by HRP results in the production of phenoxy radicals, which can react with the other EGCG molecules to form EGCG dimers. In fact, the yellow brown color of HA-EGCG hydrogel suggested the existence of EGCG dimers (Zhu et al., 2000; Tanaka et al., 2009; Dai et al., 2020; Xu et al., 2021).

The injectability of hydrogel was depicted in Figure 2A, which can be easily pushed out by a 26-gauge syringe without clogging. This injectable ability of the HA-EGCG hydrogel provides the possibility of intra-articular injection as a cell carrier. As shown in Figure 2B, the value of G' surpassed G'' and maintained constant in the time sweep mode suggesting the constructed polymer networks were stable. In addition, the representative strain amplitude sweep of hydrogel

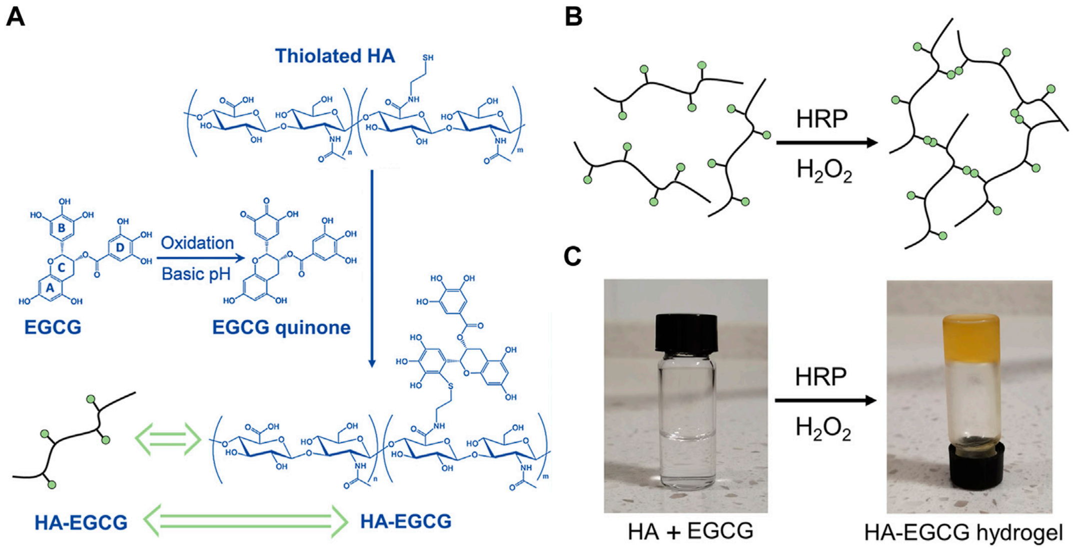

FIGURE 1
Preparation of HA-EGCG hydrogel. **(A)** Synthetic scheme of HA-EGCG conjugate. **(B)** Schematic diagram illustrating the formation of HA-EGCG hydrogel through oxidative coupling between two EGCG moieties catalyzed by HRP and H_2O_2. **(C)** Gross images of HA-EGCG conjugate solution (left) and HA-EGCG hydrogel (right) catalyzed by HRP and H_2O_2.

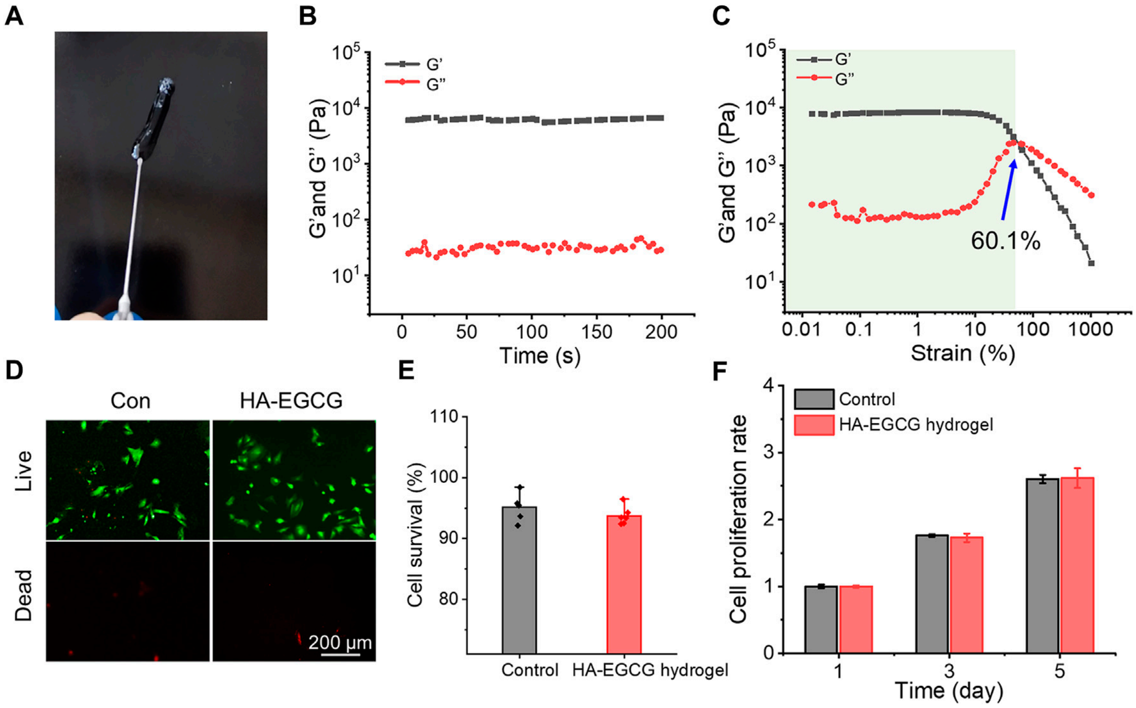

FIGURE 2
Characterization and biocompatibility of HA-EGCG hydrogel. **(A)** The injectability of HA-EGCG hydrogel extruding by a 26-gauge syringe. **(B)** Evolution of the G′ and G″ values over time for the HA-EGCG hydrogel. **(C)** Dependence of the G′ and G″ values over strain for the HA-EGCG hydrogel. **(D)** Calcein AM/PI staining of ADSCs. **(E)** Quantitative analysis of the survival rates of ADSCs (n = 6). **(F)** CCK-8 assay of ADSCs to detect cell proliferation (n = 3).

indicated that the values of G′ and G″ decreased with the strain range from 0.1% to 1000%, showing the typical viscoelastic behavior of hydrogels. In particular, the curves of G′ and G″ intersected at the strain of 60.1%, which was a crucial strain value for the breakdown of the polymer networks (Figure 2C). The viscosity of the hydrogels was tested by a viscometer. The result was revealed that the HA-EGCG

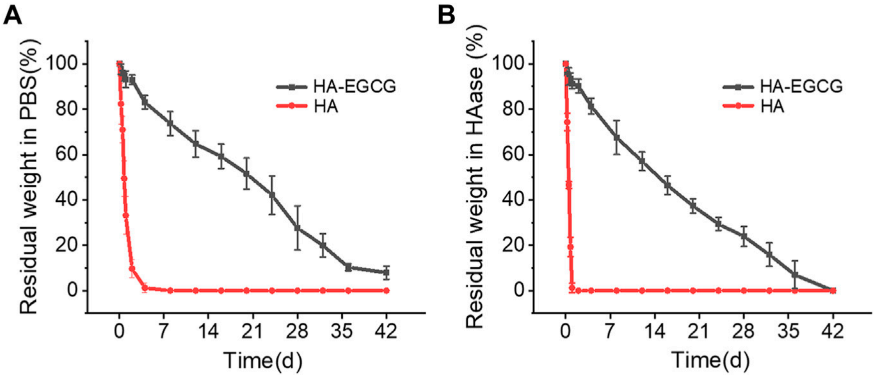

FIGURE 3
Degradation profiles of HA-EGCG hydrogel in PBS and HAase. **(A)** Degradation rate of the HA-EGCG hydrogel in PBS (n = 3). **(B)** Degradation of HA-EGCG hydrogel in PBS containing 15 units/mL HAase (n = 3).

hydrogel had high viscoelasticity, with viscosity index of 170 Pas and elasticity ratio of 51%, which is a favorable material for intra-articular injection.

As a carrier for stem cell delivery, the biocompatibility of the prepared hydrogel is crucial (Bai et al., 2020). As exhibited in Figure 2D, almost all the ADSCs seeded in the HA-EGCG hydrogel were stained with Calcein AM, indicating that they were living cells. As the control group for standardization, the survival rate of ADSCs seeded in the plates was 95.1 ± 2.19%, which was not significantly different from that cultured with the HA-EGCG hydrogel (93.7 ± 1.5%) (Figure 2E). In addition, the proliferation rates of ADSCs cultured in different substrates increased with the prolongation of culture time, and there was no significant difference between groups (Figure 2F). These outcomes proved that the HA-EGCG hydrogel has excellent biocompatibility and can well maintain the cellular activity of ADSCs encapsulated in it, thus making it eligible as candidates for cell delivery carrier.

Degradation resistance of HA-EGCG hydrogel

HA with high viscoelasticity widely exists in joint synovial fluid, which plays an important role in shock absorption and lubrication (Donovan et al., 2022). Intra-articular injection of HA has been widely recommended in clinical practice and is considered a cost-effective treatment strategy for OA (Dai et al., 2020; Xu et al., 2021). However, the rapid degradation of HA in the articular cavity makes this administration strategy need to be repeated every week for several times. This repeated joint cavity puncture may bring some clinical complications, such as pain and joint cavity infection (Patil et al., 2022; Sax et al., 2022). To address these challenges, the HA-EGCG hydrogel with long-term degradation resistance was prepared by peroxidase catalyzed oxidative coupling process between EGCG moieties. As displayed in Figure 3A, the degradation time of HA-EGCG hydrogel in PBS was significantly prolonged, and there was still 51.57 ± 6.8% and 7.9 ± 2.9% residual amounts on the 20th and 42nd day. As a contrast, commercial HA almost completely degraded in PBS within 2 days.

In addition, in the presence of HAase (15 units/mL), the residual amounts of HA-EGCG hydrogel on the 20th was 37.3 ± 3.2%, and completely degraded on the 42nd day (Figure 3B). The results showed that HA-EGCG hydrogel exhibited significantly better resistance to HAase mediated hydrogel degradation than commercial HA. Specifically, commercial HA was completely degraded within 24 h, while about 91.2% of the HA-EGCG hydrogel still existed within the same time period. The HAase inhibitory capacity of HA-EGCG hydrogel may be conducive to improving the stability of its application in the joint cavity, thereby reducing the adverse effects of repeated administration.

HA-EGCG hydrogel scavenging ROS and protecting cell viability under oxidative stress

Considering the ROS accumulated microenvironment in the joint cavity of OA, hydrogel, as a cell delivery carrier, endowed with the ability of scavenging ROS, is a design strategy that needs to be included. As displayed in Figure 4A, commercial HA failed to show visible H_2O_2 scavenging capacity during the whole process. However, HA-EGCG conjugate endowed the hydrogel with excellent ROS-scavenging ability. Specifically, a time-dependent H_2O_2 scavenging efficacy detection assay exhibited that the HA-EGCG hydrogel decomposed approximately 46% of H_2O_2 in the first 60 min, and almost complete elimination was detected in the 120 min.

In addition, to imitate the oxidative stress microenvironment of OA *in vitro*, the ADSCs were cultured with 100 μM H_2O_2. The cells incubated under normal conditions without additional H_2O_2 introduced was set as the normal control group for comparisons. Cellular ROS eliminating ability of the HA-EGCG hydrogel was evaluated by a ROS-specific probe DCFH-DA (Figure 4B). As exhibited in Figure 4C, ADSCs in the H_2O_2+HA-EGCG group showed significantly lower green fluorescence intensity compared to the H_2O_2 group ($p < 0.001$) and H_2O_2+HA group ($p < 0.01$), indicating that the HA-EGCG hydrogel can subside the intracellular ROS efficiently to a normal standard like the Normal group. By continuously ROS-scavenging, a non-oxidative stress microenvironment was expected to construct, which was conducive to maintaining cell vitality. As depicted in Figure 4D, with the protection of HA-EGCG hydrogel, delivered ADSCs were almost green stained live cells under oxidative stress marked by Calcein

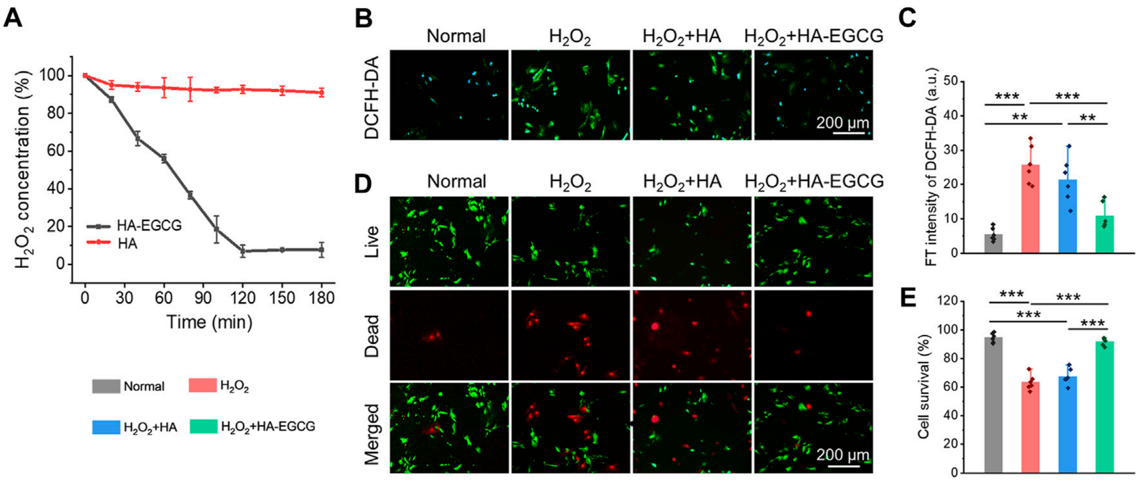

FIGURE 4
ROS-scavenging and cell viability protecting under oxidative stress. **(A)** Decomposition of H_2O_2 with HA-EGCG hydrogel and commercial HA (n = 3). **(B)** Intercellular ROS level validated by a ROS probe (DCFH-DA) after different treatments. **(C)** The quantitative analysis of fluorescence intensity of DCFH-DA to evaluate the ROS depletion. **(D)** Calcein AM/PI staining of ADSCs. **(E)** Quantitative analysis of the survival rates of ADSCs (n = 6) (*$p < 0.05$, **$p < 0.01$, and ***$p < 0.001$).

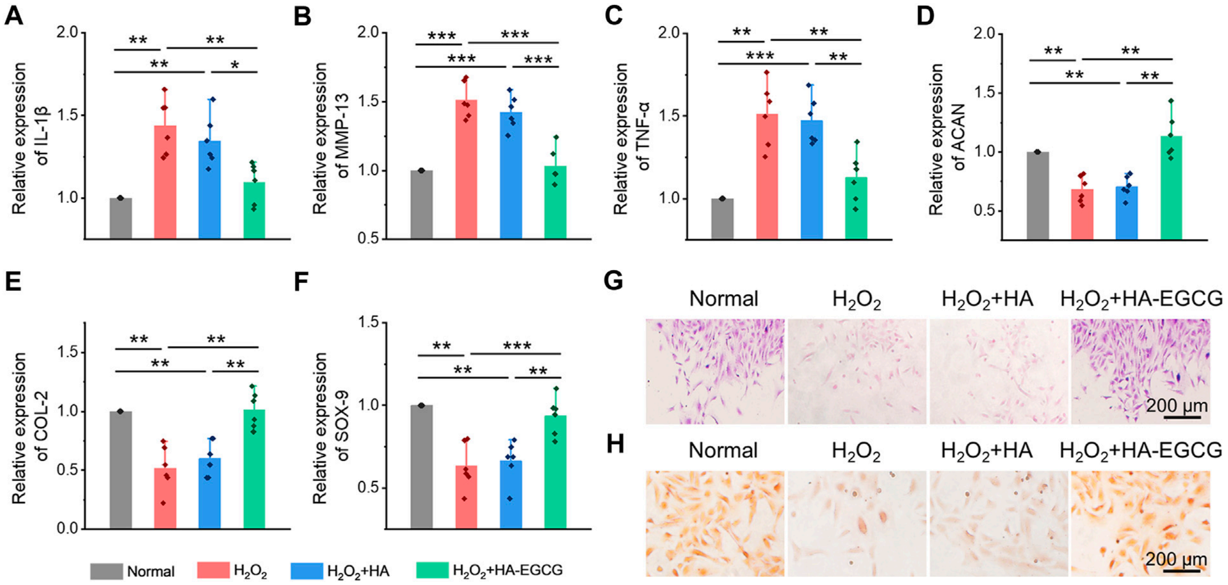

FIGURE 5
Inhibition inflammatory cytokines expression and induction chondrogenic differentiation of ADSCs under oxidative stress. **(A–C)** Real-time PCR analysis of inflammatory cytokines IL-1β, MMP-13, and TNF-α in ADSCs under oxidative stress (*n* = 6). **(D–F)** Real-time PCR analysis of chondrogenic-related genes ACAN, COL-2, and SOX-9 in ADSCs after chondrogenic induction (*n* = 6). **(G)** Alcain blue staining of ADSCs. **(H)** Safranine O staining of ADSCs (*$p < 0.05$, **$p < 0.01$, and ***$p < 0.001$).

AM/PI assay. Quantitative analysis displayed that the cell survival rates in Normal group, H_2O_2 group, H_2O_2+HA group, and H_2O_2+HA-EGCG group, were 94.5 ± 3.2%, 63.4 ± 5.5%, 67.5 ± 5.7%, and 92.0 ± 2.7%, respectively (Figure 4E). These results showed that the hydrogel with ROS-scavenging ability can well maintain the cell vitality of ADSCs under oxidative stress, which is expected to be used as a delivery carrier of stem cells to protect their functions in the joint cavity of OA.

HA-EGCG hydrogel inhibited inflammatory cytokines expression and protected chondrogenic differentiation of ADSCs under oxidative stress

Analysis has proved that H_2O_2 can induce cells to produce excessive ROS, which participates in many signal pathways by activating various cytokines to amplify inflammation reaction,

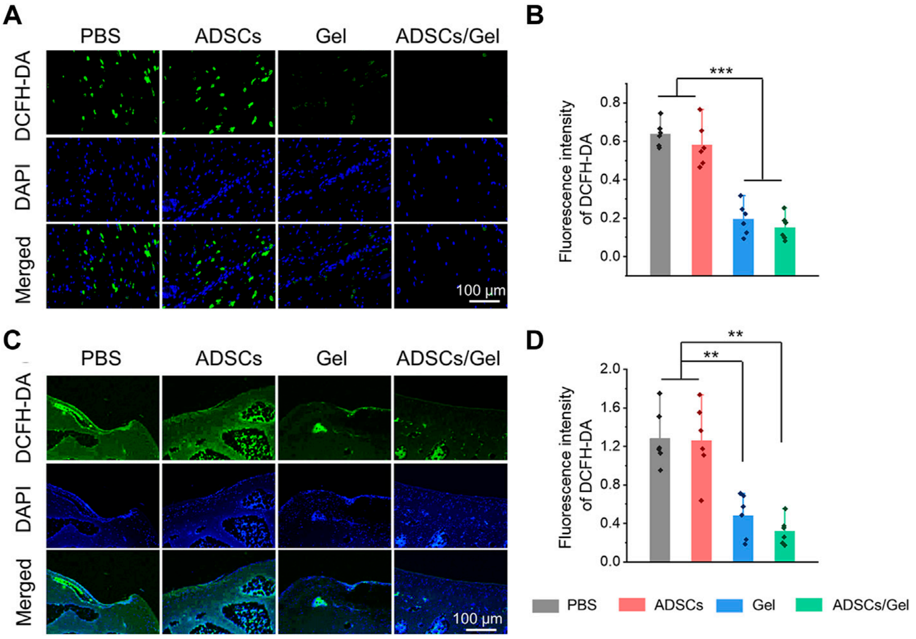

FIGURE 6
HA-EGCG hydrogel scavenging ROS in the joint cavity. **(A)** DCFD-DA labeling of ROS level in synovial tissues. **(B)** Quantitative analysis of the fluorescence intensity of DCFD-DA in synovial tissues (*n* = 6). **(C)** DCFD-DA labeling of ROS level in articular cartilage. **(D)** Quantitative analysis of the fluorescence intensity of DCFD-DA in articular cartilage (*n* = 6) ($*p < 0.05$, $**p < 0.01$, and $***p < 0.001$).

impede cell viability, and prohibit chondrogenesis in OA (Hou et al., 2021). Herein, ADSCs cultured under oxidative stress were collected, and the expression of chondrogenic markers and inflammatory cytokines was detected by the real-time PCR. As showed in Figures 5A–C, when cells were treated with H_2O_2 (H_2O_2 group), the expression of inflammatory factors, including IL-1β, MMP-13, and TNF-α, increased significantly, while the addition of commercial HA (H_2O_2+HA group) cannot reverse this inflammatory state. However, co-cultured with HA-EGCG hydrogel (H_2O_2+HA-EGCG group), the level of inflammatory cytokines can be corrected and restored to a concentration roughly similar to that of the Normal group. Accordingly, this ROS-scavenging hydrogel alleviated the oxidative stress state and decreased the expression of inflammatory factors in cells, and ultimately facilitated the expression of chondrogenic related genes, such as ACAN, COL-2, and SOX-9 (Figures 5D–F). In addition, Alcain blue and Safranine O staining further verified that the HA-EGCG hydrogel was conducive to chondrogenic differentiation of ADSCs in the microenvironment of oxidative stress (Figures 5G, H). These results fully demonstrated that the HA-EGCG hydrogel inhibited the expression of inflammatory cytokines and induced cartilage differentiation of ADSCs under oxidative stress. It means that the HA-EGCG hydrogel as a protective carrier for cell delivery has a potential prospect in the treatment of OA.

ROS-scavenging in synovial and cartilage tissues

The excessive oxidative stress caused by the imbalance between the production and elimination of ROS is regarded as a potential event to activate and accelerate pathological process of OA (Blanco et al., 2018). Previous study has rigorously shown that ROS will oxidize and subsequently destroy the homeostasis of cartilage, promote catabolism by enhancing chondrocyte apoptosis, and finally lead to excessive inflammation and degradation of cartilage matrix (Bolduc et al., 2019). Therefore, the researchers think that scavenging excessive ROS can improve the local microenvironment in the joint cavity and is a potential therapeutic strategy for OA. Herein, the ROS level in synovial tissues and articular cartilage tissues represents the severity of local oxidative stress, which is closely relevant to the progress of OA. At the 12th week after intra-articular injection therapy, we evaluated the ROS changes in synovial tissues by ROS probe (DCFH-DA), as exhibited in Figure 6A. The fluorescence intensity of the images indicated that intra-articular injection of HA-EGCG hydrogel or ADSCs incorporated HA-EGCG hydrogel can effectively reduce the ROS accumulation in the synovium of OA animals and relieve oxidative stress, compared with the PBS group and ADSCs group (Figure 6B). Furthermore, the level of ROS in articular cartilage also decreased significantly in the Gel group and ADSCs/Gel group (Figures 6C,D). These results proved that HA-EGCG hydrogel can remove ROS accumulated in the synovium and cartilage of OA, create a favorable microenvironment for transplanted stem cells, and thus starting the subsequent repair process effectively.

HA-EGCG hydrogel induced synovial macrophage polarization and alleviated synovitis

OA is a chronic disease that involves all tissues of the joint and is featured with synovial inflammation, cartilage matrix progressive

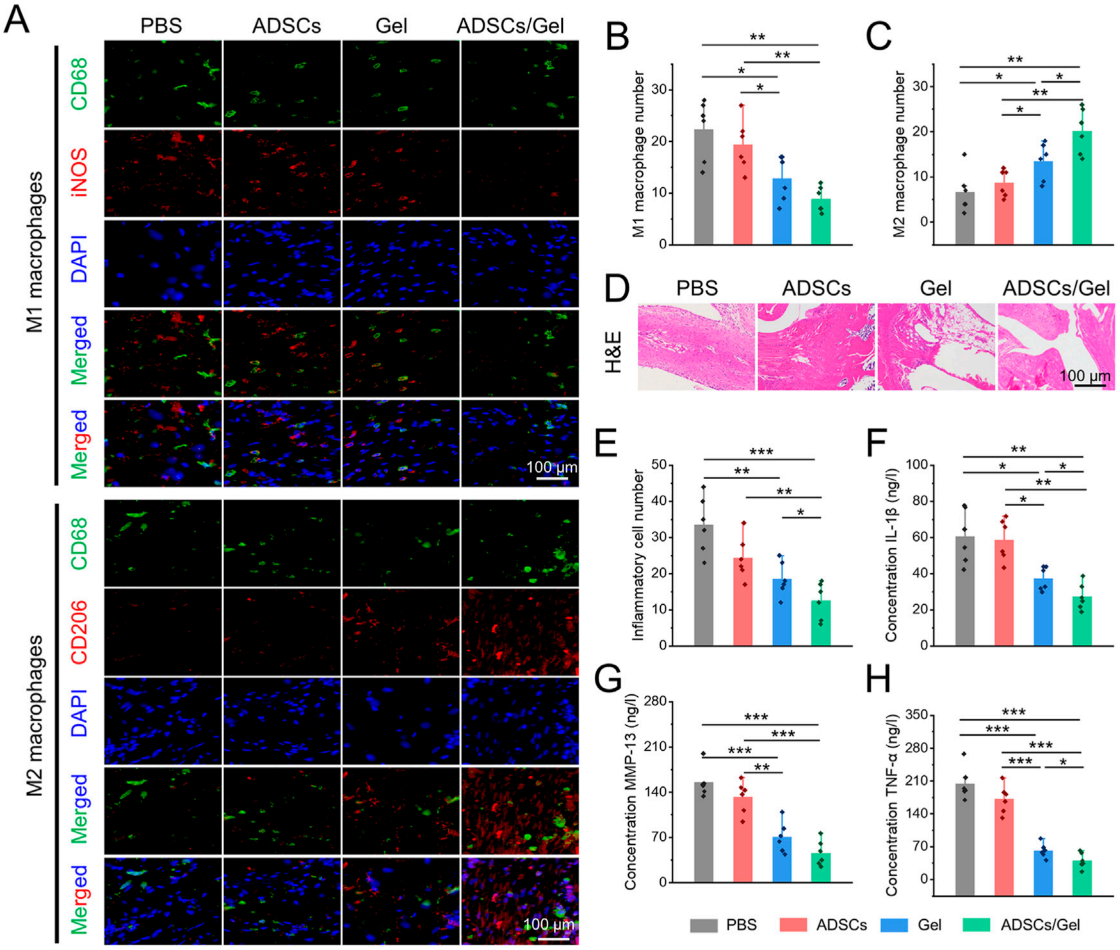

FIGURE 7
Intra-articular injection of ADSCs loaded HA-EGCG hydrogel induced synovial macrophages polarization and alleviated synovitis. **(A)** Immunofluorescence of CD68 plus iNOS to co-label M1 macrophages and CD68 plus CD163 to co-label M2 macrophages. **(B)** Quantitative analysis of the number of M1 macrophages per field ($n = 6$). **(C)** Quantitative analysis of the number of M2 macrophages per field ($n = 6$). **(D)** H&E staining of synovial tissues. **(E)** Quantitative analysis of the number of inflammatory cells infiltration in synovial tissues ($n = 6$). **(F–H)** The concentrations of various pro-inflammatory cytokines, including IL-1β, MMP-13, and TNF-α in synovial tissues by ELISA ($n = 6$) (*$p < 0.05$, **$p < 0.01$, and ***$p < 0.001$).

degeneration, subchondral osteosclerosis and exposure, and osteophyte formation (Zhang et al., 2022). Among them, synovial inflammation, as an initiating factor, is tied to the pathological aggravation of OA (Arra et al., 2020). Various evidences have indicated that the accumulation of ROS interacts with synovitis and worsens, which may show an important influence in the development of OA (Liu et al., 2022; Sunk et al., 2022). Inflammatory reaction exists in synovial tissues, that is, the severity of synovitis is associated with the symptoms of OA and the progress of disease to a large extent. A large number of macrophages with different activation states were observed in the synovium of OA patients at different stages (Yin J. et al., 2022; Jia et al., 2022). Among them, M1 phenotype macrophages are the main subgroups of inflammatory cytokines production, cartilage degradation, and osteophyte formation in the OA state, while M2 type macrophages have a protective effect on OA by secreting some anti-inflammatory factors (Lv et al., 2022; Wang et al., 2022). Previous studies demonstrated that inhibiting macrophages conversion to M1 type and promoting its polarization to M2 phenotype can alleviate the synovitis and delay the progress of OA (Zhang et al., 2018; Li D. et al., 2022; Wang and He, 2022). Therefore, regulating the polarization of synovial macrophages may be an alternative mean to manage OA.

Herein, immunofluorescence double staining was carried out to label the polarization of synovial macrophages *in vivo* after intra-articular injection of therapeutic agents (Figure 7A**)**. Specifically, M1 macrophages co-stained by CD68 plus iNOS in the Gel group and ADSCs/Gel group was prominently decreased compared with PBS group and ADSCs group (Figure 7B). As illustrated in Figure 7C, the number of M2 phenotype macrophages in synovium, which were labeled by CD68 plus CD163, in the PBS group, ADSCs group, Gel group, and ADSCs/Gel group were 6.7 ± 4.6, 8.7 ± 3.0, 13.5 ± 4.1, and 20.7 ± 5.0, respectively. In general, after intra-articular injection of HA-EGCG hydrogel, the M1 phenotype polarization of synovial macrophages in OA rats was significantly reduced, and the M2 phenotype polarization was significantly improved. It is worth noting that the HA-EGCG hydrogel loaded with ADSCs (ADSCs/Gel group) was more conducive to inducing the polarization of synovial macrophages to M2 type than the administration HA-EGCG hydrogel alone (Gel group), which may be attributed to the immune regulation of stem cells to enhance this polarization induction. Predictably, this

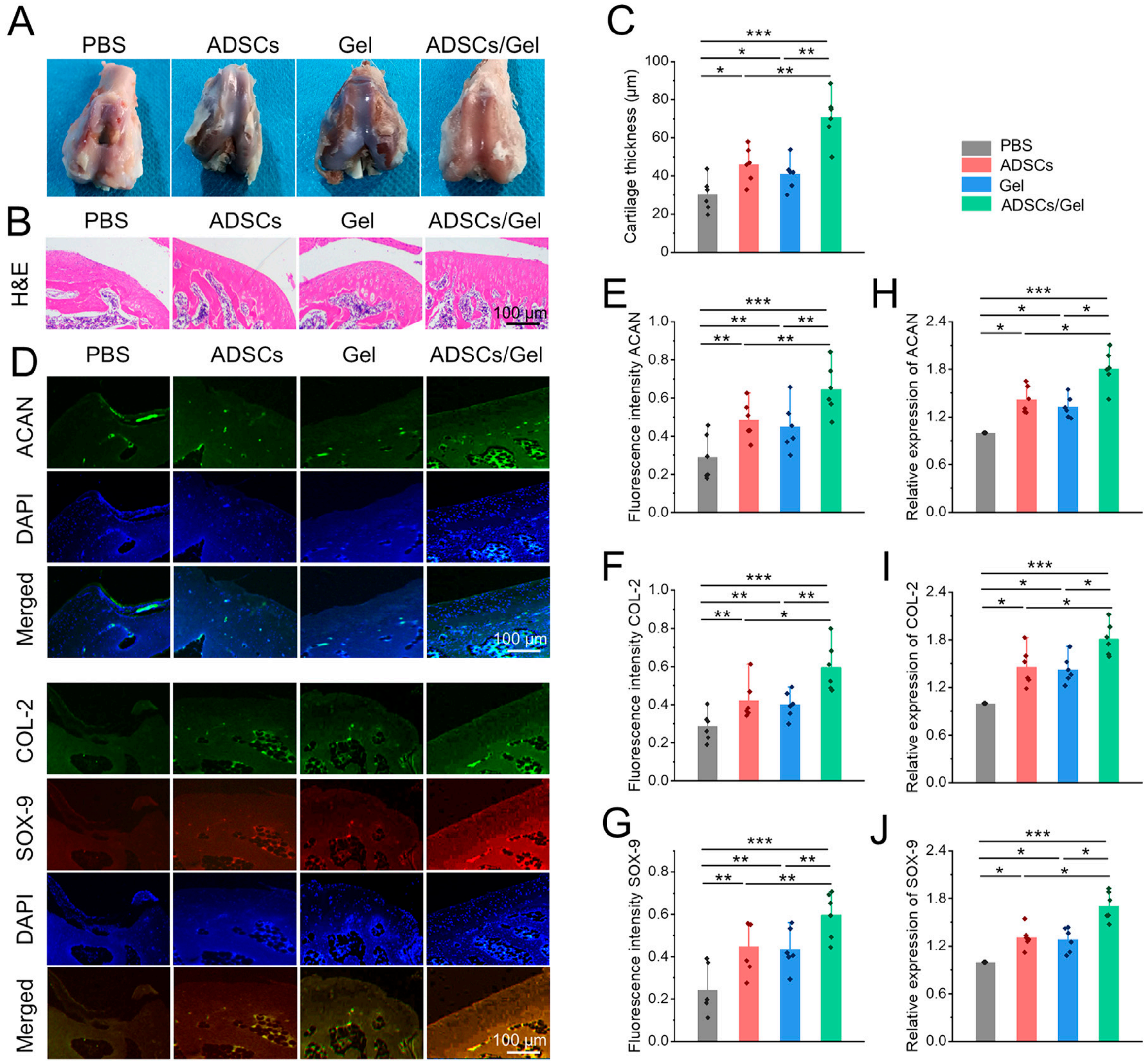

FIGURE 8
Intra-articular injection of ADSCs loaded HA-EGCG hydrogel repair the damaged cartilage in OA. **(A)** Gross observation of articular cartilages. **(B)** H&E staining of articular cartilage. **(C)** Quantitative analysis of the thickness of articular cartilage ($n = 6$). **(D)** Immunofluorescence of ACAN, COL-2, and COX-9 of the cartilage samples. **(E–G)** Quantitative analysis of fluorescence intensity of ACAN, COL-2, and COX-9 in the images ($n = 6$). **(H–J)** Real-time PCR detection the mRNA expression of ACAN, COL-2, and COX-9 in the cartilage samples (n = 6) (*$p < 0.05$, **$p < 0.01$, and ***$p < 0.001$).

effect of inducing pro-inflammatory macrophages to transform into an anti-inflammatory phenotype significantly inhibited synovial inflammation and inflammatory cell infiltration in each high-power field of the microscope through H&E staining in histology (Figures 7D,E).

In addition, the concentrations of various inflammatory cytokines (including IL-1β, MMP-13, and TNF-α) in synovial tissues were further evaluated by ELISA assays to confirm the severity of synovitis. As depicted in Figures 7F–H–H, these pro-inflammatory cytokines were decreased obviously in the Gel group and ADSCs/Gel group. In particular, the expression of IL-1β and TNF-α in the ADSCs/Gel group was markedly lower than that in the Gel group. In a word, these results indicated that intra-articular administration of HA-EGCG hydrogel or ADSCs loaded HA-EGCG hydrogel induced synovial macrophages polarization from M1 phenotype to M2, thus alleviating synovial inflammation and suppressing the concentrations of pro-inflammatory cytokines (including IL-1β, MMP-13, and TNF-α) in OA synovium. In general, these results have proved that the HA-EGCG hydrogel can remove the accumulated ROS and reduce the inflammatory state of synovium in OA joints, which reversed the adverse pathological microenvironment for ADSCs loaded in it, and provided great prospects for stem cells to repair damaged cartilage in the articular cavity.

HA-EGCG hydrogel relieved cartilage destruction in OA

The classic features of OA are erosion of cartilage surface, thinning of cartilage thickness, and subchondral bone exposure (Yue and Berman, 2022). With the great progress of cell therapy, intra-articular injection of stem cells has gradually become a new strategy to manage OA. Among them, MSCs are considered as a kind of alternative seed cells to treat OA because of their extensive sources, easy access, great potential for self-proliferation and multi-differentiation, and ability to regulate inflammation (Barry and Murphy, 2013; Bertoni et al., 2021; Hwang et al., 2021). Numerous previous clinical studies have systematically demonstrated that intra-articular injection of MSCs can improve cartilage damage and relieve pain in patients with OA (Aletto et al., 2022; Carvalho Schweich-Adami et al., 2022; Gunay et al., 2022). Specifically, ADSCs significantly reduced OA cartilage damage in rats, which can be achieved by down-regulating MMP-13 and COL-X and up-regulating COL-2. In addition, The paracrine action of ADSCs can show regulatory effects in chondrocyte proliferation, anabolism, and catabolism, as well as restore IL-1β Induced abnormal expression of molecular markers, including ACAN, COL-2, SOX-9, COL-X, SOX-6, IL-6, MMP-3, MMP-13, ADAMTS5, and ADAMTS9 in chondrocytes (Yan et al., 2022). However, after intra-articular delivering of MSCs, only a few cells adhere to the cartilage defects, their chondrogenic differentiation ability and paracrine action are not prominent in the harsh pathological microenvironment of joint cavity (Chang et al., 2016; Ha et al., 2019). Therefore, by regulating the ROS accumulation in the joint cavity to create a favorable microenvironment, it will contribute to the ADSCs to repair the OA articular cartilage effectively. Herein, HA-EGCG hydrogel as a cell protective carrier was used to incorporate ADSCs for intra-articular injection. The HA-EGCG hydrogel scavenged the accumulated ROS and alleviated progressive synovitis, thus improving the pathological microenvironment in OA joints. By regulating and improving the ROS accumulated microenvironment, the loaded ADSCs can maintain better cell vitality and chondrogenic differentiation potential, and it is expected to obtain better cartilage repair effect in OA. Gross observation of articular cartilages in the ADSCs/Gel group showed an intact appearance (Figure 8A). As showed in Figure 8B, H&E staining revealed that although the cartilage in the ADSCs group and Gel group showed an overall complete histomorphology, the thickness of the articular cartilage layer became thin and uneven, and the arrangement of deep layer chondrocytes was irregular and loose, even vacuolated. However, after intra-articular injection of ADSCs loaded HA-EGCG hydrogel, the histological morphology of cartilage was almost normal, and the thickness of cartilage layer was significantly higher than that of the PBS group ($p < 0.001$), ADSCs group ($p < 0.01$), and Gel group ($p < 0.01$), respectively (Figure 8C).

Subsequently, the chondrogenic markers in the articular cartilage were observed by immunofluorescence staining (Figure 8D). As exhibited in Figures 8E–G–G, the fluorescence intensity of ACAN, COL-2, and SOX-9 in the articular cartilage was obviously enhanced in the ADSCs/Gel group compared with the other three groups. In addition, at the gene level, the mRNA expression of ACAN, COL-2, and SOX-9 in the ADSCs/Gel group were also the highest among all experimental groups (Figures 8H,J–JFigures 8H,J). These results indicated that after the harsh microenvironment characterized by ROS accumulation in the OA articular cavity was improved, intra-articular injection of ADSCs loaded HA-EGCG hydrogel could maximize the role of enhancing anabolism of chondrocytes, and reducing the degradation of cartilage matrix, thereby greatly improving the pathological progress of OA.

Conclusion

In this study, HA-EGCG hydrogel was prepared as a protective carrier of ADSCs for intra-articular injection in OA. The naturally derived injectable hydrogels with good biocompatibility and durable retention can capture the redundant ROS continuously and efficiently, thus protecting ADSCs from ROS-mediated death and bioactivity inhibition, including cell survival, proliferation and chondrogenic differentiation. Intra-articular administration of this ADSCs loaded hydrogel significantly induced synovial macrophages polarization to M2 phenotype and reduce synovial inflammation, thus maximizing the role of ADSCs on repairing cartilage destruction in OA, which providing a great potential for OA management.

Data availability statement

The original contributions presented in the study are included in the article/supplementary material, further inquiries can be directed to the corresponding author.

Ethics statement

All animal procedures and manipulations in this study were conducted following approval of the Committee on Ethics of Naval Medical University and in compliance with the Shanghai Changzheng Hospital Institutional Animal Care and Use Committee [CZEC (2017)-13].

Author contributions

HL and DX: Conceptualization, Investigation, Writing original draft, and Manuscript revision. CG: Data curation, Visualization, and Writing original draft. XW: Conceptualization, Methodology. LL: Supervision, Writing—review & editing.

Funding

This research was financially supported by the Medical Discipline Construction Project of Pudong Health Committee of Shanghai (Grant No. PWYgf 2021-03).

Conflict of interest

The authors declare that the research was conducted in the absence of any commercial or financial relationships that could be construed as a potential conflict of interest.

Publisher's note

References

Ahmad, N., Ansari, M. Y., and Haqqi, T. M. (2020). Role of iNOS in osteoarthritis: Pathological and therapeutic aspects. *J. Cell Physiol.* 235, 6366–6376. doi:10.1002/jcp.29607

Aletto, C., Giordano, L., Quaranta, M., Zara, A., Notarfrancesco, D., and Maffulli, N. (2022). Short-term results of intra-articular injections of stromal vascular fraction for early knee osteoarthritis. *J. Orthop. Surg. Res.* 17, 310. doi:10.1186/s13018-022-03196-0

Arra, M., Swarnkar, G., Ke, K., Otero, J. E., Ying, J., Duan, X., et al. (2020). LDHA-mediated ROS generation in chondrocytes is a potential therapeutic target for osteoarthritis. *Nat. Commun.* 11, 3427. doi:10.1038/s41467-020-17242-0

Bai, H., Cui, Y., Wang, C., Wang, Z., Luo, W., Liu, Y., et al. (2020). 3D printed porous biomimetic composition sustained release zoledronate to promote osteointegration of osteoporotic defects. *Mater. Des.* 189, 108513. doi:10.1016/j.matdes.2020.108513

Barry, F., and Murphy, M. (2013). Mesenchymal stem cells in joint disease and repair. *Nat. Rev. Rheumatol.* 9, 584–594. doi:10.1038/nrrheum.2013.109

Bertoni, L., Jacquet-Guibon, S., Branly, T., Desance, M., Legendre, F., Melin, M., et al. (2021). Evaluation of allogeneic bone-marrow-derived and umbilical cord blood-derived mesenchymal stem cells to prevent the development of osteoarthritis in an equine model. *Int. J. Mol. Sci.* 22, 2499. doi:10.3390/ijms22052499

Blanco, F. J., Valdes, A. M., and Rego-Pérez, I. (2018). Mitochondrial DNA variation and the pathogenesis of osteoarthritis phenotypes. *Nat. Rev. Rheumatol.* 14, 327–340. doi:10.1038/s41584-018-0001-0

Bolduc, J. A., Collins, J. A., and Loeser, R. F. (2019). Reactive oxygen species, aging and articular cartilage homeostasis. *Free Radic. Biol. Med.* 132, 73–82. doi:10.1016/j.freeradbiomed.2018.08.038

Cao, D., Zhang, Y., Zhang, H., Zhong, L., and Qian, X. (2009). Systematic characterization of the covalent interactions between (-)-epigallocatechin gallate and peptides under physiological conditions by mass spectrometry. *Rapid Commun. Mass Spectrom.* 23, 1147–1157. doi:10.1002/rcm.3985

Carvalho Schweich-Adami, L., Da Silva, R. A., Menezes, J. N. D. S., Baranoski, A., Kassuya, C. a. L., Bernardi, L., et al. (2022). The intra-articular injection of adipose-derived stem cells decreases pain and reduces inflammation in knee osteoarthritis, with or without the addition of platelet-rich plasma also improves functionality. *J. Tissue Eng. Regen. Med.* 16, 900–912. doi:10.1002/term.3337

Chang, Y.-H., Liu, H.-W., Wu, K.-C., and Ding, D.-C. (2016). Mesenchymal stem cells and their clinical applications in osteoarthritis. *Cell Transplant.* 25, 937–950. doi:10.3727/096368915x690288

Csaki, C., Schneider, P. R. A., and Shakibaei, M. (2008). Mesenchymal stem cells as a potential pool for cartilage tissue engineering. *Ann. Anatomy-Anatomischer Anzeiger* 190, 395–412. doi:10.1016/j.aanat.2008.07.007

Dai, W., Ruan, C., Zhang, Y., Wang, J., Han, J., Shao, Z., et al. (2020). Bioavailability enhancement of EGCG by structural modification and nano-delivery: A review. *J. Funct. Foods* 65, 103732. doi:10.1016/j.jff.2019.103732

Donovan, R. L., Edwards, T. A., Judge, A., Blom, A. W., Kunutsor, S. K., and Whitehouse, M. R. (2022). Effects of recurrent intra-articular corticosteroid injections for osteoarthritis at 3 months and beyond: A systematic review and meta-analysis in comparison to other injectables. *Osteoarthr. Cartil.* 30, 1658–1669. doi:10.1016/j.joca.2022.07.011

Gunay, A. E., Karaman, I., Guney, A., Karaman, Z. F., Demirpolat, E., Gonen, Z. B., et al. (2022). Assessment of clinical, biochemical, and radiological outcomes following intra-articular injection of wharton jelly-derived mesenchymal stromal cells in patients with knee osteoarthritis: A prospective clinical study. *Medicine* 101, e30628. doi:10.1097/md.0000000000030628

Ha, C.-W., Park, Y.-B., Kim, S. H., and Lee, H.-J. (2019). Intra-articular mesenchymal stem cells in osteoarthritis of the knee: A systematic review of clinical outcomes and evidence of cartilage repair. *Arthroscopy-the J. Arthrosc. Relat. Surg.* 35, 277-288.e2, doi:10.1016/j.arthro.2018.07.028

Hou, W., Ye, C., Chen, M., Gao, W., Xie, X., Wu, J., et al. (2021). Excavating bioactivities of nanozyme to remodel microenvironment for protecting chondrocytes and delaying osteoarthritis. *Bioact. Mater* 6, 2439–2451. doi:10.1016/j.bioactmat.2021.01.016

Huang, H., Lou, Z., Zheng, S., Wu, J., Yao, Q., Chen, R., et al. (2022). Intra-articular drug delivery systems for osteoarthritis therapy: Shifting from sustained release to enhancing penetration into cartilage. *Drug Deliv.* 29, 767–791. doi:10.1080/10717544.2022.2048130

Hwang, J. J., Rim, Y. A., Nam, Y., and Ju, J. H. (2021). Recent developments in clinical applications of mesenchymal stem cells in the treatment of rheumatoid arthritis and osteoarthritis. *Front. Immunol.* 12, 631291. doi:10.3389/fimmu.2021.631291

Jia, H., Duan, L., Yu, P., Zhou, Y., Liu, R., and Wang, H. (2022). Digoxin ameliorates joint inflammatory microenvironment by downregulating synovial macrophage M1-like-polarization and its-derived exosomal miR-146b-5p/Usp3&Sox5 axis. *Int. Immunopharmacol.* 111, 109135. doi:10.1016/j.intimp.2022.109135

Kang, D., Lee, J., Jung, J., Carlson, B. A., Chang, M. J., Chang, C. B., et al. (2022). Selenophosphate synthetase 1 deficiency exacerbates osteoarthritis by dysregulating redox homeostasis. *Nat. Commun.* 13, 779. doi:10.1038/s41467-022-28385-7

Khan, N. M., Ahmad, I., and Haqqi, T. M. (2018). Nrf2/ARE pathway attenuates oxidative and apoptotic response in human osteoarthritis chondrocytes by activating ERK1/2/ELK1-P70S6K-P90RSK signaling axis. *Free Radic. Biol. Med.* 116, 159–171. doi:10.1016/j.freeradbiomed.2018.01.013

Kim, J., Kim, H. Y., Song, S. Y., Go, S. H., Sohn, H. S., Baik, S., et al. (2019). Synergistic oxygen generation and reactive oxygen species scavenging by manganese ferrite/ceria Co-decorated nanoparticles for rheumatoid arthritis treatment. *ACS Nano* 13, 3206–3217. doi:10.1021/acsnano.8b08785

Lee, F., Chung, J. E., Xu, K., and Kurisawa, M. (2015). Injectable degradation-resistant hyaluronic acid hydrogels cross-linked via the oxidative coupling of green tea catechin. *ACS Macro Lett.* 4, 957–960. doi:10.1021/acsmacrolett.5b00544

Li, D., Ruan, G., Zhang, Y., Zhao, Y., Zhu, Z., Ou, Q., et al. (2022). *Metformin attenuates osteoarthritis by targeting chondrocytes, synovial macrophages and adipocytes*. Oxford): Rheumatology.

Li, H., Wang, D., Yuan, Y., and Min, J. (2017). New insights on the MMP-13 regulatory network in the pathogenesis of early osteoarthritis. *Arthritis Res. Ther.* 19, 248. doi:10.1186/s13075-017-1454-2

Li, Y., Xie, W., Xiao, W., and Dou, D. (2022). Progress in osteoarthritis research by the national natural science foundation of China. *Bone Res.* 10, 41. doi:10.1038/s41413-022-00207-y

Li, Z., Zhao, Y., Huang, H., Zhang, C., Liu, H., Wang, Z., et al. (2022a). A nanozyme-immobilized hydrogel with endogenous ROS-scavenging and oxygen generation abilities for significantly promoting oxidative diabetic wound healing. *Adv. Healthc. Mater.* 11, 202201524. doi:10.1002/adhm.202201524

Li, Z., Zhao, Y., Liu, H., Ren, M., Wang, Z., Wang, X., et al. (2021). pH-responsive hydrogel loaded with insulin as a bioactive dressing for enhancing diabetic wound healing. *Mater. Des.* 210, 110104. doi:10.1016/j.matdes.2021.110104

Li, Z., Zhao, Y., Wang, Z., Ren, M., Wang, X., Liu, H., et al. (2022b). Engineering multifunctional hydrogel-integrated 3D printed bioactive prosthetic interfaces for osteoporotic osseointegration. *Adv. Healthc. Mater.* 11, 2102535. doi:10.1002/adhm.202102535

Lin, X., Tsao, C. T., Kyomoto, M., and Zhang, M. (2022). Injectable natural polymer hydrogels for treatment of knee osteoarthritis. *Adv. Healthc. Mater.* 11, 2101479. doi:10.1002/adhm.202101479

Liu, C., Bae, K. H., Yamashita, A., Chung, J. E., and Kurisawa, M. (2017). Thiol-mediated synthesis of hyaluronic acid-epigallocatechin-3-O-gallate conjugates for the formation of injectable hydrogels with free radical scavenging property and degradation resistance. *Biomacromolecules* 18, 3143–3155. doi:10.1021/acs.biomac.7b00788

Liu, L., Luo, P., Yang, M., Wang, J., Hou, W., and Xu, P. (2022). The role of oxidative stress in the development of knee osteoarthritis: A comprehensive research review. *Front. Mol. Biosci.* 9, 1001212. doi:10.3389/fmolb.2022.1001212

Lv, G., Wang, B., Li, L., Li, Y., Li, X., He, H., et al. (2022). Exosomes from dysfunctional chondrocytes affect osteoarthritis in Sprague-Dawley rats through FTO-dependent regulation of PIK3R5 mRNA stability. *Bone Jt. Res.* 11, 652–668. doi:10.1302/2046-3758.119.bjr-2021-0443.r2

Maumus, M., Guerit, D., Toupet, K., Jorgensen, C., and Noel, D. (2011). Mesenchymal stem cell-based therapies in regenerative medicine: Applications in rheumatology. *Stem Cell Res. Ther.* 2, 14. doi:10.1186/scrt55

Molnar, V., Pavelic, E., Vrdoljak, K., Cemerin, M., Klaric, E., Matisic, V., et al. (2022). Mesenchymal stem cell mechanisms of action and clinical effects in osteoarthritis: A narrative review. *Genes* 13, 949. doi:10.3390/genes13060949

Patil, P., Nene, S., Shah, S., Singh, S. B., and Srivastava, S. (2022). Exploration of novel drug delivery systems in topical management of osteoarthritis. *Drug Deliv. Transl. Res* [ahead of print]. doi:10.1007/s13346-022-01229-z

Sax, O. C., Douglas, S. J., Pervaiz, S. S., Salem, H. S., Nabet, A., Mont, M. A., et al. (2022). Intra-articular hip injections prior to total hip arthroplasty: Infection and cost-related associations. *Orthopedics* 6, 1–8. doi:10.3928/01477447-20221003-05

Shao, Y., Zhao, C., Pan, J., Zeng, C., Zhang, H., Liu, L., et al. (2021). BMP5 silencing inhibits chondrocyte senescence and apoptosis as well as osteoarthritis progression in mice. *Aging* 13, 9646–9664. doi:10.18632/aging.202708

Shoukrie, S. I., Venugopal, S., Dhanoa, R. K., Selvaraj, R., Selvamani, T. Y., Zahra, A., et al. (2022). Safety and efficacy of injecting mesenchymal stem cells into a human knee joint to treat osteoarthritis: A systematic review. *Cureus J. Med. Sci.* 14, e24823. doi:10.7759/cureus.24823

Stocco, E., Barbon, S., Piccione, M., Belluzzi, E., Petrelli, L., Pozzuoli, A., et al. (2019). Infrapatellar fat pad stem cells responsiveness to microenvironment in osteoarthritis: From morphology to function. *Front. Cell Dev. Biol.* 7, 323. doi:10.3389/fcell.2019.00323

Sunk, I. G., Amoyo-Minar, L., Niederreiter, B., Soleiman, A., Kainberger, F., Smolen, J. S., et al. (2022). Dorso-ventral osteophytes of interphalangeal joints correlate with cartilage damage and synovial inflammation in hand osteoarthritis: A histological/radiographical study. *Arthritis Res. Ther.* 24, 226. doi:10.1186/s13075-022-02911-w

Tanaka, T., Matsuo, Y., and Kouno, I. (2009). Chemistry of secondary polyphenols produced during processing of tea and selected foods. *Int. J. Mol. Sci.* 11, 14–40. doi:10.3390/ijms11010014

Wang, L., and He, C. (2022). Nrf2-mediated anti-inflammatory polarization of macrophages as therapeutic targets for osteoarthritis. *Front. Immunol.* 13, 967193. doi:10.3389/fimmu.2022.967193

Wang, S., Xiao, L., Prasadam, I., Crawford, R., Zhou, Y., and Xiao, Y. (2022). Inflammatory macrophages interrupt osteocyte maturation and mineralization via regulating the Notch signaling pathway. *Mol. Med.* 28, 102. doi:10.1186/s10020-022-00530-4

Xu, F.-W., Lv, Y.-L., Zhong, Y.-F., Xue, Y.-N., Wang, Y., Zhang, L.-Y., et al. (2021). Beneficial effects of green tea EGCG on skin wound healing: A comprehensive review. *Molecules* 26, 6123. doi:10.3390/molecules26206123

Yan, B., Lv, S., Tong, P., Yan, L., Chen, Z., Zhou, L., et al. (2022). Intra-articular injection of adipose-derived stem cells ameliorates pain and cartilage anabolism/catabolism in osteoarthritis: Preclinical and clinical evidences. *Front. Pharmacol.* 13, 854025. doi:10.3389/fphar.2022.854025

Yang, D., Cao, G., Ba, X., and Jiang, H. (2022). Epigallocatechin-3-O-gallate promotes extracellular matrix and inhibits inflammation in IL-1 beta stimulated chondrocytes by the PTEN/miRNA-29b pathway. *Pharm. Biol.* 60, 589–599. doi:10.1080/13880209.2022.2039722

Yin, B., Ni, J., Witherel, C. E., Yang, M., Burdick, J. A., Wen, C., et al. (2022). Harnessing tissue-derived extracellular vesicles for osteoarthritis theranostics. *Theranostics* 12, 207–231. doi:10.7150/thno.62708

Yin, J., Zeng, H., Fan, K., Xie, H., Shao, Y., Lu, Y., et al. (2022). Pentraxin 3 regulated by miR-224-5p modulates macrophage reprogramming and exacerbates osteoarthritis associated synovitis by targeting CD32. *Cell Death Dis.* 13, 567. doi:10.1038/s41419-022-04962-y

Yue, L., and Berman, J. (2022). What is osteoarthritis? *Jama* 327, 1300. doi:10.1001/jama.2022.1980

Zeng, W., Wang, G., Liao, X., and Pei, C. (2022). Efficacy of intra-articular injection of platelet-rich plasma combined with mesenchymal stem cells in the treatment of knee osteoarthritis: A systematic review and meta-analysis. *Int. J. Clin. Pract.* 2022, 1–9. doi:10.1155/2022/2192474

Zhang, H., Lin, C., Zeng, C., Wang, Z., Wang, H., Lu, J., et al. (2018). Synovial macrophage M1 polarisation exacerbates experimental osteoarthritis partially through R-spondin-2. *Ann. Rheum. Dis.* 77, 1524–1534. doi:10.1136/annrheumdis-2018-213450

Zhang, Y., Li, S., Jin, P., Shang, T., Sun, R., Lu, L., et al. (2022). Dual functions of microRNA-17 in maintaining cartilage homeostasis and protection against osteoarthritis. *Nat. Commun.* 13, 2447. doi:10.1038/s41467-022-30119-8

Zhao, Y. P., Lin, Z. G., Lin, S. D., Xia, L. P., Zhang, Z. Y., and Zhao, Y. (2022). Recommendations on the diagnosis and treatment of osteoarthritis in China. *Zhonghua nei ke za zhi* 61, 1136–1143. doi:10.3760/cma.j.cn112138-20220416-00280

Zhu, N. Q., Sang, S. M., Huang, T. C., Bai, N. S., Yang, C. S., and Ho, C. T. (2000). Antioxidant chemistry of green tea catechins: Oxidation products of (-)-epigallocatechin gallate and (-)-epigallocatechin with peroxidase. *J. Food Lipids* 7, 275–282. doi:10.1111/j.1745-4522.2000.tb00178.x

Zhu, W., Tang, H., Cao, L., Zhang, J., Li, J., Ma, D., et al. (2022). Epigallocatechin-3-O-gallate ameliorates oxidative stress-induced chondrocyte dysfunction and exerts chondroprotective effects via the Keap1/Nrf2/ARE signaling pathway. *Chem. Biol. Drug Des.* 100, 108–120. doi:10.1111/cbdd.14056

frontiers | Frontiers in Bioengineering and Biotechnology

TYPE Review
PUBLISHED 27 January 2023
DOI 10.3389/fbioe.2023.1118468

EDITED BY
Fengxuan Han,
Soochow University, China

REVIEWED BY
Genglei Chu,
The First Affiliated Hospital of Soochow University, China
Ting Liang,
Soochow University, China

*CORRESPONDENCE
Yayi Xia,
✉ xiayy@lzu.edu.cn

SPECIALTY SECTION
This article was submitted to Tissue Engineering and Regenerative Medicine, a section of the journal Frontiers in Bioengineering and Biotechnology

RECEIVED 07 December 2022
ACCEPTED 06 January 2023
PUBLISHED 27 January 2023

CITATION
Yang C, Teng Y, Geng B, Xiao H, Chen C, Chen R, Yang F and Xia Y (2023), Strategies for promoting tendon-bone healing: Current status and prospects.
Front. Bioeng. Biotechnol. 11:1118468.
doi: 10.3389/fbioe.2023.1118468

Strategies for promoting tendon-bone healing: Current status and prospects

Chenhui Yang[1,2,3,4], Yuanjun Teng[1,2,3], Bin Geng[1,2,3], Hefang Xiao[1,2,3], Changshun Chen[1,2,3], Rongjin Chen[1,2,3], Fei Yang[1,2,3] and Yayi Xia[1,2,3]*

[1]Department of Orthopedics, Lanzhou University Second Hospital, Lanzhou, China, [2]Orthopaedics Key Laboratory of Gansu Province, Lanzhou University Second Hospital, Lanzhou, China, [3]The Second School of Clinical Medical, Lanzhou University, Lanzhou, China, [4]Department of Orthopedic, Tianshui Hand and Foot Surgery Hospital, Tianshui, China

Tendon-bone insertion (TBI) injuries are common, primarily involving the rotator cuff (RC) and anterior cruciate ligament (ACL). At present, repair surgery and reconstructive surgery are the main treatments, and the main factor determining the curative effect of surgery is postoperative tendon-bone healing, which requires the stable combination of the transplanted tendon and the bone tunnel to ensure the stability of the joint. Fibrocartilage and bone formation are the main physiological processes in the bone marrow tract. Therefore, therapeutic measures conducive to these processes are likely to be applied clinically to promote tendon-bone healing. In recent years, biomaterials and compounds, stem cells, cell factors, platelet-rich plasma, exosomes, physical therapy, and other technologies have been widely used in the study of promoting tendon-bone healing. This review provides a comprehensive summary of strategies used to promote tendon-bone healing and analyses relevant preclinical and clinical studies. The potential application value of these strategies in promoting tendon-bone healing was also discussed.

KEYWORDS

tendon-bone insertion, anterior cruciate ligament, rotator cuff, tendon-bone healing, stem cells, cell factor, platelet-rich plasma, exosome

1 Introduction

In recent years, with the extensive development of sports activities, the incidence of tendon-bone insertion (TBI) injury has increased. TBI injuries are common in rotator cuff (RC) and anterior cruciate ligament (ACL) injuries. More than 30 million TBI injuries are reported worldwide each year (Maffulli et al., 2003). Ligaments are essential for the proper movement and stability of joints. Ligament injury often leads to abnormal joint motion, secondary damage to articular cartilage and other structures, and even degenerative joint changes ((Moses et al., 2012), (von Porat et al., 2004)). Currently, the main treatment for TBI injuries is tendon/ligament repair and reconstruction, which re-establishes the physical structure of the joint through tendon grafting. In the process of tendon transplantation, tendon graft should be fixed through bone tunnel. The main factor that determines the success of surgery is the good fusion of the graft tendon with the bone tunnel. Although autologous ligament repair and reconstruction techniques have made great progress, there are still limitations. The main disadvantages of autologous tendon transplantation are the longer tendon-bone healing time and the higher recurrence rate [(Goradia et al., 2000), (Rodeo et al., 1993)].

Studies have shown that failure of tendon-bone healing can lead to failure of surgery. Scar tissue formation often occurs in tendon-bone healing, and the limited mechanical properties of scar tissue can easily lead to tendon re-injury (Galatz et al., 2004). It has been reported that the

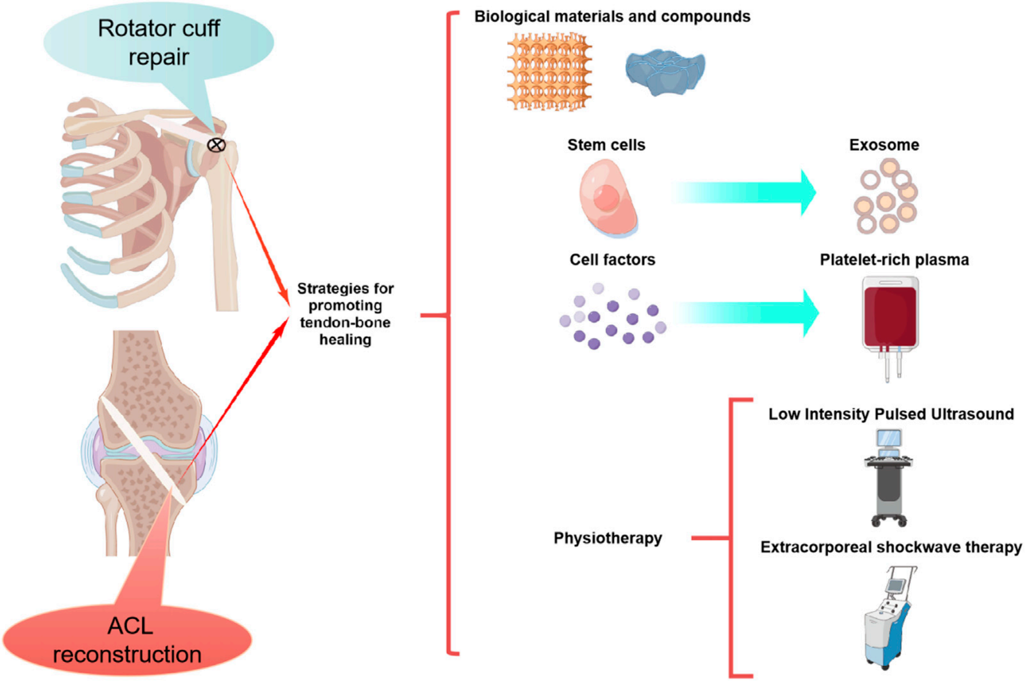

FIGURE 1
Strategies for promoting tendon-bone healing were demonstrated by Figdraw.

failure rate of RC prostheses is 20%–94% (Galatz et al., 2004; Xu et al., 2021), while the failure rate of ACL reconstruction is 10%–25% (Vergis and Gillquist, 1995). Additionally, tendon-bone healing can lead to complications such as knee joint relaxation, cartilage and meniscus damage, and post-traumatic osteoarthritis (Levine et al., 2013; Musahl and Karlsson, 2019). Therefore, tendon-bone healing is essential for ligament repair and reconstruction.

In order to promote tendon-bone healing, it is essential to understand the physiological process in the bone tunnel. There is evidence that the tendon-bone healing process begins with the growth of fibrous tissue cells between bone and tendon along the length of the bone tunnel, gradually forming a layer of collagen fibers. As the collagen layer matures, the trabecular bone around the tendon is reconstructed, and the tendon-bone interface increases in strength. Ultimately, the strength of the tendon-bone interface is determined by the bone's entry, mineralization, and maturation (Rodeo et al., 1993). Effective bone ingrosion promotes tendon-bone healing and is an important factor in speeding recovery and restoring limb function. In addition to the mesenchymal stem cells (MSCs) participating in tissue repair through differentiation, this physiological processes also involve the regulation of a wide range of cellular factors.

Researchers have been developing techniques to promote bone growth during tendon transplantation for the past 10 years, and have developed a number of therapeutic strategies based on the physiological process of tendon-bone healing. Among them, biomaterials (Lacheta and Braun, 2022), platelet-rich plasma (PRP) (Figueroa et al., 2015), cell factors (Zhu et al., 2022a), stem cells (Xu et al., 2021), exosomes (Xu et al., 2022a)and physical therapy (Lai et al., 2021) and other technologies have been widely used in the basic research of promoting tendon-bone healing, and have achieved good efficacy. Some of these technologies have also been applied in clinical practice. In this review, preclinical and clinical studies are analyzed to summarize current strategies used to promote tendon-bone healing. To provide theoretical basis for clinical treatment of promoting tendon-bone healing, we discussed the potential application value of the above strategies.

2 Strategies to promote tendon-bone healing

It is well known that the main factors determining the perfect healing of the tendon-bone interface are the formation of blood vessels and bone (Zhao et al., 2022). In recent years, researchers have directly developed stem cells, cell factor, physical and other treatments for these two factors. Since drug localization and sustained release are difficult due to the specificity of joint local administration, biomaterials and compounds have been developed for adjuvant drug therapy. Furthermore, PRP, stem cells that overexpressed target genes and marrow mesenchymal stem cell-derived exosomes (MSC-Exos) have been developed in addition to stem cell and cytokine therapy (Figure 1). Numerous preclinical studies have been conducted using the above methods, and good results have been achieved (Tables 1–8).

2.1 Biological materials and compounds

With the rapid development of bioengineering technology over the past few years, the research of biomaterials and compounds for promoting tendine-bone healing has also made rapid progress. Biological products such as Calcium phosphate (Cap), Biological

TABLE 1 Preclinical studies of biomaterials and compounds used to promote tendon-bone healing.

Intervening measure	Method of delivery	Treatment outcomes	Animal model	References
Cap	Soaking the tendon graft	The Cap hybrid tendon can promote sineoskeletal healing at the articular foramen of the anterior femoral and posterior tibial tunnels.	Goat ACL reconstruction	Mutsuzaki et al. (2016)
Cap	Soaking the tendon graft	The microstructures of Cap hybrid tendon grafts contain low crystalline apatite and type I collagen, and thus resemble the microstructures of bone, enhancing the formation of new bone in the bone tunnel.	Rats ACL reconstruction	Mutsuzaki et al. (2017)
Strontium-enriched Cap cement (Sr-CPC)	Coating the tendon graft	Sr-CPC promotes osteoblast-like cell proliferation, increases alkaline phosphatase (ALP) activity and the expression of type Ⅰ collagen, osteocalcin, and osteostatin, and accelerates healing in bone tunnels.	Rabbit ACL reconstruction	Kuang et al. (2013)
Simvastatin coupled gelatin hydrogel	Local administration	Local low-dose simvastatin coupled gelatin hydrogel promotes early tendon-bone healing through angiogenesis and osteogenesis.	Rabbit ACL reconstruction	Oka et al. (2013)
Strontium-enriched Cap cement (Sr-CPC)	Local administration	Sr-CPC accelerates graft healing in bone tunnels.	Rabbit ACL reconstruction	Kuang et al. (2014)
Demineralized bone matrix(DBM)	Local administration	Tendon-bone healing is enhanced by DBM, which promotes early differentiation of mesenchymal cells into chondrogenic and osteoblastic lineages.	Rabbit ACL reconstruction	Hsu and Wang, (2014)
Kartogenin (KGN)	Local injection	KGN induces chondrogenic differentiation of stem cells and promotes tendon-bone healing.	Model of Achilles tendon and patellar tendon injury in rabbits	Zhang and Wang, (2014)
Ca-5(PO$_4$)(2)SiO$_4$ (CPS) HA	Local administration	Both CPS and HA bioceramics contribute to cell attachment and proliferation, and promote new bone formation.	Rat RC repair model	Zhao et al. (2014a)
bFGF-loaded electrospun poly(PLGA) fibrous membrane	Local administration	bFGF-PLGA membrane facilitates cell attachment and proliferation, and accelerates tendon-bone reconstruction.	Rat RC repair model	Zhao et al. (2014b)
Biomimetic nanofiber membrane of polycaprolactone/nanoHA/collagen(PCL/nHAp/Col)	Wrapping graft tendon	PCL/nHAp/Col nanofiber membrane can effectively promote the healing of tendon and host bone and improve the mechanical strength during ACL reconstruction.	Rabbit ACL reconstruction	Han et al. (2015)
Microfibers of poly (3-caprolactone) (PCL) and nanofibers of chitosan	Local implanting	The PCL-chitosan scaffold enhanced new bone formation and collagen and glycosaminoglycan expression, and it also enhanced the strength of the regenerated TBI site.	Rat RC repair model	Zhao et al. (2015)
Biodegradable high-purity magnesium (HP Mg)	Local implanting	HP Mg is a biodegradable interfering screw that has the potential to promote the regeneration of fibrocartilage implants in ACL reconstruction.	Rabbit ACL reconstruction	Cheng et al. (2016)
Biodegradable polylactide bolt as the bone anchor and apoly (D,L-lactide-co-glycolide) nanofibrous membrane embedded with collagen as a biomimic patch	Local implanting	The composite polymer of nanofiber membrane can effectively promote rabbit tendon reconstruction, reduce tunnel enlargement and enhance tendon-bone fusion.	Rabbit ACL reconstruction	Chou et al. (2016)
Electrospun silk fibroin (SF) mat	Coating the tendon graft	SF mat can promote tendon-bone healing in soft tissue graft.	Rabbit ACL reconstruction	Zhi et al. (2016)
Collagen gel loaded with BMP-2	Local injection	Collagen gel loaded with BMP-2 can be used to enhance the healing of the tendon-bone interface.	Rabbit RC repair model	Lee et al. (2017)
P(2) porous titanium-coated constructs (DJO Surgical, Austin, TX, United States)	Local implanting	Osseointegration P2 porous titanium-coated prosthesis reduces superficial and deep tissue infection. Thus, tendon-bone healing can be improved with P (2) porous titanium implants.	Rat RC repair model	Tucker et al. (2017)
Mg screws	Local implanting	Mg screw has good corrosion resistance, degradation will not cause bone tunnel widening. Mg screw can promote tendon-bone healing.	Rabbit ACL reconstruction	Wang et al. (2017a)

(Continued on following page)

TABLE 1 (*Continued*) **Preclinical studies of biomaterials and compounds used to promote tendon-bone healing.**

Intervening measure	Method of delivery	Treatment outcomes	Animal model	References
Polyvinylpyrrolidone-iodine (PVP-I)	Soaking the tendon graft	PVP-I promotes tendon-bone healing through osteogenesis.	Rabbit achilles tendon repair model	Zhang et al. (2017a)
Dual-layer aligned-random scaffold (ARS)	Local implanting	ARS can effectively enhance the fusion of tendon and bone and promoting the maturation of collagen tissue.	Rabbit achilles tendon repair model	Cai et al. (2018)
Tendon-derived hydrogel (tHG)	Local administration	tHG can induce ADSCs to locate at the site of tendon injury to improve tendon-bone healing.	Rat tendon repair model	Franklin et al. (2020)
Chitosan/gelatin/β-glycerol phosphate(C/G/GP) hydrogels	Local administration	Collagenase C/G/GP hydrogel promotes tendon-bone healing.	Rabbit ACL reconstruction	Huang et al. (2020a)
Silk-collagen scaffold with both ends modified by HA	Local implanting	The silk-collagen scaffold promote bone fusion, which has great potential for clinical application.	Rabbit ACL reconstruction	Bi et al. (2021)
Amorphous calcium phosphate (ACP) nanoparticles	Local administration	ACP nanoparticles improve the biomechanical strength of the tendon-bone junction, promote osteogenesis and angiogenesis.	Rat RC repair model	Liao et al. (2021)
Mg-pretreated periosteum (M-P)	Coating the tendon graft	M-P significantly increased the formation of fibrocartilage, and prevented bone loss around the tunnel and more bone growth into the tendon graft.	Rabbit ACL reconstruction	Wang et al. (2021)
Fibrin Glue-Kartogenin Complex(FG-KGN)	Local administration	FG-KGN complex can effectively promote the regeneration and formation of fibrochondral tissue.	Rabbit RC repair model	Zhu et al. (2021)
HA incorporated polylactic acid (PLLA) aligned nanofibrous membranes	Coating the tendon graft	Electrospun PLLA-HA nanofiber membrane can better induce bone formation of BMSCs.	Rat RC repair model	Lv et al. (2022)
HA/type I collagen (Hap/Col I) paste	Local injection	Hap/Col I provides and microenvironment for early cell attachment and proliferation, further osteogenic expression and extracellular matrix deposition.	Canine ACL reconstruction	Jiang et al. (2023)
Natural fish scale (FS) modified by calcium silicate nanoparticles (CS NPs)	Local fixation	CS-FS promotes the repair of transitional tissue, and plays a more active integration role in promoting the repair of bone-tendon interface.	Rat and rabbit RC repair model	Han et al. (2023)

nanofiber scaffolds, magnesian products and hydrogel have been widely used in preclinical studies and have achieved good results (Table 1).

Cap material has the advantage of promoting bone formation and has been widely used to enhance bone regeneration. In order to explore the effect of Cap on tendon-bone healing, MUTSUZAKI H et al. (Mutsuzaki et al., 2016; Mutsuzaki et al., 2017) used Cap to soak tendon grafts to try to improve tendon-bone healing. In the treatment of the goat ACL reconstruction model, Cap hybrid tendon grafts showed significant histological improvement in both bone tunnels and increased *in-situ* force under tibial preload applied at high flexion angles. This research suggests that this technique may promote tendon-bone healing by enhancing osteogenesis. Liao et al. (2021) recently studied the application of amorphous Cap nanoparticles in tendon-bone healing, and found that amorphous Cap nanoparticles couldn't only improve the biomechanical strength of the tendon-bone junction by promoting osteogenesis, but also promote angiogenesis, thus promoting tendon-bone healing. Secondly, the effects of Ca-5(PO_4) (Moses et al., 2012) SiO_4 (CPS) and hydroxyapatite (HA) on promoting tendon-bone healing were compared. Zhao et al. (2014a) found that the local application of CPS and HA bioceramics both contributed to cell attachment and proliferation, and promoted the formation of new bone. Compared with HA, CPS bioceramics have a more significant effect on tendon-bone healing, which is expected to improve healing after RC injury repair. Strontium (Sr) has good bone conductivity and is widely used as a bone substitute to treat bone diseases. Strontium-enriched calcium phosphate cement (Sr-CPC) was developed by researchers (Kuang et al., 2013). It is found that Sr-CPC has the potential to enhance the fusion of graft and bone tunnel in ACL reconstruction. Preclinical studies have shown that Sr-CPC promotes osteoblast-like cell proliferation, and increases alkaline phosphatase (ALP) activity and the expression of type I collagen, osteocalcin, and osteoprotetin (Panzavolta et al., 2008; Kuang et al., 2012).

In recent years, researchers have attempted to mimic the tendon-bone healing interface through tissue engineering. However, because the tendon-bone healing interface is a transition of soft to hard tissue, the structure is complex. The interfacial connection of tendon-bone healing was observed in different animal models, and it was found that the interfacial connection was mainly composed of Sharpey-like fibers (Tabuchi et al., 2012; Kawakami et al., 2017). Based on this structural property, biological nanofiber scaffolds prepared by electrospinning technology have been developed and widely used in tissue repair of tendon-bone interface (Zhao et al., 2014b; Han et al., 2015). Biological nanofiber scaffolds have the characteristics of good biocompatibility, high aspect ratio and high porosity (Chen et al., 2009; Zhang et al.,

TABLE 2 Preclinical studies of stem cells used to promote tendon-bone healing.

Intervening measure	Method of delivery	Treatment outcomes	Animal model	References
Non-autologous transplantation of hUCB-MSCs	Local administration	hUCB-MSCs can enhance tendon-bone healing by promoting broad fibrochondrogenesis, with higher histological scores and reduced femoral and tibial tunnel widths.	Rabbit ACL reconstruction	Jang et al. (2015)
BMSCs genetically modified with BMP2 and bFGF	Local administration	Gene modified BMSCs have better structure, promote new bone formation and higher mechanical properties, and contribute to the healing process.	Rabbit ACL reconstruction	Chen et al. (2016)
ADRC	Local administration	ADRCs can be used to enhance graft healing during ACL reconstruction. Local administration facilitates the early healing process at the tendon-bone junction, both histologically and mechanically.	Rabbit ACL reconstruction	Kosaka et al. (2016)
Platelet-derived growth factor subunit B (PDGF-B) gene Modified BMSCs	Local administration	PDGF-B can increase the ultimate load and stiffness of tendon tissue, and expression of PDGF-B can enhance tendon-bone healing.	Rat RC repair model	Wang et al. (2018)
Fresh autologous bone marrow (BM)	Local administration	Local delivery of fresh autologous bone marrow was more effective than alternative therapy in promoting tendon to bone healing.	Rat autogenous tendon transplantation model	Lu et al. (2019)
hBMSCs	Local administration	The effect of hBMSCs is to accelerate graft-bone incorporation and midsubstance ligamentization as well as to enhance fibroblast proliferation, differentiation, and collagen synthesis.	Rat ACL reconstruction	Sun et al. (2019)
hBMSC	Local administration	hBMSC-CM influences macrophage polarization through the Smad2/3 signaling pathway and thus plays a role in tendon-bone healing, which is dependent on its immunomodulatory properties.	Rat RC repair model	Chen et al. (2021)
Bone marrow mononuclear cells(BMMNCs);bone marrow stromal cells (BMSCs)	Local administration	Both BMMNCs and BMSCs were equally effective at repopulating cells and healing interfacial allografts.	Rabbit ACL reconstruction	Lu et al. (2021)
ADSC sheets	Local administration	ADSC sheets can improve the biomechanical strength of the *in vivo* model, prevent bone tunnel enlargement.	Rabbit ACL reconstruction	Matsumoto et al. (2021)
BMSCs modifcated of RUNX1 with lentiviral system	Local administration	Runx1 upregulated BMSCs promote osteogenesis after ACL reconstruction by upregating the number of osteoblasts identified by ALP, osteocalcin, and osteopontin at the tendon-bone interface.	Rat ACL reconstruction	Kang et al. (2022)
De-BMSCs	Local administration	De-BMSCs transplantation can better promote bone formation at the tendon-bone interface and increase the early biomechanical strength of the reconstructed ACL.	Rabbit ACL reconstruction	Tie et al. (2022)

2010). In addition, the morphological characteristics of scaffolds play an important role in the adhesion, proliferation and differentiation of active cells (Huang et al., 2016; Mahmoodinia Maymand et al., 2018). Yin et al. (2010) studied the effect of electrospinning nanoscaffolds on the differentiation of human tendon stem/progenitor cells (hTSPCs), and the results showed that nanoscaffolds could induce the tenogenic and osteogenic differentiation of hTSPCs. Cai et al. (2018) prepared a double-layered aligned-random scaffold (ARS) by electrostatic spinning. In the experiment, ARS was used to wrap the Achilles tendon and transplant it through the bone tunnel. The results showed that ARS could effectively enhance the tendon-bone fusion by increasing the area of fibrocartilage and inducing the formation of new bone. Similarly, researchers have experimented with nanoscaffolds loaded with growth factors to promote tendon-bone healing Zhao et al. (2014b) invented an electrospun polylact-glycol ester (PLGE) fiber membrane loaded with bFGF for repairing rotator cuff tear (RCT). The results showed that electrospinning fiber membrane was conducive to cell attachment and proliferation, and accelerated sineoskeletal reconstruction. PLGE fiber membrane loaded with bFGF had a more obvious effect on sineoskeletal healing. In addition, Bi et al. (2021) prepared silk collagen scaffolds loaded with HA and used HA/sericinogen scaffolds as grafts to replace the original ACL in animal models, and the histological staining after surgery showed that a large number of mature bones were formed at the stens-bone interface. Immunohistochemical staining showed more deposition of type I collagen and osteocalcin than that of the control group. These results indicate that the direct use or drug loading of nanoengineered biological scaffolds is a promising method to promote tendon-bone healing.

Magnesium is a biodegradable biomaterial with good biocompatibility and mechanical properties, which can meet the load requirements during knee implantation and active rehabilitation (Farraro et al., 2014). Studies have shown that Mg ion can promote the growth of transplanted tendon into bone through the osteogenic differentiation pathway of stem cells (Yoshizawa et al., 2014). (Cheng et al., 2016) reported the efficacy of biodegradable high-purity magnesium (HP Mg) screw in promoting tendon-bone healing after ACL reconstruction. Research

TABLE 3 Preclinical studies on the application of cell factors to promote tendon-bone healing.

Intervening measure	Method of delivery	Treatment outcomes	Animal model	References
BMP-2	Local administration	BMP-2 induces bone formation by regulating the recruitment and differentiation of bone progenitor cells, which improves tendon-bone healing and bone formation.	Rabbit ACL reconstruction	Kim et al. (2014)
CXCL13	Local administration	CXCL13 is involved in the bone regeneration process treated by MSCs through the activation of ERK1/2by miR-23a, thus promoting tendon-bone healing.	Rat achilles tendon repair model	Tian et al. (2015)
Fibrin clots loaded with bFGF and CaPP	Local administration	Fibrin clots loaded with bFGF and CaPP enhanced cell migration and proliferation, increased bioactivity at the tendon-bone interface, and promoted tendon-bone healing.	Rabbits patellar tendon repair model	Zhang et al. (2016b)
Hyaluronic acid	Local administration	Hyaluronic acid-activated MSCs may play a key role in accelerating tendon to bone healing.	Rabbit RC repair model	Honda et al. (2017)
aFGF delivered in collagen (aFGF/collagen)	Local administration	The application of aFGF/collagen can promote early healing of the tendon-bone interface, especially when using high concentrations of aFGF/collagen.	Rabbit ACL reconstruction	Lu et al. (2018a)
Collagen sponges (CS) as a delivery device for osteoprotegerin (OPG)/BMP-2	Local administration	The combination of CS and growth factor OPG/BMP-2 can ensure the slow and stable release of OPG/BMP-2 and significantly promote tendon-bone healing.	Rabbit ACL reconstruction	Wei et al. (2020)
HA encapsulated with TGF-β1	Local administration	The addition of HA-TGF-β1 ceramic powder at the tendon-bone interface can increase the formation of bone and fibrocartilage, improve collagen tissue and enhance tendon-bone healing.	Rat RC repair model	You et al. (2018)
The GF combination of TGF-β1, Insulin-like growth factor 1, and parathyroid hormone	Local administration	GF combination can promote the proliferation and differentiation of tendon cells and improve the biomechanical and histological quality of the repaired tendon-bone interface.	Rat RC repair model	Zhu et al. (2022a)

TABLE 4 Preclinical studies of platelet-rich application to promote tendon-bone healing.

Intervening measure	Method of delivery	Treatment outcomes	Animal model	References
PRP combined with sponge carrier	Local injection	PRP significantly improved the biomechanical properties of RC tendon—bone interface.	Rat RC repair model	Ersen et al. (2014)
PRP plus bioactive glass (BG) mixture	Local administration	PRP + BG mixture can promote tendon-bone healing in tendon repair.	Rabbit RC repair model	Wu et al. (2014)
PRP	Local injection	PRP during tendon-to-bone implantation has positive effects histologically.	Rabbits ACL reconstruction	Ağır et al. (2017)
Chitosan-PRP implants	Local implanting	Chitosan-PRP implants may modulate RC healing in large animal models.	Sheep RC repair model	Deprés-Tremblay et al. (2018)
PRP Combined with Gelatin Sponge (GS)	Local implanting	PRP-GS can promote early healing of the tendon—bone junction.	Rabbit ACL reconstruction	Zhang et al. (2019a)
Combination of graphene oxide and PRP	Local implanting	GO/PRP improved the biomechanical properties of newborn tendons and made TBI tissue more stable.	Rabbit RC repair model	Bao et al. (2021)
Bone marrow-derived PRF (BM-PRF)	Local implanting	BM-PRF can enhance tendon-bone continuity and achieve better tendon-bone maturity.	Rabbits RC repair model	Uno et al. (2022)
PRF	Local administration	By promoting the formation of fibrocartilage and bone in a transitional zone between bone and tendon graft, bioactive PRF effectively promotes bone and tendon healing.	Rabbit ACL reconstruction	Wong et al. (2020)

results showed that HP Mg screw can promote the expression of BMP-2, VEGF and glycosaminoglycan in the early stage of tendon-bone healing. Based on the results of this study, magnesium ions are responsible for promoting fibroblast cartilage regeneration by acting on the above molecules. Wang et al. (2017a) compared the efficacy of titanium screw and magnesium screw in promoting tendon-bone healing. The results showed that Mg screw could significantly improve the healing quality of bone marrow tract by promoting the ossification of tendon endothelial area. It was also found that Mg screw can significantly promote the bone formation in the periscrew area at the early stage of healing, and has good corrosion resistance and doesn't cause bone tunnel enlargement after

TABLE 5 Preclinical studies of exosomes used to promote tendon-bone healing.

Intervening measure	Method of delivery	Treatment outcomes	Animal model	References
BMSC-Exos	Local administration	BMSC-Exos promotes tendon-bone healing after RC reconstruction by promoting angiogenesis and inhibiting inflammation.	Rat RC repair model	Huang et al. (2020b))
BMSC-Exos	Local administration	Local administration of BMSC-Exos promotes fibrochondrogenesis by increasing M2 macrophage polarization, thereby improving biomechanical properties.	Mouse achilles tendon repair model	Shi et al. (2020)
Mesenchymal stem cell -derived exosomes(MSC-Exos)	Local injection	MSC-Exos can significantly reduce osteoclast formation and improve the strength of tendon-bone healing, and can be used as a potential therapy for osteolysis.	Mouse achilles tendon repair model	Feng et al. (2021)
Purified exosome product (PEP)	Local injection	PEP promotes the migration and fusion of osteoblasts and tendon cells, especially in direct cell-cell contact, and accelerates tendon-bone healing for RC.	Rat RC repair model	Ren et al. (2021)
Exosomes of polyaspartic acid-polylactic acid-glycolic acid copolymer (PASP-PLGA) microcapsules	Local administration	Protein expression related to tendon regeneration and cartilage differentiation was significantly up-regulated after PASP-PLGA microcapsule exosome treatment, promoting tendon-bone interface healing after RC injury.	Rabbit RC repair model	Han et al. (2022)
Exosome derived from magnetically actuated (iron oxide nanoparticles (IONPs)	Local administration	IONP-Exos significantly prevented bone loss around the tunnel, promoted more bone inward growth in the tendon graft, and increased fibrochondrogenesis at the tendon-bone tunnel interface.	Rat ACL reconstruction	Wu et al. (2022)
BMSC-Exos	Local administration	BMSC-Exos promotes the polarization of M1 macrophages to M2 macrophages through miR-23a-3p, reduces the early inflammatory response at the tendon-bone interface, and promotes the early postoperative healing.	Rat ACL reconstruction	Li et al. (2022)
Exosomes from infrapatellar fat pad (IPFP) MSCs	Local administration	IPFP MSC-derived exosomes accelerate tendon-bone healing and intraarticular graft reconstruction, which may be related to immune regulation of macrophage polarization.	Rat ACL reconstruction	Xu et al. (2022a)

TABLE 6 Preclinical studies of physical therapy used to promote tendon-bone healing.

Intervening measure	Method of delivery	Treatment outcomes	Animal model	References
LIPUS	Local treatment	LIPUS alters the differentiation pathway of multipotent mesenchymal cells into osteoblasts and/or chondroblasts, stimulates osteogenic differentiation of osteoblasts, and significantly increases the expression of BMP, which is involved in and improves tendon-bone healing.	Sheep RC repair model	Lovric et al. (2013)
ESW	Local treatment	ESW enhances fibrocartilage regeneration at the TBI healing interface by upregating the expression of fibrochondroscope-related manufacturers and cell factors through mechanical signaling.	Rabbit patellar tendon repair model	Chow et al. (2014)
LIPUS	Local treatment	The effect of LIPUS on tendon-bone healing from the 7th day after surgery was more significant	Rabbit patellar tendon repair model	Lu et al. (2016a)
LIPUS	Local treatment	LIPUS treatment starting at the second week after surgery can accelerate bone formation during the healing process of tendon-bone junction and significantly improve the healing quality of BTJ injury.	Rabbit patellar tendon repair model	Lu et al. (2016b)
Intermittent negative pressure	Local treatment	Intermittent negative pressure in the tendon to bone healing and creep replacement plays a positive role in rabbit ACL reconstruction.	Rabbits ACL reconstruction	Sun et al. (2017)
LIPUS	Local treatment	The healing effect of LIPUS stimulation twice a day is better than that of the treatment once a day.	Rabbit patellar tendon repair model	Lu et al. (2018b)
Pulsed electromagnetic field (PEMF)	Local treatment	PEMF downregulates genes associated with fibrotic healing responses and significantly increases the rate of osteodynamic formation and the number of osteoblasts in the humeral head directly adjacent to the tendon.	Rats RC repair model	Huegel et al. (2022)
LIPUS	Local treatment	LIPUS accelerates the accumulation of early inflammatory macrophages and promotes the polarization of late anti-inflammatory macrophages (M2). LIPUS showed a higher bone volume/total volume ratio and a better TBI maturity score after treatment.	Rat RC repair model	Xu et al. (2022b)

TABLE 7 Preclinical studies of combined application in promoting tendon-bone healing.

Intervening measure	Method of delivery	Treatment outcomes	Animal model	References
PRP combined with BMSCs	Local administration	The combination of PRP and BSCs promoted more maturation of the tendon-bone interface, and more newly formed bone was found in the bone tunnel wall.	Rabbit ACL reconstruction	Teng et al. (2016)
Cortical demineralised bone matrix used with minimally manipulated MSCs	Local administration	The use of DBM with minimally treated MSCs promotes healing at the sineon-bone interface with superior mechanical and histological results.	Ovine patellar tendon repair model	Thangarajah et al. (2016)
ADSCs, PRP, and Extracellular Matrix Hydrogel	Local administration	Combined application showed greater repair capacity and biocompatibility.	Rat achilles tendon repair model	McGoldrick et al. (2017)
Kartogenin (KGN) and PRP	Local administration	KGN-PRP can induce the formation of fibrocartilage.	Rat achilles tendon repair model	Zhang et al. (2017b)
Kartogenin (KGN) with PRP	Local administration	KGN with PRP as the carrier promoted the formation of fibrochondral band between tendon graft and bone interface.	Rat achilles tendon repair model	Zhou et al. (2017)
Stromal cell-derived factor 1 (SDF-1)-releasing collagen-silk (CSF) scaffold combined with intra-articular injection of LSPCs	Local administration	This treatment strategy also improved cartilage degeneration and reduced the severity of joint fibrosis.	Rabbit ACL reconstruction	Hu et al. (2018)
DBM and BMSCs	Local administration	MSCs-enhanced DBM improved RC healing after 6 weeks and brought bone density in the RC back to pre-injury levels.	Rat RC repair model	Thangarajah et al. (2018)
BMP-12-overexpressing MSCs loaded 3D-printed PLGA scaffolds	Local administration	The 3D-printed PLGA scaffold supported by BMSCs overexpressing BMP-12 can promote the healing of the tendon—bone interface, improve collagen tissue and increase fibrocartilage in rabbit trochanteric sleeve repair.	Rabbit RC repair model	Chen et al. (2019)
MSCs and PRP	Local administration	Combination therapy induced the strongest signals associated with angiogenesis, bone formation, and *in situ* tendon formation.	Rat RC repair model	Han et al. (2019a)
BMP-2 and PRF	Local administration	The combination of bone morphogenetic protein 2 (BMP-2) and PRF (PRF) therapy has a synergistic effect on sineotone-bone healing and has great potential in the treatment of ACL reconstruction.	Rat ACL reconstruction	Han et al. (2019b)
Simvastatin and PRP	Local administration	Simvastatin combined with PRP can induce chondrogenesis of BMSCs and promote fibrochondrogenesis *in vivo*.	Rat achilles tendon repair model	Zhang et al. (2019c)
Poly lactic-co-glycolic acid (PLGA) scaffolds loaded with BMSCs	Local implanting	The implantation of BMSCs-PLGA scaffolds promoted collagen formation, increased collagen diameter at the tendon-bone interface, and improved biomechanical properties of the regenerated tendons.	Rabbit RC repair model	Chen et al. (2020)
Hierarchically demineralized cortical bone coated with stem cell-derived extracellular matrix (hDCB-ECM)	Local administration	hDCB-ECM promotes the formation of bone and fibrocartilage at the tendon-bone interface.	Rabbit RC repair model	He et al. (2021)

degradation. Therefore, Mg screw can be used instead of titanium screw in ACL reconstruction. In addition, Wang J et al. found that the release of calcitonin gene-related peptide played a significant role in promoting osteogenic differentiation by activating the cyclic adenosine monophosphate (cAMP) reaction element binding protein pathway, and this effect was significantly enhanced with the increase of magnesium ion concentration in periosteum (Zhang et al., 2016a; Wang et al., 2020). It has also been demonstrated that a higher magnesium ion concentration enhances cell adhesion strength by activating the integrin/local adhesion kinase pathway (Wang et al., 2017b). Cell migration and adhesion are mediated by periosteum proteins through the integrin/FAK pathway. (Qin et al., 2015). Therefore, Mg ions may also affect the secretion of periosteum-derived stem cells (PDSCs). Recent studies have shown that periostein can control bone regeneration potential by up-regulating PDSCs to promote osteogenic differentiation (Duchamp de Lageneste et al., 2018). Wang et al. (2021) used Mg pretreated periosteum wrapped graft tendon, and found that tendon-bone healing was significantly enhanced. These studies suggest that the mechanism of promoting bone growth through Mg ions may be a practical therapeutic strategy to enhance the healing of the tendon-bone interface.

Currently, local injection of bone cement, growth factors and cell transplantation have been identified as potential therapeutic options for promoting tendon-bone healing (Fu et al., 2014). However, how to deliver the drug at the optimal concentration and speed in the tendon-bone healing area remains one of the clinical challenges. Hydrogel microspheres have the advantages of prolonged drug retention time

TABLE 8 Clinical studies on the promotion of tendon-bone healing.

Conditions	Intervening measure	Patients (Number)	Treatment outcomes	References
ACL reconstruction	ESWT	26	ESWT significantly improves the subjective Lysholm score and decreases the middle 1/3 tibia tunnel enlargement after single hamstring autograft ACL reconstruction.	Wang et al. (2014)
RCTs	PRP	52	The application of moderately concentrated PRP improves the clinical and structural prognosis of large cuff tears. PRP can also enhance the ability of vascular repair around the injured site early on.	Pandey et al. (2016)
ACL reconstruction	ADRCs	20	ADRCs can significantly improve patient knee function and graft healing/maturation. However, this improvement wasn't statistically significant compared to a control group undergoing ACL reconstruction alone.	Alentorn-Geli et al. (2019)
ACL reconstruction	Cap hybridization method for graft tendon	8	Cap hybridization is a safe and feasible method for ACL reconstruction. In addition, the method can improve clinical efficacy.	Mutsuzaki et al. (2019)
ACL reconstruction	Allogeneic hUCB-MSCs	10	Allogeneic hUCB-MSCs were safely used for ACL reconstruction without treatment-related adverse events. However, studies haven't shown any evidence of clinical advantage.	Moon et al. (2021)
ACL reconstruction	PRP	85	PRP can promote graft tendon-bone healing and improve early postoperative status and joint function.	Chen et al. (2022)
ACL reconstruction	PRP	30	PRP had no significant effect on promoting tendon-bone healing and improving knee function. However, PRP may promote intraarticular graft maturation.	Gong et al. (2022)

and high drug loading efficiency, and have become a potential excellent drug carrier in the biomedical field. Franklin et al. (2020) demonstrated that hydrogel alone could also promote tendon-bone healing by inducing ADSCs to gather at the tendon-bone interface. Oka et al. (2013) implanted simvastatin coupled gelatin hydrogel into the bone tunnel reconstructed by ACL. It has been found that simvastatin coupled gelatin hydrogel can promote tendon-bone healing through angiogenesis and osteogenesis in the early stage. Similarly, (Lee et al., 2017) confirmed that collagen gel could be used as an effective carrier of BMP-2 to enhance the healing of the tendon-bone interface. Other researchers have combined hydrogels with collagenase for tendon-bone healing. In addition, (Huang et al., 2020a) studied and prepared chitosan/gelatin/β-glycerophosphoric acid (C/G/GP) hydrogel, which was used in combination with collagenase carrier at the tendon-bone junction. The results showed a significant increase in total bone volume in the model treated with collagenase and hydrogel. The above studies indicate that hydrogel alone or as a drug carrier can promote tendon-bone healing, so hydrogel technology may be a promising avenue for the treatment of tendon injuries in the future.

2.2 Stem cells

In addition to self-regeneration, Bone marrow mesenchymal stem cells (BMSCs) can differentiate into a variety of cell types, and are widely used in tissue repair and regeneration (Xu et al., 2021). Conventional BMSCs were collected from the pelvis, femur, tibia, and humerus. Some recent studies have shown that BMSCs can be obtained from synovial and adipose tissues, so these tissues have been widely used in tendon-bone repair (De Bari et al., 2001; Hanahan and Weinberg, 2011). Stem cells from different sources have different differentiation ability, and the direction of stem cell differentiation is also regulated by cell factors. Therefore, with the application of combined cytokine and gene overexpression strategies, various types of stem cells have the ability to improve tendon-bone healing (Table 2).

Human umbilical cord blood MSCs (hUCB-MSCs) are used in the study of promoting tendon-bone healing. Jang et al. (2015) studied the safety of non-autologous hUCB-MSCs in animal models of ACL reconstruction and the efficacy of promoting tendon-bone healing. This study found that non-autologous hUCB-MSCs transplantation could be used for ACL reconstruction without early immune rejection. Secondly, more broad fibrochondrocytes were formed and histological scores were higher during tendon-bone healing, and the bone tunnel width was significantly reduced. This study confirms the therapeutic potential of non-autologous hUCB-MSCs in promoting tendon to bone healing. However, it is difficult for hUCB-MSCs to be widely carried out due to ethical factors. Recently, (Tie et al., 2022) compared the efficacy of dedifferentiated osteoblast BMSCs (De-BMSCs) and BMSCs in ACL reconstruction. In this study, De-BMSCs were shown to increase the early biomechanical strength of ACL reconstructions by stimulating bone formation at the tendon-bone interface. The results of this study suggest that De-BMSC transplantation might be more effective for bone formation in the tunnel during tendon repair and reconstruction.

With the increase of stem cell sources, adipose-derived stem cells (ADSCs) have been gradually applied in the study of tendon repair. It has been demonstrated in rabbit ACL reconstruction models that ADSCs can enhance tendon-bone healing (Kosaka et al., 2016) Both histologically and mechanically, local administration promoted the early healing process of the tendon-bone junction. Similarly, (Matsumoto et al., 2021) studied the effect of ADSCs grafts on the biomechanical strength of the tendon-bone interface after ACL reconstruction. The results displayed that ADSCs tablets could enhance the biomechanical intensity of rabbit model and prevent the enlargement of bone tunnel. However, (Kaizawa et al., 2019) found that hydrogel loaded with ADRCs didn't significantly improve tendon-bone healing after RC repair in a chronic RCT model. Therefore, more studies are needed to examine the efficacy of ADRCs in promoting tendon-bone healing after RCT repair.

Furthermore, significant progress has been made in the identification of clonability, pluripotency and self-renewal ability of tendon-derive stem cell (TSCs) in humans and mice (Bi et al., 2007). Studies have shown that TSCs have stronger clonability than BMSCs (Tan et al., 2012). These cells not only have universal stem cell properties similar to BMSCs, but also feature high expression of genes and proteins associated with tendons (Bi et al., 2007). In recent years, researchers have also explored the effectiveness of TSCs in the repair of tendon-bone injury. Shen et al. (2012) investigated the effectiveness of knitted silky collagen sponge scaffolds seeded with TSCs. After operation, the growth of fibroblasts increased and lymphocyte infiltration decreased at the implantation site of TSCs allogeneic scaffolds. Moreover, the structural and biomechanical properties of the allogeneic TSCs transplantation group were improved. This study demonstrated that the woven silk-collagen sponge scaffolds of allogeneic TPCs improve RC tendon regeneration by differentiating into tendon cells and secreting anti-inflammatory cytokines. Although MSCs are commonly used for tendon-bone junction repair isolated from various tissues, the use of TSCs to repair tendon-bone junctions may be beneficial because the tendon environment is ideal and familiar, facilitating transplantation and differentiation between transplanted cells (Lui and Wong, 2012). The research of TSCs in the treatment of tendon-bone junction injuries is still in its infancy. Further studies are needed to test the efficacy of tspc application in large animal models and to determine its efficacy *in vivo*.

Researchers have also investigated the effect of human bone marrow stem cells (hBMSCs) on tendon-bone healing. Sun et al. (2019) explored the effect of hBMSCs on tendon-bone fusion in a rat model. The results demonstrated that hBMSCs could accelerate tendon-bone fusion by enhancing fibroblast proliferation, differentiation and collagen synthesis. Similarly, (Chen et al., 2021) examined the effect of hBMSCs on promoting tendon-bone healing in RC repair models. The results of this study show that hBMSCs are capable of promoting tendon-bone healing following RC injuries in rats. Further studies confirmed that the benefits of hBMSCs on tendon-bone healing are related to the regulation of macrophages, and hBMSCs affect the polarization of macrophages through the Smad2/3 signaling pathway. In addition, (Lu et al., 2021) compared Bone marrow mononuclear cells (BMMNCs) and bone marrow stromal cells (BMSC) to promote tenon-bone healing in ACL reconstruction models. In this study, BMMNCs and BMSC were found to be equally effective in promoting tendon-bone healing. These studies suggest that the collection of hBMSCs or mononuclear cells from peripheral blood may also be a potential therapeutic option for promoting tendon-bone healing.

The differentiation ability of BMSCs varies due to different sources. Therefore, the researchers used genetic engineering to modify MSCs to target differentiation to promote tendon-bone healing. Chen et al. (2016) evaluated the effects of BMP2 and bFGF gene modified BMSCs on tendon-bone healing. This study confirmed that BMSCs genetically modified with BMP2 or bFGF can better promote new bone formation, resulting in higher mechanical properties of bone tissue, and thus more effectively promote tendon-bone healing. The study also found that the combination of overexpression of the two genes was more effective than single overexpression therapy. Similarly, (Wang et al., 2018) modified BMSCs by platelet-derived growth factor subunit B (PDGF-B) on tendon-bone healing after RCT repair. This study also found that BMSCs overexpressing PDGF-B could enhance tendon-bone healing after RCT repair. In addition, a recent study by (Kang et al., 2022) found that RUNt-related transcription factor 1 (RUNX1) gene modified MSCs also produced better efficacy in tendon-bone healing. The above studies indicate that genetic engineering technology can make up for the lack of differentiated ability of BMSCs from different sources.

2.3 Cell factors

A growing body of research has focused on promoting tendon-bone healing within bone tunnels through the application of cell factors, such as transforming growth factor (TGF), bone morphogenetic protein (BMP), fibroblast factor (FGF), CXCL13, Hyaluronic acid, etc., (Tian et al., 2015; Honda et al., 2017; Lu et al., 2018a; You et al., 2018; Wei et al., 2020). Local application of cell factors has been studied to promote tendon-bone healing and has shown good efficacy in animal models of tendon repair (Table 3).

Transforming growth factor β (TGF-β) family exerts a crucial function in connective tissue development (Kim et al., 2011). TGFβ1 has been shown to promote the formation of fibrous tissue at the site of tendon healing by inhibiting the matrix metalloproteinase pathway (Arimura et al., 2017), and has also been reported to effectively enhance the biomechanical properties of tendons or ligaments (Anaguchi et al., 2005). You et al. (2018) tried to apply TGFβ1-coated HA to repair RCTs, and found that it could significantly enhance the healing of the tendon-bone interface. Further studies showed that the addition of HA-TGFβ1 ceramic powder at the tendon-bone interface could increase the formation of bone and fibrocartilage and improve the collagen structure. Recently, (Zhu et al., 2022a) explored the efficacy of the combination of TGFβ1, insulin-like growth factor 1 and parathyroid hormone in improving the repaired tendon-bone interface. This study found that the combination of cytokine therapy significantly improved the quality of tendon-bone healing and the formation of a mature tendon-bone interface. These studies suggest that TGFβ1 alone or in combination can improve tendon-bone healing, providing a theoretical basis for further clinical application.

BMP-2, a widely distributed glycoprotein in bone matrix, can induce bone formation *in vivo* by regulating the recruitment and differentiation of bone progenitor cells (Bessa et al., 2008). Tendon-bone healing has been demonstrated to be enhanced by BMP-2 by increasing the biomechanical strength between the two (Ma et al., 2007). Due to its short half-life and structural instability, BMP-2 requires high doses, resulting in adverse effects (Carragee et al., 2011). KIM J G et al.[82] evaluated the effect of local application of BMP-2 on bone formation and tendon-bone healing. The results showed that BMP-2 alone could promote new bone formation and bone maturation at the tendon-bone interface, thereby improving the biomechanical strength at the tendon-bone interface. In addition, Huang et al. used Collagen sponge ES (CS) combined with BMP-2 to repair bone defects in rats, and the results showed that using CS as a carrier could effectively promote tendon-bone healing (Huang et al., 2015). Similarly, (Wei et al., 2020) studied the effect of CS as a delivery device of OPG/BMP-2 on tendon-bone healing. It was found that the combination of CS and growth factor OPG/BMP-2 can induce the slow and stable release of OPG/BMP-2, and significantly promote the tendon-bone healing in the ACL model.

As members of the FGF family, both acid fibroblast growth factor (aFGF) and bFGF significantly promoted the mitosis of osteoblasts and chondrocytes, and stimulated the formation of new capillaries (Ide et al., 2009; de Girolamo et al., 2015). Therefore, researchers began to try to use aFGF and bFGF to improve tendon-bone healing. Lu et al. (2018a) applied collagen containing different concentrations of aFGF to the tendon-bone interface to evaluate the influence of aFGF/collagen on the healing of the sineoskeletal interface. According to the results, the application of aFGF/collagen composite could promote the early healing of the tendon-bone interface through the growth of new bone, especially the application of high concentration of aFGF/collagen. In addition, (Ide et al., 2009) also demonstrated that local tendon repair with bFGF-treated tendons showed early improvements in bone growth and biomechanical strength at the tendon-bone interface. The results of these studies suggest that FGF may enhance tendon-bone healing, particularly in the early stages after reconstruction.

In the process of cell migration, CXC chemokine ligand 13 (CXCL13) plays a significant role (Zhou et al., 2013). The inflammatory cytokine IL-6 significantly induces CXCL13 expression in human osteoblasts, while CXCL13 expression is not obvious in osteoclasts (Singh et al., 2009), suggesting that CXCL13 may play a role in tendon-bone healing. Tian et al. (2015) evaluated the effect of CXCL13 on tendon-bone healing in rats. The results demonstrated that CXCL13 acted on MSCs through the activation of ERK1/2 signaling pathway by miR-23a, thus promoting tendon-bone healing. Furthermore, hyaluronic acid belongs to the glycosaminoglycan family and is usually found in the synovial fluid of joints, cartilage and other tissues. There is evidence that HA plays an important role in repairing tissue damage (Neuman et al., 2015). Honda et al. (2017) explored the effect of hyaluronic acid on tendon-bone healing after RCT repair. It was found that hyaluronic acidon accelerated tendon-bone healing, enhanced biomechanical strength, and increased chondroid formation and tendon maturation at the tendon-bone interface in tendon repair models. These studies suggest that both CXCL13 and hyaluronic acidon can promote tendon-bone healing by activating the MSCs pathway, and they are also potential candidate cell factors for promoting tendon-bone healing.

2.4 Platelet-rich plasma

Because many cell factors are involved in tendon repair, cell factors are widely used in tendon repair. PRP, as a source of cell factors, has been shown to improve inflammation, promote cell proliferation, and enhance angiogenesis (Lang et al., 2018; Santos et al., 2018). PRP has also been identified as a potential therapy for accelerating tendon repair. Studies on the application of PRP in the repair of soft tissue wounds have confirmed its efficacy in promoting the healing of tissue wounds (Table 4). PRP is involved in tissue remodeling, chondrogenic differentiation, and wound healing by releasing cell factors (Mehrabani et al., 2019).

There have been numerous studies investigating the efficacy of PRP in reconstructing the ACL and repairing the RCT. Ağır et al. (2017) evaluated the effect of PRP on tendon-bone healing in ACL reconstruction. The results demonstrated that the use of PRP during tendon implantation into the bone tunnel could promote tendon-bone healing by inducing fibrochondral formation early on. Besides, in order to optimize the release of PRP in the joint, the role of PRP combined with drug carriers in promoting tendon-bone healing was also explored.

Zhang et al. (2019a) explored the effect of PRP combined with gelatin sponge (GS) on tendon-bone healing. It has been shown *in vitro* that GS-loaded PRP can prolong its bioactivity time and promote BMSC proliferation. PRP promotes early healing of tendon-bone junctions in a model of ACL reconstruction. However, (Ersen et al., 2014) previously found that PRP improved the biomechanical properties of RC tendon-bone interface regardless of whether GS was applied. The different models used in the two studies may account for the different results. PRP in combination with other biomaterials has also been studied to promote tendon-bone healing. Graphene oxide (GO) can promote tissue repair by improving the physical properties of tissues. Bao et al. (2021) prepared PRP gel containing different concentrations of GO to promote tendon-bone healing in rabbit tendon reconstruction model after RC injury. The results demonstrated that the addition of GO enhanced the biomechanical properties of the newly formed tendons and made the tendon-bone interface more stable. Therefore, the combination of PRP and GO has great potential in the treatment of RCT. In addition, platelet-rich fibrin (PRF), as a concentrated product of PRP, has also been used in the study of promoting tendon-bone healing. A recent study by (Uno et al., 2022) found that PRF significantly enhanced tendon-bone continuity in the RCT model, and at the same time achieved better tendon-bone maturation. Consequently, PRP and its concentrate have great potential to promote tendon-bone healing.

2.5 Exosome

In recent years, more and more evidence shows that BMSCs are effective in the treatment of joint diseases (Zhang et al., 2019b). BMSCs are involved in many regulatory functions through the paracrine capacity of exosomes (Kourembanas, 2015). Exosomes are bilayer extracellular vesicles containing small RNAs and proteins and are considered to be important mediators for genetic exchange and communication between cells. Recently, researchers have found that stem cell-derived exosomes can improve the healing rate of tendon repair (Zhang et al., 2021). Therefore, many studies have been carried out on exosomes in promoting tendon-bone healing, providing more theoretical basis for promoting tendon-bone healing (Table 5).

The number of studies on exosomes that promote tendon-bone healing has increased significantly in recent years. Huang et al. (2020b) Xu et al. (2022a) explored the role of bone marrow mesenchymal stem cell-derived exosomes (BMSC-Exos) in tendon-bone healing after RC and ACL reconstruction respectively. The results confirmed that BMSC-Exos can increase angiogenesis and bone growth at the tendon-bone interface, which may be related to immune regulation of macrophage polarization. Further studies by (Shi et al., 2020) found that local administration of BMSC-Exos promoted the formation of fibrocartilage by mediating the polarization of M2 macrophages, thus improving the biomechanical properties of the tendon-bone interface. In addition, LI Z et al.[117] observed the effect of BMSCs-Exos on ACL reconstruction posterior tendon bone healing and its possible mechanism *in vitro* and *in vivo*. According to the results, BMSC-Exos promoted the polarization of M1 macrophages to M2 macrophages through miR-23a-3p, reduced the early inflammatory response at the tendon-bone interface, and promoted early healing after ACL reconstruction. BMSC-Exos could be used in the repair of tendons and bones based on the findings of this study. In conclusion, BMSCs-Exos has been shown to be an effective and viable natural drug for enhancing tendon-bone healing, suggesting that BMSCs-Exos may be a promising therapeutic strategy.

2.6 Physiotherapy

In recent years, non-invasive physical therapy has been gradually applied to promote tendon-bone healing. Low intensity pulsed ultrasound (LIPUS), as a non-invasive physiotherapy technique, has been shown to promote recovery from musculoskeletal injuries. LIPUS transmits high frequency acoustic pressure waves and mechanical stresses through the skin to biological tissues. It has been successfully demonstrated in animal models and clinical trials to stimulate bone growth and thus promote fracture healing (Hannemann et al., 2014). In addition, it has been shown that extracorporeal shock wave (ESW) can promote tendon-bone healing by upregating the expression of fibrochondrogenic cell factors through mechanical signaling. LIPUS and ESW, as non-invasive physical therapy, have also been studied in the field of promoting tendon-bone healing, and have achieved good efficacy (Kuo et al., 2007; Greve et al., 2009) (Table 6).

In 2013, Lovric et al. (2013) conducted the first study to test the effect of LIPUS on the initial tendon-bone healing in RC sheep model. The results suggest that LIPUS may help RC repair in the initial stages of tendon-bone healing. Afterwards, LU H's team conducted a large number of studies in this field (Lu et al., 2016a; Lu et al., 2016b; Lu et al., 2018b). First, they determined the optimal time for LIPUS treatment, and the study found that LIPUS treatment on the 7th day after surgery had a more significant impact on tendon-bone healing. Further studies showed that LIPUS accelerated bone formation during tendon-bone healing from the second week after treatment, significantly improving the quality of tendon-bone healing. Finally, they evaluated the dose-effect of LIPUS stimulation on tendon-bone healing. The study found that LIPUS stimulation twice a day was better for muscle and bone healing than the treatment once a day. Recently, (Xu et al., 2022b) observed in rats RC tear model that macrophage polarization may be a potential mechanism for LIPUS treatment of TBI repair. In conclusion, LIPUS therapy, as a non-invasive physical therapy, has been thoroughly studied in terms of promoting the mechanism of tendon-bone healing and the selection of treatment time and frequency. These results indicate that LIPUS therapy, as a technique to promote tendon-bone healing, may be widely used in clinic.

ESW is another potential non-invasive form of physical therapy that promotes tendon-bone healing. Chow et al. (2014) explored the effect of ESW on fibrocartilage regeneration during tendon-bone healing. It was found that ESW upregulated the expression of cell factors related to fibrocartilage production by providing mechanical signals, thus accelerating fibrocartilage regeneration at the healing interface. More studies are needed to confirm the efficacy and mechanism of ESW in promoting tendon-bone healing. In addition, intermittent negative pressure and Pulsed electromagnetic field (PEMF) therapy have been preliminarily explored to promote tenoon-bone healing after tendon repair with positive results (Sun et al., 2017; Huegel et al., 2022). More research is needed to confirm their specific efficacy and mechanism.

2.7 Combination therapy

In recent years, the physiological mechanism of tendon-bone healing has gradually become clear. Researchers are also trying to combine these methods to enhance their efficacy in promoting tendon-bone healing after tendon injury. Stem cells, cell factors, PRP and biomaterials were used in combination with each other, and positive effects were achieved (Table 7).

At present, stem cell and PRP therapy techniques are the mainstream methods to promote tendon-bone healing. The combined application of the two is also widely used in this field. Teng et al. (2016) studied the ability of PRP combined with BMSCs to promote tendon-bone healing. Studies have shown that PRP-BMSCs promote more mature healing of the tendon-bone interface, and the joint shows a higher functional load. Similarly, (Han et al., 2019a) explored the efficacy of combined MSCs and PRP in RC damage repair model. The results showed significantly enhanced signals related to angiogenesis, bone formation, and *in situ* tendon formation induced by combination therapy. The above studies confirm that the combination of MSCs and PRP can synergistically promote tendon-bone healing, which has great hope for promoting the treatment of tendon-bone healing. In addition, (McGoldrick et al., 2017) prepared extracellular matrix hydrogel loaded with PRP and ADSCs in order to make the drug release in the joint more lasting and better. It showed superior repair ability and biocompatibility in the rat model of Achilles tendon injury repair. Therefore, optimizing the effect of drug release based on the combination of stem cells and PRP may offer greater hope for promoting tendon-bone healing.

It was found that the combination of MSCs and demineralized bone matrix (DBM) can also enhance the role of MSCs in promoting tendon-bone healing. Thangarajah et al. (2016) explored the effect of DBM combined with MSCs on improving the function of the tendon-bone interface. In the treatment of patella tendon injury repair model, it was found that the combination effectively promoted the healing of the tendon-bone interface. Similarly, (Thangarajah et al., 2018) also studied the effect of the combination of DBM and MSCs on RCT healing. The results also showed that the combination of the two methods enhanced RC healing at an early stage and restored bone mineral density in the RC to pre-injury levels. These studies suggest that tendon repair using DBM and MSCs can achieve better tendon-bone healing early after surgery, and further studies are needed to determine its efficacy.

Furthermore, researchers have provided a new strategy for promoting tendon-bone healing. Combining biological scaffolds with tissue-specific stem cells may be a promising protocol for promoting tendon-bone healing. Hu et al. (2018) explored the synergistic therapeutic effect of collagen-filament scaffolds combined with derived stem cells on ACL regeneration. It was found that this treatment strategy significantly improved cartilage degeneration and reduced the severity of joint fibrosis. Similarly, (Chen et al., 2020) developed polylactic acid-glycolic acid (PLGA) scaffolds loaded with BMSCs. In a rabbit RCT repair model, it was found to promote tendon-bone healing by improving the biomechanical properties of the regenerated tendon. Besides, (Chen et al., 2019) studied the efficacy of scaffolds loaded with gene-edited BMSCs in improving RC repair. BMP-12 overexpressed rabbit BMSCs were used in this study. The results demonstrated that the PLGA scaffold loaded with BMSCs overexpressing BMP-12 could promote the healing of the tendon-bone interface, improve collagen tissue and increase fibrocartilage in rabbit RCT repair. In conclusion, biological scaffolds combined with MSCs are an effective strategy to improve tendon-bone healing, especially the combined use of MSCs that can be directed differentiation after gene modification.

3 Clinical study on promoting tendon-bone healing

As mentioned earlier, numerous strategies have been used in preclinical studies to promote tendon-bone healing, and some therapeutic strategies have also been used in clinical studies. Relevant clinical studies on stem cells and PRP have achieved certain curative effect, however, due to the lack of abundant clinical studies, some studies have produced negative curative effect (Table 8). Therefore, more clinical studies are needed to verify the safety and effectiveness of the above strategies, so as to accelerate their clinical application.

Currently, preclinical studies have shown that stem cell applications help promote tendon-bone healing after ACL reconstruction. However, the current clinical research results haven’t made a breakthrough. Alentorn-Geli et al. (2019) explored the clinical efficacy of ADRCs in the treatment of patients with ACL reconstruction. A matched cohort of 20 patients who underwent ADRCs infiltration followed by ACL reconstruction was compared with 19 patients who underwent the same surgery without ADRCs infiltration. The results found that patients treated with ADRCs at the time of ACL reconstruction had significantly improved knee function and graft maturity at 12 months. In addition, (Moon et al., 2021) studied whether allogeneic hUCB-MSCs could improve the clinical effect of human ACL reconstruction (KCT0000917). Allogeneic hUCB-MSCs were found to be safe for ACL reconstruction with no treatment-related adverse events at a 2-year follow-up. However, this study did not demonstrate a clinical advantage over allogeneic hUCB-MSCs. The application of stem cells to promote tendon-bone healing needs more clinical studies. After all, stem cells from different sources can differentiate in very different directions.

Studies of PRP in promoting tendon-bone healing have shown similar results to stem cells. Chen et al. (2022) retrospectively studied the effect of PRP on tendon-bone healing after ACL reconstruction. The results confirm that PRP can promote graft muscle and bone healing and improve knee function early. Recently, (Gong et al., 2022) studied the effect of PRP on tendon-bone healing and intraarticular graft maturation after ACL reconstruction (NCT04659447). In this study, it was found that PRP had no significant effect on reducing bone tunnel widening, accelerating tendon-bone healing, and improving knee joint function. However, this study have shown that PRP may promote the maturation of intraarticular grafts. In addition, (Pandey et al., 2016) performed PRP treatment on 52 RCT patients undergoing arthroscopic repair. The results showed that the application of moderately concentrated PRP could improve the clinical outcome of large cuff tear. PRP can also enhance the growth of blood vessels around the repair site early on. These studies suggest that PRP may promote tendon-bone healing at an early stage by promoting intraarticular graft maturation. However, more clinical studies are needed to confirm.

Preclinical studies have shown that Cap hybridization can promote fibrochondrogenesis of transplanted tendons. In the study (Mutsuzaki et al., 2019), eight patients underwent ACL reconstruction of quadriceps tendon transplantation by Cap hybridization. The patients were followed up for 2 months to 4 years. The results show that the Cap hybridization method is safe and feasible for ACL reconstruction in clinical trials, and can improve clinical outcomes. This study is only a one-arm clinical study, and its clinical efficacy needs to be verified by more controlled studies.

In addition, there are few clinical studies on physical therapy to promote tendon-bone healing. Wang et al. (2014) evaluated the influence of extracorporeal shock wave therapy (ESWT) on human ACL reconstruction. In this study, 26 patients underwent ESWT immediately after ACL reconstruction. Tibial tunnel radiographs in ESWT group were significantly lower than those in control group at 2 years after surgery ($p = 0.018$). The study results confirmed that ESWT significantly improved the subjective lysholm score of patients in the early stage after ACL reconstruction, and the tibial tunnel was significantly less than the control group in the long term. This study showed that ESWT after ACL reconstruction not only improved the clinical symptoms in the early stage, but also prevented the enlargement of the bone marrow tract in the long term. In the future, more clinical studies are needed to accelerate the pace of clinical application of this technology. Besides, a meta-analysis conducted by W. C. (Lai et al., 2021) evaluated the efficacy of LIPUS on tendon-to-bone healing. A total of 28 animal studies and two human studies met the inclusion criteria. Animal experiments demonstrated that LIPUS treatment significantly improved collagen content and organization, bone formation, fibrocartilage remodeling, and mechanical strength compared with control. Nevertheless, LIPUS for tendon injury disorders hasn’t improved clinical outcomes in human trials. The results of this study indicate that LIPUS is still not clinically effective in promoting tendine-bone healing. Therefore, more mechanism studies are needed to determine the mechanism by which physical therapy promotes tendine-bone healing, so as to regulate the selection of timing and parameters of physical therapy, so as to achieve better efficacy in promoting tendine-bone healing.

4 Discussion

It is well known that the major factor affecting recovery after ligament repair and reconstruction is tendon-bone healing (Mao et al., 2021). The main process of tendon-bone healing is the formation of fibrocartilage and mineralized bone (Zhao et al., 2022). As a result, numerous strategies have been developed to promote tendon-bone healing by promoting fibrochondral and bone formation pathways. This paper summarizes the current therapeutic measures used to promote tendon-bone healing, including biological materials, and compounds, stem cells, cell factors, and physical therapy. In addition, PRP and exosomes have been developed on the basis of stem cell and cytokine therapy. At present, most of the above research methods have achieved gratifying results in preclinical studies. However, due to the relatively few clinical studies, most of the above strategies have not been widely carried out in clinical practice.

MSCs transplantation has been widely used in tendon and bone repair, and has shown good efficacy in promoting tendon-bone healing (Jang et al., 2015; Xu et al., 2019; Chen et al., 2021). Different MSCs from different sources have different differentiation directions, which leads to different MSCs play different roles in promoting tendon-bone healing. Therefore, tissue-derived MSCs such as synovium and adipose tissue are being developed for application in tendon-bone healing (Kosaka et al., 2016; Matsumoto et al., 2021). Researchers have also attempted to combine MSCs and PRP for tendon-bone healing, and achieved good results (Teng et al., 2016; Han et al., 2019a). In recent years, researchers have found that MSCs exercise their biological regulatory function by secreting exosomes. A large number of studies have been conducted on the application of MSCs-Exos to promote tendon-bone healing, and preliminary results have been gratifying (Shi et al., 2020; Ren et al., 2021; Han et al., 2022; Li et al., 2022). In addition, with the development of genetic engineering technology, researchers have also begun to modify MSCs through gene modification methods, such as BMP2 and bFGF (76), so that they can target differentiation and promote tendon-bone healing. Therefore, genetically modified stem cell techniques and stem-cell derived exosomes may be promising strategies for promoting tendine-bone healing in the future. PRP contains abundant cell factors that can promote tendon and bone tissue repair, so it is widely used in tendon, bone tissue and wound repair (Figueroa et al., 2015). PRP has been shown in basic studies to be beneficial to tendon-bone interface healing early by promoting fibro chondral formation. However, PRP hasn't achieved satisfactory efficacy in clinical studies. Recently, Zhu et al. (2022b) conducted a systematic review and meta-analysis to explore the clinical efficacy of PRP in ACL reconstruction. A total of 14 Chinese and English studies were included in this study. The results showed that PRP in ACL reconstruction can reduce postoperative pain and improve knee function in the short to medium term, but not in the long term. The study also found that PRP didn't improve knee stability or tunnel enlargement, nor did it accelerate graft healing. There are also limitations in this study. The injection volume, concentration, intensity and injection times of PRP in the study were different in different studies. Secondly, the source of the transplanted tendon during ACL reconstruction is also different. Therefore, more studies are needed in the future to further verify the role of PRP in promoting tendine-bone healing on the one hand, and determine the method and specific dosage of PRP on the other hand, so as to facilitate its widespread clinical promotion. RCT repair and ACL reconstruction surgery determined that local administration was the preferred option (Saab et al., 2022). However, local application of the drug may result in short joint retention time or incongruous onset of the drug and the physiological stages of tendon-bone healing (Zhao et al., 2022). Hydrogel microspheres have the advantages of minimally invasive, prolonged drug retention time and high drug loading efficiency, and have become a promising drug carrier in the biological field. Currently, it has been used to promote tendon-bone healing as a drug delivery tool and has shown good function in joint local administration (Zhao et al., 2022). It is believed that with the rapid development of biomaterial technology, hydrogel microspheres may be the most effective drug carrier to promote tendon-bone healing.

Physical therapy is widely used in sports medicine because of its non-trauma. It also shows great potential in promoting tendon-bone healing (Chow et al., 2014; Lu et al., 2016b). The study of Wang et al. (2014) confirmed that ESWT could avoid the enlargement of bone marrow tract in the long term after ACL reconstruction. As mentioned above, most of the previous strategies mainly act on the early stage of tendon-bone healing, and most of the long-term curative effects aren't obvious. Therefore, physical therapy in combination with other therapies that promote tendon-bone healing may compensate for the long-term lack of efficacy of these methods.

5 Conclusion

Therefore, tendon-bone healing determines the outcome of RCT repair and ACL reconstruction. As a result, researchers have tried a variety of strategies to promote tendon-bone healing. At present, biomaterials and compounds, stem cells, cell factors, PRP, exosomes, physical therapy and other technologies have been widely used in the study of promoting tendon-bone healing, and have achieved good efficacy. With the gradual maturation of these techniques and further study of the mechanism of tendon-bone healing, the strategies to promote tendon-bone healing will certainly make breakthroughs.

Author contributions

All authors conceptualized and wrote the manuscript. CY and YX additionally performed literature and data analysis. YT has modified the language and content of this article. All authors contributed to the article and approved the submitted version.

Acknowledgments

Thanks to all the authors who participated in the design and literature analysis of this paper, as well as to the Second Hospital of Lanzhou University for facilitating this paper.

Conflict of interest

The authors declare that the research was conducted in the absence of any commercial or financial relationships that could be construed as a potential conflict of interest.

Publisher's note

References

Ağır, İ., Aytekin, M. N., Küçükdurmaz, F., Kocaoğlu, B., Çetinel, S., and Karahan, M. (2017). The effect of platelet-rich plasma in bone-tendon integration. *Adv. Clin. Exp. Med.* 26 (2), 193–199. doi:10.17219/acem/61384

Alentorn-Geli, E., Seijas, R., Martínez-De la Torre, A., Cuscó, X., Steinbacher, G., Álvarez-Díaz, P., et al. (2019). Effects of autologous adipose-derived regenerative stem cells administered at the time of anterior cruciate ligament reconstruction on knee function and graft healing. *J. Orthop. Surg. Hong. Kong)* 27 (3), 230949901986758. doi:10.1177/2309499019867580

Anaguchi, Y., Yasuda, K., Majima, T., Tohyama, H., Minami, A., and Hayashi, K. (2005). The effect of transforming growth factor-beta on mechanical properties of the fibrous tissue regenerated in the patellar tendon after resecting the central portion. *Clin. Biomech. (Bristol, Avon)* 20 (9), 959–965. doi:10.1016/j.clinbiomech.2005.05.012

Arimura, H., Shukunami, C., Tokunaga, T., Karasugi, T., Okamoto, N., Taniwaki, T., et al. (2017). TGF-β1 improves biomechanical strength by extracellular matrix accumulation without increasing the number of tenogenic lineage cells in a rat rotator cuff repair model. *Am. J. Sports Med.* 45 (10), 2394–2404. doi:10.1177/0363546517707940

Bao, D., Sun, J., Gong, M., Shi, J., Qin, B., Deng, K., et al. (2021). Combination of graphene oxide and platelet-rich plasma improves tendon-bone healing in a rabbit model of supraspinatus tendon reconstruction. *Regen. Biomater.* 8 (6), rbab045. doi:10.1093/rb/rbab045

Bessa, P. C., Casal, M., and Reis, R. L. (2008). Bone morphogenetic proteins in tissue engineering: The road from laboratory to clinic, part II (BMP delivery). *J. Tissue Eng. Regen. Med.* 2 (2-3), 81–96. doi:10.1002/term.74

Bi, F., Chen, Y., Liu, J., Wang, Y., Xu, D., and Tian, K. (2021). Anterior cruciate ligament reconstruction in a rabbit model using a silk-collagen scaffold modified by hydroxyapatite at both ends: A histological and biomechanical study. *J. Orthop. Surg. Res.* 16 (1), 139. doi:10.1186/s13018-021-02281-0

Bi, Y., Ehirchiou, D., Kilts, T. M., Inkson, C. A., Embree, M. C., Sonoyama, W., et al. (2007). Identification of tendon stem/progenitor cells and the role of the extracellular matrix in their niche. *Nat. Med.* 13 (10), 1219–1227. doi:10.1038/nm1630

Cai, J., Wang, J., Ye, K., Li, D., Ai, C., Sheng, D., et al. (2018). Dual-layer aligned-random nanofibrous scaffolds for improving gradient microstructure of tendon-to-bone healing in a rabbit extra-articular model. *Int. J. Nanomedicine* 13, 3481–3492. doi:10.2147/ijn.S165633

Carragee, E. J., Hurwitz, E. L., and Weiner, B. K. (2011). A critical review of recombinant human bone morphogenetic protein-2 trials in spinal surgery: Emerging safety concerns and lessons learned. *Spine J.* 11 (6), 471–491. doi:10.1016/j.spinee.2011.04.023

Chen, B., Li, B., Qi, Y. J., Ni, Q. B., Pan, Z. Q., Wang, H., et al. (2016). Enhancement of tendon-to-bone healing after anterior cruciate ligament reconstruction using bone marrow-derived mesenchymal stem cells genetically modified with bFGF/BMP2. *Sci. Rep.* 6, 25940. doi:10.1038/srep25940

Chen, M., Patra, P. K., Lovett, M. L., Kaplan, D. L., and Bhowmick, S. (2009). Role of electrospun fibre diameter and corresponding specific surface area (SSA) on cell attachment. *J. Tissue Eng. Regen. Med.* 3 (4), 269–279. doi:10.1002/term.163

Chen, P., Cui, L., Chen, G., You, T., Li, W., Zuo, J., et al. (2019). The application of BMP-12-overexpressing mesenchymal stem cells loaded 3D-printed PLGA scaffolds in rabbit rotator cuff repair. *Int. J. Biol. Macromol.* 138, 79–88. doi:10.1016/j.ijbiomac.2019.07.041

Chen, P., Cui, L., Fu, S. C., Shen, L., Zhang, W., You, T., et al. (2020). The 3D-printed PLGA scaffolds loaded with bone marrow-derived mesenchymal stem cells augment the healing of rotator cuff repair in the rabbits. *Cell Transpl.* 29, 096368972097364. doi:10.1177/0963689720973647

Chen, R. J., Zhu, H. Z., Gu, X. Y., and Xiang, X. X. (2022). Effects of platelet-rich plasma on tendon-bone healing after anterior cruciate ligament reconstruction. *Orthop. Surg.* 14 (1), 88–95. doi:10.1111/os.13175

Chen, W., Sun, Y., Gu, X., Cai, J., Liu, X., Zhang, X., et al. (2021). Conditioned medium of human bone marrow-derived stem cells promotes tendon-bone healing of the rotator cuff in a rat model. *Biomaterials* 271, 120714. doi:10.1016/j.biomaterials.2021.120714

Cheng, P., Han, P., Zhao, C., Zhang, S., Wu, H., Ni, J., et al. (2016). High-purity magnesium interference screws promote fibrocartilaginous entheses regeneration in the anterior cruciate ligament reconstruction rabbit model via accumulation of BMP-2 and VEGF. *Biomaterials* 81, 14–26. doi:10.1016/j.biomaterials.2015.12.005

Chou, Y. C., Yeh, W. L., Chao, C. L., Hsu, Y. H., Yu, Y. H., Chen, J. K., et al. (2016). Enhancement of tendon&ndash;bone healing via the combination of biodegradable collagen-loaded nanofibrous membranes and a three-dimensional printed bone-anchoring bolt. *Int. J. Nanomedicine* 11, 4173–4186. doi:10.2147/ijn.S108939

Chow, D. H., Suen, P. K., Huang, L., Cheung, W. H., Leung, K. S., Ng, C., et al. (2014). Extracorporeal shockwave enhanced regeneration of fibrocartilage in a delayed tendon-bone insertion repair model. *J. Orthop. Res.* 32 (4), 507–514. doi:10.1002/jor.22566

De Bari, C., Dell'Accio, F., Tylzanowski, P., and Luyten, F. P. (2001). Multipotent mesenchymal stem cells from adult human synovial membrane. *Arthritis Rheum.* 44 (8), 1928–1942. doi:10.1002/1529-0131(200108)44:8<1928::aid-art331>3.0.co;2-p

de Girolamo, L., Galliera, E., Volpi, P., Denti, M., Dogliotti, G., Quaglia, A., et al. (2015). Why menisci show higher healing rate when repaired during ACL reconstruction? Growth factors release can be the explanation. *Knee Surg. Sports Traumatol. Arthrosc.* 23 (1), 90–96. doi:10.1007/s00167-013-2712-8

Deprés-Tremblay, G., Chevrier, A., Hurtig, M. B., Snow, M., Rodeo, S., and Buschmann, M. D. (2018). Freeze-dried chitosan-platelet-rich plasma implants for rotator cuff tear repair: Pilot ovine studies. *ACS Biomater. Sci. Eng.* 4 (11), 3737–3746. doi:10.1021/acsbiomaterials.7b00354

Duchamp de Lageneste, O., Julien, A., Abou-Khalil, R., Frangi, G., Carvalho, C., Cagnard, N., et al. (2018). Periosteum contains skeletal stem cells with high bone regenerative potential controlled by Periostin. *Nat. Commun.* 9 (1), 773. doi:10.1038/s41467-018-03124-z

Ersen, A., Demirhan, M., Atalar, A. C., Kapicioğlu, M., and Baysal, G. (2014). Platelet-rich plasma for enhancing surgical rotator cuff repair: Evaluation and comparison of two application methods in a rat model. *Arch. Orthop. Trauma Surg.* 134 (3), 405–411. doi:10.1007/s00402-013-1914-3

Farraro, K. F., Kim, K. E., Woo, S. L., Flowers, J. R., and McCullough, M. B. (2014). Revolutionizing orthopaedic biomaterials: The potential of biodegradable and bioresorbable magnesium-based materials for functional tissue engineering. *J. Biomech.* 47 (9), 1979–1986. doi:10.1016/j.jbiomech.2013.12.003

Feng, W., Jin, Q., Ming-Yu, Y., Yang, H., Xu, T., You-Xing, S., et al. (2021). MiR-6924-5p-rich exosomes derived from genetically modified Scleraxis-overexpressing PDGFRα(+) BMMSCs as novel nanotherapeutics for treating osteolysis during tendon-bone healing and improving healing strength. *Biomaterials* 279, 121242. doi:10.1016/j.biomaterials.2021.121242

Figueroa, D., Figueroa, F., Calvo, R., Vaisman, A., Ahumada, X., and Arellano, S. (2015). Platelet-rich plasma use in anterior cruciate ligament surgery: Systematic review of the literature. *Arthroscopy* 31 (5), 981–988. doi:10.1016/j.arthro.2014.11.022

Franklin, A., Gi Min, J., Oda, H., Kaizawa, Y., Leyden, J., Wang, Z., et al. (2020). Homing of adipose-derived stem cells to a tendon-derived hydrogel: A potential mechanism for improved tendon-bone interface and tendon healing. *J. Hand Surg. Am.* 45 (12), 1180.e1e12–1180.e121180. doi:10.1016/j.jhsa.2020.05.003

Fu, S. C., Cheuk, Y. C., Yung, S. H., Rolf, C. G., and Chan, K. M. (2014). Systematic review of biological modulation of healing in anterior cruciate ligament reconstruction. *Orthop. J. Sports Med.* 2 (3), 232596711452668. doi:10.1177/2325967114526687

Galatz, L. M., Ball, C. M., Teefey, S. A., Middleton, W. D., and Yamaguchi, K. (2004). The outcome and repair integrity of completely arthroscopically repaired large and massive rotator cuff tears. *J. Bone Jt. Surg. Am.* 86 (2), 219–224. doi:10.2106/00004623-200402000-00002

Gong, H., Huang, B., Zheng, Z., Fu, L., and Chen, L. (2022). Clinical use of platelet-rich plasma to promote tendon-bone healing and graft maturation in anterior cruciate ligament reconstruction-A randomized controlled study. *Indian J. Orthop.* 56 (5), 805–811. doi:10.1007/s43465-021-00533-z

Goradia, V. K., Rochat, M. C., Grana, W. A., Rohrer, M. D., and Prasad, H. S. (2000). Tendon-to-bone healing of a semitendinosus tendon autograft used for ACL reconstruction in a sheep model. *Am. J. Knee Surg.* 13 (3), 143–151.

Greve, J. M., Grecco, M. V., and Santos-Silva, P. R. (2009). Comparison of radial shockwaves and conventional physiotherapy for treating plantar fasciitis. *Clin. (Sao Paulo)* 64 (2), 97–103. doi:10.1590/s1807-59322009000200006

Han, F., Li, T., Li, M., Zhang, B., Wang, Y., Zhu, Y., et al. (2023). Nano-calcium silicate mineralized fish scale scaffolds for enhancing tendon-bone healing. *Bioact. Mater* 20, 29–40. doi:10.1016/j.bioactmat.2022.04.030

Han, F., Zhang, P., Sun, Y., Lin, C., Zhao, P., and Chen, J. (2015). Hydroxyapatite-doped polycaprolactone nanofiber membrane improves tendon-bone interface healing for anterior cruciate ligament reconstruction. *Int. J. Nanomedicine* 10, 7333–7343. doi:10.2147/ijn.S92099

Han, L., Fang, W. L., Jin, B., Xu, S. C., Zheng, X., and Hu, Y. G. (2019). Enhancement of tendon-bone healing after rotator cuff injuries using combined therapy with mesenchymal stem cells and platelet rich plasma. *Eur. Rev. Med. Pharmacol. Sci.* 23 (20), 9075–9084. doi:10.26355/eurrev_201910_19310

Han, L., Hu, Y. G., Jin, B., Xu, S. C., Zheng, X., and Fang, W. L. (2019). Sustained BMP-2 release and platelet rich fibrin synergistically promote tendon-bone healing after anterior cruciate ligament reconstruction in rat. *Eur. Rev. Med. Pharmacol. Sci.* 23 (20), 8705–8712. doi:10.26355/eurrev_201910_19264

Han, L., Liu, H., Fu, H., Hu, Y., Fang, W., and Liu, J. (2022). Exosome-delivered BMP-2 and polyaspartic acid promotes tendon bone healing in rotator cuff tear via Smad/RUNX2 signaling pathway. *Bioengineered* 13 (1), 1459–1475. doi:10.1080/21655979.2021.2019871

Hanahan, D., and Weinberg, R. A. (2011). Hallmarks of cancer: The next generation. *Cell.* 144. 646–674. doi:10.1016/j.cell.2011.02.013

Hannemann, P. F., Mommers, E. H., Schots, J. P., Brink, P. R., and Poeze, M. (2014). The effects of low-intensity pulsed ultrasound and pulsed electromagnetic fields bone growth stimulation in acute fractures: A systematic review and meta-analysis of randomized controlled trials. *Arch. Orthop. Trauma Surg.* 134 (8), 1093–1106. doi:10.1007/s00402-014-2014-8

He, S. K., Ning, L. J., Yao, X., Hu, R. N., Cui, J., Zhang, Y., et al. (2021). Hierarchically demineralized cortical bone combined with stem cell-derived extracellular matrix for regeneration of the tendon-bone interface. *Am. J. Sports Med.* 49 (5), 1323–1332. doi:10.1177/0363546521994511

Honda, H., Gotoh, M., Kanazawa, T., Ohzono, H., Nakamura, H., Ohta, K., et al. (2017). Hyaluronic acid accelerates tendon-to-bone healing after rotator cuff repair. *Am. J. Sports Med.* 45 (14), 3322–3330. doi:10.1177/0363546517720199

Hsu, S. L., and Wang, C. J. (2014). The use of demineralized bone matrix for anterior cruciate ligament reconstruction: A radiographic, histologic, and immunohistochemical study in rabbits. *J. Surg. Res.* 187 (1), 219–224. doi:10.1016/j.jss.2013.09.025

Hu, Y., Ran, J., Zheng, Z., Jin, Z., Chen, X., Yin, Z., et al. (2018). Exogenous stromal derived factor-1 releasing silk scaffold combined with intra-articular injection of progenitor cells promotes bone-ligament-bone regeneration. *Acta Biomater.* 71, 168–183. doi:10.1016/j.actbio.2018.02.019

Huang, C. Y., Hu, K. H., and Wei, Z. H. (2016). Comparison of cell behavior on pva/pva-gelatin electrospun nanofibers with random and aligned configuration. *Sci. Rep.* 6, 37960. doi:10.1038/srep37960

Huang, R. L., Chen, G., Wang, W., Herller, T., Xie, Y., Gu, B., et al. (2015). Synergy between IL-6 and soluble IL-6 receptor enhances bone morphogenetic protein-2/absorbable collagen sponge-induced bone regeneration via regulation of BMPRIA distribution and degradation. *Biomaterials* 67, 308–322. doi:10.1016/j.biomaterials.2015.07.047

Huang, Y., He, B., Wang, L., Yuan, B., Shu, H., Zhang, F., et al. (2020). Bone marrow mesenchymal stem cell-derived exosomes promote rotator cuff tendon-bone healing by promoting angiogenesis and regulating M1 macrophages in rats. *Stem Cell Res. Ther.* 11 (1), 496. doi:10.1186/s13287-020-02005-x

Huang, Y. M., Lin, Y. C., Chen, C. Y., Hsieh, Y. Y., Liaw, C. K., Huang, S. W., et al. (2020). Thermosensitive chitosan-gelatin-glycerol phosphate hydrogels as collagenase carrier for tendon-bone healing in a rabbit model. *Polym. (Basel)* 12 (2), 436. doi:10.3390/polym12020436

Huegel, J., Chan, P. Y. W., Weiss, S. N., Nuss, C. A., Raja, H., Waldorff, E. I., et al. (2022). Pulsed electromagnetic field therapy alters early healing in a rat model of rotator cuff injury and repair: Potential mechanisms. *J. Orthop. Res.* 40 (7), 1593–1603. doi:10.1002/jor.25185

Ide, J., Kikukawa, K., Hirose, J., Iyama, K., Sakamoto, H., Fujimoto, T., et al. (2009). The effect of a local application of fibroblast growth factor-2 on tendon-to-bone remodeling in rats with acute injury and repair of the supraspinatus tendon. *J. Shoulder Elb. Surg.* 18 (3), 391–398. doi:10.1016/j.jse.2009.01.013

Jang, K. M., Lim, H. C., Jung, W. Y., Moon, S. W., and Wang, J. H. (2015). Efficacy and safety of human umbilical cord blood-derived mesenchymal stem cells in anterior cruciate ligament reconstruction of a rabbit model: New strategy to enhance tendon graft healing. *Arthroscopy* 31 (8), 1530–1539. doi:10.1016/j.arthro.2015.02.023

Jiang, Q., Wang, L., Liu, Z., Su, J., Tang, Y., Tan, P., et al. (2023). Canine ACL reconstruction with an injectable hydroxyapatite/collagen paste for accelerated healing of tendon-bone interface. *Bioact. Mater* 20, 1–15. doi:10.1016/j.bioactmat.2022.05.003

Kaizawa, Y., Franklin, A., Leyden, J., Behn, A. W., Tulu, U. S., Sotelo Leon, D., et al. (2019). Augmentation of chronic rotator cuff healing using adipose-derived stem cell-seeded human tendon-derived hydrogel. *J. Orthop. Res.* 37 (4), 877–886. doi:10.1002/jor.24250

Kang, K., Geng, Q., Cui, L., Wu, L., Zhang, L., Li, T., et al. (2022). Upregulation of Runt related transcription factor 1 (RUNX1) contributes to tendon-bone healing after anterior cruciate ligament reconstruction using bone mesenchymal stem cells. *J. Orthop. Surg. Res.* 17 (1), 266. doi:10.1186/s13018-022-03152-y

Kawakami, Y., Takayama, K., Matsumoto, T., Tang, Y., Wang, B., Mifune, Y., et al. (2017). Anterior cruciate ligament-derived stem cells transduced with BMP2 accelerate graft-bone integration after ACL reconstruction. *Am. J. Sports Med.* 45 (3), 584–597. doi:10.1177/0363546516671707

Kim, H. M., Galatz, L. M., Das, R., Havlioglu, N., Rothermich, S. Y., and Thomopoulos, S. (2011). The role of transforming growth factor beta isoforms in tendon-to-bone healing. *Connect. Tissue Res.* 52 (2), 87–98. doi:10.3109/03008207.2010.483026

Kim, J. G., Kim, H. J., Kim, S. E., Bae, J. H., Ko, Y. J., and Park, J. H. (2014). Enhancement of tendon-bone healing with the use of bone morphogenetic protein-2 inserted into the suture anchor hole in a rabbit patellar tendon model. *Cytotherapy* 16 (6), 857–867. doi:10.1016/j.jcyt.2013.12.012

Kosaka, M., Nakase, J., Hayashi, K., and Tsuchiya, H. (2016). Adipose-derived regenerative cells promote tendon-bone healing in a rabbit model. *Arthroscopy* 32 (5), 851–859. doi:10.1016/j.arthro.2015.10.012

Kourembanas, S. (2015). Exosomes: Vehicles of intercellular signaling, biomarkers, and vectors of cell therapy. *Annu. Rev. Physiol.* 77, 13–27. doi:10.1146/annurev-physiol-021014-071641

Kuang, G. M., Yau, W. P., Lam, W. M., Wu, J., Chiu, K. Y., Lu, W. W., et al. (2012). An effective approach by a chelate reaction in optimizing the setting process of strontium-incorporated calcium phosphate bone cement. *J. Biomed. Mater Res. B Appl. Biomater.* 100 (3), 778–787. doi:10.1002/jbm.b.32511

Kuang, G. M., Yau, W. P., Lu, W. W., and Chiu, K. Y. (2014). Local application of strontium in a calcium phosphate cement system accelerates healing of soft tissue tendon grafts in anterior cruciate ligament reconstruction: Experiment using a rabbit model. *Am. J. Sports Med.* 42 (12), 2996–3002. doi:10.1177/0363546514549536

Kuang, G. M., Yau, W. P., Lu, W. W., and Chiu, K. Y. (2013). Use of a strontium-enriched calcium phosphate cement in accelerating the healing of soft-tissue tendon graft within the bone tunnel in a rabbit model of anterior cruciate ligament reconstruction. *Bone Jt. J.* 95-b (7), 923–928. doi:10.1302/0301-620x.95b7.30748

Kuo, Y. R., Wu, W. S., Hsieh, Y. L., Wang, F. S., Wang, C. T., Chiang, Y. C., et al. (2007). Extracorporeal shock wave enhanced extended skin flap tissue survival via increase of topical blood perfusion and associated with suppression of tissue pro-inflammation. *J. Surg. Res.* 143 (2), 385–392. doi:10.1016/j.jss.2006.12.552

Lacheta, L., and Braun, S. (2022). Limited evidence for biological treatment measures for cartilage and tendon injuries of the shoulder. *Knee Surg. Sports Traumatol. Arthrosc.* 30 (4), 1132–1137. doi:10.1007/s00167-021-06499-7

Lai, W. C., Iglesias, B. C., Mark, B. J., and Wang, D. (2021). Low-intensity pulsed ultrasound augments tendon, ligament, and bone-soft tissue healing in preclinical animal models: A systematic review. *Arthroscopy* 37 (7), 2318e3–2333.e3. doi:10.1016/j.arthro.2021.02.019

Lang, S., Loibl, M., and Herrmann, M. (2018). Platelet-rich plasma in tissue engineering: Hype and hope. *Eur. Surg. Res.* 59 (3-4), 265–275. doi:10.1159/000492415

Lee, K. W., Lee, J. S., Jang, J. W., Shim, Y. B., and Lee, K. I. (2017). Tendon-bone interface healing using an injectable rhBMP-2-containing collagen gel in a rabbit extra-articular bone tunnel model. *J. Tissue Eng. Regen. Med.* 11 (5), 1435–1441. doi:10.1002/term.2041

Levine, J. W., Kiapour, A. M., Quatman, C. E., Wordeman, S. C., Goel, V. K., Hewett, T. E., et al. (2013). Clinically relevant injury patterns after an anterior cruciate ligament injury provide insight into injury mechanisms. *Am. J. Sports Med.* 41 (2), 385–395. doi:10.1177/0363546512465167

Li, Z., Li, Q., Tong, K., Zhu, J., Wang, H., Chen, B., et al. (2022). BMSC-derived exosomes promote tendon-bone healing after anterior cruciate ligament reconstruction by regulating M1/M2 macrophage polarization in rats. *Stem Cell Res. Ther.* 13 (1), 295. doi:10.1186/s13287-022-02975-0

Liao, H., Yu, H. P., Song, W., Zhang, G., Lu, B., Zhu, Y. J., et al. (2021). Amorphous calcium phosphate nanoparticles using adenosine triphosphate as an organic phosphorus source for promoting tendon-bone healing. *J. Nanobiotechnology* 19 (1), 270. doi:10.1186/s12951-021-01007-y

Lovric, V., Ledger, M., Goldberg, J., Harper, W., Bertollo, N., Pelletier, M. H., et al. (2013). The effects of low-intensity pulsed ultrasound on tendon-bone healing in a transosseous-equivalent sheep rotator cuff model. *Knee Surg. Sports Traumatol. Arthrosc.* 21 (2), 466–475. doi:10.1007/s00167-012-1972-z

Lu, C. C., Ho, C. J., Huang, H. T., Lin, S. Y., Chou, S. H., Chou, P. H., et al. (2021). Effect of freshly isolated bone marrow mononuclear cells and cultured bone marrow stromal cells in graft cell repopulation and tendon-bone healing after allograft anterior cruciate ligament reconstruction. *Int. J. Mol. Sci.* 22 (6), 2791. doi:10.3390/ijms22062791

Lu, D., Yang, C., Zhang, Z., and Xiao, M. (2018). Enhanced tendon-bone healing with acidic fibroblast growth factor delivered in collagen in a rabbit anterior cruciate ligament reconstruction model. *J. Orthop. Surg. Res.* 13 (1), 301. doi:10.1186/s13018-018-0984-x

Lu, H., Chen, C., Qu, J., Chen, H., Chen, Y., Zheng, C., et al. (2016). Initiation timing of low-intensity pulsed ultrasound stimulation for tendon-bone healing in a rabbit model. *Am. J. Sports Med.* 44 (10), 2706–2715. doi:10.1177/0363546516651863

Lu, H., Liu, F., Chen, C., Wang, Z., Chen, H., Qu, J., et al. (2018). Low-intensity pulsed ultrasound stimulation for tendon-bone healing: A dose-dependent study. *Am. J. Phys. Med. Rehabil.* 97 (4), 270–277. doi:10.1097/phm.0000000000000844

Lu, H., Liu, F., Chen, H., Chen, C., Qu, J., Xu, D., et al. (2016). The effect of low-intensity pulsed ultrasound on bone-tendon junction healing: Initiating after inflammation stage. *J. Orthop. Res.* 34 (10), 1697–1706. doi:10.1002/jor.23180

Lu, J., Chamberlain, C. S., Ji, M. L., Saether, E. E., Leiferman, E. M., Li, W. J., et al. (2019). Tendon-to-Bone healing in a rat extra-articular bone tunnel model: A comparison of fresh autologous bone marrow and bone marrow-derived mesenchymal stem cells. *Am. J. Sports Med.* 47 (11), 2729–2736. doi:10.1177/0363546519862284

Lui, P. P., and Wong, O. T. (2012). Tendon stem cells: Experimental and clinical perspectives in tendon and tendon-bone junction repair. *Muscles Ligaments Tendons J.* 2 (3), 163–168.

Lv, Y., Sang, X., Tian, Z., Jiang, S., Li, C., Guo, Q., et al. (2022). Electrospun hydroxyapatite loaded L-polylactic acid aligned nanofibrous membrane patch for rotator cuff repair. *Int. J. Biol. Macromol.* 217, 180–187. doi:10.1016/j.ijbiomac.2022.07.061

Ma, C. B., Kawamura, S., Deng, X. H., Ying, L., Schneidkraut, J., Hays, P., et al. (2007). Bone morphogenetic proteins-signaling plays a role in tendon-to-bone healing: A study of rhBMP-2 and noggin. *Am. J. Sports Med.* 35 (4), 597–604. doi:10.1177/0363546506296312

Maffulli, N., Wong, J., and Almekinders, L. C. (2003). Types and epidemiology of tendinopathy. *Clin. Sports Med.* 22 (4), 675–692. doi:10.1016/s0278-5919(03)00004-8

Mahmoodinia Maymand, M., Soleimanpour-Lichaei, H. R., Ardeshirylajimi, A., Soleimani, M., Enderami, S. E., Nojehdehi, S., et al. (2018). Improvement of hepatogenic differentiation of iPS cells on an aligned polyethersulfone compared to random nanofibers. *Artif. Cells Nanomed Biotechnol.* 46 (4), 853–860. doi:10.1080/21691401.2017.1345929

Mao, Z., Fan, B., Wang, X., Huang, X., Guan, J., Sun, Z., et al. (2021). A systematic review of tissue engineering scaffold in tendon bone healing *in vivo*. *Front. Bioeng. Biotechnol.* 9, 621483. doi:10.3389/fbioe.2021.621483

Matsumoto, T., Sato, Y., Kobayashi, T., Suzuki, K., Kimura, A., Soma, T., et al. (2021). Adipose-derived stem cell sheets improve early biomechanical graft strength in rabbits after anterior cruciate ligament reconstruction. *Am. J. Sports Med.* 49 (13), 3508–3518. doi:10.1177/03635465211041582

McGoldrick, R., Chattopadhyay, A., Crowe, C., Chiou, G., Hui, K., Farnebo, S., et al. (2017). The tissue-engineered tendon-bone interface: *In vitro* and *in vivo* synergistic effects of adipose-derived stem cells, platelet-rich plasma, and extracellular matrix hydrogel. *Plast. Reconstr. Surg.* 140 (6), 1169–1184. doi:10.1097/prs.0000000000003840

Mehrabani, D., Seghatchian, J., and Acker, J. P. (2019). Platelet rich plasma in treatment of musculoskeletal pathologies. *Transfus. Apher. Sci.* 58 (6), 102675. doi:10.1016/j.transci.2019.102675

Moon, S. W., Park, S., Oh, M., and Wang, J. H. (2021). Outcomes of human umbilical cord blood-derived mesenchymal stem cells in enhancing tendon-graft healing in anterior cruciate ligament reconstruction: An exploratory study. *Knee Surg. Relat. Res.* 33 (1), 32. doi:10.1186/s43019-021-00104-4

Moses, B., Orchard, J., and Orchard, J. (2012). Systematic review: Annual incidence of ACL injury and surgery in various populations. *Res. Sports Med.* 20 (3-4), 157–179. doi:10.1080/15438627.2012.680633

Musahl, V., and Karlsson, J. (2019). Anterior cruciate ligament tear. *N. Engl. J. Med.* 380 (24), 2341–2348. doi:10.1056/NEJMcp1805931

Mutsuzaki, H., Fujie, H., Nakajima, H., Fukagawa, M., Nomura, S., and Sakane, M. (2016). Effect of calcium phosphate-hybridized tendon graft in anatomic single-bundle ACL reconstruction in goats. *Orthop. J. Sports Med.* 4 (8), 232596711666265. doi:10.1177/2325967116662653

Mutsuzaki, H., Kinugasa, T., and Sakane, M. (2019). Safety and feasibility of using calcium phosphate hybridization method for quadriceps tendon-bone graft in anterior cruciate ligament reconstruction. *J. Orthop.* 16 (5), 422–425. doi:10.1016/j.jor.2019.04.004

Mutsuzaki, H., Nakajima, H., Nomura, S., and Sakane, M. (2017). Differences in placement of calcium phosphate-hybridized tendon grafts within the femoral bone tunnel during ACL reconstruction do not influence tendon-to-bone healing. *J. Orthop. Surg. Res.* 12 (1), 80. doi:10.1186/s13018-017-0583-2

Neuman, M. G., Nanau, R. M., Oruña-Sanchez, L., and Coto, G. (2015). Hyaluronic acid and wound healing. *J. Pharm. Pharm. Sci.* 18 (1), 53–60. doi:10.18433/j3k89d

Oka, S., Matsumoto, T., Kubo, S., Matsushita, T., Sasaki, H., Nishizawa, Y., et al. (2013). Local administration of low-dose simvastatin-conjugated gelatin hydrogel for tendon-bone healing in anterior cruciate ligament reconstruction. *Tissue Eng. Part A* 19 (9-10), 1233–1243. doi:10.1089/ten.TEA.2012.0325

Pandey, V., Bandi, A., Madi, S., Agarwal, L., Acharya, K. K., Maddukuri, S., et al. (2016). Does application of moderately concentrated platelet-rich plasma improve clinical and structural outcome after arthroscopic repair of medium-sized to large rotator cuff tear? A randomized controlled trial. *J. Shoulder Elb. Surg.* 25 (8), 1312–1322. doi:10.1016/j.jse.2016.01.036

Panzavolta, S., Torricelli, P., Sturba, L., Bracci, B., Giardino, R., and Bigi, A. (2008). Setting properties and *in vitro* bioactivity of strontium-enriched gelatin-calcium phosphate bone cements. *J. Biomed. Mater Res. A* 84 (4), 965–972. doi:10.1002/jbm.a.31412

Qin, J., Yuan, F., Peng, Z., Ye, K., Yang, X., Huang, L., et al. (2015). Periostin enhances adipose-derived stem cell adhesion, migration, and therapeutic efficiency in Apo E deficient mice with hind limb ischemia. *Stem Cell Res. Ther.* 6 (1), 138. doi:10.1186/s13287-015-0126-x

Ren, Y., Zhang, S., Wang, Y., Jacobson, D. S., Reisdorf, R. L., Kuroiwa, T., et al. (2021). Effects of purified exosome product on rotator cuff tendon-bone healing *in vitro* and *in vivo*. *Biomaterials* 276, 121019. doi:10.1016/j.biomaterials.2021.121019

Rodeo, S. A., Arnoczky, S. P., Torzilli, P. A., Hidaka, C., and Warren, R. F. (1993). Tendon-healing in a bone tunnel. A biomechanical and histological study in the dog. *J. Bone Jt. Surg. Am.* 75 (12), 1795–1803. doi:10.2106/00004623-199312000-00009

Saab, M., Hildebrand, F., Martel, B., and Blanchemain, N. (2022). Materials enhancing anterior cruciate ligament tendon graft to bone healing show favorable results, in animal models, vivo: A systematic review. *Arthroscopy* 39 (2), 529–548. doi:10.1016/j.arthro.2022.05.011

Santos, S., Sigurjonsson Ó, E., Custódio, C. A., and Mano, J. (2018). Blood plasma derivatives for tissue engineering and regenerative medicine therapies. *Tissue Eng. Part B Rev.* 24 (6), 454–462. doi:10.1089/ten.TEB.2018.0008

Shen, W., Chen, J., Yin, Z., Chen, X., Liu, H., Heng, B. C., et al. (2012). Allogenous tendon stem/progenitor cells in silk scaffold for functional shoulder repair. *Cell Transpl.* 21 (5), 943–958. doi:10.3727/096368911x627453

Shi, Y., Kang, X., Wang, Y., Bian, X., He, G., Zhou, M., et al. (2020). Exosomes derived from bone marrow stromal cells (BMSCs) enhance tendon-bone healing by regulating macrophage polarization. *Med. Sci. Monit.* 26, e923328. doi:10.12659/msm.923328

Singh, S., Singh, R., Sharma, P. K., Singh, U. P., Rai, S. N., Chung, L. W., et al. (2009). Serum CXCL13 positively correlates with prostatic disease, prostate-specific antigen and mediates prostate cancer cell invasion, integrin clustering and cell adhesion. *Cancer Lett.* 283 (1), 29–35. doi:10.1016/j.canlet.2009.03.022

Sun, Y., Chen, W., Hao, Y., Gu, X., Liu, X., Cai, J., et al. (2019). Stem cell-conditioned medium promotes graft remodeling of midsubstance and intratunnel incorporation after anterior cruciate ligament reconstruction in a rat model. *Am. J. Sports Med.* 47 (10), 2327–2337. doi:10.1177/0363546519859324

Sun, Z., Wang, X., Ling, M., Wang, W., Chang, Y., Yang, G., et al. (2017). Acceleration of tendon-bone healing of anterior cruciate ligament graft using intermittent negative pressure in rabbits. *J. Orthop. Surg. Res.* 12 (1), 60. doi:10.1186/s13018-017-0561-8

Tabuchi, K., Soejima, T., Kanazawa, T., Noguchi, K., and Nagata, K. (2012). Chronological changes in the collagen-type composition at tendon-bone interface in rabbits. *Bone Jt. Res.* 1 (9), 218–224. doi:10.1302/2046-3758.19.2000109

Tan, Q., Lui, P. P., Rui, Y. F., and Wong, Y. M. (2012). Comparison of potentials of stem cells isolated from tendon and bone marrow for musculoskeletal tissue engineering. *Tissue Eng. Part A* 18 (7-8), 840–851. doi:10.1089/ten.TEA.2011.0362

Teng, C., Zhou, C., Xu, D., and Bi, F. (2016). Combination of platelet-rich plasma and bone marrow mesenchymal stem cells enhances tendon-bone healing in a rabbit model of anterior cruciate ligament reconstruction. *J. Orthop. Surg. Res.* 11 (1), 96. doi:10.1186/s13018-016-0433-7

Thangarajah, T., Sanghani-Kerai, A., Henshaw, F., Lambert, S. M., Pendegrass, C. J., and Blunn, G. W. (2018). Application of a demineralized cortical bone matrix and bone marrow-derived mesenchymal stem cells in a model of chronic rotator cuff degeneration. *Am. J. Sports Med.* 46 (1), 98–108. doi:10.1177/0363546517727512

Thangarajah, T., Shahbazi, S., Pendegrass, C. J., Lambert, S., Alexander, S., and Blunn, G. W. (2016). Tendon reattachment to bone in an ovine tendon defect model of retraction using allogenic and xenogenic demineralised bone matrix incorporated with mesenchymal stem cells. *PLoS One* 11 (9), e0161473. doi:10.1371/journal.pone.0161473

Tian, F., Ji, X. L., Xiao, W. A., Wang, B., and Wang, F. (2015). CXCL13 promotes the effect of bone marrow mesenchymal stem cells (MSCs) on tendon-bone healing in rats and in C3HIOT1/2 cells. *Int. J. Mol. Sci.* 16 (2), 3178–3187. doi:10.3390/ijms16023178

Tie, K., Cai, J., Shi, H., Li, X., Shangguan, Y., and Chen, L. (2022). Autologous dedifferentiated osteogenic bone marrow mesenchymal stem cells promote bone formation in a rabbit model of anterior cruciate ligament reconstruction versus bone marrow mesenchymal stem cells. *Arthroscopy* 38 (7), 2246e1–2254.e1. doi:10.1016/j.arthro.2022.01.021

Tucker, J. J., Gordon, J. A., Zanes, R. C., Zuskov, A., Vinciguerra, J. D., Bloebaum, R. D., et al. (2017). P(2) porous titanium implants improve tendon healing in an acute rat supraspinatus repair model. *J. Shoulder Elb. Surg.* 26 (3), 529–535. doi:10.1016/j.jse.2016.09.006

Uno, T., Maruyama, M., Satake, H., Takakubo, Y., Toyono, S., Xing, L., et al. (2022). Effectiveness of bone marrow-derived platelet-rich fibrin on rotator cuff healing in a rabbit degenerative model. *Am. J. Sports Med.* 50 (12), 3341–3354. doi:10.1177/03635465221116084

Vergis, A., and Gillquist, J. (1995). Graft failure in intra-articular anterior cruciate ligament reconstructions: A review of the literature. *Arthroscopy* 11 (3), 312–321. doi:10.1016/0749-8063(95)90009-8

von Porat, A., Roos, E. M., and Roos, H. (2004). High prevalence of osteoarthritis 14 years after an anterior cruciate ligament tear in male soccer players: A study of radiographic and patient relevant outcomes. *Ann. Rheum. Dis.* 63 (3), 269–273. doi:10.1136/ard.2003.008136

Wang, C. J., Ko, J. Y., Chou, W. Y., Hsu, S. L., Ko, S. F., Huang, C. C., et al. (2014). Shockwave therapy improves anterior cruciate ligament reconstruction. *J. Surg. Res.* 188 (1), 110–118. doi:10.1016/j.jss.2014.01.050

Wang, J. L., Xu, J. K., Hopkins, C., Chow, D. H., and Qin, L. (2020). Biodegradable magnesium-based implants in orthopedics-A general review and perspectives. *Adv. Sci. (Weinh)* 7 (8), 1902443. doi:10.1002/advs.201902443

Wang, J., Xu, J., Fu, W., Cheng, W., Chan, K., Yung, P. S., et al. (2017). Biodegradable magnesium screws accelerate fibrous tissue mineralization at the tendon-bone insertion in anterior cruciate ligament reconstruction model of rabbit. *Sci. Rep.* 7, 40369. doi:10.1038/srep40369

Wang, J., Xu, J., Song, B., Chow, D. H., Shu-Hang Yung, P., and Qin, L. (2017). Magnesium (Mg) based interference screws developed for promoting tendon graft incorporation in bone tunnel in rabbits. *Acta Biomater.* 63, 393–410. doi:10.1016/j.actbio.2017.09.018

Wang, J., Xu, J., Wang, X., Sheng, L., Zheng, L., Song, B., et al. (2021). Magnesium-pretreated periosteum for promoting bone-tendon healing after anterior cruciate ligament reconstruction. *Biomaterials* 268, 120576. doi:10.1016/j.biomaterials.2020.120576

Wang, L. L., Yin, X. F., Chu, X. C., Zhang, Y. B., and Gong, X. N. (2018). *Retracted*: Platelet-derived growth factor subunit B is required for tendon-bone healing using bone marrow–derived mesenchymal stem cells after rotator cuff repair in rats. *J. Cell Biochem.* 119 (11), 8897–8908. doi:10.1002/jcb.27143

Wei, B., Wang, C., Yan, C., Tang, B., Yu, X., Zhang, H., et al. (2020). Osteoprotegerin/bone morphogenetic protein 2 combining with collagen sponges on tendon-bone healing in rabbits. *J. Bone Min. Metab.* 38 (4), 432–441. doi:10.1007/s00774-019-01078-w

Wong, C. C., Yeh, Y. Y., Yang, T. L., Tsuang, Y. H., and Chen, C. H. (2020). Augmentation of tendon graft-bone tunnel interface healing by use of bioactive platelet-rich fibrin scaffolds. *Am. J. Sports Med.* 48 (6), 1379–1388. doi:10.1177/0363546520908849

Wu, X. D., Kang, L., Tian, J., Wu, Y., Huang, Y., Liu, J., et al. (2022). Exosomes derived from magnetically actuated bone mesenchymal stem cells promote tendon-bone healing through the miR-21-5p/SMAD7 pathway. *Mater Today Bio* 15, 100319. doi:10.1016/j.mtbio.2022.100319

Wu, Y., Dong, Y., Chen, S., and Li, Y. (2014). Effect of platelet-rich plasma and bioactive glass powder for the improvement of rotator cuff tendon-to-bone healing in a rabbit model. *Int. J. Mol. Sci.* 15 (12), 21980–21991. doi:10.3390/ijms151221980

Xu, J., Ye, Z., Han, K., Zheng, T., Zhang, T., Dong, S., et al. (2022). Infrapatellar fat pad mesenchymal stromal cell-derived exosomes accelerate tendon-bone healing and intra-articular graft remodeling after anterior cruciate ligament reconstruction. *Am. J. Sports Med.* 50 (3), 662–673. doi:10.1177/03635465211072227

Xu, Q., Sun, W. X., and Zhang, Z. F. (2019). High expression of VEGFA in MSCs promotes tendon-bone healing of rotator cuff tear via microRNA-205-5p. *Eur. Rev. Med. Pharmacol. Sci.* 23 (10), 4081–4088. doi:10.26355/eurrev_201905_17909

Xu, Y., Zhang, W. X., Wang, L. N., Ming, Y. Q., Li, Y. L., and Ni, G. X. (2021). Stem cell therapies in tendon-bone healing. *World J. Stem Cells* 13 (7), 753–775. doi:10.4252/wjsc.v13.i7.753

Xu, Z., Li, S., Wan, L., Hu, J., Lu, H., and Zhang, T. (2022). Role of low-intensity pulsed ultrasound in regulating macrophage polarization to accelerate tendon-bone interface repair. *J. Orthop. Res.* doi:10.1002/jor.25454

Yin, Z., Chen, X., Chen, J. L., Shen, W. L., Hieu Nguyen, T. M., Gao, L., et al. (2010). The regulation of tendon stem cell differentiation by the alignment of nanofibers. *Biomaterials* 31 (8), 2163–2175. doi:10.1016/j.biomaterials.2009.11.083

Yoshizawa, S., Brown, A., Barchowsky, A., and Sfeir, C. (2014). Magnesium ion stimulation of bone marrow stromal cells enhances osteogenic activity, simulating the effect of magnesium alloy degradation. *Acta Biomater.* 10 (6), 2834–2842. doi:10.1016/j.actbio.2014.02.002

You, X., Shen, Y., Yu, W., and He, Y. (2018). Enhancement of tendon-bone healing following rotator cuff repair using hydroxyapatite with TGFβ1. *Mol. Med. Rep.* 17 (4), 4981–4988. doi:10.3892/mmr.2018.8499

Zhang, C., Li, Q., Deng, S., Fu, W., Tang, X., Chen, G., et al. (2016). bFGF- and CaPP-loaded fibrin clots enhance the bioactivity of the tendon-bone interface to augment healing. *Am. J. Sports Med.* 44 (8), 1972–1982. doi:10.1177/0363546516637603

Zhang, J., and Wang, J. H. (2014). Kartogenin induces cartilage-like tissue formation in tendon-bone junction. *Bone Res.* 2, 14008. doi:10.1038/boneres.2014.8

Zhang, J., Yuan, T., Zheng, N., Zhou, Y., Hogan, M. V., and Wang, J. H. (2017). The combined use of kartogenin and platelet-rich plasma promotes fibrocartilage formation in the wounded rat Achilles tendon entheses. *Bone Jt. Res.* 6 (4), 231–244. doi:10.1302/2046-3758.64.Bjr-2017-0268.R1

Zhang, K., Wang, H., Huang, C., Su, Y., Mo, X., and Ikada, Y. (2010). Fabrication of silk fibroin blended P(LLA-CL) nanofibrous scaffolds for tissue engineering. *J. Biomed. Mater Res. A* 93 (3), 984–993. doi:10.1002/jbm.a.32504

Zhang, M., Zhen, J., Zhang, X., Yang, Z., Zhang, L., Hao, D., et al. (2019). Effect of autologous platelet-rich plasma and gelatin sponge for tendon-to-bone healing after rabbit anterior cruciate ligament reconstruction. *Arthroscopy* 35 (5), 1486–1497. doi:10.1016/j.arthro.2018.11.014

Zhang, P., Zhi, Y., Fang, H., Wu, Z., Chen, T., Jiang, J., et al. (2017). Effects of polyvinylpyrrolidone-iodine on tendon-bone healing in a rabbit extra-articular model. *Exp. Ther. Med.* 13 (6), 2751–2756. doi:10.3892/etm.2017.4359

Zhang, R., Ma, J., Han, J., Zhang, W., and Ma, J. (2019). Mesenchymal stem cell related therapies for cartilage lesions and osteoarthritis. *Am. J. Transl. Res.* 11 (10), 6275–6289.

Zhang, X., Cai, Z., Wu, M., Huangfu, X., Li, J., and Liu, X. (2021). Adipose stem cell-derived exosomes recover impaired matrix metabolism of torn human rotator cuff tendons by maintaining tissue homeostasis. *Am. J. Sports Med.* 49 (4), 899–908. doi:10.1177/0363546521992469

Zhang, Y., Xu, J., Ruan, Y. C., Yu, M. K., O'Laughlin, M., Wise, H., et al. (2016). Implant-derived magnesium induces local neuronal production of CGRP to improve bone-fracture healing in rats. *Nat. Med.* 22 (10), 1160–1169. doi:10.1038/nm.4162

Zhang, Y., Yu, J., Zhang, J., and Hua, Y. (2019). Simvastatin with PRP promotes chondrogenesis of bone marrow stem cells *in vitro* and wounded rat Achilles tendon-bone interface healing *in vivo*. *Am. J. Sports Med.* 47 (3), 729–739. doi:10.1177/0363546518819108

Zhao, S., Peng, L., Xie, G., Li, D., Zhao, J., and Ning, C. (2014). Effect of the interposition of calcium phosphate materials on tendon-bone healing during repair of chronic rotator cuff tear. *Am. J. Sports Med.* 42 (8), 1920–1929. doi:10.1177/0363546514532781

Zhao, S., Zhao, J., Dong, S., Huangfu, X., Li, B., Yang, H., et al. (2014). Biological augmentation of rotator cuff repair using bFGF-loaded electrospun poly(lactide-co-glycolide) fibrous membranes. *Int. J. Nanomedicine* 9, 2373–2385. doi:10.2147/ijn.S59536

Zhao, S., Zhao, X., Dong, S., Yu, J., Pan, G., Zhang, Y., et al. (2015). A hierarchical, stretchable and stiff fibrous biotemplate engineered using stagger-electrospinning for augmentation of rotator cuff tendon-healing. *J. Mater Chem. B* 3 (6), 990–1000. doi:10.1039/c4tb01642d

Zhao, X., Zhou, Y., Li, J., Zhang, C., and Wang, J. (2022). Opportunities and challenges of hydrogel microspheres for tendon-bone healing after anterior cruciate ligament reconstruction. *J. Biomed. Mater Res. B Appl. Biomater.* 110 (2), 289–301. doi:10.1002/jbm.b.34925

Zhi, Y., Liu, W., Zhang, P., Jiang, J., and Chen, S. (2016). Electrospun silk fibroin mat enhances tendon-bone healing in a rabbit extra-articular model. *Biotechnol. Lett.* 38 (10), 1827–1835. doi:10.1007/s10529-016-2158-4

Zhou, S. B., Wang, J., Chiang, C. A., Sheng, L. L., and Li, Q. F. (2013). Mechanical stretch upregulates SDF-1α in skin tissue and induces migration of circulating bone marrow-derived stem cells into the expanded skin. *Stem Cells* 31 (12), 2703–2713. doi:10.1002/stem.1479

Zhou, Y., Zhang, J., Yang, J., Narava, M., Zhao, G., Yuan, T., et al. (2017). Kartogenin with PRP promotes the formation of fibrocartilage zone in the tendon-bone interface. *J. Tissue Eng. Regen. Med.* 11 (12), 3445–3456. doi:10.1002/term.2258

Zhu, J., Shao, J., Chen, Y., Zhao, G., Li, L., Fu, Q., et al. (2021). Fibrin glue-kartogenin complex promotes the regeneration of the tendon-bone interface in rotator cuff injury. *Stem Cells Int.* 2021, 1–8. doi:10.1155/2021/6640424

Zhu, M., Lin Tay, M., Lim, K. S., Bolam, S. M., Tuari, D., Callon, K., et al. (2022). Novel growth factor combination for improving rotator cuff repair: A rat *in vivo* study. *Am. J. Sports Med.* 50 (4), 1044–1053. doi:10.1177/03635465211072557

Zhu, T., Zhou, J., Hwang, J., and Xu, X. (2022). Effects of platelet-rich plasma on clinical outcomes after anterior cruciate ligament reconstruction: A systematic review and meta-analysis. *Orthop. J. Sports Med.* 10 (1), 232596712110615. doi:10.1177/23259671211061535

frontiers | Frontiers in Bioengineering and Biotechnology

TYPE Original Research
PUBLISHED 15 February 2023
DOI 10.3389/fbioe.2023.1118487

OPEN ACCESS

EDITED BY
Fengxuan Han,
Soochow University, China

REVIEWED BY
Xiaolin Li,
Shanghai Jiao Tong University, China
Hongzhao Qi,
Qingdao University, China
Heyong Yin,
Affiliated Beijing Friendship Hospital,
Capital Medical University, China

*CORRESPONDENCE
Ming Zhang,
✉ zhangming1@pkuih.edu.cn
Jia Li,
✉ leejia301@126.com

[†]These authors have contributed equally to this work and share first authorship

SPECIALTY SECTION
This article was submitted to Tissue Engineering and Regenerative Medicine, a section of the journal Frontiers in Bioengineering and Biotechnology

RECEIVED 07 December 2022
ACCEPTED 02 February 2023
PUBLISHED 15 February 2023

CITATION
Zhang T, Qin X, Gao Y, Kong D, Jiang Y, Cui X, Guo M, Chen J, Chang F, Zhang M, Li J and Yin P (2023), Functional chitosan gel coating enhances antimicrobial properties and osteogenesis of titanium alloy under persistent chronic inflammation.
Front. Bioeng. Biotechnol. 11:1118487.
doi: 10.3389/fbioe.2023.1118487

Functional chitosan gel coating enhances antimicrobial properties and osteogenesis of titanium alloy under persistent chronic inflammation

Ti Zhang[1,2†], Xiaoyan Qin[3†], Yuan Gao[4†], Dan Kong[4], Yuheng Jiang[1,5], Xiang Cui[1,2], Miantong Guo[3], Junyu Chen[1,2], Feifan Chang[1,2], Ming Zhang[6]*, Jia Li[1,2]* and Pengbin Yin[1,2]

[1]Department of Orthopedics, The Fourth Medical Center of Chinese PLA General Hospital, Beijing, China, [2]National Clinical Research Center for Orthopedics, Sports Medicine and Rehabilitation, Beijing, China, [3]College of Life Science and Technology, Beijing University of Chemical Technology, Beijing, China, [4]The First Medical Center of Chinese PLA General Hospital, Beijing, China, [5]Department of Orthopedics, General Hospital of Southern Theater Command of PLA, Guangzhou, China, [6]International Hospital, Peking University, Beijing, China

Titanium is widely used as surgical bone implants due to its excellent mechanical properties, corrosion resistance, and good biocompatibility. However, due to chronic inflammation and bacterial infections caused by titanium implants, they are still at risk of failure in interfacial integration of bone implants, severely limiting their broad clinical application. In this work, chitosan gels crosslinked with glutaraldehyde were prepared and successfully loaded with silver nanoparticles (nAg) and catalase nanocapsules (n (CAT)) to achieve functionalized coating on the surface of titanium alloy steel plates. Under chronic inflammatory conditions, n (CAT) significantly reduced the expression of macrophage tumor necrosis factor (TNF-α), increased the expression of osteoblast alkaline phosphatase (ALP) and osteopontin (OPN), and enhanced osteogenesis. At the same time, nAg inhibited the growth of *S. aureus* and *E. coli*. This work provides a general approach to functional coating of titanium alloy implants and other scaffolding materials.

KEYWORDS

titanium alloy, persistent chronic inflammatory environment, functional coating, anti-inflammatory, bacteriostasis, bone formation

Introduction

Titanium (Ti) is one of the most commonly used materials in orthopedic implants due to its good biocompatibility, excellent corrosion resistance, and outstanding mechanical properties (Xu et al., 2020; Wang et al., 2021). Although Ti alloys implants have achieved good efficacy in fixing fractures, correcting deformities, and joint replacements, there is still limitation of Ti alloy implants, especially early bacteria adhesion and then biofilm formation on the implant surface, leading to implant-associated infections, which is the main cause of the high rate of implant failure in clinical practice (Muruve et al., 2017; Kim et al., 2020). The persistent chronic inflammatory response that results in poor integration of the Ti implant interface with bone is one of the main causes of implant failure. When implanting an osseous biomaterial, the cues for the onset of the inflammatory response begin with preparation for surgery (Franz et al., 2011), and even aseptic inflammation associated with the nature of the implant 'foreign body' can lead to poor integration of the material with the bone (Chuang et al., 2002; Chrcanovic et al., 2014a; Chrcanovic et al., 2014b). Infection of the tissues surrounding the implant interface caused by bacterial infection also contributes to the development of a persistent chronic inflammatory response at the implant site, which can severely inhibit osseointegration and even lead to non-union (Gao et al., 2019; Wu et al., 2021).

The initial immune response triggered by the implantation of orthopedic biomaterials is mainly induced by innate immune cells of the myeloid lineage (Anderson, 1988; Donath et al., 1992), which secreted signaling molecules, such as chemokines and cytokines, create a microenvironment at the implantation site that directly determines the success or failure of the integration between the material and the bone. Macrophages, as the first innate immune cells to come into contact with the implant surface after implantation, are rapidly activated after migration to the injury site following tissue injury and present two functional phenotypes, one of which is a macrophage phenotype that promotes an inflammatory response. This macrophage phenotype is found to be disproportionately present in the clinic around pure titanium grafts (Rao et al., 2012; Mantovani et al., 2013). Such macrophage-mediated persistent chronic inflammation is detrimental to bone repair. The production of persistent tumor necrosis factor (TNF-α), interleukin 6 (IL-6), inducible nitrogen oxide synthase (iNOS), and reactive oxygen species (ROS) such as H_2O_2 can severely alter osteoblast activity and differentiation capacity leading to bone resorption (Devasconcellos et al., 2012; Muruve et al., 2017; Li et al., 2020). Therefore, how to effectively improve osteogenesis and integration of the bone-implant interface on the surface of the Ti alloy implant in a persistent chronic inflammatory environment remains the focus of bone implant research.

Modification of the surface of bone implants has become an effective strategy for promoting bone formation and enhancing the integration of bone graft interfaces. Zhu et al. (2015) used inductively coupled plasma-based dry etching techniques, bone formation is promoted by altering the microstructure of the surface of the material. Gulati et al. (2017), on the other hand, significantly improved stem cell differentiation through the coexistence of micron-scale spherical particles and nanoscale vertical tubular arrays of microsurface structures constructed by 3D printing and anodic oxidation techniques. At the same time, Zhao et al. (2020) conferred excellent antibacterial capacity and osseointegration capacity on steel plates by preparing a functional coating of a zinc oxide/collagen type I composite (Col-I). It was also found that coating titanium alloy surfaces with metallic tantalum successfully activated the Wnt/beta signaling pathway and transformed the growth factor beta/fruit fly parent against decaying proteins (Smad), thus accelerating natural mineral deposition in body fluids and effectively promoting osteogenesis. However, these approaches have focused on the effects of biomaterials on BMSCs and osteoblasts.

In contrast, integrating the implant-bone interface is a complex biological process with immune-inflammatory responses triggered by various cell types. Therefore, it is essential to focus on the regulatory effect of titanium implant surface modification on osteoblasts in the microenvironment of persistent inflammation after implant implantation. In our pre-experiments, our team demonstrated that catalase effectively breaks down H_2O_2 in inflammatory environments and reduces the expression of associated pro-inflammatory cytokines to effectively treat inflammatory related diseases (Qin et al., 2020; Li et al., 2021; Yan et al., 2022). And our group developed nanocapsules based on the formation of free radical reactions to provide reasonable protection for further applications of catalase in complex environments *in vivo* (Zhu et al., 2015; Tian et al., 2016; Zhang et al., 2017; Xu et al., 2019).

In this work, we prepared chitosan gel crosslinked with glutaraldehyde to coat the titanium alloy surface, in which silver nanoparticles (nAg) and catalase nanocapsules (n (CAT)) were loaded. Based on the experimental results, the presence of nAg conferred an excellent antibacterial ability on the titanium alloy (Chimutengwende-Gordon et al., 2014; Huang et al., 2014; Cochis et al., 2015; Unosson et al., 2015; Cheng et al., 2022; Xiong et al., 2022; Yazdani-Ahmadabadi et al., 2022). Furthermore, osteoblast differentiation experiments found that n (CAT) effectively relieved inhibition of osteoblast differentiation in a chronic inflammatory environment and promoted osteogenesis; this could ultimately help improve the immunoinflammatory microenvironment at the implant-bone interface, providing a new idea for better integration of the implant-bone interface (Scheme 1).

Materials and methods

Materials

All reagents were used as received unless otherwise specified. Sandpaper was purchased from 3M (Minnesota, America). Silver nanoparticles were purchased from Feynman Nanomaterials Technology Co. Ltd (Liaoning China). Chitosan was obtained from Source leaf (Shanghai, China). Glutaraldehyde, acetic acid, nitric acid, hydrofluoric acid, sodium hydroxide, and sodium bicarbonate were purchased from Macklin (Shanghai, China). *Staphylococcus aureus* (*S. aureus,* CMCC26003) was obtained from Haibo Bio (Qingdao, China). *Escherichia coli* (*E. coli*, ATCC25922) was purchased from Xuanya Biotechnology Co. Ltd (Shanghai, China). Catalase (CAT) from Aspergillus niger was purchased from Sunson Industry Group (Beijing, China). Trypsin was purchased from Sigma Aldrich (St. Louis, MO), 2-methacryloyloxyethyl phosphorylcholine (MPC) was obtained from Anqing Kuangyou Biomaterials Co. Ltd. N-(3-Aminopropyl) methacrylamide hydrochloride (APM) was purchased from HEOWNS (Tianjin, China). N,N-methylenebisacrylamide (BIS), and ammonium persulfate (APS) were obtained from FuChen (Tianjin, China). N,N,N′,N′-tetramethylethylenediamine (TEMED) was purchased from Sangon Biotech (Shanghai, China). Mouse peritoneal macrophages (RAW264.7) were obtained from Northana Bio (Qingdao, China). Nutritional agar, Cell Counting Kit-8 (CCK-8), Bicinchoninic Acid (BCA) Protein Assay Kit, Catalase Activity Assay Kit, Endotoxin Erasol, phalloidin and DAPI were purchased from Beijing Solarbio Science and Technology Co. Ltd. (Beijing, China). Mouse TNF-α enzyme-linked immunosorbent assay (ELISA) kit, mouse IL-6 ELISA kit, and mouse IL-10

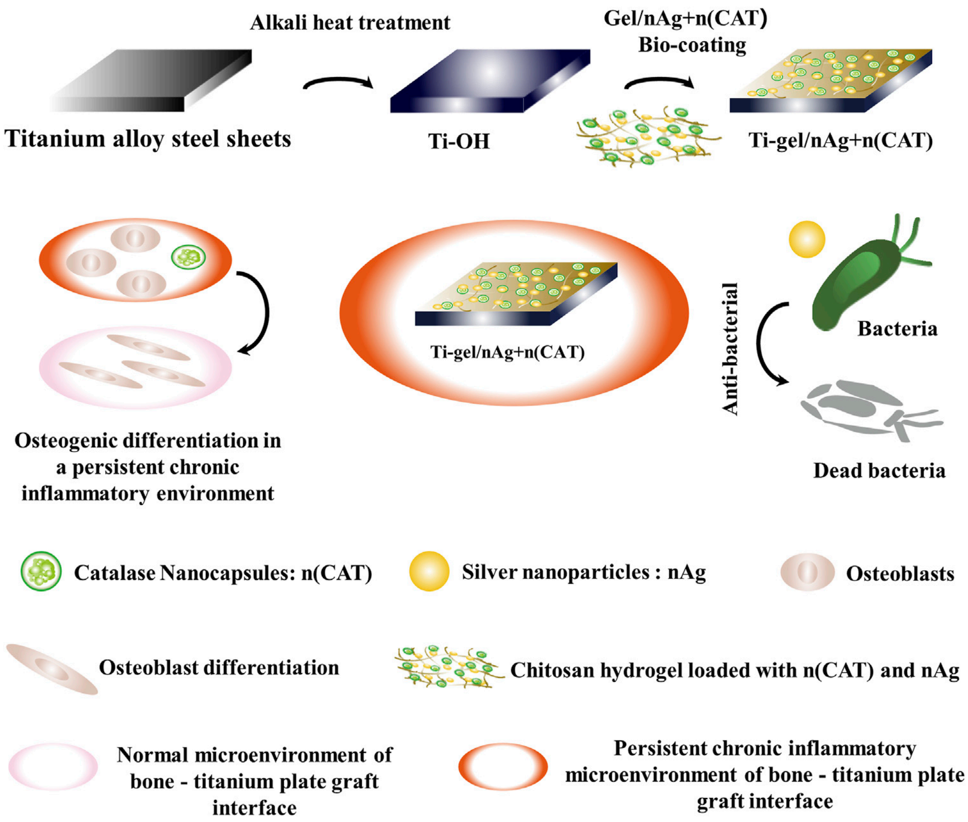

SCHEME 1
Schematic approach to antimicrobial and osteogenic differentiation in a persistent chronic inflammatory environment after coating titanium alloy steel plates with chitosan gel loaded with catalase nanocapsules (n (CAT)) and silver nanoparticles (nAg). The nano-silver in the gel coating provides effective antibacterial protection. At the same time, catalase nanocapsules effectively reduce the inhibition of osteoblast differentiation by removing hydrogen peroxide from the persistent chronic inflammatory environment and ultimately promote osteoblast differentiation by improving the persistent chronic inflammatory environment at the bone-titanium alloy graft interface.

ELISA kit were purchased from PeproTech (Suzhou, China). BCA protein concentration determination kit, fluorescein isothiocyanate (FITC), dexamethasone, ascorbic acid, sodium β-glycerophosphate, Alizarin Red Staining Solution, 4% paraformaldehyde solution, and 25% glutaraldehyde solution were also obtained from Solarbio (Beijing, China). DMEM, α-MEM medium, penicillin/streptomycin (P/S, 1%), and fetal bovine serum (FBS) were purchased from Gibico (Australia). BCIP/NBT alkaline phosphatase (ALP) color development kit, Live/dead cell double staining kit (Calcein AM/PI), and CCK-8 kit were purchased from Biyuntian (Shanghai, China). Osteopontin (OPN) was obtained from Abcam (United Kingdom). Ultrapure water with a resistivity of 18.2 MΩ cm was used throughout.

Instruments

Transmission electron microscopy (TEM) images were acquired on the Tecnai T12 cryo-electron microscope (FEI) using an acceleration voltage of 120 kV. Dynamic light scattering (DLS) measurements were performed on a Zetasizer Nano instrument (Malvern) with a 10-mW helium-neon laser and thermoelectric temperature controller. FTIR measurements were performed using an FTIR spectrometer (Nicolet 6700, Thermo). Fluorescence intensity imaging was performed using an automatic multifunction imaging analysis system (OI600-MF-Touch). The rheological properties of chitosan hydrogels were measured at 37°C using an ARES-LS2 rheometer (TA Instruments, New Castle, DE). Cell adhesion to the surface of the material, the cytoskeleton, and the fluorescence images of the OPN were observed using a confocal laser scanning microscope (Leica TCS SP8). Fluorescence intensity was measured with a microplate reader (Multiskan GO, Thermo). Fluorescently stained cells were imaged with an upright fluorescence microscope (Nikon, Japan). UV absorption measurement was used by NANODROP (Thermo).

Synthesis

Synthesis of Ti-OH. First, the surface of the titanium alloy plate was sanded with 800, 1200, and 2000 grit sandpaper until the surface was smooth and flat, and the polished titanium alloy plate was named Ti alloy plate. The Ti alloy plate was then immersed in a mixed acid solution of nitric acid (25%, v/v), hydrofluoric acid (3%, v/v), and water for 1 min and then removed and rinsed with deionized water. After drying the Ti surface with dust-free paper, it was placed in a 2 mol/L sodium hydroxide solution and reacted at 80°C for 4 h to obtain treated Ti treated with alkali (Ti-OH). Soak Ti and Ti-OH in a 75% ethanol solution for 15 min to obtain sterile Ti and Ti-OH.

Synthesis of Chitosan Gels. 7.5 mg of chitosan was dissolved in 185 μL of acetic acid solution (2%, v/v), and 15 μL of glutaraldehyde solution (2%, v/v) was added to the completely dissolved chitosan solution, mixed well and left to form a gel at room temperature for 2 h. To obtain sterile chitosan gels, the chitosan was pretreated with UV light for 30 min and the acetate and glutaraldehyde solutions were filtered through a 0.22 μm filter membrane on an ultra-clean bench. The gels were prepared on the ultra-clean table described above to obtain sterile gels.

Synthesis of n(CAT). CAT nanocapsules, denoted as n (CAT). It was synthesized as previously reported (Qin et al., 2020). Briefly, CAT was thoroughly mixed with MPC, APM, BIS, TEMED, and APS in a molar ratio of 1:21600: 2400: 2400: 4800: 2400 in 10 mM pH 7.0 PBS buffer. A free radical polymerization reaction was initiated by the final addition of APS and TEMED. The reaction was carried out at 4°C for 2 h and then dialyzed in 10 mM pH 7.0 PBS buffer using a cellulose membrane (MWCO 100 kDa) to remove unreacted monomers and initiators. The dialyzed solution is then purified by passing it through a phenyl sepharose CL-4B column (GE) in the presence of a 10xPBS elution buffer. Finally, the purified solution was concentrated using an ultrafiltration tube to obtain n (CAT). Sterile n (CAT) was obtained by filtration using a 0.22 μm membrane on an Ultraclean table.

Synthesis of n(CAT)-FITC. For imaging purposes, n (CAT) was fluorescently labeled with FITC (Ex 490 nm, Em 525 nm). Briefly, n (CAT) and FITC were mixed in a 1: 5 M ratio and incubated at room temperature for 48 h in the dark. Then, the combination used to be considerably dialyzed into 10 mM pH 7.0 PBS buffer with the use of a cellulose membrane (MWCO 10 kDa) to remove unreacted FITC and eventually obtain FITC-labeled n (CAT) (denoted as n (CAT)-FITC).

Synthesis of Gel/nAg, Gel/n(CAT) and Gel/nAg + n(CAT). Chitosan gels loaded with nAg, n (CAT) and nAg + n (CAT) were denoted as gel/nAg, gel/n (CAT) and gel/nAg + n (CAT). According to the steps above in the preparation of chitosan, nAg or n (CAT) was added to the completely dissolved chitosan solution, where the concentration of nAg was 20 ppm and the enzyme activity of n (CAT) was added at 16 μg/ml, well mixed. The 2% glutaraldehyde solution was then added and well mixed to obtain the drug-loaded pregel solution, and the drug-loaded pregel solution was left to stand at room temperature for 2 h to obtain gel/nAg, gel/n (CAT) and gel/nAg + n (CAT). After the sterile raw material for the preparation of drug-loaded chitosan gels was obtained according to the method described above, the gels were prepared on an ultraclean table to obtain sterile gel/nAg, gel/n (CAT), and gel/nAg + n (CAT).

Synthesis of Ti-gel, Ti-gel/n(CAT) and Ti-gel/nAg. The chitosan gels and drug-loaded chitosan gel-coated titanium alloy steel sheets were denoted as Ti-gel, Ti-gel/n (CAT), Ti-gel/nAg, Ti-gel/nAg + n (CAT) and Ti-gel/nAg + n (CAT)-FITC. On the basis of the above methods, sterile Ti-OH, chitosan gel, and drug-carrying chitosan gel were prepared. Briefly, after adding 200 μL drops of pre-gelatinization solution to the Ti-OH surface and leaving it for 3 min to completely gel, it was then placed in a sterile well plate and placed in an oven at 37°C overnight resulting in sterile Ti-gel, Ti-gel/n (CAT), Ti-gel/nAg, Ti-gel/nAg + n (CAT), and Ti-gel/nAg + n (CAT)-FITC. The above operation was performed in a sterile ultra-clean table.

Cell culture

Isolation and Culture of BMSCs. Bone marrow-derived MSCs (BMSCs) were collected from the femur and tibia of 1-month-old New Zealand rabbits. Approximately 2–5 ml of fresh bone marrow was removed from the rabbit femurs and tibias and cultured in α-MEM (10% fetal bovine serum, 1% P/S) for 5 days (37°C, 5% CO_2, 95% relative humidity). When non-adherent cells were removed, most adherent cells were considered BMSCs. After reaching 80%–90% fusion, primary BMSCs were passaged in a 1: 3 ratio with 0.25% trypsin/EDTA. Subsequently, 2-4 generations of BMSCs were used for *in vitro* cytotoxicity and value-added adhesion assays.

Isolation and Culture of Osteoblasts. Osteoblasts were collected from the skulls of newborn C57 mice. The skulls were digested in 500 μl of 0.25% trypsin solution at 37°C for 10 min, followed by washing with a-MEM medium. The digestion reaction was then continued by adding 600 μl of 0.2% (2 mg/ml) type II collagenase solution for 30 min at 37°C. The skulls were further excised and placed in a type II collagenase solution for 60 min at 37°C. The digest was centrifuged at 1500 r/min for 5 min, the supernatant was discarded and the precipitated fraction was resuspended in α-MEM containing 10% FBS and 1% P/S. Resuspension was transferred to culture flasks (37°C, 5% CO_2, 95% relative humidity), and the culture medium was changed every 2–3 days (Zheng et al., 2020). The primary osteoblasts obtained were used for subsequent osteogenic differentiation experiments.

Culture of Mouse Peritoneal Macrophages (RAW264.7). Mouse peritoneal macrophages (RAW264.7) were purchased from Northana Bio and cultured using a DMEM medium containing 10% FBS and 1% P/S for subsequent cytokine assay experiments.

Determination of the concentration and activity of CAT and n (CAT)

Protein Concentration Assay. The concentration of CAT and n (CAT) was determined by optical absorption measurements using an extinction coefficient of $\varepsilon = 324000\ M^{-1}\,cm^{-1}$ at 405 nm (Samejima and Yang, 1963).

Catalase Activity Assay. The activity of CAT and n (CAT) was tested using a catalase activity assay kit. Briefly, 1 ml of H_2O_2 solution (pH = 7.4, 0.1 M HEPES buffer, H_2O_2 concentration 0.03% w/v) and 35 μL of the sample were added to a 1 ml quartz cuvette. After mixing for 5 s, the absorbance at 240 nm was measured immediately (A1) and after 1 min (A2). The following equation calculates the activity of catalase:

$$\boldsymbol{Catalase\,activity\ (U/mL) = \left[\Delta A \times V_{total} \div (\varepsilon \times d)\, 10^{6}\right] \div V_{sample} \div T}$$
$$\boldsymbol{= 678 \times \Delta A}$$

Where $\Delta \boldsymbol{A} = \boldsymbol{A1} - \boldsymbol{A2}$; $\boldsymbol{V_{total}}$ stands for the total volume of the reaction system, 1.035 Ml; $\boldsymbol{\varepsilon}$ stands for the molar absorptivity of H2O2, 43.6 L/mol/cm; $\boldsymbol{d}$ stands for the optical path of the cuvette, 1cm; $\boldsymbol{V_{sample}}$ stands for the volume of the sample added, 0.035 ml; $\boldsymbol{T}$ stands for the reaction time, 1min.

Characterizations of the n (CAT)

Dynamic Light Scattering (DLS) Measurement. The particle size distribution of CAT and n (CAT) was measured using a Zetasizer Nano instrument. The instrument is equipped with a 10-mW HeNe laser and a thermoelectric temperature controller to measure the particle size of CAT and n (CAT) at a measurement temperature of 25°C and a scattering angle of 90° (n = 3).

Transmission Electron Microscopy (TEM). The sample was prepared as previously described (Tian et al., 2016; Qin et al., 2020). Briefly, a 1% (w/v) solution of phosphotungstic acid was used to stain n (CAT) and was added dropwise to the copper web. Finally, the morphology of n (CAT) on the copper web was observed using an HT7700 field emission electron microscope at 100 kV.

Characterizations of chitosan gels

Rheology (TA) Measurements of Chitosan Gels. The mechanical properties of the chitosan hydrogels were determined using an ARES-LS2 rheometer (TA Instruments, New Castle, DE). The rheometer has a 25 mm stainless steel upper cone and a temperature-controlled Peltier base plate on which a 2 cm diameter, 2 mm thick hydrogel sample was placed. The samples were dynamically scanned at 37°C, 1Hz, and with a 1% strain applied for 900 s to determine the mechanical properties of the hydrogel (n = 3).

Fourier Transform Infrared Spectroscopy (FT-IR). Infrared spectroscopy was performed on freeze-dried chitosan hydrogel samples using a Jasco FT/IR-6200 spectrometer (Jasco, OK, United States) equipped with a deuterated triglyceride sulfate detector (Pike Technologies, WI, United States). Chitosan hydrogels were prepared as previously described and then freeze-dried at -20°C before subjecting them to FTIR analysis. Thirty-two scans from 600 to 4000 cm $^{-1}$ were taken for each measurement to obtain spectra with a nominal resolution of 4 cm $^{-1}$.

Characterizations of the Ti, Ti-OH, and Ti-gel/nAg + n (CAT)

SEM-EDS. The morphology and element composition of the surface of Ti, Ti-OH, Ti-gel/nAg + n (CAT) samples were measured using a field-induced emission scanning electron microscope (FE-SEM; Sigma500, Zeiss, Germany) equipped with an energy dispersion X-ray spectrometer. The entire observation process was operated at a constant accelerating voltage of 5 kV in a vacuum environment. Before imaging, samples were sputter coated with gold to increase conductivity.

Fluorescence Imaging. Optical imaging was used to further confirm the successful coating of fluorescently labeled n (CAT) on Ti surfaces achieved using an automated multifunctional imaging analysis system (OI-600MF-Touch, Guang Yi Bio, Guangzhou).

Water Contact Angle (WAC) Assay Hydrophilic testing of Ti, Ti-OH and Ti-gel/nAg + n (CAT) surface using a contact angle goniometer (DSA100, Dataphysics Instruments GmbH, Filderstadt, Germany). Briefly, the material was placed on the stage and raised so that the material being examined would come into contact with water droplets from the injector. Then, the stage was lowered to remove the droplets. Finally, a photo of the water droplets was taken after 10 s. The five-point fitting becoming approach was once used to measure the static water contact angle.

Antibacterial assay

Bacterial Culture. Nutrient agar was dissolved in deionized water at 10% (m/v) to obtain a solid medium for bacteria; mix 10 g of peptone, 3 g of beef paste, and 5 g of sodium chloride dissolved in 1 L of distilled water to obtain a liquid medium. Both mediums were autoclaved at 121°C for 20 min and used to culture *E. coli* and *S. aureus.* Individual colonies were picked and placed in 5 ml of liquid medium and incubated in a constant temperature incubator at 37°C with shaking at 180r/min for 12 h to obtain freshly cultured bacterial broth.

Inhibition Zone Assay. The antimicrobial activity of Ti-Gel/nAg was studied by inhibition zone assay analysis. 1 ml of freshly cultured mycelium was taken and diluted in a 1000-fold gradient with 1xPBS buffer. Then 100 μL of the diluent was added to the solid medium. After uniform coating, the material was placed in the middle of a solid medium and incubated for a total of 12 h at 37°C to observe the formation of the inhibition zone.

Bacterial Survival Rate Assay. After centrifugation with 1 ml of fresh bacterial solution, the supernatant was discarded, resuspended in a sterile 1 ml of 1× PBS buffer, further diluted 1000 times gradiently, then the material was immersed in a diluted 4 ml bacterial solution and co-incubated at 37°C for 12 h. After co-culture, the co-cultivated bacterial solution was again diluted in a 1000-fold gradient using 1xPBS buffer. After incubation at 37°C for 24 h, 100 uL of diluted bacterial solution was taken and evenly spread on solid medium and colonies on the surface of agar plates were counted and the experiment was repeated 3 times for each group (n = 3). The bacterial survival rate was obtained through the following equation.

$$\boldsymbol{Bacterial\,survival}\ (\%) = \frac{\boldsymbol{Is}}{\boldsymbol{Ic}} \times \mathbf{100}\%$$

Where *Is* the number of colonies in the test sample and *Ic* is the total number of colonies of the control bacteria.

Cytotoxicity of n (CAT) and nAg

Fourth-generation BMSCs were used to study the toxic effects of n (CAT) and nAg at the cellular level. First, BMSCs were seeded at a density of 5 × 10^3 cells/well in 96-well plates and incubated overnight at 37°C to adhere them to the wall. Subsequently, 100 μL of the n (CAT) solution (100, 200, 500, 1000, and 2000 ng/ml) and the nAg solution (5, 10, 15, 20, 25 ppm), prediluted with serum-free medium, were added and incubated with cells for 24 h at 37°C. Finally, 10 μL of CCK-8 reagent was added to each well and incubated for 2–3 h at 37°C. The absorbance was measured at 450 nm using a multifunctional enzyme marker (EnSpire PerkinElmer) microplate reader. The absorbance value in the blank wells was 100%, which was used to convert the relative cell viability of the experimental group. (n = 5).

Adhesion and proliferation assay of BMSCs on the surface of Ti and Ti-gel/nAg + n (CAT)

Fourth-generation BMSCs were used to study the ability of cells to adhere to Ti and Ti-gel/nAg + n (CAT) surfaces for value-added. Sterile Ti and Ti-gel/nAg + n (CAT) were prepared as previously described. Ti and Ti-gel/nAg + n (CAT) were pre-equilibrated in medium for 2 h. BMSCs were seeded on Ti and Ti-gel/nAg + n (CAT) surfaces at a density of 2.5×10^4 cells per well. The surface of the material was rinsed 3 times with PBS to remove loosely attached cells, followed by adding 0.5 ml of α-MEM medium containing 10% CCK-8 and incubation at 37°C for 2–3 h before measuring the OD at 450 nm. The previous measurements were repeated on days 2, 3, and 4. At the same time, BMSCs were inoculated on the surface of Ti and Ti-gel/nAg + n (CAT) materials in the same way; cells were stained with Ghost Cyclin/DAPI labeled with Rhodamine and Calcein AM/PI at different time points, then live-dead and cell morphology were observed using fluorescence microscopy (Nikon japonica) and confocal fluorescence microscopy (Leica TCS SP8), respectively.

Osteogenic differentiation assay of osteoblasts cultured on the surface of gel and Gel/n (CAT) in a persistent chronic inflammatory environment

Osteoblasts were used in a persistent chronic inflammatory environment to study the ability of osteogenic differentiation on different surfaces of materials. The sterile gel and gel/n (CAT) were prepared using the method described above. First, by interfering with the formation of a persistent chronic inflammatory environment by adding 100 μM H_2O_2 to the osteoblast induction medium and then investigating the osteoblast differentiation capacity on the gel and gel/n (CAT) surface. Gel and Gel/n (CAT) were pre-equilibrated in medium for 2 h. Osteoblasts were inoculated on the Gel and Gel/n (CAT) surface at a density of 1×10^4 cells per well. After 2 days of incubation, the α-MEM medium was replaced with an osteogenic induction medium and the culture was changed daily until days 7 and 14.

Alizarin Red and Alkaline Phosphatase Staining. Alizarin red staining was performed on day 7 of the osteogenic differentiation culture according to the previous method. Cells were fixed in 4% tissue fixative for 15 min, rinsed three times with 1xPBS solution, followed by Alizarin Red staining solution for 30 min. On day 14, alkaline phosphatase staining (ALP) was performed and the ALP working solution was prepared according to the instructions for the ALP kit (Beyotime, C3206). Cells were fixed in 4% tissue fixative for 15 min. They were washed three times with 1 x PBS solution and subsequently stained with ALP working solution for 60 min. All staining results were observed with a biological scanning electron microscope (SU8010 Thermo) and quantitatively analyzed using ImagePro software.

Cytokine expression ability of macrophages on the surface of Ti and Ti-gel/n (CAT) in a persistent chronic inflammatory environment

RAW264.7 macrophages were used to study cytokine expression on different surface surfaces of materials in a persistent chronic inflammatory environment. Sterile Ti, Ti-gel/n (CAT) and chronic inflammatory environments were obtained according to the method previously described to study the anti-inflammatory capacity of macrophages on their surfaces. The macrophages were inoculated at 2×10^4 per well on the surface of Ti and Ti-gel/nAg + n (CAT), and after 24 h of incubation, the cell supernatant was aspirated. The concentrations of TNF-α, IL-6, and IL-10 in the supernatant were measured using ELISA kits (PeproTech, Suzhou, China).

OPN immunofluorescence staining of osteoblasts on Ti and Ti-gel/n (CAT) in a persistent chronic inflammatory environment *via* n (CAT)

Osteoblasts were inoculated onto the Ti and Ti-gel/n (CAT) surfaces at a density of 1×10^4 cells per well according to the previous method. After 2 days of incubation, the α-MEM medium was replaced with an osteogenic induction medium. The medium was changed daily until day 7, when immunofluorescence staining for OPN was performed. Briefly, cells were fixed in 4% tissue fixative for 15 min, rinsed three times with 1 x PBS solution, followed by further treatment of the samples with 0.3%–0.5% Triton X-100, immediately followed by the addition of 10% goat serum for 1 h at room temperature to block non-specific binding. After adding primary antibodies to the samples overnight at 4°C, secondary antibodies Alexa Fluor 647 goat anti-mouse IgG (Abcam) were added and incubated at room temperature for 2 h. The cytoskeleton and nuclei were then treated with rhodamine-labeled ghost pencil cyclic peptide and DAPI. Finally, the OPN fluorescence images of the surfaces of different materials were observed by a fluorescence confocal microscope. (Nikon).

Statistical analysis

As indicated, all results are presented as the mean ± standard error of the mean (s.e.m.). Three statistical methods, including T-test, one-way ANOVA and two-way ANOVA were used in this article. All statistical analyses were performed with Prism Software (Prism 8.0.1).

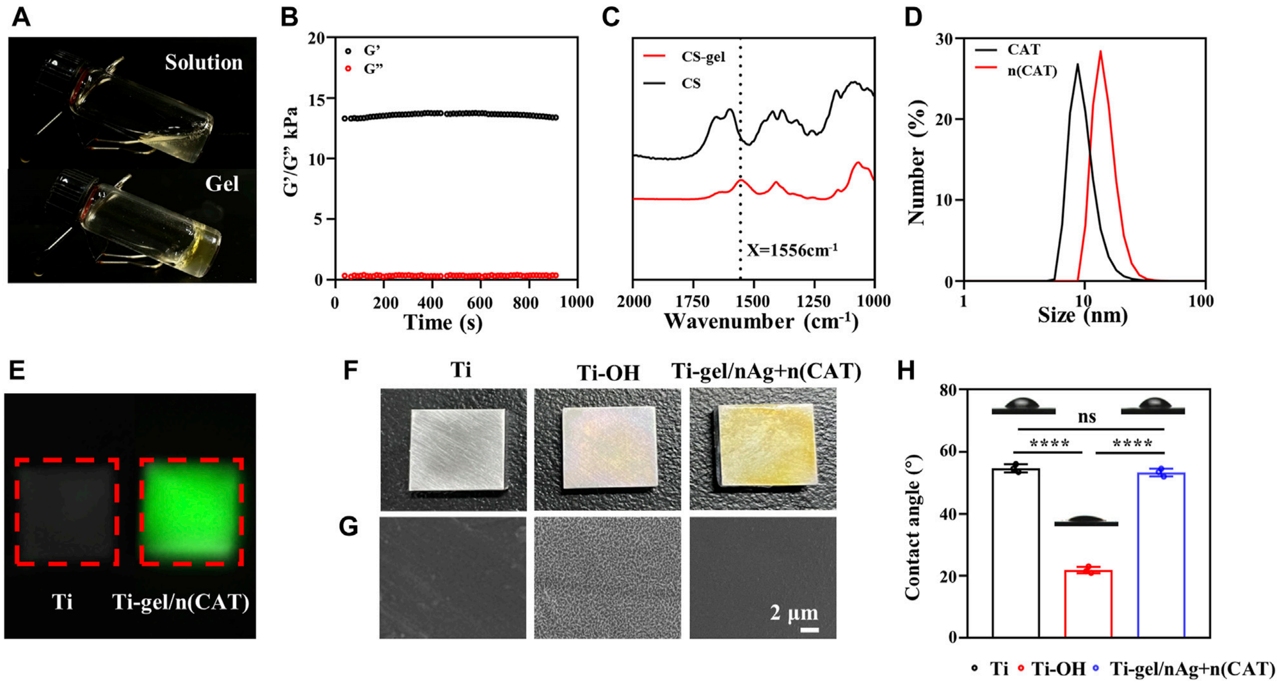

FIGURE 1
Characterization of gel, n (CAT), and Ti-gel/nAg + n (CAT). **(A)** Physical diagram of the gel. **(B)** Young's modulus of the gel. **(C)** FT-IR spectra of chitosan and gel. **(D)** DSL of CAT and n (CAT). **(E)** Fluorescent images of Ti and Ti-gel/n (CAT). **(F and G)** Physical diagram and SEM of Ti, Ti-OH, and Ti-gel/nAg + n (CAT). **(H)** Ti, Ti-OH, and Ti-gel/nAg + n (CAT) water contact angle. (n = 3, ns means that there are no significant differences, *****p* < 0.0001).

Results and Discussions

Characterization of gel, n (CAT) and Ti-gel/nAg + n (CAT)

Characterization of gel

By preparing a chitosan hydrogel that can be loaded with bioactive substances, the surface of a titanium alloy steel plate is coated to impart bioactivity and its related characterization. Figure 1A shows the physical diagram of the chitosan solution in a gel. Its mechanical properties were measured using a rheometer. The results show that the elastic modulus of the chitosan gel was significantly higher than the viscous modulus (G'> G″), suggesting that the system was similar to a solid-like colloid and that the system was indeed transformed from a chitosan solution to a hydrogel colloid. The trend of the curve was stable, indicating that the chitosan gel cross-linked system was stable (Figure 1B). Compared to chitosan, the chitosan gel had a characteristic peak glutaraldehyde cross-linking band at 1556cm^{-1} (amide II). (Li et al., 2013). This shows that the chitosan hydrogel system is indeed formed by glutaraldehyde crosslinking (Figure 1C). These results are evidence of the successful synthesis of chitosan gels.

Characterization of n (CAT)

Catalase nanocapsules were prepared and characterized as previously described. The DLS results confirmed that the hydrodynamic radius of the CAT was 7.58 nm, while the hydrodynamic radius of n (CAT) reached 13.6 nm (Figure 1D). Further TEM results showed that n (CAT) has a spherical morphology with an average diameter of about 20 nm (Supplementary Figure S1A), which was consistent with the DLS results. This result indicated that the monomers and BIS cross-linkers incubated with CAT formed a thin layer of polymer shell around the CAT. These results collectively demonstrate the successful synthesis of n (CAT). Compared to CAT, n (CAT) exhibited a similar enzymatic activity (Supplementary Figure S1B), showing that the nanopolymer shell layer did not affect the CAT enzymatic activity, and the prepared n (CAT) can be used for subsequent experiments. Next, n (CAT) was fluorescently labeled with FITC to investigate the effect of loading n (CAT) and nAg for the gel formation of the chitosan solution. As shown in Supplementary Figure S1C, the chitosan solution loaded with n (CAT) and nAg formed a gel well and n (CAT) was evenly distributed in the gel. The gel/n (CAT)-FITC was further coated on the surface of Ti-OH, as can be seen by fluorescence imaging that n (CAT) was uniformly distributed on the surface of Ti-OH, indicating that the loading of n (CAT) by Ti-OH was achieved successfully (Figure 1E).

Characterization of Ti-gel/nAg + n (CAT)

The microscopic morphological changes of Ti, Ti-OH, and Ti-gel/nAg + n (CAT) surfaces were investigated. As can be seen in the physical image in Figure 1F, the surface of Ti-OH shows a blue metallic luster compared to Ti, while the surface of Ti-gel/nAg + n (CAT) after the drug-loaded chitosan gel coating is pale yellow. From further SEM images (Figure 1G), which showed that the Ti surface is smooth and that the Ti-OH surface showed a porous mesh structure compared to Ti. Further treatment with the drug-loaded

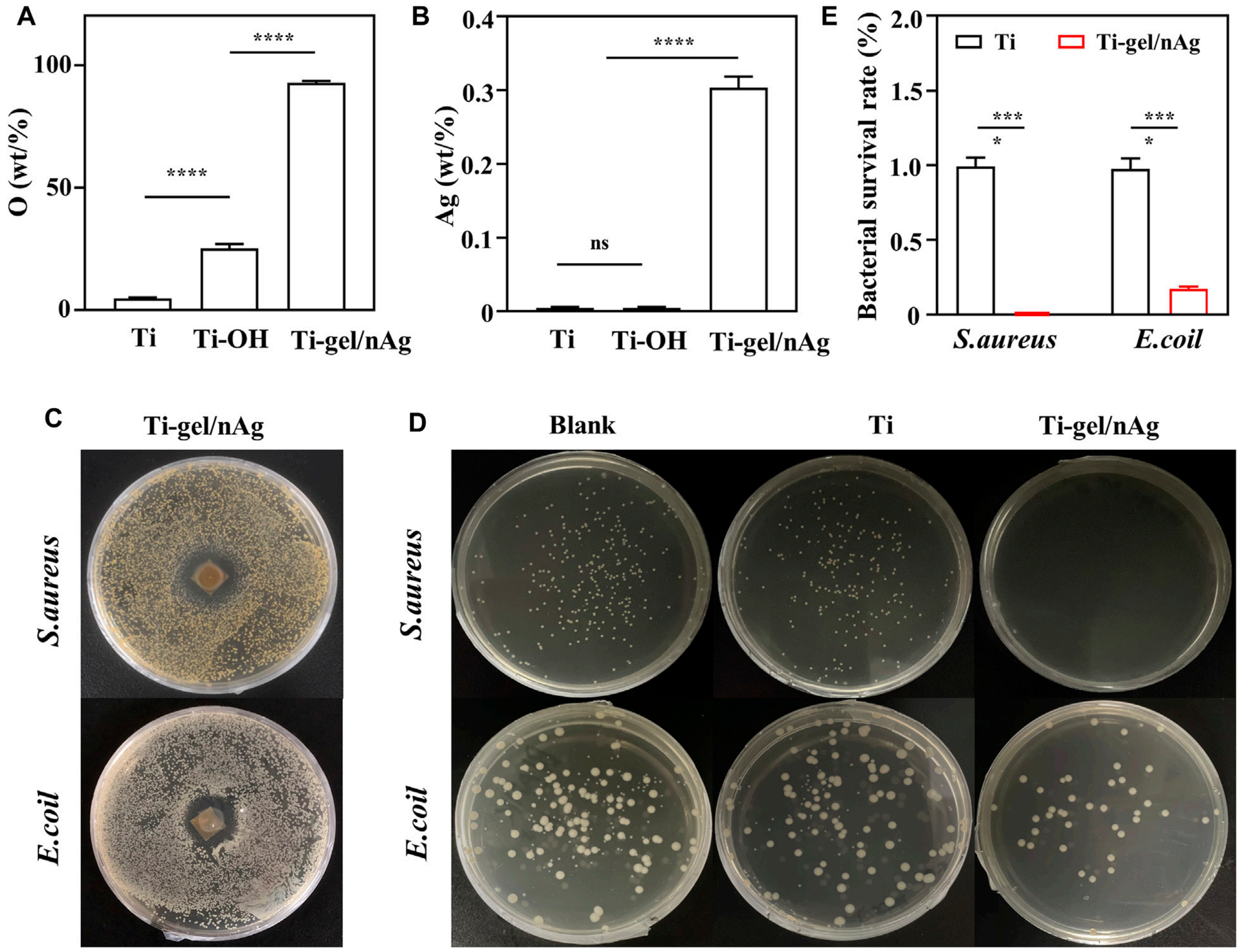

FIGURE 2
The surface elemental composition and antibacterial capacity of Ti and Ti-gel/nAg. **(A)** Relative elemental O and Ag **(B)** content of Ti, Ti-OH, and Ti-gel/nAg. **(C)** Inhibition zone of Ti and Ti-gel/nAg after co-culture with *S. aureus/E. coil* for 12 h **(D)** CFU of Ti and Ti-gel/nAg after co-culture with *S. aureus/E. coil* for 12 h **(E)** Bacterial survival of Ti and Ti-gel/nAg after co-culture with *S. aureus/E. coil* for 12 h (n = 3, ns means no significant difference, $^{***}p < 0.001$).

gel coating restored the smooth surface of Ti-gel/nAg + n (CAT). Meanwhile, the hydrophilicity of different materials' surfaces was measured by detecting the contact angle of these surfaces with water. The angle of contact with water on the surface of Ti-OH (21.8°) was found to decrease significantly compared to that of Ti (54.7°) (Figure 1H). In comparison, the water contact angle of the Ti-gel/nAg + n (CAT) surface after the drug-loaded chitosan gel coating was restored to 53.3°, basically the same as that of the untreated Ti surface. All of these results indicated that the Ti-OH surface was successfully coated with the drug-loaded chitosan gel and that the coating treatment did not affect the excellent hydrophilicity of Ti itself.

Characterization of the anti-bacterial ability of Ti-gel/nAg

The Ti-OH surface was then coated with gel-nAg to investigate the antibacterial ability of Ti-gel/nAg. The elements on the Ti, Ti-OH, and Ti-gel/nAg surfaces were determined by EDS. Supplementary Figure S2A shows the full spectrum of the point sweep energy spectra of the Ti, Ti-OH, and Ti-gel/nAg surfaces. Further semiquantitative elemental analysis of O and Ag on their surfaces revealed a significant increase in O element on the Ti-gel/nAg surface compared to Ti (Figure 2A), which was due to the high amount of oxygen in chitosan. The Ag element content also showed the same variation as oxygen (Figure 2B), demonstrating a successful loading of nAg on the surface of titanium alloy steel plates. *S. aureus* and *E. coli* as representatives of Gram-positive and Gram-negative bacteria, respectively (Huang et al., 2019), these two bacteria were selected for inhibition zone and bacterial survival tests to investigate the anti-bacterial ability of Ti-gel/nAg. After co-culture of Ti-gel/nAg on agar plates coated with *S. aureus* and *E. coli*, a clear antibacterial circle appeared in the medium (Figures 2C, D), indicating that Ti-gel/nAg had some inhibitory ability on *S. aureus* and *E. coli* growth. Furthermore, as seen by the bacterial survival test (Figure 2E), in the control medium and Ti-treated, a similar number of colony units were observed to form, while, after

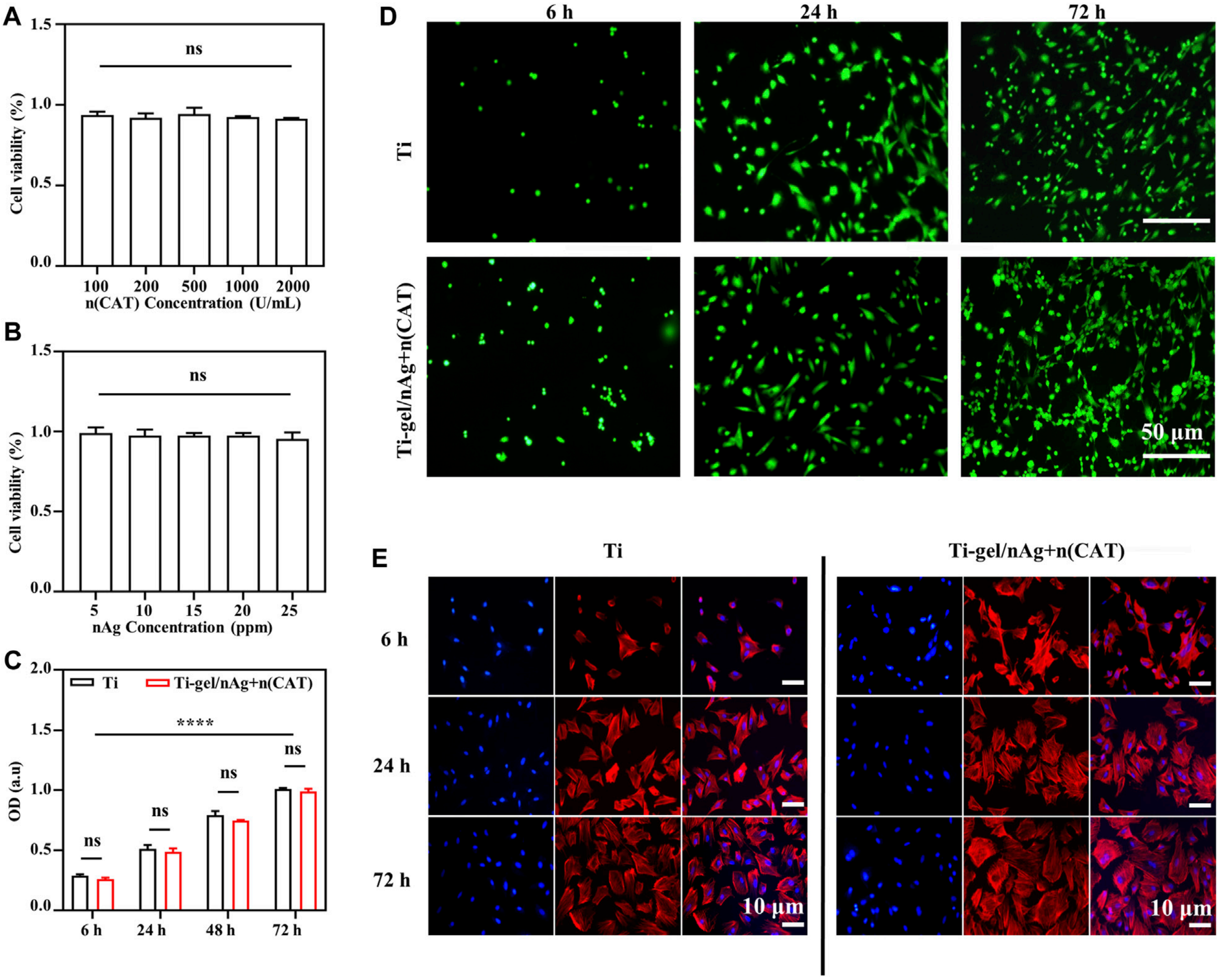

FIGURE 3
The adhesion and cell proliferation of BMSCs on the surface of Ti-gel/nAg + n (CAT). **(A,B)** Cell viability at different concentrations of n (CAT) and nAg. **(C,D)** BMSC fluorescence images adhered to different surfaces at different time points, and BMSC proliferation profiles were obtained by the CCK-8 assay. **(E)** Cell morphology of BMSCs growth on different surfaces at different time points. (n = 3, ns means that there are no significant differences, ****$p < 0.0001$).

Ti-gel/nAg treatment, no colony formation of *S. aureus* was observed in the medium. The same trend was observed in the results of the bacterial survival test for *E. coli*, with a significant reduction in the number of *E. coli* colonies in the medium after the Ti-gel/nAg treatment compared to the control and Ti-treated *E. coli* colonies. After calculating the bacterial survival rate, it was found that the survival rate of *S. aureus* in Ti-gel/nAg treatment was 0, and that of *E. coli* was only 0.17%. The above results demonstrate that Ti-gel/nAg has a good antibacterial ability.

BMSCs adhesion and proliferation on Ti-gel/nAg + n (CAT)

To test the biocompatibility of Ti-gel/nAg + n (CAT) surfaces, BMSCs were selected to investigate the effects of drug-laden chitosan gel coating on the surface of titanium alloy steel plates on cell behavior, such as value-added adhesion and cell morphology. First, the cytotoxicity of n (CAT) and nAg was investigated, and it was found that the concentration of n (CAT) enzyme activity of 100-2000u/mL (Figure 3A) and the nAg concentration of 5–25ppm were not significantly toxic to cells (Figure 3B). Then, it was found that the OD values of BMSCs in Ti and Ti-gel/nAg + n (CAT) were not significantly different at different time points in adhesion and proliferation (Figure 3C), and the OD values gradually increased with time, indicating that the cells had a good proliferation ability on the material surface. Meanwhile, consistent results were also observed on the live-dead stained fluorescence images of the Ti and Ti-gel/nAg + n (CAT) surfaces (Figure 3D), and with good cell morphology on the Ti and Ti-gel/nAg + n (CAT) surfaces at all time points (Figure 3E). All of these results collectively demonstrate the good biocompatibility of Ti-gel/nAg + n (CAT) for further application *in vitro*.

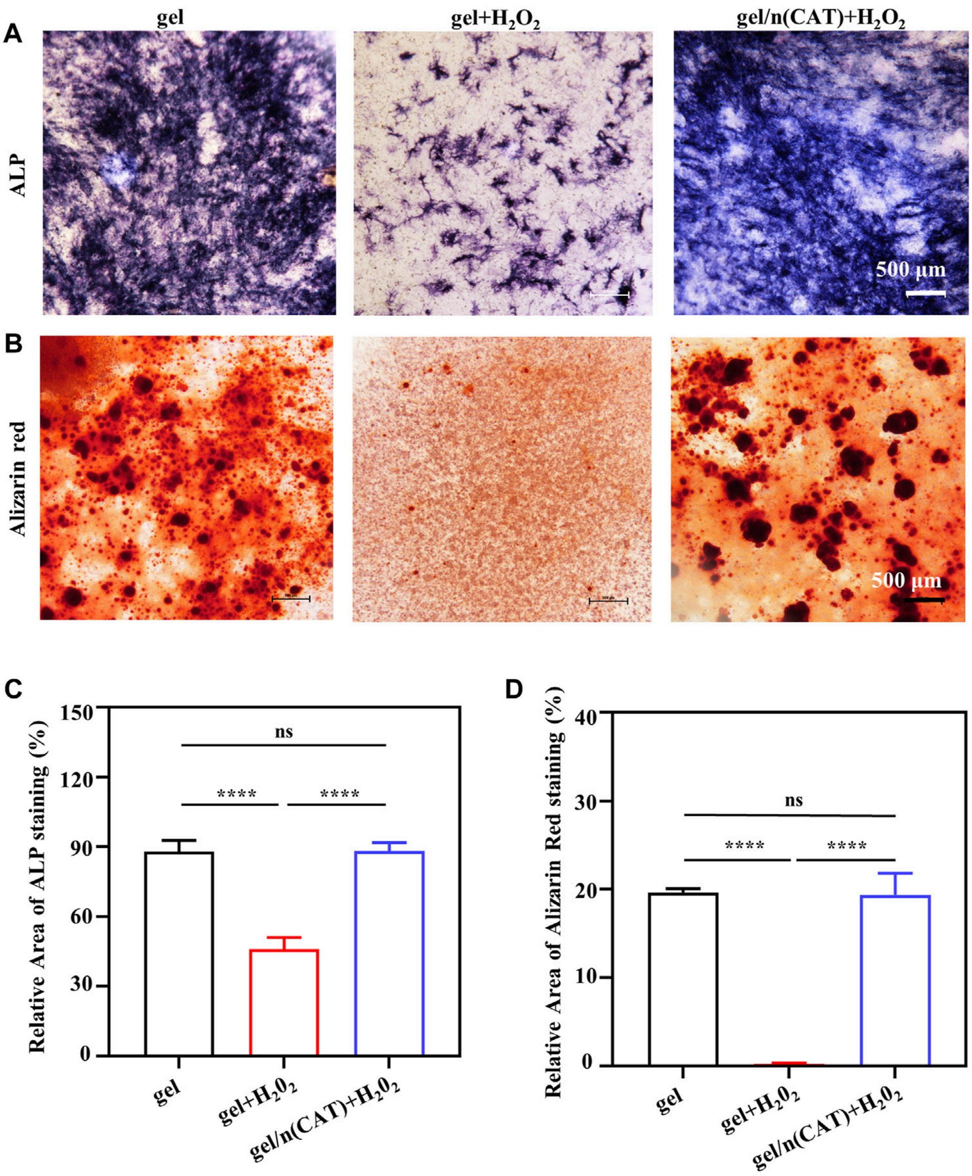

FIGURE 4
Osteogenic differentiation of osteoblasts by gel-n (CAT) in a persistent chronic inflammatory environment *in vitro*. **(A)** ALP staining of induced BMSCs for 7 days. **(B)** Alizarin Red Staining of induced BMSCs for 14 days. **(C)** Quantitative analysis of ALP and **(D)** Alizarin Red Staining images were analyzed by ImageJ software. (n = 3, ns means that there are no significant differences, ****$p < 0.0001$).

Effect of Gel/n (CAT) on osteoblasts osteogenic differentiation in a persistent chronic inflammatory environment *in Vitro*

ALP is a precise marker of the early stage of osteogenic differentiation. Meanwhile, calcium deposition is one of the vital signs and symptoms of late osteogenic differentiation, which can be specially examined using ARS. As a result of the opaque nature of the titanium alloy steel plate material, the staining phenomena ALP and ARS could not be observed. Gel/n (CAT) was used as a model for the application of Ti-gel/n (CAT) to investigate the effect of a persistent chronic inflammatory environment on osteogenic differentiation of osteoblasts on the surface of different materials. Osteoblasts on the surface of different materials were stained for ALP and ARS on day 7 and day 14 of osteogenic differentiation culture in a chronic inflammatory environment.

Figure 4A shows the ALP staining of osteoblasts on the gel surface under different environments. The degree and extent of ALP staining are significantly reduced in the chronic inflammatory environment compared to the gel in the normal environment. This is due to that the persistent chronic inflammatory environment greatly inhibits osteogenic differentiation of osteoblasts. While ALP staining of osteoblasts on the surface of gel/n (CAT) in the same persistent chronic inflammatory environment showed a significant increase in the degree and extent of ALP staining compared to gel (Figure 4A), indicating that n (CAT) effectively relieved inhibition of osteogenic differentiation of osteoblasts by the chronic inflammatory environment.

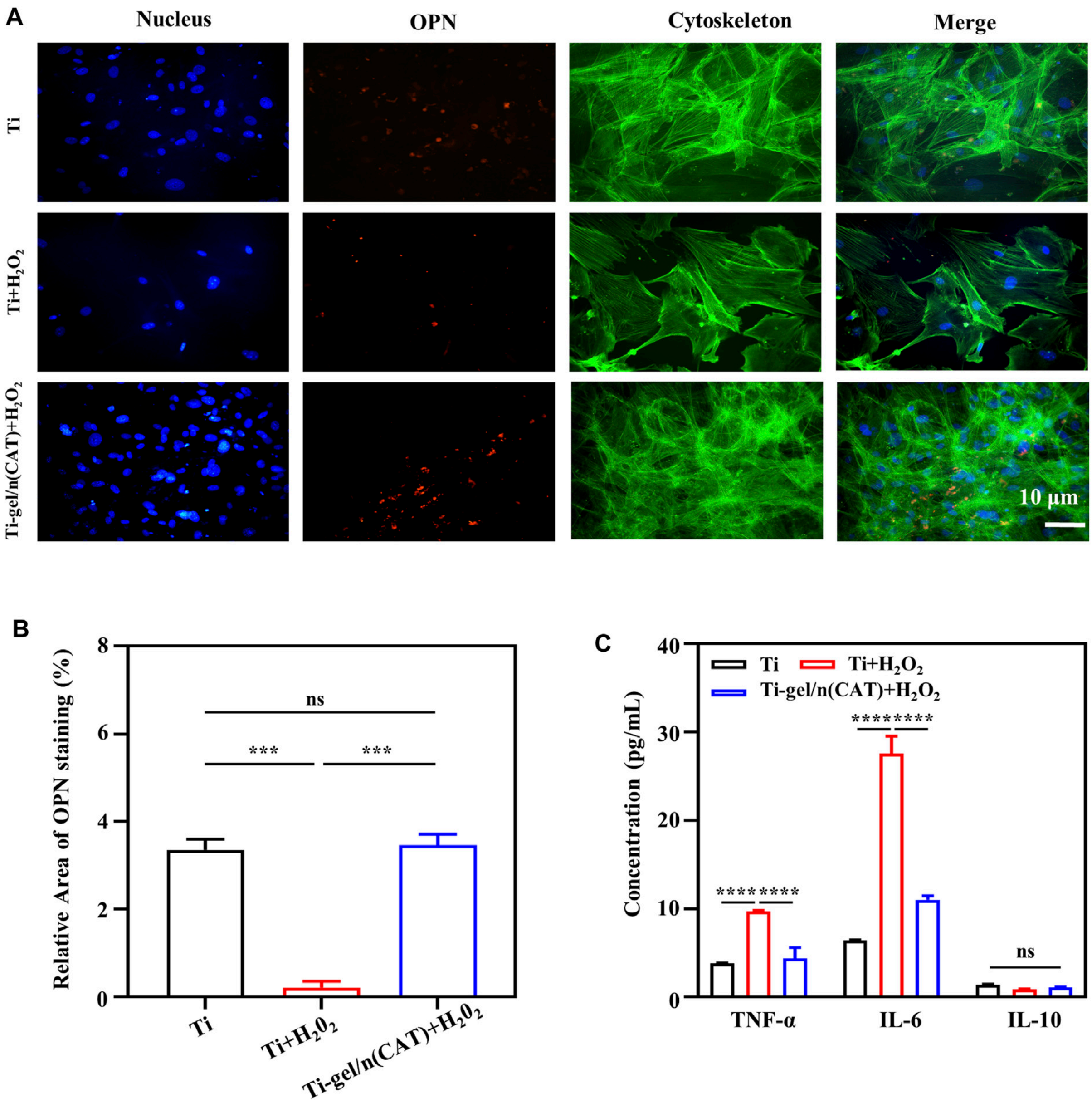

FIGURE 5
OPN expression by osteoblasts on the surface of different materials in a persistent chronic inflammatory environment. **(A,B)** Immunofluorescence images of OPN staining on different surfaces of the material. The OPN was stained in red, and the quantitative analysis of the OPN immunofluorescence images was analyzed using ImageJ software. **(C)** Cytokine expression levels of macrophages on different material surfaces. (n = 3, ns means that there are no significant differences, ***p < 0.001, ****p < 0.0001).

The ARS staining results showed the same trend as the ALP staining (Figure 4B). Furthermore, by quantifying the area of ALP and ARS staining (Figures 4C, D), it was found that the area percentage of ALP staining and ARS staining of cells on the gel surface in the persistent chronic inflammatory environment was reduced to 45.97 and 0.25 compared to 88.31 and 19.63 in the normal environment; while for osteoblasts on the gel/n (CAT) surface in the same chronic inflammatory environment, the staining area of ALP and ARS up to 88.21 and 19.35 were not significantly different from the area of ALP and ARS staining of osteoblasts on the gel surface in the normal environment (Figures 4C, D). All the results suggest that gel/n (CAT) has an excellent ability to contribute to bone differentiation in a chronic inflammatory environment.

Effect of Ti-gel/n (CAT) on osteopontin expression in osteoblasts in a persistent chronic inflammatory environment *in Vitro*

Osteopontin (OPN) is closely associated with bone formation and development. To investigate the level of osteoblast OPN expression on the surface of different materials under persistent chronic inflammatory conditions. On day 7 of the osteogenic differentiation culture in a persistent chronic inflammatory environment, immunofluorescence staining was used to investigate the expression of the OPN protein by osteoblasts on the surface of the material in different environments. The intensity of OPN fluorescence of the Ti surface was significantly weaker than that under a normal environment (Figure 5A). On the intensity of the OPN fluorescence of the Ti-gel/n (CAT) surface under the same persistent chronic inflammatory environment was significantly enhanced compared to that of the Ti-gel (Figure 5B). Further quantification result of the percentage of OPN fluorescence area showed that the persistent chronic inflammatory environment led to a decrease in the percentage of OPN fluorescence area on the Ti surface from 3.35 to 0.204. While the percentage of OPN fluorescence area on the Ti gel/n (CAT) surface reached as high as 3.46, which was not significantly different from the percentage of OPN fluorescence area on the Ti surface in normal environment. The above results fully demonstrate that Ti-gel/n (CAT) can effectively increase OPN expression in a persistent chronic inflammatory environment (Figures 5A, B) thereby promoting osteoblast osteogenesis differentiation (Figures 4A, B).

In a persistent chronic inflammatory environment, H_2O_2 can act as a signaling molecule to trigger the release of a variety of cytokines and chemokines from immune-responsive cells to enhance the inflammatory response. At the same time, pro-inflammatory factor tumor necrosis factor-α (TNF-α), pro-inflammatory factor interleukin-6 (IL-6), and anti-inflammatory factor interleukin-10 (IL-10), which are secreted by monocytes such as macrophages, play an important role in the inflammatory response (Qin et al., 2020; Li et al., 2021; Yan et al., 2022). To further explore the effect of Ti-gel/n (CAT) on the expression levels of inflammatory cytokines associated with macrophages RAW267.4 in a chronic inflammatory setting. As shown in Figure 5C, the expression levels of TNF-α and IL-6 both increased significantly in macrophages on the Ti surface in a persistent chronic inflammatory environment compared to the Ti surface in a normal environment, indicating that a persistent chronic inflammatory environment improved the expression of relevant pro-inflammatory factors. In the same chronic inflammatory environment, the expression levels of TNF-α and IL-6 cytokines were significantly reduced in macrophages on the surface of Ti-gel/n (CAT) compared to Ti. These results demonstrate that Ti-gel/n (CAT) can effectively reduce the expression of pro-inflammatory factors in the persistent chronic inflammatory environment, and its mechanism of contributing to bone in the persistent chronic inflammatory environment *in vivo* is likely to be achieved by reducing the expression levels of pro-inflammatory factors.

Conclusion

In summary, we have developed a strategy for surface functionalization of titanium alloys through functional coating of the Ti surface with chitosan gel containing nAg and n (CAT), in which nAg significantly enhanced the antibacterial ability of the Ti surface, and n (CAT) effectively promoted osteogenic differentiation of osteoblasts in a persistent chronic inflammatory environment. In addition, as a general approach, our strategy can be extended to the bioactive functionalization of other implants for various medical applications.

Data availability statement

The original contributions presented in the study are included in the article/Supplementary Material, further inquiries can be directed to the corresponding authors.

Ethics statement

The animal study was reviewed and approved by Ethics Committee of Chinese PLA General Hospital.

Author contributions

JL, XC: funding acquisition and editing. MZ and PY: conceptualization and editing. DK, YJ, TZ, XQ, and YG: performed the cell experiments and analysis. JC, MG, and FC: formal analysis. TZ, XQ, MZ, and JL: writing–original draft preparation. All authors contributed to the article have read and agreed to the published version of the manuscript.

Funding

This research was funded by China Postdoctoral Science Foundation China (Grant/Award Number: 2020M683740), Equipment research project (Grant/Award Number: LB20211A010020) and Fundamental Strengthening Project (Grant/Award Number: 2020-JCJQ-ZD-264-2-04).

Acknowledgments

We would like to thank each of the authors for their contribution to this study. And thank our families for their support.

Conflict of interest

The authors declare that the research was conducted in the absence of any commercial or financial relationships that could be construed as a potential conflict of interest.

Publisher's note

Supplementary material

The Supplementary Material for this article can be found online at: https://www.frontiersin.org/articles/10.3389/fbioe.2023.1118487/full#supplementary-material

References

Anderson, J. M. (1988). Inflammatory response to implants. *ASAIO J.* 34, 101–107. doi:10.1097/00002480-198804000-00005

Cheng, X., Pei, X., Xie, W., Chen, J., Li, Y., Wang, J., et al. (2022). pH-triggered size-tunable silver nanoparticles: Targeted aggregation for effective bacterial infection therapy. *Small* 18, e2200915. doi:10.1002/smll.202200915

Chimutengwende-Gordon, M., Pendegrass, C., Bayston, R., and Blunn, G. (2014). Preventing infection of osseointegrated transcutaneous implants: Incorporation of silver into preconditioned fibronectin-functionalized hydroxyapatite coatings suppresses *Staphylococcus aureus* colonization while promoting viable fibroblast growth *in vitro*. *Biointerphases* 9, 031010. doi:10.1116/1.4889977

Chrcanovic, B. R., Albrektsson, T., and Wennerberg, A. (2014a). Periodontally compromised vs. periodontally healthy patients and dental implants: A systematic review and meta-analysis. *J. Dent.* 42, 1509–1527. doi:10.1016/j.jdent.2014.09.013

Chrcanovic, B. R., Albrektsson, T., and Wennerberg, A. (2014b). Reasons for failures of oral implants. *J. Oral Rehabil.* 41, 443–476. doi:10.1111/joor.12157

Chuang, S. K., Wei, L. J., Douglass, C. W., and Dodson, T. B. (2002). Risk factors for dental implant failure: A strategy for the analysis of clustered failure-time observations. *J. Dent. Res.* 81, 572–577. doi:10.1177/154405910208100814

Cochis, A., Azzimonti, B., Della Valle, C., Chiesa, R., Arciola, C. R., and Rimondini, L. (2015). Biofilm formation on titanium implants counteracted by grafting gallium and silver ions. *J. Biomed. Mater Res. A* 103, 1176–1187. doi:10.1002/jbm.a.35270

Devasconcellos, P., Bose, S., Beyenal, H., Bandyopadhyay, A., and Zirkle, L. G. (2012). Antimicrobial particulate silver coatings on stainless steel implants for fracture management. *Mater Sci. Eng. C Mater Biol. Appl.* 32, 1112–1120. doi:10.1016/j.msec.2012.02.020

Donath, K., Laass, M., and GüNZL, H. J. (1992). The histopathology of different foreign-body reactions in oral soft tissue and bone tissue. *Virchows Arch. A Pathol. Anat. Histopathol.* 420, 131–137. doi:10.1007/bf02358804

Franz, S., Rammelt, S., Scharnweber, D., and Simon, J. C. (2011). Immune responses to implants - a review of the implications for the design of immunomodulatory biomaterials. *Biomaterials* 32, 6692–6709. doi:10.1016/j.biomaterials.2011.05.078

Gao, Q., Feng, T., Huang, D., Liu, P., Lin, P., Wu, Y., et al. (2019). Antibacterial and hydroxyapatite-forming coating for biomedical implants based on polypeptide-functionalized titania nanospikes. *Biomater. Sci.* 8, 278–289. doi:10.1039/c9bm01396b

Gulati, K., Prideaux, M., Kogawa, M., Lima-Marques, L., Atkins, G. J., Findlay, D. M., et al. (2017). Anodized 3D-printed titanium implants with dual micro- and nano-scale topography promote interaction with human osteoblasts and osteocyte-like cells. *J. Tissue Eng. Regen. Med.* 11, 3313–3325. doi:10.1002/term.2239

Huang, Q., Liu, X., Zhang, R., Yang, X., Lan, C., Feng, Q., et al. (2019). The development of Cu-incorporated micro/nano-topographical bio-ceramic coatings for enhanced osteoblast response. *Appl. Surf. Sci.* 465, 575–583. doi:10.1016/j.apsusc.2018.09.208

Huang, Y. H., Chen, M. H., Lee, B. H., Hsieh, K. H., Tu, Y. K., Lin, J. J., et al. (2014). Evenly distributed thin-film Ag coating on stainless plate by tricomponent Ag/silicate/PU with antimicrobial and biocompatible properties. *ACS Appl. Mater Interfaces* 6, 20324–20333. doi:10.1021/am5057213

Kim, J. Y., Choi, H., Park, J. H., Jung, H. D., and Jung, Y. S. (2020). Effects of anti-resorptive drugs on implant survival and peri-implantitis in patients with existing osseointegrated dental implants: A retrospective cohort study. *Osteoporos. Int.* 31, 1749–1758. doi:10.1007/s00198-019-05257-3

Li, B., Shan, C. L., Zhou, Q., Fang, Y., Wang, Y. L., Xu, F., et al. (2013). Synthesis, characterization, and antibacterial activity of cross-linked chitosan-glutaraldehyde. *Mar. Drugs* 11, 1534–1552. doi:10.3390/md11051534

Li, F., Yan, R., Wu, J., Han, Z., Qin, M., Liu, C., et al. (2021). An antioxidant enzyme therapeutic for sepsis. *Front. Bioeng. Biotechnol.* 9, 800684. doi:10.3389/fbioe.2021.800684

Li, Q., Shen, A., and Wang, Z. (2020). Enhanced osteogenic differentiation of BMSCs and M2-phenotype polarization of macrophages on a titanium surface modified with graphene oxide for potential implant applications. *RSC Adv.* 10, 16537–16550. doi:10.1039/c9ra10563h

Mantovani, A., Biswas, S. K., Galdiero, M. R., Sica, A., and Locati, M. (2013). Macrophage plasticity and polarization in tissue repair and remodelling. *J. Pathol.* 229, 176–185. doi:10.1002/path.4133

Muruve, N., Feng, Y., Platnich, J., Hassett, D., Irvin, R., Muruve, D., et al. (2017). A peptide-based biological coating for enhanced corrosion resistance of titanium alloy biomaterials in chloride-containing fluids. *J. Biomater. Appl.* 31, 1225–1234. doi:10.1177/0885328217692949

Qin, M., Cao, Z., Wen, J., Yu, Q., Liu, C., Wang, F., et al. (2020). An antioxidant enzyme therapeutic for COVID-19. *Adv. Mater* 32, e2004901. doi:10.1002/adma.202004901

Rao, A. J., Gibon, E., Ma, T., Yao, Z., Smith, R. L., and Goodman, S. B. (2012). Revision joint replacement, wear particles, and macrophage polarization. *Acta Biomater.* 8, 2815–2823. doi:10.1016/j.actbio.2012.03.042

Samejima, T., and Yang, J. T. (1963). Reconstitution of acid-denatured catalase. *J. Biol. Chem.* 238, 3256–3261. doi:10.1016/s0021-9258(18)48655-3

Tian, H., Du, J., Wen, J., Liu, Y., Montgomery, S. R., Scott, T. P., et al. (2016). Growth-factor nanocapsules that enable tunable controlled release for bone regeneration. *ACS Nano* 10, 7362–7369. doi:10.1021/acsnano.5b07950

Unosson, E., Rodriguez, D., Welch, K., and Engqvist, H. (2015). Reactive combinatorial synthesis and characterization of a gradient Ag-Ti oxide thin film with antibacterial properties. *Acta Biomater.* 11, 503–510. doi:10.1016/j.actbio.2014.09.048

Wang, Z., Mei, L., Liu, X., and Zhou, Q. (2021). Hierarchically hybrid biocoatings on Ti implants for enhanced antibacterial activity and osteogenesis. *Colloids Surf. B Biointerfaces* 204, 111802. doi:10.1016/j.colsurfb.2021.111802

Wu, S., Xu, J., Zou, L., Luo, S., Yao, R., Zheng, B., et al. (2021). Long-lasting renewable antibacterial porous polymeric coatings enable titanium biomaterials to prevent and treat peri-implant infection. *Nat. Commun.* 12, 3303. doi:10.1038/s41467-021-23069-0

Xiong, J., Cao, Y., Zhao, H., Chen, J., Cai, X., Li, X., et al. (2022). Cooperative antibacterial enzyme-Ag-polymer nanocomposites. *ACS Nano* 16, 19013–19024. doi:10.1021/acsnano.2c07930

Xu, D., Wu, D., Qin, M., Nih, L. R., Liu, C., Cao, Z., et al. (2019). Efficient delivery of nerve growth factors to the central nervous system for neural regeneration. *Adv. Mater* 31, e1900727. doi:10.1002/adma.201900727

Xu, N., Fu, J., Zhao, L., Chu, P. K., and Huo, K. (2020). Biofunctional elements incorporated nano/microstructured coatings on titanium implants with enhanced osteogenic and antibacterial performance. *Adv. Healthc. Mater.* 9, 2000681. doi:10.1002/adhm.202000681

Yan, R., Ren, J., Wen, J., Cao, Z., Wu, D., Qin, M., et al. (2022). Enzyme therapeutic for ischemia and reperfusion injury in organ transplantation. *Adv. Mater* 34, e2105670. doi:10.1002/adma.202105670

Yazdani-Ahmadabadi, H., Felix, D. F., Yu, K., Yeh, H. H., Luo, H. D., Khoddami, S., et al. (2022). Durable surfaces from film-forming silver assemblies for long-term zero bacterial adhesion without toxicity. *ACS Cent. Sci.* 8, 546–561. doi:10.1021/acscentsci.1c01556

Zhang, X., Xu, D., Jin, X., Liu, G., Liang, S., Wang, H., et al. (2017). Nanocapsules of therapeutic proteins with enhanced stability and long blood circulation for hyperuricemia management. *J. Control Release* 255, 54–61. doi:10.1016/j.jconrel.2017.03.019

Zhao, S., Xu, Y., Xu, W., Weng, Z., Cao, F., Wan, X., et al. (2020). Tremella-like ZnO@col-I-decorated titanium surfaces with dual-light-defined broad-spectrum antibacterial and triple osteogenic properties. *ACS Appl. Mater Interfaces* 12, 30044–30051. doi:10.1021/acsami.0c05413

Zheng, H., Tian, Y., Gao, Q., Yu, Y., Xia, X., Feng, Z., et al. (2020). Hierarchical micro-nano topography promotes cell adhesion and osteogenic differentiation via integrin α2-PI3K-akt signaling Axis. *Front. Bioeng. Biotechnol.* 8, 463. doi:10.3389/fbioe.2020.00463

Zhu, S., Nih, L., Carmichael, S. T., Lu, Y., and Segura, T. (2015). Enzyme-responsive delivery of multiple proteins with spatiotemporal control. *Adv. Mater* 27, 3620–3625. doi:10.1002/adma.201500417

frontiers | Frontiers in Bioengineering and Biotechnology

TYPE Original Research
PUBLISHED 31 March 2023
DOI 10.3389/fbioe.2023.1103709

Check for updates

OPEN ACCESS

EDITED BY
Christopher Mccormick,
University of Strathclyde, United Kingdom

REVIEWED BY
Genglei Chu,
The First Affiliated Hospital of Soochow University, China
Ting Liang,
Soochow University, China

*CORRESPONDENCE
Hongbin Liu,
✉ liuhongbin999@163.com

†These authors have contributed equally to this work

SPECIALTY SECTION
This article was submitted to Tissue Engineering and Regenerative Medicine, a section of the journal Frontiers in Bioengineering and Biotechnology

RECEIVED 20 November 2022
ACCEPTED 24 March 2023
PUBLISHED 31 March 2023

CITATION
Yu W, Zhou H, Feng X, Liang X, Wei D, Xia T, Yang B, Yan L, Zhao X and Liu H (2023), Mesenchymal stem cell secretome-loaded fibrin glue improves the healing of intestinal anastomosis. *Front. Bioeng. Biotechnol.* 11:1103709. doi: 10.3389/fbioe.2023.1103709

Mesenchymal stem cell secretome-loaded fibrin glue improves the healing of intestinal anastomosis

Wenwen Yu[1†], Haicun Zhou[2†], Xueliang Feng[1†], Xiaoqin Liang[1], Dengwen Wei[3], Tianhong Xia[4], Bin Yang[4], Long Yan[4], Xiaochen Zhao[4] and Hongbin Liu[1*]

[1]The Second Clinical Medical College, Lanzhou University, Lanzhou, China, [2]Department of Breast Surgery, Gansu Maternal and Child Healthcare Hospital, Lanzhou, China, [3]Department of Abdominal Surgery, Gansu Provincial Cancer Hospital, Gansu Provincial Academic Institute for Medical Research, Lanzhou, China, [4]Key Laboratory of Stem Cells and Gene Drugs of Gansu Province, The 940th Hospital of Joint Logistics Support Force of Chinese People's Liberation Army, Lanzhou, China

Anastomotic leakage is a serious complication following gastrointestinal surgery and one of the leading causes of patient mortality. Despite the significant clinical and economic burden, there are currently no reliable treatment options to improve the healing of intestinal anastomosis and subsequently prevent anastomotic leakage. Recently, the development of regenerative medicine has shown promise for improving anastomotic healing. Recent studies have illustrated that stem cell-derived secretome can enhance tissue regeneration without the safety and ethical limitations of stem cell transplantation. Herein, we developed a fibrin glue topical delivery system loaded with mesenchymal stem cells (MSCs)-derived secretome for controlled delivery of bioactive factors, and evaluated its application potential in improving the healing of intestinal anastomosis. Under *in vitro* conditions, the MSCs secretome significantly promoted cell proliferation viability in a dose-dependent manner and resulted in the controlled release of growth factors *via* fibrin glue delivery. We established a rat surgical anastomotic model and experimentally found that MSCs secretome-loaded fibrin glue enhanced anastomotic bursting pressure, increased granulation tissue formation and collagen deposition, and significantly promoted anastomotic healing. Mechanistically, fibrin glue accelerated cell proliferation, angiogenesis, and macrophage M2 polarization at the surgical anastomotic site by releasing bioactive factors in the secretome, and it also alleviated the inflammatory response and cell apoptosis at the anastomotic site. Our results demonstrated for the first time that MSCs-derived secretome could promote the healing of intestinal anastomosis. Considering the accessibility and safety of the cell-free secretome, we believed that secretome-loaded fibrin glue would be a cell-free therapy to accelerate the healing of intestinal anastomosis with great potential for clinical translation.

KEYWORDS

stem cell secretome, fibrin glue, anastomotic healing, cell-free therapy, drug delivery system, regenerative medicine

1 Introduction

Anastomotic leakage is a serious clinical syndrome induced by the infiltration of intestinal contents into the abdominal cavity due to failed anastomotic healing following intestinal resection and anastomosis. It can easily progress to severe abdominal infection and sepsis, and it is also one of the main causes of death (Huang et al., 2020). It has been reported that the incidence of anastomotic leakage following gastroesophageal surgery is 7%–12%, and the incidence of that after colorectal surgery is 3%–19% (Khan et al., 2012; Wang et al., 2019). It is estimated that at least one million patients worldwide suffer from anastomotic leakage-related complications after surgery annually (Rose et al., 2015). With improved surgical techniques for gastrointestinal surgery, improved surgical instruments, and accumulated experience in perioperative management in recent years, the incidence and mortality of anastomotic leakage have been reduced (Reischl et al., 2021). However, studies have shown that still more than half of patients cannot benefit from these interventions (Khan et al., 2012; Kiran et al., 2015). Therefore, unfavorable healing of surgical anastomosis has been an intractable problem in clinical practice.

Stem cell-based regenerative therapies are considered a promising scheme as stem cells have the ability to differentiate into intestinal cells or promote intestinal cell proliferation (Flatres et al., 2019; Lightner, 2019; Kent et al., 2021; Zhang et al., 2022). Several preclinical studies investigated the role of stem cell transplantation in accelerating the healing of intestinal anastomosis, and preliminary results indicated that stem cell transplantation has the potential to protect surgical anastomosis (Maruya et al., 2017; Van de Putte et al., 2017; Sukho et al., 2018; Morgan et al., 2020; Pan et al., 2020). However, the potential tumorigenicity, immune intolerance, and other safety risks related to stem cell transplantation, coupled with the strict supervision of stem cell clinical trials by regulatory authorities, have hampered the clinical translation of stem cell therapies for tissue regeneration and repair (Deng et al., 2018; Nathan and Ustun, 2019). In recent years, de-cellular modalities associated with stem cells have attracted extensive attention. Mesenchymal stem cells (MSCs) can secrete numerous bioactive components such as cytokines, growth factors, exosomes, and even extracellular matrix (Lee et al., 2017; Rahimi et al., 2021; Chouw et al., 2022; Lei et al., 2022; Tang et al., 2022), collectively referred to as the secretome, and these bioactive factors and paracrine signaling molecules exert critical roles in tissue repair and regeneration. The secretome, which can be dissolved in a medium after secretion by MSCs *in vitro*, is thus also referred to as a “conditioned medium”. Multiple fundamental studies support the application of MSC-derived secretome in the reconstruction of injured organs or tissues (Rhatomy et al., 2020; Lin et al., 2021). Furthermore, clinical trials have shown that MSCs-derived secretome is promising in the treatment of hereditary pulmonary arterial hypertension (Hansmann et al., 2022), protection against skin aging (Sushmitha et al., 2018; Liang et al., 2022), and hair regeneration (Shin et al., 2018). Although the MSCs-derived secretome holds strong potential to promote regeneration and repair, unfortunately, there are currently no reports on its role in anastomotic healing.

In light of these findings, we aimed to assess the effect of MSCs secretome on anastomotic healing in a rat model. To ensure the local release of MSCs secretome at the anastomotic site, we incorporated MSCs secretome into an FDA-approved fibrin glue (FG) and developed a topical delivery system (Secretome/FG), which could rapidly form an intestinal patch through gelatinization at the anastomotic site (Figure 1). *In vitro* experiments revealed that the MSCs secretome could boost the viability of key cells involved in wound healing dose-dependently. In a rat model of anastomosis, MSCs secretome-loaded fibrin glue (Secretome/FG) significantly improved the healing of surgical anastomosis, which might provide a novel strategy to accelerate anastomotic healing, contributing to the clinical translation of MSCs secretome-based therapies for anastomotic repair.

2 Materials and methods

2.1 Cell culture

Human umbilical vein endothelial cells (HUVEC, passage 5) and endothelial cell medium were procured from Beijing BNCC Science & Technology Co., Ltd. (Beijing, China). Human intestinal epithelial cells (Caco-2), mouse macrophages (Raw264.7), and mouse fibroblasts (L929) were commercially available from Shanghai Fuheng Science & Technology Co., Ltd. (Shanghai, China) and cultured in high-glucose Dulbecco’s modified Eagle’s medium (DMEM) supplemented with 10% FBS (Gibco, Amarillo, United States). Human umbilical cord mesenchymal stem cells (hucMSCs), donated by the Key Laboratory of Stem Cell and Gene Drug of Gansu Province, were isolated from human umbilical cord tissues and cultured in low-glucose DME containing 10% FBS (Gibco). Cells were placed in standard cell culture flasks and cultured at 37°C with 5% CO_2 and a relative humidity of 95%. The medium was renewed every 2-3 days, and upon reaching 80%-90% confluence, the cells were passaged using trypsin-EDTA (Solarbio, Beijing, China).

2.2 Preparation of MSCs secretome and Secretome/FG delivery system

Secretome was obtained from the conditioned medium of hucMSCs at passage 3–5. To obtain MSCs secretome, MSCs were plated at 2×10^6 cells per 15 cm culture dish and cultured in DMEM containing 10% FBS until 70% confluence (approximately 0.9×10^6 cells). 20 mL of serum-free medium (Gibco) without FBS was added to the MSCs and cultured for another 2 days (approximately 1.4×10^7 cells and at least 90% live cells). The supernatant was collected and centrifuged (2000×g) to remove debris and dead cells. After the removal of impurities using a 0.22 μM syringe (Beyotime, Shanghai, China), the hucMSCs conditioned medium (secretome) was collected. Secretome was concentrated using Amnicon Ultra Centrifugal Filter Units with a molecular cutoff of 3 kDa (Millipore, Germany), and the concentrated secretome was preserved in a −80°C freezer for later use. For animal study, we used 40 μL of 25-fold concentrated secretome to ultimately obtain 100 μL of 10-fold concentrated secretome (approximately 1.2 mg/mL) in the mixture with fibrin glue for injection. Fibrin glue (Specification: 5 mL; Bioseal Biotech, Guangzhou, China) is mainly consisted of fibrinogen powder and thrombin-containing catalyst fines. To

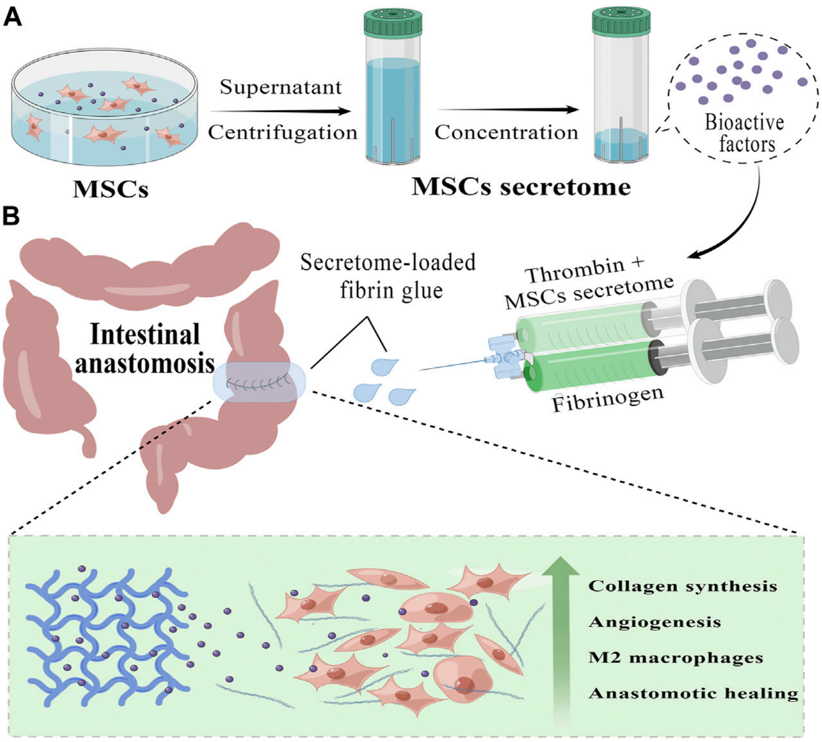

FIGURE 1
Preparation and application of MSCs secretome-loaded fibrin glue (by Figdraw). **(A)** We collect the secretome from the conditioned medium of human umbilical cord mesenchymal stem cells (hucMSCs) and further concentrate it into different secretome concentrates with protein ultrafiltration tubs, which contain a variety of bioactive factors that promote tissue repair. **(B)** Using a convenient mixed injection, we can rapidly form an MSCs secretome-loaded fibrin glue (Secretome/FG) patch covering the surgical anastomosis tightly. By slowly releasing bioactive factors, Secretome/FG promotes collagen synthesis and angiogenesis, regulates macrophage M2 polarization, and ultimately improves the healing of ischemic intestinal anastomosis.

prepare Secretome/FG, the thrombin-containing catalyst fines were first incorporated into MSCs secretome solution to produce mixed MSCs secretome-catalyst suspension. Then, the fibrinogen powder was immersed in ultrapure water to generate a fibrinogen solution. Finally, MSCs secretome-catalyst suspension and fibrinogen solution were separately filled into the two chambers of a dual-chambered syringe (Bioseal Biotech) at a 1:1 ratio, which was then equipped with a droplet head (Bioseal Biotech). Using this syringe, the solution was directly pushed and smeared onto the surgical anastomosis.

2.3 Cell proliferation assay

To analyze the pro-proliferative ability of MSCs secretome *in vitro*, cell viability was quantified using a cell counting kit-8 (CCK-8; Yeasen Biotech, China) according to the manufacturer's instructions. Briefly, MSCs were seeded into 96-well plates at a density of 1,500 cells per well and treated with 0-, 1.25-, 2.5-, 5-, 10-, and 20-fold concentrated MSCs secretome for 1, 2, and 3 days. At the end of the treatment, the medium was removed and 100 μL of medium containing 10% CCK-8 were added into each well and incubated for an hour at 37°C. The absorbance at 450 nm was measured using a microplate reader. Cell viability was calculated according to the formula {cell viability = [(As-Ab)/(Ac-Ab)]*100%}.

2.4 Measurement of growth factors

ELISA kits were employed to quantify cytokine concentrations according to the manufacturer's protocol. Growth factors to be measured include human basic fibroblast growth factor (FGF-2; Jinglai Biotechnology, Shanghai, China), human vascular endothelial growth factor (VEGF; Jinglai Biotechnology), human insulin-like growth factor 1 (IGF-1; Jinglai Biotechnology), rat transforming growth factor-β1 (TGF-β1; Jinglai Biotechnology), rat VEGF (Jinglai Biotechnology), rat FGF-2 (Jinglai Biotechnology), rat interleukin-1β (IL-1β; Jinglai Biotechnology), rat tumor necrosis factor-α (TNF-α; Jinglai Biotechnology), rat interleukin 4 (IL-4; Jinglai Biotechnology), and rat interleukin 10 (IL-10; Jinglai Biotechnology).

2.5 Controlled release ability of MSCs secretome

To assess the release of growth factors (FGF-2, VEGF, and IGF-1) from Secretome/FG, their levels were quantified by ELISA. A 100 μL fibrin glue containing 10-fold MSCs secretome was incubated at 500 μL PBS (37°C, 5% CO_2). On days 0.5, 1, 2, 3, 5, 7, 10, and 14, half of the PBS was collected. An equal volume of fresh PBS was added to the test tube for further detection. The concentration of FGF-2 released in the culture medium was measured using a human FGF-2 ELISA kit (Jinglai Biotechnology). The concentration of VEGF released in the culture medium was measured using a human VEGF ELISA kit (Jinglai Biotechnology). The concentration of IGF-1 released in the culture medium was measured with a human IGF-1 ELISA kit (Jinglai Biotechnology).

2.6 Animal experiments

Male Sprague-Dawley rats (200–220 g) were provided by the 940th Hospital of Joint Logistics Support Force of PLA and housed under a natural light/dark cycle at 25°C with free access to food and water. Rats were fasted from 12 h before surgery until 24 h after surgery. The rats were anesthetized with an intraperitoneal injection of 2% pentobarbital sodium (40 mg/kg), and their abdomens were shaved after anesthesia. Next, a laparotomy was performed using a sterile surgical technique. Through a careful exploration of the abdominal viscera, the ileum was dissected at 2 cm proximal to the cecum (ligation of the mesenteric vascular arch at the proximal and distal 0.5 cm of the ileal anastomosis before ileum dissection is essential to reduce bleeding and improve survival). After that, the broken ends of the intestinal tubes were sutured using a 6–0 absorbable surgical suture (Jinhuan, Shanghai, China), and then the ileum was ligated (anastomosis). We used 12 sutures for a full-thickness interrupted varus suture to construct the anastomosis to make it completely “sealed”. After anastomosis, to ensure no anastomotic leakage, we clipped the proximal and distal ends of the anastomosis simultaneously and injected normal saline into the vicinity of the anastomosis through a syringe fitted with a 26G needle (Shinva, Zhibo, China). No fluid outflow represented a successful surgical anastomosis. To testify to the therapeutic effect of MSCs secretome-loaded fibrin glue, rats were assigned into four groups according to different interventions, including the negative control group (NC; without any treatment after intestinal anastomosis), the MSCs secretome intravenous injection group (Secretome-iv; tail vein injection of 100 μL 10-fold MSCs secretome), the fibrin glue group (FG; smeared with 100 μL fibrin glue at surgical anastomosis), and the MSCs secretome-loaded fibrin glue group (Secretome/FG; smeared with 100 μL fibrin glue containing 10-fold MSCs secretome at surgical anastomosis). The abdomen was closed, and the rat was placed on a warm pad. The whole surgical process was done by three surgeons. The baseline conditions of rats were constantly observed after surgery, and the changes in the weight of feces and body weight were recorded. The rats were reanesthetized with sodium pentobarbital on day 7 following the operation. At first, the baseline conditions, such as intestinal adhesions, anastomotic abscesses, or infections in the abdominal cavity, were evaluated, and then the ileal anastomotic tissues were collected for further analysis. Lastly, the rats were euthanized with carbon dioxide.

2.7 Anastomotic bursting pressure assessment

The anastomotic bursting pressure is an important index reflecting the strength of anastomotic healing. After PBS washes, a 3 mm catheter was placed on one side of the isolated intestinal stump, and both sides of the stump were sutured with 3-0 silk sutures (Jinhuan) to close the lumen. The catheter was connected to an infusion syringe and a manometer, the isolated intestinal tract containing anastomosis was immersed in water, and air was injected into the intestinal tract using a syringe. The anastomotic bursting pressure was defined as the intraluminal pressure where air leakage was initially observed.

2.8 Histological analyses

On day 7 after surgery, the intestinal anastomotic tissues were collected and fixed with 4% paraformaldehyde (Servicebio, China) after PBS rinses. Next, the anastomotic tissues were embedded with paraffin and sliced into 5-μM-thick sections (surgical anastomotic tissues after repair) for later use. Histological sections were subjected to hematoxylin and eosin (HE) staining and Masson-Trichrome-Goldner (MTG) staining as per standard protocols to assess the level of inflammation, granulation tissue formation, and collagen expression in the anastomotic tissues.

Cell proliferation, angiopoiesis, and macrophage polarization in tissues were assessed by immunofluorescence. Sections were probed using Anti-CD86 (1:200; Affinity, Jiangsu, China), anti-CD206 (1: 200; Affinity), anti-CD31 (1:500; Servicebio, Wuhan, China), anti-α-SMA (1:1,000; Servicebio), and anti-Ki-67 (1:1,000; Servicebio), followed by incubation with corresponding secondary antibodies at room temperature. Ultimately, the tissues were counterstained with DAPI. Images were recorded with a fluorescence microscope (OLYMPUS, 1X71 + DP71).

2.9 TUNEL staining

To assess the apoptosis in tissues surrounding the anastomosis, TUNEL staining was performed using a Fluorescein (FITC) Tunel Cell Apoptosis Detection Kit (Servicebio) according to the manufacturer’s instructions. The percentage of apoptotic cells was determined depending on the proportion of FITC- and DAPI-positive nuclei.

2.10 Statistical analysis

All experimental data were expressed as mean ± standard deviation and analyzed statistically by GraphPad Prism 8 and SPSS 25.0 software. Statistical group comparisons were done by one-way analysis of variance (ANOVA) and *t*-test accordingly. For all comparisons, *p*-values <0.05 were considered statistically significant.

3 Results

3.1 Identification of MSCs secretome

We characterized the key components and bioactivity of the extracted MSCs secretome. At first, we determined the expression of FGF-2, VEGF, and IGF-1, which have been previously reported to be expressed in the MSCs secretome (Chen et al., 2021; Liang et al., 2022). ELISA results showed that these factors were all expressed in

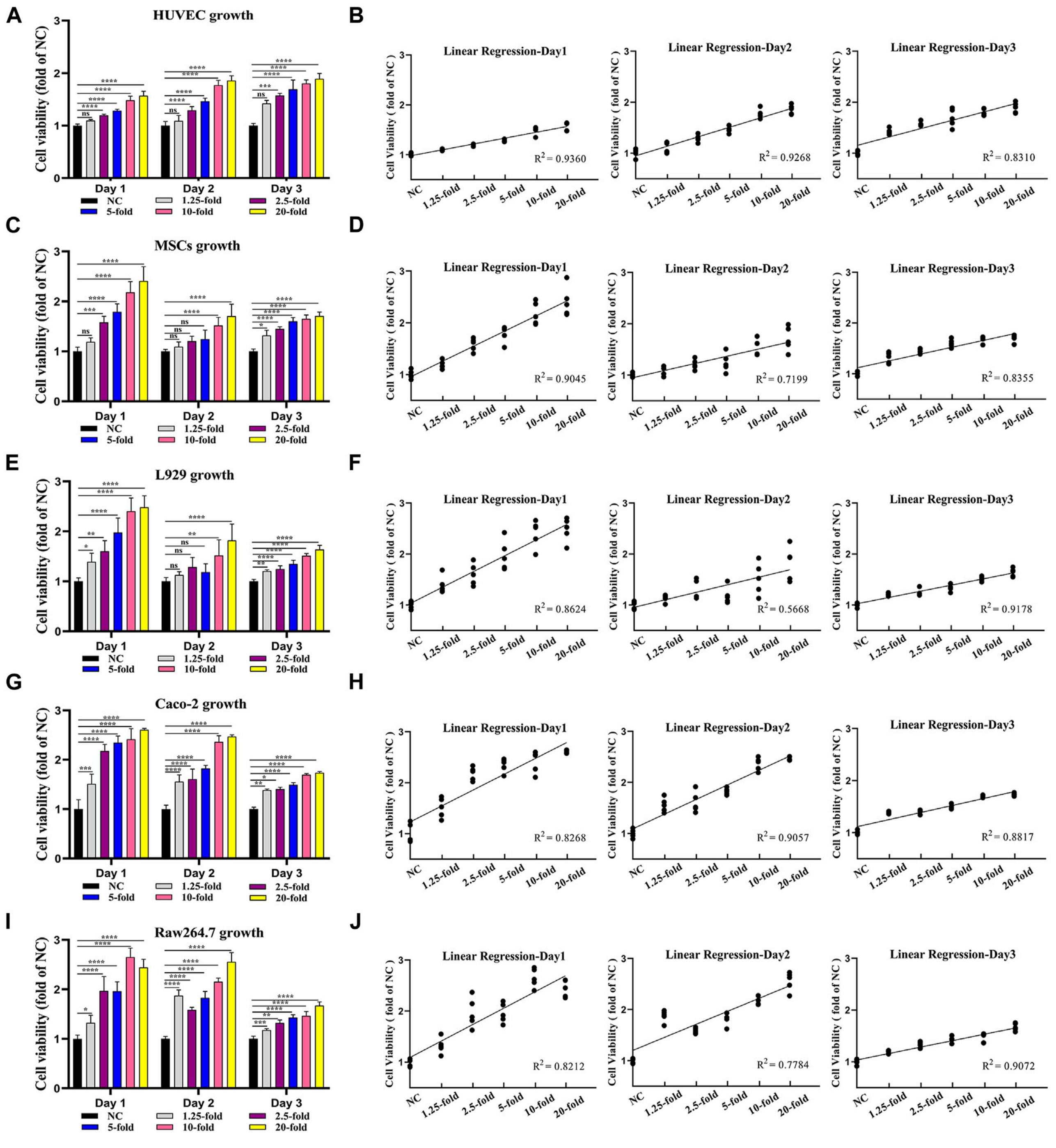

FIGURE 2
MSCs secretome enhances the viability of key cells for tissue healing in a dose-dependent manner. Vascular endothelial cells (HUVEC) **(A)**, mesenchymal stem cells (MSCs) **(C)**, fibroblasts (L929) **(E)**, intestinal epithelial cells (Caco-2) **(G)**, and macrophages (Raw264.7) **(I)** are treated with various MSCs secretome concentrations (1.25-, 2.5-, 5-, 10-, and 20-fold), and cell viability is measured using the CCK-8 assay on day 1, day 2, and day 3. The linear regression relation between MSCs secretome concentration and cell viability, including HUVEC **(B)**, MSCs **(D)**, L929 **(F)**, Caco-2 **(H)**, and Raw264.7 **(J)** ($n = 5$ per group; ANOVA). ****$p < 0.0001$, ***$p < 0.001$, **$p < 0.01$, *$p < 0.05$, ns ≥ 0.05.

the MSCs secretome. The concentrations of FGF-2, VEGF, and IGF-1 were 302.6 pg/mL, 580.01 pg/mL, and 714.05 pg/mL, respectively. Surprisingly, the aforementioned growth factors have also been reported to promote anastomotic repair (Oines et al., 2014; Li et al., 2017).

Next, to determine the bioactivity of the extracted MSCs secretome, we tested the effect of MSCs secretome on cell viability by CCK-8 assay (Figures 2A, J). Five kinds of wound healing-related cell lines (vascular endothelial cells HUVEC, mesenchymal stem cells MSCs, fibroblasts L929, intestinal

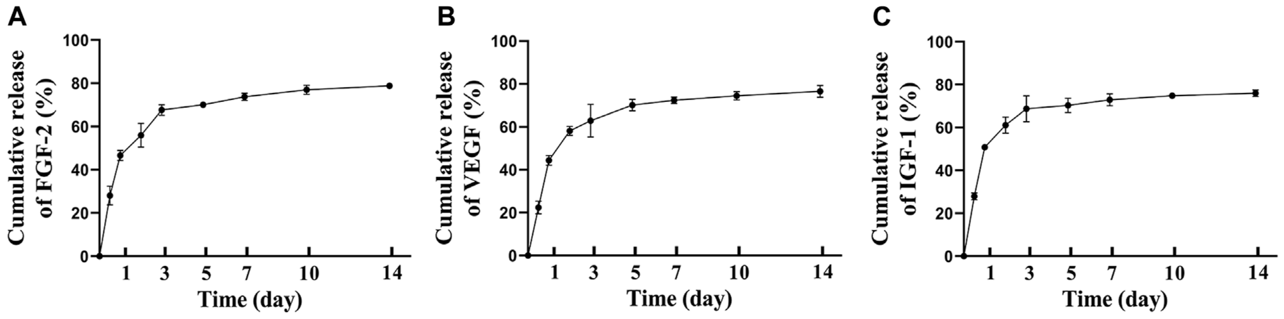

FIGURE 3
Controlled release of MSCs secretome from fibrin glue *in vitro*. The cumulative release of FGF-2**(A)**, VEGF**(B)**, IGF-1**(C)** from MSCs secretome-loaded fibrin glue; *n* = 3 per group.

epithelial cells Caco-2, and macrophages Raw264.7) were cultured in the medium containing MSCs secretome at different concentrations (1.25-, 2.5-, 5-, 10-, and 20-fold), and the cell proliferation was assessed on days 0, 1, 2, and 3. Almost all cell lines treated with MSCs secretome showed significant increases in cell numbers on days 1, 2, and 3 compared with the non-treated cells (absence of MSCs secretome). Similarly, when comparing most groups on the same day, the higher the concentration of MSCs' secretome, the greater the viability of cells (Figures 2A, C, E, G, I). To further investigate the relationship between MSCs secretome concentration and cell viability, we performed linear regression analysis. Linear regression results revealed a strong positive correlation between MSCs secretome concentration and cell viability, regardless of cell type (Figures 2B, D, F, H, J). These results indicated that the MSCs secretome could enhance cell viability in a dose-dependent manner.

Taken together, the above-mentioned results demonstrated that our collected MSCs secretome contained key growth factors and that the MSCs secretome could promote the viability of key cells involved in the healing process, showing good biological activity.

3.2 Secretome/FG could release the growth factors for up to 10 days

After incorporating MSCs secretome into fibrin glue, we analyzed the release kinetics of MSCs secretome from Secretome/FG, and the release profiles of therapeutic proteins were measured using FGF-2, VEGF, and IGF-1 as model proteins. Based on ELISA results, the cumulative protein release curves of FGF-2 (Figure 3A), VEGF (Figure 3B), and IGF-1 (Figure 3C) all showed a rapid release in the first 3 days, followed by a sustained release period of up to 7 days. It was demonstrated that the Secretome/FG delivery system could control the sustained release of bioactive factors from the MSCs secretome.

3.3 Secretome/FG improves the anastomotic healing

We then hypothesized that MSCs secretome-loaded Secretome/FG might promote surgical anastomosis healing. To verify this, we established a rat model of ischemic ileal anastomosis to test the therapeutic effects. Figure 4A shows a schematic of groups and the experimental design for a 7 days animal study. Figures 4B, C present schematic drawings of blood vessel ligation to induce ischemia in intestinal anastomosis.

Firstly, in order to determine the optimal therapeutic concentration of MSCs secretome loaded into fibrin glue, we conducted animal experiments to screen the therapeutic dose. The secretome of MSCs was loaded into fibrin glue at various concentrations (0-, 1.25-, 2.5-, 5-, 10-, and 20-fold), and six concentration gradient groups were established. After successful animal modeling, Secretome/FG containing different secretome concentrations was smeared onto the surgical anastomosis of rats using a dual-chamber syringe for treatment. The therapeutic effect was preliminary evaluated after 7 days by measuring the anastomotic bursting pressure of rats (Figure 4D). The results showed that, compared with the fibrin glue group (NC, 0-fold concentration), the anastomotic bursting pressure increased in all other treatment groups except for the 1.25-fold concentration group. Among all the treatment groups, the anastomotic bursting pressure was highest in the 10-fold and 20-fold secretome concentration groups, and no significant difference was noted between these two groups. Therefore, we chose the Secretome/FG containing 10-fold secretome as the candidate for further animal experiments (Figure 4E).

After determining the appropriate therapeutic concentration of MSCs secretome in the Secretome/FG delivery system, we developed a rat model of ischemic ileal anastomosis to evaluate the therapeutic effect of MSCs secretome. The rats were assigned into four groups according to different interventions, including the NC group, Secretome-iv group, FG group, and Secretome/FG group. No death was observed before euthanasia of the rats.

By analyzing changes in body weight after surgery, the results revealed an average increase of 6.6 g in the body weight of the Secretome/FG group, which was higher than that of other groups (Figure 4F). Also, the weight of defecation was significantly increased in the Secretome/FG group as compared to other groups (Figure 4G). It was indicated that the intestinal function and food intake of rats were restored following the treatment with Secretome/FG. On the 7th day after surgery, the rats were dissected, and abdominal adhesions were evaluated using the rating scale at

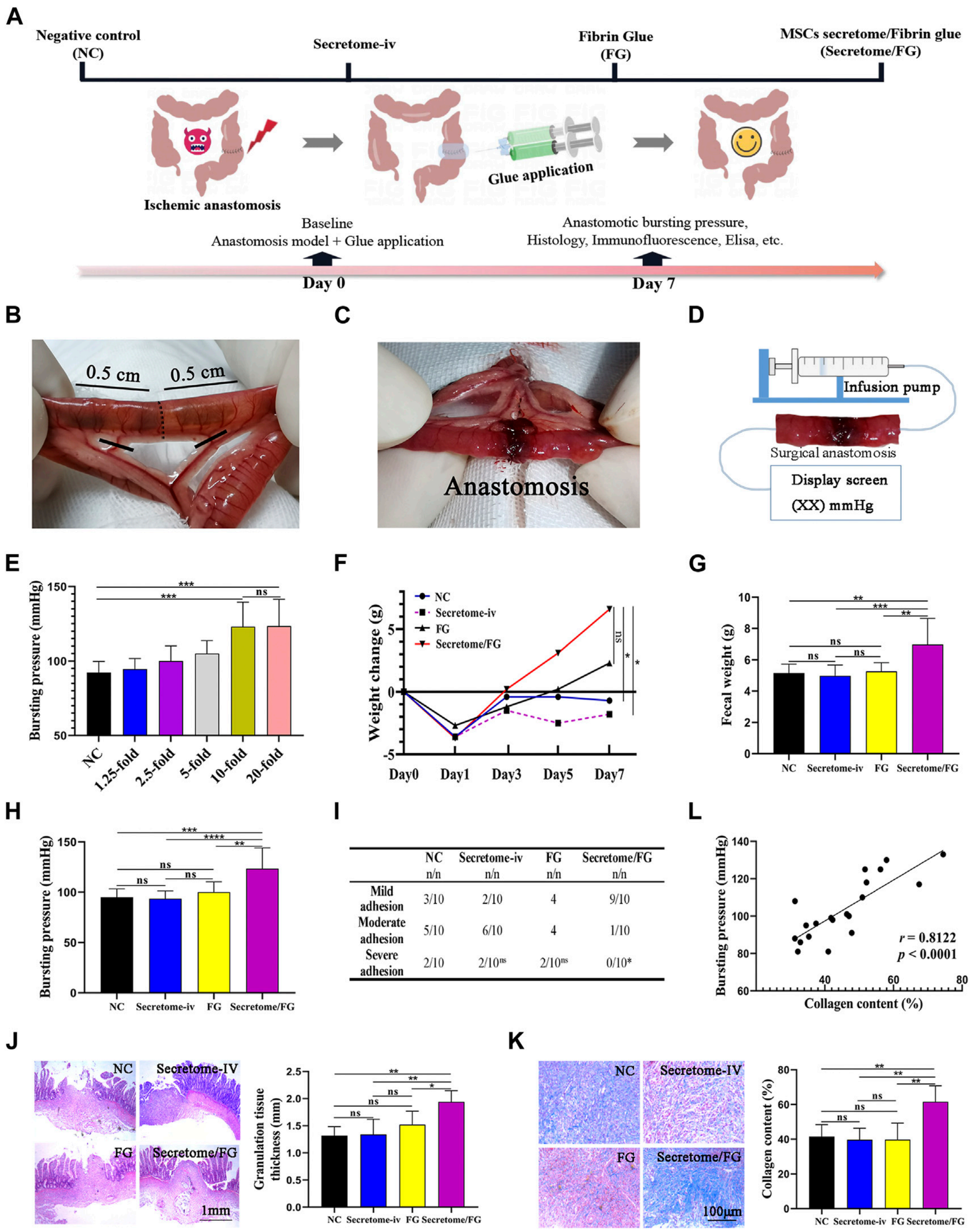

	NC n/n	Secretome-iv n/n	FG n/n	Secretome/FG n/n
Mild adhesion	3/10	2/10	4	9/10
Moderate adhesion	5/10	6/10	4	1/10
Severe adhesion	2/10	$2/10^{ns}$	$2/10^{ns}$	0/10*

FIGURE 4
MSCs secretome-loaded fibrin glue (Secretome/FG) improves intestinal anastomosis healing in a rat model. **(A)** Schematic of groups and the experimental design for a 7 days animal study. **(B, C)** Schematic drawings of blood vessel ligation to induce ischemia in intestinal anastomosis. **(D)** The method for detecting anastomotic bursting pressure, which is the maximum pressure measured by a pressure transducer during the continuous infusion of air into the sealed isolated intestine containing surgical anastomosis. **(E)** Screening of optimal secretome concentration by bursting pressure analysis of intestinal anastomosis. Overall, MSCs secretome at a concentration of 10-fold is the optimal concentration to improve intestinal anastomosis healing (*n* = 10 per group; ANOVA). **(F, G)** The change in body weight and fecal weight indicates that the rats treated with Secretome/FG promoted a significant recovery of gastrointestinal function at POD 7 compared with the negative control group (NC) (*n* = 10 per group; ANOVA). **(H)** The comparison of anastomotic bursting pressure by different interventions (*n* = 10 per group; ANOVA). **(I)** The scoring analysis reveals that Secretome/FG reduced the abdominal adhesion on the 7th day after surgery compared with other interventions (*n* = 10 per group; Chi-Square Test). **(J, K)** The histological and quantitative analysis by HE and Masson staining shows that the repair of intestinal anastomosis depends on the regenerated granulation tissues for all interventions, in which the granulation tissues are the thickest with the most collagen content for the Secretome/FG treatment (*n* = 5 per group; ANOVA). **(L)** The correlation analysis of individual bursting pressure values with collagen content (*n* = 5 per group; Pearson's correlation analysis). ****$p < 0.0001$, ***$p < 0.001$, **$p < 0.01$, *$p < 0.05$, ns ≥ 0.05.

specific sites. The results showed that all groups had varying degrees of abdominal adhesions. Whereas, compared with other groups, the adhesions between the surgical sites were reduced in the Secretome/FG group (Figure 4I). In addition, a pressure sensor was used to record the bursting pressure after slow and continuous air perfusion into the isolated small intestine. The results suggested that the Secretome/FG treatment could strengthen the healing strength of the surgical anastomosis because the bursting pressure of the rats in this group was the highest (Figure 4H).

Granulation tissue formation and collagen deposition are the main factors determining sufficient tissue strength and, thus, anastomotic healing (Thompson, Chang, and Jobe, 2006). Hence, we performed HE staining and MTG staining to assess the granulation tissue regeneration and collagen deposition at the anastomotic site. As shown in Figures 4J, K, the thickness of granulation tissues at the anastomosis was increased, and the collagen deposition was more significant in the Secretome/FG group than in other groups. In fact, the collagen content was also positively correlated with the bursting pressure of surgical anastomosis in all rats (Figure 4L). To sum up, the above-mentioned results illustrated that the Secretome/FG treatment could improve the healing strength of intestinal anastomosis in rats and increase the granulation tissue thickness and collagen content, thus improving the healing of the surgical anastomosis; whereas, the single intravenous injection of MSCs secretome exhibited no promoting effect on the anastomotic healing (Figures 4H, J, K).

3.4 Secretome/FG creates a beneficial microenvironment for the anastomotic healing

To reveal the microenvironment changes of intestinal anastomotic tissues after the treatment of secretome-loaded Secretome/FG, we conducted immunofluorescence and ELISA to examine the phenotypic changes in surgical anastomotic tissues closely related to tissue repair after different interventions, such as tissue proliferation, angiogenesis, and macrophage polarization. We first analyzed the expression of the proliferation protein Ki67 in anastomotic tissues to evaluate the proliferation surrounding the anastomosis. Immunofluorescence results exhibited that Ki67 was expressed at the highest level in the anastomotic tissues of the Secretome/FG group in comparison with the Secretome-iv, FG, and NC groups (Figure 5A). These results suggested that the Secretome/FG treatment boosted cell proliferation at the anastomotic site. Additionally, we also assessed the cell apoptosis in anastomotic tissues using TUNEL staining and found that the Secretome/FG treatment reduced cell apoptosis in tissues (Figure 5B).

As local hypoxia caused by tissue damage might affect collagen synthesis and degradation, blood perfusion is critical for the repair and protection of anastomotic tissue (Strowitzki et al., 2019). To evaluate angiogenesis, we performed a quantitative analysis of new blood vessels formed in the regenerated granulation tissues through immunofluorescent staining for CD31, a vascular biomarker. The results suggested that a large number of new blood vessels were formed after treatment with Secretome/FG (Figures 5C, D). To further validate the promoting role of Secretome/FG in cell proliferation and angiogenesis, we examined the expression of growth factors VEGF, TGF-β1, and FGF-2 in anastomotic tissues, which are key effector factors to promote cell proliferation, collagen synthesis, and angiogenesis. The ELISA results displayed the highest VEGF, TGF-β1, and FGF-2 levels in the Secretome/FG group (Figure 5E).

Excessive inflammatory cells can degrade collagen in intestinal anastomosis, and macrophages exert a crucial regulatory role in anastomotic inflammation (Thompson, Chang, and Jobe, 2006). Given the distinct cellular functions of classically activated macrophages (pro-inflammatory, M1) and alternatively activated macrophages (wound healing, M2), we examined macrophage polarization infiltrating into the anastomotic tissues through CD86 immunofluorescent staining and CD206 immunofluorescent staining, respectively. The result showed that the Secretome/FG treatment achieved the lowest proportion of M1 macrophage polarization (CD86) and the highest proportion of M2 macrophage polarization (CD206) in the regenerated granulation tissues among all of the interventions (Figures 5F, G). We then measured the expression of inflammatory factors in anastomotic tissues to further validate the anti-inflammatory and pro-reparative effects of Secretome/FG treatment, because pro- and anti-inflammatory cytokines are key effector factors underlying macrophage immunomodulatory effects. ELISA results showed that the Secretome/FG treatment reduced the levels of pro-inflammatory IL-1β and TNF-α and elevated the levels of anti-inflammatory IL-4 and IL-10 in the anastomosis (Figures 5H, I).

Collectively, these results demonstrated that the secretome-loaded Secretome/FG delivery system could facilitate cell proliferation and angiogenesis *in vivo*, regulate macrophage M2 polarization, reduce inflammatory reaction and cell apoptosis surrounding the anastomosis, and increase collagen synthesis, offering a beneficial microenvironment for rapid anastomotic healing.

4 Discussion

To our knowledge, this study was the first to investigate the application of MSCs derivatives in intestinal anastomotic repair. This study is mainly aimed at investigating the potential application of MSCs secretome-based therapy in surgical anastomosis. In this study, In order to apply MSCs secretome to the local anastomotic site to exert therapeutic effects, we developed a fibrin glue delivery system loaded with MSCs-derived secretome (Secretome/FG), which could rapidly form a stable intestinal patch *in situ* in the intestinal anastomosis after application. Our results showed that the Secretome/FG delivery system could significantly improve anastomotic healing *via* sustained release of the bioactive factors from the MSCs secretome. Specifically, upon application of the Secretome/FG at surgical anastomosis in rats, the released bioactive factors showed strong promoting effects on anastomotic healing by elevating anastomotic bursting pressure and increasing anastomotic granulation tissue regeneration and collagen deposition. Mechanistically, the MSCs secretome could enhance cell proliferation and angiogenesis, regulate the local immune response, and reduce cell apoptosis, yielding a favorable

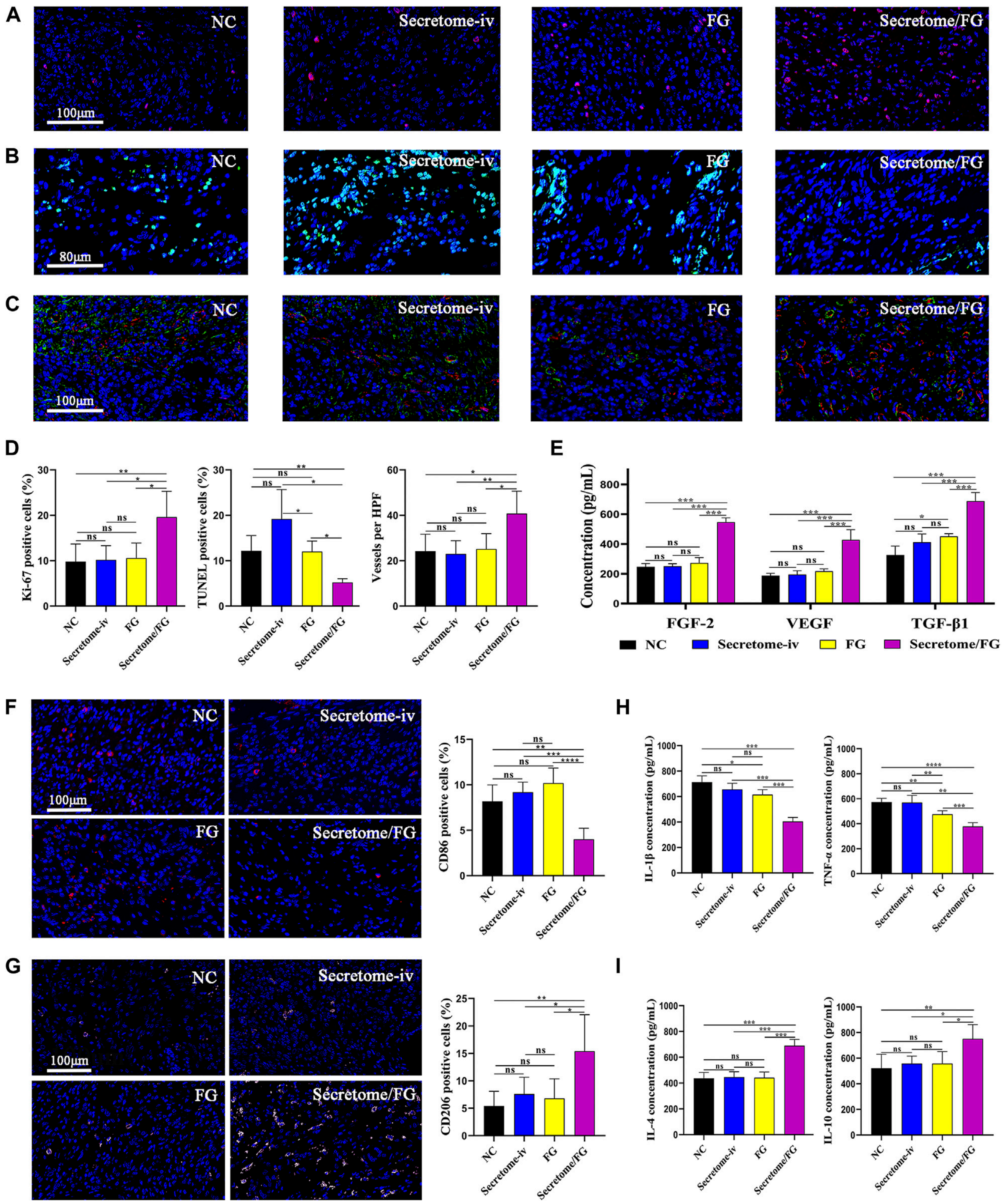

FIGURE 5
Secretome/FG creates a beneficial tissue microenvironment for the healing of intestinal anastomosis. **(A, B, and C)** Immunofluorescence staining of proliferation, apoptosis, and neovessel formation in regenerated granulation tissues for the different interventions. **(D)** Quantitative analysis of proliferation **(A)**, apoptosis **(B)**, and neovessel formation **(C)** ($n = 5$ per group; ANOVA). **(E)** Quantitative analysis of FGF-2, VEGF, and TGF-β1 in regenerated granulation tissues by ELISA for the different interventions ($n = 5$ per group; ANOVA). **(F, G)** The immunofluorescence staining results show that the Secretome/FG treatment achieves the lowest proportion of M1 macrophage polarization (CD86) and the highest proportion of M2 macrophage polarization (CD206) in the regenerated granulation tissues among all of the interventions. **(H, I)** ELISA quantification of pro-inflammatory factor (IL-1β, TNF-α) and anti-inflammatory factor (IL-4, IL-10) in regenerated granulation tissues for the different interventions ($n = 5$ per group; ANOVA). $^{****}p < 0.0001$, $^{***}p < 0.001$, $^{**}p < 0.01$, $^{*}p < 0.05$, ns ≥ 0.05.

(promoting wound healing) microenvironment in the intestinal anastomosis.

The utility of stem cell technology for the repair and regeneration of the injured intestine has been a major focus, and stem cell-based regenerative therapies hold promise for anastomotic healing (Flatres et al., 2019; Lightner, 2019; Kent et al., 2021; Zhang et al., 2022). In fact, studies have reported the utilization of stem cell patches in animal experiments to promote anastomotic healing with positive outcomes (Maruya et al., 2017; Van de Putte et al., 2017; Sukho et al., 2018; Morgan et al., 2020; Pan et al., 2020). To date, however, no stem cell-related technology has yet been implemented into clinical practice in the field of anastomotic healing, and its application may be limited by tumorigenic risk as well as low retention and survival post-transplantation (Deng et al., 2018; Nathan and Ustun, 2019). A large body of evidences have indicated that MSCs can play a significant role in tissue repair and regeneration by releasing paracrine factors such as cytokines, chemokines, hormones, and exosomes (Lee et al., 2017; Rahimi et al., 2021; Chouw et al., 2022; Lei et al., 2022; Tang et al., 2022), which are secreted into the culture medium *in vitro* known as "conditioned medium" or "secretome". As a cell-free technique, transplantation of MSCs secretome is more convenient, safer, cost-effective, and easier to preserve than transplantation of MSCs, with greater potential for clinical translation (Rhatomy et al., 2020). It is also the key reason why we chose the MSCs secretome as a therapeutic agent in our study. We harvested the secretome from the culture medium of MSCs and subsequently detected several growth factors that have been reported to promote surgical anastomotic healing, such as FGF-2, VEGF, and IGF-1 (Oines et al., 2014; Li et al., 2017), which are essential key factors involved in tissue repair and regeneration. *In vitro* studies also found that the MSCs secretome accelerated the viability of key cells involved in tissue repair in a dose-dependent manner. In the rat animal model, the secretome-loaded Secretome/FG delivery system showed strong promoting effects on healing by increasing collagen deposition surrounding the anastomosis. Similar to the promoting role of the MSCs secretome in organ repair after damage such as myocardial infarction (Tang et al., 2022), skin wounds (Lin et al., 2021), and renal injury (Yim et al., 2019), our results also demonstrated the efficacy of the MSCs secretome in improving anastomotic healing.

To improve the utilization efficiency and targetability of drugs, the application of biomaterials as drug delivery vehicles has been extensively studied (Wang et al., 2022). Fibrin glue imitates the final step of the clotting process, and because of its rapid *in situ* gelation properties, it can adhere to the tissue interface, forming a natural barrier. As a result, fibrin glue has been widely used as a hemostatic or tissue sealing agent in clinical practice for decades. In addition, to further ensure safety, tissue adhesion and gelation properties, a commercially available fibrin glue (fibrin adhesive) was used (Spicer and Mikos, 2010; Miller et al., 2019). Recently, fibrin glue has been investigated as a topical delivery carrier for growth factors or drugs, showing positive efficacy by releasing these drug proteins (Willerth et al., 2007; Whelan, Caplice, and Clover, 2014; Viale et al., 2018). Herein, to ensure safety and gelation properties, we used a commercially available fibrin glue as the carrier of MSCs secretome. Our results demonstrated that controlled delivery of the MSCs secretome through fibrin glue seemed to be an effective approach to promote surgical anastomotic repair. Firstly, our *in vitro* experiments showed that MSCs secretome-loaded fibrin glue could sustainably release FGF-2, VEGF, and IGF-1 for up to 10 days, which was similar to the findings of other studies that fibrin glue can exert therapeutic effects through the sustained release of growth factors for extended periods (Tredwell et al., 2006; Yang et al., 2009; Zhou et al., 2011; Al Kayal et al., 2022). The results of subsequent animal experiments suggested its good regenerative potential for repair and also validated fibrin glue as an effective carrier for MSCs secretome. Interestingly, intravenous administration of MSCs secretome alone did not improve anastomotic healing, and at least 10-fold intravenous administration of MSCs secretome was not as effective as topical delivery of fibrin glue loaded with the same MSCs secretome dose. It is well known that drugs administered intravenously have some limitations: 1. Susceptibility to degradation by the complex microenvironment of the circulatory system; 2. Lack of disease targeting; and 3. Poor bioavailability, often requiring an increased drug dose or frequency of administration to be therapeutically effective. This may mainly explain why the intravenous secretome (100 μL in total) did not work *in vivo* in this work. Perhaps increasing the dose or frequency of drug administration would have led to different experimental results. Meanwhile, it also revealed that the local drug delivery system described in our work has more therapeutic advantages than previous studies (Oines et al., 2014) that reported using intravenous drug administration for anastomotic repair. Since the application of the MSCs secretome for anastomosis has not been previously investigated, it has been difficult to make direct comparisons of the efficacy of different modes of administration with other studies. However, other similar studies indirectly confirmed the plausibility of our findings. In a rat model of renal ischemia-reperfusion, Tarng et al. (Tarng et al., 2016) observed improvement of the renal function only in the treatment group that was intravenously injected with highly concentrated 50-fold secretome (4 mL in total). Also, Van Koppen et al. (Van Koppen et al., 2012) observed significant changes in renal function after injection with high-dose 25-fold secretome (2 mL in total) only. However, Hyung et al. reported that, after local injection of the 100-fold or 25-fold secretome (200 μL 10-fold concentrated secretome)-loaded biomaterial into the kidney, a significant improvement was observed in renal function. These results showed the importance of the topical sustained release of bioactive factors and also implied that the topical use of biomaterials at the anastomosis for effective controlled delivery of MSCs secretome seemed to be a requisite for improving anastomotic healing.

In fact, studies in the field of intestinal anastomotic healing have employed fibrin glue as the scaffold to deliver exogenous growth factors VEGF (Li et al., 2017), and growth hormone (Li et al., 2007; Wang et al., 2009), demonstrating fibrin glue's application potential as a sustained-release carrier for growth factors. However, compared with MSCs secretome therapy, this kind of mono-factor therapy has significant disadvantages. At first, this therapy is not regulated by endogenous negative feedback mechanisms and has the potential to cause tissue hyperproliferation and carcinogenesis (Vajanto et al., 2002; Li et al., 2017; Tamburello et al., 2022). Secondly, this therapy has limited efficacy because tissue repair is accomplished by the concerted action of multiple factors, whereas MSCs secretome therapy has the advantage of containing numerous bioactive factors (Rhatomy et al., 2020). This was also substantiated by our *in vitro* and *in vivo* findings that the MSCs secretome promoted the proliferation of various cells involved in tissue repair, and the numerous bioactive factors released in animal models formed a microenvironment beneficial for granulation tissue formation and collagen synthesis.

As MSCs secretome and fibrin glue have been widely applied as a regenerative drug or tool in various diseases (Spicer and Mikos, 2010; Shin et al., 2018; Miller et al., 2019), our MSCs secretome-loaded fibrin glue delivery system could be easily modified for more interesting biological applications, thus offering great clinical therapeutic potential. In addition to the aforementioned advantage that the MSCs secretome itself is rich in multiple bioactive factors (Rhatomy et al., 2020), the MSCs secretome could be rapidly prepared and stored while being cost-effective as a therapeutic strategy, showing advantages in clinical applications. Furthermore, fibrin glue is a commercialized biomaterial that can be prepared into a variety of agents such as applicators, injections, or sprays depending on clinical treatment needs. Treatment with a combination of MSCs secretome and fibrin glue could contribute to better and faster recovery of patients from surgical anastomosis than before, thus reducing surgical risks and hospital costs.

At last, several limitations existed in this study. Although we identified that the MSCs secretome could promote tissue regeneration, the exact beneficial components of the secretome and the potential mechanisms of intestinal regeneration warrant additional investigations. A comprehensive understanding of the therapeutic efficacy of the MSCs secretome in intestinal regeneration will contribute to a more successful clinical translation of this approach. Next, there is still potential for further improvement in the controlled release properties of the fibrin-based scaffolds used in this study. The development of advanced materials with better MSCs secretome loading techniques and release properties may improve the therapeutic efficacy of secretome. Additionally, the rat model used here could not completely simulate the clinical scenario, and measures such as the mode of intestinal anastomosis and perioperative management all differ from clinical practice, leading to the possibility of some differences in the results. In the future, we intend to conduct experiments in porcine models to explore the application potential of a combined strategy based on the MSCs secretome and biomaterials for anastomotic healing, laying the foundation for future clinical trials.

5 Conclusion

MSCs secretome-based therapy is a novel and promising cell-free therapeutic strategy for tissue repair, but its role and reliable delivery system in surgical anastomotic healing remain unknown. Herein, we developed a fibrin glue delivery system loaded with MSCs secretome (Secretome/FG) to induce collagen deposition, cell proliferation, and angiogenesis and regulate macrophage polarization in surgical anastomosis *via* sustained release of bioactive factors in MSCs secretome, which provided a basis for the repair of surgical anastomotic damage. We demonstrated for the first time that the MSCs secretome could promote the healing of intestinal anastomosis. Because the raw material was easily available, simple to use, and biocompatible, this approach can be easily translated into clinical settings. Conclusively, this work demonstrated that this MSCs secretome-based cell-free therapy had significant potential for the rapid repair of intestinal anastomosis.

Date availability statement

The original contributions presented in the study are included in the article/supplementary material, further inquiries can be directed to the corresponding author.

Ethics statement

The animal study was reviewed and approved by the 940th Hospital of Joint Logistics Support Force of Chinese People's Liberation Army.

Author contributions

WY, HZ, and HL developed the concept of this study and designed the experiments. WY, HZ, XF, XL, DW, TX, BY, LY, and XZ performed experiments, data collection, and data analysis. WY, HZ, and XF performed data interpretation and manuscript writing and editing. All authors approved the final article.

Funding

This research was supported by the National Natural Science Foundation of China (No. 21772080), the Natural Science Foundation of Gansu Province (21JR1RA186, 21JR11RA173, 21JR11RA193), the Youth Science and Technology Fund Program of Gansu Province (22JR5RA1014), and the Health Industry Research Program of Gansu Province (GSWSKY 2021-043).

Conflict of interest

The authors declare that the research was conducted in the absence of any commercial or financial relationships that could be construed as a potential conflict of interest.

Publisher's note

References

Al Kayal, T., Buscemi, M., Cavallo, A., Foffa, I., Soldani, G., and Losi, P. (2022). Plasminogen-loaded fibrin scaffold as drug delivery system for wound healing applications. *Pharmaceutics* 14, 251. doi:10.3390/pharmaceutics14020251

Chen, W., Sun, Y., Gu, X., Cai, J., Chen, S., Zhang, X., et al. (2021). Conditioned medium of human bone marrow-derived stem cells promotes tendon-bone healing of the rotator cuff in a rat model. *Biomaterials* 271, 120714. doi:10.1016/j.biomaterials.2021.120714

Chouw, A., Milanda, T., Sartika, C. R., Kirana, M. N., Halim, D., and Faried, A. (2022). Potency of mesenchymal stem cell and its secretome in treating COVID-19. *Regen. Eng. Transl. Med.* 8, 43–54. doi:10.1007/s40883-021-00202-5

Deng, J., Zhang, Y., Xie, Y., Zhang, L., and Tang, P. (2018). Cell transplantation for spinal cord injury: Tumorigenicity of induced pluripotent stem cell-derived neural stem/progenitor cells, *Stem Cells Int.*, 2018, 1–7. doi:10.1155/2018/5653787

Flatres, C., Loffet, E., Neunlist, M., and Mahe, M. M. (2019). Façonner l'intestin à partir des cellules souches pluripotentes humaines. *Med. Sci. Paris.* 35, 549–555. doi:10.1051/medsci/2019096

Hansmann, G., Chouvarine, P., Diekmann, F., Giera, M., Ralser, M., Mülleder, M., et al. (2022). Human umbilical cord mesenchymal stem cell-derived treatment of severe pulmonary arterial hypertension. *Nat. Cardiovasc Res.* 1, 568–576. doi:10.1038/s44161-022-00083-z

Huang, J., Ren, H., Jiang, Y., Wu, X., and Ren, J. (2020). Technique advances in enteroatmospheric fistula isolation after open abdomen: A review and outlook. *Front. Surg.* 7, 559443. doi:10.3389/fsurg.2020.559443

Kent, I., Freund, M., Agarwal, S., and Wexner, S. (2021). The application of regenerative medicine in colorectal surgery. *Surgery* 171, 867–872. doi:10.1016/j.surg.2021.08.026

Khan, O., Nizar, S., Vasilikostas, G., and Wan, A. (2012). Minimally invasive versus open oesophagectomy for patients with oesophageal cancer: A multicentre, open-label, randomised controlled trial. *J. Thorac. Dis.* 4, 465–466. doi:10.3978/j.issn.2072-1439.2012.08.16

Kiran, R. P., Murray, A., Chiuzan, C., Estrada, D., and Forde, K. (2015). Combined preoperative mechanical bowel preparation with oral antibiotics significantly reduces surgical site infection, anastomotic leak, and ileus after colorectal surgery. *Ann. Surg.* 262, 416–425. doi:10.1097/SLA.0000000000001416

Lee, S. Y., Kwon, B., Lee, K., Son, Y. H., and Chung, S. G. (2017). Therapeutic mechanisms of human adipose-derived mesenchymal stem cells in a rat tendon injury model. *Am. J. Sports Med.* 45, 1429–1439. doi:10.1177/0363546517689874

Lei, F., Li, M., Lin, T., Zhou, H., Wang, F., and Su, X. (2022). Treatment of inflammatory bone loss in periodontitis by stem cell-derived exosomes. *Acta biomater.* 141, 333–343. doi:10.1016/j.actbio.2021.12.035

Li, Y., Bao, Y., Jiang, T., Tan, L., Liu, F., and Li, J. (2007). Combination of fibrin glue with growth hormone augments healing of incomplete intestinal anastomoses in a rat model of intra-abdominal sepsis: A dynamic study. *J. Invest. Surg.* 20, 301–306. doi:10.1080/08941930701598826

Li, Z., Wang, W., Wang, X., Jiang, L., Wang, F., and Liu, Q. (2017). Sustained-released mixture of vascular endothelial growth factor 165 and fibrin glue strengthens healing of ileal anastomoses in a rabbit model with intraperitoneal infection. *Ann. Surg. Treat. Res.* 93, 159–165. doi:10.4174/astr.2017.93.3.159

Liang, X., Li, J., Yan, Y., Xu, Y., Wang, X., Wu, H., et al. (2022). Efficacy of microneedling combined with local application of human umbilical cord-derived mesenchymal stem cells conditioned media in skin brightness and rejuvenation: A randomized controlled split-face study. *Front. Med. (Lausanne)* 9, 837332. doi:10.3389/fmed.2022.837332

Lightner, A. L. (2019). Stem cell therapies for inflammatory bowel disease. *Curr. Gastroenterol. Rep.* 21, 16. doi:10.1007/s11894-019-0672-y

Lin, H., Chen, H., Zhao, X., Chen, Z., Zhang, P., Tian, Y., et al. (2021). Advances in mesenchymal stem cell conditioned medium-mediated periodontal tissue regeneration. *J. Transl. Med.* 19, 456. doi:10.1186/s12967-021-03125-5

Maruya, Y., Kanai, N., Kobayashi, S., Koshino, K., Okano, T., Eguchi, S., et al. (2017). Autologous adipose-derived stem cell sheets enhance the strength of intestinal anastomosis. *Regen. Ther.* 7, 24–33. doi:10.1016/j.reth.2017.06.004

Miller, R., Wormald, J. C. R., Wade, R. G., and Collins, D. P. (2019). Systematic review of fibrin glue in burn wound reconstruction. *Br. J. Surg.* 106, 165–173. doi:10.1002/bjs.11045

Morgan, A., Zheng, A., Linden, K. M., Zhang, P., Brown, S. A., Carpenter, J. P., et al. (2020). Locally transplanted adipose stem cells reduce anastomotic leaks in ischemic colorectal anastomoses: A rat model. *Dis. Colon Rectum* 63, 955–964. doi:10.1097/DCR.0000000000001667

Nathan, S., and Ustun, C. (2019). Complications of stem cell transplantation that affect infections in stem cell transplant recipients, with analogies to patients with hematologic malignancies. *Infect. Dis. Clin. North Am.* 33, 331–359. doi:10.1016/j.idc.2019.01.002

Oines, M. N., Krarup, P. M., Jorgensen, L. N., and Agren, M. S. (2014). Pharmacological interventions for improved colonic anastomotic healing: A meta-analysis. *World J. Gastroenterol.* 20, 12637–12648. doi:10.3748/wjg.v20.i35.12637

Pan, H., Lam, P. K., Tong, S. W., Leung, K. K., Teoh, A. Y., and Ng, E. K. (2020). Mesenchymal stem cells combined with tissue fusion technology promoted wound healing in porcine bowel anastomosis. *Stem Cells Int.* 2020, 1–14. doi:10.1155/2020/5142797

Rahimi, B., Panahi, M., Saraygord-Afshari, N., Taheri, N., Bilici, M., Jafari, D., et al. (2021). The secretome of mesenchymal stem cells and oxidative stress: Challenges and opportunities in cell-free regenerative medicine. *Mol. Biol. Rep.* 48, 5607–5619. doi:10.1007/s11033-021-06360-7

Reischl, S., Wilhelm, D., Friess, H., and Neumann, P. A. (2021). Innovative approaches for induction of gastrointestinal anastomotic healing: An update on experimental and clinical aspects. *Langenbecks Arch. Surg.* 406, 971–980. doi:10.1007/s00423-020-01957-1

Rhatomy, S., Prasetyo, T. E., Setyawan, R., Soekarno, N. R., Romaniyanto, F., Sedjati, A. P., et al. (2020). Prospect of stem cells conditioned medium (secretome) in ligament and tendon healing: A systematic review. *Stem Cells Transl. Med.* 9, 895–902. doi:10.1002/sctm.19-0388

Rose, J., Weiser, T. G., Hider, P., Wilson, L., and Bickler, S. W. (2015). Estimated need for surgery worldwide based on prevalence of diseases: A modelling strategy for the WHO global Health estimate. *Lancet Glob. Health* 3, S13–S20. doi:10.1016/S2214-109X(15)70087-2

Shin, H., Chong, H. W., Chung, W. K., and Park, B. S. (2018). Up-to-date clinical trials of hair regeneration using conditioned media of adipose-derived stem cells in male and female pattern hair loss. *Curr. Stem Cell Res. Ther.* 12, 524–530. doi:10.2174/1574888X12666170504120244

Spicer, P. P., and Mikos, A. G. (2010). Fibrin glue as a drug delivery system. *J. Control Release* 148, 49–55. doi:10.1016/j.jconrel.2010.06.025

Strowitzki, M. J., Ritter, A. S., Kimmer, G., and Schneider, M. (2019). Hypoxia-adaptive pathways: A pharmacological target in fibrotic disease? *Pharmacol. Res.* 147, 104364. doi:10.1016/j.phrs.2019.104364

Sukho, P., Boersema, G. S. A., Kops, N., Lange, J. F., Kirpensteijn, J., Hesselink, J. W., et al. (2018). Transplantation of adipose tissue-derived stem cell sheet to reduce leakage after partial colectomy in A rat model. *J. Vis. Exp.* 138, 57213. doi:10.3791/57213

Sushmitha, S., Antara, B., Rosa, Di, Jothimani, G., Gopinath, M., Murugesan, R., et al. (2018). Concise review on clinical applications of conditioned medium derived from human umbilical cord-mesenchymal stem cells (UC-MSCs). *Int. J. Hematol. Oncol. Stem Cell Res.* 12, 230–234.

Tamburello, M., Altieri, B., Sbiera, I., Sigala, S., Berruti, A., Fassnacht, M., et al. (2022). FGF/FGFR signaling in adrenocortical development and tumorigenesis: Novel potential therapeutic targets in adrenocortical carcinoma. *Endocrine* 77, 411–418. doi:10.1007/s12020-022-03074-z

Tang, J., Cui, X., Zhang, Z., Xu, Y., Guo, J., Soliman, B. G., et al. (2022). Injection-free delivery of MSC-derived extracellular vesicles for myocardial infarction therapeutics. *Adv. Healthc. Mater* 11, e2100312. doi:10.1002/adhm.202100312

Tarng, D. C., Tseng, W. C., Lee, P. Y., Chiou, S. H., and Hsieh, S. L. (2016). Induced pluripotent stem cell-derived conditioned medium attenuates acute kidney injury by downregulating the oxidative stress-related pathway in ischemia-reperfusion rats. *Cell Transpl.* 25, 517–530. doi:10.3727/096368915X688542

Thompson, S. K., Chang, E. Y., and Jobe, B. A. (2006). Clinical review: Healing in gastrointestinal anastomoses, part I. *Microsurgery* 26, 131–136. doi:10.1002/micr.20197

Tredwell, S., Jackson, J. K., Hamilton, D., Lee, V., and Burt, H. M. (2006). Use of fibrin sealants for the localized, controlled release of cefazolin. *Can. J. Surg.* 49, 347–352.

Vajanto, I., Rissanen, T. T., Rutanen, J., Hiltunen, M. O., Tuomisto, T. T., Arve, K., et al. (2002). Evaluation of angiogenesis and side effects in ischemic rabbit hindlimbs after intramuscular injection of adenoviral vectors encoding VEGF and LacZ. *J. Gene Med.* 4, 371–380. doi:10.1002/jgm.287

Van de Putte, D., Demarquay, C., Van Daele, E., Moussa, L., Vanhove, C., Benderitter, M., et al. (2017). Adipose-derived mesenchymal stromal cells improve the healing of colonic anastomoses following high dose of irradiation through anti-inflammatory and angiogenic processes. *Cell Transpl.* 26, 1919–1930. doi:10.1177/0963689717721515

van Koppen, A., Joles, J. A., van Balkom, B. W., Lim, S. K., de Kleijn, D., Giles, R. H., et al. (2012). Human embryonic mesenchymal stem cell-derived conditioned medium rescues kidney function in rats with established chronic kidney disease. *Plos One* 7, e38746. doi:10.1371/journal.pone.0038746

Viale, M., Monticone, M., Maric, I., Giglio, V., Profumo, A., Aprile, A., et al. (2018). Characterization of drug release from fibrin gels loaded with different pharmaceutical and experimental doxorubicin formulations. *Pharmacol. Rep.* 70, 760–765. doi:10.1016/j.pharep.2018.02.014

Wang, C., Min, J. B., Kim, S. N., Park, W., Park, H. H., Kim, T. H., et al. (2022). Biomaterials as therapeutic drug carriers for inflammatory bowel disease treatment. *J. Control Release* 345, 1–19. doi:10.1016/j.jconrel.2022.02.028

Wang, F., Ren, J., Wang, G., Ren, H., Hong, Z., and Wu, X. (2019). Early active drainage by fine tube bundles improves the clinical outcome of anastomotic leak after abdominal surgery: A pilot randomized, controlled trial in two tertiary hospitals in China. *Surg. Infect. (Larchmt)* 20, 208–214. doi:10.1089/sur.2018.177

Wang, P., Wang, J., Zhang, W., Li, Y., and Li, J. (2009). Effect of the combination of fibrin glue and growth hormone on intestinal anastomoses in a pig model of traumatic shock associated with peritonitis. *World J. Surg.* 33, 567–576. doi:10.1007/s00268-008-9889-x

Whelan, D., Caplice, N. M., and Clover, A. J. (2014). Fibrin as a delivery system in wound healing tissue engineering applications. *J. Control Release* 196, 1–8. doi:10.1016/j.jconrel.2014.09.023

Willerth, S. M., Johnson, P. J., Maxwell, D. J., Parsons, S. R., Doukas, M. E., and Sakiyama-Elbert, S. E. (2007). Rationally designed peptides for controlled release of nerve growth factor from fibrin matrices. *J. Biomed. Mater Res. A* 80, 13–23. doi:10.1002/jbm.a.30844

Yang, P., Wang, C., Shi, Z., Huang, X., Dang, X., Xu, S., et al. (2009). Prefabrication of vascularized porous three-dimensional scaffold induced from rhVEGF₁₆₅: A preliminary study in rats. *Cells Tissues Organs* 189, 327–337. doi:10.1159/000142162

Yim, H. E., Kim, D. S., Chung, H. C., Shing, B., Moon, K. H., George, S. K., et al. (2019). Controlled delivery of stem cell-derived trophic factors accelerates kidney repair after renal ischemia-reperfusion injury in rats. *Stem Cells Transl. Med.* 8, 959–970. doi:10.1002/sctm.18-0222

Zhang, H. M., Yuan, S., Meng, H., Hou, X. T., Li, J., Xue, J. C., et al. (2022). Stem cell-based therapies for inflammatory bowel disease. *Int. J. Mol. Sci.* 23, 8494. doi:10.3390/ijms23158494

Zhou, W., Zhao, M., Zhao, Y., and Mou, Y. (2011). A fibrin gel loaded with chitosan nanoparticles for local delivery of rhEGF: Preparation and *in vitro* release studies. *J. Mater Sci. Mater Med.* 22, 1221–1230. doi:10.1007/s10856-011-4304-9

Frontiers in Bioengineering and Biotechnology

TYPE Original Research
PUBLISHED 04 May 2023
DOI 10.3389/fbioe.2023.1142610

EDITED BY
Junxi Wu,
University of Strathclyde, United Kingdom

REVIEWED BY
Luzhong Zhang,
Nantong University, China
Peter X. Ma,
University of Michigan, United States

*CORRESPONDENCE
Qian Chen,
✉ Qian_Chen@brown.edu

‡PRESENT ADDRESS
Shuang Zhu, Department of Joints and Orthopedics, Orthopedic Center, Zhujiang Hospital of Southern Medical University, Guangzhou, China

†These authors share first authorship

RECEIVED 11 January 2023
ACCEPTED 20 April 2023
PUBLISHED 04 May 2023

CITATION
Li NY, Vorrius B, Ge J, Qiao Z, Zhu S, Katarincic J and Chen Q (2023), Matrilin-2 within a three-dimensional lysine-modified chitosan porous scaffold enhances Schwann cell migration and axonal outgrowth for peripheral nerve regeneration.
Front. Bioeng. Biotechnol. 11:1142610.
doi: 10.3389/fbioe.2023.1142610

Matrilin-2 within a three-dimensional lysine-modified chitosan porous scaffold enhances Schwann cell migration and axonal outgrowth for peripheral nerve regeneration

Neill Y. Li[1,2†], Brandon Vorrius[1†], Jonathan Ge[1], Zhen Qiao[1], Shuang Zhu[1‡], Julia Katarincic[1] and Qian Chen[1*]

[1]Laboratory of Molecular Biology and Nanomedicine, Department of Orthopaedics, Warren Alpert Medical School of Brown University, Providence, RI, United States, [2]Department of Orthopaedics, Duke University School of Medicine, Durham, NC, United States

Background: Matrilin-2 is a key extracellular matrix protein involved in peripheral nerve regeneration. We sought to develop a biomimetic scaffold to enhance peripheral nerve regeneration by incorporating matrilin-2 within a chitosan-derived porous scaffold. We hypothesized that the use of such a novel biomaterial delivers microenvironmental cues to facilitate Schwann cell (SC) migration and enhance axonal outgrowth during peripheral nerve regeneration.

Materials and Methods: The effect of matrilin-2 on SC migration was evaluated with agarose drop migration assay on matrilin-2 coated dishes. SC adhesion was determined with SCs cultured atop tissue culture dishes coated with matrilin-2. Various formulations of chitosan vs matrilin-2 in scaffold constructs were examined with scanning electron microscopy. The effect of the matrilin-2/chitosan scaffold on SC migration in the collagen conduits was determined by capillary migration assays. Neuronal adhesion and axonal outgrowth were evaluated with three-dimensional (3D) organotypic assay of dorsal root ganglions (DRG). DRG axonal outgrowth within the scaffolds was determined by immunofluorescence staining of neurofilaments.

Results: Matrilin-2 induced SC migration and enhanced its adhesion. A formulation of 2% chitosan with matrilin-2 demonstrated an optimal 3D porous architecture for SC interaction. Matrilin-2/chitosan scaffold enabled SCs to migrate against gravity within conduits. Chemical modification of chitosan with lysine (K-chitosan) further improved DRG adhesion and axonal outgrowth than the matrilin-2/chitosan scaffold without lysine modification.

Conclusion: We developed a matrilin-2/K-chitosan scaffold to mimic extracellular matrix cues and provide a porous matrix to enhance peripheral nerve regeneration. Taking advantage of matrilin-2's capability to stimulate SC migration and adhesion, we formulated a porous matrilin-2/chitosan scaffold to support axongal outgrowth. Chemical modification of chitosan with lysine further improved matrilin-2 bioactivity in the 3D scaffold. The 3D porous matrilin-2/K-chitosan scaffolds have high potential for enhancing nerve repair by stimulating SC migration, neuronal adhesion, and axonal outgrowth.

KEYWORDS

nerve regeneration, scaffold, chitosan, matrilin-2, schwann cell, axon, porous, lysine

Introduction

Despite adequate management, patients with major peripheral nerve injuries (PNI) undertake a long recovery to regain motor and sensory function. As a result, the potential and permanence for a significant reduction in quality of life and independence are high. PNI may occur following motor vehicle accidents, penetrating wounds, or crush injuries leaving the nerve lacerated, compressed, stretched, or avulsed (Rotshenker, 2015). Depending on the state and chronicity of the injury, the nerve may not be amenable to repair by primary end-to-end coaptation. If there is nerve loss or need for excision in which direct repair would cause excessive tension, means to reconstruct the gap through artificial conduit, acellular nerve allograft (ANA), or autograft may be utilized depending on the distance to reconstruct.

Currently, the use of conduits *versus* allograft or autograft depends on the extent of nerve injury and the length of gapping between nerve ends that require repair (Ducic et al., 2012). Nerve conduits have been produced from a variety of materials including type I collagen, polyglycolic acid, porcine small intestine submucosa, and chitosan (Zhang et al., 2021; Zhang et al., 2022; Wang et al., 2023). The tubular and hollow structure may restrict the use of conduits to short gaps of around 5 mm with a maximum of less than 10 mm in small nerve diameters as their construction lacks the internal architecture to support more considerable cross-sectional regeneration and distances (Shin et al., 2009; Giusti et al., 2012; Lin et al., 2013). For longer gaps, ANAs have become more commonly used. ANAs provide the native architecture and platform for regeneration, but the processing and use of detergents to remove cells, extracellular matrix (ECM) proteins, and growth factors conducive to nerve regeneration, limit the length and robustness of regeneration that become more suited for nerve autograft. Autografts are the gold standard for bridging gaps in PNI. The use of autograft provides the native architecture and proteins that critically form the ECM as well as growth factors to facilitate the best microenvironment for regeneration. However, harvesting nerve from another part of the body can lead to adverse effects such as incision site complications, neuromas at the repair site, and loss of sensory function (Giusti et al., 2012).

Given the positives and negatives of each modality, we sought to construct a readily available graft that features a biomimetic scaffold within a multichannel three-dimensional cross-sectional architecture inherent to nerves to bridge longer gaps than currently used conduits to achieve a more robust regenerative response. To initiate a biomimetic environment, we sought to exploit the properties of the ECM protein family of matrilins (Wang et al., 2014). In nerve, matrilin-2 is expressed in the perineurium and upregulated by Schwann cells (SCs) following injury (Korpos et al., 2015). Matrilin-2 belongs to an oligomeric multi-adhesion adaptor protein family named matrilins with a wide distribution in the ECM of different tissues. They interact among various ECM ligands including collagen, fibrillin, laminin, and fibronectin (Piecha et al., 1999). Such interactions are mediated by the metal-ion-dependent adhesion site (MIDAS) (Kim et al., 2016). Notably, the lysine residue is often involved in the interaction of ECM ligands (Mäki et al., 2005). The broad distribution of matrilin-2 allows it to mediate ECM protein adhesion and assembly (Segat et al., 2000; Piecha et al., 2002). Matrilin-2 enhances axonal outgrowth and SC migration upon its application *in-vitro* and *ex-vivo* and further verified in MATN2 knockout mouse models (Malin et al., 2009).

The aim of this study is to utilize matrilin-2 in a reconstructive environment for nerve repair. We hypothesized that increased cross-sectional and longitudinal presence of matrilin-2 improves the ability for SCs to adhere and migrate, thereby enhancing the rate of axonal outgrowth and ultimately neural regeneration. To test this hypothesis, we first examined whether matrilin-2 maintained chemotactic properties of SC migration *in vitro*. We then developed a scaffold with the cross-sectional architecture that hosts matrilin-2 utilizing material well suited in a neural regenerative environment. Utilizing iterations of the scaffold, we demonstrate that axonal outgrowth of neonatal dorsal root ganglions (DRG) was improved compared to currently used conduits. We further identified that chemical modification of chitosan with lysine further improved neuronal adhesion, SC migration, and axonal outgrowth by enhancing matrilin-2 conjugation to form matrilin-2/K-chitosan scaffold.

Materials and methods

Cell culture

S16 SCs were purchased from American Type Culture Collection (ATCC, Manassas, VA) and were cultured per ATCC protocol in DMEM/F-12 supplemented with 10% FBS and 1% Penicillin-Streptomycin. All media and supplements were purchased from Thermo Fisher Scientific (Waltham, MA).

Agarose migration and cell adhesion assays

Recombinant human matrilin-2 protein was purchased from R&D systems (Minneapolis, MN), coated onto 22 mm tissue glass coverslips at 20ug/ml as described previously (Malin et al., 2009) and incubated overnight. The agarose migration assay was performed as previously described (Chernousov et al., 2001). The agarose for the drop migration assay was diluted to a 0.03% concentration. After 24 h of incubation, the cells were visualized under phase-contrast microscopy.

For cellular adhesion, SCs were placed atop matrilin-2 coated plates and incubated for 24 h. Cells were then fixed at room temperature with 4% paraformaldehyde for 10 min. Subsequently, cells were washed with PBS, followed by permeabilization for 30 min using 0.1% Triton X-100. Cells were stained with rhodamine phalloidin (Cell Signaling Technology, Danvers, MA) for immunofluorescent imaging. After 30 min, the cells were washed three times with PBS and incubated in 4′,6′-diamidino-2-phenylindole dihydrochloride (1:1,000; Sigma-Aldrich, St. Louis, MO) for 5 min at room temperature to counterstain the cell

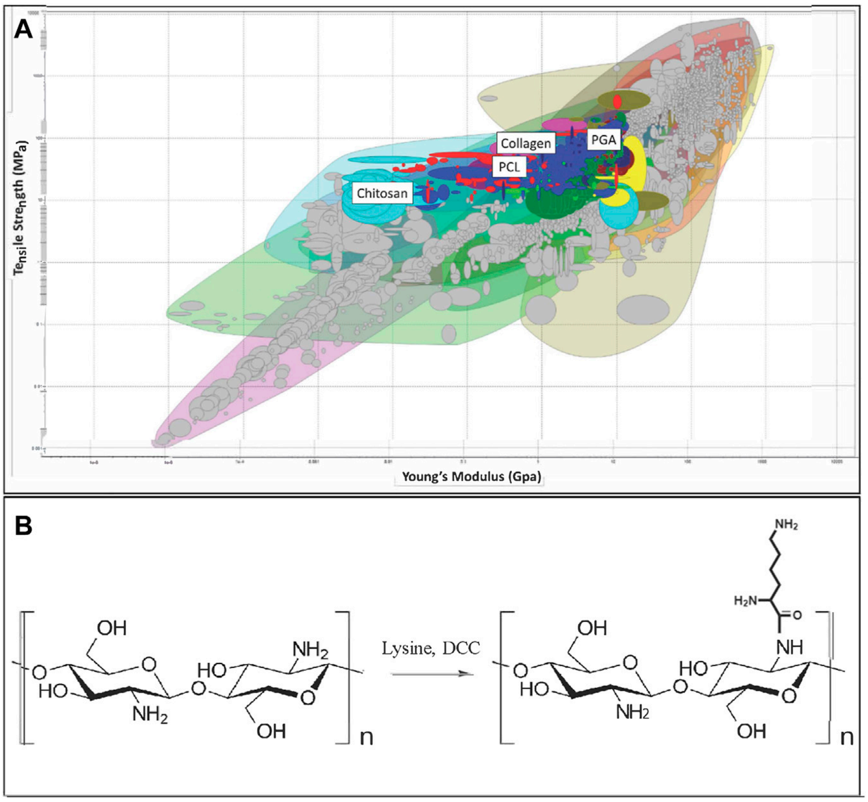

FIGURE 1
(A) Initial array of materials with tensile strength and Young's Modulus as constraints. Materials highlighted include Polyglycolic Acid (PGA), Polycaprolactone (PCL), collagen, and chitosan. **(B)** Chitosan structure (Left) and chemical modification of chitosan by Lysine (K-chitosan).

nuclei. The specimens were washed three times with PBS, each for 5 min, and were then mounted with an antifade solution. Immunolabeled cells were examined *via* fluorescence microscopy (Zeiss Axiovision Z1, Oberkochen, Germany). All experiments were carried out in triplicate.

Material survey and evaluation

Given the wide variety of materials previously utilized for nerve repair, a material selection search was performed to determine an ideal material to interact with matrilin-2 in the formation of a scaffold. The CES Edupack Database of Natural and Man-Made materials (Ansys, Canonsburg, PA) was utilized to comprehensively examine available options. The database was used with an initial filter of material of tensile strength of 12–100 Megapascals. The following parameter was Young's Modulus with biological reference to 0.067 GPa for peripheral nerves (Borschel et al., 2003). This was set to a constraint of 0.005–10 Gigapascals (GPa). This range included polymer-based rubbers as a point of interest as well as chitosan (0.014 GPa), which has the lowest Young's Modulus of the currently used materials in nerve conduits. The upper constraint of the modulus was set to 10.0 GPa to include a large variance of potential materials. PGA had the highest Young's Modulus of currently used materials with 6.1–7.2 GPa (Figure 1A).

Scaffold formulation with Matrilin-2 and chitosan

Unless otherwise specified, all chemicals were obtained from Sigma-Aldrich (St. Louis, MO). Chitosan was dissolved in acetic acid in the development of various concentrations of chitosan at 1%, 2%, and 3%. Matrilin-2 was then added within a physiologic concentration level of 10 ug/mL as exemplified by Malin et al. (Jonas et al., 2014). 50uL of solutions were then pipetted into 2 mm × 2 mm sectioned pieces of a collagen conduit (Integra, Princeton, NJ). These units were then flash-frozen and lyophilized. Scaffolds were then fixed and imaged under scanning electron microscopy to detail their microarchitecture.

Capillary migration study

S16 SCs were cultured as described above and stained with Vybrant Dil Cell-Labeling Solution (ThermoFisher Scientific, Waltham, MA). The cells were then seeded into a 24-well cell culture plate. A 5 mm long empty or scaffold-filled conduit was then placed vertically atop the cells, in which the cross-section of the conduit faced the cells. SCs were incubated for 24 h to allow for migration up the conduit and/or scaffold. The conduits were then longitudinally sectioned and fixed onto slides to visualize the SC migration under fluorescence.

Chitosan modification with lysine

To improve upon neuronal and SC interaction with matrilin-2 given poor adherence of DRGs during the 3D organotypic assay, chitosan was modified with lysine to enhance conjugation with matrilin-2 (Figure 1B). 100ml of 2% (w/v) chitosan aqueous solution was prepared with the addition of 1% (v/v%) acetic acid solution under vigorous mechanical stirring at room temperature to form homogeneous gel. Lysine was added at a lower molar ratio (0.1mM, 0.0146 g) than the free amine groups on the chitosan chain. The solution was stirred for 1 h to again form a homogeneous gel. Afterwards, 0.1mMol (0.0206 g) DCC (N,N′-Dicyclohexylcarbodiimide), dissolved in 150 µl 99% ethanol, was added to trigger the coupling reaction of chitosan and lysine. This reaction was carried out in room temperature, with gentle agitation for 1 h. Upon reaction completion, the gel was filtered to remove dicyclohexylurea (DCU). For crosslinking of lysine-modified chitosan (K-chitosan), 100 µl glutaraldehyde (25% in H_2O) was added dropwise into the gel solution under vigorous stirring. The pH of the above system was then adjusted to 10.0 using NaOH (10% w/v) to instigate a crosslinking reaction for 2 h at 60 °C. The gel was then filtered and purified with DI-H2O in a dialysis bag for 4 h to remove unreacted chemicals and side products (trace amount DCU *etc.*). Matrilin-2 was then added in a similar fashion as described above to construct the matrilin-2 conjugated K-chitosan scaffold (matrilin-2/K-chitosan).

Three-dimensional organotypic assay for DRG-Based axonal outgrowth

The assay was performed as described by (Tajdaran et al., 2019). Rat DRGs were purchased from BrainBits LLC (Springfield, IL). 2mm diameter collagen conduits were sectioned into 5 mm lengths. The conduits were separated into three groups: 1) collagen conduit with chitosan scaffold only, 2) conduit with matrilin-2/chitosan scaffold, and 3) conduit with matrilin-2/K-chitosan scaffold. Each conduit was placed separately into a 9-well tissue culture dish with each filled with media composed of neurobasal media, B27 supplement at 50X, NGF at 50 ng/ml, 1% Pencillin/Streptomycin, and Glutamax 100X. The conduits and associated scaffolds were allowed to incubate in the neurobasal media for 4 h at 37C. DRGs were then placed into each conduit or conduit and scaffold and allowed to incubate for 48 h at 37C.

After incubation, media was removed from the wells and the conduits were rinsed with PBS x 5 min, three times. Paraformaldehyde 4% was then used to fix the DRG and conduits overnight. The DRG and conduits were then rinsed with PBS x 5 min, 3 times, and then placed in incremental increases of sucrose starting with 10%–20% to 30% which was soaked overnight. The samples were then placed into trays and frozen individually in O.C.T compound embedding medium. The samples were cryosectioned longitudinally at the 200, 400, 600, 800, 1,000, 1,200, 1,400, 1,600, and 1800 µm levels and cut at 10 µm thickness. The collected sections were then processed for H&E and immunofluorescence staining. For immunofluorescence analysis, sections were washed, blocked (5% normal goat serum), and incubated with Anti-Neurofilament-L mouse monoclonal antibody (1:50, Santa Cruz) overnight at 4C. The sections were then washed and incubated with donkey anti-mouse Alexa Fluor 568 (1:200, In) for 2 h at room temperature. Sections were then washed and visualized under fluorescent microscopy.

Results

Selection of chitosan as a structural scaffold

We selected polymer candidates for a nerve regeneration scaffold by considering material properties as described in Methods and Materials (Figure 1A). We set the minimum tensile strength to 12 MPa and eliminated materials lacking appropriate elasticity according to the Young’s Modulus (Supplementary Figure S1). PGA, one of the previously described materials utilized for nerve conduits, was eliminated according to these criteria (Figure 1A). Next, by applying the criterion “Biological and natural materials,” the search was refined to include only chitosan, collagen, and collagen-related natural materials leather, and ligament (Supplementary Figure S1). This refinement was made because the biocompatibility of these materials would be important to interact with extracellular matrix proteins, growth factors, and chemokines, while also permitting cellular adherence.

We ultimately chose chitosan as the scaffold-forming material, taking into consideration that chitosan has a lower Young’s Modulus than that of collagen and peripheral nerve. This property could be beneficial as chitosan poses less resistance to stretching and yet maintains the tensile strength of a normal nerve. Such material property not only reduces the likelihood of material tearing during manufacturing, but also allows SCs to migrate and guide axonal regeneration during movement at the reconstruction site. We expect that as the SCs produce matrix during the regenerative process, the Young’s Modulus would be increased to approximate that of a healthy nerve (Borschel et al., 2003). Thus, we selected chitosan as the primary structural component of the scaffold within a collagen conduit. Previous tissue engineering research found success with chitosan and collagen interaction to improve mechanical strength, biodegradation rate, and cell proliferation, which are crucial for optimal axonal regeneration (Ma et al., 2003; Tangsadthakun et al., 2006).

Matrilin-2 increased Schwann cell migration and adhesion

To determine the suitability of matrilin-2 as a bioactive component of the scaffold for nerve repair, we quantified its effect on Schwann Cell (SC) migration and adhesion. Agarose drop migration assay demonstrated a significantly greater migration of SCs atop matrilin-2 compared to no-matrilin-2 (Figures 2A,B). There was a significant increase in SC migration distance (180 ± 20 µm) atop matrilin-2 compared to no-matrilin-2 (0 µm) ($p < 0.0001$) (Figure 2C). SC adhesion was also significantly improved when incubated with matrilin-2 compared to no-matrilin-2 (Figures 2D,E). Quantification of adhered cells demonstrated a significantly greater adhesion profile on matrilin-2 compared to no-matrilin-2 ($p < 0.001$) (Figure 2F).

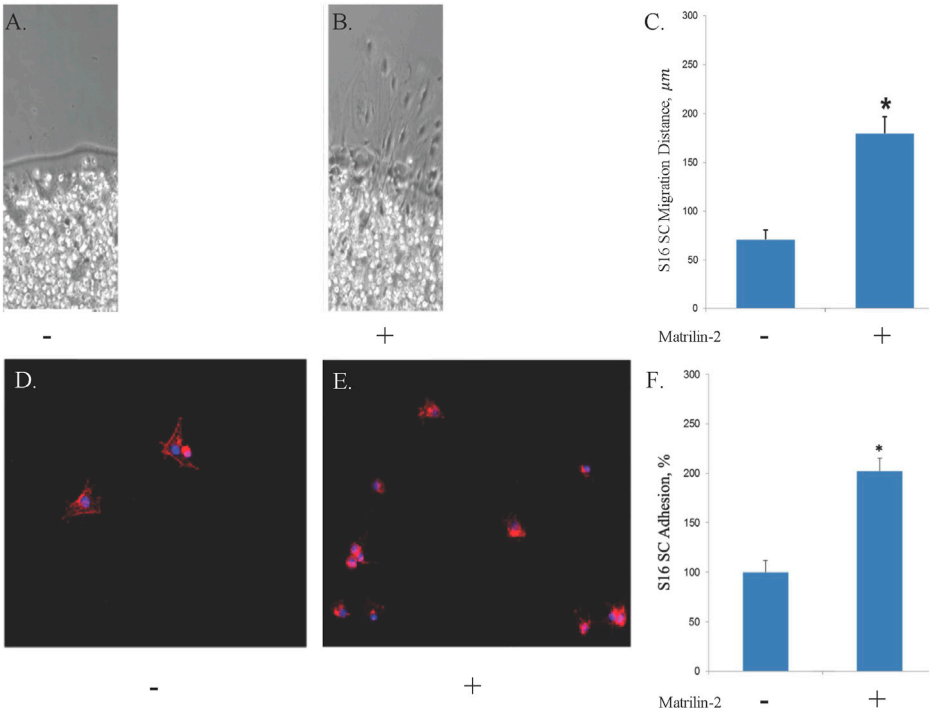

FIGURE 2
A-C, S16 SC agarose drop migration assay visualized by phase-contrast microscopy. Tissue glass coverslips coated with **(A)** ribonuclease-free water or **(B)** matrilin-2. Scale bar: 20 μm. **(C)** Quantification of migration distances noting significantly increased migration atop matrilin-2 compared to water. * denotes statistical significance of $p < 0.0001$. D-F, Fluorescent microscopy of Schwann cell adherence on tissue glass covered with **(D)** ribonuclease-free water and **(E)** matrilin-2. **(F)** Fluorescent profile denoting cellular presence was measured with Matrilin-2 compared against water noting a significantly greater presence of fluorescence and cellular adherence with matrilin-2. * denotes statistical significance of $p < 0.01$.

Matrilin-2/chitosan Scaffold induced SC migration within the collagen conduit

To test different formulations of the matrilin-2/chitosan scaffold within the collagen conduit, we performed scanning electron microscopy (SEM) imaging. A collagen conduit by itself presented a cross-sectional internal hollow tubular structure (Figure 3A). Matrilin-2 with 2% chitosan formed an internal scaffold with porous structures (Figure 3B). The pore sizes measured around 50 μm (Figure 3D). In contrast, matrilin-2 with 3% chitosan formed an amorphous scaffold without regular-sized pores (Figure 3C). The scaffold composed of matrilin-2 with 2% chitosan, referred to as matrilin-2/chitosan hereinafter was chosen for testing its biological activity. The matrilin-2/chitosan scaffold within the collagen conduit stimulated upward migration of fluorescently labeled SCs within the collagen conduit after 24h incubation, while a collagen conduit without the scaffold failed to do so (Figures 4A–C). The average upward migration distance in the scaffold was 383.43 μm (Figure 4D).

Matrilin-2/K-chitosan scaffold induced DRG adhesion and axonal outgrowth

To further improve matrilin-2 and chitosan interaction in the scaffold, we chemically modified chitosan with lysine (Figure 1B). Lysine is an important residue to mediate ECM crosslinking (Mäki et al., 2005). Scanning electron microscopy showed an irregular, dense, and gapped matrix with chitosan alone (Figures 5A,B). In matrilin-2/chitosan scaffold, a more porous structure was formed (Figures 5C,D). Chitosan modified with lysine (K-chitosan) presented a 2D cross-sectional architecture network (Figure 5 E, F). In contrast, matrilin-2/K-chitosan presented a 3D porous network structure with notable porosity and depth (Figures 5G,H). Such 3D porous structures are consistent with the natural channels noted in peripheral nerve structures (Jenq et al., 1987).

To determine whether the matrilin-2/K-chitosan scaffold facilitates growth of DRGs in the collagen conduit, we first evaluated DRG adherence on the cross-sectional surface of the scaffold. H&E histological analysis was performed on the cross sections of the collagen conduit with and without the scaffold (Figure 6). The scaffold with chitosan only presented a dense structure without DRG adherence (Figure 6A). The scaffold with matrilin-2/chitosan demonstrated a more porous architecture however no DRG adhesion (Figure 6B). The scaffold with matrilin-2/K-chitosan demonstrated the most porous structure and a multi-channel architecture (Figures 6C,D). It facilitated the adhesion of the DRG to the matrilin-2/K-chitosan scaffold (Figure 6D).

To evaluate axonal outgrowth in the scaffolds, we performed immunofluorescence analysis with an antibody against neurofilament. The presence of neuronal cells in the scaffolds was detected by the DAPI nuclear staining. There was no DAPI staining in

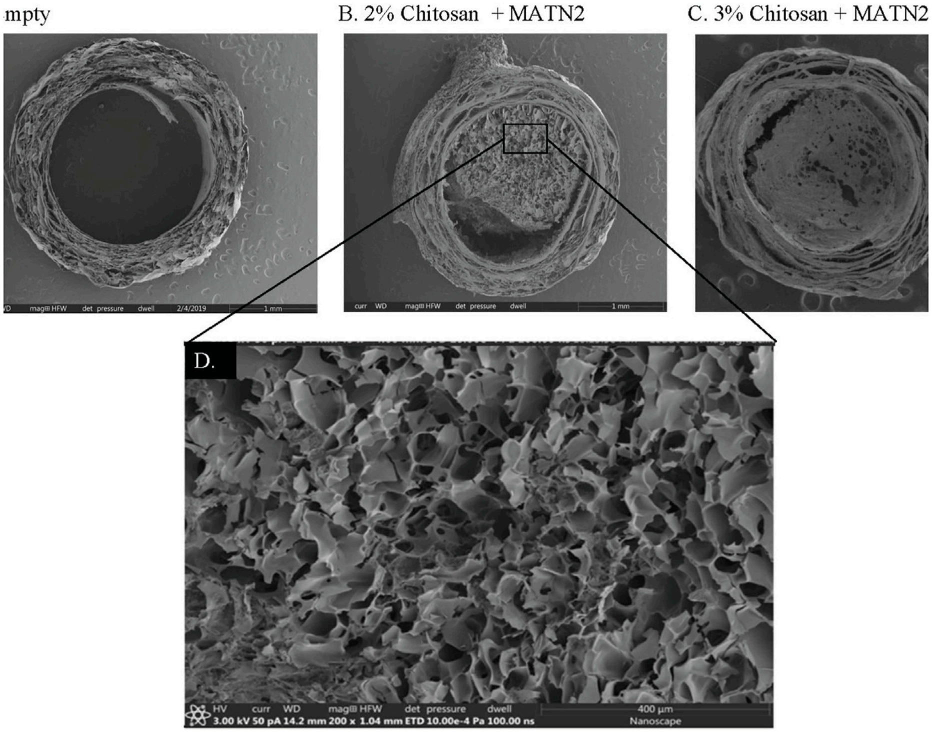

FIGURE 3
Scanning electron microscopy of **(A)** empty collagen conduit, **(B)** collagen conduit filled with matrilin-2 and 2% chitosan, and **(C)** collagen conduit filled with matrilin-2 and 3% chitosan. **(D)** Magnification of the matrilin-2 and 2% chitosan scaffold detailing porous structures measuring around 50 µm.

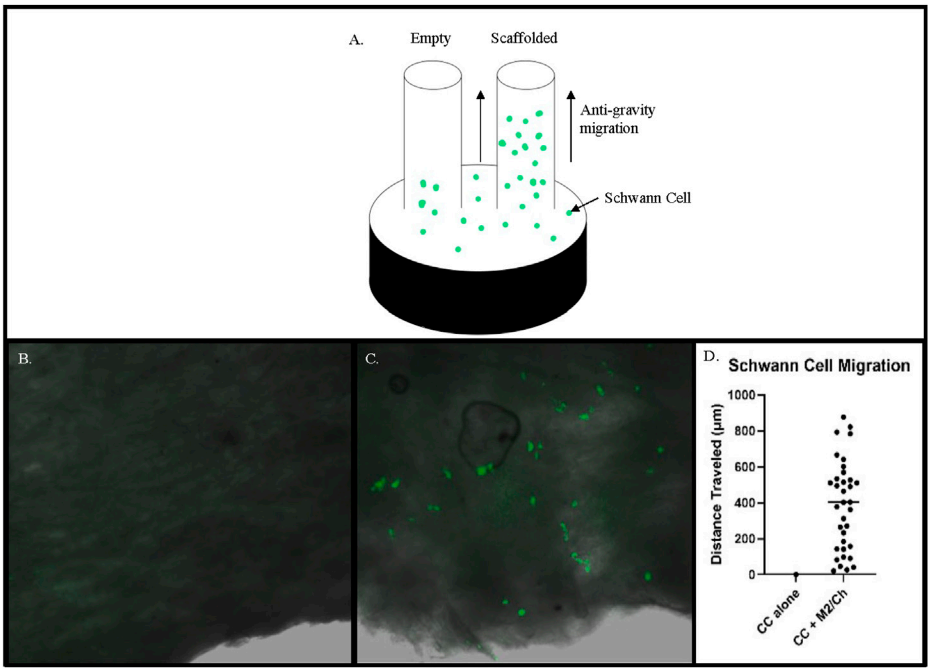

FIGURE 4
(A) Schematic of a modified capillary migration study that demonstrated negligible upward migration of Schwann cells in **(B)** empty collagen conduit (CC) while **(C)** Matrilin-2/Chitosan scaffold (M2/Ch) demonstrated migration of fluorescently labeled Schwann cells. **(D)** Quantification of distances traveled noted an average distance of 383.43 µm.

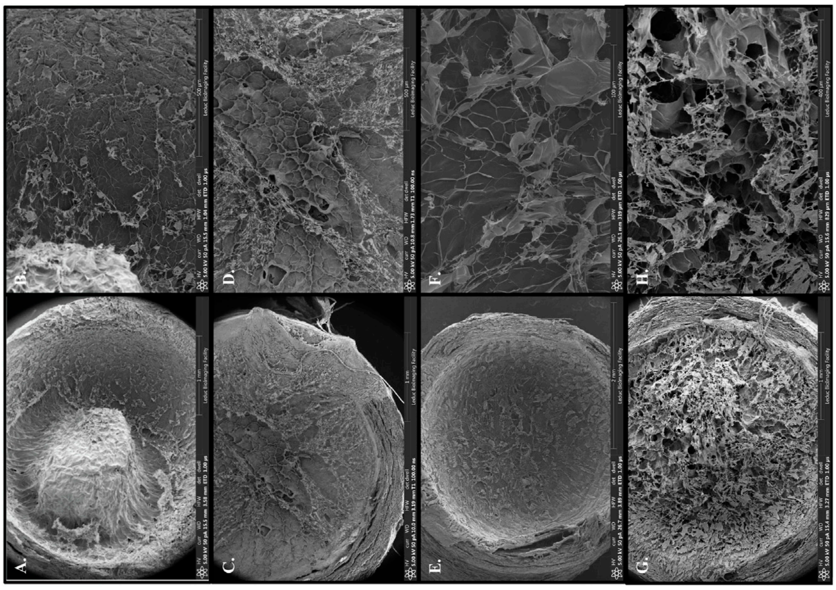

FIGURE 5
Scanning electron microscopy with overview of collagen conduit and scaffold components: **(A)** 2% chitosan, **(C)** matrilin-2/chitosan, **(E)** 2% chitosan modified with lysine (K-chitosan), **(G)** matrilin-2/K-chitosan. Scanning electron microscopy with focus on porosity of varying scaffold structures and components: **(B)** 2% chitosan with a dense and gapped matrix, **(D)** matrilin-2/chitosan with a more porous matrix, **(F)** K-chitosan with a dense and less gapped matrix, and **(H)** matrilin-2/K-chitosan a more 3D porous network.

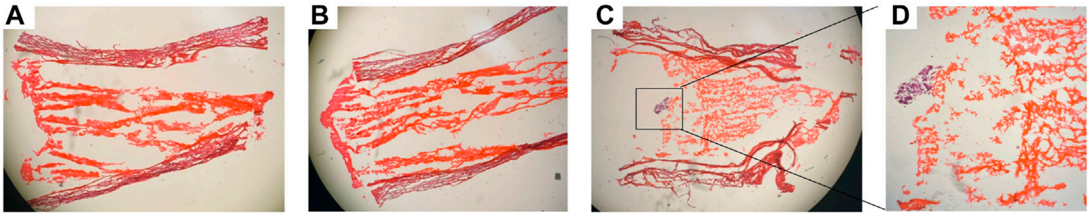

FIGURE 6
H&E staining of conduit demonstrating **(A)** collagen conduit with chitosan scaffold, **(B)** collagen conduit matrilin-2/chitosan scaffold, **(C)** collagen conduit with matrilin-2/K-chitosan scaffold with dorsal root ganglion (DRG) [black box]. **(D)** DRG at higher power adhere to matrilin-2/K-chitosan scaffold within collagen conduit.

the chitosan-alone scaffold (data not shown). Although neuronal cells were observed in the matrilin-2/chitosan scaffold in the collagen conduit (Figure 7A), only residual neurofilament staining was observed (Figure 7B). In contrast, a greater number of neuronal cells comprising the DRG was observed in the matrilin-2/K-chitosan scaffold (Figure 7C). Numerous neurofilaments representing robust axonal outgrowth were observed in the matrilin-2/K-chitosan scaffold (Figure 7D).

Discussion

In this study, we developed a novel 3D matrilin-2/K-chitosan porous scaffold for promoting axonal regeneration. Currently, commercially available, hollow collagen conduits are often used in clinical practice to assist with short gap distances. We demonstrated a significant superiority of the 3D porous matrilin-2/K-chitosan scaffold compared to not only the hollow collagen conduit, but also a scaffold comprising chitosan alone, or chitosan with matrilin-2. Our data indicated that the matrilin-2/K-chitosan scaffold forms a 3D porous network that is not only favorable to peripheral nerve regeneration structurally, but also induces Schwann cell migration, DRG neuronal cell adhesion, and axonal outgrowth biologically.

First, we identified chitosan as an optimal biomaterial for engineering a scaffold to stabilize matrilin-2 through materials analysis. Chitosan is a derivative of chitin, a natural polymer that makes up the structure of an invertebrate exoskeleton (Yi et al., 2018). The chitin is modified to contain a positively charged amine group on the oligosaccharide chain during a deacetylation reaction to create chitosan. The positive charge of the chitosan has been shown to

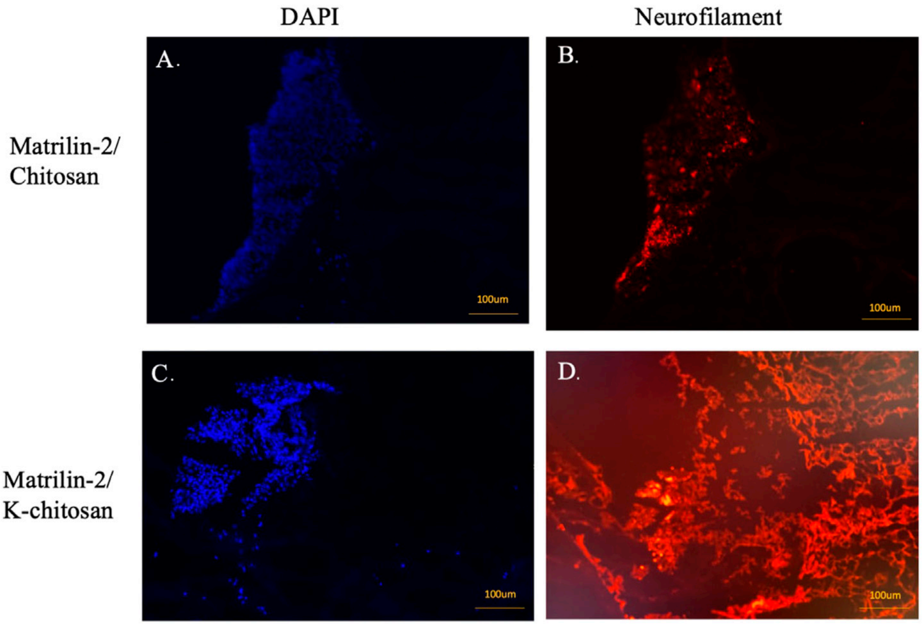

FIGURE 7
Immunofluorescent imaging of matrilin-2/chitosan and matrilin-2/K-chitosan scaffold. **(A)** DAPI staining of neuronal cells adhered to end of conduit with matrilin-2/chitosan scaffold and **(B)** neurofilament staining of matrilin-2/chitosan demonstrating minimal axonal outgrowth from neuronal cells seen of same DAPI field. **(C)** DAPI staining of cluster of neuronal cells adhered to the end of conduit and matrilin-2/K-chitosan scaffold and **(D)** neurofilament staining of same DAPI field demonstrating axonal outgrowth. Scale marked at 100uM.

enable cell adhesion and migration. In addition, chitosan has been demonstrated to be biocompatible and biodegradable and has been utilized to create nerve conduits (Yi et al., 2018)' (Neubrech et al., 2018). Chitosan degradation products have been noted to improve upon peripheral nerve regeneration through stimulating SC proliferation and inducing macrophage infiltration (Wang et al., 2016; Zhao et al., 2017). However, chitosan lacks the ability to hold a cross-sectional structure without a crosslinker between its oligo-chains. With this understanding, matrilin-2 was utilized to successfully integrate and stabilize chitosan to create a porous multi-channel cross-sectional architecture when applied to a collagen conduit. We found that chitosan not only has material properties similar to those of the native nerve, but its chemical structure also allowed conjugating with matrilin-2 to form a scaffold. Constructing scaffolds with various concentrations of chitosan demonstrated that the 2% chitosan scaffold presented the best porous microarchitecture with matrilin-2.

Second, matrilin-2 was chosen to be the second important component of the scaffold based on its structural as well as biological activities. We sought to utilize the native presence of matrilin-2 in the neuronal tissues with its biological cues and structural interactions with the ECM and SCs. These properties are important for forming a biomimetic scaffold with not only a porous microarchitecture allowing nerve growth, but also the capability of enhancing SC cellular adhesion and migration and promoting axonal regeneration (Malin et al., 2009) Indeed, matrilin-2 facilitated greater SC migration and adhesion *in vitro*. Such results were consistent with prior literature showing matrilin-2 enhanced SC migration and adhesion greater than fibronectin or laminin (Malin et al., 2009). Matrilin-2 also increased axonal outgrowth from DRGs (Malin et al., 2009). Structurally, matrilin-2 serves as a hinge molecule in the ECM by forming an oligomeric structure (Klatt et al., 2011). Matrilin forms not only a filamentous structure by itself (Piecha et al., 1999), but also a filamentous network by interacting with other ECM ligands including collagens and proteoglycans (Wang et al., 2014). The broad interaction of matrilin-2 allows it act not only as a mediator between ECM proteins, but also induce a chemotactic property for SC migration. Further establishment of cellular interactions with matrilin-2 within the microenvironment of peripheral nerve regeneration will help to better elucidate its mediating role between injury response and induction of regeneration.

Although the matrilin-2/chitosan scaffold induced SC migration against gravity in the collagen conduit, it failed to facilitate DRG adhesion or axonal outgrowth during the 3D organotypic assay. Thus, we focused on the creation of a 3D biomimetic extracellular matrix environment to improve the efficiency of cellular adhesion and migration during peripheral nerve regeneration. The modification of chitosan with lysine provides a greater interaction of matrilin-2 with chitosan by adding a free amine group that is less sterically hindered. Lysine has further been used to augment hydrogels to promote neurite outgrowth by improving bioactivity through delivery of positive charges (Cai et al., 2012a; 2012b). Indeed, we observed a notably increased porosity and depth of the 3D network in the matrilin-2/K-chitosan scaffold than that without lysine modification. Such porous structure mimics the native channels observed in native peripheral nerves (Jenq et al., 1987). Prior research of lysine has also demonstrated that its presence creates a hydrophilic surface and surface charge that improves the environment for cellular adhesion (Wang et al., 2018). Differences in nerve cell affinity were observed through various binding patterns of lysine with chitosan (Cheng et al., 2004). Lysine also improved the affinity, differentiation, and growth of neurons. Our study demonstrated that the 3D matrilin-2/K-chitosan scaffold not only presented an optimal porous cross-sectional architecture, but also supported DRG affinity and induced axonal outgrowth.

A limitation of this study is that the novel scaffolds were tested with SCs *in vitro* and with DRG *ex-vivo*. We plan to analyze the scaffold with an *in-vivo* rat sciatic nerve model to further understand its impact on peripheral nerve regeneration compared to an empty conduit and autograft. Ultimately, this work serves as a template for establishing a scaffold capable of integrating crucial extracellular matrix proteins, chemokines, and growth proteins. It creates a biomimetic microenvironment that improves the adhesion and infiltration of SCs through the site of bridging during nerve regeneration. By optimizing SC behavior towards a reparative phenotype following nerve repair, the environment for axonal regeneration is better established and maintained, thus allowing for a more rapid recovery from potentially devastating injuries to peripheral nerves.

Conclusion

The delivery of matrilin-2, a crucial extracellular matrix protein upregulated during nerve injury, to assist in creating a biomimetic environment to help bridge critical nerve gaps has yet to be thoroughly explored, leaving much of its biomedical properties and potential untapped. Integrating matrilin-2 into chitosan modified with lysine scaffold produced a porous internal structure that promoted Schwann cell migration DRG adhesion and axonal outgrowth. Such findings demonstrate the potential of using chitosan and matrilin-2 to engineer a 3D microenvironment to improve upon SC response following injury. Ultimately, our scientific premise lies in generating nerve grafts that not only have the multi-channel microarchitecture of nerve, but are bioactive in their interaction with SC adhesion, migration, and reparative activity. Such a novel scaffold supports the pathway for axonal outgrowth and becomes a promising, reliable, and readily available therapeutic for nerve repair.

Data availability statement

The raw data supporting the conclusion of this article will be made available by the authors, without undue reservation.

Author contributions

NL and BV performed most of the experiments, analyzed data, and drafted the manuscript. JG assisted with experiments and editing of the manuscript. ZQ assisted with the chitosan augmentation with lysine. SZ assisted with the agarose migration and cell adhesion assays. JK critically revised the manuscript with insight into clinical context. QC assisted in designing the study and provided critical guidance of the work and revisions to the manuscript.

Funding

The project was supported by funds from the American Foundation for Surgery of the Hand (Award 3968) to NL, NIGMS/NIH (P30 GM122732) and NIA/NIH (R01AG080141) to QC.

Conflict of interest

The authors declare that the research was conducted in the absence of any commercial or financial relationships that could be construed as a potential conflict of interest.

Publisher's note

Supplementary material

The Supplementary Material for this article can be found online at: https://www.frontiersin.org/articles/10.3389/fbioe.2023.1142610/full#supplementary-material

References

Borschel, G. H., Kia, K. F., Kuzon, W. M., and Dennis, R. G. (2003). Mechanical properties of acellular peripheral nerve. *J. Surg. Res.* 114, 133–139. doi:10.1016/S0022-4804(03)00255-5

Cai, L., Lu, J., Sheen, V., and Wang, S. (2012a). Optimal poly(l-lysine) grafting density in hydrogels for promoting neural progenitor cell functions. *Biomacromolecules* 13, 1663–1674. doi:10.1021/bm300381d

Cai, L., Lu, J., Sheen, V., and Wang, S. (2012b). Promoting nerve cell functions on hydrogels grafted with poly(l-lysine). *Biomacromolecules* 13, 342–349. doi:10.1021/bm201763n

Cheng, M., Gong, K., Li, J., Gong, Y., Zhao, N., and Zhang, X. (2004). Surface modification and characterization of chitosan film blended with poly-L-lysine. *J. Biomater. Appl.* 19, 59–75. doi:10.1177/0885328204043450

Chernousov, M. A., Stahl, R. C., and Carey, D. J. (2001). Schwann cell type V collagen inhibits axonal outgrowth and promotes Schwann cell migration via distinct adhesive activities of the collagen and noncollagen domains. *J. Neurosci.* 21, 6125–6135. doi:10.1523/jneurosci.21-16-06125.2001

Ducic, I., Fu, R., and Iorio, M. L. (2012). Innovative treatment of peripheral nerve injuries. *Ann. Plast. Surg.* 68, 180–187. doi:10.1097/sap.0b013e3182361b23

Giusti, G., Willems, W. F., Kremer, T., Friedrich, P. F., Bishop, A. T., and Shin, A. Y. (2012). Return of motor function after segmental nerve loss in a rat model: Comparison of autogenous nerve graft, collagen conduit, and processed allograft (AxoGen). *J. Bone Jt. Surg. - Ser. A* 94, 410–417. doi:10.2106/JBJS.K.00253

Jenq, C. B., Jenq, L. L., and Coggeshall, R. E. (1987). Nerve regeneration changes with filters of different pore size. *Exp. Neurol.* 97, 662–671. doi:10.1016/0014-4886(87)90123-3

Jonas, A., Thiem, S., Kuhlmann, T., Wagener, R., Aszodi, A., Nowell, C., et al. (2014). Axonally derived matrilin-2 induces proinflammatory responses that exacerbate autoimmune neuroinflammation. *J. Clin. Investigation* 124, 5042–5056. doi:10.1172/JCI71385

Kim, D. I., Jensen, S. C., Noble, K. A., Kc, B., Roux, K. H., Motamedchaboki, K., et al. (2016). An improved smaller biotin ligase for BioID proximity labeling. *Mol. Biol. Cell.* 27, 1188–1196. doi:10.1091/mbc.E15-12-0844

Klatt, A. R., Becker, A. K. A., Neacsu, C. D., Paulsson, M., and Wagener, R. (2011). The matrilins: Modulators of extracellular matrix assembly. *Int. J. Biochem. Cell. Biol.* 43, 320–330. doi:10.1016/j.biocel.2010.12.010

Korpos, É., Deák, F., and Kiss, I. (2015). Matrilin-2, an extracellular adaptor protein, is needed for the regeneration of muscle, nerve and other tissues. *Neural Regen. Res.* 10, 866. doi:10.4103/1673-5374.158332

Lin, M. Y., Manzano, G., and Gupta, R. (2013). Nerve allografts and conduits in peripheral nerve repair. *Hand Clin.* 29, 331–348. doi:10.1016/j.hcl.2013.04.003

Ma, L., Gao, C., Mao, Z., Zhou, J., Shen, J., Hu, X., et al. (2003). Collagen/chitosan porous scaffolds with improved biostability for skin tissue engineering. *Biomaterials* 24, 4833–4841. doi:10.1016/s0142-9612(03)00374-0

Mäki, J. M., Sormunen, R., Lippo, S., Kaarteenaho-Wiik, R., Soininen, R., and Myllyharju, J. (2005). Lysyl oxidase is essential for normal development and function of the respiratory system and for the integrity of elastic and collagen fibers in various tissues. *Am. J. Pathology* 167, 927–936. doi:10.1016/S0002-9440(10)61183-2

Malin, D., Sonnenberg-Riethmacher, E., Guseva, D., Wagener, R., Aszódi, A., Irintchev, A., et al. (2009). The extracellular-matrix protein matrilin 2 participates in peripheral nerve regeneration. *J. Cell. Sci.* 122, 995–1004. doi:10.1242/jcs.040378

Neubrech, F., Sauerbier, M., Moll, W., Seegmüller, J., Heider, S., Harhaus, L., et al. (2018). Enhancing the outcome of traumatic sensory nerve lesions of the Hand by additional use of a chitosan nerve tube in primary nerve repair: A randomized controlled bicentric trial. *Plast. Reconstr. Surg.* 142, 415–424. doi:10.1097/PRS.0000000000004574

Piecha, D., Muratoglu, S., Mörgelin, M., Hauser, N., Studer, D., Kiss, I., et al. (1999). Matrilin-2, a large, oligomeric matrix protein, is expressed by a great variety of cells and forms fibrillar networks. *J. Biol. Chem.* 274, 13353–13361. doi:10.1074/jbc.274.19.13353

Piecha, D., Wiberg, C., Mörgelin, M., Reinhardt, D. P., Deák, F., Maurer, P., et al. (2002). Matrilin-2 interacts with itself and with other extracellular matrix proteins. *Biochem. J.* 367, 715–721. doi:10.1042/BJ20021069

Rotshenker, S. (2015). Traumatic injury to peripheral nerves. *Nerves Nerve Inj.* 23, 863–873. doi:10.1016/B978-0-12-802653-3.00088-9

Segat, D., Frie, C., Nitsche, P. D., Klatt, A. R., Piecha, D., Korpos, E., et al. (2000). Expression of matrilin-1, -2 and -3 in developing mouse limbs and heart. *Matrix Biol.* 19, 649–655. doi:10.1016/S0945-053X(00)00112-8

Shin, R. H., Friedrich, P. F., Crum, B. A., Bishop, A. T., and Shin, A. Y. (2009). Treatment of a segmental nerve defect in the rat with use of bioabsorbable synthetic nerve conduits: A comparison of commercially available conduits. *J. Bone Jt. Surg. - Ser. A* 91, 2194–2204. doi:10.2106/JBJS.H.01301

Tajdaran, K., Chan, K., Zhang, J., Gordon, T., and Borschel, G. H. (2019). Local FK506 dose-dependent study using a novel three-dimensional organotypic assay. *Biotechnol. Bioeng.* 116, 405–414. doi:10.1002/bit.26853

Tangsadthakun, C., Kanokpanont, S., Sanchavanakit, N., Banaprasert, T., and Damrongsakkul, S. (2006). Properties of collagen/chitosan scaffolds for skin tissue engineering fabrication of collagen/chitosan scaffolds. *J. Mater. Mat. Min.* 16, 37–44.

Wang, J., Tian, L., Chen, N., Ramakrishna, S., and Mo, X. (2018). The cellular response of nerve cells on poly-L-lysine coated PLGA-MWCNTs aligned nanofibers under electrical stimulation. *Mater. Sci. Eng. C* 91, 715–726. doi:10.1016/j.msec.2018.06.025

Wang, Y., Zhao, Y., Sun, C., Hu, W., Zhao, J., Li, G., et al. (2016). Chitosan degradation products promote nerve regeneration by stimulating Schwann cell proliferation via miR-27a/FOXO1 Axis. *Mol. Neurobiol.* 53, 28–39. doi:10.1007/s12035-014-8968-2

Wang, Y., Zhu, L., Wei, L., Zhou, Y., Yang, Y., and Zhang, L. (2023). A bio-orthogonally functionalized chitosan scaffold with esterase-activatable release for nerve regeneration. *Int. J. Biol. Macromol.* 229, 146–157. doi:10.1016/j.ijbiomac.2022.12.113

Wang, Z., Luo, J., Iwamoto, S., and Chen, Q. (2014). Matrilin-2 is proteolytically cleaved by ADAMTS-4 and ADAMTS-5. *Molecules* 19, 8472–8487. doi:10.3390/molecules19068472

Yi, S., Xu, L., and Gu, X. (2018). Scaffolds for peripheral nerve repair and reconstruction. *Exp. Neurol.* 319, 112761. doi:10.1016/j.expneurol.2018.05.016

Zhang, L., Yao, K., Wang, Y., Zhou, Y. L., Fu, Z., Li, G., et al. (2021). Brain-targeted dual site-selective functionalized poly(β-amino esters) delivery platform for nerve regeneration. *Nano Lett.* 21, 3007–3015. doi:10.1021/acs.nanolett.1c00175

Zhang, L., Yao, K., Wei, J., Li, G., Lin, Y., Zhou, Y. L., et al. (2022). Convenient *in situ* synthesis of injectable lysine-contained peptide functionalized hydrogels for spinal cord regeneration. *Appl. Mater Today* 27, 101506. doi:10.1016/j.apmt.2022.101506

Zhao, Y., Wang, Y., Gong, J., Yang, L., Niu, C., Ni, X., et al. (2017). Chitosan degradation products facilitate peripheral nerve regeneration by improving macrophage-constructed microenvironments. *Biomaterials* 134, 64–77. doi:10.1016/j.biomaterials.2017.02.026

frontiers | Frontiers in Bioengineering and Biotechnology

TYPE Original Research
PUBLISHED 22 June 2023
DOI 10.3389/fbioe.2023.1185251

Lipoaspirate fluid derived factors and extracellular vesicles accelerate wound healing in a rat burn model

Yue Wu[1,2,3], Pengyu Hong[1,2,3], Pan Liu[1,2,3], Qi Zhang[1,2,3], Yue Zhang[1,2,3], Baohua Yang[1,2,3], Huixing Liu[4], Lei Liu[1,2,3]*, Weidong Tian[1,2,3] and Mei Yu[1,2]*

[1]State Key Laboratory of Oral Disease, National Engineering Laboratory for Oral Regenerative Medicine, National Clinical Research Center for Oral Diseases, West China School of Stomatology, Sichuan University, Chengdu, China, [2]Engineering Research Center of Oral Translational Medicine, Ministry of Education, Sichuan University, Chengdu, China, [3]Department of Oral and Maxillofacial Surgery, West China Hospital of Stomatology, Sichuan University, Chengdu, China, [4]Sichuan Huamel Zixin Medical Aesthetic Hospital, Chengdu, Sichuan, China

Check for updates

OPEN ACCESS

EDITED BY
Junxi Wu,
University of Strathclyde, United Kingdom

REVIEWED BY
Jia Xian Law,
National University of Malaysia, Malaysia
Chengliang Deng,
Affiliated Hospital of Zunyi Medical University, China

*CORRESPONDENCE
Mei Yu,
✉ yumei925@hotmail.com
Lei Liu,
✉ drliulei@163.com

RECEIVED 13 March 2023
ACCEPTED 14 June 2023
PUBLISHED 22 June 2023

CITATION
Wu Y, Hong P, Liu P, Zhang Q, Zhang Y, Yang B, Liu H, Liu L, Tian W and Yu M (2023), Lipoaspirate fluid derived factors and extracellular vesicles accelerate wound healing in a rat burn model. *Front. Bioeng. Biotechnol.* 11:1185251. doi: 10.3389/fbioe.2023.1185251

Background: The regenerative capabilities of derivatives derived from the fat layer of lipoaspirate have been demonstrated. However, the large volume of lipoaspirate fluid has not attracted extensive attention in clinical applications. In this study, we aimed to isolate the factors and extracellular vesicles from human lipoaspirate fluid and evaluate their potential therapeutic efficacy.

Methods: Lipoaspirate fluid derived factors and extracellular vesicles (LF-FVs) were prepared from human lipoaspirate and characterized by nanoparticle tracking analysis, size-exclusion chromatography and adipokine antibody arrays. The therapeutic potential of LF-FVs was evaluated on fibroblasts *in vitro* and rat burn model *in vivo*. Wound healing process was recorded on days 2, 4, 8, 10, 12 and 16 post-treatment. The scar formation was analyzed by histology, immunofluorescent staining and scar-related gene expression at day 35 post-treatment.

Results: The results of nanoparticle tracking analysis and size-exclusion chromatography indicated that LF-FVs were enriched with proteins and extracellular vesicles. Specific adipokines (adiponectin and IGF-1) were detected in LF-FVs. *In vitro*, LF-FVs augmented the proliferation and migration of fibroblasts in a dose-dependent manner. *In vivo*, the results showed that LF-FVs significantly accelerated burn wound healing. Moreover, LF-FVs improved the quality of wound healing, including regenerating cutaneous appendages (hair follicles and sebaceous glands) and decreasing scar formation in the healed skin.

Conclusion: LF-FVs were successfully prepared from lipoaspirate liquid, which were cell-free and enriched with extracellular vesicles. Additionally, they were found to improve wound healing in a rat burn model, suggesting that LF-FVs could be potentially used for wound regeneration in clinical settings.

Abbreviations: CE, crude extract; COL I, collagen I; EVs, extracellular vesicles; HFF, human foreskin fibroblasts; LF-FVs, lipoaspirate fluid derived factors and extracellular vesicles; NTA, nanoparticle tracking analysis; SEC, size-exclusion chromatography; TFF, tangential flow filtration; TGF-β1, transforming growth factor-β1; α-SMA, α-smooth muscle actin.

KEYWORDS

extracellular vesicles, adipokines, lipoaspirate fluid, rat burn model, wound healing

1 Introduction

Burn injuries represent a significant disease burden on the world's population, with nearly 9 million injuries and an estimated 120,000–180,000 deaths annually (James et al., 2020). At present, standard nursing, early excision, and skin grafting have been used to treat burn injuries (Las Heras et al., 2020; Shahin et al., 2020), however, the long-term medical treatment (Bailey et al., 2019) and severe complications such as permanent scarring and disfigurement (Tan et al., 2017) cause heavy burden to patients, in addition, skin grafting has the disadvantages such as limited source, additional surgical trauma and possible complications including necrosis, contraction and infection of the donor area (Stekelenburg et al., 2016; Ozhathil et al., 2021). Therefore, there is an increasing need for a more effective and ideal treatment strategy.

Adipose tissue has garnered special attention in wound healing and scar repair as a rich source of bioactive substances (Cai et al., 2020; Guo et al., 2022). Scholars have found that fat grafting could significantly accelerate burn wound healing and improve scar quality (Klinger et al., 2008; Klinger et al., 2020). He et al. confirmed the inductive effect of cell-free adipose tissue extract prepared from human subcutaneous adipose tissue on wound healing in C57BL/6 mice (He et al., 2019). Wang et al. obtained adipose tissue extract from healthy female adipose tissue and demonstrated that it could accelerate diabetic wound healing in db/db mice through pro-angiogenic and anti-inflammatory activities (Wang et al., 2020). Paracrine cytokines and extracellular vesicles (EVs) were reportedly the main factors through which adipose tissue and its derivatives exert their biological effects (Bellei et al., 2022; Li et al., 2022). Lipoaspirate waste is typically divided into two parts: a fat layer and a liquid layer. Various adipose tissue derivatives (adipose-derived stem cells conditioned medium, adipose-derived stem cells extracellular vesicles and adipose tissue extract, *etc.*) are produced from the fat layer of lipoaspirate waste, which play an important role in the field of tissue repair and regenerative medicine, particularly in scar repair and wound healing (Cai et al., 2020; Bellei et al., 2022). Despite the efficient therapeutic efficacy exhibited by the secretome of these cultured cells/tissue, several hurdles must be addressed before translating this therapy from bench-to-bedside. For example, isolation of cells using enzymatic digestion that increases the risk of biological contamination and the secretome harvested from cultured cells/tissues requires considerable cell expansion, specific laboratory equipment and time-consuming steps (Mazini et al., 2020; Poulos, 2018). Based on the effectiveness and feasibility of adipose-derived therapies in the field of wound healing and scar prevention, we speculated that a variety of bioactive factors, including growth factors and extracellular vesicles, could be extracted from the discarded lipoaspirate fluids and play a therapeutic role in repairing burn skin wounds.

This study presented a novel method to obtain a cell-free liquid portion from lipoaspirate fluids, the "lipoaspirate fluid derived factors and extracellular vesicles" (LF-FVs). The contents of LF-FVs were detected and the therapeutic effects of LF-FVs on burn wound healing and scar reduction in rats were investigated with two administration methods (local injection and topical spray).

2 Materials and methods

2.1 LF-FVs preparation

Healthy donors (1) no infectious diseases such as syphilis and acquired immune deficiency syndrome (AIDS) (2) 18<BMI<30 were included in this study. Human lipoaspirate fluid was collected from 4 patients (4 women) as waste material from liposuction surgery in Sichuan HUAMEI ZIXIN medical aesthetic hospital after written consent. The mean age was 31 years (range, 22–40 years). Detailed information about patients was listed in Supplementary Table S1. The procedures were approved by the Institutional Review Board of Sichuan University West China Hospital of Stomatology (Approval number, WCHSIRB-D-2021-028).

After collection, the lipoaspirate fluid is differentially centrifuged at 300 g for 10 min and 2,000 g for 10 min to remove cells and tissue debris. The supernatant is then further centrifuged at 15,000 g for 1 h to remove the fraction of large EVs. After the third centrifugation, the supernatant was collected to obtain crude extract of lipoaspirate fluid (CE). The volume of CE was further concentrated through tangential flow filtration (TFF) using 500 kDa molecular weight cut-off capsule (Millipore), the remaining concentrated fluid was named as LF-FVs (Figure 1).

2.2 Nanoparticle tracking analysis (NTA)

The particle concentration and size distribution of isolated LF-FVs samples were determined with Zeta View (Particle Metrix, Germany) as per the manufacturer's instructions.

2.3 Size-exclusion chromatography (SEC)

1 mL LF-FVs were overlaid on top of the Sepharose-4B (4B200-100mL, CAS:9012-36-6) in 10 mL disposable plastic column (Thermo, 29924). A total of 30 sequential fractions of 500 μL were collected according to the manufacturer's protocol. The particle number and protein concentration of SEC fractions were detected by NTA, and the bicinchoninic protein assay (BCA Protein Assay Kit, KeyGEN BioTECH) respectively.

2.4 Adipokine antibody array

Adipokines in LF-FVs were analyzed using Quantibody® Human Obesity Array 3 (QAH-ADI-3) (RayBiotech, United States) according to the manufacturer's protocol. The fluorescence signals were visualized through a laser scanner

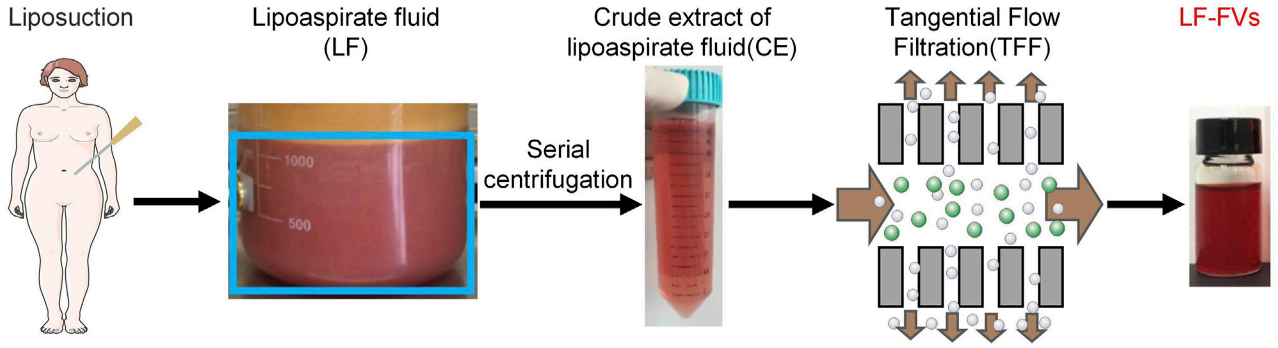

FIGURE 1
Schematic illustration of LF-FVs preparation.

equipped with a Cy3 wavelength. Signal intensities were quantified with the microarray analysis software (GenePix).

2.5 Cell culture

Fibroblasts are critical in supporting wound healing. One of the most available sources of human fibroblasts is the foreskin (Bainbridge, 2013; Ramenzoni et al., 2017). In the current study, human foreskin fibroblasts (HFF) were purchased from Shanghai Institute of Biochemistry and Cell Biology (China) and cultured in Dulbecco's modified Eagle's medium supplemented with 10% fetal bovine serum and penicillin/streptomycin (P/S; 1000 UI/mL) at 37°C in humidified air containing 5% CO_2.

2.6 Cell proliferation assay

1 x 10^3 HFF were seeded into 96-well plates and cultured with medium containing LF-FVs at the appropriate concentrations (0, 10, 50, 100, 250 μg/mL) (0.1 mL per well) before Cell Counting Kit-8 assay (CCK8, KeyGEN BioTECH, Nanjing, China). Untreated cells (0 μg/mL) served as the control group. The optical density (OD) value was detected at 450 nm using the Multiskan Go Spectrophotometer (Thermo Fisher Scientific) from day 1 to day 6 (n = 5).

2.7 Cell scratch assay

Confluent HFF monolayers were scratched with a sterile 200 μL pipette tip, washed twice in PBS to remove debris and cocultured with LF-FVs at the indicated concentrations (0, 10, 50, 100, 250 μg/mL). The initial (0 h after scratching) and final (16 h after scratching) images were captured by phase-contrast microscope (Olympus), and the scratch area was analyzed by ImageJ software. The data were expressed as the relative percentage of wound healing = $[(A_0 - A_t)/A_0] \times 100\%$, where A_0 is the initial wound area (t = 0) and A_t is remaining wound area at 16 h.

2.8 Transwell assay

Transwell assay was performed using 24-well transwell inserts (8 μm pore, Corning, Unites States). 2 x 10^3 HFF were plated into the upper chamber, then cultured in 500 μL complete medium (containing 10% FBS) supplementing LF-FVs at the indicated concentrations (0, 10, 50, 100, 250 μg/mL). After incubation for 24 h, non-migrated cells were removed by cotton swab and migrated cells were fixed with 4% paraformaldehyde and stained with 0.1% crystal violet (Sigma, United States). The number of migrated cells was calculated under an optical microscope at a ×100 magnification (Olympus).

2.9 *In vivo* experiments

The rats were purchased from Dashuo experimental animal Co., Ltd. (Chengdu, China). All operations of animals were approved by the Institutional Review Board of Sichuan University West China Hospital of Stomatology (WCHSIRB-D-2020-269). The third-degree burns were performed on the dorsum of SD (Sprague Dawley) male rats as previously described (Foubert et al., 2016; Dong et al., 2020; Zhou et al., 2019). Briefly, male 5-week-old SD rats (n = 27) were anesthetized by intraperitoneal injection of 1% pentobarbital. One burn (20 mm in diameter) was made on the shaved dorsum of each rat using a round metal hot iron (diameter, 20 mm) of a temperature-controlled burner (YLS-5Q, China). Two days after burning, wound sites were excised to create a fresh full-thickness wound. 27 rats were randomly divided into 3 groups: (1) control group (PBS injected subdermally into the superficial fascia of the wound, 0.25 mL/wound, n = 9), (2) local injection of LF-FVs (5 mg LF-FVs/0.25 mL/wound, n = 9) and (3) topical spray of LF-FVs directly onto the wound bed (5 mg LF-FVs/0.25 mL/wound, n = 9). The dosage of LF-FVs for local injection and topical spray was based on the preliminary results of the pre-experiment *in vivo*. For local injection, LF-FVs were locally injected subdermally into the superficial fascia around the wounds at 5 injection sites (50 μL per site) to provide a dose of 5 mg LF-FVs. For topical spray, 250 μL LF-FVs were sprayed directly onto the wound bed, after each spray, the rats were positioned in hand until sprayed solution dried. Local injection of LF-FVs were administered every 2 days, and the topical spray of LF-FVs were administered every day. After the treatments, the wounds were exposed while the rats were kept individually with food and water in animal room. The wound areas were photographed on days 2, 4, 8, 10, 12, 16 and 35 post-treatment and quantified using ImageJ software. The wound area at different time points (Wound Area_T) was compared to the wound area on the excision day (Wound Area_0) and indicated as (% of wound = Wound Area_T/Wound Area_0 x 100%). Additionally, the area of unhealed wounds at different time points was represented by a contour-like wound tracing pattern to represent the speed of burn wound healing more clearly.

The skin-wound repair process was classically divided into four phases, namely, hemostasis (hours), inflammation (days), proliferation (1–2 weeks), and remodeling (>2 weeks). We assumed that 35 days after wounding could be considered in the progress of the remodeling phase (Hu et al., 2021). At 35 days, the rats were euthanized via cervical dislocation under general anesthesia and skin tissues were harvested for further testing. For each group, 4 of 9 skin samples were preserved in a 4% paraformaldehyde for histology; 4 skin samples were dissolved in Buffer RL1 (Vazyme, China) for real-time PCR; and 1 sample was dissolved in a RIPA Lysis Buffer (KeyGEN, China) for western blot.

2.10 Quantitative real-time polymerase chain reaction (qRT-PCR)

RNA was isolated from skin tissue using FastPure® Cell/Tissue Total RNA Isolation Kit (Vazyme, China) following the manufacturer's protocol. qRT-PCR was performed with the SYBR Green PCR master mix (Vazyme, China) using the QuantStudio™ 6 Flex Real-Time PCR System (Applied Biosystems). Relative gene expressions were analyzed using the $2^{-\Delta\Delta CT}$ method with GAPDH as the endogenous control (Supplementary Table S2).

2.11 Western blot analysis

Briefly, the skin tissue samples were dissolved in RIPA Lysis Buffer (KeyGEN, China), resolved on a 10% polyacrylamide gel, and blotted on to a nitrocellulose membrane. The membranes were blocked and then incubated with primary antibodies against TGF-β1 (Abcam, ab92486), α-SMA (ab5694), COL I (ab270993) and β-actin (Zen Bioscience, 200068-8F10) at 4°C overnight, followed by horseradish peroxidase (HRP)-conjugated secondary antibodies for 1 h at room temperature. Immobilon Western Chemiluminescent HRP Substrate (Millipore) was used for the detection following the manufacturer's instructions. β-actin was used as an internal loading control. Signals were visualized with an ImageQuant LAS 4000 mini (GE Healthcare).

2.12 Histological staining

Wound skin samples at 35 days were fixed overnight with 4% paraformaldehyde in PBS at 4°C, dehydrated using graded ethanol and paraffin-embedded and sectioned into 5 μm slides for H&E staining, masson's trichrome staining and picrosirius red staining (Chantre et al., 2018; Wang et al., 2017). To assess the relative degree of scar formation, the epidermal thickness was quantified according to H&E staining under an Olympus VS.200 Whole Slide Scanner. The thickness of the epidermis is defined as the distance between the stratum basal and stratum granulosum and measured manually using OlyVIA software based on the scale bar. To assess the relative degree of skin regeneration, skin appendage (hair follicles and sebaceous glands) density was determined according to masson's trichrome staining. Five fields of each tissue section containing the epidermis in the healed skin were randomly selected, then the hair follicles and sebaceous glands were counted per field 500 μm × 1000 μm with OlyVIA software. The mean and standard error was showed from 4 skin samples. Following picrosirius red staining, the images of the stained sections were obtained by Olympus VS. 200 Whole Slide Scanner. All counts and measurements were finished by two authors in a double-blinded fashion.

2.13 Immunofluorescence staining

The disappearance of myofibroblasts is important for the prevention of scar formation, so the presence of myofibroblasts in wound tissue was detected by immunofluorescence staining. Briefly, the sections were incubated with primary antibodies anti-α-SMA (Abcam, ab5694) and anti-COL I (Abcam, ab270993) at 4°C overnight. After PBST washing, sections were incubated with secondary antibody Alexa Fluor 555 goat anti-rabbit (Invitrogen, A21428) and Alexa Fluor 488 goat anti-rabbit (Invitrogen, A11008) at room temperature for 1 h. The images of the stained sections were obtained by confocal microscopy at ×200 magnification (Olympus FV1000, Japan).

2.14 Statistics

Statistical analyses were performed using GraphPad Prism software (v.6.0, GraphPad). Results are expressed as mean value ± standard deviation. One-way ANOVA with Tukey posthoc test was used to determine the level of significance. In all figures, we used * to denote *p*-values, Values of $p < 0.05$ were accepted as significant and no significance $p > 0.05$.

3 Results

3.1 Characteristics of LF-FVs

To evaluate the optimal TFF parameter, the volumes of crude extract from 4 patients were concentrated at 5 fold, 10 fold or 15 fold through TFF to obtain 5x, 10x or 15x LF-FVs. The protein concentration in CE, 5x, 10x and 15x LF-FVs were 3.29 ± 0.53, 8.35 ± 1.79, 23.70 ± 4.75, 40.57 ± 6.44 mg/mL respectively (Figure 2A). The particle numbers in CE, 5x, 10x and 15x LF-FVs were 3.43 ± 3.04, 10.72 ± 5.39, 51.75 ± 17.91 and 60.67 ± 29.94 ($\text{x}10^{11}$ particles/mL), respectively (Figure 2B). The median diameter of the particles in 5x, 10x and 15x LF-FVs was 131.00 ± 4.00, 138.00 ± 4.41 and 138.40 ± 7.51 nm respectively (Figure 2C).

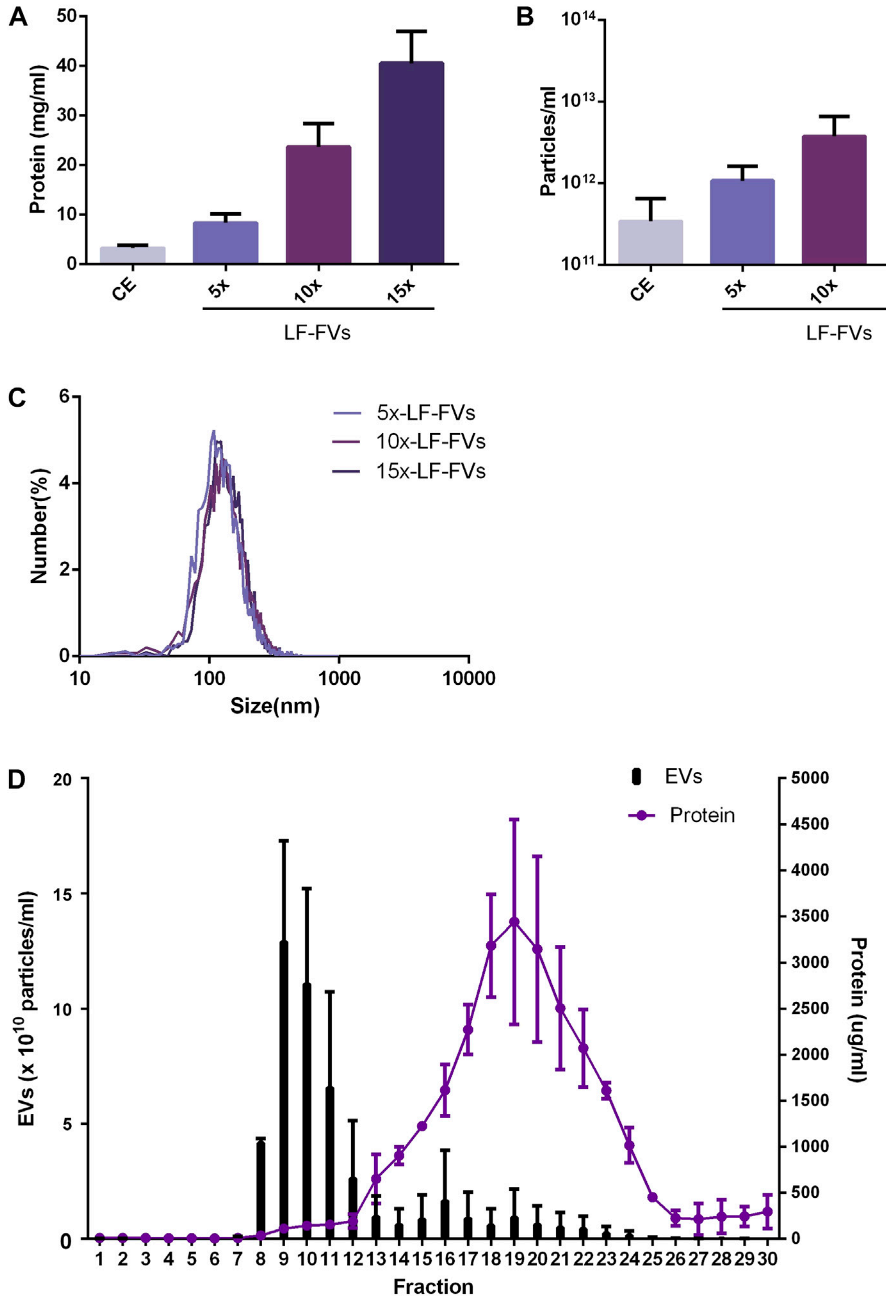

FIGURE 2
Characterization of LF-FVs with indicated TFF concentration fold. **(A)** Protein concentration was determined by the bicinchoninic protein assay. **(B)** The concentration of particles was detected by NTA (particles/mL). **(C)** The size distribution of 5x, 10x and 15x LF-FVs was measured by NTA. **(D)** particle and protein concentration measurements of size-exclusion chromatography fractions from LF-FVs.

10x LF-FVs from 4 patients were further analyzed by size-exclusion chromatography respectively. The protein concentration increased in fractions 12-25, with a peak at fraction 19. Fractions 8-12 were accompanied by the increase in particle concentration, with a peak at fraction 9. The results suggested that both soluble proteins and EVs were enriched in LF-FVs (Figure 2D). To further quantify the soluble proteins in LF-FVs, Quantibody® Human Obesity Array 3 were applied for 10x LF-FVs from 4 patients respectively. Among the 40 specific adipokines, two adipokines (adiponectin and IGF-1) were highly expressed in LF-FVs, of which concentrations were 4.60 ± 0.10 and 1.46 ± 0.33 (x10^5 pg/mL) respectively (Table 1). However, a few adipokines (such as IL-8, IL-1b, AgRP and Pepsinogen II) were not detected.

To avoid the inconsistent results caused by heterogeneity of LF-FVs from different patients, the 10x LF-FVs from 4 patients were pooled for subsequent analysis.

TABLE 1 | The concentrations of adipokines in LF-FVs (pg/ml).

Adipokines	LF-FVs-1	LF-FVs-2	LF-FVs-3	LF-FVs-4	Mean
Adiponectin	456,645.40	466,811.00	447,634.50	468,411.40	459875.58
TSP-1	156,188.40	123,340.70	94,174.70	201,408.40	143778.05
IGF-1	159,129.80	161,233.10	96,734.30	166,776.00	145968.30
Adipsin	70,722.60	72,858.70	59,598.60	74,250.80	69357.67
Chemerin	15,975.00	42,234.20	45,800.20	35,486.70	34874.03
CRP	13,276.80	8,560.70	10,688.90	44,579.60	19276.50
SAA	13,160.90	6,026.20	5,164.60	37,527.80	15469.88
Leptin	3,133.30	158.60	2,927.30	12,668.20	4721.85
RBP4	9,459.20	10,230.20	9,214.00	10,069.10	9743.13
Procalcitonin	6,563.90	11,310.60	8,944.60	9,197.10	9004.05
ANGPTL4	5,702.00	1,724.30	4,498.90	5,865.40	4447.65
TGFb1	2,843.20	2,354.60	3,560.00	2,753.50	2877.83
Pepsinogen I	1,276.90	1,683.60	852.30	1,018.80	1207.90
Insulin	1,651.20	1,373.20	1,205.00	1,254.70	1371.03
MSP	1,486.40	837.40	91.70	1,528.50	986.00
PAI-1	495.40	575.80	78.40	1,212.10	590.43
IGFBP-2	1,050.30	1,439.40	913.50	1,154.00	1139.30
TNF RI	472.40	989.30	237.40	549.00	562.03
Lipocalin-2	579.90	431.40	455.80	934.60	600.43
IL-1ra	540.50	546.60	413.00	310.80	452.73
IGFBP-1	188.60	455.10	482.20	467.70	398.40
GH	471.00	489.20	418.90	354.30	433.35
TNF RII	332.90	434.40	111.90	342.00	305.30
OPG	310.90	371.30	3.30	118.00	200.88
IFNg	365.30	242.60	322.90	282.10	303.23
IL-6	343.90	322.90	350.80	310.00	331.90
TNFa	231.60	222.10	176.80	189.50	205.00
Resistin	54.90	52.70	89.60	63.90	65.28
IL-10	65.50	44.60	51.90	62.30	56.08
VEGF	16.80	26.60	38.50	51.00	33.23
Pepsinogen II	14.10	0.00	138.30	0.00	38.10
IL-12p70	25.50	16.90	13.40	15.40	17.80
BDNF	15.40	20.10	13.50	21.70	17.68
IL-12p40	11.70	19.10	12.80	10.50	13.53
AgRP	6.30	9.50	5.50	0.00	5.33
PDGF-BB	3.50	2.40	2.90	6.50	3.83
Prolactin	7.20	0.00	749.20	9.30	191.43
RANTES	1.40	0.00	0.40	1.90	0.93
IL-1b	1.40	1.20	1.50	0.00	1.03
IL-8	0.00	0.00	0.00	0.00	0.00

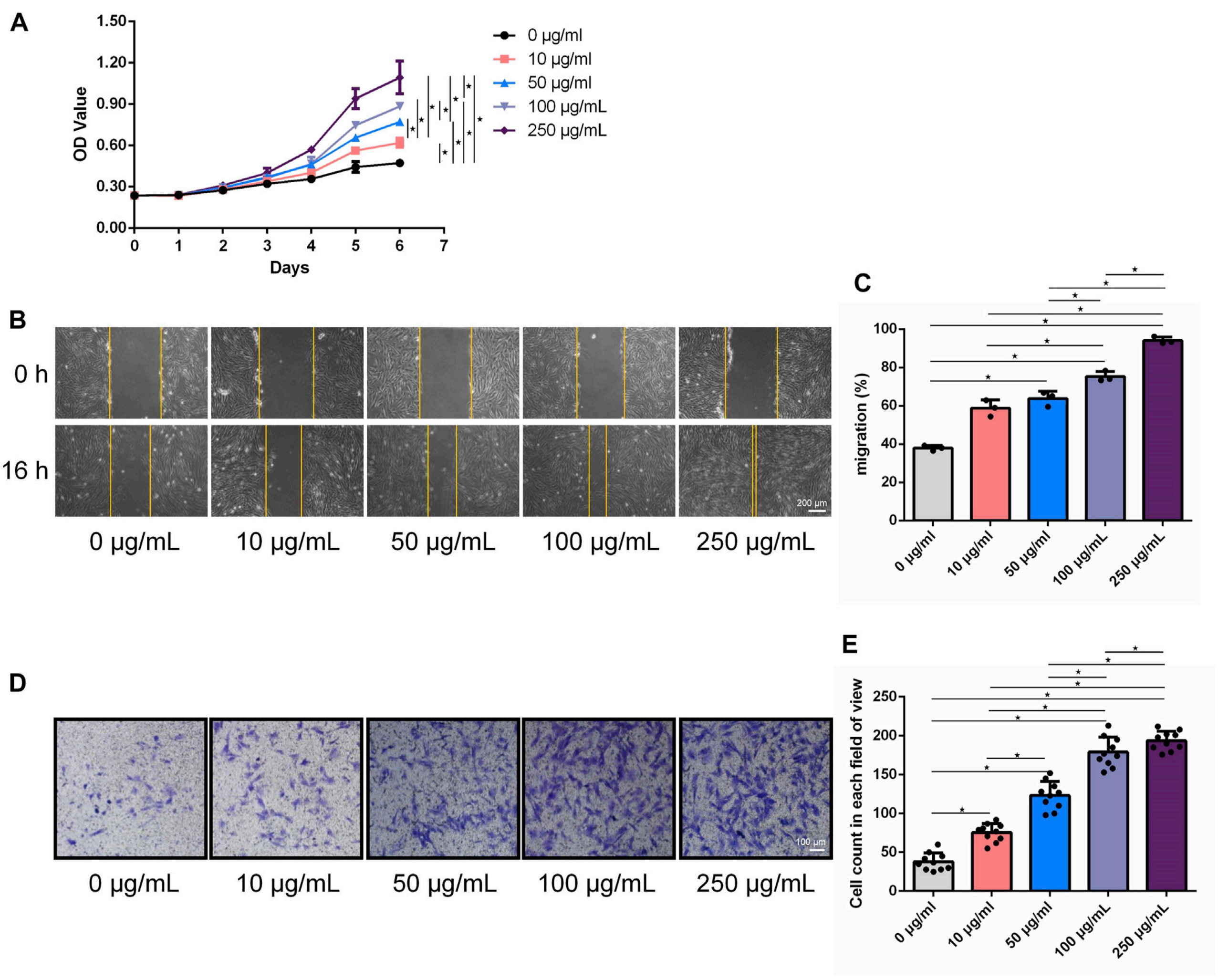

FIGURE 3
LF-FVs promoted HFF proliferation and migration. **(A)** Growth curves of HFF which were co-cultured with LF-FVs at indicated concentrations. **(B)** Representative images of scratch assay in HFF that co-cultured with LF-FVs at indicated concentrations and **(C)** relative quantification. Scale bars = 200 μm. **(D)** The migration of HFF that co-cultured with LF-FVs at indicated concentrations was detected by the transwell assay and **(E)** relative quantification. Scale bars = 100 μm. ($^{*}p < 0.05$).

3.2 LF-FVs promoted HFF proliferation and migration *in vitro*

Growth curves of HFF cultured with LF-FVs at different concentrations were plotted with CCK-8 assay (Figure 3A). At day 6, the proliferation of HFF was promoted by 31.35% ± 12.74%, 63.16% ± 8.29%, 87.49% ± 14.65% and 130.55% ± 16.86% with the addition of LF-FVs at 10, 50, 100 and 250 μg/mL, respectively ($p < 0.05$). In the scratch assay, the relative migrated HFF cells coverage at 16 h was 37.91% ± 1.38%. With the addition of LF-FVs at 10, 50, 100 and 250 μg/mL, cells coverage was 58.75% ± 4.27%, 63.76% ± 3.81%, 75.18% ± 2.74%, 94.04% ± 1.83% respectively ($p < 0.05$) (Figures 3B; C). In transwell assay, the numbers of migrated cells were 38.00 ± 11.24, 75.60 ± 11.55, 123.30 ± 17.94, 179.00 ± 19.18 and 193.70 ± 12.28 in the group treated with 0, 10, 50, 100, 250 μg/mL LF-FVs respectively (Figures 3D, E).

3.3 LF-FVs accelerated wound healing in burn wound

The therapeutic effects of LF-FVs through local injection or topical spray were evaluated in a rat burn model (Figure 4A). The wounds were photographed at the indicated time points (2d, 4d, 8d, 10d, 12d, 16d, and 35d) to discover the rate of wound closure (Figures 4B, C). Wound closure was faster in LF-FVs injection (31.49% ± 3.94%) and LF-FVs spray (23.63% ± 6.76%) groups compared to the PBS injection group (63.58% ± 9.13%) on day 8 ($p < 0.05$). On day 16, reepithelialization was completed in LF-FVs injection (0.85% ± 1.17%) and LF-FVs spray (0.42% ± 0.94%) groups except for the PBS injection group (17.90% ± 2.67%) ($p < 0.05$) (Figure 4D). Moreover, no significant difference was observed between the LF-FVs injection group and LF-FVs spray group at any time point during wound healing ($p > 0.05$).

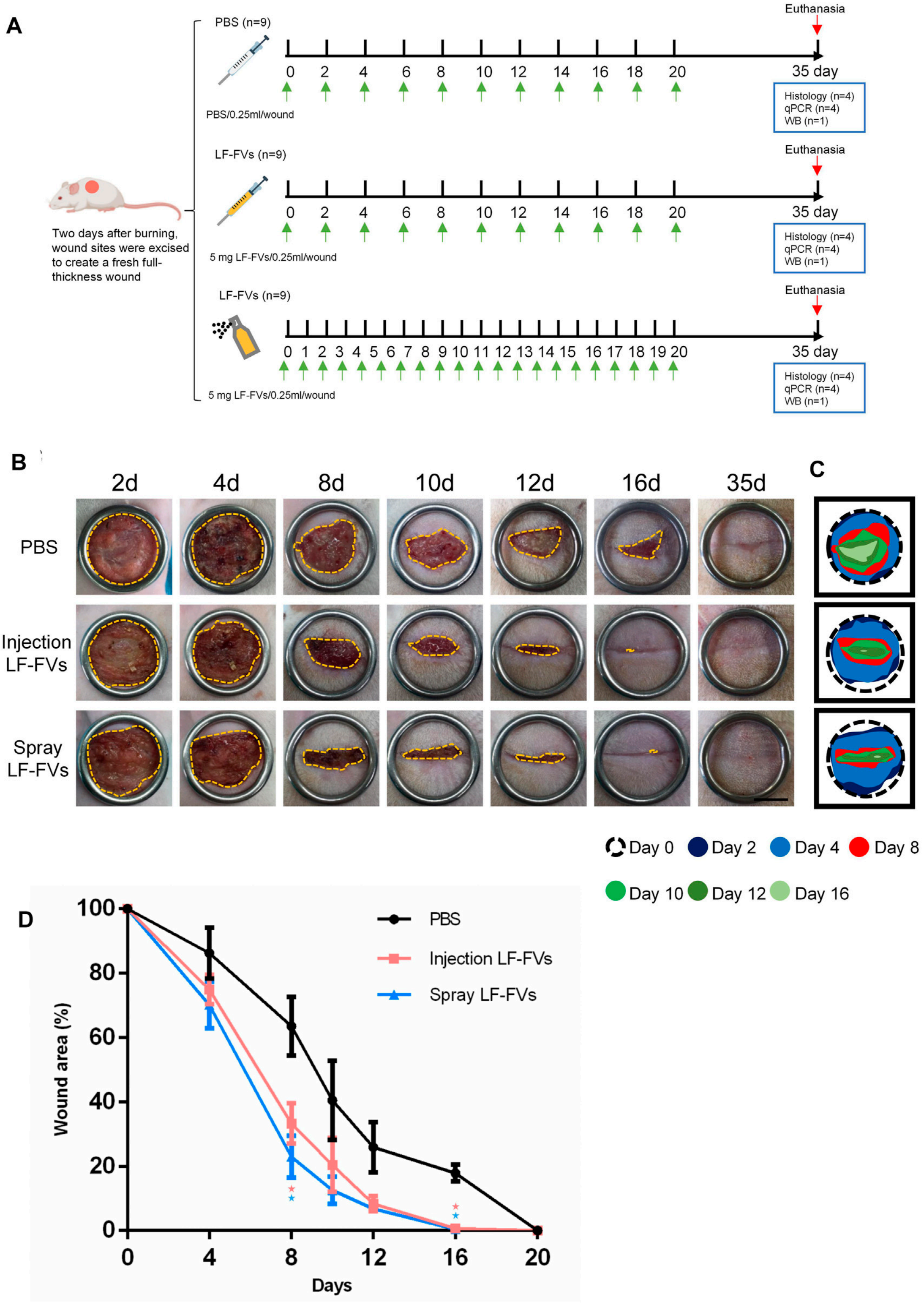

FIGURE 4
Burn wound healing was accelerated by LF-FVs. **(A)** Schematic representation of the experimental design. **(B)** Macro images of skin burn wounds at 2d, 4d, 8d,10d,12d, 16d and 35d. Scale bars = 1 cm. **(C)** Wound edge traces were established for each time point. **(D)** Quantification of the wound area. (**p* < 0.05).

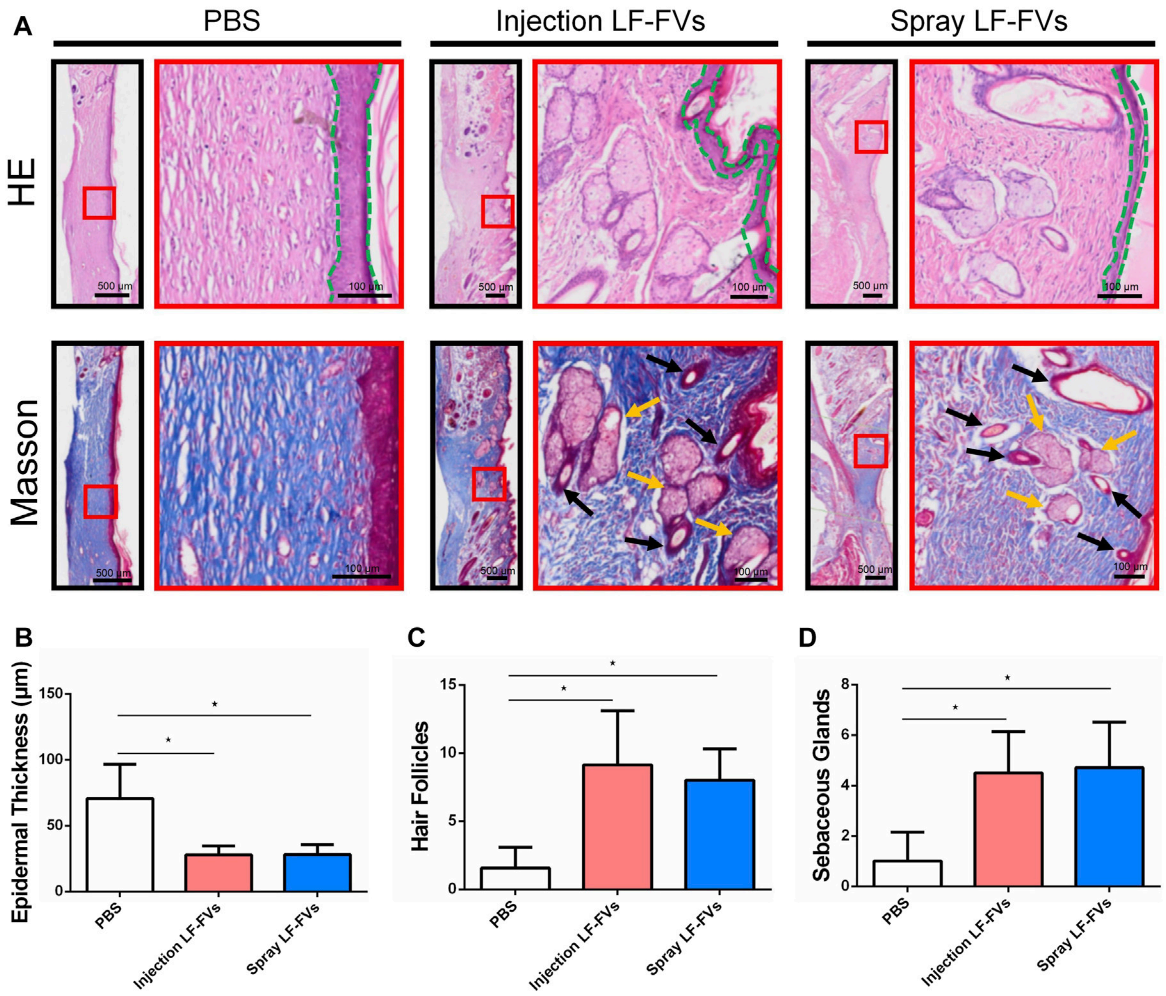

FIGURE 5
LF-FVs improved skin appendages regeneration at 35d post-treatment. **(A)** The microstructure of the healing skin was investigated by H&E and Masson staining. Green dashed lines delimit the epidermal layer in the skin tissue. Black and orange arrows mark the presence of hair follicles and sebaceous glands, respectively. Quantitative analysis of **(B)** epidermal thickness, **(C)** hair follicles and **(D)** sebaceous glands in the healing skin. (**p* < 0.05).

3.4 LF-FVs improved skin appendages regeneration

At day 35 post-treatment, epithelial thickness was 70.71 ± 25.89 μm in the PBS injection group, while thinner epithelial was detected in the LF-FVs injection group (27.85 ± 6.67 μm) and LF-FVs spray group (28.11 ± 7.64 μm) (Figures 5A, B). Masson's staining showed an increase of hair follicles in the LF-FVs injection group (5.82-fold) and LF-FVs spray group (5.09-fold) compared to PBS injection group ($p < 0.05$) (Figure 5C). The numbers of sebaceous glands in the LF-FVs injection group (4.50-fold) and LF-FVs spray group (4.71-fold) were also higher compared to PBS injection group ($p < 0.05$) (Figure 5D).

3.5 LF-FVs inhibited scar formation

TGF-β1, α-SMA, and COL I are crucial scar–related molecules involved in cicatricial diseases (Desmouliere, 1993; Xiao et al., 2017; Wei et al., 2019). Immunofluorescence results implied the less presence of a-SMA and COL I (Figures 6A,B) in LF-FVs treated groups than those in the control group at day 35 post-treatment. The decreased expression of scar-related genes also was detected by real-time PCR in the LF-FVs injection group (TGF-β1, 42.50% ± 25.40%; α-SMA, 44.30% ± 21.40%; COL I, 25.90% ± 10.90%) and LF-FVs spray group (TGF-β1, 38.60% ± 21.90%; α-SMA, 49.60% ± 29.70%; COL I, 40.20% ± 26.50%) compared to the PBS injection group ($p < 0.05$), while there was no significant difference between LF-FVs injection group and LF-FVs spray group ($p > 0.05$) (Figure 6C). Western blot further confirmed the decreased levels of TGF-β1, α-SMA, and COL I in the LF-FVs treated groups (Figure 6D) Picrosirius red staining showed that COL I, which displayed the orange-red birefringence, were regularly organized in a reticular pattern in all the groups. However, bundles of COL III, which showed the green-colored birefringence, were only evident in the LF-FVs treated groups (Figure 6E).

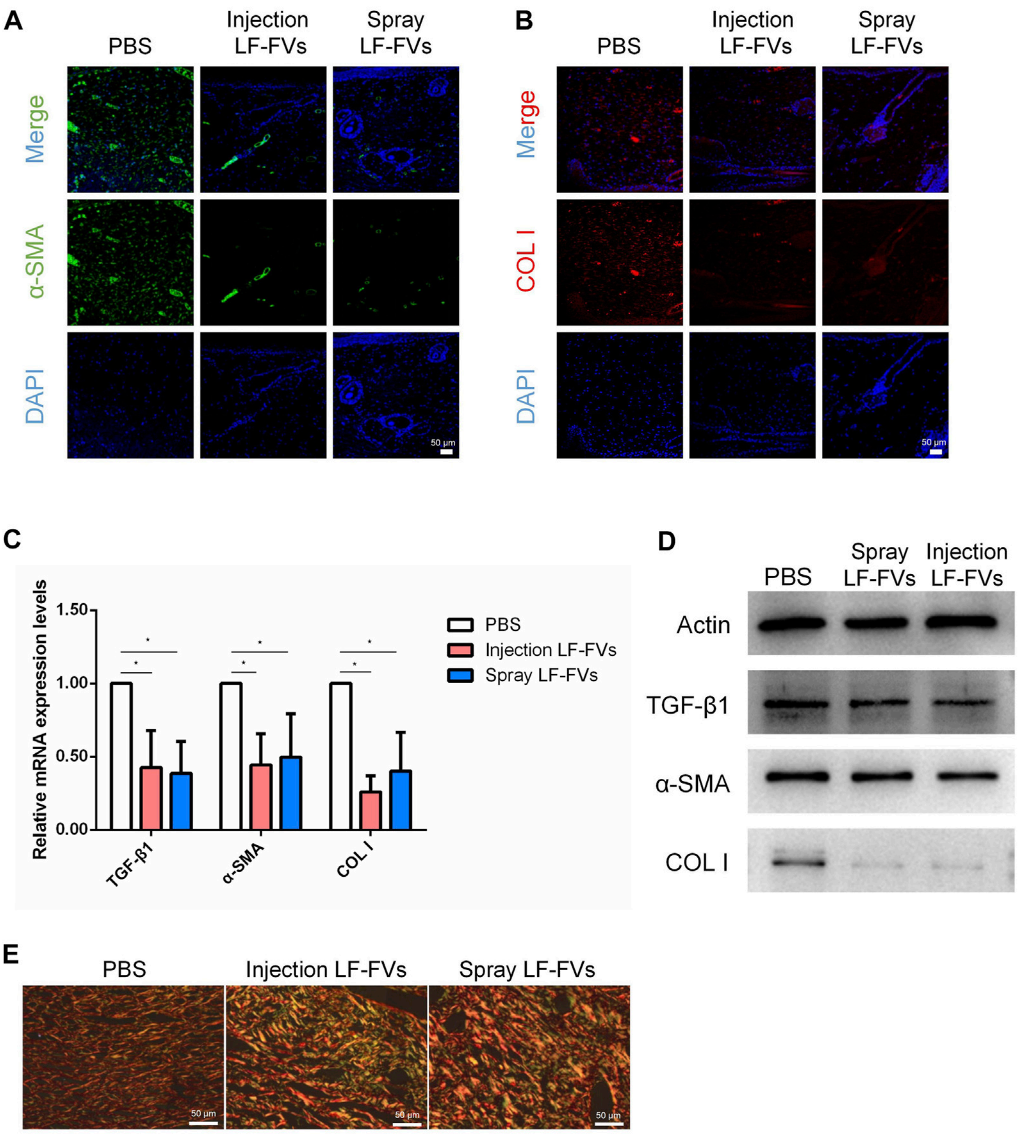

FIGURE 6

LF-FVs inhibited scar formation at 35d post-treatment. **(A, B)** Expression of α-SMA and COL I were detected using immunofluorescence staining at 35d post-treatment. Scale bars = 50 μm; magnification, ×200. **(C)** LF-FVs deceased mRNA levels of TGF-β1, α-SMA and COL I at 35d post-treatment. ($^{*}p < 0.05$). **(D)** The expression of TGF-β1, α-SMA and COL I were detected by western blot at 35d post-treatment following LF-FVs treatment. **(E)** Skin in burn wound revealed by picrosirius red-polarization. Scale bars = 50 μm.

4 Discussion

In recent years, studies have shown adipose tissue is not only an organ for energy storage, but also an endocrine organ (Ouchi et al., 2011). It can play an important role in the field of tissue engineering/regenerative medicine by secreting cytokines and extracellular vesicles in autocrine or paracrine manners (He et al., 2022). However, cell-based therapies have been hindered by various issues, such as cell survival, safety, immunogenicity, cell preservation, transportation and cost-efficiency for clinical applications (Poulos, 2018). Lipoaspirate fluid is a part of lipoaspirate waste and few attempts have been made to study the effects of lipoaspirate fluid. In this study, we aimed to develop a method of preparing new biological products from lipoaspirate fluid as raw material. For the first time, the present study developed a novel method to prepare a cell-free, EVs-rich product (LF-FVs) derived from human lipoaspirate fluid, which promoted the proliferation and migration of skin fibroblasts *in vitro* and accelerated burn wound healing in rats. Moreover, both early intervention with local injection or topical spray of LF-FVs improved the regeneration of burned skin and reduced scar formation.

In the past few years, extracellular vesicles have gained increasing interest from the scientific community. Studies have shown that EVs could be used in many fields of tissue repair and regenerative medicine (Nagelkerke et al., 2021; Wu et al., 2021). However, lipoaspirate fluid has not attracted extensive attention in clinical applications. There are many harvesting methods for extracellular vesicles, including sucrose gradient centrifugation; ultrafiltration; immunoaffinity magnetic bead separation; ExoQuick extraction (Tiwari et al., 2021; Wang et al., 2022). The most commonly used method is ultracentrifugation (Thery et al., 2018; Wang et al., 2019). However, ultracentrifugation results in low recovery rates, has time-consuming centrifugation steps (Coumans et al., 2017), frequently damages the EVs structure, and causes the coprecipitation of contaminants (Zheng et al., 2013). On the contrary, tangential flow filtration is operated under controlled low pressure and flow conditions (Shankaran et al., 2001), providing a suitable method to gently sieve out microparticles, avoiding sample manipulation that could lead to the formation of artificial nanoparticles during the concentration step (Paterna et al., 2022). Moreover, TFF differs from conventional dead-end filtration, as fluid flows tangentially across the surface, avoiding filter cake formation (Haraszti et al., 2018). Our study indicated that TFF was an efficient method for obtaining EVs-enriched product from lipoaspirate fluid.

LF-FVs do not contain cells, therefore can be assumed to be nonimmunogenic (Zakrzewski et al., 2014; Hu et al., 2022) and overcome challenges such as low survival rate of implanted cells or the potential risk of tumorigenicity (Ben-David and Benvenisty, 2011;; Poulos 2018). Moreover, LF-FVs do not require the use of cell cryopreservation solution which suggests that LF-FVs maybe be easily stored, transported at low temperature and serve as a potential “off-the-shelf” product for clinical use (Hu et al., 2022). In this study, xenogeneic human LF-FVs promoted burn wound healing in rats, and the results provided the possibility of future allogeneic application of LF-FVs in the clinic.

The therapeutic effect of LF-FVs on burn wounds was examined. Wound healing is a complex process usually divided into four orderly overlapping stages: clotting, inflammatory, proliferative and remodeling (Las Heras et al., 2020). Fibroblasts play an important role in scar formation and injury repair. In this study, we revealed that LF-FVs promoted the proliferation and migration of fibroblasts *in vitro* in a dose-dependent manner and LF-FVs treatment could significantly accelerate the healing of burn wounds. The potential mechanism of LF-FVs to accelerate burn wound healing may be due to the enriched EVs (Narauskaitė et al., 2021) and various active factors (Table 1) (such as adiponectin (Ryu et al., 2019)) in LF-FVs.

In this study, only the short-term effect of LF-FVs in rat third-degree burn model was observed, we plan to investigate the long-term treatment effects of LF-FVs by topical spray in a porcine burn model with optimal dosage in the future. Moreover, the application of LF-FVs could be further extended, for example, diabetic wounds, adipose tissue regeneration, skin sclerosis as well as skin rejuvenation.

5 Conclusion

To summarize, the present study demonstrates a novel method to prepare a cell-free and extracellular vesicle-rich liquid extract from human lipoaspirate fluid. LF-FVs, which were rich in extracellular vesicles, could promote fibroblast proliferation and migration *in vitro* and improve wound healing in a rat burn model. These findings suggest that LF-FVs might be a feasible and effective approach to inducing wound regeneration in the clinic.

Data availability statement

The original contributions presented in the study are included in the article/Supplementary Material further inquiries can be directed to the corresponding author.

Ethics statement

The animal study was reviewed and approved by the West China Hospital of Stomatology Sichuan University. Written informed consent was obtained from the individual(s) for the publication of any potentially identifiable images or data included in this article.

Author contributions

YW: Investigation, Methodology and Writing original draft; MY: conceptualization, Writing—review and editing; PH, PL, and QZ: Methodology and Visualization; YZ and BY: Visualization; HL: lipoaspirate sample preparation; LL and WT: funding acquisition, Project administration and Supervision. All authors contributed to the article and approved the submitted version.

Funding

This work was supported by National Natural Science Foundation of China (U21A20369 and 81670951), Key Technology R&D Program of Sichuan Province (2019YFS0312) and Applied Basic Research Project of Sichuan Province (2020YJ0278).

Acknowledgments

The authors acknowledge the support from National Natural Science Foundation of China, Key Technology R&D Program of Sichuan Province and Applied Basic Research Project of Sichuan Province.

Conflict of interest

The authors declare that the research was conducted in the absence of any commercial or financial relationships that could be construed as a potential conflict of interest.

Supplementary material

The Supplementary Material for this article can be found online at: https://www.frontiersin.org/articles/10.3389/fbioe.2023.1185251/full#supplementary-material

References

Bailey, M. E., Sagiraju, H. K. R., Mashreky, S. R., and Alamgir, H. (2019). Epidemiology and outcomes of burn injuries at a tertiary burn care center in Bangladesh. *Burns*. 45, 957–963. doi:10.1016/j.burns.2018.12.011

Bainbridge, P. (2013). Wound healing and the role of fibroblasts. *J. Wound Care*. 22(8), 407–408. doi:10.12968/jowc.2013.22.8.407

Bellei, B., Migliano, E., and Picardo, M. (2022). Research update of adipose tissue-based therapies in regenerative dermatology. *Stem Cell Rev Rep*. 18(6), 1956–1973. doi:10.1007/s12015-022-10328-w

Bellei, B., Migliano, E., and Picardo, M. (2022). Therapeutic potential of adipose tissue-derivatives in modern dermatology. *Exp. Dermatol*. 31(12), 1837–1852. doi:10.1111/exd.14532

Ben-David, U., and Benvenisty, N. (2011). The tumorigenicity of human embryonic and induced pluripotent stem cells. *Nat. Rev. Cancer*. 11(4), 268–277. doi:10.1038/nrc3034

Cai, Y., Li, J., Jia, C., He, Y., and Deng, C. (2020). Therapeutic applications of adipose cell-free derivatives: A review. *Stem Cell Res Ther*. 11(1), 312. doi:10.1186/s13287-020-01831-3

Chantre, C. O., Campbell, P. H., Golecki, H. M., Buganza, A. T., Capulli, A. K., and Deravi, L. F., (2018). Production-scale fibronectin nanofibers promote wound closure and tissue repair in a dermal mouse model. *Biomaterials*. 166, 96–108. doi:10.1016/j.biomaterials.2018.03.006

Coumans, F. A. W., Brisson, A. R., Buzas, E. I., Dignat-George, F., Drees, E. E. E., and El-Andaloussi, S., (2017). Methodological guidelines to study extracellular vesicles. *Circ Res*. 120(10), 1632–1648. doi:10.1161/CIRCRESAHA.117.309417

Desmoulière, A., Geinoz, A., Gabbiani, F., and Gabbiani, G. (1993). Transforming growth factor-beta 1 induces alpha-smooth muscle actin expression in granulation tissue myofibroblasts and in quiescent and growing cultured fibroblasts. *J Cell Biol*. 122(1), 103–111. doi:10.1083/jcb.122.1.103

Dong, Y., Cui, M., Qu, J., Wang, X., Kwon, S. H., and Barrera, J., (2020). Conformable hyaluronic acid hydrogel delivers adipose-derived stem cells and promotes regeneration of burn injury. *Acta Biomater*. 108, 56–66. doi:10.1016/j.actbio.2020.03.040

Foubert, P., Gonzalez, A. D., Teodosescu, S., Berard, F., Doyle-Eisele, M., and Yekkala, K., (2016). Adipose-derived regenerative cell therapy for burn wound healing: A comparison of two delivery methods. *Adv. Wound Care (New Rochelle)*. 5(7), 288–298. doi:10.1089/wound.2015.0672

Guo, X., Schaudinn, C., Blume-Peytavi, U., Vogt, A., and Rancan, F. (2022). Effects of adipose-derived stem cells and their conditioned medium in a human *ex vivo* wound model. *Cells*. 11(7), 1198. doi:10.3390/cells11071198

Haraszti, R. A., Miller, R., Stoppato, M., Sere, Y. Y., Coles, A., and Didiot, M. C., (2018). Exosomes produced from 3D cultures of MSCs by tangential flow filtration show higher yield and improved activity. *Mol. Ther.*, 26(12), 2838–2847. doi:10.1016/j.ymthe.2018.09.015

He, C., Dai, M. J., Zhou, X. J., Long, J., Tian, W. D., and Yu, M. (2022). Comparison of two cell-free therapeutics derived from adipose tissue: Small extracellular vesicles versus conditioned medium. *Stem Cell Res Ther*. 13(1), 86. doi:10.1186/s13287-022-02757-8

He, Y., Xia, J., Chen, H., Wang, L., Deng, C., and Lu, F. (2019). Human adipose liquid extract induces angiogenesis and adipogenesis: A novel cell-free therapeutic agent. *Stem Cell Res Ther*. 10(1), 252. doi:10.1186/s13287-019-1356-0

Hu, C., Chu, C., Liu, L., Wang, C., Jin, S., and Yang, R., (2021). Dissecting the microenvironment around biosynthetic scaffolds in murine skin wound healing. *Sci Adv*. 7(22), eabf0787. doi:10.1126/sciadv.abf0787

Hu, J. C., Zheng, C. X., Sui, B. D., Liu, W. J., and Jin, Y. (2022). Mesenchymal stem cell-derived exosomes: A novel and potential remedy for cutaneous wound healing and regeneration. *World J. Stem Cells*. 14(5), 318–329. doi:10.4252/wjsc.v14.i5.318

James, S. L., Lucchesi, L. R., Bisignano, C., Castle, C. D., Dingels, Z. V., and Fox, J. T., (2020). Epidemiology of injuries from fire, heat and hot substances: Global, regional and national morbidity and mortality estimates from the global burden of disease 2017 study. *Inj Prev*. 26. i36, doi:10.1136/injuryprev-2019-043299

Klinger, M., Marazzi, M., Vigo, D., and Torre, M. (2020). Fat injection for cases of severe burn outcomes: A new perspective of scar remodeling and reduction. *Aesthetic Plast Surg*. 44(4), 1278–1282. doi:10.1007/s00266-020-01813-z

Klinger, M., Marazzi, M., Vigo, D., and Torre, M. (2008). Fat injection for cases of severe burn outcomes: A new perspective of scar remodeling and reduction burn outcomes: A new perspective of scar remodeling and reduction. *Aesthetic Plast Surg*. 32(3), 465–469. doi:10.1007/s00266-008-9122-1

Las Heras, K., Igartua, M., Santos-Vizcaino, E., and Hernandez, R. M. (2020). Chronic wounds: Current status, available strategies and emerging therapeutic solutions. *J. Control Release*. 328, 532–550. doi:10.1016/j.jconrel.2020.09.039

Li, C., Wei, S., Xu, Q., Sun, Y., Ning, X., and Wang, Z. (2022). Application of ADSCs and their exosomes in scar prevention exosomes in scar prevention, *Stem Cell Rev Rep*. 18(3), 952–967. doi:10.1007/s12015-021-10252-5

Mazini, L., Rochette, L., Admou, B., Amal, S., and Malka, G. (2020). Hopes and limits of adipose-derived stem cells (ADSCs) and mesenchymal stem cells (MSCs) in wound healing. *Int J Mol. Sci*. 21(4), 1306. doi:10.3390/ijms21041306

Nagelkerke, A., Ojansivu, M., van der Koog, L., Whittaker, T. E., Cunnane, E. M., and Silva, A. M., (2021). Extracellular vesicles for tissue repair and regeneration: Evidence, challenges and opportunities. *Adv Drug Deliv Rev*. 175, 113775. doi:10.1016/j.addr.2021.04.013

Narauskaitė, D., Vydmantaitė, G., Rusteikaitė, J., Sampat, R., Rudaitytė, A., and Stašytė, G., (2021). Extracellular vesicles in skin wound healing. *Pharm. (Basel)*. 14(8), 811. doi:10.3390/ph14080811

Ouchi, N., Parker, J. L., Lugus, J. J., and Walsh, K. (2011). Adipokines in inflammation and metabolic disease. *Nat Rev Immunol*. 11(2), 85–97. doi:10.1038/nri2921

Ozhathil, D. K., Tay, M. W., Wolf, S. E., and Branski, L. K. (2021). A narrative review of the history of skin grafting in burn care. *Med. Kaunas*. 57(4), 380. doi:10.3390/medicina57040380

Paterna, A., Rao, E., Adamo, G., Raccosta, S., Picciotto, S., and Romancino, D., (2022), Isolation of extracellular vesicles from microalgae: A renewable and scalable bioprocess. *Front Bioeng Biotechnol*. 10, 836747. doi:10.3389/fbioe.2022.836747

Poulos, J. (2018). The limited application of stem cells in medicine: A review. *Stem Cell Res Ther*. 9(1), 1. doi:10.1186/s13287-017-0735-7

Ramenzoni, L. L., Weber, F. E., Attin, T., and Schmidlin, P. R. (2017). Cerium chloride application promotes wound healing and cell proliferation in human foreskin fibroblasts. *Mater. (Basel)*. 10(6), 573. doi:10.3390/ma10060573

Ryu, J., Loza, C. A., Xu, H., Zhou, M., Hadley, J. T., and Wu, J., (2019). Potential roles of adiponectin isoforms in human obesity with delayed wound healing. *Cells*. 8(10), 1134. doi:10.3390/cells8101134

Shahin, H., Elmasry, M., Steinvall, I., and Söberg F, El-Serafi, A. (2020). Vascularization is the next challenge for skin tissue engineering as a solution for burn management. *Burns Trauma*. 8, tkaa022. doi:10.1093/burnst/tkaa022

Shankaran, H., and Neelamegham, S. (2001). Effect of secondary flow on biological experiments in the cone-plate viscometer: Methods for estimating collision frequency, wall shear stress and inter-particle interactions in non-linear flow. *Biorheology*, 38(4), 275–304. doi:10.1016/S0006-3495(01)76233-9

Stekelenburg, C. M., Simons, J. M., Tuinebreijer, W. E., and van Zuijlen, P. P. (2016). Analyzing contraction of full thickness skin grafts in time: Choosing the donor site does matter. *Burns*. 42(7), 1471–1476. doi:10.1016/j.burns.2016.02.001

Tan, J., and Wu, J. (2017). Current progress in understanding the molecular pathogenesis of burn scar contracture. *Burns Trauma*. 5, 14. doi:10.1186/s41038-017-0080-1

Théry, C., Witwer, K. W., Aikawa, E., Alcaraz, M. J., Anderson, J. D., and Andriantsitohaina, R., (2018). Minimal information for studies of extracellular vesicles 2018 (MISEV2018): A position statement of the international society for extracellular vesicles and update of the MISEV2014 guidelines. *J. Extracell. Vesicles*. 7(1), 1535750. doi:10.1080/20013078.2018.1535750

Tiwari, S., Kumar, V., Randhawa, S., and Verma, S. K. (2021). Preparation and characterization of extracellular vesicles. *Am J Reprod Immunol*. 85(2), e13367. doi:10.1111/aji.13367

Wang, C., Song, W., Chen, B., Liu, X., and He, Y. (2019). Exosomes isolated from adipose-derived stem cells: A new cell-free approach to prevent the muscle degeneration associated with torn rotator cuffs adipose-derived stem cells: A new cell-free approach to prevent the muscle degeneration associated with torn rotator cuffs. *Am J Sports Med*. 47(13), 3247–3255. doi:10.1177/0363546519876323

Wang, L., Hu, L., Zhou, X., Xiong, Z., Zhang, C., and Shehada, H. M. A., (2017). Exosomes secreted by human adipose mesenchymal stem cells promote scarless cutaneous repair by regulating extracellular matrix remodelling. *Sci Rep*. 7(1), 13321. doi:10.1038/s41598-017-12919-x

Wang, X., Deng, M., Yu, Z., Cai, Y., Liu, W., and Zhou, G., (2020). Cell-free fat extract accelerates diabetic wound healing in db/db mice. *Am J Transl. Res*. 12(8), 4216, doi:10.1186/s13287-022-02813-3

Wang, Y., Cheng, L., Zhao, H., Li, Z., Chen, J., and Cen, Y., (2022). The therapeutic role of ADSC-EVs in skin regeneration. *Front. Med. (Lausanne)*. 9, 858824. doi:10.3389/fmed.2022.858824

Wei, P., Xie, Y., Abel, P. W., Huang, Y., Ma, Q., and Li, L., (2019). Transforming growth factor (TGF)-β1-induced miR-133a inhibits myofibroblast differentiation and pulmonary fibrosis. *Cell Death Dis*. 10(9), 670. doi:10.1038/s41419-019-1873-x

Wu, P., Zhang, B., Ocansey, D. K. W., Xu, W., and Qian, H. (2021). Extracellular vesicles: A bright star of nanomedicine. *Biomaterials*. 269, 120467. doi:10.1016/j.biomaterials.2020.120467

Xiao, K., Luo, X., Wang, X., and Gao, Z. (2017). MicroRNA-185 regulates transforming growth factor-β1 and collagen-1 in hypertrophic scar fibroblasts. *Mol Med Rep*. 15(4), 1489–1496. doi:10.3892/mmr.2017.6179

Zakrzewski, J. L., van den Brink, M. R., and Hubbell, J. A. (2014). Overcoming immunological barriers in regenerative medicine. *Nat Biotechnol*. 32(8), 786–794. doi:10.1038/nbt.2960

Zheng, H., Jiménez-Flores, R., and Everett, D. W. (2013). Bovine milk fat globule membrane proteins are affected by centrifugal washing processes. *J Agric Food Chem*. 61(35), 8403–8411. doi:10.1021/jf402591f

Zhou, X., Ning, K., Ling, B., Chen, X., Cheng, H., and Lu, B., (2019). Multiple injections of autologous adipose-derived stem cells accelerate the burn wound healing process and promote blood vessel regeneration in a rat model. *Stem Cells Dev*. 28(21), 1463–1472. doi:10.1089/scd.2019.0113

frontiers | Frontiers in Bioengineering and Biotechnology

TYPE Original Research
PUBLISHED 25 July 2023
DOI 10.3389/fbioe.2023.1217655

OPEN ACCESS

EDITED BY
Junxi Wu,
University of Strathclyde, United Kingdom

REVIEWED BY
Thomas Biedermann,
University of Zurich, Switzerland
Mahmut Parmaksiz,
Ankara University, Türkiye

*CORRESPONDENCE
Maxime Abellan Lopez,
✉ maxime.abellanlopez@gmail.com

RECEIVED 05 May 2023
ACCEPTED 06 July 2023
PUBLISHED 25 July 2023

CITATION
Abellan Lopez M, Hutter L, Pagin E, Vélier M, Véran J, Giraudo L, Dumoulin C, Arnaud L, Macagno N, Appay R, Daniel L, Guillet B, Balasse L, Caso H, Casanova D, Bertrand B, Dignat F, Hermant L, Riesterer H, Guillemot F, Sabatier F and Magalon J (2023), *In vivo* efficacy proof of concept of a large-size bioprinted dermo-epidermal substitute for permanent wound coverage. *Front. Bioeng. Biotechnol.* 11:1217655. doi: 10.3389/fbioe.2023.1217655

In vivo efficacy proof of concept of a large-size bioprinted dermo-epidermal substitute for permanent wound coverage

Maxime Abellan Lopez[1,2]*, Laurence Hutter[3], Etienne Pagin[3], Mélanie Vélier[2,4], Julie Véran[2,4], Laurent Giraudo[2,4], Chloe Dumoulin[2,4], Laurent Arnaud[5], Nicolas Macagno[6], Romain Appay[6], Laurent Daniel[6], Benjamin Guillet[2,7], Laure Balasse[2], Hugo Caso[1], Dominique Casanova[1,2], Baptiste Bertrand[1,2], Françoise Dignat[2,4], Loïc Hermant[3], Hélène Riesterer[3], Fabien Guillemot[3], Florence Sabatier[2,4] and Jérémy Magalon[2,4]

[1]Plastic Surgery Department, Hôpital de la Conception, AP-HM, Marseille, France, [2]Aix-Marseille Université, INSERM, Institut National de Recherche Pour l'Agriculture, l'Alimentation et l'Environnement, Centre de Recherche en Cardiovasculaire et Nutrition (C2VN), Marseille, France, [3]Poietis, Pessac, France, [4]Cell Therapy Department, Hôpital de la Conception, AP-HM, INSERM CIC BT 1409, Marseille, France, [5]Vascular Biology Department, Hôpital de la Timone, AP-HM, Marseille, France, [6]Anatomy and Pathology Department, INSERM U1263, C2VN, Hôpital de la Timone, Marseille, France, [7]Centre Européen de Recherche en Imagerie Médicale (CERIMED), Aix-Marseille Université, Centre National de la Recherche Scientifique, Marseille, France

Introduction: An autologous split-thickness skin graft (STSG) is a standard treatment for coverage of full-thickness skin defects. However, this technique has two major drawbacks: the use of general anesthesia for skin harvesting and scar sequelae on the donor site. In order to reduce morbidity associated with STSG harvesting, researchers have developed autologous dermo-epidermal substitutes (DESs) using cell culture, tissue engineering, and, more recently, bioprinting approaches. This study assessed the manufacturing reliability and *in vivo* efficacy of a large-size good manufacturing practice (GMP)-compatible bioprinted human DES, named Poieskin®, for acute wound healing treatment.

Methods: Two batches (40 cm^2 each) of Poieskin® were produced, and their reliability and homogeneity were assessed using histological scoring. Immunosuppressed mice received either samples of Poieskin® (*n* = 8) or human STSG (*n* = 8) immediately after longitudinal acute full-thickness excision of size 1 × 1.5 cm, applied on the skeletal muscle plane. The engraftment rate was assessed through standardized photographs on day 16 of the follow-up. Moreover, wound contraction, superficial vascularization, and local

---

Abbreviations: ANOVA, analysis of variance; ALI, air–liquid interface; APAFIS, Autorisation de Projet Utilisant des Animaux à des Fins Scientifiques (Project Authorization Using Animals for Scientific Purposes); ATMP, advanced therapeutic medicinal products; BMI, body mass index; CI, confidence interval; CT, computed tomography; DES, dermo-epidermal substitute; FDG, fluorodeoxyglucose; GMP, good manufacturing practice; HSTSG: human STSG; LAB, laser-assisted bioprinting; LASER, light amplification by stimulated emission; NGB, Next-Generation Bioprinter; PET, positron emission tomography; ROI, region of interest; SD, standard deviation; STSG, split-thickness skin graft.

inflammation were evaluated via standardized photographs, laser Doppler imaging, and PET imaging, respectively. Histological analysis was finally performed after euthanasia.

Results: Histological scoring reached 75% ± 8% and 73% ± 12%, respectively, displaying a robust and homogeneous construct. Engraftment was comparable for both groups: 91.8% (SD = 0.1152) for the Poieskin® group *versus* 100% (SD = 0) for the human STSG group. We did not record differences in either graft perfusion, PET imaging, or histological scoring on day 16.

Conclusion: Poieskin® presents consistent bioengineering manufacturing characteristics to treat full-thickness cutaneous defects as an alternative to STSG in clinical applications. Manufacturing of Poieskin® is reliable and homogeneous, leading to a clinically satisfying rate of graft take compared to the reference human STSG in a mouse model. These results encourage the use of Poieskin® in phase I clinical trials as its manufacturing procedure is compatible with pharmaceutical guidelines.

KEYWORDS

skin substitute, wound healing, multimodal bioprinting, laser-assisted bioprinting, large size, good manufacturing practice compatible

1 Introduction

Full-thickness skin defects are mainly represented by acute carcinologic excisions, donor-site scarring of reconstructive procedures, burn injuries, and traumatic and chronic wounds. Patients suffering from these types of lesions need to be properly and promptly treated. An autologous split-thickness skin graft (STSG) is the reference treatment for skin coverage, especially when the defect is large and reaches the hypodermis. STSG of 200–500 µm thick is harvested using a dermatome and can be mechanically expanded for higher coverage capacity. In the case of severe burn injuries, it remains the only surgical solution to ensure patient survival, and surgeons need to manage with a donor-site shortage. However, this technique has some significant drawbacks such as the use of general anesthesia, leaving a noticeable scar on the donor site, and long-term stiffness (Voineskos et al., 2009).

Technological advances, including cell-based therapy and tissue engineering, have fostered the development of skin substitutes for temporary (Salisburry et al., 1973; Tavis et al., 1979; Ramakrishnan and Jayaraman, 1997; Pegg, 2002) and permanent wound coverage to overcome STSG limitations. *In vitro* manufacturing of the epidermal layer was initiated in 1975, when Rheinwald and Green managed to culture autologous keratinocytes from a small cutaneous biopsy (Rheinwald and Green, 1975). Since then, a large area of the epidermal layer can be produced by cell culture into keratinocytes sheets (Renner et al., 2009; Sheridan, 2009; Ortega-Zilic et al., 2010; Takami et al., 2014) or directly in a suspension to spray (Moustafa et al., 2007; Límová, 2010; Kirsner et al., 2012) on a vascularized ground. More challenging projects have proposed autologous dermo-epidermal skin reconstruction. Self-assembly manufacturing techniques have already been validated to produce large-size substitutes (from 35 to 45 cm^2) used in burn injuries and chronic wound applications (NCT02145130, 2014; NCT03229564, 2017; NCT03394612, 2018; Boa et al., 2013; CHU de Quebec-Universite Laval, 2014; Germain et al., 2018; Auger, 2022; Blok et al., 2013; Blok, 2016; NCT01655407, 2016). However, this handmade manufacturing method remains difficult to implement in therapeutic and industrial applications in an automated manner.

In this context, 3D bioprinting offers clear advantages over conventional skin tissue engineering. This technology enables the generation of different functional tissues with appropriate architectures and cell compositions of different sizes with high throughput and reproducibility (Lee et al., 2009; Lee et al., 2010; Lee et al., 2010; Zhao et al., 2012; Baltazar et al., 2020) as it can print layer-by-layer different types of cells combined in a selected matrix. Because of its multilayered structure, skin is a perfect example of the strengths and benefits of 3D bioprinting approaches, overcoming some of the limitations of traditional tissue engineering strategies (Arslan-Yildiz et al., 2016; Miri et al., 2019; Yu et al., 2020). This approach has been investigated on animal models since 2013 for skin engineering (Cubo et al., 2016; Albanna et al., 2019; Baltazar et al., 2020; Jorgensen et al., 2020). Although these works formally use 3D bioprinting techniques, the manufacturing methods described (Lee et al., 2009; Cubo et al., 2016) are far from the good manufacturing practice (GMP) requirements necessary to bring this innovative technology to the clinical level. Furthermore, none of these studies manufactured a large-size dermo-epidermal substitute (DES) compliant with a potential therapeutic application in a GMP-compatible protocol compared with the current reference treatment, autologous STSG.

We developed a manufacturing process for a DES, named Poieskin®, based on the combination of extrusion bioprinting for biomaterials and laser-assisted bioprinting (LAB) for cell seeding, leveraging the advantages of high volumes and speed deposition of the matrix and high resolution and viability maintenance of cells. These two approaches were combined in the same equipment referred to as the Next-Generation Bioprinting (NGB) system designed to meet the regulatory GMP requirements for advanced therapy medicinal product (ATMP) manufacturing (EMA, 2018).

Herein, we report the reliability and homogeneity of a large-size (40 cm^2) GMP-compatible DES, named Poieskin®, as well as its efficacy and safety in the treatment of acute wound healing on an immunosuppressed murine model as part of the Poieskin® preclinical development program.

2 Methods

2.1 Ethics declaration

In this preclinical study, the authors manufactured batches of Poieskin® under GMP-compatible conditions using cells harvested from patient biopsies. Human skin biopsies for Poieskin® production and human split-thickness skin graft (HSTSG) controls were surgical residues removed during plastic surgeries on healthy volunteer patients (BIOPSKIN study number NCT04925323).

All animal experiments were conducted in accordance with the Aix-Marseille University Institutional Animal Care and Use Committee (CE14, Aix-Marseille University) and the French Ministry of Research (project authorization #33645 on 29 November 2021), according to the European Union directive 2010/63/EU and the recommendations of the Declaration of Helsinki. The study was approved by the National Animal Care and Ethics Committee (no. APAFIS 2020012015402650). Trained and authorized operators performed all animal experiments.

2.2 Human split-thickness skin

Poieskin® wound healing efficacy was compared to HSTSG as a control group. Tissue was harvested from healthy donor patients during mammaplasty procedures (after obtaining written informed consent) using an electrical dermatome (Acculan 3Ti® Dermatome, Aesculap, Hazelwood, MO, United States) set to harvest 0.2–0.3-mm-thick skin, according to the STSG defined thickness range. HSTSG was collected 1 hour before the grafting procedure and was transferred in a sterile container with 0.9% NaCl solution to the center for *in vivo* transplantation.

2.3 Poieskin® biofabrication

Human dermal fibroblasts and epidermal keratinocytes were extracted from a skin biopsy. We used two 4-cm^2 skin biopsies to produce two 40-cm^2 skin substitutes. Keratinocytes and fibroblasts were isolated from human donor skin. The hypodermis compartment was manually deleted, and the skin biopsy was cut into small pieces. The epidermis and dermis were separated after overnight incubation at 4°C in 2.4 U/mL of dispase. Collagenase NB5 was used at a concentration of 0.25 U/mL for fibroblast isolation and trypsine 0.05% for keratinocyte separation.

The viability and concentration of keratinocytes and fibroblasts in viable nucleated cells were checked after each trypsination using an automated cell counter Luna X7 (Logos Biosystems, Villeneuve-d'Ascq, France).

After primary seeding, keratinocytes and fibroblasts were detached using trypsin-EDTA and cryopreserved in 10% DMSO + 90% FBS for storage at −150°C. For tissue production, keratinocytes and fibroblasts were thawed and further cultured and amplified *ex vivo*.

Keratinocytes were grown on an allogeneic feeder layer of irradiated human fibroblasts (WCB-3C, AP-HM, Marseille, France) and cultured in a keratinocyte medium containing 58% Dulbecco–Vogt modified Eagle's medium, 30% Ham's F12, 2 mM GlutaMAX, 10% bovine FetalClone II serum, 10 ng/mL human epidermal growth factor, and 20 μg/mL gentamicin.

Fibroblasts were grown in fibroblast media containing alphaMEM, 5% platelet lysate, 2 UI/mL heparin, 100 U/mL penicillin, and 20 μg/mL gentamicin.

In preparation for dermis bioprinting, human dermal fibroblasts (passage 3) were suspended in DPBS to obtain a bioink containing 12.5 million viable nucleated cells/mL for LAB. Meanwhile, bovine collagen ink was formulated at 4 mg/mL using 10X DPBS, water for injection (WFI), and NaOH for extrusion bioprinting at 4°C. Dermal architecture consisted of depositing three layers of collagen and fibroblasts by extrusion and LAB, respectively.

After bioprinting, the dermis was cultured for 5 days in dermis maturation media containing alphaMEM supplemented with 3% platelet lysate, 2 UI/mL heparin, 100 U/mL penicillin, 20 μg/mL gentamicin, and 50 μg/mL laroscorbine.

Keratinocytes (passage 2) were suspended in DMEM to obtain a bioink containing 70 million viable nucleated cells/mL for LAB.

After bioprinting keratinocytes onto the bioprinted dermis, the skin constructs were cultured under immersed conditions for 2 days in a dedicated medium containing 58% Dulbecco–Vogt modified Eagle's medium, 30% Ham's F12 , 3% platelet lysate, 10 ng/mL human epidermal growth factor, 100 U/mL penicillin, 20 μg/mL gentamicin, and 50 μg/mL laroscorbine.

Cells were expanded before being formulated into bio-inks and bioprinted using an NGB bioprinter, in a GMP-compatible process, which has been defined by the use of GMP reagents and culture media for all the steps of the Poieskin® manufacturing process and the conformity to the acceptance criteria on the final Poieskin® product (size = 40 cm^2 ± 10%; dermal thickness >200 μm; histological score >50; and sterility of culture media including the specific absence of mycoplasms). Two 40-cm^2 DESs were produced through a multistep protocol (Figure 1A). First, the multilayer dermal compartment was sequentially obtained by printing human primary fibroblast patterns on a bovine collagen (SYMATESE, Chaponost, France) layer printed by bioextrusion (Figure 1B). Second, the epidermal compartment was obtained by printing human primary keratinocyte patterns on the dermal equivalent (Figure 1C). Then, both 40-cm^2 DESs were matured at the air–liquid interface (ALI) for the final epidermal differentiation for 6 days with a culture medium containing 58% Dulbecco–Vogt modified Eagle's medium, 30% Ham's F12, 3% platelet lysate supplemented with 0.8% human serum albumin, 0.4 μg/mL hydrocortisone, 0.12 UI/mL insulin, 100 U/mL penicillin, and 20 μg/mL gentamicin. We prepared a 1.6X ALI medium and then mixed it with agarose to obtain a final medium of 1X ALI medium and agarose 0.75%. We allowed it to gelify and then placed the Poieskin on top of it (it does not sink in the gelified medium) so that the air–liquid interface is maintained.

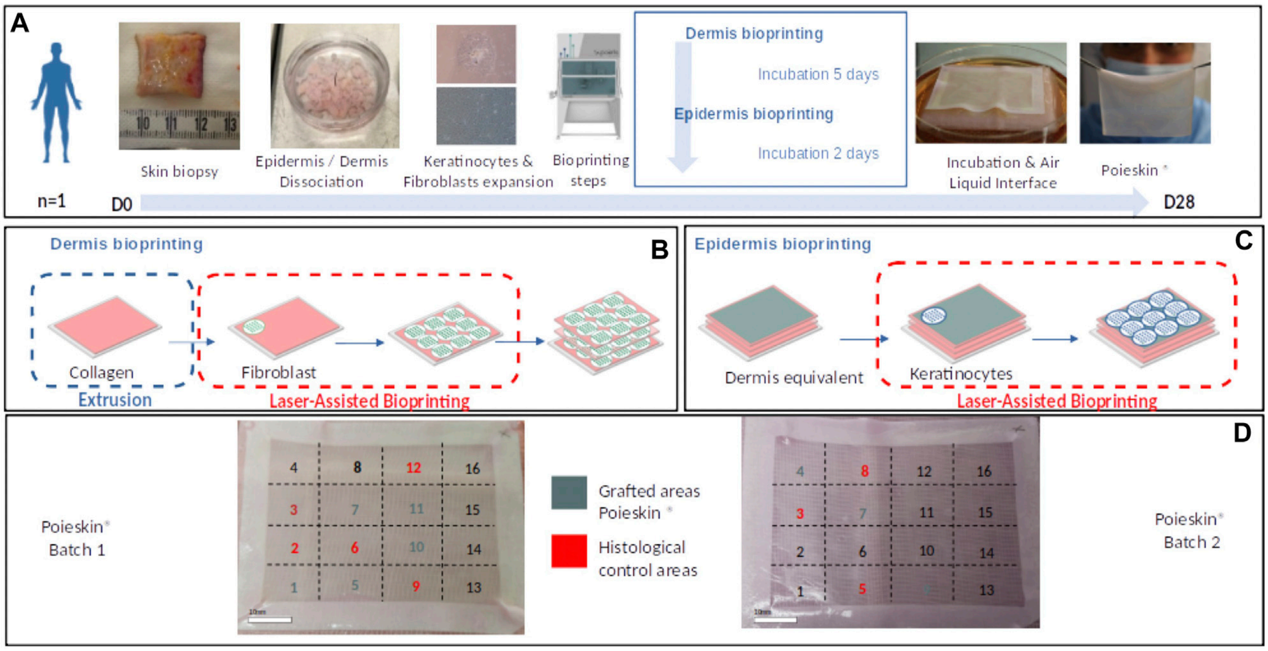

FIGURE 1
(A) Summary of main Poieskin® manufacturing steps. **(B)** Dermis bioprinting steps: successive bioprinting of collagen layers with extrusion bioprinting and fibroblast layers with laser-assisted bioprinting (LAB). **(C)** Epidermis bioprinting steps: keratinocyte deposition with LAB. **(D)** Final repartition of Poieskin® product batches 1 and 2 between histological control and grafts on mice.

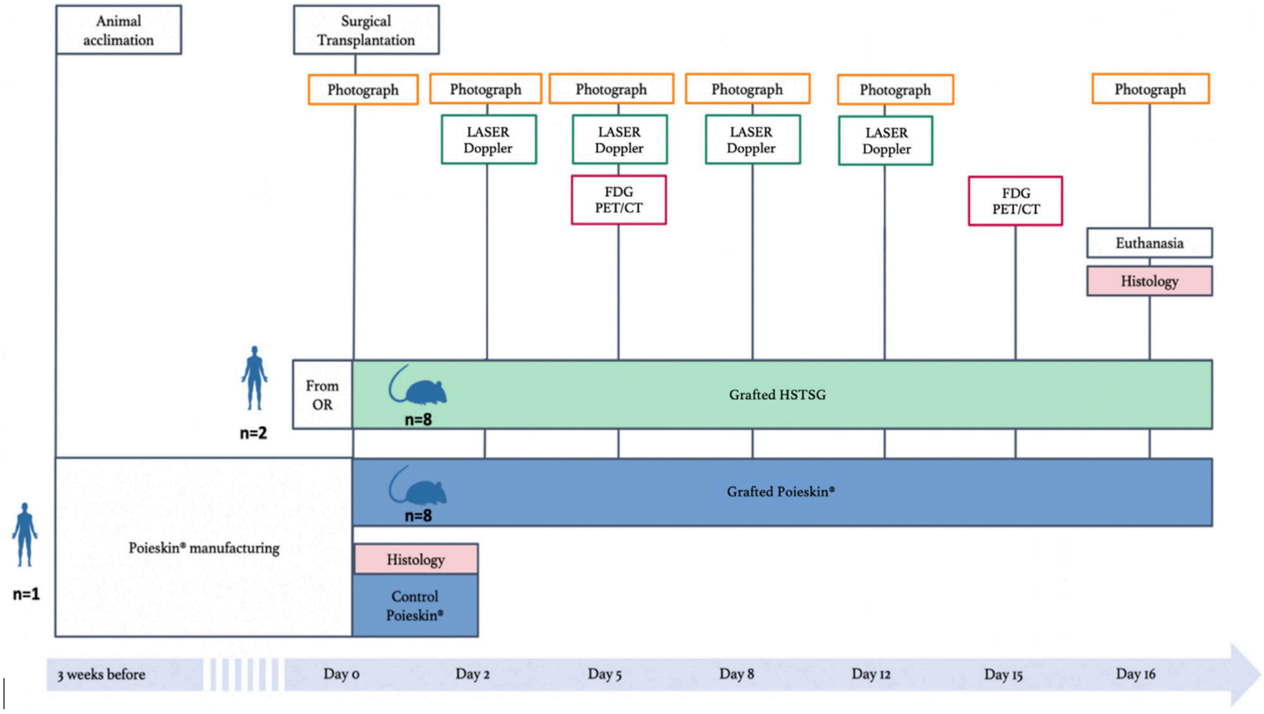

FIGURE 2
Study design comparing human split-thickness skin graft (HSTSG) to Poieskin® (OR, operating room).

On day 6 of the ALI, the DESs were placed on gelified ALI media at room temperature for 6 h and transported from the manufacturing facilities (Poietis, Pessac, France) to the animal facilities (CERIMED, Marseille, France) for grafting. Before grafting, the DESs were cultured at the ALI with fresh ALI media for 24 h. Throughout fabrication, in-process characterizations were performed. Eight areas of 1.5 cm^2 were selected for the grafting procedure, and eight additional areas of the same dimensions were used for control tests (Figure 1D).

Mechanical behavior was assessed by a senior plastic surgeon whose conformity was defined to be robust enough not to break when packaged, manipulated, and applied to the surgical site.

2.4 Homogeneity and quality control of Poieskin® biofabrication

Control samples from 40-cm^2 Poieskin® to be grafted were analyzed to characterize the production features, as well as sections of the wound samples 16 days after grafting. Thickness measurements were made on the histology images using ImageJ software (National Institute of Health, Bethesda, United States).

The quality of the DES was assessed from histological sections after staining with Masson's trichrome (described in Section 2.11). *POIETIS* developed a scoring grid to evaluate dermal and epidermal structures, excluding skin appendages, in order to quantitatively assess the quality of the evaluated samples. The semiquantitative score and associated parameters are presented in Supplementary Table S1.

2.5 *In vivo* preclinical study design

The study was designed to demonstrate the non-inferiority of Poieskin® compared to the reference HSTSG in a relevant animal model (Figure 2). Immunosuppressed female NMRI-Foxn1$^{nu/nu}$ mice (aged 7 weeks and weighing 20–23 g) were purchased from Janvier Laboratories (Genest-Saint-Isle, France). They were allowed to acclimatize for 2 weeks before the experiments. Eight mice received a Poieskin® graft, while eight others received HSTSG on their back immediately after a cutaneous excision of 1 × 1.5 cm. The primary endpoint was the area measurement of the graft taken on standardized photographs in a 16-day follow-up. Moreover, the following secondary endpoints were evaluated: area percentage of wound contraction, superficial vascularization assessed by laser Doppler imaging, local inflammation by PET imaging, and histological analysis after euthanasia.

2.6 Surgical transplantation

The initiation of the surgical procedure in mice was synchronized to the end of Poieskin® maturation and surgical harvesting of HSTSG, in order to perform both treatments on the same day, without delay, under comparable conditions. The mice received a subcutaneous injection of buprenorphine at a dose of 0.1 mg/kg 30 min before general anesthesia by sevoflurane initiation in an induction chamber (8%; 1 L/min). Anesthesia was maintained via a nose cone (2.5%–3%; 0.5 L/min) with spontaneous ventilation on an electric heater carpet at 37°C. Protective collyrium was then administered. The procedure began by cleaning with iodine after marking a 1 × 1.5 cm longitudinal rectangular cutaneous area to excise on the back of the mice. Before incision, the mice received long-term local analgesia by a subcutaneous back-forward injection of ropivacaine at 4 mg/kg around the surgical site. Then, surgical ×2.5 magnifying loupes were used in the surgical procedures.

The surgical protocol consisted of three steps: i) realization of an acute full-thickness longitudinal 1 × 1.5 cm excision using a scalpel no. 15. Any continuous bleeding was coagulated using bipolar forceps. Scarring was followed by immediate covering (with Poieskin® or HSTSG). Grafts were custom-sized according to the defect (1.5 cm^2) from larger samples, using a scalpel no. 23, withdrawn from a 40-cm^2 Poieskin® specimen, or from a fresh human split-thickness skin sample for the HSTSG group. They were manipulated using microsurgical tweezers (without teeth); ii) application of an immediate graft on the skeletal muscles by plan and fixation surgical methods to the skin with 14 separate Prolene® 6–0 (Ethicon Inc., Johnson & Johnson, New Brunswick, NJ, United States) stitches using a microsurgical holder and scissors; iii) application of custom-sized dressing on the graft of a non-adherent, non-absorbent UrgoTul® interface (Laboratoires URGO, Chenôve, France) and then a non-woven surgical pad was fixed using an adhesive Tegaderm® bandage (3 M, Saint Paul, MN, United States). We checked before awakening that the dressing did not induce any hindrance to chest expansion, limb mobility, and fecal or urinary tract.

During postoperative surveillance, the mice were placed under a heating lamp until awakening and then placed into an individually ventilated cage in a loose housing room. The general health condition was monitored daily. Analgesic subcutaneous injections of buprenorphine (0.1 mg/kg/day for the first week and then 0.05 mg/kg/day) could be administered, if necessary. No antibiotic was administered. Dressings were first changed on day 2 and then on days 5, 8, 10, 12, and 15 under general anesthesia.

2.7 Photograph analysis

Standardized photographs were taken preoperatively (day 0) on days 2, 5, 8, and 12 and finally on day 16 immediately before the mice were euthanized. The camera (Canon PowerShot SX220 HS, Tokyo, Japan) was placed vertically 35 cm above the operating site, and the view was zoomed to ×2, taking a centimeter ruler in the range in order to harmonize the area measurement performed using ImageJ software (National Institute of Health, Bethesda, United States). We analyzed the evolution of engraftment and retraction ratios. The engraftment ratio is defined as the vascularized epithelialized graft area divided by the total scarring area at the same time. On the other hand, the retraction ratio is calculated as the total scarring area at a specific moment divided by the total scarring area on day 0.

2.8 Graft perfusion analysis

Laser Doppler perfusion imaging (PIM2, Perimed, Craponne, France) was used to assess skin graft perfusion after surgery on days 2, 6, 12, and 16 post-surgery under sevoflurane anesthesia. The mice were induced with 8% sevoflurane in air, followed by 3% sevoflurane in air, and placed on a 37°C heated carpet. The results were expressed as an optical density ratio of the graft area to a healthy back skin area.

2.9 [18F]-FDG MicroPET/CT imaging

The mice were injected with 6.4 ± 1.5 MBq/100 μL [18 F]-FDG in the caudal vein on days 5 and 15 after surgery. MicroPET/CT images were acquired 60 min after injection during a 20-min imaging session. MicroPET/CT imaging was performed using a nanoScan PET/CT camera (Mediso, Budapest, Hungary) under isoflurane anesthesia. The mice were induced with 4% isoflurane in air, followed by 1.5% isoflurane in air (Isovet from Piramal, Voorschoten, Netherlands). Quantitative region-of-interest (ROI) analysis of the PET signal was performed on attenuation- and decay-corrected PET images using VivoQuant software v4.0patch1 (Invicro, Boston, MA, United States). Tissue standardized uptake values were expressed as the ratio of the graft area to the healthy back skin area.

For both techniques (laser Doppler and [18F]-FDG MicroPET/CT), the screened areas were divided into several ROIs. Unaffected skin on the neck and lumbar area served as controls to assess vascularization and local inflammation evolution of the grafts.

2.10 Histological analysis and immunostaining

On day 0, control DESs were fixed with 4% (w/v) formaldehyde for 8 h at room temperature. At the end of the 16-day follow-up, the mice were euthanized with a lethal overdose of sevoflurane inhaled into an induction chamber associated with cervical dislocation. The surgical sites were then entirely harvested, taking laterally 3-mm-width margins and vertically from the underlying musculoskeletal system to the cutaneous envelope, in order to collect an exhaustive sample for histological analysis. Sections of the wound samples were immediately fixed with 4% (w/v) formaldehyde at room temperature for 48 h and maintained at 4°C for 72 h.

2.11 Histology and immunostaining

Fixed samples were dehydrated in successive ethanol and xylene solutions prior to paraffin embedding using a Histokinette (Leica, Wetzlar, Germany). Sections of 5 μm were generated using a microtome (Leica) and then stained with Masson's trichrome dyes before imaging by light microscopy (Eclipse Ts2, Nikon, Tokyo, Japan). The histological characteristics of all grafts, Poieskin® and HSTSG, were analyzed by an independent skilled pathologist who was blinded to the samples, using NDP2 viewing software (Hamamatsu Photonics, Hamamatsu, Japan) and a semi-quantitative scoring system as previously described.

Previously processed slides were permeabilized with 1X citrate buffer at pH 6 for 20 min at 98°C. Non-specific interactions were limited by incubation with a 2% (w/v) BSA-DPBS solution (bovine serum albumin, Merck, Burlington, Massachusetts, United States; Dulbecco's phosphate-buffered saline, Dutscher) for 10 min. The samples were then incubated overnight at 4°C with primary antibodies, namely, K5 (1/200, Abcam, AB52635), K10 (1/200, Merck Millipore MAB3230), Coll1 (1/500, Abcam, Ab138492) (specific for human and bovine collagen 1 and does not stain mouse collagen 1), αSMA (1/200, Abcam, Ab5694) (Prost-Squarcioni et al., 2008) (Ruiter et al., 1993), and loricrin (1/200, Abcam, Ab85679) antibodies (Matsui and Amagai, 2015). After washing, secondary goat anti-rabbit Alexa Fluor 488 (1/200, Thermo Fisher Scientific, 10729174), secondary goat anti-rabbit Alexa Fluor 594 (1/200, Molecular Probes, R10477), and goat anti-mouse Alexa Fluor 488 (1/200, Thermo Fisher Scientific, 10256302) antibodies were added for 1 h at room temperature. The samples were counterstained with DAPI (1/1000, PK-CA707-40043, PromoCell, Heidelberg, Germany). Immunofluorescence images were captured using the Eclipse Ts2 microscope (Nikon) and analyzed using ImageJ software (National Institute of Health, Bethesda, United States).

The protein structure of the samples was analyzed by immunohistochemistry. Bovine type I collagen, which was used as a biomaterial in Poieskin®, allowed for the identification of the location of Poieskin® and HSTSG. Cytokeratin 5 staining highlighted basal- and spinous-layer keratinocytes of human origin. The association of K10, K5, and loricrin staining revealed the epidermal maturation gradient, as they represent the basal, supra-basal, and corneal layers, respectively. αSMA was used to identify myofibroblasts or pericytes that could reveal neovascularization with a circular shape surrounding a lumen.

2.12 Statistical analysis

Statistical analysis was performed using GraphPad Prism 4.0 (GraphPad Software, La Jolla, CA, United States). The data that support the findings of this study are available on request from the corresponding author. The normality of data distributions was assessed using Shapiro–Wilk and Kolmogorov–Smirnov tests, and all data passed the normality test. Two-way ANOVA statistical tests were used for the analysis with multiple factor interactions (FDG-CT, graft take, and graft retraction). The engraftment ratio was defined as the vascularized epithelialized graft area divided by the total scarring area at the same time, whereas the retraction ratio corresponded to the total scarring area during evaluation divided by the total scarring area on day 0. A mixed-effect analysis was used for the analysis of laser Doppler imaging because values for performing two-way ANOVA were missing. Ultimately, ordinary one-way ANOVA was used for comparing the histological scorings. Graphs display the mean ± standard deviation (SD).

3 Results

The cells were harvested from a skin biopsy of a 25-year-old woman without co-morbidities (BMI was 24.6 kg/m^2). The obtained Poieskin® batches were intact after shipment and easy to manipulate after the final differentiation. All defined acceptance criteria were compliant for both final Poieskin® batches. The total thickness of Poieskin® grafts in two batches was 292 ± 26 μm and 226 ± 31 μm, respectively, which were considered optimal for grafting compared

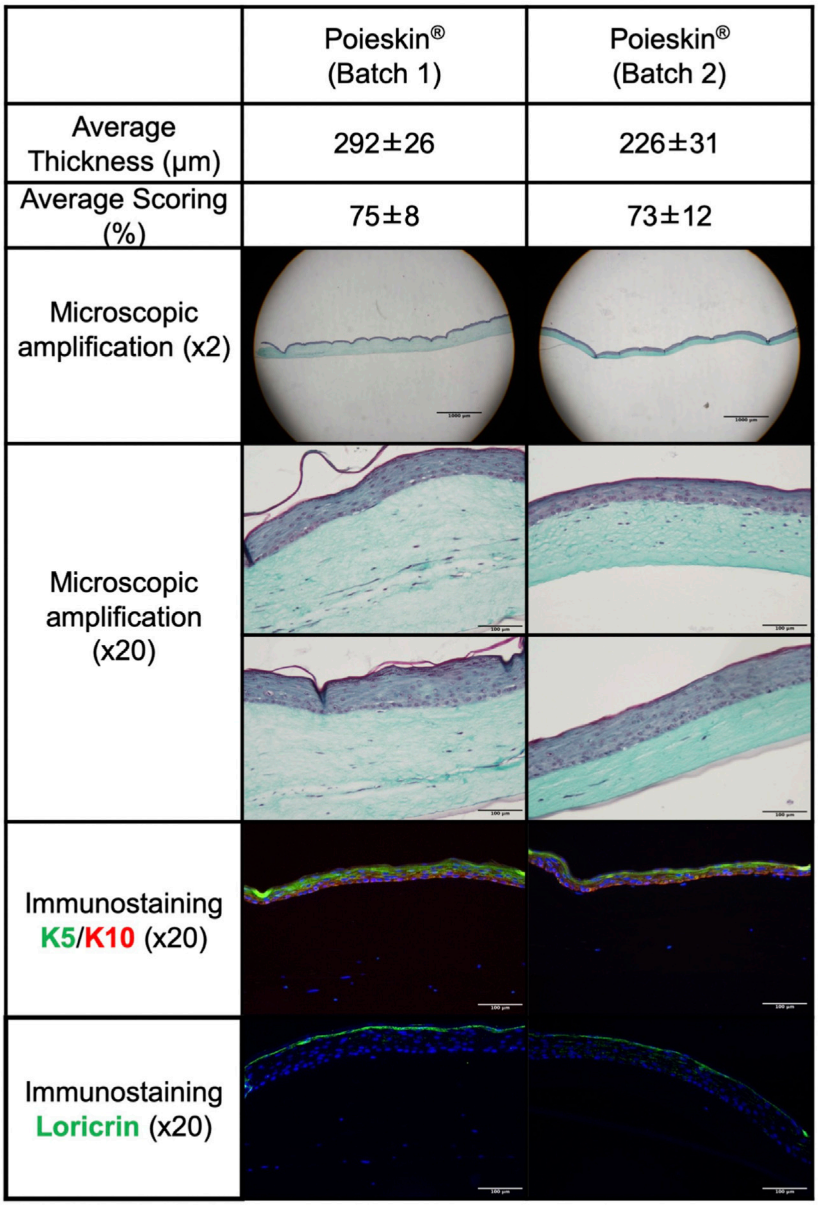

	Poieskin® (Batch 1)	Poieskin® (Batch 2)
Average Thickness (µm)	292±26	226±31
Average Scoring (%)	75±8	73±12
Microscopic amplification (x2)		
Microscopic amplification (x20)		
Immunostaining K5/K10 (x20)		
Immunostaining Loricrin (x20)		

FIGURE 3
Histological and immunostaining characterization of Poieskin® manufacturing: Poieskin® batch 1: area 6 control of mouse 2, scoring = 78, and thickness = 355 ± 33 µm; Poieskin® batch 2: area 3 control of mouse 6, scoring = 81, and thickness = 219 ± 45 µm.

with HSTSG. According to the assessed scoring parameters of the dermal, epidermal, and basement membrane features, the histological structure of Poieskin® was of reliable quality, with an average score of 75% ± 8% for batch 1 (n = 5) and 73% ± 12% for batch 2 (n = 3), well above the 50% compliance threshold. Samples within each batch were homogeneous regardless of their initial localization. Immunohistochemistry with anti-cytokeratin 5 and 10 revealed the presence of a proliferative layer of keratinocytes, as well as satisfactory differentiation of the upper layers of the epidermis, characterized by switching from cytokeratin 5 to 10. Furthermore, immunohistochemistry with anti-loricrin demonstrated the presence of a well-defined stratum corneum (Figure 3). Detailed information about the viability, doubling population, and concentration in viable nucleated cells before bioprinting and scoring and histological images are given in Supplementary Table S2 and Supplementary Figure S1, respectively.

A total of 16 subjects (n = 16) were included receiving either HSTSG (n = 8) or Poieskin® (n = 8). One mouse which received HSTSG died during surgery. HSTSG donor patients were 67- and 44-year-old women without co-morbidities (BMI was 27.0 kg/m^2 and 27.3 kg/m^2, respectively). The conformity with the mechanical behavior was observed for both batches, as shown in Supplementary Video S1. Based on ImageJ software analysis, the mean graft take percentage was 91.8% (SD = 0.1152) on day 16 for Poieskin® and 100% (SD = 0) for HSTSG (Figure 4). We did not observe a significant difference in graft take between the two groups (mean

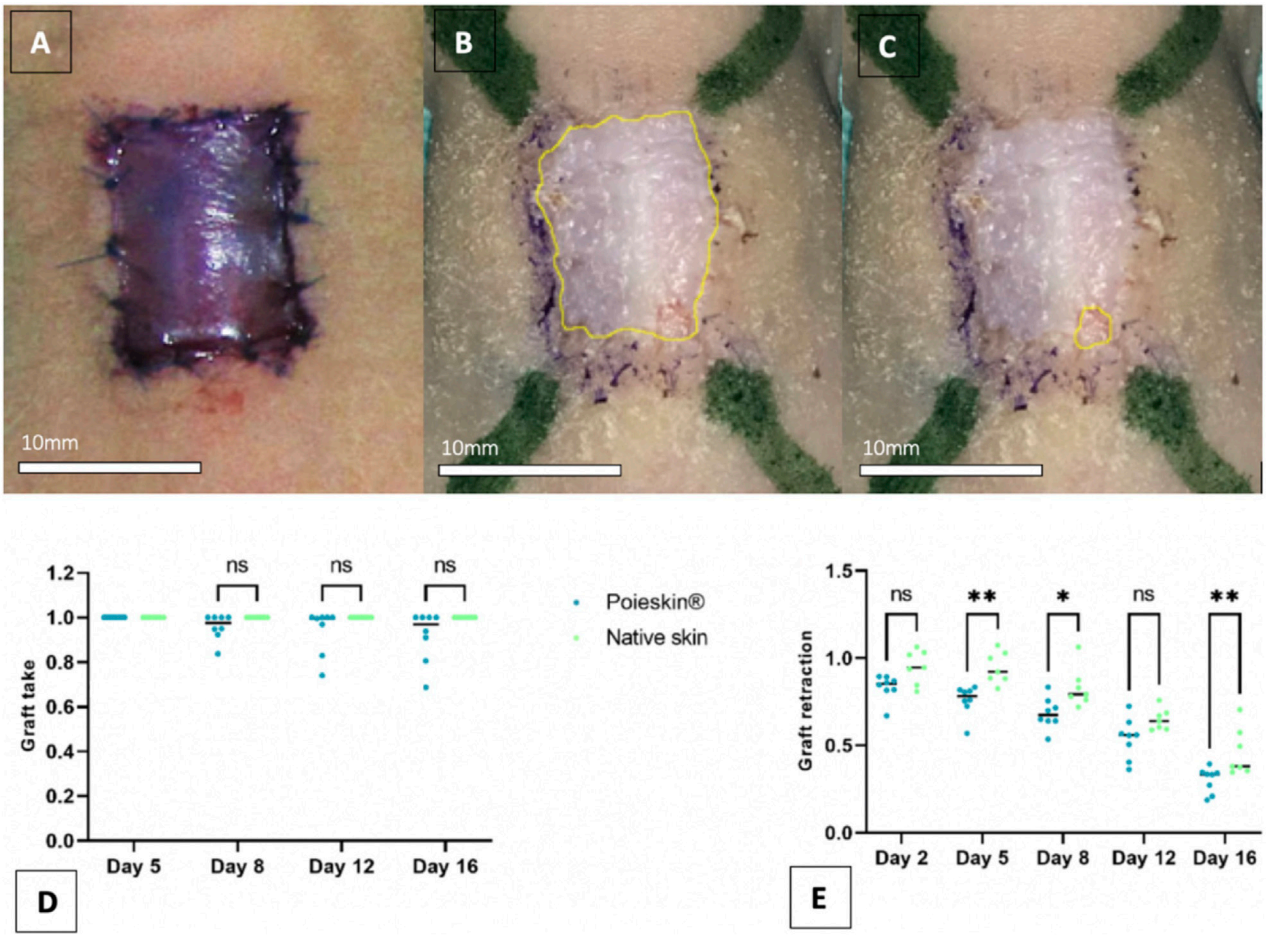

FIGURE 4
Grafted area measurements on standardized photographs ((**A)** Photograph of grafted Poieskin® on day 0; **(B)** photograph of grafted Poieskin® on day 16 with contouring of the total scarring area; **(C)** photograph of grafted Poieskin® on day 16 with contouring of the graft lysed area; **(D)** assessment of graft take; **(E)** assessment of graft retraction; HSTSG, human split-thickness skin graft).

difference: −0.08225; 95% CI (−0.2177 to 0.05315); $p = 0.2942$). The retraction evolution of grafts ran faster for Poieskin® than for HSTSG with a significant difference on day 16 (mean difference: −16.0%; 95% CI (−29.04 to −29.15); $p = 0.0095$). An example of the macroscopic aspect suggesting the quality of graft take, the difference in pigmentation, and the pliability is presented in Supplementary Video S2.

Cutaneous perfusion assessment by laser Doppler imaging showed that the global optical density of the graft decreased over time (Figure 5). However, no significant difference was observed between the two groups ($p = 0.1951$ on day 16). No deaths, adverse events, clinical inflammation, or infection were observed during the entire procedure. Local inflammation assessment by [18F]-FDG MicroPET/CT imaging did not reveal any increasing metabolic activity in the grafted area (Figure 6). We did not observe any significant differences between Poieskin® and HSTSG on either day 5 ($p = 0.9998$) or day 15 ($p = 0.5109$). Collagen 1 staining confirmed the presence of both Poieskin® and HSTSG *in situ* 16 days after grafting on mice. On the other hand, mouse collagen was not stained as expected. Cytokeratin 5 staining highlighted basal and spinous layer keratinocytes of human origin. αSMA was used to identify myofibroblasts or pericytes that could reveal neovascularization with a circular shape surrounding a lumen. Based on our specific histological scoring, the mean score of Poieskin® was 75% (SD = 8.31; $n = 8$), and the mean score of HSTSG was 83% (SD = 4.99; $n = 7$) (Figure 7). We did not record a significant difference in scoring between Poieskin® and HSTSG with a mean difference of 7.964 (SD = 3.588) points (95% CI = 0.2121 to 15.72; $p = 0.2423$).

4 Discussion

This study demonstrated for the first time the reliability and homogeneity of a bioprinted large-sized DES under GMP-compatible conditions.

The NGB multimodal bioprinting manufacturing equipment successfully delivered functional DESs for *in vivo* grafting. The manufacturing process was completed within 28 days of initial biopsy procurement, and the substitutes' thickness met the defined specifications set by clinicians. Histology and immunostaining analyses confirmed the presence of mandatory skin structures related to dermal and epidermal compartments.

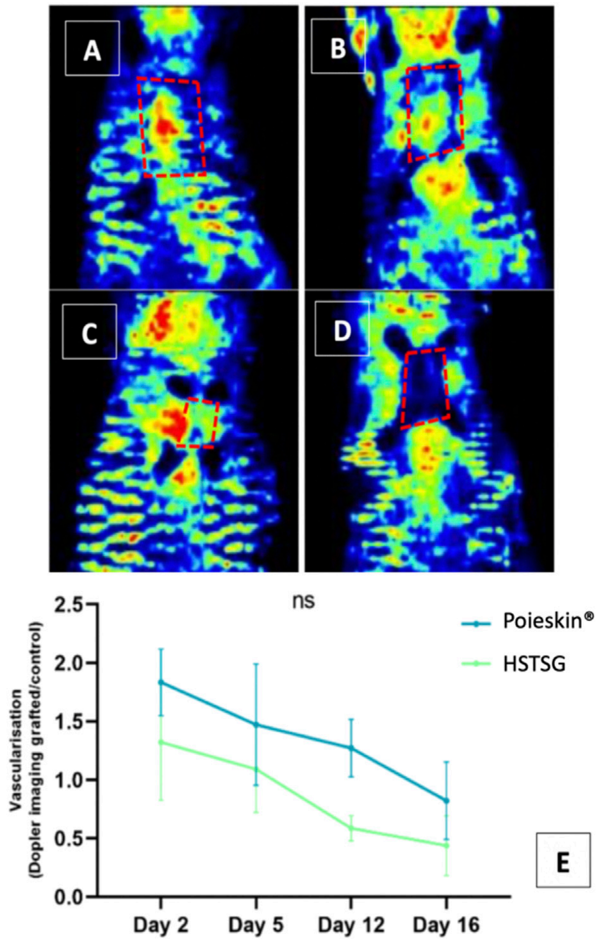

FIGURE 5
Graft perfusion assessment by laser Doppler (**(A)** Poieskin® condition on day 2; **(B)** HSTSG condition on day 2; **(C)** Poieskin® condition on day 16; **(D)** HSTSG condition on day 16; **(E)** evolution of the optical density ratio for both conditions).

Indeed, we were able to obtain two 40-cm^2 batches with similar histological characteristics. The histological scoring was previously validated on more than 150 histological skin models (data not shown) by four independent operators to select and adjust the appropriate criteria and thresholds for the final version. In this study, the scoring grid was then used by an independent pathologist to calculate the score of the Poieskin batches.

We also assessed the safety and efficacy of Poieskin® in a relevant immunosuppressed mouse model compared to the reference method, HSTSG.

Inflammation, as an expression of local infection, was monitored by TEP-CT FDG. We did not observe any increment and recorded variations that were close to the background signal. As no side effects occurred during the study, we could infer that Poieskin® grafting is a safe procedure.

Furthermore, we reported an average engraftment of Poieskin® of 91.8% 16 days after grafting, which was similar to the reference method. Qualitative observations of the grafted Poieskin® samples showed that some microscopic aspects of HSTSG, which were not included in the printing pattern, appeared on day 16, such as intra-dermal micro-vessels, dermal papilla, and a coherent morphological continuum of the epidermal layer at the scar border. This endpoint is encouraging, and we assume that Poieskin® could be an alternative to STSG in superficial full-thickness skin defects which are mainly represented by acute carcinologic excisions, donor-site scarring of reconstructive procedures, burn injuries (from deep second to third degree), and traumatic and chronic wounds. These indications are nowadays properly treated by 200–300 μm autologous STSG. The cutoff ratio deeming the success or failure of skin graft take is not consensual. It depends on intrinsic and extrinsic factors (such as the location, thickness, or type/etiology of the defect) and varies from 50% to 90% in the literature (Birchall et al., 1991; Kirsner et al., 1995; Thourani et al., 2003; Shores et al., 2012; Reddy et al., 2014; Lauerman et al., 2018; Braza and Fahrenkopf, 2022). In clinical applications of skin grafts, we consider an engraftment of over 80% of the graft area on days 15–21 as successful since the patient does not require additional procedures. In this study, we observed that seven out of eight mice grafted with Poieskin® were above this 80% cutoff on day 16.

The skin graft area is known to shrink over time due to fibroblasts differentiating into myofibroblasts, inducing contraction. This is sometimes a desired effect as it decreases the size of the lesion, but

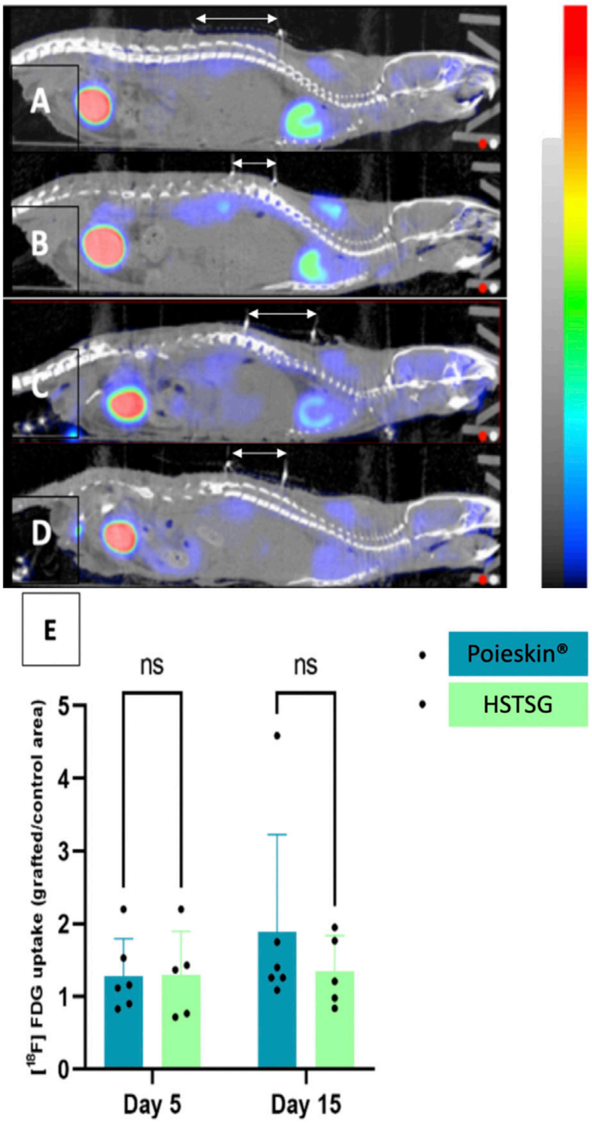

FIGURE 6
[18F]-FDG MicroPET/CT imaging (CT signal from −500 to 3,500 HU; PET signal from 0 to 8 Bq) 1 h after IV injection. Grafts are located below the white arrows (**(A)** Poieskin® on day 5; **(B)** HSTSG on day 5; **(C)** Poieskin® on day 15; **(D)** HSTSG on day 15; **(E)** metabolic activity measurements).

it can stiffen adjacent articulations. Here, we recorded differences in the kinetics of area reduction: Poieskin® showed faster contraction than HSTSG, reaching approximately 69% of contraction *versus* 54% for HSTSG, from day 5. According to our assumption, a poorer reticulation of the constructed dermis in Poieskin® could induce faster graft dehydration *in situ* than that in HSTSG. The phenotype and organization of fibroblasts in the dermis could also be involved in this contraction phenomenon (Douillet et al., 2022).

Nevertheless, the Poieskin® texture turned out to be more elastic but without pigmentation compared to HSTSG, with a softer appearance. Although not significant, this observation was consistent with the difference in the optical density on the laser Doppler assessment between Poieskin® and HSTSG. Indeed, the lower optical density of HSTSG (which showed 100% graft take) cannot be due to hypoperfusion but might be a result of human skin texture characteristics that present a thicker stratum corneum and greater pigmentation due to the presence of melanocytes. It suggests that laser Doppler is not suitable for comparing perfusion of skin with different textures.

From a general perspective, the animal model represents a difficult setting for the skin graft procedure. Indeed, recipient site immobilization is not possible, enhancing shear forces, while aseptic conditions under the dressings are hard to maintain. Furthermore, the inflammation phenomenon is underestimated in the immunosuppressed mice model we selected. This could have influenced the results of the TEP-CT FDG we described. The choice to perform the grafting procedure just after the acute full-thickness excision is also a matter of discussion. Although this model is classically used to assess the skin graft procedure (Michael et al., 2013; Cubo et al., 2016; Kim et al., 2018; Albanna et al., 2019; Baltazar et al., 2020; Jorgensen et al., 2020), this corresponds to a worst-case scenario compared to clinical applications where grafts are

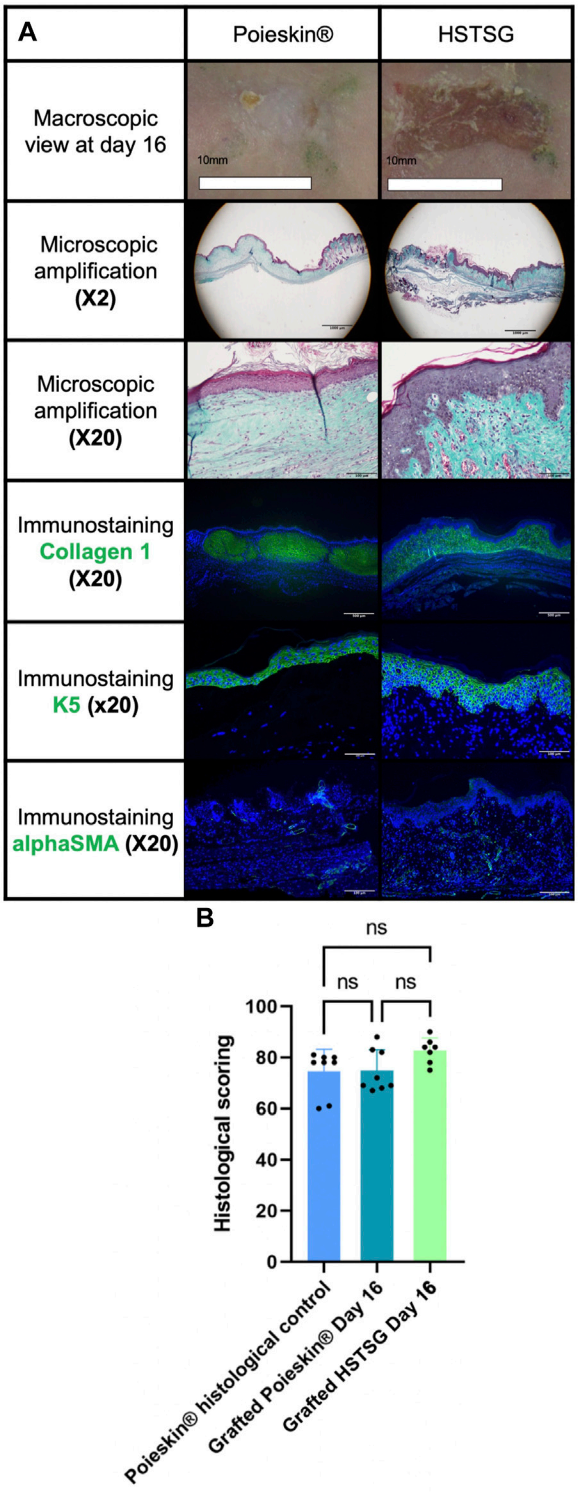

FIGURE 7
Results of histological analysis. **(A)** Representative images of the histological aspects of Poieskin® (mouse 8, batch 2, area 9, scoring = 69, and thickness >300 μm) and human split-thickness skin graft (HSTSG) (mouse 9, scoring 84, and thickness >300 μm); **(B)** exhaustive results of histological scoring for Poieskin® control, grafted Poieskin®, and grafted HSTSG.

applied after granulation tissue formation, which is rich in neovessels and promotes graft take. In clinical settings, granulation tissue appears after 21 days from the hypodermis layer, which suggests that Poieskin® manufacturing will need to be slightly shortened due to process duration optimization.

Different authors have already studied the *in vivo* efficacy of a bioprinting DES, but none of them were able to provide a GMP-compatible and large-size DES (Michael et al., 2013; Cubo et al., 2016; Baltazar et al., 2020; Jorgensen et al., 2020; Yang et al., 2022). Indeed, the largest reported production ever does not exceed 10 cm × 2 cm (Cubo et al., 2016), although Poieskin® is an 8 cm × 5 cm sheet comparable to the handmade manufacturing method that has already been tested in humans (Blok et al., 2013; Boa et al., 2013; Blok, 2016; Germain et al., 2018; Meuli et al., 2019). Their findings are mainly focused on the histology and immunohistochemistry qualitative evaluation of the DES, with a follow-up varying from 11 days to 8 weeks. Only Jorgensen et al. (2020) reported wound closure using the epithelialization rate of 50.4% at 21 days, which appears to be lower than that of Poieskin®. It is important to note that none of these studies compared bioprinted DES to STSG engraftment, which is considered the reference treatment from a clinical perspective.

It is important to note that Poieskin® has undergone rigorous GMP readiness assessments, including in-depth selection and risk analysis of starting and raw materials, accurate process step and cell characterization with quality controls during batch development, and a validated quality control strategy with appropriate in-process controls, all of which have been submitted and discussed with the French National Agency for Medicines and Health Products Safety (data not shown). The manufacturing process for Poieskin® has been designed to meet GMP requirements for automated manufacturing equipment for ATMPs, and the automated bioprinting equipment NGB has been qualified to operate in a grade A environment. Additionally, sterilization of all specific consumables has been validated, and the entire process and manufacturing conditions of Poieskin® have been validated with a dedicated aseptic process simulation test.

We believe that these results are important for the scientific community for two main reasons. First, there is a significant clinical need for large-scale DES products that have not been commercialized yet. Second, while bioprinting approaches have shown potential in recent years, most preclinical studies have been conducted on limited-size DESs that do not comply with GMP requirements. In this context, our original results support the use of Poieskin® in humans as it represents a reliable and homogeneous large-size DES with a reproducible architecture and comparable features to HSTSG in terms of engraftment, safety, and surgical use.

5 Conclusion

In conclusion, for the first time, we described a GMP-compatible manufacturing method that produces a 3D bioprinted DES. Poieskin® has consistent bioengineering and manufacturing characteristics and can be used as an alternative to STSG in clinical applications to treat full-thickness cutaneous defects.

Data availability statement

The original contributions presented in the study are included in the article/Supplementary Material further inquiries can be directed to the corresponding author.

Ethics statement

The studies involving human participants were reviewed and approved by BIOPSKIN study number NCT04925323 CE14, Aix-Marseille University. The patients/participants provided their written informed consent to participate in this study. The animal study was reviewed and approved by the National Animal Care and Ethics Committee (no. APAFIS 2020012015402650).

Author contributions

ML, HC, DC, BB, BG, and LB performed animal experimentation, imaging, and data collection. LaH, EP, LoH, HR, and FG performed statistical analysis. LaH, EP, LoH, HR, FG, JV, LG, CD, LA, HC, FS, and JM performed biofabrication and in-process controls. NM, RA, and LD performed histological analysis. All authors contributed to the article and approved the submitted version.

Conflict of interest

Author FG is the CEO and founder of POIETIS.

The remaining authors declare that the research was conducted in the absence of any commercial or financial relationships that could be construed as a potential conflict of interest.

Publisher's note

Supplementary material

The Supplementary Material for this article can be found online at: https://www.frontiersin.org/articles/10.3389/fbioe.2023.1217655/full#supplementary-material

References

Albanna, M., Binder, K. W., Murphy, S. V., Kim, J., Qasem, S. A., Zhao, W., et al. (2019). *In situ* bioprinting of autologous skin cells accelerates wound healing of extensive excisional full-thickness wounds. *Sci. Rep. 12 févr* 9 (1), 1856. doi:10.1038/s41598-018-38366-w

Arslan-Yildiz, A., El Assal, R., Chen, P., Guven, S., Inci, F., and Demirci, U. (2016). Towards artificial tissue models: Past, present, and future of 3D bioprinting. *Biofabrication. 1 mars* 8 (1), 014103. doi:10.1088/1758-5090/8/1/014103

Auger, D. F. A. (2022). Sass 2: Self assembled skin substitute for the autologous treatment of severe burn wounds in acute stage of burn trauma. Avaliable At: https://clinicaltrials.gov/ct2/show/NCT02350205.

Baltazar, T., Merola, J., Catarino, C., Xie, C. B., Kirkiles-Smith, N. C., Lee, V., et al. (2020). Three dimensional bioprinting of a vascularized and perfusable skin graft using human keratinocytes, fibroblasts, pericytes, and endothelial cells. *Tissue Eng. Part a. mars* 26 (5-6), 227–238. doi:10.1089/ten.tea.2019.0201

Birchall, M. A., Varma, S., and Milward, T. M. (1991). The moriarty sign: An appraisal. *Br. J. Plast. Surg. mars* 44 (2), 149–150. doi:10.1016/0007-1226(91)90051-k

Blok, C. (2016). A phase II randomized multicenter study on efficacy and safety of cultured autologous skin (Tiscover®) and acellular dermal matrix (AS210) in chronic (Arterio-)Venous ulcers. Avaliable At: https://clinicaltrials.gov/ct2/show/NCT02360358.

Blok, C. S., Vink, L., de Boer, E. M., van Montfrans, C., van den Hoogenband, H. M., Mooij, M. C., et al. (2013). Autologous skin substitute for hard-to-heal ulcers: Retrospective analysis on safety, applicability, and efficacy in an outpatient and hospitalized setting. *Wound Repair Regen. Off. Publ. Wound Heal Soc. Eur. Tissue Repair Soc. Oct.* 21 (5), 667–676. doi:10.1111/wrr.12082

Boa, O., Cloutier, C. B., Genest, H., Labbé, R., Rodrigue, B., Soucy, J., et al. (2013). Prospective study on the treatment of lower-extremity chronic venous and mixed ulcers using tissue-engineered skin substitute made by the self-assembly approach. *Adv. Skin. Wound Care* 26 (9), 400–409. doi:10.1097/01.asw.0000433102.48268.2a

Braza, M. E., and Fahrenkopf, M. P. (2022). "Split-thickness skin grafts," in *StatPearls* (Treasure Island (FL): StatPearls Publishing). Avaliable At: http://www.ncbi.nlm.nih.gov/books/NBK551561/.

CHU de Quebec-Universite Laval (2014). Treatment of cutaneous ulcers with a novel biological dressing. Avaliable At: https://clinicaltrials.gov/ct2/show/NCT00207818.

Cubo, N., Garcia, M., Del Cañizo, J. F., Velasco, D., and Jorcano, J. L. (2016). 3D bioprinting of functional human skin: Production and *in vivo* analysis. *Biofabrication. 5 déc* 9 (1), 015006. doi:10.1088/1758-5090/9/1/015006

Douillet, C., Nicodeme, M., Hermant, L., Bergeron, V., Guillemot, F., Fricain, J. C., et al. (2022). From local to global matrix organization by fibroblasts: A 4D laser-assisted bioprinting approach. *Biofabrication. 24 janv* 14 (2), 025006. doi:10.1088/1758-5090/ac40ed

EMA (2018). *New guidelines on good manufacturing practices for advanced therapies*. Bruxelles, Belgium: European Commission. Avaliable At: https://www.ema.europa.eu/en/news/new-guidelines-good-manufacturing-practices-advanced-therapies.

Germain, L., Larouche, D., Nedelec, B., Perreault, I., Duranceau, L., Bortoluzzi, P., et al. (2018). Autologous bilayered self-assembled skin substitutes (SASSs) as permanent grafts: A case series of 14 severely burned patients indicating clinical effectiveness. *Eur. Cell. Mater* 36, 128–141. doi:10.22203/ecm.v036a10

Jorgensen, A. M., Varkey, M., Gorkun, A., Clouse, C., Xu, L., Chou, Z., et al. (2020). Bioprinted skin recapitulates normal collagen remodeling in full-thickness wounds. *mai* 26 (9-10), 512–526. doi:10.1089/ten.tea.2019.0319

Kim, B. S., Kwon, Y. W., Kong, J. S., Park, G. T., Gao, G., Han, W., et al. (2018). 3D cell printing of *in vitro* stabilized skin model and *in vivo* pre-vascularized skin patch using tissue-specific extracellular matrix bioink: A step towards advanced skin tissue engineering. *juin* 168, 38–53. doi:10.1016/j.biomaterials.2018.03.040

Kirsner, R. S., Marston, W. A., Snyder, R. J., Lee, T. D., Cargill, D. I., and Slade, H. B. (2012). Spray-applied cell therapy with human allogeneic fibroblasts and keratinocytes for the treatment of chronic venous leg ulcers: A phase 2, multicentre, double-blind, randomised, placebo-controlled trial. *Lancet Lond Engl.* 380 (9846), 977–985. doi:10.1016/s0140-6736(12)60644-8

Kirsner, R. S., Mata, S. M., Falanga, V., and Kerdel, F. A. (1995). Split-thickness skin grafting of leg ulcers. The University of Miami Department of Dermatology's experience (1990-1993). *Dermatol Surg. Off. Publ. Am. Soc. Dermatol Surg. Al. août* 21 (8), 701–703. doi:10.1111/j.1524-4725.1995.tb00273.x

Lauerman, M. H., Scalea, T. M., Eglseder, W. A., Pensy, R., Stein, D. M., and Henry, S. (2018). Efficacy of wound coverage techniques in extremity necrotizing soft tissue infections. *Am. Surg. 1 Nov.* 84 (11), 1790–1795. doi:10.1177/000313481808401137

Lee, W., Debasitis, J. C., Lee, V. K., Lee, J. H., Fischer, K., Edminster, K., et al. (2009). Multi-layered culture of human skin fibroblasts and keratinocytes through three-dimensional freeform fabrication. *Biomaterials* 30 (8), 1587–1595. doi:10.1016/j.biomaterials.2008.12.009

Lee, W., Lee, V., Polio, S., Keegan, P., Lee, J. H., Fischer, K., et al. (2010a). On-demand three-dimensional freeform fabrication of multi-layered hydrogel scaffold with fluidic channels. *Biotechnol. Bioeng. 15 avr* 105 (6), 1178–1186. doi:10.1002/bit.22613

Lee, Y. B., Polio, S., Lee, W., Dai, G., Menon, L., Carroll, R. S., et al. (2010b). Bio-printing of collagen and VEGF-releasing fibrin gel scaffolds for neural stem cell culture. *Exp. Neurol. juin* 223 (2), 645–652. doi:10.1016/j.expneurol.2010.02.014

Límová, M. (2010). Active wound coverings: Bioengineered skin and dermal substitutes. *Surg. Clin. North Am. déc* 90 (6), 1237–1255. doi:10.1016/j.suc.2010.08.004

Matsui, T., and Amagai, M. (2015). Dissecting the formation, structure and barrier function of the stratum corneum. *Int. Immunol. juin* 27 (6), 269–280. doi:10.1093/intimm/dxv013

Meuli, M., Hartmann-Fritsch, F., Hüging, M., Marino, D., Saglini, M., Hynes, S., et al. (2019). A cultured autologous dermo-epidermal skin substitute for full-thickness skin defects: A phase I, open, prospective clinical trial in children. *Plast. Reconstr. Surg. juill* 144 (1), 188–198. doi:10.1097/prs.0000000000005746

Michael, S., Sorg, H., Peck, C. T., Koch, L., Deiwick, A., Chichkov, B., et al. (2013). Tissue engineered skin substitutes created by laser-assisted bioprinting form skin-like structures in the dorsal skin fold chamber in mice. *PloS One* 8 (3), e57741. doi:10.1371/journal.pone.0057741

Miri, A. K., Mostafavi, E., Khorsandi, D., Hu, S. K., Malpica, M., and Khademhosseini, A. (2019). Bioprinters for organs-on-chips. *Biofabrication* 11 (4), 042002. doi:10.1088/1758-5090/ab2798

Moustafa, M., Bullock, A. J., Creagh, F. M., Heller, S., Jeffcoate, W., Game, F., et al. (2007). Randomized, controlled, single-blind study on use of autologous keratinocytes on a transfer dressing to treat nonhealing diabetic ulcers. *Regen. Med. Nov.* 2 (6), 887–902. doi:10.2217/17460751.2.6.887

NCT01655407 (2016). Safety and efficacy study of autologous engineered skin substitute to treat partial- and full-thickness burn wounds - full text view - ClinicalTrials.gov. Avaliable At: https://clinicaltrials.gov/ct2/show/NCT01655407.

NCT02145130 (2014). Phase I study for autologous dermal substitutes and dermo-epidermal skin substitutes for treatment of skin defects - full text view - ClinicalTrials.gov. Avaliable At: https://clinicaltrials.gov/ct2/show/NCT02145130.

NCT03229564 (2017). Study with an autologous dermo-epidermal skin substitute for the treatment of burns in children - full text view - ClinicalTrials.gov. Avaliable At: https://clinicaltrials.gov/ct2/show/NCT03229564.

NCT03394612 (2018). Study with an autologous dermo-epidermal skin substitute for the treatment of full-thickness skin defects in adults and children - full text view - ClinicalTrials.gov. Avaliable At: https://clinicaltrials.gov/ct2/show/NCT03394612.

Ortega-Zilic, N., Hunziker, T., Läuchli, S., Mayer, D. O., Huber, C., Baumann Conzett, K., et al. (2010). EpiDex® Swiss field trial 2004-2008. *Dermatol Basel Switz.* 221 (4), 365–372. doi:10.1159/000321333

Pegg, D. E. (2002). The history and principles of cryopreservation. *Semin. Reprod. Med.* 20, 005–014. doi:10.1055/s-2002-23515

Prost-Squarcioni, C., Fraitag, S., Heller, M., and Boehm, N. (2008). Functional histology of dermis. *Ann. Dermatol Venereol. janv* 135 (12), 1S5–20. doi:10.1016/S0151-9638(08)70206-0

Ramakrishnan, K. M., and Jayaraman, V. (1997). Management of partial –thickness burn wounds by amniotic membrane: A cost-effective treatment in developing countries. *Burns* 23 (1), S33–S36. doi:10.1016/s0305-4179(97)90099-1

Reddy, S., El-Haddawi, F., Fancourt, M., Farrant, G., Gilkison, W., Henderson, N., et al. (2014). The incidence and risk factors for lower limb skin graft failure. *Dermatol Res. Pract.* 2014, 1–3. doi:10.1155/2014/582080

Renner, R., Harth, W., and Simon, J. C. (2009). Transplantation of chronic wounds with epidermal sheets derived from autologous hair follicles--the Leipzig experience. *Int. Wound J. juin* 6 (3), 226–232. doi:10.1111/j.1742-481x.2009.00609.x

Rheinwald, J. G., and Green, H. (1975). Seria cultivation of strains of human epidemal keratinocytes: The formation keratinizin colonies from single cell is. *Cell.* 6, 331–343. doi:10.1016/s0092-8674(75)80001-8

Ruiter, D. J., Schlingemann, R. O., Westphal, J. R., Denijn, M., Rietveld, F. J., and De Waal, R. M. (1993). Angiogenesis in wound healing and tumor metastasis. *Behring Inst. Mitt. août* 92, 258–272.

Salisburry, R. E., Wilmore, D. W., and Silverstein, P. (1973). Biological dressing for skin graft donor site. *Arch. Surg.* 106, 705–706.

Sheridan, R. (2009). Closure of the excised burn wound: Autografts, semipermanent skin substitutes, and permanent skin substitutes. *Clin. Plast. Surg. Oct.* 36 (4), 643–651. doi:10.1016/j.cps.2009.05.010

Shores, J. T., Hiersche, M., Gabriel, A., and Gupta, S. (2012). Tendon coverage using an artificial skin substitute. *J. Plast. Reconstr. Aesthetic Surg. JPRAS. Nov.* 65 (11), 1544–1550. doi:10.1016/j.bjps.2012.05.021

Takami, Y., Yamaguchi, R., Ono, S., and Hyakusoku, H. (2014). Clinical application and histological properties of autologous tissue-engineered skin equivalents using an acellular dermal matrix. *J. Nippon. Med. Sch. Nippon. Ika Daigaku Zasshi* 81 (6), 356–363. doi:10.1272/jnms.81.356

Tavis, M. J., Thornton, J. W., and Bartlett, R. H. (1979). A new composite skin prothesis. *Burns* 8, 123–130.

Thourani, V. H., Ingram, W. L., and Feliciano, D. V. (2003). Factors affecting success of split-thickness skin grafts in the modern burn unit. *J. Trauma. mars* 54 (3), 562–568. doi:10.1097/01.ta.0000053246.04307.2e

Voineskos, S. H., Ayeni, O. A., McKnight, L., and Thoma, A. (2009). Systematic review of skin graft donor-site dressings. *Plast. Reconstr. Surg. juill* 124 (1), 298–306. doi:10.1097/prs.0b013e3181a8072f

Yang, Y., Xu, R., Wang, C., Guo, Y., Sun, W., and Ouyang, L. (2022). Recombinant human collagen-based bioinks for the 3D bioprinting of full-thickness human skin equivalent. *Int. J. Bioprinting* 8 (4), 611. doi:10.18063/ijb.v8i4.611

Yu, J., Park, S. A., Kim, W. D., Ha, T., Xin, Y. Z., Lee, J., et al. (2020). Current advances in 3D bioprinting technology and its applications for tissue engineering. *Polym. 11 déc* 12 (12), 2958. doi:10.3390/polym12122958

Zhao, L., Lee, V. K., Yoo, S. S., Dai, G., and Intes, X. (2012). The integration of 3-D cell printing and mesoscopic fluorescence molecular tomography of vascular constructs within thick hydrogel scaffolds. *Biomater. juill* 33 (21), 5325–5332. doi:10.1016/j.biomaterials.2012.04.004

Frontiers in Bioengineering and Biotechnology

TYPE Original Research
PUBLISHED 28 July 2023
DOI 10.3389/fbioe.2023.1215233

Sustained release of a highly specific GSK3β inhibitor SB216763 in the PCL scaffold creates an osteogenic niche for osteogenesis, anti-adipogenesis, and potential angiogenesis

Weimin Gong[1†], Molin Li[1†], Lizhou Zhao[1†], Pengtao Wang[1], Xiaofang Wang[1], Bo Wang[1], Xing Liu[2*] and Xiaolin Tu[1*]

[1]Laboratory of Skeletal Development and Regeneration, Institute of Life Sciences, Chongqing Medical University, Chongqing, China, [2]Department of Orthopedics, Ministry of Education Key Laboratory of Child Development and Disorders, National Clinical Research Center for Child Health and Disorders, Children's Hospital of Chongqing Medical University, Chongqing, China

OPEN ACCESS

EDITED BY
Junxi Wu,
University of Strathclyde, United Kingdom

REVIEWED BY
Guya Diletta Marconi,
University of Studies G. d'Annunzio Chieti and Pescara, Italy
Donghai Li,
Sichuan University, China

*CORRESPONDENCE
Xing Liu,
xtu@cqmu.edu.cn
Xiaolin Tu,
liuxingda@126.com

†These authors have contributed equally to this work

RECEIVED 01 May 2023
ACCEPTED 20 July 2023
PUBLISHED 28 July 2023

CITATION
Gong W, Li M, Zhao L, Wang P, Wang X, Wang B, Liu X and Tu X (2023), Sustained release of a highly specific GSK3β inhibitor SB216763 in the PCL scaffold creates an osteogenic niche for osteogenesis, anti-adipogenesis, and potential angiogenesis.
Front. Bioeng. Biotechnol. 11:1215233.
doi: 10.3389/fbioe.2023.1215233

The safe and effective use of Wnt signaling is a hot topic in developing osteogenic drugs. SB216763 (S33) is a widely used highly specific GSK3β inhibitor. Here, we show that S33 initiates canonical Wnt signaling by inhibiting GSK3β activity in the bone marrow stromal cell line ST2 and increases osteoblast marker alkaline phosphatase activity, osteoblast marker gene expression including *Alpl*, *Col1α1*, and *Runx2*, promoting osteogenic differentiation and mineralization of ST2 cells. In addition, S33 suppressed the expression of adipogenic transcription factors *Pparg* and *Cebpa* in ST2 cells to suppress adipogenesis. ICRT-14, a specific transcriptional inhibitor of Wnt signaling, reversed the effects of S33 on the differentiation of ST2 cells. S33 also increased the expression of osteoclast cytokines *RANKL* and *Opg* but decreased the *RANKL/Opg* ratio and had the potential to inhibit osteoclast differentiation. In addition, we printed the PSCI3D (polycaprolactone, S33, cell-integrated 3D) scaffolds using a newly established integrated 3D printing system for hard materials and cells. S33 sustained release in the hydrogel of the scaffold with 25.4% release on day 1% and 81.7% release over 7 days. Cells in the scaffolds had good cell viability. The ratio of live/dead cells remained above 94% for 7 days, while the cells in the scaffolds proliferated linearly, and the proliferative activity of the PSCI3D scaffold group increased 1.4-fold and 1.7-fold on days 4 and 7, respectively. Similarly, in PSCI3D scaffolds, osteogenic differentiation of st2 cells was increased. The alkaline phosphatase activity increased 1.4- and 4.0-fold on days 7 and 14, respectively, and mineralization increased 1.7-fold at 21 days. In addition, PSCI3D conditioned medium promoted migration and tubulogenesis of HUVECs, and S33 upregulated the expression of *Vegfa*, a key factor in angiogenesis. In conclusion, our study suggests that S33 functions in osteogenesis, anti-adipogenesis, and potential inhibition of osteoclast differentiation. And the sustained release of S33 in PSCI3D scaffolds creates a safe osteogenic niche, which promotes cell proliferation, osteogenesis, and angiogenesis and has application prospects.

KEYWORDS

SB216763, Wnt signaling, osteogenesis, adipogenesis, angiogenesis, PCL and cell integrated 3D scaffold, sustained release

Introduction

More effective osteogenic drugs with fewer side effects remain a research hotspot. Teriparatide (PTH), abalopathide (PTHrP), and romosozumab (sclerotin antibody) are anabolic drugs approved for the treatment of osteoporosis. PTH and PTHrP act through PTH receptors to regulate the fate of BMSCs towards osteoblasts or adipocytes in bone (Fan et al., 2017) and to promote angiogenesis as well (Cohn-Schwartz et al., 2022), but PTH and PTHrP should not be used for a long time because of the risk of inducing osteosarcoma (Neer et al., 2001). Sclerostin antibodies activate the Wnt/β-catenin pathway to promote bone formation and reduce bone resorption (McClung et al., 2014). However, sclerotin antibodies may lead to vascular calcification (Golledge and Thanigaimani, 2022), increasing the risk of severe cardiovascular disease (Saag et al., 2017).

Targeting Wnt signals may be an effective way for drug development (Baron and Kneissel, 2013). The Wnt signaling is associated with cell proliferation, differentiation, polarization, and migration (Wodarz and Nusse, 1998). *ß*-catenin levels are critical regulators of Wnt signaling. They can be regulated by a ubiquitin-dependent proteolysis system when the Wnt ligand binds to the receptor Frizzled and the co-receptor low-density lipoprotein (Lrp) 5/6 to form a complex, which inhibits the effect of the *ß*-catenin destruction complex, resulting in reduced *ß*-catenin phosphorylation to stabilize *ß*-catenin in the cytoplasm. Increased *ß*-catenin enters the nucleus to cooperate with the transcription factor Tcf/Lef to activate the transcription of Wnt target genes (Nusse and Clevers, 2017). GSK3β is a member of the complex, and inhibiting its activity can disable the *ß*-catenin destruction complex, effectively activating Wnt/β-catenin signaling. This makes GSK3β a target for drug development (MacDonald et al., 2009).

SB216763 (S33) is a widely used GSK3β inhibitor with more than 500 articles published as searched by title/abstract in PubMed. S33 inhibits GSK3β activity by competitively inhibiting ATP activity (Coghlan et al., 2000). S33 is highly selective and does not affect the activity of 24 other serine/threonine and tyrosine protein kinases under complete inhibition of GSK3 activity. S33 has been used in many disease-related studies, such as neurogastrointestinal disorders (Zhang et al., 2017), denervated muscle atrophy (Weng et al., 2018), and bronchopulmonary dysplasia (Hummler et al., 2013), but its effects on mesenchymal stem cell differentiation and osteoporosis have not been reported.

In this study, we found that S33 initiates canonical Wnt signaling in the bone marrow stromal cell line ST2 and preosteoblastic cell line MC3T3-E1, promoting osteogenesis in a dose-dependent manner. S33 increases the activity of osteoblast marker alkaline phosphatase and the expression of osteoblast marker genes *Alpl*, *Col1α1*, and *Runx2*. In addition, S33 inhibits the transcription factor of adipogenesis *Pparg* and *Cebpα* to inhibit adipogenesis and potential osteoclast differentiation. These features make S33 a promising candidate drug suitable for drug development in preventing and treating elderly osteoporosis.

The materials in the orthopedic market are mostly metal, ceramic, polymer materials, etc., but the current gold standard for bone transplantation is still autologous bone transplantation (Herrmann et al., 2015). Because pure material grafts have low biological activity and lack bone regeneration ability, they are prone to loosening, graft failure, or inevitable revision outcomes 5—20 years after surgeries (Cha et al., 2019). Revision is a headache for orthopedic surgeons because it takes a lot of cost and time and impacts patients' quality of life. Bone tissue engineering technology, especially 3D biological printing technology, has successfully achieved the personalized shape adaptation of tissue engineering scaffolds through live cell printing, creating a suitable biological microenvironment for cell adhesion, proliferation, and differentiation (Kang et al., 2022).

3D printing can solve the problem of shape matching, but the research of orthopedic materials failed to be considered from the perspective of bone developmental biology, resulting in effective bone regeneration.1 Therefore, the lack of biological activity is still a bottleneck problem. To address the biological activity of orthopedic materials and achieve a breakthrough in the "0″status of grafts combined with hard materials and stem cells in the current graft market, an integrated 3D tissue and organ printer (ITOP, in 2016) prints structures containing supportive hard materials and stem cells, forming vascularized bone in the body (Kang et al., 2016). This work has been featured as an industry milestone and a direction for future medical applications in journals with high-impact factors, such as Nature Reviews (Lieben, 2016; Malda and Groll, 2016; Pashuck and Stevens, 2016). However, 7 years later, there has been no breakthrough in the construction of biomimetic bones, and such research is still limited to 3D printing for the production of vascularized bones (Wang S. et al., 2022). There are few reports about other cells or tissues forming in orthopedic materials. The reason could be the lack of an osteogenic microenvironment with developmental function (Grosso et al., 2017).

Endowing hard material osteogenic niches is an improved approach to addressing bottlenecks (Liu et al., 2022; Wang et al., 2023). In this study, we tried to sustainably release S33 in hard material (PSCI3D) scaffolds, creating an osteogenic niche that completely solves cell survival and growth in the scaffolds, with a cell survival rate as high as 94.0%. Within 7 days, the proliferative activity of the cells increases linearly, while S33 is slowly released by 81.7%; however, amazingly, the scaffolds keep better osteoblast differentiation and mineralization after 7 days. Thus, the sustained release of S33 creates a safe osteogenic niche, which bionomically reconstructs functional bone with osteogenesis, angiogenesis, anti-adipogenesis, and potentially anti-osteoclastogenesis in the scaffold.

Materials and methods

Reagents and cells

Chemicals: S33 and ICRT-14 were purchased from MCE (Shanghai, China). Lyophilized Gelatin Methacryloyl (GelMA) and a photo-cross-linking agent (LAP) were obtained from Sunp Biotech (Beijing, China). Polycaprolactone (PCL) was obtained from Sigma (St Louis, MO, USA), while Trizol was purchased from Invrogen (Thermo Fisher Scientific, Carlsbad, CA, USA). Alizarin red S was obtained from Solarbao Biotechnology (Beijing, China), and Matrigel was purchased from Corning (Costar; Corning, NY, USA). Lipo 8000 and an enhanced chemiluminescence (ECL) reagent were obtained from Beyotime Biotechnology (Shanghai, China).

Assay kits: The BCIP/NBT alkaline phosphatase (AP) color-rendering kit, live/dead viability assay kit, alkaline phosphatase activity assay kit, cytoplasmic and nuclear protein extraction kit, and modified Oil Red O staining Kit and DAPI staining solution were all obtained from Beyotime Biotechnology (Shanghai, China). AG RNAex Pro Reagent and reverse transcription reaction kits were obtained from Accurate Biology (Hunan, China), while the CCK8 assay kit was purchased from MCE (Shanghai, China).

Antibodies: Wanlei (Shenyang, China) provided anti-β-catenin, anti-β-actin, and anti-lamin B antibodies, while Beyotime Biotechnology (Shanghai, China) supplied FITC-labeled goat anti-rabbit IgG (H + L) and HRP-labeled goat anti-rabbit IgG (H + L).

Plasmid: The Wnt signaling reporter construct and its control, TopFlash and FopFlash plasmids, were acquired from Addgene (Cambridge, MA, USA).

Cell culture reagents and cell lines: Gibco (Beijing, China) supplied *a*-MEM, DMEM, penicillin, and streptomycin, while Sigma (St. Louis, MO, USA) provided *ß*-glycerophosphate, ascorbic acid, dexamethasone, Indomethacin, and IBMX. Fetal bovine serum (FBS) was purchased from Biological Industries (Israel), and Wnt3a-expressing cells, control L cells, and human umbilical vein endothelial cells (HUVECs) were obtained from the American Type Culture Collection (ATCC, Manassas, VA, USA). Additionally, ST2 and MC3T3-E1 cells were acquired from Dr. Steve Teitelbaum.

Cell culture and differentiation

ST2, Wnt3a, and control L cells were grown in a growth medium comprising 90% *a*-MEM, 10% FBS, 50U/mL penicillin, and 50 μg/mL streptomycin at 37°C and 5% CO_2, with half of the medium being refreshed every 2 days. To induce osteogenic differentiation, cells were cultured in an osteogenic medium containing 10 mM *ß*-glycerophosphate and 50 μg/mL ascorbic acid, with medium replacement every 1–2 days. Adipogenic differentiation was induced by culturing the cells in an adipogenic medium consisting of 0.5 μM dexamethasone, 0.5 mM IBMX, and 60 μM Indomethacin in DMEM, with medium replacement every 3–4 days.

Modulation of Wnt signaling

To activate and obstruct Wnt signaling, S33, and ICRT-14 were used, respectively. While S33 was employed at different concentrations to stimulate Wnt signaling, DMSO was the control. ICRT-14 was utilized to decrease the binding efficiency of *ß*-catenin to the N-terminal domain of T-cell factor 4 (TCF4) to stop *ß*-catenin activity (Gonsalves et al., 2011). And ST2 cells were split in each well of a 24-well plate at a density of 2×10^4 cells and treated with S33 and ICRT-14 for 72 h to verify the specificity of Wnt signaling.

Integrated 3D printing

As previously described in our earlier report (Wang P. et al., 2022), GelMA hydrogel was utilized to load both cells and S33. To prepare the GelMA solution, 0.5% (w/v) lithium phenyl-2, 4, 6-trimethylbenzoylphosphinate (LAP) photo-initiator was added to a mixture of 0.25 mL *a*-MEM and either 10 μM S33 or 5×10^5 ST2 cells. Pre-melt at 95°C for 30 min to reach the optimal temperature for PCL printing; melted PCL was then extruded at 400 μm diameter with an interval of 1,100 μm and a printing speed of 2 mm/s. At 25°C, S33 or cell-loaded GelMA solution was printed between the PCL strips at a printing speed of 5 mm/s, with a beam diameter of 300 μm and an interval of 500 μm (Billiet et al., 2014). Once a layer was printed, the GelMA hydrogel was crosslinked under 405 nm blue light for 10s before printing resumed vertically for the next layer. After printing three layers, the PCL, S33, cell integrated 3D (PSCI3D) scaffold was successfully fabricated.

Cell viability

To assess cell viability, we employed the same methods described in our previous report (Wang B. et al., 2022). Both live/dead assay kit and CCK8 proliferation activity assay were utilized for this purpose.

Live/dead assay

The live/dead cell assay was performed with a kit. Following culturing for 1, 4, and 7 days, the scaffold underwent washing with PBS and subsequent incubation in a mixture at room temperature. The mixture was prepared according to Calcein AM: PI: assay buffer = 1: 1: 1,000. Calcein AM for living cells, and PI for dead cells. The scaffold was then incubated for 0.5 h in a 37°C incubator before being imaged with a laser scanning confocal microscope (Nikon, Japan). Using ImageJ, the cell viability was quantified.

Cell proliferative activity

Cell proliferative activity was measured by the CCK8 kit. For the proliferation of ST2 cells, they were seeded in 96-well plates at a density of 2,000 cells per well and treated with varying concentrations of S33 for 24, 48, and 72 h. After treatment, 90 μL PBS and 10 μL CCK8 solution were added to each well and incubated at 37°C for 2 h. The absorbance at 450 nm was measured by a spectrophotometer (Thermo Fisher Scientific). For PSCI3D scaffolds, perform as above after 1, 4, and 7 days of incubation.

Gene expression analysis

To analyze gene expression, total RNA was extracted from the cells using Trizol (Tu et al., 2012b). The cDNA was synthesized using AG RNAex Pro Reagent, and the cDNA was used as templates for quantitative real-time polymerase chain reaction (qPCR) to detect genes with primer sets (Tables 1, 2). The housekeeping gene glyceraldehyde-3-phosphate dehydrogenase (Gapdh) was used to normalize the mRNA expression levels, and the 2-Δ Ct method was applied (Tu et al., 2015).

Osteogenic differentiation

Alkaline phosphatase staining

Alkaline Phosphatase Staining (AP staining) was performed according to a previously reported method (Tu et al., 2007).

TABLE 1 Sequences of primers used for RT-PCR (mouse).

Primer	Forward (5′-3′)	Reverse (5′-3′)
Gapdh	GCACAGTCAAGGCCGAGAAT	GCCTTCTCCATGGTGGTGAA
beta-actin	AGAGGGAAATCGTGCGTGAC	CCATACCCAAGAAGGAAGGCT
Lef1	TACCCCAGCCAGTGTCAACA	TCCATGATAGGCTTGATGACTTTC
Axin2	TGCAGGAGGCGGTACAGTTC	GCTGGAAGTGGTAAAGCAGCTT
Alpl	CACGGCGTCCATGAGCAGAAC	CAGGCACAGTGGTCAAGGTTGG
Runx2	CCGGTCTCCTTCCAGGAT	GGGAACTGCTGTGGCTTC
Bglap	CAGCGGCCCTGAGTCTGA	GCCGGAGTCTGTTCACTACCTTA
Col1a1	GACAGGCGAACAAGGTGACAGCAGAGG	CAGGAGAACCAGGAGAACCAGGAG
Ibsp	CAGAGGAGGCAAGCGTCACT	GCTGTCTGGGTGCCAACACT
Pparg	GCCAAGGTGCTCCAGAAGATGAC	GTGAAGGCTCATGTCTGTCTCTGTC
Cebpa	GCCAAACTGAGACTCTTC	TGGCATCTCTGTGTCAAC
RANKL	CATGACGTTAAGCAACGG	AGGGAAGGGTTGGACA
Opg	ACGGACAGCTGGCACACCAG	CTCACACACTCGGTTGTGGG
Vegfa	AGAAGGAGGAGGGCAGAATCATCAC	GGGCACACAGGA TGGCTTGAAG

TABLE 2 Sequences of primers used for RT-PCR (human).

Primer	Forward (5′-3′)	Reverse (5′-3′)
GAPDH	GGAGCGAGATCCCTCCAAAAT	GGCTGTTGTCATACTTCTCATGG
VEGFA	AGAGGGAAATCGTGCGTGAC	CCATACCCAAGAAGGAAGGCT

Following treatment with S33 for 3 days, ST2 cells were washed with PBS and fixed in 3.7% formaldehyde for 5 min. Next, washed thrice with PBS and subjected to staining using the BCIP/NBT alkaline phosphatase color development kit. For the PSCI3D scaffold, staining was carried out for 4 hours after culturing for 7 and 14 days. The plates and scaffolds were stained for 30 min and 4 h, respectively. Results were recorded using a digital camera.

AP biochemical activity assay

The cells were subjected to a previously reported assay to measure the alkaline phosphatase (AP) biochemical activity (Tu et al., 2007). Briefly, 0.3 mL of 10 mM Tris/HCl (pH 7.4) was added to each well, and the cells were scraped and sonicated three times for 10 s each. Centrifuged at 13,000 rpm for 3 min, the supernatant was collected and analyzed using an AP detection kit, following the manufacturer's instructions.

Mineralization assay (Alizarin Red S staining)

ST2 cells and PSCI3D scaffold were cultured in a growth medium for 3 days and 7 days, respectively. The medium was then changed to osteogenic medium for both cell types and cultured for 14 days. To analyze matrix mineralization, cells, and scaffold were stained with 0.4% Alizarin Red S for 0.5 h and imaged under a microscope. After that, they were washed with PBS at room temperature and destained with 10% cetylpyridinium chloride for 1 h. The quantitation of mineralization was performed by measuring the absorbance of the washing solution at 562 nm.

Plasmid transfection and reporter gene activity assay

The experimental protocol followed previous reports (Luo et al., 2022). ST2 cells were cultured into 24-well plates and transfected with TopFlash and FopFlash plasmids using Lipo8000 for 24 h. Transfected ST2 cells were continued to be treated with S33 for 48 h. Luciferase activity was measured using a dual luciferase reporter analysis system, and the results were presented as normalized values.

Detection of changes of *ß*-catenin content

Immunofluorescence was used to detect *ß*-catenin in the treated cells, as previously reported (Liu et al., 2022). The cells were first treated with S33 or DMSO for 24 h, then washed with PBS and fixed with 4% paraformaldehyde. To allow for permeabilization, the cells were treated with PBS-T for 30 min, then blocked with 1% BSA for 0.5 h. Immunostaining was carried out using a rabbit polyclonal anti-mouse *ß*-catenin antibody (diluted 1:50) and FITC-labeled goat anti-rabbit IgG (H + L) secondary antibody (diluted 1:500). After three washes with PBS, the cells were incubated with DPAI (diluted 1:5000) for 5 min and washed again with PBS. Then, images were captured using a fluorescence microscope.

Adipogenesis assay

Adipogenic differentiation

To induce adipogenic differentiation, the ST2 cells were cultured in an adipogenic medium (0.5 μM dexamethasone, 0.5 mM IBMX, 60 μM Indomethacin, and *a*-MEM was replaced by DMEM). Lipid droplets were observed microscopically after 7 days of stimulation with S33, followed by Oil Red O staining.

Oil Red O staining

ST2 cells were washed once with PBS. Then the cells were fixed with 3.7% formaldehyde for 5 min. ST2 cells were then washed three times with PBS at room temperature, stained with a modified Oil Red O staining kit per instruction, and photographed under a microscope.

Western blotting

As we previously described (Tu et al., 2012a), the cytoplasmic and nuclear proteins were isolated from ST2 cells using a cytoplasmic and nuclear protein extraction kit. Samples containing 10 μg of protein were separated using a 10% SDS/PAGE gel and transferred onto a PVDF membrane (Millipore). Following blocking in 5% non-fat milk for 2 h, the membranes were incubated overnight at 4°C with the appropriate primary antibody: rabbit polyclonal anti-mouse *ß*-catenin antibody (diluted 1:1,000), mouse polyclonal anti-Lamin-B (diluted 1:1,000), or anti-β-actin (diluted 1:1,000) antibodies. After washing three times with TBS-T, the membranes were incubated with a secondary antibody, goat anti-rabbit IgG (H + L) (diluted 1:5000) for 1 h at room temperature. Following three additional washes with TBS-T, an enhanced chemiluminescence (ECL) reagent was used. The bands were measured by Bio-Rad XRS (Bio-Rad, Hercules, CA, US).

S33 release experiment in scaffold

As reported (Wang et al., 2021), different concentrations of S33 were prepared ranging from 0.1 to 2 mg/mL, measuring the absorbance at 220 nm. A standard curve was then generated for absorbance values for S33 concentration. The PSCI3D scaffolds were placed in a 6-well plate, and added 4 mL of purified water. The plates were then incubated at 37°C. 1 mL of culture medium was measured for absorbance values at 220 nm and repeated at each time point. Then, the standard curve was used to obtain the change of S33 release in the PSCI3D scaffold over time. To maintain the volume, add 2 mL of fresh water back to the plate.

Angiogenesis assay

PSCI3D scaffold conditioned medium preparation

After culturing the PSCI3D scaffold or DMSO control scaffold in a complete medium for 3 days, a conditioned medium (CM) was collected after that. Then they were stored at – 80°C until use. Wnt3a and the control L conditioned medium were collected in the same manner as previously reported (Vinyoles et al., 2014). Wnt3a-expressing cells and control L cells were cultured in complete medium for 3 days, and the conditioned medium (CM) was collected and stored at −80°C until use.

Cell migration assay

As previously reported (Liu et al., 2022), 1 × 10^5 HUVECs were seeded in DMEM without FBS in the upper chamber. The lower chamber was filled with 700 μL DMEM containing 10% FBS and 300 μL CM, then placed at 37°C for 48 h. Migrated cells in the upper chamber were fixed with 3.7% formaldehyde for 5 min. Staining is then performed with a crystal violet stain for 1–2 min. Finally, stained cells were counted and quantified with ImageJ.

Tube formation assay

As we previously reported (Wang P. et al., 2022), HUVECs were seeded onto 24-well plates, which were pre-coated with 200 μL/well Matrigel at a density of 2 × 10^4 per well and then incubated with 700 μL complete medium and 300 μL of PSCI3D scaffold conditioned medium for 6 h. The structures were observed and counted microscopically. Vascular tubular networks formed by HUVECs were quantified with ImageJ.

Statistical analysis

GraphPad Prism 8.0.1 software was used for statistical analysis. Each experiment was independently repeated three times, and the results were presented as means ± SD (standard deviation). Differences between multiple groups were analyzed using One-Way ANOVA, while differences between groups split into two independent variables were analyzed using Two-Way ANOVA. Student's t-test was used for analyzing differences between two comparable groups. A significant difference was defined as $p < 0.05$.

Results

S33 inactivates GSK3β to activate canonical Wnt signaling

As a highly selective GSK3β inhibitor, S33 can inhibit the activity of GSK3β without affecting the activity of other kinases (Zhu et al., 2019). Phosphorylation of GSK3β at SER9 leads to the inactivation of its enzymatic activity, a critical step in activating canonical Wnt signaling by inhibiting GSK3β. As shown in Figure 1A, s33 upregulated the phosphorylation level of SER9 of GSK3β in a dose-dependent manner in ST2 cells, whereas total GSK3β levels remained unchanged. Inactivation of GSK3β decreased the levels of phosphorylated *ß*-catenin and stabilized *ß*-catenin in the cytoplasm, and the stabilized *ß*-catenin entered the nucleus to activate Wnt signaling (MacDonald et al., 2009; Baron and Kneissel, 2013). The effect of S33 on intracellular *ß*-catenin levels was investigated by Western blotting. Compared with DMSO controls, *ß*-catenin protein content in cytosolic and nuclear fractions also increased progressively with increasing concentrations of S33 (Figure 1B).

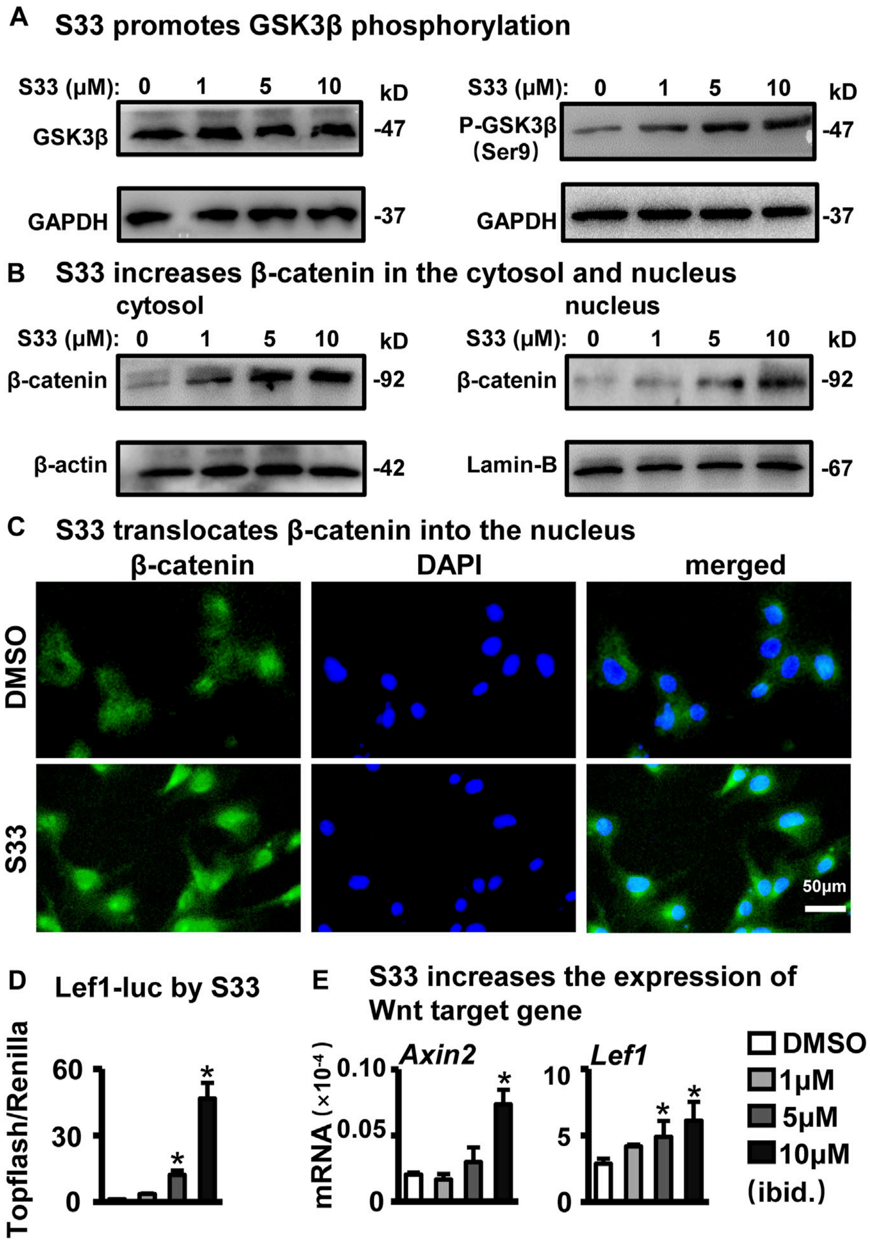

FIGURE 1
Effect of S33 on canonical Wnt signaling. **(A,B)** Western blotting detection of protein GSK3β, P-GSK3β, and *ß*-catenin expression in the cytoplasm and nucleus of ST2 cells treated with different concentrations of S33 **(C)** Immunofluorescence staining of *ß*-catenin in ST2 cells. Scale bar = 50 μm. **(D)** Luciferase activity of ST2 cells **(E)** Expression of Wnt targets genes. *, $p < 0.05$, compared with the DMSO group, n = 3.

To verify whether *ß*-catenin nuclear entry was increased, immunofluorescence staining by an anti-β-catenin antibody detected changes in *ß*-catenin levels in the nuclei of ST2 cells treated with 10 μM S33. Consistent with WB results, 10 μM S33 significantly promoted *ß*-catenin nuclear entry (Figure 1C).

Next, to determine the effect of S33 on canonical Wnt signaling transduction, we transfected ST2 cells with TopFlash (the synthetic *ß*-catenin/Tcf-dependent luciferase reporter) and FopFlash (the negative control reporter for *ß*-catenin/Tcf-binding element mutation) plasmids for 8 h followed by stimulation with S33 for 48 h, and then measured luciferase activity. The results showed that S33 upregulated TopFlash reporter activity in a dose-dependent manner without affecting the activity of the negative control reporter FopFlash (Figure 1D).

Finally, Wnt target genes were detected. The results showed that the expression of Wnt target gene *Lef1* was increased in a concentration-dependent manner, and *Axin2* also showed a significant increase after treatment with 10 μM S33 (Figure 1E).

The above results showed that S33 concentration-dependently inhibits GSK3β activity by increasing GSK3β phosphorylation level and *ß*-catenin content in the nucleus, effectively activating Wnt signaling in ST2 cells.

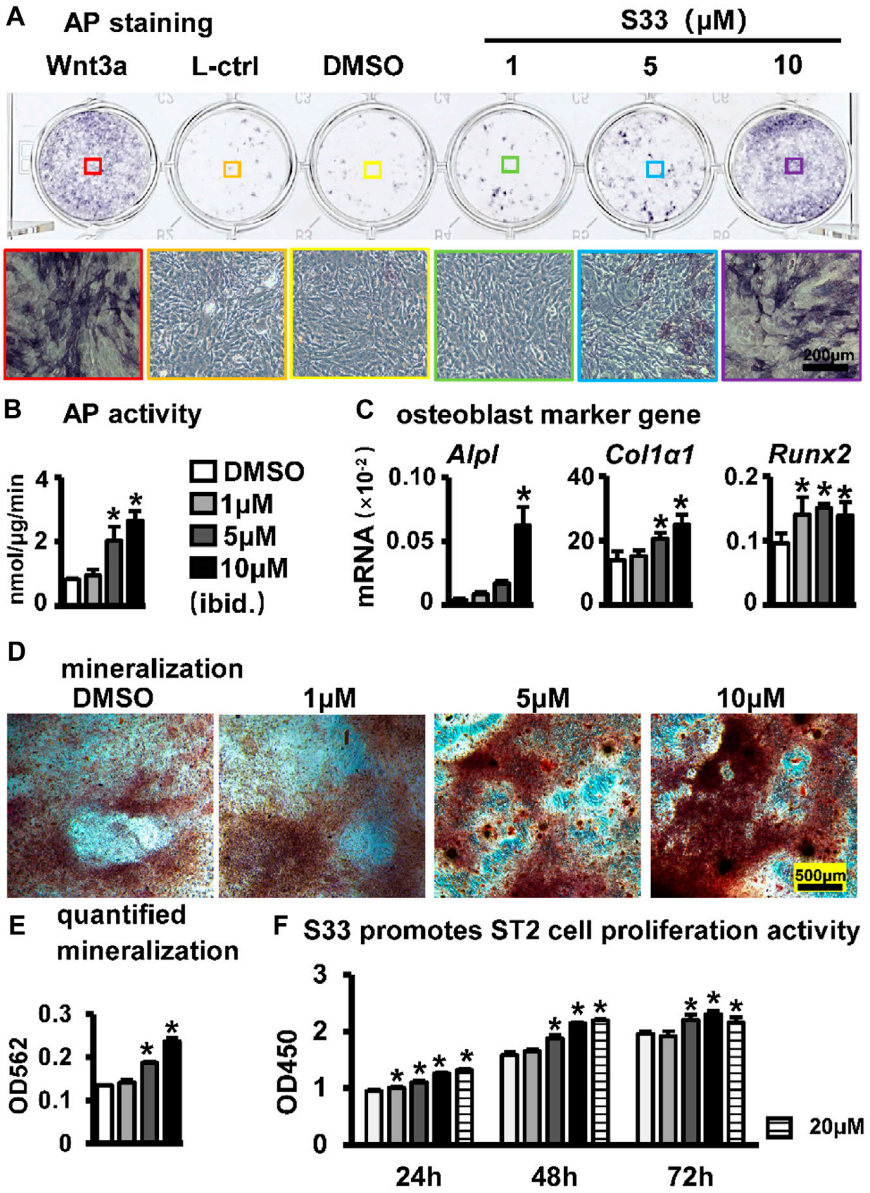

FIGURE 2
Effect of S33 on osteogenic differentiation. **(A)** ST2 cells were treated with different concentrations of S33 for 3 days, followed by AP staining. Positive and negative controls were established using Wnt3a and control L conditioned medium, respectively, scale bar = 200 μm **(B)** AP biochemical activity assay. **(C)** Expression of osteoblast marker genes **(D)** Images under the microscope of Alizarin Red S staining of bone nodules, scale bar = 500 μm. **(E)** Quantitative analysis of mineralization **(F)** CCK8 assay. *, $p < 0.05$, compared with the DMSO group, n = 3.

S33 promotes osteogenic differentiation and proliferation of ST2 cells

To assess the effect of S33 on the osteogenic differentiation of ST2 cells following the activation of canonical Wnt signaling, osteogenic differentiation analysis was performed after ST2 cells were treated with different concentrations of S33. For AP staining, conditioned media from Wnt3a and control L cells were used as positive and negative controls, respectively. Wnt3a-expressing cells were able to secrete Wnt3a protein, which promotes osteogenic differentiation of ST2 cells (Tu et al., 2007), whereas control L cells are the control of Wnt3a-expressing cells. AP staining showed that S33 increased AP expression in ST2 cells in a dose-dependent manner (Figure 2A). Subsequent quantitative AP activity assay results showed that AP activity also increased dose-dependent (Figure 2B). Meanwhile, qPCR results indicated that S33 upregulated the expression of osteoblast marker genes *Alpl*, *Col1α1*, and *Runx2* (Figure 2C).

To further assess changes in extracellular matrix (ECM) mineralization, Alizarin Red S staining and mineralization quantification were performed in ST2 cells cultured with an osteogenic medium containing different concentrations of S33 for 14 days. Similarly, S33 promoted calcium deposition in a concentration-dependent manner (Figure 2D), with

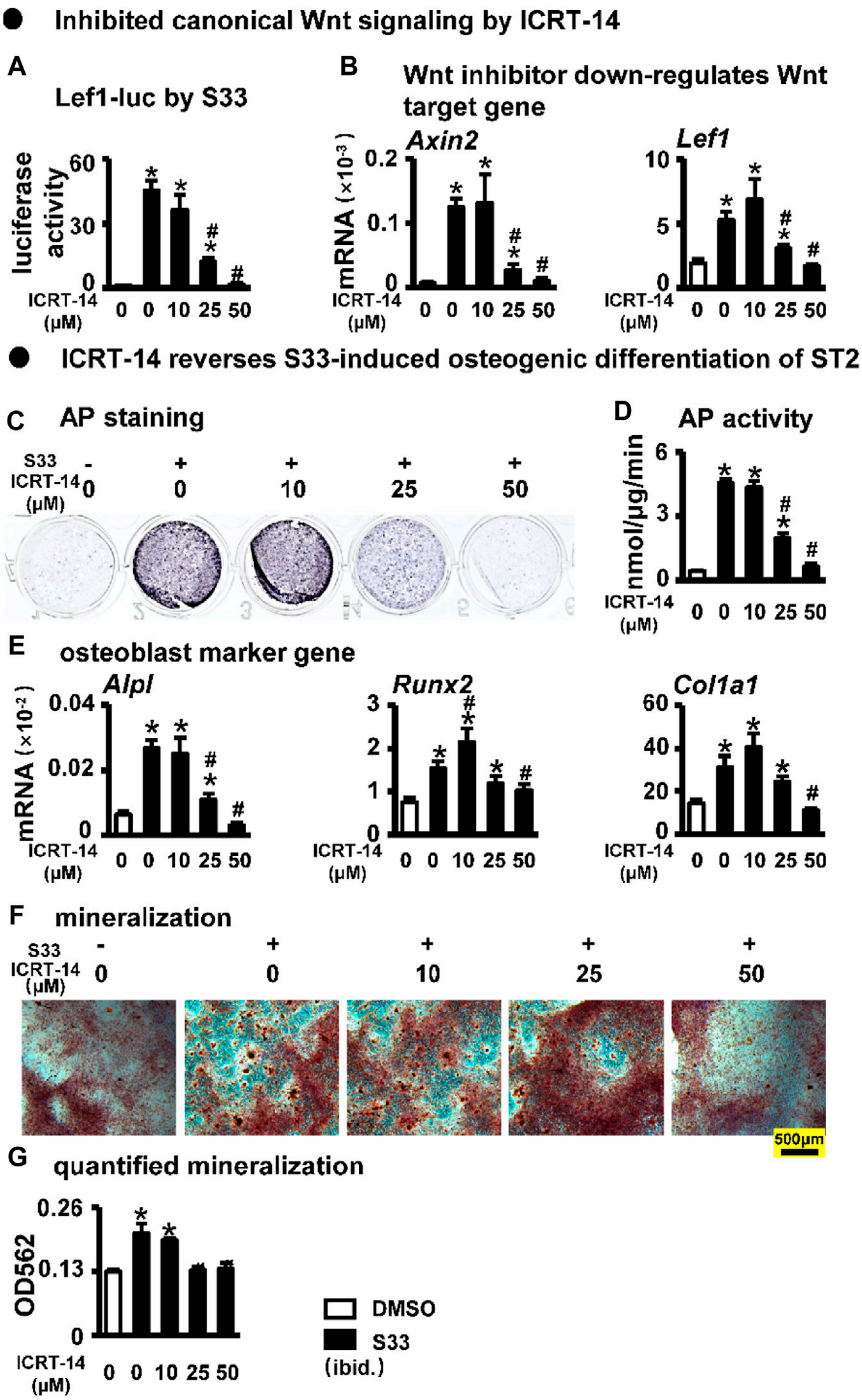

FIGURE 3
Effect of inhibiting Wnt signaling on osteogenic differentiation. **(A)** Luciferase activity. After transfection of ST2 cells with TopFlash/FopFlash plasmids, the cells were treated with S33 (10 μM) and different concentrations of inhibitors for 3 days. **(B)** Expression of Wnt target genes **(C)** AP staining. **(D)** AP biochemical activity assay **(E)** Expression of osteoblast marker genes. **(F)** Alizarin Red S staining was performed after ST2 cells were treated with ICRT-14 and S33 for 14 days and photographed under a microscope, scale bar = 500 μm, and quantification assay **(G)** was performed after this. *, $p <$ 0.05, compared with the DMSO group, n = 3.

mineralization quantified 1.8-fold higher than the control at 10 μM (Figure 2E).

The CCK8 assay was used to assess the effect of S33 on the proliferative activity of ST2 cells at different concentrations. After ST2 cells were treated with S33, our results showed that S33 not only had no cytotoxicity to ST2 cells in the concentration range of 0—20 μM but also promoted cell proliferation in a concentration-dependent manner (Figure 2F).

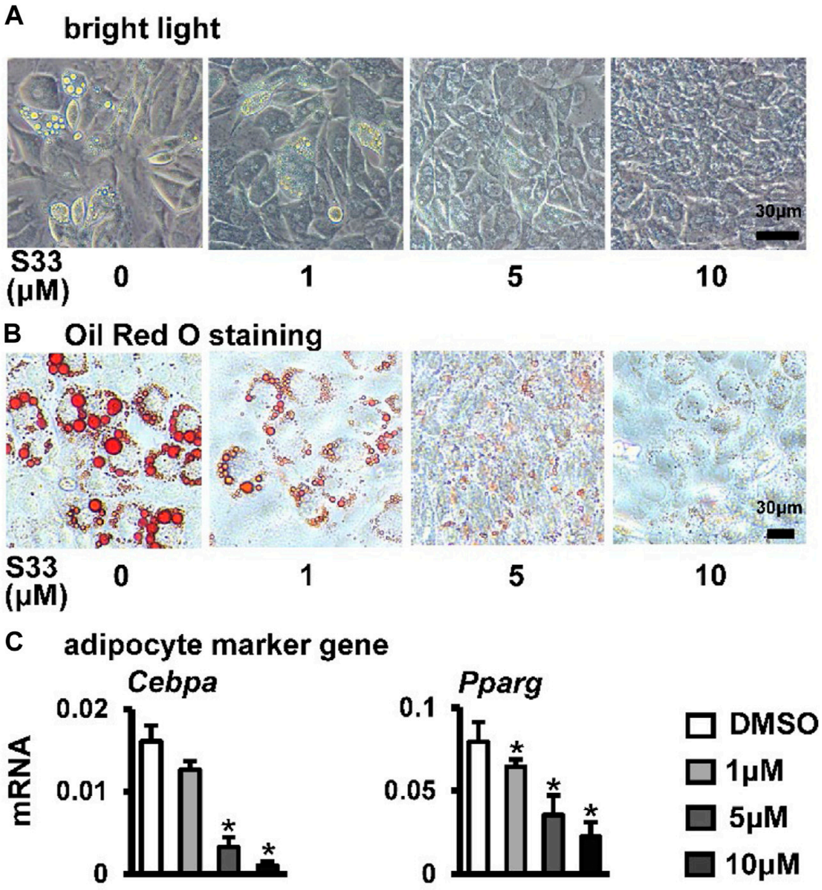

FIGURE 4
Effect of S33 on adipogenic differentiation. **(A)** Lipid droplets in ST2 cells treated with different concentrations of S33 for 7 days in the adipogenic medium under bright light, scale bar = 30 μm **(B)** Oil Red O staining images of lipid droplets in ST2 cells. Scale bar = 30 μm **(C)** qPCR detects the mRNA expression of *Pparg* and *Cebpa* after 3 days of S33 treatment. *, $p < 0.05$, compared with the DMSO group, n = 3.

The above results showed that S33 promoted osteogenic differentiation and proliferation of ST2 cells in a concentration-dependent manner.

Inhibition of canonical Wnt signaling reverses S33-induced increase of osteogenic differentiation in ST2 cells

To investigate whether S33 promotes osteogenic differentiation by activating canonical Wnt signaling in ST2 cells, we used the Wnt/β-catenin/Tcf-mediated transcriptional antagonist ICRT-14 for experiments. We used different concentrations of ICRT-14 and 10 μM of S33 to act on ST2 cells for 3 days. The results showed that TopFlash reporter activity was inhibited in ICRT-14 treatment in a dose-dependent way (Figure 3A), and the expression of Wnt target genes *Axin2* and *Lef1* were significantly decreased (Figure 3B), demonstrating that Wnt signaling was effectively inhibited by ICRT-14.

We then treated ST2 cells with ICRT-14 and S33 for 3 days. AP staining and biochemical quantification showed that AP activity was significantly inhibited by ICRT-14 treatment (Figures 3C, D). qPCR results showed that the expression of osteoblast marker genes *Alpl*, *Col1α1*, and *Runx2* was decreased to DMSO levels at a concentration of 50 μM ICRT-14 (Figure 3E). Alizarin Red S staining and mineralization quantification results showed that ICRT-14 decreased the mineralization induced by S33 in ST2 cells also in a dose-dependent manner (Figures 3F, G).

These results indicate that S33 promotes osteogenic differentiation of ST2 cells by activating the canonical Wnt signaling.

S33 inhibits adipogenic differentiation of ST2 cells

Osteogenic and adipogenic differentiation are closely linked, while Wnt signaling can inhibit preadipocyte differentiation by down-regulating key adipogenic transcription factors *Cebpa*, *Pparg* (Xu et al., 2016). Therefore, we investigated whether activation of canonical Wnt signaling by S33 inhibits adipogenic differentiation. After ST2 cells were cultured with adipogenic medium for 7 days, it was observed microscopically that the cytoplasm of ST2 cells was basically occupied by lipid droplets in the DMSO group, while no significant lipid droplet was formed in the S33-treated cells (Figure 4A). And subsequent Oil Red O staining

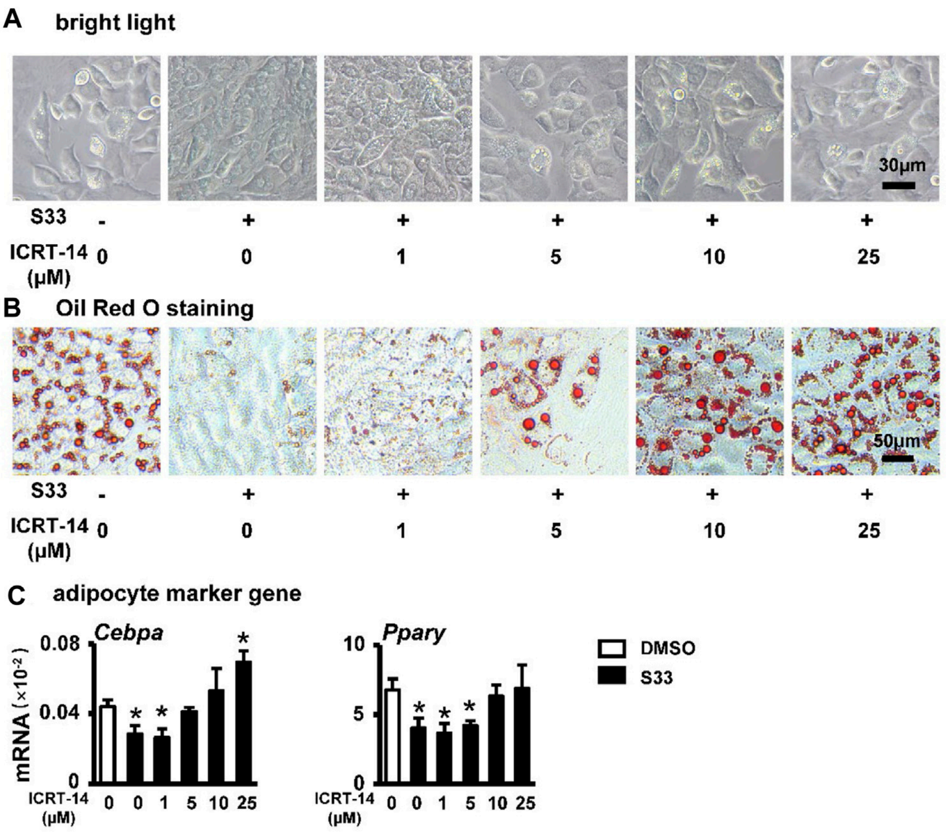

FIGURE 5
Effect of inhibiting Wnt signaling on adipogenic differentiation. **(A)** Expression of *Pparg* and *Cebpa* of ST2 cells treated with S33 and different concentrations of ICRT-14 in adipogenic medium for 3 days. To observe the changes in lipid droplet formation, ST2 cells were treated with S33 and different concentrations of ICRT-14 for 7 days in an adipogenic medium **(B)** Lipid droplets in ST2 cells under bright light, scale bar = 30 μm **(C)** Oil Red O staining images of lipid droplets in ST2 cells, scale bar = 50 μm *, $p < 0.05$, compared with the DMSO group, n = 3.

also showed a concentration-dependent reduction in lipid droplet accumulation with S33 treatment compared to the DMSO group (Figure 4B). In addition, S33 concentration-dependently inhibited the expression of *Cebpa* and *Pparg* in ST2 cells (Figure 4C).

The above results showed that S33 concentration-dependently inhibits adipogenic differentiation of ST2 cells.

Inhibition of canonical Wnt signaling reverses S33-mediated reduction in adipogenic differentiation of ST2 cells

To investigate whether S33 still inhibits adipogenic differentiation by activating canonical Wnt signaling in ST2 cells, we again used different concentrations of ICRT-14 and 10 μM of S33 to act together in ST2 cells. After 7 days of adipogenic induction, lipid droplet accumulation in ST2 cells was reproduced with increasing concentrations of ICRT-14 (Figure 5A). This was also confirmed by Oil Red O staining. The size and density of lipid droplets in the cells basically returned to DMSO control levels after ICRT-14 concentration reached 10 μM (Figure 5B). In addition, adipogenesis-related gene assays also showed that ICRT-14 rescued S33-suppressed expression of *Cebpa* and *Pparg* (Figure 5C).

The above results clearly indicate that S33 inhibits adipogenic differentiation of ST2 cells through canonical Wnt signaling.

S33 promotes cell proliferation in the PSCI3D scaffold

We established PCL, S33, and cell integrated 3D printing (PSCI3D) systems (Wang P. et al., 2022) to study the function of S33. ST2 cells and S33 were mixed in GelMA hydrogel for integrated printing with PCL into a 3D scaffold for a rapid test of S33 on osteoblast differentiation (Figure 6A). The release of small molecular drugs from hydrogels plays an important role in such regard (Oliva et al., 2017), so we first test the release of S33 in the GelMA hydrogels. The experimental results showed that 25.4% of S33 was released after 1st day of culture, 81% within 7 days, and 84% within 9 days. The release content of S33 gradually decreased with time and did not show burst release (Figure 6B).

The cell survival rate of ST2 was measured by live/dead cell assay within 7 days of culture in the PSCI3D scaffold. The results showed that ST2 exhibited high cell viability in both DMSO and S33 groups within 7 days, >91% (Figures 6C, D). The cell proliferation activity assay showed that in the PSCI3D scaffold, the proliferation activity

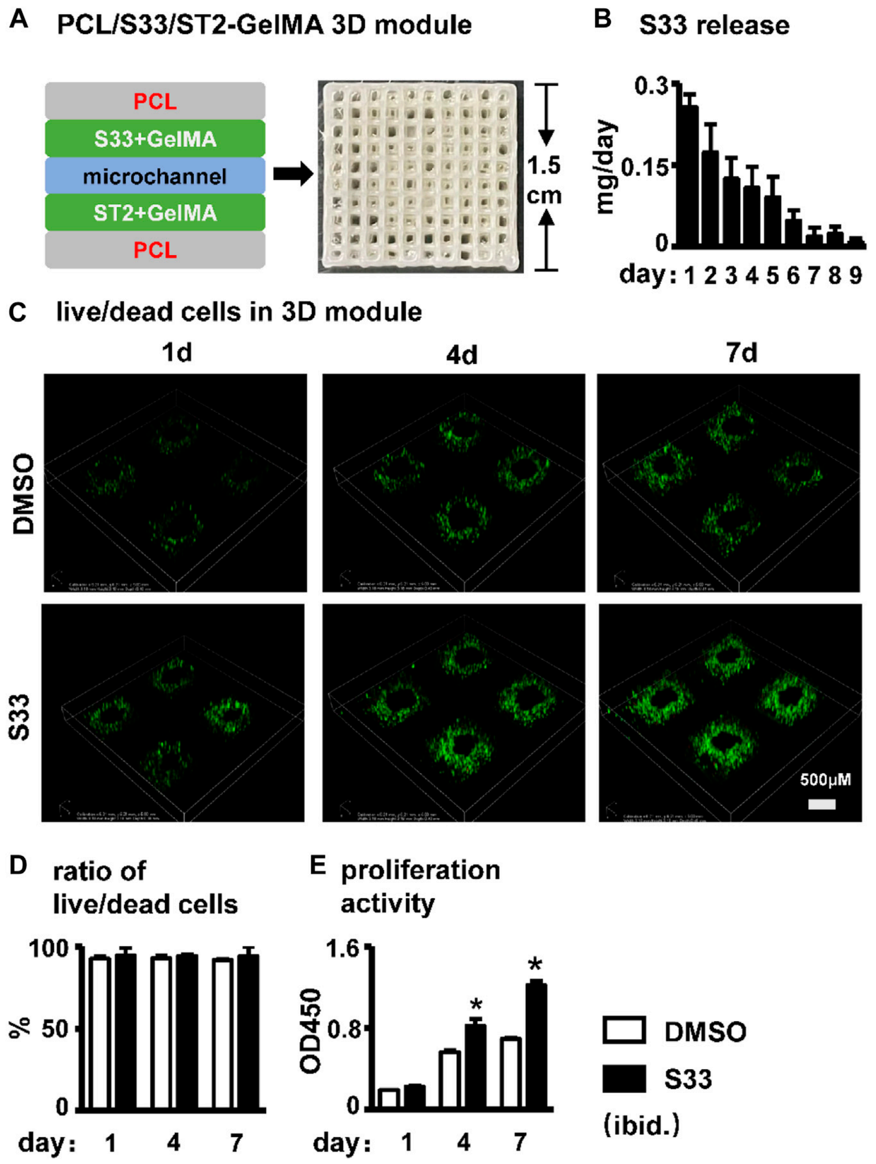

FIGURE 6
Effect of cell viability and proliferation activity in PSCI3D scaffold. **(A)** Schematic diagram of the PSCI3D scaffold and the printed scaffold **(B)** Cumulative release of S33 from PSCI3D scaffold. **(C)** Live/dead cell staining of cells at 1, 4, and 7 days in PSCI3D scaffold, scale bar = 500 μm **(D)** Live/dead cell ratio **(E)** CCK8 assay for cell proliferation activity. *, $p < 0.05$, compared with the DMSO group, n = 3.

of ST2 cells in the S33 treated group increased linearly by 40% and 70% at 4 and 7 days of culture (Figure 6E).

The above results showed that S33 in the PSCI3D scaffold did not show a burst release phenomenon, and the scaffold provided a good microenvironment for cells to grow and proliferate.

S33 promotes osteogenic differentiation and mineralization in the PSCI3D scaffold

AP staining and biochemical activity assays were performed on the PSCI3D scaffold after 7 and 14 days of culture. Compared with the DMSO group, the S33 group showed enhanced AP staining at both 7 and 14 days (Figure 7A) and increased AP activity by 1.4- and 4.0-fold, respectively (Figure 7B), demonstrating that S33 significantly promoted osteogenic differentiation in PSCI3D scaffold. This was further confirmed by qPCR in the upregulated expression of the osteoblast markers *Alpl*, *Col1a1*, and *Runx2* by S33 treatment compared to DMSO control at both 7 and 14 days, and *Bglap* expression was also increased by S33 treatment after 14 days of culture (Figure 7C).

To perform the mineralization assay, the PSCI3D scaffold was cultured in a complete medium for 7 days, followed by another 14 days in an osteogenic medium. The results of Alizarin Red S staining and quantification showed a higher number of mineral nodules in S33 treated group (Figure 7D). Additionally, mineralization was increased by approximately 1.7-fold (Figure 7E).

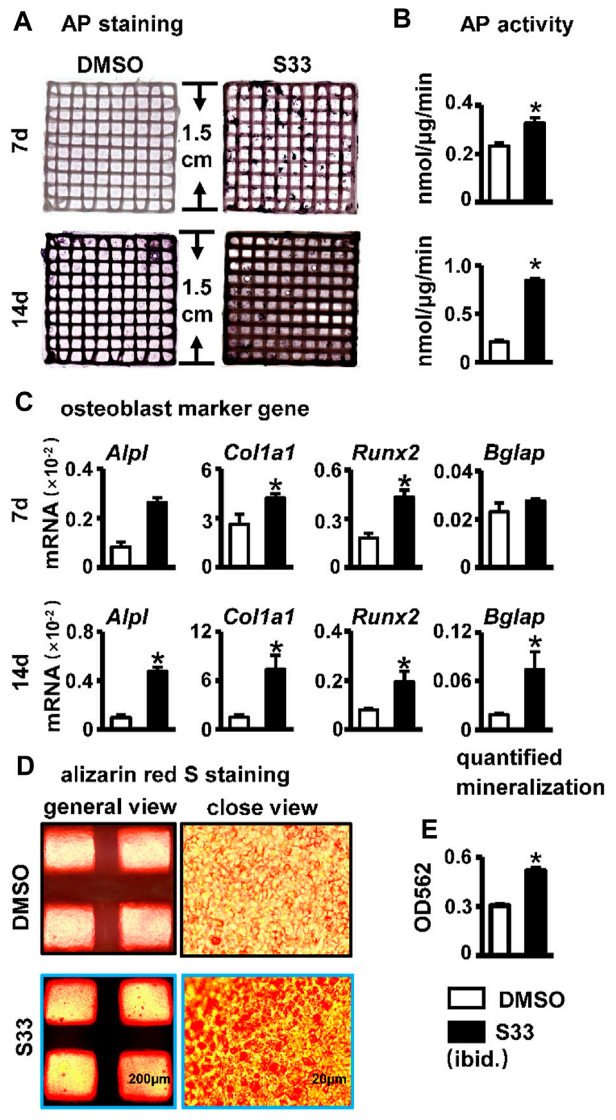

FIGURE 7
Effect of osteogenic differentiation and mineralization in PSCI3D scaffold. **(A)** AP staining of PSCI3D scaffold cultured for 7 and 14 days. **(B)** AP biochemical activity assay. **(C)** Expression of osteoblast marker genes in PSCI3D scaffold **(D)** Images under the microscope of Alizarin red S staining of bone nodules in PSCI3D scaffold, scale bars: 200 μm for the general view and 20 μm for the close view **(E)** Quantitative analysis of mineralization in PSCI3D scaffold. *, $p < 0.05$, compared with the DMSO group, n = 3.

S33 indirectly promotes angiogenesis

Blood vessels are essential in bone regeneration and deliver nutrients for cell growth (Peng et al., 2020). Therefore, we examined the effect of the conditioned medium of the PSCI3D scaffold on angiogenesis. The conditioned medium of the PSCI3D scaffold facilitated the migration of HUVEC cells (Figure 8A). Migrated cells were increased by 1.9-fold compared to the controls (Figure 8B). Then, we cultured HUVEC cells in 24-well plates pre-coated with Matrigel and observed the formation of tubules after 6 h in the conditioned medium. We found that the conditioned medium increased vascular tubule formation in the PSCI3D group compared with the control medium (Figure 8C), formed nodes and branching lengths were increased by 1.82 and 1.73-fold, respectively, and total lengths by 1.64-fold compared to the control group (Figure 8D). The angiogenic process is heavily influenced by the significant role played by the vascular endothelial growth factor *Vegfa* (Sun, 2012), and qPCR results showed increased *Vegfa* expression in ST2 cells in the PSCI3D scaffold (Figure 8E).

The above results showed that S33 may have a pro-angiogenic effect when acting *in vivo*.

Discussion

In this study, we investigated the osteogenic effect of GSK3β inhibitor S33. We utilized S33 to inhibit GSK3β kinase activity and confirmed that S33 is a potent Wnt agonist in murine bone marrow stromal cell ST2. We then show that S33 specifically stimulates osteogenesis and inhibits adipogenesis by downregulating *Pparg* and *Cebpa* expression via canonical Wnt signaling. Inhibition of Wnt signaling by the Wnt transcriptional inhibitor ICRT-14 disrupts the bone-promoting and adipogenesis-inhibiting effects of S33, respectively. In view of the characteristics of increased adipogenesis and decreased osteogenesis of BMSCs in elderly patients with osteoporosis, S33 may have a potential therapeutic effect.

The effect of S33 in promoting osteogenic differentiation was also reproduced in MC3T3-E1 cells (Supplementary Figures S1A–E). Because MC3T3-E1 cells are pre-osteoblasts and have exceeded the common cellular stage of osteogenesis and adipogenesis in the development of osteoblasts, they cannot be induced into adipocytes. Therefore, the inhibitory effect of S33 on adipogenic differentiation has not been detected in the MC3T3-E1 stage.

We printed the PSCI3D functional scaffold using a newly developed PCL and cell integrated 3D bioprinting technology to simulate the developmental microenvironment *in vivo*. In the PSCI3D scaffold, the survival rate of cells reached 94% within 7 days, so ST2 cells grew linearly and greatly increased cell proliferation activity. High proliferation activity and survival rate guarantee subsequent osteogenic differentiation and mineralization. And we also found that the conditioned medium of the PSCI3D scaffold could effectively promote the migration and tubule formation of HUVEC cells, indicating that the PSCI3D scaffold enhances angiogenesis, which is essential for bone formation.

S33 has a variety of biological functions and may have translational application value in the treatment of osteoporosis. At present, PTH, PTHrP, and sclerostin antibodies for the treatment of osteoporosis are all protein drugs that have defects such as immunogenicity, easy degradation, high price, short half-life, and poor permeability (Vargason et al., 2021). These side effects limit their use to some extent. However, small molecule drugs have been a research hotspot due to their good stability, solubility, easier processing, and low cost (Vargason et al., 2021). Like anti-sclerostin antibodies, the small molecule S33 acts through the Wnt/β-catenin pathway to promote osteogenic differentiation, in addition to inhibiting adipogenic differentiation, promoting angiogenesis, and has the potential to inhibit osteoclast differentiation. We found that S33 increased *Opg* expression in ST2 cells and decreased the *RANKL/Opg* ratio, potentially inhibiting osteoclast differentiation (Supplementary Figure S3).

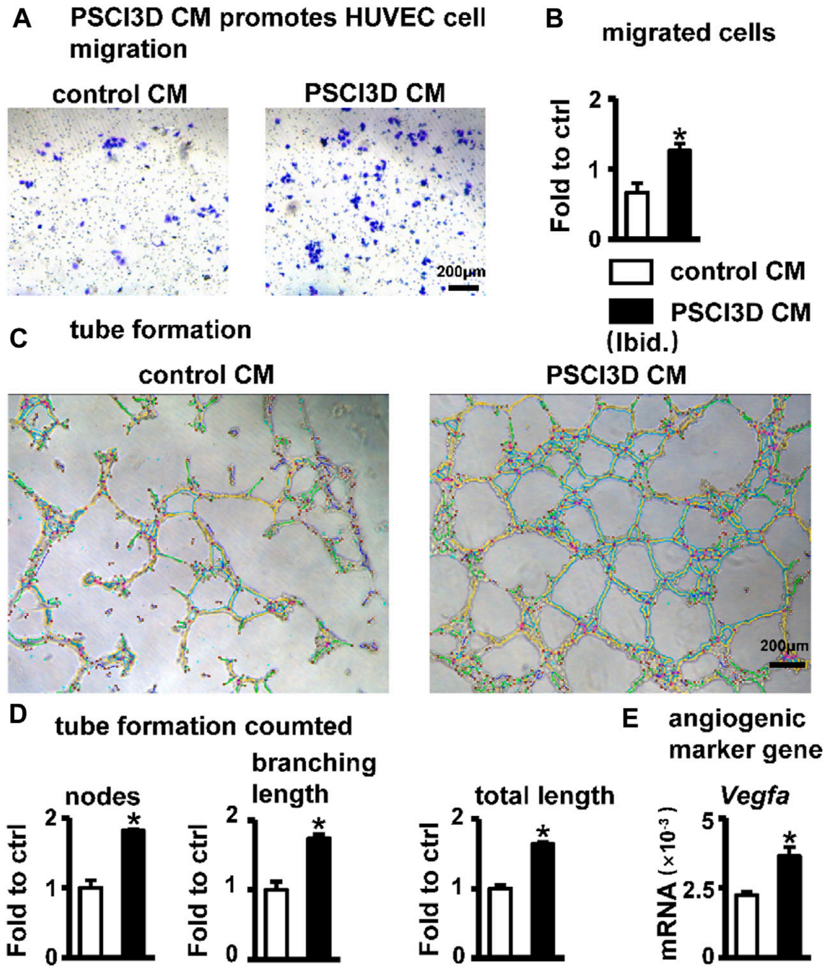

FIGURE 8
Effect of PSCI3D conditioned medium (CM) on angiogenesis in HUVEC cells. **(A)** Images of endothelial cell migration assay in the transwell chamber with conditioned medium for 48h, scale bar = 200 μm **(B)** Quantification of migrated cells. **(C)** Images of vascular tubules forming in HUVECs upon PSCI3D CM **(D)** Calculation of formed nodes, branching length, and total length **(E)** Expression of angiogenic marker *Vegfa*. *, $p < 0.05$, compared with the control CM group, n = 3.

S33 is an effective and safe osteogenic drug. The Canonical Wnt pathway is important in cell proliferation, differentiation, polarization, and migration (Wodarz and Nusse, 1998). Therefore, the safety of drugs targeting this pathway is very important when developing drugs (Kahn, 2014). In the PSCI3D scaffold, the sustained-release system released 25.6% of S33 on the first day and slowly released 81.7% within 7 days. At 7 days, S33 promoted osteoblast differentiation, which increased by 1.4-fold compared to the control group, but at 14 days, osteoblast differentiation increased even higher, reaching 4.0-fold. Although the concentration of S33 is very low at 7 days, the affected ST2 cells can continue to proliferate and differentiate. Thus, the drug's effect is limited to the local area and does not affect the tissues and cells around the scaffold. In addition, the conditioned medium of the PSCI3D scaffold promotes angiogenesis (Figures 8A–E). This indicates that the released S33 forms a developmental microenvironment guiding cells to proliferate and differentiate into osteoblasts. After slowly releasing most of S33 within 7 days, it can still maintain the osteogenic differentiation of the cells, and the microenvironment may secrete angiogenic factors such as *Vegfa* for angiogenesis. Therefore, the development microenvironment formed in the PSCI3D scaffold promotes osteogenic differentiation and angiogenesis.

Another important innovation in this study is the preparation of the PSCI3D scaffold by alternately printing strips of PCL, cell-laden hydrogel, and S33-laden hydrogel through a newly developed integrated 3D bioprinting technology, which creates an osteogenic niche. Printing hard materials together with cells has been a huge challenge because the problem of low cell survival rate cannot be well solved, making cells unable to differentiate subsequently (Valot et al., 2019). In 2016, Kang et al. established an ITOP to print PCL and stem cell scaffold that can induce bone vascularization after implantation *in vivo* (Kang et al., 2016), becoming a milestone in 3D bioprinting technology. However, in the following period, 3D bioprinting technology was still limited by the lack of a developmentally functional microenvironment and failed to make a further breakthrough.

As we previously reported (Wang P. et al., 2022), we reserved space for cells to exchange substances by alternately printing strips of PCL, cell-laden hydrogel, and S33-laden hydrogel. This resulted in a 45.3% and 75.4% increase in cell proliferation activity at 4 days and 7 days of cultivation in a 3D environment, which was a little greater than that in a two-dimensional environment. And we also provided mechanical support for cell adhesion and proliferation through blue light-curable GelMA hydrogel. These methods have greatly improved the survival rate of cells, which can remain above 94% within 7 days, slightly higher than that in 2D culture (unpublished data). In addition, S33 in the hydrogel can still function for a long time after releasing most of the S33 at 7 days, well mimicking the effect of S33 on cells *in vivo* in a three-dimensional environment. Therefore, our reconstructed PSCI3D scaffold can simulate the developmental microenvironment *in vivo* and rapidly verify the effect of S33 on cell differentiation *in vivo*, which also provides a possible method for the rapid identification of the *in vivo* effect of drugs in the future.

Another interesting function of S33's ability is to promote angiogenesis. We found that PSCI3D conditioned medium exhibits a significant angiogenic effect (Figures 8A–E). To exclude the impact of residual S33 in a conditioned medium, we used S33 to directly stimulate HUVECs, but unfortunately, no angiogenesis function was found (Supplementary Figures S2A–C). However, our previous work reveals that osteocyte with SKL2001-activated Wnt signaling promotes angiogenesis (Liu et al., 2022). Thus, similar to the previous mode, S33 may indirectly promote angiogenesis by stimulating ST2 cells to release angiogenic factors such as *Vegfa* (Figure 8E), but the specific mechanism needs further investigation.

Conclusion

All in all, we found that SB216763, a highly specific GSK3β inhibitor has multiple functions such as osteogenic and anti-adipogenic effects and angiogenic potential, and S33 may also have another potential to inhibit osteoclastogenesis. These features make S33 a good candidate drug for therapeutics against elderly osteoporosis. Amazingly, when S33 is almost released in the PSCI3D scaffold at 7 days of cultivation, it creates an osteogenic microenvironment to produce better effects of osteoblast differentiation and mineralization. For the time being, we call this drug sustained-release in the 3D scaffold creating an osteogenic niche that continues to play a role in bone formation. The PSCI3D scaffold can be used as a bioactive material to bionically reconstruct artificial bone organs.

Data availability statement

The datasets presented in this study can be found in online repositories. The names of the repository/repositories and accession number(s) can be found in the article/Supplementary Material.

Author contributions

Conceptualization, WG, BW, XL, and XT; methodology, WG, ML, and XW; investigation, WG, ML, and LZ; data analysis, WG, LZ, and ML; writing—original draft preparation, WG, ML, LZ, and XT; Writing—review and editing, WG, PW, and XT; funding acquisition, XL and XT; resources, XL and XT; supervision, XT. All authors contributed to the article and approved the submitted version.

Funding

This research was funded by the National Natural Science Foundation of China U1601220, 81672118, and 82072450 (XT), and Chongqing Science and Technology Commission—Basic Sci-ence and Frontier Technology Key Project cstc2015jcyjBX0119 and CSTB2022NSCQ-LZX0048 (XT), and CQMU Program for Youth Innovation in Future Medicine (No. W0203) (XL).

Acknowledgments

The authors appreciate Jie Chen and Guangliang Liu for their technical help.

Conflict of interest

The authors declare that the research was conducted in the absence of any commercial or financial relationships that could be construed as a potential conflict of interest.

Publisher's note

Supplementary material

The Supplementary Material for this article can be found online at: https://www.frontiersin.org/articles/10.3389/fbioe.2023.1215233/full#supplementary-material

References

Baron, R., and Kneissel, M. (2013). WNT signaling in bone homeostasis and disease: From human mutations to treatments. *Nat. Med.* 19, 179–192. doi:10.1038/nm.3074

Billiet, T., Gevaert, E., De Schryver, T., Cornelissen, M., and Dubruel, P. (2014). The 3D printing of gelatin methacrylamide cell-laden tissue-engineered constructs with high cell viability. *Biomaterials* 35, 49–62. doi:10.1016/j.biomaterials.2013.09.078

Cha, G. D., Kang, D., Lee, J., and Kim, D. H. (2019). Bioresorbable electronic implants: History, materials, fabrication, devices, and clinical applications. *Adv. Healthc. Mater* 8, e1801660. doi:10.1002/adhm.201801660

Coghlan, M. P., Culbert, A. A., Cross, D. A., Corcoran, S. L., Yates, J. W., Pearce, N. J., et al. (2000). Selective small molecule inhibitors of glycogen synthase kinase-3 modulate glycogen metabolism and gene transcription. *Chem. Biol.* 7, 793–803. doi:10.1016/s1074-5521(00)00025-9

Cohn-Schwartz, D., Schary, Y., Yalon, E., Krut, Z., Da, X., Schwarz, E. M., et al. (2022). PTH-induced bone regeneration and vascular modulation are both dependent on endothelial signaling. *Cells* 11, 897. doi:10.3390/cells11050897

Fan, Y., Hanai, J-I., Le, P. T., Bi, R., Maridas, D., Demambro, V., et al. (2017). Parathyroid hormone directs bone marrow mesenchymal cell fate. *Cell Metab.* 25, 661–672. doi:10.1016/j.cmet.2017.01.001

Golledge, J., and Thanigaimani, S. (2022). Role of sclerostin in cardiovascular disease. *Arteriosclerosis, Thrombosis, Vasc. Biol.* 42, e187–e202. doi:10.1161/ATVBAHA.122.317635

Gonsalves, F. C., Klein, K., Carson, B. B., Katz, S., Ekas, L. A., Evans, S., et al. (2011). An RNAi-based chemical genetic screen identifies three small-molecule inhibitors of the Wnt/wingless signaling pathway. *Proc. Natl. Acad. Sci. U. S. A.* 108, 5954–5963. doi:10.1073/pnas.1017496108

Grosso, A., Burger, M. G., Lunger, A., Schaefer, D. J., Banfi, A., and Di Maggio, N. (2017). It takes two to tango: Coupling of angiogenesis and osteogenesis for bone regeneration. *Front. Bioeng. Biotechnol.* 5, 68. doi:10.3389/fbioe.2017.00068

Herrmann, M., Verrier, S., and Alini, M. (2015). Strategies to stimulate mobilization and homing of endogenous stem and progenitor cells for bone tissue repair. *Front. Bioeng. Biotechnol.* 3, 79. doi:10.3389/fbioe.2015.00079

Hummler, S. C., Rong, M., Chen, S., Hehre, D., Alapati, D., and Wu, S. (2013). Targeting glycogen synthase kinase-3β to prevent hyperoxia-induced lung injury in neonatal rats. *Am. J. Respir. Cell Mol. Biol.* 48, 578–588. doi:10.1165/rcmb.2012-0383OC

Kahn, M. (2014). Can we safely target the WNT pathway? *Nat. Rev. Drug Discov.* 13, 513–532. doi:10.1038/nrd4233

Kang, H-W., Lee, S. J., Ko, I. K., Kengla, C., Yoo, J. J., and Atala, A. (2016). A 3D bioprinting system to produce human-scale tissue constructs with structural integrity. *Nat. Biotechnol.* 34, 312–319. doi:10.1038/nbt.3413

Kang, X., Zhang, X-B., Gao, X-D., Hao, D-J., Li, T., and Xu, Z-W. (2022). Bioprinting for bone tissue engineering. *Front. Bioeng. Biotechnol.* 10, 1036375. doi:10.3389/fbioe.2022.1036375

Lieben, L. (2016). Regenerative medicine: The future of 3D printing of human tissues is taking shape. *Nat. Rev. Rheumatol.* 12, 191. doi:10.1038/nrrheum.2016.29

Liu, Y., Ruan, X., Li, J., Wang, B., Chen, J., Wang, X., et al. (2022). The osteocyte stimulated by Wnt agonist SKL2001 is a safe osteogenic niche improving bioactivities in a polycaprolactone and cell integrated 3D module. *Cells* 11, 831. doi:10.3390/cells11050831

Luo, C., Xu, W., Tang, X., Liu, X., Cheng, Y., Wu, Y., et al. (2022). Canonical Wnt signaling works downstream of iron overload to prevent ferroptosis from damaging osteoblast differentiation. *Free Radic. Biol. Med.* 188, 337–350. doi:10.1016/j.freeradbiomed.2022.06.236

Macdonald, B. T., Tamai, K., and He, X. (2009). Wnt/β-Catenin signaling: Components, mechanisms, and diseases. *Dev. Cell* 17, 9–26. doi:10.1016/j.devcel.2009.06.016

Malda, J., and Groll, J. (2016). A step towards clinical translation of biofabrication. *Trends Biotechnol.* 34, 356–357. doi:10.1016/j.tibtech.2016.03.003

Mcclung, M. R., Grauer, A., Boonen, S., Bolognese, M. A., Brown, J. P., Diez-Perez, A., et al. (2014). Romosozumab in postmenopausal women with low bone mineral density. *N. Engl. J. Med.* 370, 412–420. doi:10.1056/NEJMoa1305224

Neer, R. M., Arnaud, C. D., Zanchetta, J. R., Prince, R., Gaich, G. A., Reginster, J. Y., et al. (2001). Effect of parathyroid hormone (1-34) on fractures and bone mineral density in postmenopausal women with osteoporosis. *N. Engl. J. Med.* 344, 1434–1441. doi:10.1056/NEJM200105103441904

Nusse, R., and Clevers, H. (2017). Wnt/β-Catenin signaling, disease, and emerging therapeutic modalities. *Cell* 169, 985–999. doi:10.1016/j.cell.2017.05.016

Oliva, N., Conde, J., Wang, K., and Artzi, N. (2017). Designing hydrogels for on-demand therapy. *Accounts Chem. Res.* 50, 669–679. doi:10.1021/acs.accounts.6b00536

Pashuck, E. T., and Stevens, M. (2016). From clinical imaging to implantation of 3D printed tissues. *Nat. Biotechnol.* 34, 295–296. doi:10.1038/nbt.3503

Peng, Y., Wu, S., Li, Y., and Crane, J. L. (2020). Type H blood vessels in bone modeling and remodeling. *Theranostics* 10, 426–436. doi:10.7150/thno.34126

Saag, K. G., Petersen, J., Brandi, M. L., Karaplis, A. C., Lorentzon, M., Thomas, T., et al. (2017). Romosozumab or alendronate for fracture prevention in women with osteoporosis. *N. Engl. J. Med.* 377, 1417–1427. doi:10.1056/NEJMoa1708322

Sun, W. (2012). Angiogenesis in metastatic colorectal cancer and the benefits of targeted therapy. *J. Hematol. Oncol.* 5, 63. doi:10.1186/1756-8722-5-63

Tu, X., Chen, J., Lim, J., Karner, C. M., Lee, S-Y., Heisig, J., et al. (2012a). Physiological notch signaling maintains bone homeostasis via RBPjk and Hey upstream of NFATc1. *PLoS Genet.* 8, e1002577. doi:10.1371/journal.pgen.1002577

Tu, X., Delgado-Calle, J., Condon, K. W., Maycas, M., Zhang, H., Carlesso, N., et al. (2015). Osteocytes mediate the anabolic actions of canonical Wnt/β-catenin signaling in bone. *Proc. Natl. Acad. Sci. U. S. A.* 112, E478–E486. doi:10.1073/pnas.1409857112

Tu, X., Joeng, K. S., Nakayama, K. I., Nakayama, K., Rajagopal, J., Carroll, T. J., et al. (2007). Noncanonical Wnt signaling through G protein-linked PKCδ activation promotes bone formation. *Dev. Cell* 12, 113–127. doi:10.1016/j.devcel.2006.11.003

Tu, X., Rhee, Y., Condon, K. W., Bivi, N., Allen, M. R., Dwyer, D., et al. (2012b). Sost downregulation and local Wnt signaling are required for the osteogenic response to mechanical loading. *Bone* 50, 209–217. doi:10.1016/j.bone.2011.10.025

Valot, L., Martinez, J., Mehdi, A., and Subra, G. (2019). Chemical insights into bioinks for 3D printing. *Chem. Soc. Rev.* 48, 4049–4086. doi:10.1039/c7cs00718c

Vargason, A. M., Anselmo, A. C., and Mitragotri, S. (2021). The evolution of commercial drug delivery technologies. *Nat. Biomed. Eng.* 5, 951–967. doi:10.1038/s41551-021-00698-w

Vinyoles, M., Del Valle-Pérez, B., Curto, J., Viñas-Castells, R., Alba-Castellón, L., García De Herreros, A., et al. (2014). Multivesicular GSK3 sequestration upon Wnt signaling is controlled by p120-catenin/cadherin interaction with LRP5/6. *Mol. Cell* 53, 444–457. doi:10.1016/j.molcel.2013.12.010

Wang, B., Khan, S., Wang, P., Wang, X., Liu, Y., Chen, J., et al. (2022a). A highly selective GSK-3β inhibitor CHIR99021 promotes osteogenesis by activating canonical and autophagy-mediated Wnt signaling. *Front. Endocrinol.* 13, 926622. doi:10.3389/fendo.2022.926622

Wang, L., Fu, H., Wang, W., Liu, Y., Li, X., Yang, J., et al. (2021). Notoginsenoside R1 functionalized gelatin hydrogels to promote reparative dentinogenesis. *Acta Biomater.* 122, 160–171. doi:10.1016/j.actbio.2020.12.031

Wang, P., Wang, X., Wang, B., Li, X., Xie, Z., Chen, J., et al. (2022b). 3D printing of osteocytic Dll4 integrated with PCL for cell fate determination towards osteoblasts *in vitro*. *Bio-Design Manuf.* 5, 497–511. doi:10.1007/s42242-022-00196-1

Wang, S., Zhao, S., Yu, J., Gu, Z., and Zhang, Y. (2022c). Advances in translational 3D printing for cartilage, bone, and osteochondral tissue engineering. *Small (Weinheim Der Bergstrasse, Ger.* 18, e2201869. doi:10.1002/smll.202201869

Wang, X., Ma, Y., Chen, J., Liu, Y., Liu, G., Wang, P., et al. (2023). A novel decellularized matrix of Wnt signaling-activated osteocytes accelerates the repair of critical-sized parietal bone defects with osteoclastogenesis, angiogenesis, and neurogenesis. *Bioact. Mater.* 21, 110–128. doi:10.1016/j.bioactmat.2022.07.017

Weng, J., Wang, Y-H., Li, M., Zhang, D-Y., and Jiang, B-G. (2018). GSK3β inhibitor promotes myelination and mitigates muscle atrophy after peripheral nerve injury. *Neural Regen. Res.* 13, 324–330. doi:10.4103/1673-5374.226403

Wodarz, A., and Nusse, R. (1998). Mechanisms of Wnt signaling in development. *Annu. Rev. Cell Dev. Biol.* 14, 59–88. doi:10.1146/annurev.cellbio.14.1.59

Xu, C., Wang, J., Zhu, T., Shen, Y., Tang, X., Fang, L., et al. (2016). Cross-talking between PPAR and WNT signaling and its regulation in mesenchymal stem cell differentiation. *Curr. Stem Cell Res. Ther.* 11, 247–254. doi:10.2174/1574888x10666150723145707

Zhang, Y., Seid, K., Obermayr, F., Just, L., and Neckel, P. H. (2017). Activation of Wnt signaling increases numbers of enteric neurons derived from neonatal mouse and human progenitor cells. *Gastroenterology* 153, 154–165.e9. doi:10.1053/j.gastro.2017.03.019

Zhu, B., Xue, F., Zhang, C., and Li, G. (2019). Ginkgolide B promotes osteoblast differentiation via activation of canonical Wnt signalling and alleviates osteoporosis through a bone anabolic way. *J. Cell. Mol. Med.* 23, 5782–5793. doi:10.1111/jcmm.14503

Frontiers in Bioengineering and Biotechnology

TYPE Original Research
PUBLISHED 25 August 2023
DOI 10.3389/fbioe.2023.1169385

Comparison of the 3D-microstructure of human alveolar and fibula bone in microvascular autologous bone transplantation: a synchrotron radiation µ-CT study

Jonas Wüster[1]*, Bernhard Hesse[2,3], Rene Rothweiler[4], Emely Bortel[2], Christian Gross[4], Shima Bakhtiyari[2], Andrew King[5], Elodie Boller[3], Javier Gerber[2], Carsten Rendenbach[1], Tobias Fretwurst[4], Saskia Preissner[1], Max Heiland[1], Katja Nelson[4] and Susanne Nahles[1]

[1]Department of Oral and Maxillofacial Surgery, Berlin Institute of Health, Charité–Universitätsmedizin Berlin, Corporate Member of Freie Universität Berlin, Humboldt-Universität zu Berlin, Berlin, Germany, [2]Xploraytion GmbH, Berlin, Germany, [3]European Synchrotron Radiation Facility, Grenoble, France, [4]Department of Oral- and Craniomaxillofacial Surgery, Faculty of Medicine, Medical Center, University of Freiburg, Freiburg, Germany, [5]Synchrotron Soleil, Saint-Aubin, France

EDITED BY
Junxi Wu,
University of Strathclyde, United Kingdom

REVIEWED BY
Berit Zeller-Plumhoff,
Helmholtz-Zentrum Hereon GmbH,
Germany
Ting Liang,
Soochow University, China

*CORRESPONDENCE
Jonas Wüster,
✉ jonas.wuester@charite.de

RECEIVED 19 February 2023
ACCEPTED 01 August 2023
PUBLISHED 25 August 2023

CITATION
Wüster J, Hesse B, Rothweiler R, Bortel E, Gross C, Bakhtiyari S, King A, Boller E, Gerber J, Rendenbach C, Fretwurst T, Preissner S, Heiland M, Nelson K and Nahles S (2023), Comparison of the 3D-microstructure of human alveolar and fibula bone in microvascular autologous bone transplantation: a synchrotron radiation µ-CT study.
Front. Bioeng. Biotechnol. 11:1169385.
doi: 10.3389/fbioe.2023.1169385

Introduction: Autologous bone transplantation is successfully used in reconstructive surgery of large/critical-sized bone defects, whereby the microvascular free fibula flap is still regarded as the gold standard for the reconstruction of such defects in the head and neck region. Here, we report the morphological and lacunar properties of patient-paired bone samples from eight patients from the jaw (AB; recipient site) and the fibula (FB; donor site) on the micron length-scale using Synchrotron µ-CT. Insights into differences and similarities between these bone structures could offer a better understanding of the underlying mechanism for successful surgical outcomes and might clear the path for optimized, nature-inspired bone scaffold designs.

Methods: Spatial vessel-pore arrangements, bone morphology, fluid-simulation derived permeability tensor, osteocyte lacunar density, and lacunar morphology are compared.

Results: The orientation of the vessel system indicates a homogenous vessel orientation for AB and FB. The average mineral distance (50%) to the closest vessel boundary is higher in AB than in FB (the mean is 96 µm for AB vs. 76 µm for FB; p = 0.021). Average osteocyte lacunar density is found to be higher in AB than in FB (mean 22,874 mm^3 vs. 19,376 mm^3 for FB; p = 0.038), which might compensate

---

Abbreviations: 3D, three-dimensional; AB, alveolar bone; BV, bone volume; CAD/CAM, critical-sized and/or complex bone; CSBD, critical-sized bone defect; CT, computed tomography; IC, iliac crest; IPS, intracortical pore system; LCN, osteocyte lacunar–canalicular system; LOA, level of alignment; N.Lc, number of lacunae; SA, surface area; SR µ-CT, synchrotron radiation micro-computed tomography; Tb.Sp, trabecular separation; Tb.Th, trabecular thickness; TV, total volume; VXL, voxel; VOI, volume of interest.

for the high distance from the mineral to the nearest vessel. No significant differences in lacunar volume are found between paired AB and FB.

Discussion: A comparable vessel network and similar distribution of vessel porosity between AB and FB may allow the FB graft to exhibit a high regeneration potential when connected to AB, and this might correlate with a high osteoinductive and osteoconductive potential of FB when connected to AB. Since widely used and potent synthetic bone grafts exist, new insight into the bone structure of well-established autologous bone grafts, such as the free fibula flap, could help to improve the performance of such materials and therefore the design of 3D scaffolds.

KEYWORDS

osteocyte lacunae, bone microarchitecture, SR micro-CT, synchrotron, free fibula flap, bone vessel orientation, scaffold

1 Introduction

Bone healing is known to be a complex physiological process involving multiple interacting cells and signalling molecules (Vidal et al., 2020). In general, minor fractures and small bone defects heal spontaneously, whereas critical-sized and/or complex bone defects (CSBDs) still present a challenge in reconstructive surgery. Normally, CSBDs exceed the intrinsic capacity of bone healing, which might lead to delayed or insufficient bone union (Vidal et al., 2020). Defects with a length greater than 1–2 cm and a loss of more than 50% of bone circumference are generally defined as CSBDs in literature (Keating et al., 2005; Sanders et al., 2014). Animal studies demonstrated that the critical size for segmental mandibula defects in minipigs is 6 cm when the periosteum is preserved and 2 cm when the periosteum is removed (Ma et al., 2009). Since bone remodelling in pigs and humans is comparable (1.2–1.5 mm/day vs. 1.0–1.5 mm/day, respectively) (Pearce et al., 2007), these animal studies provide a valuable way to determine CSBD in humans. In oncological head and neck surgery, the required quantity of bone generally exceeds the potential of self-healing and osseous free flaps with microsurgical anastomosis are therefore often needed for reconstruction. The free fibula flap (FFF) has become the gold standard for autologous reconstruction of such defects resulting from oncological head and neck surgery (Fliss et al., 2021). Advantages of FFF are sufficient quantity of bone, possibility of ideal contouring, vascular supply, and a long pedicle (Chaine et al., 2009; López-Arcas et al., 2010; Verhelst et al., 2019; Rosen et al., 2022). Lately, by using CAD/CAM planning for FFF, a high accuracy of reconstruction and improved aesthetic and functional outcome could be achieved (Mahendru et al., 2020).

On the other hand, it is known that FFF harvesting may lead to severe donor site morbidities, which are divided into early and late complications. Early complications include infections, wound dehiscence, and delayed wound healing (Zimmermann et al., 2002; Chaine et al., 2009; Ling and Peng, 2012). Late complications comprise chronic pain, gait abnormality, limited range of motion in the ankle, and reduced sensory deficit and muscle strength, which may especially impair a patient's quality of life (Chaine et al., 2009; Ling and Peng, 2012). This is linked to a rising demand for a synthetic three-dimensional (3D) bone scaffold with predictable anatomic traits that might replace FFF in the future. Therefore, an understanding of skeletal site-specific 3D microarchitecture as well as the physical and cellular properties of the human jaw as a recipient site and the donor bone is essential. Synchrotron micro computed-tomography (SR μ-CT) of alveolar bone (AB) and iliac crest (IC) reveals a site-specific distribution of the intracortical pore system (IPS) and osteocyte lacunar density (Rothweiler et al., 2022). On a nanostructural level, proteome-based profiling of patient-paired human AB and IC, highlights site-specific and interindividual differences (Fretwurst et al., 2022). These insights into site-specific properties may be important for the understanding of mineral homeostasis as well as mechanical and clinical performance of bone transplants regarding an osseous union with jawbones (Rothweiler et al., 2022) and may help explain the clinical success of IC in major (>5 mm) avascular bone augmentations (Nelson et al., 2006; Heberer et al., 2009; Fretwurst et al., 2015; Troeltzsch et al., 2016).

It is known that a physiological framework promotes superior ingrowth of vessels and migration of osteogenic cells, resulting in improved bone formation (Qu et al., 2021), which is seen as the main driving force for bone regeneration in nonviable and synthetic bone substitute scaffolds (Weber, 2019). Vascularization as a main factor for ideal molecular exchange and functional performance is recognized and has led to promising advances in bone tissue engineering (Sharma et al., 2019; Chen et al., 2020; Gonçalves et al., 2021). The significance of vessel orientation in 3D scaffolds was largely ignored (Sharma et al., 2019) until blood vessel supply, osteocytes, and their lacunar-canaliculi network (LCN) as well as their role in bone metabolism were recently closely examined-for example, in femoral bone (Carter et al., 2013a; Dong et al., 2014; Hesse et al., 2014; Portier et al., 2020).

It is well known that LCN plays a fundamental role in cell–cell contact, nutrition, signalling molecules, and even interactions with extracellular tissue (Hesse et al., 2015; Bortel et al., 2022). Besides the important role of LCN in mechanosensation and transduction processes of osteocytes (Burger and Klein-Nulend, 1999; Vatsa et al., 2008; Schneider et al., 2010), it has been reported that LCN is involved in bone remodelling (Currey, 2014).

To date, SR μ-CT has neither been used in a study to examine bone samples of the fibula bone (FB) as a donor, nor of the jaw bone (AB), as a recipient site in an individual. Further, it is unknown

TABLE 1 Patient data.

Patient #	Gender	Age (years)	Sample	Biopsy origin	Diagnosis
1* #	Male	52	54A	Mandible region 32/33	OSCC
			54F	Fibula	
2* #	Male	60	55A	Mandible region 32/33	OS
			55F	Fibula	
3* #	Male	62	56A	Mandible region 33/34	OSCC
			56F	Fibula	
4*	Male	73	57A	Mandible region 43	OSCC
			57F	Fibula	
5#	Female	53	63A	Mandible region 34	OSCC
			63F	Fibula	
6#	Female	66	67A	Maxilla region 32	BCC
			67F	Fibula	
7#	Female	47	68A	Mandible region 34	OSCC
			68F	Fibula	
8#	Male	70	69A	Mandible region 44	OSCC
			69F	Fibula	
$N = 8$	62.5% male 37.5% female	Ø 60.38 years	$N = 16$	Recipient site: 87.5% mandible ($n = 7$), 12.5% maxilla ($n = 1$); Donor site: 100% fibula	Diagnosis: 75% OSCC ($n = 6$); 12.5% BCC ($n = 1$); 12.5% OS ($n = 1$)

In total, 8 patients were included. All patients' data such as gender, diagnosis (BCC = basal cell carcinoma; OSCC = oral squamous cell carcinoma; OS = osteosarcoma), age, sample and biopsy origin are provided in this table. *patients included in the 2.27 µm series; #patients included in the 640 nm series.

whether bone transplants for microsurgical anastomosis require specific morphological properties for the reconstruction of CSBDs or if a microarchitecture related to the recipient bone site might be favourable. Moreover, fluid simulation-derived orientation-dependent permeability properties may be of relevance, since a better match in terms of spatial orientation of the FB when connected to AB, could lead to an improved supply of nutrients and subsequently to bony union in the segmental gap. Therefore, the fluid simulation-derived permeability tensor was analysed to gain insights into the orientation-dependent permeability of AB and FB.

In order to provide a better understanding of the microarchitecture of human AB and FB, patient-paired samples were analysed and compared using SR µ-CT down to a voxel-size of 640 nm. It is demonstrated that SR µ-CT represents an ideal tool for 3D imaging of the bone microarchitecture without sample destruction. Additionally, spatial arrangement of the intracortical-pore system as well as osteocyte lacunar density and lacunar morphology were analysed and compared.

2 Materials and methods

The Ethics Committee of the Faculty of Medicine Charité Berlin approved this study (EA4/161/18). The study was performed in accordance with the Helsinki Declaration of 1964 as revised in 2013.

2.1 Patients

In total, 8 patients (females: 3; males: 5; mean age: 60.38 years; age range: 47–73 years) were treated at the Department of Oral and Maxillofacial Surgery, Charité–Universitätsmedizin Berlin, Germany and were consecutively enrolled between September 2018 and May 2020. Seven patients received a partial resection of the mandible, whereas one patient received a resection of the maxilla. A resection of the mandible or the maxilla was required due to oral squamous cell carcinoma ($n = 6$), basal cell carcinoma ($n = 1$), or osteosarcoma ($n = 1$). Primary CAD/CAM-planned reconstruction with a free fibula flap (FFF) was performed in all patients, whereby the CAD/CAM planning procedure followed a previously described workflow (Kreutzer et al., 2022). Informed consent was obtained from all participants included in this study. Patients with medication affecting bone metabolism (e.g., immunosuppressants and antiresorptive agents), were not included in this research.

2.2 Sample harvesting and preparation

In each patient, two bone samples were harvested (one AB and one FB sample). All samples were retrieved using an oscillating saw. The AB samples were taken from the vicinity of the connecting area of the original bone to FFF during bone contouring. Since all FFF's were CAD/CAM-planned and raised using CAD/CAM templates, the slice of bone between two segments (which was not further used) was taken as the FB sample. Patient data are listed in Table 1.

After harvesting, the bone samples were fixed in 4% neutral buffered formalin. Subsequently, dehydration in ascending alcohol series (water, 70%/80%/96%/100% ethanol) for three days each followed. The samples were defatted in xylene and infiltrated, embedded, and polymerized in Technovit® 9100 New (Heraues Kulzer, Wehrheim, Germany). Technovit® 9100 New was used according to the manufacturer's manual (Kulzer, 2012). All Technovit® blocks were cut to a size of 5 mm × 5 mm using a band saw (Proxxon S.A., Wecker, Luxembourg).

2.3 Synchrotron computed tomography imaging

Samples of four patients were SR µ-CT scanned at a voxel size of 2.27 µm, and samples from seven patients (including 3 that were analyzed at the 2.27 voxel-size setup) were scanned at 640 nm voxel size to address the difference in bone morphology at two different voxel-sizes [Figures for all samples are listed in Supplementary Figure S1 (2.27 µm), respectively Supplementary Figure S2 (640 nm)]. The imaging of the 640 nm data was performed at Synchrotron Soleil, France. A SR µ-CT setup of the Psiché (PSICHÉ) beamline was used with a beam energy of 45 keV and a sample to detector distance of 45 mm. For each sample, a total of 5600 projections were exposed for 40 ms each and were recorded over an angle of 360° using a Hamamatsu ORCA Flash sCMOS camera. Phase retrieval and image reconstruction was performed using Paganin's method (Paganin et al., 2002) and a filtered back projection algorithm, respectively with a delta/beta ratio of approximately 65. Data of 2.27 µm voxel-size were acquired at the beamline ID 19 of the European Synchrotron Radiation Facility (ESRF) in Grenoble, France using 46.9 keV beam energy and a sample detector distance of 460 mm. For each sample, 4000 radiographs over an angle of 360° were recorded at an acquisition time per frame of 20 ms. A pco.edge 5.5 camera (PCO AG, Kelheim, Germany) was used. As with the 640 nm data, reconstruction was carried out using Paganin's method in combination with the conventional filtered back projection algorithm employing a delta/beta ratio of 350 (Paganin et al., 2002).

2.4 Segmentation of samples

For all samples, representative volumes of interest (VOIs) were selected with a particular emphasis on artifact-free and physiological bone anatomy. In FB, cortical regions were chosen; and AB was mostly assigned to the cortical bone. The VOI of the 640 nm scan was set within the VOI scanned at 2.27 µm. Within each VOI, different tissue regions were segmented into mineralized tissue, vessel pores, and osteocyte lacunae. For both voxel-sizes (2.27 and 640 nm), inhouse-developed MATLAB (R2018b, The MathWorks Inc., Natick, MA, United States) scripts combining several different morphological operations were used. To obtain the mineral mask on the binarized data, a closing of all pores (vessel pores and osteocyte lacunae) within the mineralized region was achieved by a Euclidian distance map coupled to a thresholding step. Combining the mineral mask and the inverse of the binarized data resulted in a mask containing vessel pores. Osteocyte lacunae were extracted from the gray value data with a bottom-hat transformation and a following thresholding step. A connected component analysis was used to size and filter osteocyte lacunae between 30 and 8,000 µm^3 and with length and width below 130 and 30 µm.

2.5 Digital bone morphometry and osteocyte lacunae segmentation

For all VOIs, the following parameters of bone morphometry were obtained: bone volume (BV), total volume (TV), bone surface area (SA), porosity (1-BV/TV), specific bone surface (SA/BV), osteocyte lacunae density (N.Lc/BV), mineral distance [(50%) $L_{dist,min50}$], mineral distance [(95%) $L_{dist,min95}$], vessel distance [(50%) $L_{dist,\ vessel50}$], vessel distance [(95%) $L_{dist,\ vessel95}$], and blood vessel volume (Vv.). Additionally, 640 nm scans were used to extract the shape of the individual lacunae, which were described by the ratio of the lacunae axes lengths (L_1/L_3; L_2/L_3; L_1/L_2, with L_1 being the longest and L_3 being the shortest axis). A detailed summary of the characterized morphological parameters is given in Table 2.

2.6 Absolute permeability and tensor of absolute permeability

Fluid simulation was performed for all 2.27 µm scans. The tensor of permeability was calculated through the Absolute Permeability Tensor Calculation module (Thermo Scientific Avizo Software, XLab Module, Version 2020.2). This tensor enables the computation of permeability in all three spatial directions as well as the computation of eigenvectors and their associated eigenvalues. The ratios of three eigenvalues (E1, E2 and E3) to each other were determined to quantify the anisotropic behavior of absolute permeability (with E1>E2>E3). The termination conditions for the simulations were that either the convergence criterion was smaller than 10^{-5} or the number of iterations reached 10^6. Tensor calculation is based on a mathematical approach which considers the sample to be representative of an infinite or macroscopic material. It provides the intrinsic permeability tensor by solving the closure problem derived from the Strokes equation by volume averaging (Whitaker, 1999). All samples were computationally aligned in the same way to ensure comparability. Therefore, the bone surface was located within the x–z plane, where the anatomical long axis was parallel to the *z*-axis of the global coordinate system.

2.7 Quantifying orientation of the vessel pore

Morphological skeletonization was used to extract central segments of all branches of the vessel pore network. The angles

TABLE 2 All parameters extracted to characterize bone morphology (Bouxsein et al., 2010; Dempster et al., 2013).

Parameter	Symbol	Unit	Calculation/Reference	Voxel-size
Total volume	TV	mm^3	Total bone volume, comprising mineral and pore volumes	2.27 µm
				640 nm
Mineral volume	BV	mm^3		2.27 µm
				640 nm
Lacunar volume	LcV	µm^3		2.27 µm
				640 nm
Lacunar porosity	Lc_V/BV	%	$Lc_V/BV*100$	2.27 µm
				640 nm
Lacunar density	NLc/BV	1/ mm^3		2.27 µm
				640 nm
Mineral distance (50%)	$L_{dist,min50}$	µm	Distance maps, histogram and cumulative summation	2.27 µm
				640 nm
Mineral distance (95%)	$L_{dist,min95}$	µm	Distance maps, histogram and cumulative summation	2.27 µm
				640 nm
Vessel distance (50%)	$L_{dist,\ vessel50}$	µm	Distance maps, histogram and cumulative summation	2.27 µm
				640 nm
Vessel distance (95%)	$L_{dist,\ vessel95}$	µm	Distance maps, histogram and cumulative summation (Dong et al., 2014)	2.27 µm
				640 nm
Mean value of lacunar volume	$\tilde{V}_{lac}$	µm^3		2.27 µm
				640 nm
Standard deviation of lacunar volume	σl_{ac}	µm^3		2.27 µm
				640 nm
Blood vessel volume	VV	µm^3		2.27 µm
				640 nm
Vessel porosity	VV/BV	%	Vv/BV*100	2.27 µm
				640 nm
Level of alignment	LOA	-	Product of the variance of theta s_Θ and the variance of phi s_Φ ($LOA = s_\Phi \cdot s_\Theta$)	2.27 µm
Angle Phi	Φ	°	Angle between a segment and the *z*–axis. Phi = 0° if the segment is parallel to a bone´s long axis	2.27 µm
Angle Theta	Θ	°	Projected angle between a segment and the *x*–axis. The segment is parallel to a bone's surface if theta = 0°	2.27 µm
Ratio EV mean	EV mean	-	Mean of the ratios of the eigenvectors of the permeability tensor [(E2/E1) + (E3/E1)]/2	640 nm
Principal Axis Length ratio L1/L3	L_1/L_3	-	Ratio of the longest and shortest axes of the osteocyte lacunae	640 nm
Principal Axis Length ratio L1/L2	L_1/L_2	-	Ratio of the longest and second-longest axes of the osteocyte lacunae L_1/L_2	640 nm
Principal Axis Length ratio L2/L3	L_2/L_3	-	Ratio of the second-longest and shortest axes of the osteocyte lacunae L_2/L_3	640 nm

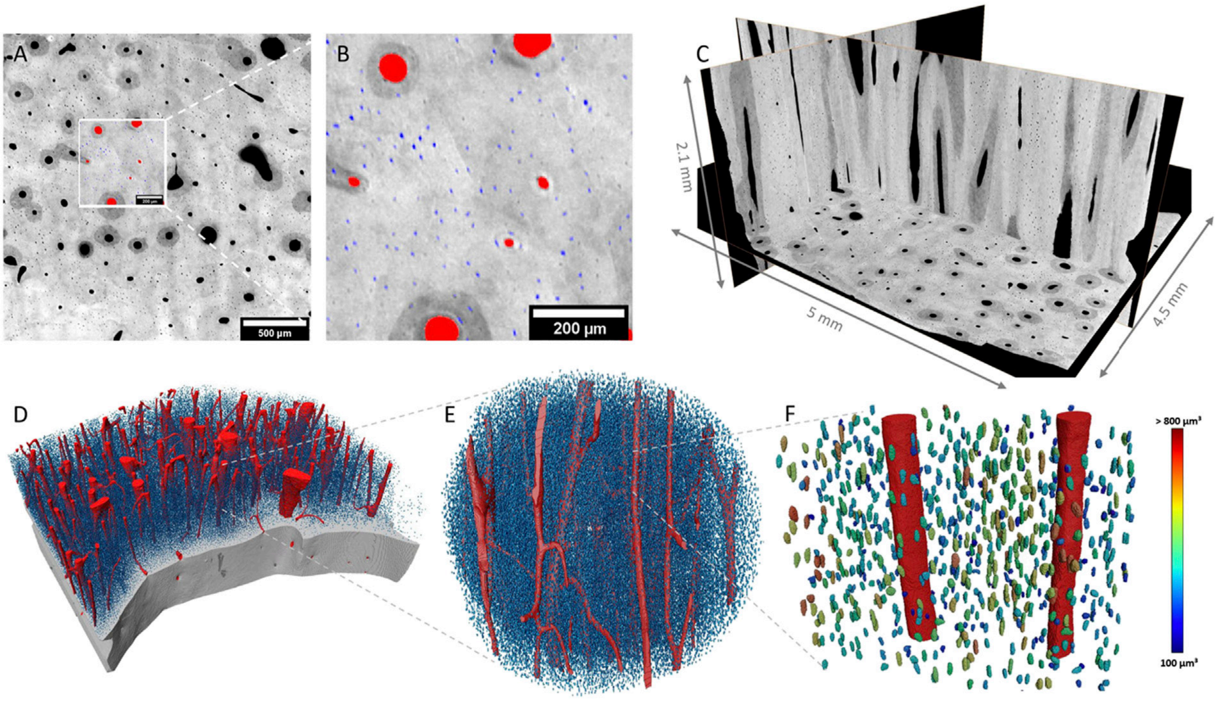

FIGURE 1
2D and 3D representation of raw and segmented data of sample 54F. Mineralized bone tissue is displayed in different shades of grey, while segmented vessels are labeled in red and lacunae in blue. **(A)** Illustrates a 2D slice inside the bone where the zoomed-in region shown in **(B)** is displayed. **(C)** Shows 3D orientation of the bone in various/selected layers. **(D)** Shows a 3D rendering of the segmented structures, where the bone is virtually cut open to reveal a vessel system and lacunae. **(E,F)** represent a selected section of D in high resolution. In **(F)**, lacunae are color-coded according to their volume.

theta and phi were computed for every segment of the skeleton to allow a quantification of spatial orientation. Phi is herein defined as the angle between the segment and the z-axis, with phi = 0° meaning that the segment is parallel to the bone's long axis. Theta is defined as the projected angle between the segment and the x-axis, resulting in a segment that is parallel to the bone's surface if theta = 0°. Histograms showing the distribution of theta and phi for all segments in each sample were calculated and the variance of the amplitudes of phi and theta was extracted. Highly aligned segments result in heterogeneous histograms with a prominent peak and thus a high variance. In contrast, equally distributed vessel orientations show a homogeneous histogram and thus a small variance. To quantify the alignment of the vessel pores, we used a recently introduced descriptor (Bortel et al., 2022)- the level of alignment (LOA), which is defined as the product of the variance of theta s_Θ and the variance of phi s_Φ (LOA = $s_\Phi \cdot s_\Theta$).

2.8 Statistics

Statistical hypothesis tests (ANOVA, Kruskal–Wallis, Mann–Whitney and t-test) with *post hoc* testing (Bonferroni) were performed using IBM SPSS Statistics (version 25.0, IBM Corp., Armonk, NY, United States). p-values ≤ 0.05 were considered statistically significant.

3 Results

3.1 Comparison of bone morphometric parameters

The data collected at the ESRF at 2.27 µm voxel-size provided a larger field of view than did the scans collected at PSICHÉ at a higher spatial voxel-size and were thus used to quantify vessel morphology and lacunar density. The data collected at the 640 nm voxel-size provided a small field of view but allowed for the shape analysis of the osteocyte lacunae.

3.2 Bone gross morphology at 2.27 µm voxel-size

SR µ-CT data of the 2.27 µm voxel-size scans (AB, FB and n = 4/each) were successfully segmented and bone gross morphology parameters were extracted as described in Table 2. Figure 1 illustrates bone sample 54F in 3D and the corresponding segmentation. In Figure 1A, it can be observed that the vessel pores in the horizontal slice mainly run perpendicular to this plane. The segmented vessels are labelled in red, while the lacunae are labelled in blue (Figures 1A, B). Orthogonal grey value slices (1C) of the bone of sample 54F are dark grey, indicating air or soft tissue compartments, while bright grey values refer to high densities of

TABLE 3 Bone morphological parameters extracted for AB and FB samples at a voxel-size of 2.27 µm.

Sample	Vessel porosity (%)	Lacunar density (per mm^3)	Mineral distance (50%) (µm)	Mineral distance (95%) (µm)	Vessel distance (50%) (µm)	Mineral volume in mm^3	Vessel distance (95%) (µm)	Vessel Surface/ Vessel volume (1/mm)	Vessel Surface/ Total volume (1/mm)	Vessel Surface/ Bone volume (1/mm)
54A	15.82	20,228	98	226	29	17.5	120	22.8	2.6	2.9
54F	3.82	18,208	84	196	11	28.9	42	53.6	2.0	2.1
55A	3.65	24,108	93	205	10	3.7	43	60.5	2.2	2.3
55F	5.84	17,882	81	195	11	15.2	37	52.5	3.1	3.3
56A	3.22	23,984	93	188	9	13.5	31	59.7	1.9	2.0
56F	6.38	21,873	60	125	10	18.0	33	57.2	3.6	3.9
57A	10.63	23,175	101	213	26	25.3	92	23.1	2.5	2.8
57F	11.62	19,541	78	179	22	21.8	76	28.9	3.4	3.8
t-test p =	Not significant	**0.038**	**0.021**	Not significant	Not significant	Not significant	Not significant	Not significant	Not significant	Not significant

The bold values provide statistically significant values.

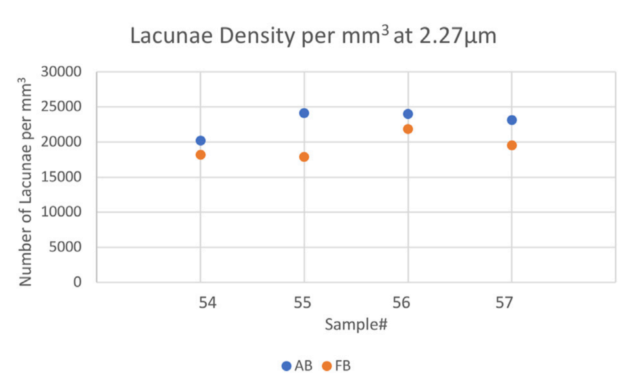

FIGURE 2
Scatterplot showing the Lacunar Density of the 2.27 µm voxelsize setup per mm^3 for AB and FB samples 54–57. Blue indicates AB, orange represents FB.

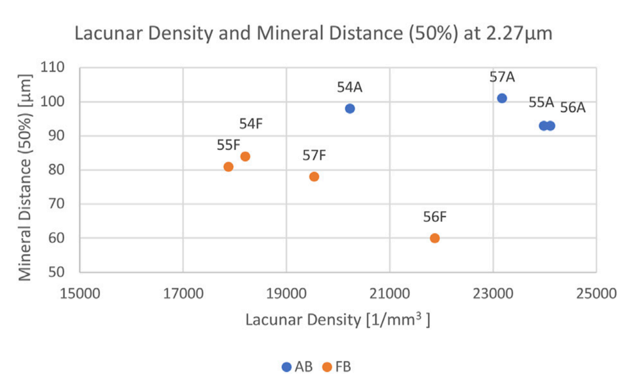

FIGURE 3
Scatterplot showing the relation between Lacunar Density per mm^3 (x-axis) and Mineral Distance (50%) (y-axis) for AB (blue) and FB (orange) samples 54–57. Each sample is labelled.

the mineralized phase. A 3D rendering of Figure 1A is given in Figure 1D: each of the blue dots refers to a single lacuna (here 18,208 mm^3). In the zoom-in in Figure 1F, the lacunae are color-coded according to their volume.

The mean vessel porosity was found to be 8.3% for AB and 6.9% for FB. At the same time, the mean vessel distance was higher for AB than it was for FB. This was observed in the mean vessel distance of 50% (AB: 18.5 µm and FB: 13.5 µm) as well as for the mean vessel distance of 95% (AB: 71.5 µm and FB: 47 µm). On average the median distance (i.e. 50%) of the mineralized bone tissue to the closest vessel pore boundary was found to be 96 µm (minimum: 93 µm; maximum: 101 µm) for AB and 76 µm (minimum: 60 µm; maximum: 84 µm) for FB. On average, 95% of mineralized bone was found at a distance of 208 µm (minimum: 188 µm; maximum: 226 µm) for AB and 174 µm (minimum: 125 µm; maximum: 196 µm) for FB from the canal surface. The average lacunar density for AB was found to be 22,874 per mm^3 (minimum: 20,228; maximum: 24,108) and 19,376 per mm^3 (minimum: 17,882; maximum: 21,873) for FB. A summary of the results is given in Table 3 and a visualization of statistically significant results is provided in Figures 2, 3 (and Supplementary Figure S3).

Most parameters showed no significant differences between AB and FB except for lacunar density (p = 0.038) and mineral distance (50%) (p = 0.021).

3.3 Lacunae shape descriptors at 640 nm

As described, gross bone morphology parameters were also determined for 7 patient-paired bone samples at a voxel-size of 640 nm (Table 4). Mean lacunar density per mm^3 showed the same trend and was higher for AB (25,145; ranging from 20,978 to 28,416) than it was for FB (21,042; ranging from 17,807 to 23,068), thus revealing significant differences between these bone entities (p = 0.0049). Mean vessel porosity for both bone entities was comparable: it was 5.16% (1.03%–11.27%) for AB and 5.61% (2.91%–8.48%) for

TABLE 4 Lacunar shape descriptors for AB and FB samples examined at 640 nm.

Sample	Number of lacunae	Mineral volume in mm^3	Lacunar density (per mm^3)	Mean value of the lacunar volume ± SD (μm^3)	Standard deviation of lacunar volume (μm^3)	Vessel porosity (%)	Principial axis length ratio L1/ L3 ± SD (-)	Principial axis length ratio L1/ L2 ± SD (-)	Principial axis length ratio L2/ L3 ± SD (-)
54A	55,543	2.65	20,978	627 ± 295	295	11.27	2.9 ± 0.7	2.2 ± 0.7	1.3 ± 0.2
54F	85,134	4.40	19,354	698 ± 280	280	2.91	3.2 ± 0.8	2.2 ± 0.7	1.5 ± 0.3
55A	33,269	1.21	27,470	414 ± 183	183	2.07	2.8 ± 0.9	2.1 ± 0.7	1.4 ± 0.3
55F	48,039	2.33	20,625	657 ± 268	268	3.63	3.1 ± 1.0	2.1 ± 0.7	1.5 ± 0.3
56A	59,501	2.37	25,136	303 ± 145	145	3.41	3.4 ± 1.2	2.6 ± 1.0	1.4 ± 0.2
56F	14,956	0.71	20,975	604 ± 306	436	6.90	2.7 ± 0.8	2.0 ± 0.7	1.4 ± 0.2
63A	16,886	0.71	23,860	559 ± 254	254	1.07	3.2 ± 0.9	2.4 ± 0.8	1.4 ± 0.3
63F	32,253	1.39	23,279	541 ± 237	237	4.87	2.8 ± 0.7	2.2 ± 0.7	1.3 ± 0.2
67A*	10,706	0.42	25,647	431 ± 174	174	9.18	2.8 ± 0.8	2.2 ± 0.7	1.4 ± 0.2
67F	35,523	1.54	23,068	555 ± 251	251	7.24	2.9 ± 0.8	2.2 ± 0.7	1.3 ± 0.2
68A	59,441	2.09	28,416	851 ± 325	325	1.03	3.1 ± 0.8	2.4 ± 0.8	1.3 ± 0.2
68F	22,342	1.01	22,186	466 ± 185	185	5.21	2.7 ± 0.7	2.0 ± 0.7	1.4 ± 0.3
69A	36,837	1.50	24,508	685 ± 315	315	8.11	3.1 ± 0.8	2.3 ± 0.8	1.4 ± 0.3
69F	32,708	1.84	17,807	688 ± 299	299	8.48	3.0 ± 0.8	2.1 ± 0.7	1.5 ± 0.3
p-value	0.9881	Not significant	**0.004878**	Not significant	Not significant	Not significant	Not significant	**0.02946**	Not significant
p-value paired	0.9880	Not significant	**0.005549**	Not significant	Not significant	Not significant	Not significant	Not significant	Not significant

*Only sample AB was taken from the maxilla.
The bold values provide statistically significant values.

TABLE 5 Comparison between the number of lacunae when extracted from 2.27 μm data and 640 nm data.

Sample	N.Lc/mm^3 of the 2.27 μm data	N.Lc/mm^3 of the 0.6 μm data	Ratio of densities between both voxel-size data
54A	20,228	20,978	1.037
54F	18,208	19,354	1.063
55A	24,108	27,470	1.139
55F	17,882	20,625	1.153
56A	23,984	25,136	1.048
56F	21,873	20,975	0.959

Sample 56F is the only sample with a high number of lacunae in the 2.27 μm scan.

FB. For the 640 nm series, lacunae shape descriptors were additionally characterized. The mean volume of the osteocyte lacunae was found to be slightly lower in AB with a mean volume of 553 μm^3 (from 303 to 851 μm^3) than it was in FB with a mean volume of 601 μm^3 (466–698 μm^3). Principal axis length ratios were measured and compared. In AB, the mean L1/L3 and L1/L2 was found to be slightly higher (3.0 and 2.3, respectively) than it was in FB (2.9 and 2.1, respectively). Mean L2/L3 was 1.37 for AB and 1.41 for FB. Interestingly, no statistical difference in the volume of the lacunae could be found between AB and FB. Sample 67 A—the only AB harvested from the maxilla showed similar results for the lacunar shape descriptors (Table 4).

3.4 Impact of voxel-size

For 6 sample scans (54 A, 54 F, 55 A, 55 F, 56 A and 56 F), lacunar densities were compared between two different voxel-sizes (2.27 and 0.64 μm) to assess the impact of field of view positioning and the voxel-size on the lacunar density (Table 5). We found that in 5 out of 6 scans (54 A, 54 F, 55 A, 55 F and 56 A),

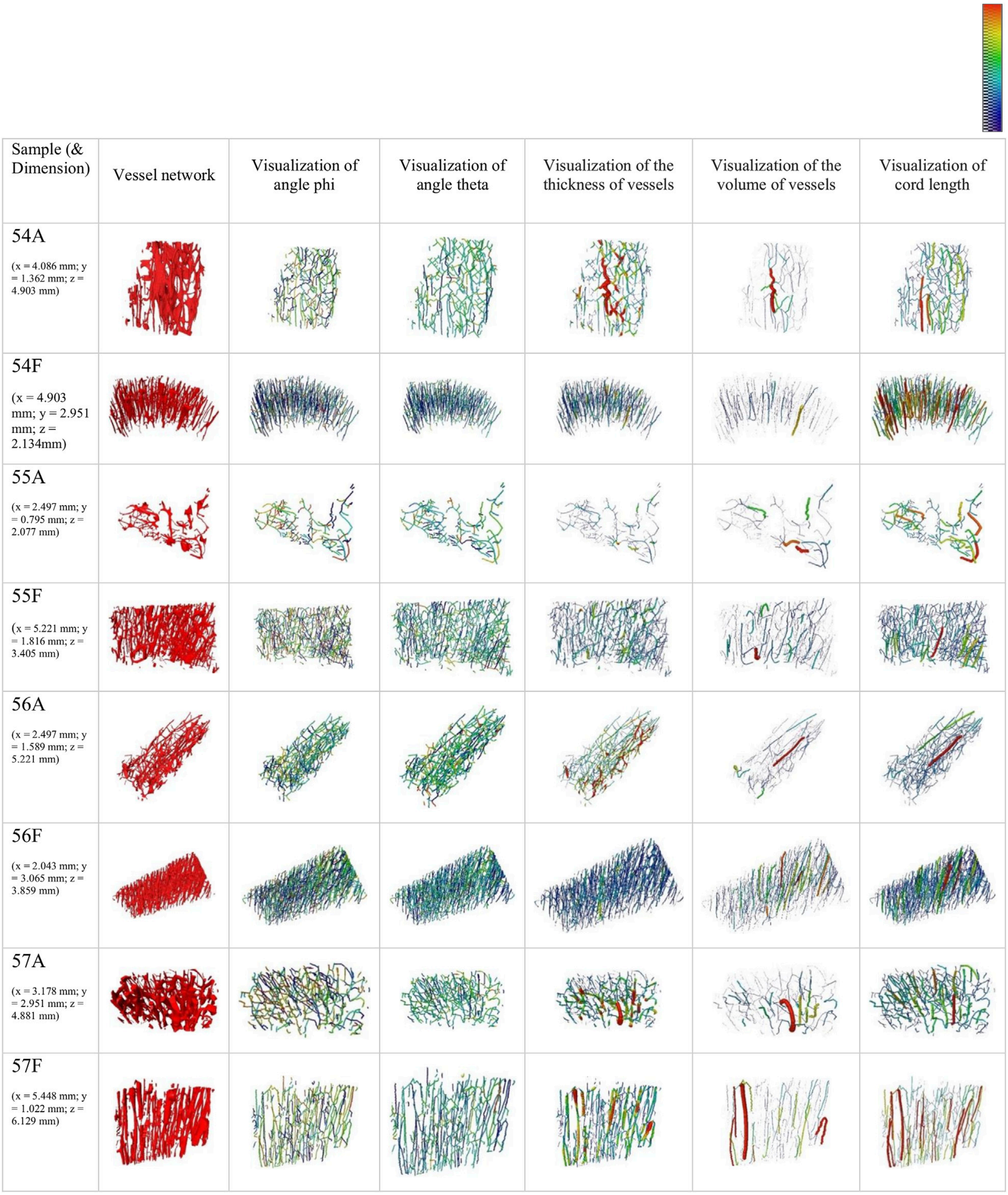

FIGURE 4
3D rendering of the segmented vessel network of 2.27 μm samples and visualization of skeletons color-coded by angles phi (colour bar: 0°–360°) and theta (colour bar 0°–90°) (column 2–4). Additionally, a visualization of pore network skeletons color-coded and weighed by thickness (colour bar: 0–30 μm) and volume (colour bar: 0 to $5 \cdot 10^6$ μm^3) and cord length (colour bar: 0–900 μm) (column 5–7) are shown. The thicker the vessels displayed, the larger the respective parameter.

lacunar density was found to be slightly higher for the high resolution data (Table 5) suggesting that not all lacunae were captured by the 2.27 μm voxel-size setup. For the one scan with the smaller lacunar density, the VOI of the 0.64 μm-setup was the smallest among the compared specimens and could therefore result in being not representative for the computation of the

TABLE 6 Orientation parameters normalised to the vessel length of the 2.27 µm series.

Sample	Phi bin var (E-03)	Theta bin var (E-03)	LOA (E-05)	LOA ratio (FB/AB)
54A	5.17	10.29	5.32	0.13
54F	1.03	6.73	0.70	
55A	3.98	6.32	2.51	0.61
55F	2.85	5.38	1.53	
56A	1.12	5.49	0.62	2.38
56F	2.68	5.50	1.47	
57A	1.19	8.47	1.01	2.71
57F	4.82	5.68	2.74	

TABLE 7 Results of fluid simulation for samples 54, 55, 56 and 57 showing the mean ratio of eigenvalues for each sample.

Sample	Ratio EV mean	Invert
54A	0.0037	273.4
54F	0.0024	425.5
55A	0.0768	13.0
55F	0.0171	58.5
56A	0.0162	61.7
56F	0.0338	29.6
57A	0.1509	6.6
57F	0.1237	8.1

Mean eigenvalues (with E1 > E2 > E3) of the permeability tensor and their ratio have already been computed. To illustrate, the invert number 273.4 means that the main permeability along the main permeability direction is 273.4 times more pronounced than it is in the orthogonal directions.

lacunar density and that the selection of a different VOI would likely result in a higher lacunar density.

3.5 Orientation of vessel network

The vessel network of AB and FB samples and the angles theta and phi as well as the visualization of the thickness, the volume of the vessels and the cord length are visualized in Figure 4. The skeleton branches are color-coded by angle, and it appears that FB samples have a high degree of alignment.

The summarized results for the orientation parameters normalized to vessel length (vessel volume) are presented in Table 6. The ratio LOA_FB/LOA_AB is smaller than 1 for samples 54 and 55 and is notable above 1 for samples 56 and 57.

Histograms of the pooled angles for phi and theta, normalized to segment length and volume, indicate a pronounced intensity between ~35° and ~55° (theta) for AB. Histograms for phi show pronounced peaks between 40° and 50° for FB.

Fluid simulations were computed for 4 paired samples, and results are listed in Table 7. Eigenvalues were computed and the means of E2/E1 and E3/E1 were calculated, revealing a more uni-directional pronounced permeability in FB than in AB in 3 of the 4 paired samples. The inverse of the mean ratio EV for each sample was calculated to highlight the consistent scale of paired AB and FB (Table 7).

4 Discussion

This study examined patient-paired AB and FB at different length scales to quantify differences in bone morphology, including permeability properties, to comprehend factors that could be relevant to the success of microvascular free fibula bone transplants in reconstructive surgery. SR µ-CT evaluation of geometrical properties of human bone has been described before and used successfully (Hesse et al., 2014). However, to the best of our knowledge, a comparison of AB and FB on a micro scale in 3D has not been performed to date.

4.1 Lacunar density and morphology

Osteocyte lacunar properties in AB, tibial bone (TB) and femoral bone (FeB) have been described before, especially regarding either a variation in osteocyte lacunar density, volume, morphology, orientation or even age-dependent changes within a femur (Carter et al., 2013b; Ashique et al., 2017). In the present study, osteocyte lacunar density was found to be significantly higher in AB compared to FB. The high number of lacunae per mm^3 found in AB, 20,228–24,108 (2.27 μm data set) and 20,978–28,416 (640 nm data set) are in accordance with previous SR μ-CT studies (Hesse et al., 2014a; Hesse et al., 2014b). Although various papers (Gauthier et al., 2018; Milovanovic and Busse, 2019) have addressed the question of inter-site variability of the osteocyte lacunar network, available data are still not fully conclusive.

Since the FB in our study was consequently standardized and harvested in the middle of diaphysis, no regional differences should occur due to different sampling locations. Gauthier et al. (2018), examined femoral diaphyses, femoral neck, and radial diaphyses and found a significantly higher lacunar density in the femoral neck compared to the radius (26,123/mm^3 vs. 21,191/mm^3). In contrast, the lacunar density of femoral diaphyses versus radial diaphyses showed merely slight differences (21,617/mm^3 vs. 21,191/mm^3) (Gauthier et al., 2018). These findings suggest that inter-site differences in one individual exist and that even anatomical regions near each other show differences in osteocyte lacunar number, which could suggest changes in bone microstructure between weight-bearing and non- or low-weight bearing areas (Gauthier et al., 2018; Milovanovic and Busse, 2019). The lacunar density of FB found in our study (17,882–21,873/mm^3 for the 2.27 μm data set and 17,807–23,860/mm^3 for the 640 nm data set) resembles the result for radial diaphyses as well as that for femoral diaphyses. Anatomically, radius and FB are comparable in terms of mechanical loading as both are low weight-bearing bones. We report that in 5 out of 6 scans, lacunar density was found to be higher for the 640 nm voxel-size data, suggesting that small lacunae were not identified when a large voxel setup was used. In only one sample does the 640 nm voxel-size data reveal a lower lacunar density, which might have originated from the heterogeneity within the individual sample. It must be noted that the analysed VOI of this particular sample was much smaller than that of the other samples. This implies that at 2.27 μm voxel-size of the used imaging setup and analysis, potentially undersegments about 5%–15% of the lacunae. Additionally, the shape of each lacuna was examined: the ratios of the lacunae principal axes lengths indicate a similar shape in the lacunae of AB and FB. The shape of the osteocyte lacunae and the potential influence on the function of osteocytes as a “mechanosensor” of the bone are assumed to be affected by mechanical loading of the bone (van Oers et al., 2015). Round osteocytes are considered to be more mechanosensitive compared to elongated osteocytes in long bones that are accustomed to high mechanical loadings (Bacabac et al., 2008). According to the assumption that variation in lacunar as well as osteocyte shape directly affects osteocytic mechanosensation and subsequently bone remodelling (van Oers et al., 2015), the findings of our study, which has a similar lacunar shape of AB and FB, might indicate comparable mechanosensitive properties. Wu et al. (2018), discovered significant differences in osteocyte surface area and orientation locally in the maxillary bone where the osteocyte surface area was 1.5 times higher and osteocyte-orientation was more cranially caudally orientated in tooth gaps compared to its orientation in edentulous parts of the maxilla, which may be related to tensile strain magnitude and orientation. Unfortunately, our data do not allow any conclusions to be drawn regarding local differences within an individual since only one AB and FB sample were examined per patient due to ethical and harvesting limitations. After transplantation, FB weight-bearing probably differs from its previous weight-bearing: dental implants are inserted when dental/prosthetic rehabilitation is done. Iezzi et al. (2020), found a higher number of osteocytes in the jawbone around immediately loaded implants compared to their number in unloaded bone sites, which suggests a change in bone matrix after dental implant loading. Changes in lacunar density of FB before and after dental implant insertion as well as after implant loading might be of particular interest. In addition, van Tol et al. (2020), showed that not only mechanical loading but also LCN architecture should be considered as a key determinant of bone adaption, which clears the way for further research. Given these preconditions, investigations of FB after dental implant insertion and weight-loading, due to prosthetic rehabilitation that affects this weight loading of the FB/neo-mandible, could help create an understanding of the process of adaption of the bone and the LCN to changes in mechanical loading.

4.2 Spatial mineral density distribution

In the present study, the mineral distance to the closest pore surface (considering 50% of all mineral volume) was found to be significantly higher in AB compared to FB, and the mineral distance (considering 95% of all mineral volume) tended to be higher in AB than in FB. Our study suggests that spatial mineral distribution is organized such that the distance to the closest vessel pore boundary is larger in AB than in FB. In contrast, AB shows a higher lacunar density than does FB, which might compensate for the great distance to the closest vessel. Recent studies have demonstrated the relation between LCN and mineralization (Roschger et al., 2019; Ayoubi et al., 2020), whereby a dense LCN is normally accompanied by a high degree of mineralization. The degree of mineralization could not be quantified in our study due to the different geometrics of the samples and the local-tomography imaging approach. The potential role of mineral exchange at the LCN interface has previously been reported in several researches (Qing et al., 2012; Kerschnitzki et al., 2013; Hesse et al., 2014a; Roschger et al., 2019).

4.3 Vessel network, porosity and permeability

The present results revealed an average vessel porosity (for the 2.27 μm samples) of 8.3% for AB and 6.9% for FB as well as 5.16% for AB and 5.61% for FB (for the 640 nm samples), which is consistent with the findings of previous studies (Feik et al., 1997; Bousson et al., 2000; Bousson et al., 2001; Kingsmill et al., 2007) and suggests similar characteristics in AB and FB. The average vascular porosity of different regions of the femur (midshaft, middiaphyseal, and midfemoral cortex) was found to be 7%–10% (Feik et al., 1997; Bousson et al., 2000; Bousson et al., 2001) and 3%–11% in the mandible (Kingsmill et al., 2007). Revascularization is described as the prime criterion for success in the regeneration of autologous bone grafts and transplants as well as for immobility and infection-free healing (Nelson et al., 2006). In order for a critical bone defect to heal, a newly formed bone requires a high vascularization (Lovett et al., 2009), which can be transferred to the osteotomy gap and the gap between FB and AB (as the recipient site). In maxillofacial surgery, the osteosynthesis normally needs to be removed (at least partially) prior to dental implant insertion (Kreutzer et al., 2022). Therefore, a sufficient osteogenesis with ossification of the osseous gap (FB and FB and AB and FB) is necessary. The rate of union in FFF is reported to be high (up to 97% after five years) (Houdek et al., 2017), which can be explained by the high number of vessels that follow the main axis of the graft and therefore allow a high blood supply leading to nutrient perfusion and mass transport. Additionally, in this area, the flow dynamic into the bone graft is often predefined by the recipient site/residual bone, where the orientation of the vessel network in FB might allow a high number of new vessel connections and a high number of vessels that can sprout into the osseous gap between AB and FB. The high and comparable number of vessels as well as the comparable vessel network between AB and FB may allow the FB graft to exhibit a high regeneration potential when connected to AB. This might correlate with a high osteoinductive and osteoconductive potential of FB when connected to AB, which is reflected in the similar distributions of vessel porosity.

Fluid simulation for most paired samples (three out of four) indicates a more pronounced relative permeability along the *z*-direction for FB compared to that in AB, which might correspond with the degree of osteoconductivity of FB. Unfortunately, only limited data on fluid flow simulation in patient-paired human bone samples exist (Rothweiler et al., 2022). Further studies on this simulation should be done, which could lead to an enhanced understanding of bone transplants if the composition of vessel pores and permeability becomes known. As aforementioned, a simplified approach with a single phase-flow was utilized (Rothweiler et al., 2022). This approach could be modified to create advanced models in subsequent studies.

A comparable SR μ-CT study (Rothweiler et al., 2022) to the current one focused on IC, which is an autologous bone graft known for its high clinical success in bone augmentation in oral and maxillofacial surgery (Nelson et al., 2006; Heberer et al., 2009; Fretwurst et al., 2015; Troeltzsch et al., 2016). Rothweiler et al. (2022), compared the bone morphology of AB (as a recipient/local bone) and IC. They found significantly more lacunae in AB compared to IC, which matches our findings for AB and FB. Moreover, AB showed a long distance for 50% and 95% of mineralized bone tissue to the closest vessel pore boundary (Rothweiler et al., 2022), which is in line with our results concerning mineral distance. This allows speculation that an increased number of osteocyte lacunae might compensate for the high average distance of the mineralized bone tissue to the nearest vessel in AB. Regarding the two different bone sites, IC and FB, AB evidently features different bone morphological characteristics that must be considered in designing 3D scaffolds for the maxilla and especially the mandible.

4.4 Limitations

The major limitation of this study is that only eight patients were included in this study, whereby samples of four patients were scanned at 2.27 μm and samples of seven patients were scanned at 640 nm voxel-size (including three patients from the 2.27 μm setup). Additionally, the samples of AB were not taken from identical regions of the mandible and one AB sample was taken from the maxilla. The segmentation of the lacunae is sensitive to the quality of the reconstructed SR μ-CT data. In turn, image quality can be a function of sample size, which also varied in different scans. Segmentation routines that are automatically adapted for each individual lacuna should be implemented for future studies. Additionally, the used voxel-size and the actual resolution must not be confused, since the resolution depends not only on the voxel-size but also on factors such as the Signal-to-Noise Ratio.

5 Conclusion

Vessel porosity, vessel network, vessel distance, as well as lacunar volume were not significantly different between AB and FB. Significant differences could be found for lacunar density and the average mineral-pore distance. Similarities in vessel orientation, porosity and vessel network might be beneficial to the osseous union of FFF and the jaw in reconstructive oral and maxillofacial surgeries. If differing lacunar density and average mineral-pore distance adversely affect the success of a bone graft/transplant, further research should be done. Additional studies on possible changes in a recipient site and the bone graft/transplant itself with regard to possible adaption mechanisms might help to create an understanding of how FB or AB contributes to the success of a transplant.

Data availability statement

The original contributions presented in the study are included in the article/Supplementary Material, further inquiries can be directed to the corresponding author.

Ethics statement

The studies involving human participants were reviewed and approved by the Ethics Committee of the Faculty of Medicine Charité Berlin (EA4/161/18). The patients/participants provided their written informed consent to participate in this study.

Author contributions

JW: conceptualization, investigation, resources, data curation, writing—original draft, visualization, and project administration. BH: supervision, methodology, validation, investigation, resources, data curation, visualization, software, and writing—original draft. RR: investigation, data curation, conceptualization, and writing—original draft. EmB: methodology, validation, investigation, resources, data curation, software, and writing—review and editing. CG: writing—review and editing. SB: methodology, software, and writing—review and editing. AK: methodology and investigation. ElB: methodology and investigation. JG: methodology, visualization, software, and writing—review and editing. CR: writing—review and editing. TF: conceptualization and writing—review and editing. SP: writing—review and editing. MH: resources, validation, supervision, conceptualization, and writing—review and editing. KN: resources, investigations, supervision, conceptualization, and writing—review and editing. SN: project administration, supervision, conceptualization, funding acquisition, and writing—original draft. All authors contributed to the article and approved the submitted version.

Acknowledgments

All authors thank the Synchrotron Soleil, Paris, France for the allocated beamtime at the PSICHÉ beamline as well as ESRF in Grenoble, France for the allocated beamtime at the ID 19 beamline.

Conflict of interest

EmB, SB, JG, and BH were employed by Xploraytion GmbH.

The remaining authors declare that the research was conducted in the absence of any commercial or financial relationships that could be construed as a potential conflict of interest.

Publisher's note

Supplementary material

The Supplementary Material for this article can be found online at: https://www.frontiersin.org/articles/10.3389/fbioe.2023.1169385/full#supplementary-material

SUPPLEMENTARY FIGURE S1
For each sample of the 2.27 µm voxel-size setup (54–57 A and F), SR-µCT images from all 3 angles (YZ; XZ:XY), the VOI, and a 3D rendering are listed. The corresponding scalebar is provided within each figure. A indicates alveoalar bone, and F fibula bone.

SUPPLEMENTARY FIGURE S2
For each sample of the 640 nm voxel-size setup (54–56 A and F, respectively 63, 67-69 A and F), SR-µCT images from all 3 angles (YZ; XZ:XY), as well as the VOI are listed. The corresponding scalebar is provided within each figure. A indicates alveoalar bone, and F fibula bone.

SUPPLEMENTARY FIGURE S3
Scatterplot showing the relation between Lacunar Density per mm^3 (x-axis) and Mineral Distance (95%) y-axis for AB and FB samples 54–57. Blue indicates AB, orange represents FB.

References

Ashique, A. M., Hart, L. S., Thomas, C. D. L., Clement, J. G., Pivonka, P., Carter, Y., et al. (2017). Lacunar-canalicular network in femoral cortical bone is reduced in aged women and is predominantly due to a loss of canalicular porosity. *Bone Rep.* 7, 9–16. doi:10.1016/j.bonr.2017.06.002

Ayoubi, M., van Tol, A. F., Weinkamer, R., Roschger, P., Brugger, P. C., Berzlanovich, A., et al. (2020). Three-dimensional interrelationship between osteocyte network and forming mineral during human bone remodeling. *bioRxiv*.2011.2020.391862. doi:10.1101/2020.11.20.391862

Bacabac, R. G., Mizuno, D., Schmidt, C. F., MacKintosh, F. C., Van Loon, J. J., Klein-Nulend, J., et al. (2008). Round versus flat: bone cell morphology, elasticity, and mechanosensing. *J. Biomech.* 41 (7), 1590–1598. doi:10.1016/j.jbiomech.2008.01.031

Blumberg, J. M., Walker, P., Johnson, S., Johnson, B., Yu, E., Lacasse, M. C., et al. (2019). Mandibular reconstruction with the scapula tip free flap. *Head. Neck* 41 (7), 2353–2358. doi:10.1002/hed.25702

Bortel, E., Grover, L. M., Eisenstein, N., Seim, C., Suhonen, H., Pacureanu, A., et al. (2022). Interconnectivity explains high canalicular network robustness between neighboring osteocyte lacunae in human bone. *Adv. NanoBiomed Res.* 2 (4), 2100090. doi:10.1002/anbr.202100090

Bousson, V., Bergot, C., Meunier, A., Barbot, F., Parlier-Cuau, C., Laval-Jeantet, A.-M., et al. (2000). CT of the middiaphyseal femur: cortical bone mineral density and relation to porosity. *Radiology* 217 (1), 179–187. doi:10.1148/radiology.217.1.r00se11179

Bousson, V., Meunier, A., Bergot, C., Vicaut, É., Rocha, M. A., Morais, M. H., et al. (2001). Distribution of intracortical porosity in human midfemoral cortex by age and gender. *J. Bone Min. Res.* 16 (7), 1308–1317. doi:10.1359/jbmr.2001.16.7.1308

Bouxsein, M. L., Boyd, S. K., Christiansen, B. A., Guldberg, R. E., Jepsen, K. J., and Müller, R. (2010). Guidelines for assessment of bone microstructure in rodents using micro-computed tomography. *J. Bone Min. Res.* 25 (7), 1468–1486. doi:10.1002/jbmr.141

Burger, E. H., and Klein-Nulend, J. (1999). Mechanotransduction in bone—Role of the lacunocanalicular network. *FASEB J.* 13 (9001), S101–S112. doi:10.1096/fasebj.13.9001.s101

Carter, Y., Thomas, C. D. L., Clement, J. G., and Cooper, D. M. L. (2013a). Femoral osteocyte lacunar density, volume and morphology in women across the lifespan. *J. Struct. Biol.* 183 (3), 519–526. doi:10.1016/j.jsb.2013.07.004

Carter, Y., Thomas, C. D. L., Clement, J. G., Peele, A. G., Hannah, K., and Cooper, D. M. L. (2013b). Variation in osteocyte lacunar morphology and density in the human femur — A synchrotron radiation micro-CT study. *Bone* 52 (1), 126–132. doi:10.1016/j.bone.2012.09.010

Chaine, A., Pitak-Arnnop, P., Hivelin, M., Dhanuthai, K., Bertrand, J. C., and Bertolus, C. (2009). Postoperative complications of fibular free flaps in mandibular reconstruction: an analysis of 25 consecutive cases. *Oral Surg. Oral Med. Oral Pathol. Oral Radiol. Endod.* 108 (4), 488–495. doi:10.1016/j.tripleo.2009.05.043

Chen, J., Hendriks, M., Chatzis, A., Ramasamy, S. K., and Kusumbe, A. P. (2020). Bone vasculature and bone marrow vascular niches in health and disease. *J. Bone Min. Res.* 35 (11), 2103–2120. doi:10.1002/jbmr.4171

Currey, J. D. (2014). New Jersey: Princeton University Press.

Dempster, D. W., Compston, J. E., Drezner, M. K., Glorieux, F. H., Kanis, J. A., Malluche, H., et al. (2013). Standardized nomenclature, symbols, and units for bone histomorphometry: a 2012 update of the report of the asbmr histomorphometry nomenclature committee. *J. Bone Mineral Res.* 28 (1), 2–17. doi:10.1002/jbmr.1805

Dong, P., Haupert, S., Hesse, B., Langer, M., Gouttenoire, P. J., Bousson, V., et al. (2014). 3D osteocyte lacunar morphometric properties and distributions in human femoral cortical bone using synchrotron radiation micro-CT images. *Bone* 60, 172–185. doi:10.1016/j.bone.2013.12.008

Feik, S., Thomas, C., and Clement, J. (1997). Age-related changes in cortical porosity of the midshaft of the human femur. *J. Anat.* 191 (3), 407–416. doi:10.1046/j.1469-7580.1997.19130407.x

Fliss, E., Yanko, R., Bracha, G., Teman, R., Amir, A., Horowitz, G., et al. (2021). The evolution of the free fibula flap for head and neck reconstruction: 21 Years of experience with 128 flaps. *J. Reconstr. Microsurg* 37 (4), 372–379. doi:10.1055/s-0040-1717101

Fretwurst, T., Gad, L. M., Nelson, K., and Schmelzeisen, R. (2015). Dentoalveolar reconstruction: modern approaches. *Curr. Opin. Otolaryngol. Head. Neck Surg.* 23 (4), 316–322. doi:10.1097/moo.0000000000000167

Fretwurst, T., Tritschler, I., Rothweiler, R., Nahles, S., Altmann, B., Schilling, O., et al. (2022). Proteomic profiling of human bone from different anatomical sites - a pilot study. *Proteomics Clin. Appl.* 16 (5), e2100049. doi:10.1002/prca.202100049

Gauthier, R., Langer, M., Follet, H., Olivier, C., Gouttenoire, P. J., Helfen, L., et al. (2018). 3D micro structural analysis of human cortical bone in paired femoral diaphysis, femoral neck and radial diaphysis. *J. Struct. Biol.* 204 (2), 182–190. doi:10.1016/j.jsb.2018.08.006

Gonçalves, R. C., Banfi, A., Oliveira, M. B., and Mano, J. F. (2021). Strategies for re-vascularization and promotion of angiogenesis in trauma and disease. *Biomaterials* 269, 120628. doi:10.1016/j.biomaterials.2020.120628

Heberer, S., Rühe, B., Krekeler, L., Schink, T., Nelson, J. J., and Nelson, K. (2009). A prospective randomized split-mouth study comparing iliac onlay grafts in atrophied edentulous patients: covered with periosteum or a bioresorbable membrane. *Clin. Oral Implants Res.* 20 (3), 319–326. doi:10.1111/j.1600-0501.2008.01638.x

Hesse, B., Männicke, N., Pacureanu, A., Varga, P., Langer, M., Maurer, P., et al. (2014a). Accessing osteocyte lacunar geometrical properties in human jaw bone on the submicron length scale using synchrotron radiation μCT. *J. Microsc.* 255 (3), 158–168. doi:10.1111/jmi.12147

Hesse, B., Langer, M., and Varga, P. (2014b). Alterations of mass density and 3D osteocyte lacunar properties in bisphosphonate-related osteonecrotic human jaw bone, a synchrotron ?CT study. *PLoS One.* 9 (2), e88481. doi:10.1371/journal.pone.0088481

Hesse, B., Varga, P., Langer, M., Pacureanu, A., Schrof, S., Männicke, N., et al. (2015). Canalicular network morphology is the major determinant of the spatial distribution of mass density in human bone tissue: evidence by means of synchrotron radiation phase-contrast nano-CT. *J. Bone Min. Res.* 30 (2), 346–356. doi:10.1002/jbmr.2324

Houdek, M. T., Bayne, C. O., Bishop, A. T., and Shin, A. Y. (2017). The outcome and complications of vascularised fibular grafts. *Bone Jt. J.* 99-b (1), 134–138. doi:10.1302/0301-620x.99b1.Bjj-2016-0160.R1

Iezzi, G., Mangano, C., Barone, A., Tirone, F., Baggi, L., Tromba, G., et al. (2020). Jawbone remodeling: a conceptual study based on synchrotron high-resolution tomography. *Sci. Rep.* 10 (1), 3777. doi:10.1038/s41598-020-60718-8

Keating, J. F., Simpson, A. H., and Robinson, C. M. (2005). The management of fractures with bone loss. *J. Bone Jt. Surg. Br.* 87 (2), 142–150. doi:10.1302/0301-620x.87b2.15874

Kerschnitzki, M., Kollmannsberger, P., Burghammer, M., Duda, G. N., Weinkamer, R., Wagermaier, W., et al. (2013). Architecture of the osteocyte network correlates with bone material quality. *J. Bone Min. Res.* 28 (8), 1837–1845. doi:10.1002/jbmr.1927

Kingsmill, V., Gray, C., Moles, D., and Boyde, A. (2007). Cortical vascular canals in human mandible and other bones. *J. Dent. Res.* 86 (4), 368–372. doi:10.1177/154405910708600413

Knitschke, M., Yonan, M., Roller, F. C., Pons-Kühnemann, J., Attia, S., Howaldt, H.-P., et al. (2022). Osseous union after jaw reconstruction with fibula-free flap: conventional vs. CAD/CAM patient-specific implants. *Cancers* 14 (23), 5774. doi:10.3390/cancers14235774

Kreutzer, K., Steffen, C., Nahles, S., Koerdt, S., Heiland, M., Rendenbach, C., et al. (2022). Removal of patient-specific reconstruction plates after mandible reconstruction with a fibula free flap: is the plate the problem? *Int. J. Oral Maxillofac. Surg.* 51 (2), 182–190. doi:10.1016/j.ijom.2021.04.003

Kulzer (2012). Polymerisation systems for histological applications [online]. Kulzer GmbH. Available at: https://www.kulzer-technik.de/media/webmedia_local/kulzer_technique/media_4/histologie_1/Prospekt_Histologie_englisch.pdf.

Ling, X. F., and Peng, X. (2012). What is the price to pay for a free fibula flap? A systematic review of donor-site morbidity following free fibula flap surgery. *Plast. Reconstr. Surg.* 129 (3), 657–674. doi:10.1097/PRS.0b013e3182402d9a

López-Arcas, J. M., Arias, J., Del Castillo, J. L., Miguel Burgueño, M., Navarro, I., Morán, M. J., et al. (2010). The fibula osteomyocutaneous flap for mandible reconstruction: a 15-year experience. *J. Oral Maxillofac. Surg.* 68 (10), 2377–84. doi:10.1016/j.joms.2009.09.027

Lovett, M., Lee, K., Edwards, A., and Kaplan, D. L. (2009). Vascularization strategies for tissue engineering. *Tissue Eng. Part B Rev.* 15 (3), 353–370. doi:10.1089/ten.TEB.2009.0085

Ma, J. L., Pan, J. L., Tan, B. S., and Cui, F. Z. (2009). Determination of critical size defect of minipig mandible. *J. Tissue Eng. Regen. Med.* 3 (8), 615–622. doi:10.1002/term.203

Mahendru, S., Jain, R., Aggarwal, A., Aulakh, H. S., Jain, A., Khazanchi, R. K., et al. (2020). CAD-CAM vs conventional technique for mandibular reconstruction with free fibula flap: a comparison of outcomes. *Surg. Oncol.* 34, 284–291. doi:10.1016/j.suronc.2020.04.012

Milovanovic, P., and Busse, B. (2019). Inter-site variability of the human osteocyte lacunar network: implications for bone quality. *Curr. Osteoporos. Rep.* 17 (3), 105–115. doi:10.1007/s11914-019-00508-y

Nelson, K., Ozyuvaci, H., Bilgic, B., Klein, M., and Hildebrand, D. (2006). Histomorphometric evaluation and clinical assessment of endosseous implants in iliac bone grafts with shortened healing periods. *Int. J. Oral Maxillofac. Implants* 21 (3), 392–398.

Paganin, D., Mayo, S. C., Gureyev, T. E., Miller, P. R., and Wilkins, S. W. (2002). Simultaneous phase and amplitude extraction from a single defocused image of a homogeneous object. *J. Microsc.* 206 (Pt 1), 33–40. doi:10.1046/j.1365-2818.2002.01010.x

Pearce, A. I., Richards, R. G., Milz, S., Schneider, E., and Pearce, S. G. (2007). Animal models for implant biomaterial research in bone: a review. *Eur. Cell. Mater* 13, 1–10. doi:10.22203/ecm.v013a01

Portier, H. J., Kewish, C. M., Chappard, C., and Pallu, S. (2020). New insights in osteocyte imaging by synchrotron radiation. *J. Spectr. Imaging* 9. doi:10.1255/jsi.2020.a3

Qing, H., Ardeshirpour, L., Pajevic, P. D., Dusevich, V., Jähn, K., Kato, S., et al. (2012). Demonstration of osteocytic perilacunar/canalicular remodeling in mice during lactation. *J. Bone Min. Res.* 27 (5), 1018–1029. doi:10.1002/jbmr.1567

Qu, M., Wang, C., Zhou, X., Libanori, A., Jiang, X., Xu, W., et al. (2021). Multi-dimensional printing for bone tissue engineering. *Adv. Healthc. Mater* 10 (11), e2001986. doi:10.1002/adhm.202001986

Roschger, A., Roschger, P., Wagermaier, W., Chen, J., van Tol, A. F., Repp, F., et al. (2019). The contribution of the pericanalicular matrix to mineral content in human osteonal bone. *Bone* 123, 76–85. doi:10.1016/j.bone.2019.03.018

Rosen, E. B., Kyle Gazdeck, R., Goldman, D. A., Panchal, H., Jones, E., Nguyen, J. P., et al. (2022). An anatomic analysis of fibula flap mandible reconstructions: implications for endosseous implant placement. *Plast. Reconstr. Surg.* 149 (6), 1419–1428. doi:10.1097/prs.0000000000009152

Rothweiler, R., Gross, C., Bortel, E., Früh, S., Gerber, J., Boller, E., et al. (2022). Comparison of the 3D-microstructure between alveolar and iliac bone for enhanced bioinspired bone graft substitutes. *Front. Bioeng. Biotechnol.* 10, 862395. doi:10.3389/fbioe.2022.862395

Sanders, D. W., Bhandari, M., Guyatt, G., Heels-Ansdell, D., Schemitsch, E. H., Swiontkowski, M., et al. (2014). Critical-sized defect in the tibia: is it critical? Results from the SPRINT trial. *J. Orthop. Trauma* 28 (11), 632–635. doi:10.1097/bot.0000000000000194

Schneider, P., Meier, M., Wepf, R., and Müller, R. (2010). Towards quantitative 3D imaging of the osteocyte lacuno-canalicular network. *Bone* 47 (5), 848–858. doi:10.1016/j.bone.2010.07.026

Sharma, D., Ross, D., Wang, G., Jia, W., Kirkpatrick, S. J., and Zhao, F. (2019). Upgrading prevascularization in tissue engineering: a review of strategies for promoting highly organized microvascular network formation. *Acta Biomater.* 95, 112–130. doi:10.1016/j.actbio.2019.03.016

Troeltzsch, M., Troeltzsch, M., Kauffmann, P., Gruber, R., Brockmeyer, P., Moser, N., et al. (2016). Clinical efficacy of grafting materials in alveolar ridge augmentation: a systematic review. *J. Craniomaxillofac Surg.* 44 (10), 1618–1629. doi:10.1016/j.jcms.2016.07.028

van Oers, R. F., Wang, H., and Bacabac, R. G. (2015). Osteocyte shape and mechanical loading. *Curr. Osteoporos. Rep.* 13 (2), 61–66. doi:10.1007/s11914-015-0256-1

van Tol, A. F., Schemenz, V., Wagermaier, W., Roschger, A., Razi, H., Vitienes, I., et al. (2020). The mechanoresponse of bone is closely related to the osteocyte lacunocanalicular network architecture. *Proc. Natl. Acad. Sci.* 117(51), 32251–32259. doi:10.1073/pnas.2011504117

Vatsa, A., Breuls, R. G., Semeins, C. M., Salmon, P. L., Smit, T. H., and Klein-Nulend, J. (2008). Osteocyte morphology in fibula and calvaria --- is there a role for mechanosensing? *Bone* 43 (3), 452–458. doi:10.1016/j.bone.2008.01.030

Verhelst, P. J., Dons, F., Van Bever, P. J., Schoenaers, J., Nanhekhan, L., and Politis, C. (2019). Fibula free flap in head and neck reconstruction: identifying risk factors for flap failure and analysis of postoperative complications in a low volume setting. *Craniomaxillofac Trauma Reconstr.* 12 (3), 183–192. doi:10.1055/s-0038-1651515

Vidal, L., Kampleitner, C., Brennan, M. Á., Hoornaert, A., and Layrolle, P. (2020). Reconstruction of large skeletal defects: current clinical therapeutic strategies and future directions using 3D printing. *Front. Bioeng. Biotechnol.* 8, 61. doi:10.3389/fbioe.2020.00061

Weber, F. E. (2019). Reconsidering osteoconduction in the era of additive manufacturing. *Tissue Eng. Part B Rev.* 25 (5), 375–386. doi:10.1089/ten.TEB.2019.0047

Whitaker, S. (1999). *The method of volume averaging*. Netherlands: Kluwer Academic Publishers.

Wu, V., van Oers, R. F. M., Schulten, E., Helder, M. N., Bacabac, R. G., and Klein-Nulend, J. (2018). Osteocyte morphology and orientation in relation to strain in the jaw bone. *Int. J. Oral Sci.* 10 (1), 2. doi:10.1038/s41368-017-0007-5

Zimmermann, C., Börner, B., Hasse, A., and Sieg, P. (2002). Donor site morbidity after microvascular fibula transfer. *Clin. oral Investig.* 5, 214–219. doi:10.1007/s00784-001-0140-5

frontiers | Frontiers in Bioengineering and Biotechnology

TYPE Review
PUBLISHED 23 October 2023
DOI 10.3389/fbioe.2023.1278124

OPEN ACCESS

EDITED BY
Junxi Wu,
University of Strathclyde, United Kingdom

REVIEWED BY
Shi-Cong Tao,
Shanghai Jiao Tong University, China
Dake Hao,
University of California, Davis,
United States

*CORRESPONDENCE
Mingxiang Cai,
✉ caimx1991@126.com
Xiangning Liu,
✉ liuxiangning2003@126.com

RECEIVED 15 August 2023
ACCEPTED 06 October 2023
PUBLISHED 23 October 2023

CITATION
Wang W, Xu Z, Liu M, Cai M and Liu X (2023), Prospective applications of extracellular vesicle-based therapies in regenerative medicine: implications for the use of dental stem cell-derived extracellular vesicles.
Front. Bioeng. Biotechnol. 11:1278124.
doi: 10.3389/fbioe.2023.1278124

Prospective applications of extracellular vesicle-based therapies in regenerative medicine: implications for the use of dental stem cell-derived extracellular vesicles

Wenhao Wang[1,2], Zinan Xu[1,2], Minyi Liu[2,3], Mingxiang Cai[1,2]* and Xiangning Liu[1,2,3]*

[1]School of Stomatology, Jinan University, Guangzhou, China, [2]Center of Stomatology, The First Affiliated Hospital of Jinan University, Guangzhou, China, [3]Clinical Research Platform for Interdiscipline, Jinan University, Guangzhou, China

In the 21st century, research on extracellular vesicles (EVs) has made remarkable advancements. Recently, researchers have uncovered the exceptional biological features of EVs, highlighting their prospective use as therapeutic targets, biomarkers, innovative drug delivery systems, and standalone therapeutic agents. Currently, mesenchymal stem cells stand out as the most potent source of EVs for clinical applications in tissue engineering and regenerative medicine. Owing to their accessibility and capability of undergoing numerous differentiation inductions, dental stem cell-derived EVs (DSC-EVs) offer distinct advantages in the field of tissue regeneration. Nonetheless, it is essential to note that unmodified EVs are currently unsuitable for use in the majority of clinical therapeutic scenarios. Considering the high feasibility of engineering EVs, it is imperative to modify these EVs to facilitate the swift translation of theoretical knowledge into clinical practice. The review succinctly presents the known biotherapeutic effects of odontogenic EVs and the underlying mechanisms. Subsequently, the current state of functional cargo loading for engineered EVs is critically discussed. For enhancing EV targeting and *in vivo* circulation time, the review highlights cutting-edge engineering solutions that may help overcome key obstacles in the clinical application of EV therapeutics. By presenting innovative concepts and strategies, this review aims to pave the way for the adaptation of DSC-EVs in regenerative medicine within clinical settings.

KEYWORDS

extracellular vesicles, engineering modification, regenerative medicine, dental stem cells, circulation time, targeting

1 Introduction

Regenerative medicine aims to restore the functionality of impaired organs or tissues. Different strategies are being explored to achieve this goal. The majority of these approaches focus on the utilization of diverse primary cells, including stem cells and their secretions (Yin et al., 2020; Nagelkerke et al., 2021). Among these approaches, stem cell transplantation stands out as the strategy with the most potential. In particular, mesenchymal stem cells (MSCs) derived from bone marrow have garnered substantial attention due to their clinical significance and extensive exploration (Ghiroldi et al., 2018; Rozier et al., 2018; Tatullo, 2019). Nonetheless, it is crucial to note that the isolation of these adults stems from human bone marrow (hBM) necessitates relatively invasive procedures that are not well accepted by patients (Beyer Nardi and da Silva Meirelles, 2006). Hence, there is a pressing need to explore alternative sources of MSCs that align more seamlessly with clinical practices in future scientific investigations. Recent years have witnessed a growing body of research reporting that dental stem cells (DSCs) are more plastic and proliferative and have better immunomodulatory properties than bone marrow stem cells (BMSCs) (Mantesso and Sharpe, 2009). Numerous studies have observed the potential of dental pulp stem cells (DPSCs) to develop not only into bone, adipose, and cartilage but also into myocytes, hepatocytes, and neurons (Iohara et al., 2006). Given their self-renewal capacity and remarkable plasticity, these cells hold promise for diverse clinical applications in both dentistry and medicine. However, it is important to acknowledge that the clinical utilization of stem cells still confronts numerous challenges. The foremost impediment to the widespread adoption of stem cell therapy, resides in its safety profile, primarily characterized by risks such as pro-inflammation, tumorigenicity, and host rejection (Caplan et al., 2019). In addition, their structural contribution to tissue regeneration is more constrained than initially believed, with only a fraction of the delivered cells successfully integrating into the host and differentiating into the intended cell type (Baraniak and McDevitt, 2010). In contrast, Valadi. et al. elucidated the role of horizontal mRNA transfer through extracellular vesicles (EVs) as a mechanism facilitating the paracrine exchange of genetic information between MSCs and other cells (Valadi et al., 2007). As elucidated in the research conducted by Gnecchi et al., MSCs exert their effect primarily through paracrine mechanisms (Gnecchi et al., 2005; Phan et al., 2018). In the field of regenerative medicine, the utilization of MSCs is primarily dependent on their capacity to produce cytokines and growth factors rather than on their inherent self-renewal and differentiation potential (Pittenger et al., 2015). Notably, EVs derived from MSCs exhibit intricate biosynthetic mechanisms and distinctive structural features. They also possess the regeneration potential inherent to MSCs of specific origin and maintain the ability to migrate their parental cells to particular tissues (Lener et al., 2015; Phinney and Pittenger, 2017). These unique attributes make MSC-derived EVs highly beneficial to the regeneration process.

Almost all tissues and cells secrete EVs and transmit signals and effector molecules across cells via circulating body fluids, making them a promising candidate for medical diagnostics and therapy. EVs comprise a homogeneous lipid bilayer in which substances, including proteins, RNAs, and metabolites, are selectively packaged. Consequently, they assume a distinctive role in facilitating intercellular communication, as highlighted in various studies (Lässer et al., 2018; Phan et al., 2018). EVs released from different sources exert influence over the regulatory processes of the cell cycle by mediating intracellular signaling, including the regulation of physiological activities such as proliferation or differentiation. Serving as pivotal molecules in intercellular communication, EVs play a major role in mediating the exchange of information within both the pathological and physiological contexts of cellular behavior, with profound implications for the function of recipient cells, (Yáñez-Mó et al., 2015). Furthermore, it is increasingly apparent that they may contribute to the pathogenesis of many diseases. EVs are divided into different types, namely, exosomes derived from endosomes (exosomes [EXO], 30–150 nm), microvesicles derived from the plasma membrane (microvesicles [MVs], 150–1,000 nm), and apoptotic cells (150–1,000 nm), and apoptotic vesicles (200–5,000 nm) released during apoptosis (Figure 1). These substances with unique biological properties can bind to specific proteins or genes to form complexes that exert therapeutic effects. Owing to the easy recognition of apoptotic vesicles and subsequent clearance by macrophages, this review dealt with EXO and MVs, which depict highly promising functions for clinical translation (Segawa and Nagata, 2015; Théry et al., 2018). EVs have risen as a compelling prospect for cell-free therapeutic schemes to promote tissue regeneration. This is attributed to their remarkable advantages, encompassing superior biosafety, the capacity to traverse biological barriers, and the ability to protect their contents from being degraded (Lazar et al., 2021; Ramasubramanian et al., 2022). Furthermore, owing to their powerful regenerative capacity and easy accessibility, the demand for stem cell-derived EVs is increasing in regenerative medicine (He et al., 2018; Liao et al., 2019; Liu and Su, 2019; Xiao et al., 2019).

However, apart from the established pharmacological role of EVs in intercellular or interorgan communication, recent research has reported that EVs can functionally transport therapeutic biological cargoes (Kamerkar et al., 2017; Poggio et al., 2019; Lathwal et al., 2021). Studies on unmodified EVs *in vivo* and circulation have reported that when administered systemically, EVs are easily recognized by the mononuclear phagocyte system and rapidly absorbed (Wiklander et al., 2015; Parada et al., 2021). Furthermore, the functional modification of EVs using bioengineering techniques is being increasingly recognized as indispensable for their effective adaptation across various clinical therapeutic scenarios (Hao et al., 2020; Cheng and Hill, 2022; Hao et al., 2022). The content of EVs, including those of proteins, lipids, and nucleic acids, can be modified. Many studies have reported that EVs exhibit the feasibility of undergoing functional modification and engineering (Alvarez-Erviti et al., 2011; Liang et al., 2021). EVs have recently emerged as a breakthrough preclinical remedy, and their superior drug delivery capabilities and modifiability have laid a solid foundation for their successful application (Bashyal et al., 2022). Engineered EVs represent a category of modified EVs synthesized by the incorporation of therapeutic molecules using bioengineering techniques. This versatile approach allows for the engineering of EVs both endogenously and exogenously, drawing upon an understanding of their biological structures and biogenesis principles. It capitalizes on the ability of primary EVs to encapsulate therapeutic cargo for precise and targeted delivery (Zipkin, 2019; Zipkin, 2020).

Recently, advances in clinical trials have increased our intuitive comprehension of the translational capabilities of EVs in various therapeutic applications. Among these, EVs derived from MSCs (MSC-EVs) have been observed to be the most prevalent type featured in these trials. Researchers have detected multiple significant EVs, both in terms of potential and clinical significance, as novel targeted delivery systems aimed at facilitating or impeding the introduction of specific bioactive substances into the body to elicit distinct biological effects.

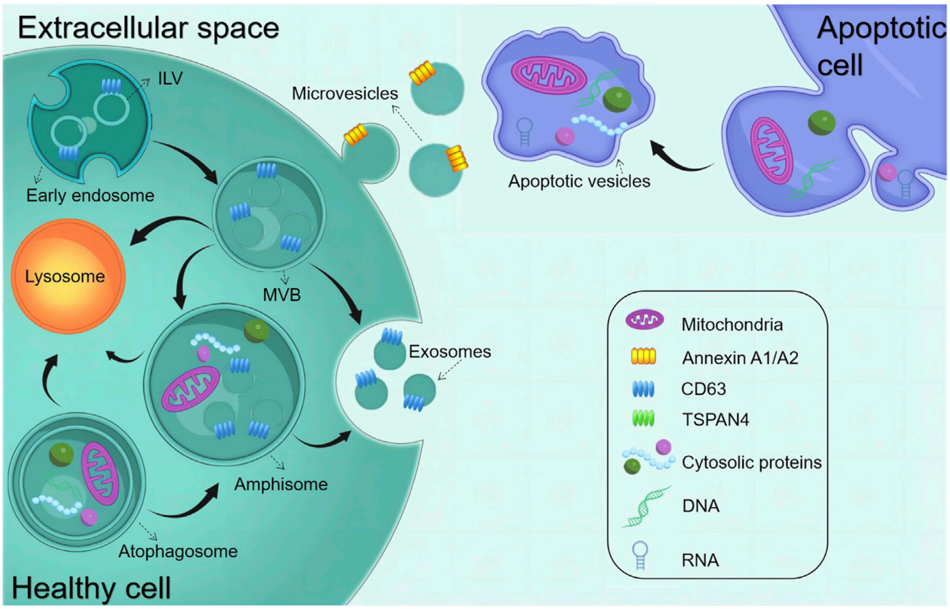

FIGURE 1
Biogenesis of common EVs. The early endosome matures and starts forming intraluminal vesicles (ILVs) (future exosomes), thereby transforming into multivesicular bodies (MVBs). MVBs can fuse with either autophagosomes or lysosomes to be degraded. MVBs are also transported to the plasma membrane to release exosomes via exocytosis. Amphisomes are formed by the fusion of autophagosomes with MVBs. Exosomes are released by the exocytosis of MVBs and amphisomes. Microvesicles are produced through plasma membrane budding and blebbing. Apoptopodia release apoptotic vesicles during apoptosis.

According to a survey of clinical trials, MSC-EVs are increasingly being used to treat diseases and deliver therapeutic agents (https://clinicaltrials.gov/ct2/home, accessed 1 May 2023) (Table 1). In three clinical trials (NCT03384433, NCT03608631, and NCT05043181), MSCs were genetically modified to overexpress EVs (Akbari et al., 2022). Furthermore, one clinical trial used plant-derived EVs loaded with curcumin to target normal colon tissues and tumors (NCT01294072). Another trial used autologous stem cell-derived EVs from human deciduous teeth to treat young and immature permanent teeth with pulp necrosis (NCT01814436). At present, MSCs are the most promising parental source of EVs owing to their varied applications, including in tissue engineering and regenerative medicine (Aheget et al., 2020; Dai et al., 2020; Yuan et al., 2021). Table 1 highlights the recent clinical trials involving MSCs or engineered EVs.

2 DSC-EVs in oral and maxillofacial tissue regeneration

2.1 Classification of DSC-EVs

Dental stem cells can be sourced from various sites within the oral cavity, encompassing the periodontal and inner pulp tissues. Researchers have identified many sites where MSCs are present in the oral cavity, which has led to a genuine interest in the dental tissues and the surrounding soft and complex support structures (Tatullo et al., 2015). Six types of dental tissue-derived stem cells have been isolated and identified in the field of oral tissue regeneration (Figure 2): dental pulp stem cells (DPSCs), stem cells from exfoliated deciduous teeth (SHEDs), stem cells from apical papilla (SCAPs), periodontal ligament stem cells (PDLSCs), dental follicle progenitor cells, and gingival MSCs (GMSCs) (Bakkar et al., 2017). DSCs differ from MSCs derived from the bone marrow (BMMSCs) or adipose tissues. These stem cells hold a distinct advantage due to their embryological origin from the neural crest, which enables them to differentiate into both dental and neural tissues. Notably, their neuro-affinity properties make them particularly intriguing for various applications (Mayo et al., 2014). Human exfoliated deciduous dental stem cells represent an immature subset of MSCs characterized by their remarkable potential for differentiation and potent capacity for proliferation. Additionally, their non-invasive and ethically unproblematic harvest makes them particularly appealing. Nakamura et al. demonstrated that SHEDs are enriched in growth factors, including transforming growth factor β2 (TGF-β2) and fibroblast growth factor-2 (FGF2) (Wu et al., 2019). The ability of apical papilla stem cells, termed SCAPs, to develop into osteoblasts, adipocytes, chondrocytes, and neuronal cells under specific culture conditions underscores their diverse functions. In the context of tooth formation, SCAPs exhibit an increased proliferation rate in comparison with PDLSCs (Chen K. et al., 2013). They have the capacity to develop into odontogenic and osteogenic progenitor cells, adipocytes, and neuronal cells (Yang B. et al., 2017). On the other hand, PDLSCs can undergo differentiation into collagen-forming cells, adipocytes, and odontogenic osteoblasts *in vitro*. They also exhibited the capacity for regeneration of odontoblasts and periodontium in various animal models (Seo et al., 2004). The dental follicle, which envelops the developing tooth as a connective capsule, houses a

TABLE 1 Recent observations and clinical trials of EVs derived from mesenchymal stem cells or engineering modification.

Trial identifier (ClinicalTrials.gov)	Trial phase	Condition	Trial purpose or intervention	Start date	Status
NCT04850469	Observation	Severe infection in children	To evaluate the application of MSC-derived exosomes	January 2022	Not yet recruiting (Estimated completion 31 December 2024)
NCT04979767	Observation	Bacterial sepsis	To define immune pathways and identify clinically useful biomarkers	15 April 2021	Recruiting
NCT04270006	Early Phase I	Periodontitis	Treatment with adipose stem cell-derived extracellular vesicles	12 February 2020	Unknown
NCT01294072	Phase I	Colon Cancer	To address the problem of curcumin delivery by using plant exosomes to deliver the drug to colon tumors and normal colon tissue	January 2011	Unknown
NCT03608631	Phase I	Adenocarcinoma	Treatment with mesenchymal stromal cell-derived extracellular vesicles along with KRAS G12D siRNA	27 January 2021	Recruiting (Estimated Completion 30 June 2023)
NCT04664738	Phase I	Skin graft	Treatment with platelet-derived extracellular vesicles	16 March 2021	Unknown
NCT05043181	Phase I	Hypercholesterolemia	To evaluate the safety and preliminary effectiveness of exosome-based older mRNA nano platform for gene therapy in Homozygous individuals	December 2021	Not yet recruiting (Estimated Completion December 2026)
NCT05402748	Phase I/II	Fistula Perianal	Treatment with placenta-MSC-derived exosomes	22 December 2021	Unknown (Estimated Completion 22 March 2023)
NCT05499156	Phase I/II	Perianal Fistula	Treatment with placenta-MSC- derived exosomes	20 January 2022	Unknown
NCT03384433	Phase I/II	Cerebrovascular Disorders	To determine the efficacy of the administration of MSC-derived exosomes in improving disability among patients with acute ischemic stroke	17 April 2019	Unknown
NCT01854866	Phase II	Malignant Pleural Effusion	Treatment with drug-packaging microparticles	May 2013	Unknown
NCT05490173	Not Applicable	Premature Birth	Treatment with exosomes derived from mesenchymal stromal cells	5 October 2022	Not yet recruiting (Estimated Completion 28 December 2026)
NCT01814436	Not Applicable	Dental Pulp Necrosis	Treatment with scaffold-free SHED-derived pellet	February 2013	Unknown

subset of MSCs called DFPCs. DFPCs possess a remarkable versatility in differentiation, with the capacity to transform into osteoblasts, adipocytes, and neural cells. Notably, DFPCs are capable of initiating neural differentiation and contributing to the regeneration of periodontal structures and bone tissue (Morsczeck et al., 2005). GMSCs are readily harvested from gingival tissues of the oral cavity with minimal damage to the organism. Furthermore, GMSCs can form connective tissue-like structures *in vivo*, and *in vitro*, they can form mineralized nodules, adipose, and chondrocyte-like matrices when cultured with different growth factors (Ge et al., 2012). These cells are superior compared to the widely acclaimed BMSCs in terms of regenerative potential (Tomar et al., 2010). DSC-EVs are involved in angiogenesis, anti-inflammation, intercellular communication, immunomodulation, osteogenesis, neuron nourishment, and promoting apoptosis in tumor cells. Owing to their accessibility, modifiability, and high proliferative capacity, DSCs have been extensively studied for regulating the development of dental, skeletal, and salivary gland tissues, repairing trauma to maxillofacial tissues, and regenerating pulpal and periodontal tissues (Li et al., 2018; Mai et al., 2021) (Table 2).

2.2 Bone and vascular tissue regeneration

Bone tissue regeneration involves the coordinated regulation of various cell types, encompassing osteoblasts, osteoclasts, chondrocytes, and endothelial cells. The crucial stages of bone regeneration are angiogenesis and osteogenesis (Qin et al., 2016). Angiogenesis is essential for bone healing because, in this process, new blood vessels are formed that provide nutrients and oxygen to the surrounding cells. A study showed that a conditioned medium deprived of EVs inhibited angiogenesis (Shabbir et al., 2015). Wu et al. reported that SHED-EVs promoted the angiogenesis as well as the proliferative and migratory capacities of human umbilical vein endothelial cells (HUVECs). This effect was mediated via the 5′AMP-activated protein kinase pathway. Additionally, they promoted the neovascularization and the formation of new bone

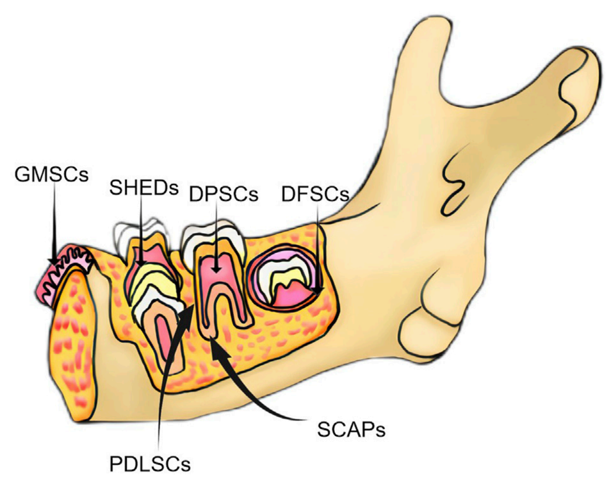

FIGURE 2
Classification of major dental-derived stem cells.

in a rat model of periodontal bone defects (Wu et al., 2019). Diomedee et al. inoculated the gingival tissues of volunteers with 3D polylactic acid scaffolds, and human gingival MSC (hGMSC)-derived EVs were found to increase calcium deposition as well as elevate RUNX2 and BMP2/4 gene expression levels and protein levels. Furthermore, EVs in PLA scaffolds significantly promoted bone and angiogenesis in rats with cortical cranial defects (Diomede et al., 2018b). Moreover, these EVs promoted the regeneration of palatal gingival tissues. Another study reported that SCAP-EVs remarkably enhanced the migratory and angiogenic capacities of HUVECs (Liu et al., 2021). Xian et al. reported that DPSC-EVs enhanced vascular endothelial cells' proliferation and angiogenic capacities and verified that these effects were achieved via the p38 mitogen-activated protein kinase (MAPK) signaling pathway (Xian et al., 2018). In another study, when Schwann cells, the primary source of odontoblasts, were co-cultured with EVs from lipopolysaccharide (LPS)-pretreated hDPSCs, they exhibited enhanced migration and osteogenic differentiation abilities (Li et al., 2021). Ivica et al. observed that hDPSC-derived small EVs encapsulated in fibrin gels promoted the migration and proliferation of human BMMSCs (hBMMSCs) (Ivica et al., 2020). Moreover, Huang et al. revealed that miR-223-3p may be pivotal in the mechanism by which LPS–hDPSCs–EXo promotes angiogenesis in HUVECs (Huang et al., 2021). Furthermore, Zhou and Pizzicannel revealed that hDPSC-EVs were critically involved in promoting angiogenesis and wound healing in the constructed mouse skin defect and rat cranial defect models, respectively. These EVs were also observed to enhance vascular and bone formation (Pizzicannella et al., 2019; Zhou et al., 2020).

2.3 Periodontal tissue regeneration

Periodontal tissues comprise the gingiva, periodontal ligament, dental bone, and alveolar bone. Periodontal tissue health is crucial to the overall masticatory function. Periodontal diseases leading to resorption or loss of the alveolar ridge can result in symptoms such as pain and bleeding. The alveolar ridge plays a vital function in providing both physical and mechanical support to the teeth. Bone loss and neovascularization are the main pathological changes during periodontal disease development. Multiple factors, including bone metabolism, osteoblasts, and matrix metalloproteinases, regulate periodontal tissue repair and reconstruction during periodontal disease development. The periodontal treatment promotes periodontal tissue regeneration by functionally reattaching the periodontal ligament to the new dental and alveolar bone (Liu et al., 2019). Traditional periodontitis therapies include scaling, periodontal scraping, systemic and topical antibiotics, and oral disinfectants. Although these treatment strategies can inhibit the progression of periodontitis in the short term, long-term efficacy regarding the condition of the patient and initiatives should be evaluated. Therefore, developing new strategies to effectively treat periodontitis and achieve periodontal tissue regeneration is imperative (Elashiry et al., 2021). Hu et al. reported that gingiva-derived MSC (GMSC)-EVs exerted an immunomodulatory effect by promoting the expression of osteogenic differentiation-related factors within PDLSCs, irrespective of whether they were in normal and inflammatory environments. Furthermore, several other studies have corroborated that GMSC-EVs possess the ability to inhibit Porphyromonas gingivalis LPS-induced nuclear factor kappa B (NF-κB) pathway activation. This inhibition triggers the activation of the Wnt/β-catenin pathway, indicating the presence of a mutually exclusive regulatory mechanism between the NF-κB and Wnt/β-catenin pathways in the peripheral inflammatory environment. GMSC-EVs were found to excel in cross-regulating these two pathways, underscoring their remarkable regulatory ability (Hu et al., 2023). Likewise, Nakaod et al. observed that locally injected GMSC-EVs considerably decreased periodontal bone resorption in a ligation-induced mouse periodontitis model (Nakao et al., 2021). Moreover, Shen et al. documented that DPSC-EVs promoted periodontal epithelial healing and alveolar bone reconstruction in a periodontitis mouse model, primarily through the delivery of miR-1246 (Shen et al., 2020). Shi et al. conducted research involving the extraction of LPS-pretreated dental follicle cell-derived EVs. The resulting data implied that these EVs promoted the osteogenic differentiation potential as well as the proliferative and migratory capacities of periodontal ligament-derived stem cells (hPDLSCs) from patients with periodontitis *in vitro*. *In vivo*, they enhanced directed periodontal ligament formation and promoted the formation of periodontal bone. These EVs were observed to be linked to decreased TRAP-positive osteoclast and RANKL/OPG expression (Shi et al., 2020). Wang et al. we're pioneers in documenting the role of SHED-EVs in promoting the osteogenic differentiation of PDLSCs *in vitro* by inducing the Wnt/β-catenin and BMP/Smad pathways. This discovery carries notable clinical implications (Wang et al., 2020). In a separate study, Wei et al. achieved the successful rescue of bone loss in mice with periodontitis by locally injecting SHED-EVs. Their *in vitro* experiments revealed that SHED-EVs exhibited a multi-faceted effect. They not only stimulated the osteogenesis and

TABLE 2 Isolation, characterization, and functions of DSC-derived EVs.

Potential application types	Origin	EV isolation methods	Identification methods	Administration	Recipients	Ref
Bone and vascular regeneration	SHED	The CM was centrifuged at 300 ×g for 10 min, 2,000 ×g for 15 min, and 10,000 ×g for 30 min, and concentrated using ultrafiltration at 100,000 ×g for 1 h	■ TEM ■ NTA ■ BCA ■ WB(CD81, CD9 and TSG101)	In vitro/in vivo	HUVEC, BMSC/SD Periodontal Defect Rat Model	Wu et al. (2019)
		The CM was centrifuged at 300× g for 10 min, 2,000 ×g for 10 min, 20,000 ×g for 30 min, and 100,000 ×g for 70 min	■ TEM ■ BCA ■ NTA ■ WB (CD9,CD63, TSG101 and Calnexin)	In vitro	PDLSCs	Wang et al. (2020)
	GMSC	ExoQuick-TC exosome isolation reagent	■ DLS ■ AFM ■ WB (CD9, CD63,CD81, and TSG101)	In vitro/in vivo	hGMSCs/Cranial injury rat model	Diomede et al. (2018b)
	SCAP	The CM was ultracentrifuge at 3,000 ×g for 20 min, 20,000 ×g for 30 min, and 120,000 ×g for 2 h	■ TEM ■ NTA ■ WB (CD9,CD63, and Alix)	In vitro/in vivo	HUVEC/palatal gingival defect mouse model	Liu et al. (2021)
	PDLSC	The CM was centrifuged at 3,000 ×g for 20 min; 16,500 ×g for 20 min; filtered using a 0.2-μm filter; and ultracentrifuged at 100,000 ×g for 70 min	■ NTA ■ Flow cytometry ■ TEM ■ WB(CD63 and CD81)	In vitro	hPDLSCs	Xie et al. (2021)
		Centrifugation for 10 min at 500 ×g, 30 min at 16,000 ×g, followed by ultracentrifugation for 70 min at 150,000 ×g	■ Flow cytometry ■ TEM ■ WB (TSG101 and CD63)	In vitro	HUVECs	Zhang et al. (2020b)
		ExoQuick-TC exosome isolation reagent	■ DLS ■ AFM	In vitro/in vivo	hPDLSCs/rat calvarial defect model	Pizzicannella et al. (2019)
		ExoQuick-TC exosome isolation reagent	■ DLS ■ AFM	In vitro/in vivo	hPDLSCs/rat calvarial defect model	Diomede et al. (2018a)
		Centrifugation at 300 ×g for 10 min, 2000 ×g for 10 min; 20,000 ×g for 30 min, followed by ultracentrifugation at 100,000 ×g for 70 min	■ TEM ■ NTA ■ WB(CD63)	In vitro	hPDLSCs	Čebatariūnienė et al. (2019)
	DPSC	The CM was centrifuged at 300 ×g for 10 min, 2,000 ×g for 10 min, and 10,000 ×g for 30 min, followed by ultracentrifugation twice at 100,000 ×g for 70 min	■ TEM ■ NTA ■ WB (Alix,HSP70, CD9, CD63 and CD81) ■ BCA	In vitro/in vivo	HUVEC/full-thickness skin defect mouse model	Zhou et al. (2020)
		The CM was centrifugated at 500 ×g for 10 min at 4°C; 2,000 ×g for 10 min; 10,000× g for 1 h at 4°C; filtered using a 0.22-μm filter; and ultracentrifuged at 100,000 ×g for 2 h	■ TEM ■ NTA ■ WB	In vitro	Schwann cells	Li et al. (2021)

(Continued on following page)

TABLE 2 (*Continued*) **Isolation, characterization, and functions of DSC-derived EVs.**

Potential application types	Origin	EV isolation methods	Identification methods	Administration	Recipients	Ref
		Exosome isolation reagent	■ TEM ■ WB (CD9, and Grp94)	In vitro	hBMMSCs	Ivica et al. (2020)
Periodontal regeneration	DPSC	The CM was centrifuged at 300 ×g for 10 min and 16,500 ×g for 20 min, followed by ultracentrifugation at 120,000 ×g for 2.5 h at 4°C	■ TEM ■ NTA ■ WB (CD9, HSP70 and TSG 101) ■ Flow Cytometry (CD 63 and CD 81)	In vitro/in vivo	Macrophages/periodontitis mouse model	Shen et al. (2020)
		Exo-spin exosome isolation reagent	■ WB (CD9 and CD63) ■ TEM	In vitro	hDPSCs	Hu et al. (2019)
		ExoQuick-TC exosome isolation reagent	■ WB (CD63 and CD9) ■ TEM	In vitro /in vivo	DPSC/hMSCs	Huang et al. (2016)
	GMSC	MagCapture TM exosome isolation kit	■ TEM ■ NTA ■ WB (CD9, CD63 and CD81)	In vitro/in vivo	Macrophage/ligature-induced periodontitis mouse model	Nakao et al. (2021)
		The CM was centrifuged at 300 ×g for 10 min and 10,000 ×g for 40 min; filtered through a 0.22-mm filter; and ultracentrifuged for 70 min at 100,000 ×g twice	■ NTA ■ TEM ■ WB(CD9, CD63, ALIX, and HSP70)	In vitro	GMSCs and PDLSCs	Hu et al. (2023)
	DFPC	Exosome isolation reagent	■ TEM ■ NTA ■ WB (CD63 and TSG101)	In vitro/in vivo	PDLCS/Periodontitis rat model	Shi et al. (2020)
	SHED	The CM was centrifuged at 300 ×g for 10 min, 2,000 ×g for 10 min, 20,000 ×g for 30 min, and 100,000 ×g for 70 min	■ TEM ■ BCA ■ NTA ■ WB (CD9,CD63, TSG101 and Calnexin)	In vitro	PDLSCs	Wang et al. (2020)
		The CM was centrifuged at 300 ×g for 10 min, 2000 ×g for 10 min, and 10,000 ×g for 60 min filtered through a 0.22-μm filter; and ultracentrifuged at 100,000 ×g for 70 min twice	■ TEM ■ WB (CD63)	In vitro/in vivo	BMSCs/OVX mouse model	Wei et al. (2020)
Pulp regeneration	DPSC	Exo-spin (Cell Guidance) exosome isolation reagent	■ WB (CD9 and CD63) ■ TEM	In vitro	hDPSCs	Hu et al. (2019)
		ExoQuick-TC exosome isolation reagent	■ WB (CD63 and CD9) ■ TEM	In vitro/in vivo	DPSC/hMSCs	Huang et al. (2016)
	SHED	The CM was centrifuged at 2,000 ×g for 10 min and 10,000 ×g for 30 min, followed by ultracentrifugation at 100,000 ×g for 70 min twice	■ TEM ■ NTA ■ WB(CD9, CD63, CD81)	In vitro/in vivo	HUVECs/SHEDs	Wu et al. (2021a)

(Continued on following page)

TABLE 2 (*Continued*) Isolation, characterization, and functions of DSC-derived EVs.

Potential application types	Origin	EV isolation methods	Identification methods	Administration	Recipients	Ref
Dentinogenesis	SCAP	The CM was centrifuged at 3,000 ×g for 20 min, 20,000 ×g for 30 min, and 120,000 ×g for 2 h	■ TEM ■ NTA ■ BCA ■ WB (CD9, and Alix)	In vitro/in vivo	BMMSCs/dentinogenic cell (in nude mice)	Zhuang et al. (2020)
	DPSC	The CM was centrifuged at 500 ×g for 10 min, 2,000 ×g for 10 min, 10,000 ×g for 1 h; filtered through 0.22-μm filter; and ultracentrifuged twice at 100,000 ×g for 2 h and 70 min at 4°C	■ BCA ■ WB (alix, CD9, CD63 and GM130) ■ TEM ■ NTA	In vitro	SCs	Li et al. (2021)
		The CM was centrifuged at 300 ×g for 10 min and 2,000 ×g for 10 min; filtered through a 0.22-μm filter; centrifuged at 4,000 ×g for 10 min; ultracentrifuged at 4,000 ×g to 200 μL and 100,000 ×g for 70 min twice	■ NTA ■ BCA ■ WB(CD9, CD63, and CD81)	In vitro/in vivo	DPSC/Rat Pulpotomy Model	Swanson et al. (2020)
Nerve tissue regeneration	GMSC	ExoQuick-TC exosome isolation reagent	■ BCA assay ■ NTA ■ WB (CD 63 and CD9)	In vitro/in vivo	SCs/Nerve damage mouse model	Mao et al. (2019)
	SHED	The CM was centrifuged at 300 ×g for 10 min, 2000 ×g for 10 min, and 20,000 ×g for 30 min, followed by ultracentrifugation at 100,000 ×g for 70 min twice	■ WB	In vitro	Human neural stem cells	Jarmalavičiūtė et al. (2015)
		The CM was centrifuged at 300 ×g for 10 min, 2,000 ×g for 10 min, and 20,000 ×g for 30 min, followed by ultracentrifugation at 100,000 ×g for 70 min twice	■ NTA ■ TEM	In vivo	PD rat model	Narbute et al. (2019)
		ExoQuick Reagent Kits	■ WB(CD81, CD63, and CD9)	In vivo	TBI rat model	Li et al. (2017)

Abbreviations: CM, conditional medium; TEM, transmission electron microscope; NTA, nanoparticle tracking analysis; DLS, dynamic light scattering; AFM, atomic force microscope.

proliferation of cells but also effectively attenuated adipogenesis and inflammatory cytokine secretion in mouse bone marrow stromal stem cells (mBMSCs) (Wei et al., 2020). The acquired data provide insights for developing novel therapeutic strategies for periodontitis and promoting periodontal tissue regeneration.

2.4 Pulp regeneration

As a highly vascularized and innervated tissue, the pulp has various functions, such as triggering immune responses to microbial insults and injuries, providing neuronal sensitivity, and promoting repair and regeneration in response to mechanical stimuli. The loss of the pulp tissue leads to the loss of tooth vitality. The root canal remains the preferred method for treating permanent necrotic teeth (Cvek, 1992). Nevertheless, new pulp regeneration therapies should be explored to maintain the biological function of the tooth. An EV-mediated pulp tissue regeneration method could serve as an effective alternative to the existing root canal treatment. Hu et al. reported that DPSC-EVs promoted the odontogenic differentiation of hDPSCs via the tumor growth factor (TGF)β1/SMAD pathway (Hu et al., 2019). Meanwhile, using a tooth fragmentation mouse model, Wu et al. demonstrated the regeneration and angiogenic ability of DSC-EVs *in vivo*. They reported that they further promoted SHED differentiation toward endothelium and increased HUVEC angiogenesis *in vitro*. Furthermore, they reported that miR-26a-rich SHED-EVs promoted angiogenesis via the TGF-β and SMAD2/3 signaling pathways, enhancing pulp tissue regeneration (Wu M. et al., 2021). Huang et al. reported that DPSCs and BMSCs endocytosed DPSC-EVs in a dose-dependent manner and activated the p38 MAPK pathway, thereby inducing DPSC differentiation and tissue regeneration. Furthermore, they validated the ability of DPSC-EVs to stimulate pulp-like tissue regeneration while considerably increasing the dentin matrix acidic phosphoprotein 1 (DMP1) and dentin sialophosphoprotein (DSPP) levels at the soft tissue–dentin junction in an *in vivo* root section model (Huang et al., 2016). The resulting data of this research provide a solid theoretical foundation for the potential application of EV therapy in promoting pulp regeneration.

2.5 Dentin regeneration

Progression infectious disease that causes hard tissue loss in the teeth, leading to pulp inflammation, thereby affecting tooth regeneration. During dental caries development, dentin-forming cells produce reactive dentin to inhibit disease progression (Farges et al., 2015). SCs primarily differentiate into dentin-forming cells after migrating to the damaged sites during tooth development and regeneration (Kaukua et al., 2014). Furthermore, Li et al. reported that hDPSC-derived EVs stimulated dentin salivary protein production and SC mineralization while increasing the expressions of DSPP, DMP1, osteocalcin, and RUNX2 genes in an isolated environment, thereby mediating the odontogenic differentiation of SCs (Li et al., 2021). Additionally, Zhuang et al. revealed that SCAP-EVs could promote the differentiation ability of dentin tissues and adult dentin cells. Moreover, SCAP-EVs exerted an effect on BMMSC proliferation *in vitro* but considerably modulated their dentin formation ability by increasing DSPP levels in BMMSC and forming mineralized nodules (Zhuang et al., 2020). Swanson et al. reported that DPSC-EVs can promote hDPSC migration and induce the mineralization process in a dose-dependent manner. Based on these findings, they developed a controlled-release platform that can be implanted into the defective sites without exogenous SC transplantation, thereby stimulating the endogenous DPSC migration from the pulp chamber and directing their differentiation fate toward a certain regenerative outcome. Using this EV delivery platform, EVs derived from hDPSCs and odontoblasts were released at the pulp interface on exposure to the body. They induced the migration and differentiation of DPSCs into dentin cells, producing reactive tertiary dentin bridges that may effectively prevent tooth necrosis (Swanson et al., 2020).

2.6 Nerve tissue regeneration

Annually, a significant number of cases involving neurological disorders, encompassing both central and peripheral nervous system disorders, are documented worldwide. Nerve damage resulting from various factors such as trauma and tumors is also prevalent, posing a substantial challenge due to the lack of effective treatment schemes. The impact of these conditions extends beyond patients themselves, affecting their families and placing a heavy burden on society (Taylor et al., 2008; Asplund et al., 2009). While autologous nerve grafting remains the established standard for rectifying nerve defects, the quest for innovative alternatives is imperative. SC-based therapies, particularly those using DSCs, offer new hope for treating neurological disorders. Reportedly, DPSCs are more suitable for treating neurodegenerative diseases than BMMSCs or adipose tissue-derived MSCs of the mesoderm (Wang et al., 2019). DSCs arising from the neural crest share features similar to those derived from the neural cells. They exhibit the capability to differentiate into various functional units, including neurons, astrocytes, and fibroblasts, which hold promise as ideal sources for cellular nerve regeneration and repair (Li et al., 2018). Among all DSCs, SCAPs exert the strongest neurotrophic effects, suggesting they may be the best EV progenitor cell source for peripheral nerve repair (Kolar et al., 2017). Mao et al. simulated clinical nerve repair *in vivo* and found that hGMSC-EVs actively facilitated axonal repair, functional recovery, and nerve regeneration in extrusion-injured mice. Furthermore, the propagation and migration of SCs were stimulated in an *ex vivo* setting (Mao et al., 2019). Li et al., using a traumatic brain injury rat model, concluded that SHED-EVs were involved in the recovery of motor function and reduced cortical damage in rats by promoting the polarized movement of microglia (Li et al., 2017). In the AKVILE study, SHED-EVs could inhibit approximately 80% of 6-hydroxydopamine (OHDA)-induced apoptosis in dopaminergic neuronal cells, suggesting the potential neuroprotective effect of SHED-EVs on human dopaminergic neurons (Jarmalavičiūtė et al., 2015). Narbute et al. achieved a significant milestone by demonstrating the therapeutic efficacy of SHED-EVs in Parkinson's disease rat models with 6-OHDA-induced medial forebrain bundle injury for the first time (Narbute et al., 2019). A. Nasirishargh et al. found that multiple exosomal miRNAs have been identified to have neuroprotective effects by promoting neurogenesis, neurite remodeling, and survival (Lazar et al., 2022). These studies contribute to a solid theoretical foundation for EV-based treatment of neurological diseases and neural tissue regeneration (Nasirishargh et al., 2021).

Overall, altering the culture conditions of donor cells, such as hypoxic or inflammatory conditions or the differentiation of donor cells, may enhance the beneficial therapeutic effects of secreted EV. However, pretreated mother cells have restricted control over the specific cargoes of these enhanced EVs as only naturally occurring cargo molecules can be enriched through these methods.

3 EV engineering strategies

3.1 Feasibility

Alongside the established pharmacological role of EVs in intercellular or interorgan communication, many recent studies have reported their functional ability to transport therapeutic cargo. EVs can be designed to transport desired components, including proteins, antibodies, drugs, and RNA of interest. Furthermore, studies have reported successfully incorporating diverse small molecules and clinical drugs into EVs (Kamerkar et al., 2017; Poggio et al., 2019; Lathwal et al., 2021). EVs exhibit therapeutic potential for various diseases, opening endless possibilities for the medical community. After their isolation, EV components can be used for endogenous and exogenous engineering at the cellular level (Hood, 2016). The present review deals with the approach to functional cargo modification (both endogenous and exogenous) of EVs. Engineering techniques for endogenous modification mainly involve the genetic engineering of source cells for overproducing proteins of interest and their fusion with EV biogenesis-related proteins, thereby exploiting the inherent ability of EVs to incorporate functional cargoes. Over the past decade, numerous endogenous engineered stents have been tested for EV cavity and surface engineering (Wiklander et al., 2019)

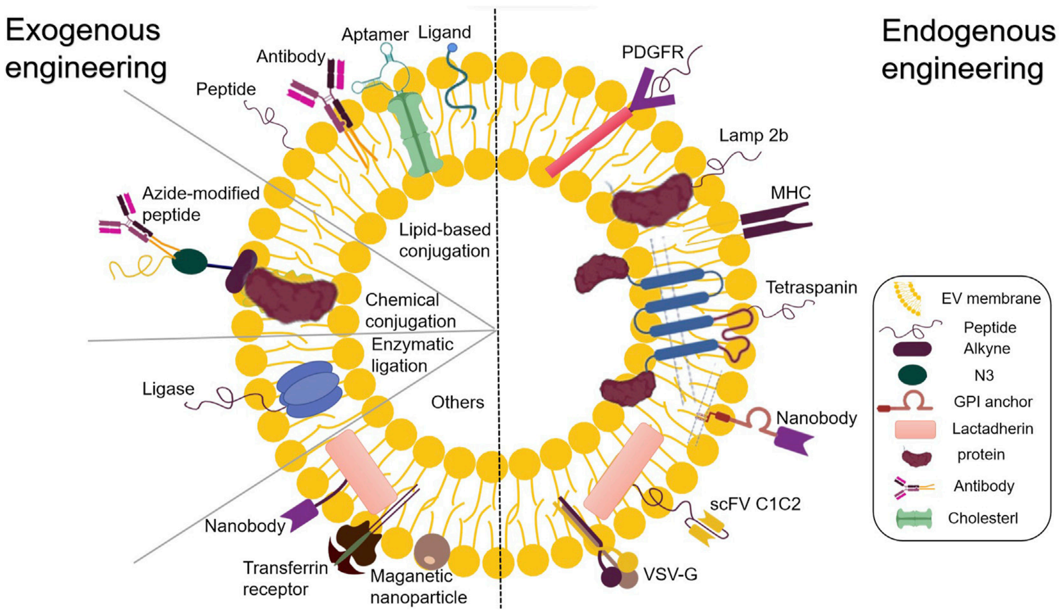

FIGURE 3
Endogenous and exogenous EV engineering strategies for therapeutic cargo loading.

(Figure 2). On the other hand, exogenous modification is achieved by incorporating functional cargoes into EVs by using cell membrane surface receptor proteins, ligands, and other molecular properties to achieve specific targeting (Rädler et al., 2023) (Figure 3).

3.2 Loading of endogenous functionalized cargo

3.2.1 Genetic and EV surface protein engineering

The utilization of miRNAs holds tremendous potential in the field of regenerative medicine. Considering the selective packaging of miRNAs within EVs by secretory cells, there has been extensive investigation into MSCs enriched for certain miRNAs *via* transfection or transduction processes. Genetic engineering strategies offer a means to generate functional EVs from cells expressing biomolecules either in the lumen or on the surface of the EV. RNA and protein sequences can be efficiently introduced into these EVs through transfection using synthetic oligonucleotides or by being expressed from a plasmid backbone (Ohno et al., 2013; Kooijmans S. A. A. et al., 2016). Parental cells can be transfected with therapeutic molecules, including RNA, proteins, ligands, and receptors, for overexpression. These molecules subsequently reach the lumen or onto the surface of EVs, presenting their unique biological properties (Lin et al., 2018; Mendt et al., 2018). This facilitates the entry of exogenous genes into the host cell. Advancements in the elucidation of the EV biogenesis pathways have improved the understanding of precise RNA sorting mechanisms, dramatically accelerating the development of EV bioengineering strategies. An integral aspect of this endeavor is the utilization of EVs as nanocarriers to construct corresponding transport systems. One possible approach for regulating the loading of nucleic acid cargoes into EVs is to fuse nucleic acid-binding proteins with EV-sorting proteins. The efficient loading of nucleic acids into EVs during biogenesis is achieved by the co-expression of the fusion protein with nucleic acids displaying compatible binding motifs (Liang et al., 2022). This approach has been successfully applied to short and long RNA sequences (Kojima et al., 2018; Wang et al., 2018). Targeted therapeutic mRNA expression within EV-derived cells allows the introduction of therapeutic proteins in EVs (Zickler and El Andaloussi, 2020).

Apart from gene transfer, another mechanism for delivering the regenerative potential of EVs involves the delivery of proteins with the capacity to influence target cells. EV can deliver proteins capable of regulating multiple aggregation pathways in its lumen (Qiu et al., 2019). V components can be engineered endogenously within the cell or exogenously after isolation (Mentkowski et al., 2018). The former can be modified by chemical engineering strategies combining metabolic engineering and click chemistry (You et al., 2021). It is worth highlighting that these covalent chemical reactions render EV functionalization more stable in comparison to non-covalent engineering methods (Armstrong et al., 2017).

The EV surface is rich in glycosylphosphatidylinositol (GPI)-anchored proteins or various transmembrane proteins, which can serve as drug carriers to augment the impact of the drug on the regulation of specific genes expressed on the target cell membrane. Different types of molecules can be used to modify these proteins. The various effector functions of these proteins, including but not limited to target cell recognition (Hoshino et al., 2015), ligand signaling (Chen et al., 2018), and induction of toxins, biological agents, and viral receptors (de Carvalho et al., 2014; Keller et al., 2020), result in a spectrum of bodily functions. Considering the presence of transmembrane molecular complexes in various forms within tissues, it is imperative to adopt a tailored approach for interactions among these complexes to achieve specific objectives. This review substantiated the feasibility of various surface-engineered scaffolds by systematically comparing EV-related transmembrane proteins. Tetraspanins (cluster of differentiation [CD]63, CD9, and CD81), lysosome-associated membrane protein (LAMP)-2b, GPI, platelet-derived growth factor receptors, and cadherins (the C1C2 structural domain) are essential in mediating cytoskeletal integration for maintaining tissue homeostasis. Prostaglandin F2 receptor negative regulator is widely used for transmembrane modifications. These transmembrane proteins play crucial roles in different tissues, mediating drug transport, promoting angiogenesis, and inducing inflammatory responses. The complex interactions among transmembrane proteins render their precise regulation difficult. Less research has been done to modify the therapeutic protein content of EV through donor cell modification. To modify the cargo of therapeutic proteins within EVs, a similar strategy to that used for miRNAs can be applied (Nagelkerke et al., 2021). Utilizing genetic engineering techniques, it is possible to create a modified exosomal membrane protein with specific signaling or homing properties. This is achieved by expressing a fusion cassette in parental cells through a gene transfer vector, such as a retroviral or lentiviral vector. Consequently, transduced cells produce EVs and express the desired polypeptide on their surface. It has been shown that cells expressing the glycoprotein (G protein) of vesicular stomatitis virus (VSV) can efficiently release VSV-G into cell-derived EVs (Montagna et al., 2018). These VSV-G-modified EVs can be loaded with protein cargo, which enhances their delivery capacity (Meyer et al., 2017). Recombinant proteins with different activities can be identified by evaluating the effective integration of the exogenous target protein or antibody into the membrane of the recipient cell. All four transmembrane proteins of EVs with the surface domains can be used for fusion with the targeting/therapeutic molecules (Corso et al., 2019; Gupta et al., 2021).

However, endogenous engineering strategies are unsuitable for personalized medicine applications because of the unfeasibility of applying this approach to the cells of the patient. Moreover, the approach is laborious and time-consuming, making it challenging to produce on a large scale, and only genetically encodable functional moieties can be used. In addition, due to the wide variety of proteins involved in EV biogenesis and cargo loading, it is challenging to determine a generic strategy for loading biotherapeutic cargo into EVs as well as the exact expression of the functional fraction in the final isolated EVs and the number of functional EVs.

3.2.2 Others

Parental cell co-incubation: This method involves co-culturing the drug with parental cells, allowing the drug to cross the cell membrane. The drug-laden EVs can be isolated after they are secreted by cells. However, the loading efficiency is typically low and strongly dependent on the gradient of drug dose, drug properties, and parental cell types (Smyth et al., 2015; Kanchanapally et al., 2019). To overcome this challenge, it has been evidenced that low currents and UV irradiation of cells may increase the rate at which nanoparticles or drugs are loaded into EVs (Ye et al., 2018; Fukuta et al., 2020).

3.3 Loading of exogenous functionalized cargo

3.3.1 Parental cell–EV co-incubation method

Isolated EVs are co-incubated with high concentrations of drugs, following which the drug passes through the EV membrane in a concentration-dependent manner. This is a simple method that helps in maintaining membrane integrity. This passive loading method is advantageous for loading hydrophobic compounds (Kugeratski et al., 2021; Tang et al., 2021). Kim et al. co-incubated paclitaxel with another anticancer drug, indocyanine green (ICG), to obtain dual-loaded EVs (Kim et al., 2022). However, this strategy is limited due to the dependence of its efficacy on the lipophilicity and concentration gradient of the drug, making it less efficient for drug loading; for example, paclitaxel and curcumin have different loading efficacies when co-incubated under the same conditions (Sun et al., 2010; Wei et al., 2019).

3.3.2 Electroporation

Electroporation is primarily applied to nucleic acids (Donoso-Quezada et al., 2020; Elsharkasy et al., 2020). An electric field can be applied to EVs suspended in a conductive solution to create pores in the EV membranes, thereby facilitating the loading of siRNAs or miRNAs, followed by restoring vesicle membrane integrity and forming drug-laden vesicles (Alvarez-Erviti et al., 2011). Kasper observed that electroporation did not alter the ability of adipose tissue-derived EVs to endogenously stimulate glioblastoma cell proliferation. However, it did lead to unfavorable morphological alterations, including EV aggregation. To counter this problem and maintain EV structural integrity, they successfully optimized a buffer system containing alginate and achieved the desired results (Johnsen et al., 2016).

3.3.3 Sonication

This method uses the principle of ultrasound to induce deformations in the EV membrane, allowing for the entry of drugs inside the EVs. This method has been used in the treatment of cancer and diabetes. The underlying principle is that the drug can flow into the EVs because of the ultrasound-induced deformations in the EV membrane. In particular, the EVs are mixed with the drug and treated in a sonic disintegrator (Kim et al., 2016). Haney successfully used this method to infuse peroxidase into EVs, increasing peroxidase activity in the cells (Haney et al., 2015).

3.3.4 Extrusion and hypotonic dialysis

This method can be utilized for the preparation of biomaterials or drug carriers, including tissue engineering scaffolds and immunomodulators. The process of extrusion entails mixing EVs with a drug, introducing this mixture into a syringe-based lipid compressor, and extruding it from a membrane with a 100–400 nm pore size. Hypotonic dialysis is achieved by transferring EVs and drugs into the dialysis membranes, placing them in a phosphate buffer, and stirring the mixture at room temperature. The EV membrane is disrupted during extrusion/dialysis and mixed violently with the drug, allowing the loading of the drug into the EV (Fuhrmann et al., 2015).

3.3.5 Freeze-thaw cycles

In this method, the drug is mixed with EVs and frozen quickly, followed by thawing at room temperature. The freeze-thaw cycle is repeated at least three times to ensure drug encapsulation. The hydrophobic nature of lipid molecules prevents the direct loading of lipids into EVs. Yuko suggested a novel method to engineer hybrid EVs by fusing EV membranes with liposomes (Sato et al., 2016).

3.3.6 Saponins

Saponins are natural glycosides with various pharmacological properties. They are known to exert adverse effects on cells; however, their protective effects, such as tumor growth inhibition and anticoagulation, have also been reported. Saponins induce the formation of tiny pores in lipid membranes, and thus, they can be used as membrane permeabilizers. This process, known as saponification, allows hydrophilic nonpermeable drugs or other molecules to enter EVs (Podolak et al., 2010; Hettich et al., 2022). In contrast to ultrasound, compression, and HP, this method preserves the standard structures of the vesicles without causing changes in size distribution or zeta potential of the loaded EVs. Furthermore, this technique enables the loading of lipid molecules into EVs without special devices. However, saponins' *in vivo* hemolytic properties must be fully considered when delivered as drugs to ensure safety and efficacy (Haney et al., 2021).

3.3.7 Exogenous modification of EV surfaces

In addition to the EV transporting proteins in its lumen capable of regulating multiple aggregation pathways, another mechanism *via* which EVs influence target cells is by means of proteins present on their surface. These surface proteins enable EVs to dock with receptors located on the surface of the target cell (French et al., 2017). In addition to chemical engineering strategies targeting the source cell membrane before EV isolation, EV membrane modification directly after EV secretion is another critical exogenous approach to EV functionalization by covalent or noncovalent methods (Liang et al., 2021). Typically, the former approach applies bioconjugation, amidation, aldehyde-amine condensation, and click chemistry to link molecules on the EV surface through chemical bonding, while the latter approach modifies EV membranes through hydrophobic insertion, receptor-ligand binding, fusion, and multivalent electrostatic interactions (Yang Y. et al., 2017; Tian et al., 2018; Wu P. et al., 2021; Guo et al., 2021). Exogenous modifications to EV surfaces are used to optimize and improve their surface structures and are performed using chemical methods. Polymers exhibiting specific biological activities are extracellular constructed, and exogenous molecules are attached to the cell membranes via chemical bonding or self-assembly. EVs are subjected to novel functionalization with artificially designed materials that have been synthesized to enhance their performance. These materials exhibit different properties enabling various biological functions, including cell recognition and drug delivery. The physical coupling of targeting ligands to surface proteins is a crucial step in this method. The integration of these molecules into EV membranes via binding affinity antibodies leads to the formation of complexes exhibiting specific biological activities. Highly selective compounds with specific affinities can be obtained by attaching a peptide or antigen fragment with a specific recognition site to the receptor molecule (Hao et al., 2022). Targeted ligands can be attached to isolated EVs in a controlled manner, which is impossible with parental cell modification methods. Methods for targeting peptides and antibodies are commonly used to achieve effective targeting after EV isolation. Isolated EVs are exogenously functionally modified using chemical reactions (click chemistry and noncovalent reactions) to attach therapeutic molecules to their surfaces. These methods involve either the chemical modification of alkynes that are EV membrane proteins or the incorporation of alkyne-modified lipids into EV membranes (Smyth et al., 2014; Tian et al., 2018; Zhu et al., 2019).

Using copper-free click chemistry, EVs containing azide lipids can be easily decorated with various functional groups (Oude Blenke et al., 2015).

Over the past decade, attempts have been made to promote inter-biomolecular linkages using magnetic, optical, and electrical interactions. Multivalent electrostatic interactions have also been used to modify EV surfaces. EV lipid bilayers can spontaneously fuse with other membrane structures. Taste et al. utilized electrostatic interactions to allow the fusion of cationic lipids with EVs (Piffoux et al., 2018). This approach has also been successfully employed for targeted drug delivery in biosensors and tissue engineering. Engineering EV surface membranes via external cationic lipids or polymer modifications can significantly improve their ability to fuse with cells. Functionalized modifications of these polymers can result in more efficient cell fusion (Nakase and Futaki, 2015; Tamura et al., 2017; Sawada et al., 2020). Similarly, Qi et al. developed an EV delivery system using magnetic fields and transferrin-coupled superparamagnetic nanoparticles to facilitate the effective binding of these nanoparticles to the surfaces of blood-derived EVs (Qi et al., 2016).

Compared with endogenous engineering techniques, exogenous modifications to EV surfaces involve a broad range of targeting ligands and offer greater flexibility in choosing chemical tools. Moreover, the time for engineered modifications was shortened, thus improving the effectiveness of EV treatment.

4 Overcoming major barriers to the clinical applications of EVs

Studies have revealed that the clearance of unmodified EVs is rapid after *in vivo* administration, especially intravenous injections. EVs that are systemically administered are rapidly cleared from the blood within 2–20 min (Wiklander et al., 2015; Morishita et al., 2017). For example, plasma-derived EVs exhibited a half-life of about 7 min in mice, whereas tumor-derived EVs were cleared from circulation more rapidly, exhibiting half-lives of around 2 min (Takahashi et al., 2013; Matsumoto et al., 2020). A pharmacokinetic study revealed that most EV doses do not reach the target tissues but accumulate nonspecifically in the liver and spleen, with a fraction directed to the kidneys, lungs, and gastrointestinal tract (Kooijmans et al., 2012; Lai et al., 2014). However, EV clearance by the spleen was reported to be the most significant (Cataldi et al., 2017).

The underlying mechanisms should be explored to develop improved versions of EVs that can escape organism capture and exhibit potent biological activities. Scientists have made significant efforts to modify EVs and demonstrated their feasibility and flexibility to undergo engineering modifications (Liang et al., 2021). In summary, the rapid clearance of EVs as therapeutic or drug delivery vehicles after administration is a limitation in certain clinical settings. To facilitate the clinical translation of EVs and broaden their application in most clinical settings, it is essential to

TABLE 3 Summary of EV targeting strategies used in regenerative medicine.

Targeting moieties	Target	Method of conjunction	Cargo	Loading method	Administration	EV/exosome origin	Application areas	Ref
RGD	αvβ3 overexpressing cells (HUVEC)	DSPE-PEG-RGD	Ac4ManNAz	Reversible permeabilization, click chemistry	*In vitro*/*in vivo* (zebrafish)	K562	Vascular regeneration	Wang et al. (2017)
CPP/CP05	Exosome/Dystrophin	CD63	PMO	Conjugated to CP05 via an amide linker	*In vivo* (Mouse mdx model)	Human serum	Muscle regeneration	Fletcher et al. (2007), Gao et al. (2018)
CAP	Chondrocytes	lamp2b	miR-140	Electroporation	*In vitro*/*in vivo* (rat osteoarthritis model)	Dendritic cells	Cartilage regeneration	Liang et al. (2020)
NP41/CP05	Exosome/Nerve tissue	CD63	None	None	*In vitro*	Human serum	Neurogenesis	Whitney et al. (2011), Gao et al. (2018)
CP05	Exosome/bone tissue	CD63	VEGF	Electroporation	*In vitro*/*in vivo* (radial defect rat model)	ATDC5	Bone & Vascular Regeneration	Gao et al. (2018), Zha et al. (2021)
RGE	Neuropilin-1	Click chemistry	Cur/SPION	Electroporation	*In vitro*/*In vivo* (orthotopic glioma mouse model)	Mouse macrophage cell	Tumor	Jia et al. (2018)
RVG	Neuronal cells	Lamp2b	BACE1 siRNA	Electroporation	*In vivo*	Dendritic cells	Neurogenesis	Alvarez-Erviti et al. (2011)
RVG	Cortical neural progenitors	Lamp2b	miRNA-124	Electroporation	*In vivo*	Dendritic cells	Neurogenesis	Alvarez-Erviti et al. (2011)

Abbreviations: Arg-Gly-Asp; RVG, rabies virus glycoprotein; Ac4ManNAz, tetra acetylated N-azidoacetyl-d-mannosamine; CP05, exosomal capture peptides; PMO, phosphorodiamidate morpholino oligomer; CPP, cell-penetrating peptide; CAP, chondrocyte-affinity peptide; NP41, NTQTLAKAPEHT; RGE, RGERPPR; VEGF, vascular endothelial growth factor; Cur, curcumin; SPION, superparamagnetic iron oxide nanoparticles.

TABLE 4 Methods for prolonging EV circulation time.

Modifying moieties	Engineering modification methods	EV origin	Main achievements	Ref
PEO	Chol-DNA	Mesenchymal stem cells	Higher stability and blood circulation time without altering tissue distribution profiles	Lathwal et al. (2021)
Dextran sulfate	Parental cell co-incubation	HEK293 and all mouse cell lines	Decreased EV liver clearance in mice and a significant increase in EV production	Watson et al. (2016)
cCHP nano gel	Polyvalent electrostatic interactions/Chol	Mouse macrophage cells	Efficient delivery in a functionally intact state	Sawada et al. (2020)
PEG	PEG-lipids	Neuro 2A	Allowed the application of a range of targeted ligands/antibodies	Kooijmans et al. (2016b)
			Improved cell specificity and prolonged circulation time	
ABD	Lamp2B	HEK-293T and AEC cells	Extended cycle time of EV and enrichment of EVs in lymph nodes	Liang et al. (2022)
PHA	MGE/click chemistry	MDA-MB-231 and HCT-116	The PHA-EVs exhibited high targeting efficiency with prolonged circulation in the bloodstream of animal models with tumor and RA	Lim et al. (2021)

Abbreviations: PEO, polyethylene oxide; PEG, polyethylene glycol; ABD, albumin binding domains; Chol, cholesteryl; PHA, PEGylated hyaluronic acid; MGE, metabolic glycoengineering; MDA-MB-231, a human breast cancer cell line; HCT-116, a human colon carcinoma cell line; HEK, human embryonic kidney cell; AEC, alveolar epithelial cell; RA, rheumatoid arthritis.

use bioengineering technologies for the function modification of these EVs. The functionalized modifications of EVs can improve their abilities to deliver therapeutic molecules to the target site, thereby enhancing their therapeutic effects (Zhang et al., 2020a). Until now, there have been relatively few studies exploring the application potential of dental-derived EVs in the field of regenerative medicine. To expedite their development, this discussion focuses on the prospects of cutting-edge engineered EV approaches with promising applications from two perspectives: targeting efficiency and *in vivo* circulation time. Tables 3, 4 summarize the applications of engineered EVs with high targeting efficiency and long circulation time.

4.1 Targeting efficiency

Research on drug delivery using EVs as carriers has rapidly progressed. Targeting determines whether EVs can deliver drugs to diseased cells or tissues precisely and efficiently (Sharif et al., 2018; Xie et al., 2019). The regenerative potential of EVs is believed to be governed by the regulation of specific intracellular pathways. However, the use of EVs may produce serious off-target effects. Hence, it is imperative to elucidate these mechanisms and their regulation in both target and off-target tissues. To address this concern, engineering modified EVs and directing them to the therapeutic site while precisely controlling the intracellular pathways influenced by modulating the therapeutic content of EVs will significantly enhance their clinical applicability (Nagelkerke et al., 2021).

In some cases, the ability to target EVs is related to the presence of specific surface proteins. Integrins on the surface of EV are considered essential mediators of their accumulation in specific tissues (Hoshino et al., 2015). Tetratransmembrane proteins and their association with integrins have also been associated with EV targeting *in vivo*. For example, EVs containing Tspan8 were notably enriched in the pancreas of mice following intravenous injection, while co-expression of β4 integrins led to their substantial accumulation in the lungs (Rana et al., 2012). Nevertheless, the inherent tissue-specific tropism of EVs is generally limited and often insufficient for determining its maximum accumulation in organs beyond the liver and spleen. Therefore, artificial targeting modifications of EVs are required.

The surface proteins of natural EVs indeed influence their biodistribution. In accordance with this fundamental principle, surface functionalization methods, which encompass chemical treatment, affinity-based immobilization, and enzymatic ligation, bestow EVs with targeting capabilities. Receptors, antibodies, ligands, peptides, RNA adaptors, and sugar fractions can be used for EV surface functionalization (Jia et al., 2018; Pham et al., 2021).

Erviti *et al.* successfully synthesized a membrane protein fused to a neuron-specific peptide and permeated the neuron-specific rabies virus glycoprotein (RVG) peptide into EVs by transfection them to target brain cells. This was then combined with electroporation to load an exogenous siRNA on EVs. The intravenous injection of RVG-EV-siRNA delivered the siRNA specifically to the brain's neurons, microglia, and oligodendrocytes, resulting in the knockdown of specific genes (Alvarez-Erviti et al., 2011). Jia integrated superparamagnetic iron oxide nanoparticles and curcumin into EVs using an electroporation method and further functionalized the EV surface with the peptide RGERPPR, thus targeting neuropilin-1 by click chemistry. Such EVs targeting gliomas exhibit therapeutic and imaging capabilities and cross the blood–brain barrier (BBB), contributing to the accurate identification of gliomas and the improved efficacy of drugs (Jia et al., 2018). Wang used a membrane modification strategy based on donor cell-assisted designing of peptide c (RGDyK)-modified EVs using click chemistry and dialysis methods. This strategy was utilized to introduce functional cargo, resulting in improved vascular targeting with a synergistic effect on therapeutic angiogenesis and angiogenic imaging (Wang et al., 2017). Liang used the endogenous genetic engineering approach to modify lysosome-associated membrane protein 2b (Lamp2b) on the EV surface to design EVs containing the chondrocyte-affinity peptide (CAP) and used an electroporation method to load the therapeutic drug onto miR-140. The *in vitro* results showed that the intracellular miR-140 level increased up to 7.5 times the original level. Simultaneously, precisely targeted delivery to deep cartilage chondrocytes, strictly confined to the cartilage interior, was successfully achieved, effectively alleviating osteoarthritis progression in a rat model (Liang et al., 2020).

Gao *et al.* targeted the second extracellular loop of CD63 for specific binding and obtained a peptide named CP05 in CD63-expressing cells; they anchored the EVs to other EVs derived from different cell cultures and human serum. The administration of EVs loaded with a CP05-modified amyotrophic protein resulted in an 18-fold increase in the amyotrophic protein levels in the muscles of amyotrophic-protein-deficient MDX mice. Further loading of muscle-targeting peptides significantly improved muscle functions. CP05 was also relatively stable in the blood after systemic administration (Gao et al., 2018). Similarly, Zha used CP05 to construct engineered EVs loaded with vascular endothelial growth factor and combined the EVs with 3D-printed porous bone scaffolds, which significantly increased the efficiency of the EVs and effectively promoted osteogenesis and angiogenesis in segmental bone defects. This study showed the potential of EVs for vascularized bone reconstruction (Zha et al., 2021). Ma *et al.* synthesized CP05 with the type I/III collagen-binding domain. The findings demonstrated that CP05 synthesis helped EVs promote the osteogenic differentiation of BMSCs. Subsequently, they applied a hydrogel containing the synthesized CP05 in combination with EVs to treat cranial bone defect in a rat model, significantly increasing the EVs' retention and stability (Ma et al., 2022).

This method did not disrupt the structural features of EV surface membranes, preserved the properties and *in vivo* distribution of EVs, offered increased modifiability, and significantly improved the efficiency of targeted drug delivery utilizing EVs. Thus, combining CP05 with various therapeutic/targeted peptide drugs is a promising means for engineering EVs.

4.2 *In vivo* circulation time

EV targeting determines the effective concentration of therapeutic agents in the targeted tissues. However, the EVs delivered to the targeted site are rapidly cleared by monocytes/macrophages or the reticuloendothelial system, resulting in reduced accumulation in the target site. Monocyte/macrophage depletion can considerably prolong the whole-body half-life of EVs in mice, suggesting that uptake by monocytes/macrophages is an important *in vivo* mechanism for clearing EVs (Bala et al., 2015; Imai et al., 2015; Morishita et al., 2015). Phagocytosis is regarded as one of the primary mechanisms of EV internalization (Hwang et al., 2015). Several engineering strategies corresponding to the mechanism of EV degradation have emerged. Macrophages recognize and phagocytose apoptotic cells by identifying phosphatidylserine (PS), a phospholipid exposed to the plasma membrane (Segawa and Nagata, 2015; Matsumura et al., 2019). As most EVs display PS on their surface (Subra et al., 2007), they are rapidly excluded from the bloodstream. The C1C2 structural domain of a PS-binding protein can mask the PS of EVs using cadherin to prolong their circulating half-life (Kooijmans et al., 2018; Longatti et al., 2018). CD47 displayed on the surface protects EVs from phagocytosis by monocytes and macrophages, thus enhancing EV retention in circulation (Belhadj et al., 2020). Importantly, macrophages may phagocytose normal erythrocytes if CD47 on the EV surface occupies the signal regulatory protein alpha site, which is typically utilized to prevent phagocytosis (Buatois et al., 2018).

Watson identified the Scavenger Receptor Class A family (SR-A) as a novel receptor for EV uptake by monocytes/macrophages. *In vivo*, the blockade of SR-A by loading dextran sulfate on EVs using the parental cell co-incubation method remarkably decreased EV clearance in hepatic tissues along with increased accumulation in tumors (Watson et al., 2016). Polymers such as polyethylene glycol (PEG) or gels to encapsulate EVs can affect their pharmacokinetics and biodistribution by improving their surface physicochemical properties (Antes et al., 2018; Choi et al., 2019). Sawad synthesized engineered EVs owing to the electrostatic interactions between amphiphilic cationic cholesteryl pullulan (cCHP) nanogel polymers and anionic EV surface membranes, which significantly improved EV circulation time and enhanced their efficient delivery *in vivo* (Sawada et al., 2020). Kooijmans developed PEG-coated EVs to avoid phagocytosis by monocytes, which increased the blood circulation time of EVs from 10 min to more than 60 min (Kooijmans S.a. A. et al., 2016; Suk et al., 2016). Choi discovered that surface modification of EVs with PEG-derived 1,2-dioctadecanoyl-sn-glycero-3-phosphoethanolamine could prolong the circulation time of EVs in a similar manner (Choi et al., 2019). These studies indicate the potential of hybrid EV nanocarriers with different biocompatibilities to transport various contents *in vivo* and ensure their effective delivery in a functional state. This provides robust support for the utilization of EV-based therapies in the fields of nanomedicine and tissue engineering.

However, the toxicity and immunogenicity of PEG carrier systems should be investigated (Shiraishi and Yokoyama, 2019). Moreover, the mentioned surface encapsulation approach may mask the natural targeting or therapeutic properties of EVs. It may not control the length and number of conjugated polymers, which can be a barrier to their translation to clinical practice. To overcome these limitations, Lathwal *et al.* created a polymer-based engineered modification platform capable of precisely controlling polymer composition, chain length, and loading, which used DNA linkers to functionalize EVs. This platform was combined with atom transfer radical polymerization technology (Baker et al., 2019; Yerneni et al., 2019) to design EV–polymer hybrids (EPHs) with considerably high stability and better pharmacokinetics. Furthermore, the EV surfaces were precisely designed by using different synthetic polymers. These polymers could be easily tuned to overcome stability- and activity-related limitations *in vitro* and *in vivo*, and the circulation time of all EPH samples was prolonged. These properties of EPH overcame some major limitations associated with the clinical application of EV-based therapies (Lathwal et al., 2021). A recent research revealed that the surface of the albumin-binding domain (ABD) was displayed on the EV surface. ABDs were either present in the extracellular loops of the selected EV-rich tetra-transmembrane proteins (CD63, CD9, and CD81), or they were directly fused to the extracellular terminus of a single transmembrane EV-sorting domain (e.g., Lamp2B).

These engineered EVs exhibited the ability to bind to human serum albumin both *in vitro* and *in vivo*. Experimental data showed that the circulation time of EVs increased significantly after they were injected via different routes in different strains of mice (Liang et al., 2022).

Thus, when EVs bind to tissue-specific targeting molecules, the circulation time of EVs *in vivo* is equally critical. The combined effect of the two may markedly accelerate the translation of EV-based therapies to clinical practice.

5 Discussion and perspectives

EVs possess unique natural targeting capabilities, have the ability to cross the BBB, and display low immunogenicity, enabling effective intercellular communication and the delivery of molecules to distant sites. These characteristics provide significant advantages over existing drug delivery vehicles. To fully exploit their potential and benefits and develop efficient and reproducible nanocarrier drug delivery systems, functionalized modifications of EVs combined with emerging bioengineering technologies are necessary to adapt them to most clinical therapeutic settings. The endogenous genetic modification of EV parental cells or the exogenous direct functionalization of isolated EV surfaces can help achieve this adaptation. Both approaches have advantages and should be selected according to specific application conditions. Notably, DSC-EVs exert a natural therapeutic effect and can be used to enhance the therapeutic effect of loaded drugs. Enhanced knowledge of the molecular content and biological functions of EVs has paved the way for the development of various engineering approaches aimed at improving the therapeutic or targeting efficacy of EVs at the preclinical stage. In addition, a more detailed understanding of specific markers and functions associated with EVs derived from different parental cells can significantly assist in establishing criteria for using optimal EV populations with maximum efficiency in therapeutic and diagnostic applications. Consequently, when selecting and designing target EVs, the natural targeting properties of different EVs should be considered because their specific target effects can more easily be further amplified by engineering modifications.

However, owing to the complexity of EV biogenesis and the wide range of engineered modification strategies, identifying a generic strategy for precisely modifying biotherapeutic cargo in EVs is challenging. Enhanced comprehension of EV biogenesis, surface markers, cargo, uptake, and function enables accurate discrimination among distinct EV types and facilitates the development of treatment schemes without adverse effects. Various engineering approaches are available to add desired functionality to EVs. Exogenous reagents can be introduced into EVs before or after vesicle formation. Genetic and chemical engineering of cells can manipulate EV cargo. Post-formation loading techniques encompass mixing, electroporation, sonication, hypotonic dialysis, extrusion, freeze-thaw cycles, and the utilization of saponin or commercially available transfection reagents. Furthermore, surface modifications of EVs can facilitate tissue-specific therapeutic delivery (Bahmani and Ullah, 2022). Hence, it is crucial to carefully choose modification techniques while also gaining a deeper comprehension of EVs. The utilization of the known molecular mechanisms associated with EVs from particular sources to guide the selection of suitable modification methods is paramount for the success of engineered EV applications.

Despite extensive endeavors to develop diverse engineering techniques for the functionalization of natural EVs and promising preclinical outcomes in regenerative medicine applications, the clinical translation of natural EVs continues to pose significant challenges. Firstly, transplantation protocols for human cells and tissues involve many ethical and policy issues related to informed consent, quality, procurement safety, processing of biological tissues, and distribution and international circulation of human cells and tissues. Maintaining regulatory order requires the coordinated operation of multiple parties. Secondly, EVs lack the capability to respond to pathological environmental stimuli as effectively as stem cells. It is important to note that clinical studies on stem cells cannot be directly transplanted to stem cell-secreted EVs because the therapeutic mechanisms of EVs may diverge significantly from those of their stem cell source. Consequently, gaining a profound understanding of EV biology and its unique action mechanisms in specific diseases is a daunting task for researchers. Furthermore, the lack of adequate and reproducible production methods remains a significant limitation to this day, and the future of EV therapy depends on the realization of high-purity isolation and mass production of EVs. Therefore, there is an urgent need to develop improved technologies for vesicle isolation, purification, characterization, and storage. In addition, such technologies should be clinically scalable to enable rapid translation of promising EV-based therapies. Despite the daunting challenges, with all the efforts to establish order in the regulatory system of stem cell banking at the local and national levels, the deepening knowledge of EV biology and therapeutic mechanisms, and the solid multidisciplinary collaborations in the fields of bioengineering, chemistry, materials science, nanotechnology, clinical medicine, and industry, these emerging positives will surely propel safe and effective EV nanotherapies toward clinical translation.

Manufactured EVs have been proposed as an alternative to natural EVs in optimizing EV therapeutics and clinical translation. Manufactured EVs, also known as synthetic lipid nanoparticles (LNPs), offer advantages over natural EVs in yield and cost-effectiveness. Synthetic LNPs are more cost-effective and accessible to manufacture on a large scale than EVs. The potential benefits of EVs over synthetic LNPs stem from their intrinsic targeting properties and immune-interacting proteins on the surface of EVs. EV is often described as having an intrinsic tissue-targeting ability when administered *in vivo*. EV from specific cancer cell lines has been shown to accumulate in specific organs after *in vivo* injection (Hoshino et al., 2015). Engineered EVs, in particular, are considered safer delivery vehicles for RNA or gene editing tools than other synthetic nanoparticles (Maugeri et al., 2019). However, any isoform protein is a potential antigen and immune target. Therefore, synthetic LNPs lacking homodimeric proteins may be advantageous in avoiding premature recognition and destruction (Chen W. C. et al., 2013). Furthermore, the growing interest in isolating EVs from different sources opens up the possibility of optimizing EV-based therapies for each specific clinical purpose. EVS released from various cell lines possess distinct properties. Obtaining well-known sources of MSCs, such as bone marrow and adipose tissue, can often be challenging. Therefore, the exploration of new alternative sources of highly plastic and accessible stem cell EVs has the potential to optimize EV therapies. DSCs have a higher proliferative capacity compared to the most widely studied BMSCs. DSCs are more acceptable to patients in terms of accessibility and prognosis. DSCs are more pleasing to patients than BMSCs and, in most cases, are benign reuse of discarded oral biologic tissues.

Furthermore, while current foundational research on DSCs tends to focus on dental applications, a significant body of research suggests that the potential of DSCs and their derived EVs extends beyond the dental field. Their therapeutic potential has been explored in diverse areas, such as the treatment of spinal cord injuries, brain injuries, myocardial infarction, wound healing, and bone replacement (Cordeiro et al., 2008). Given their self-renewal ability and strong plasticity, these cells can encompass various clinical applications in medicine and dentistry. However, it is worth noting that DSC has apparent drawbacks; one remarkable concern is whether the final amount of EV isolated from stem cells obtained from a single tooth after a normal expansion period would be sufficient to effectively treat a specific disease with EV therapy. This limitation arises because not all people have wasted wisdom teeth, and the availability of DSCs from deciduous teeth is much more limited. Consequently, this leads to very limited clinical scenarios. In this regard, establishing stem cell banks and maintaining order, as discussed earlier, are particularly critical. In addition, mature DSC acquisition and preservation programs, subsequent DSC *in vitro* expansion programs, and enrichment of derived EV biology are also essential.

6 Conclusion

EVs have great potential to become therapeutic targets, biomarkers, innovative drug delivery systems, and stand-alone therapeutic agents. However, nanotherapies utilizing EVs as regenerative medicine are still in their infancy. These vesicles play a crucial role in regulatory or pathological intercellular communication, and their circulation in the body influences their biodistribution and the effective EV dose reaching the target tissue.

In regenerative medicine, it is advisable to choose parental stem cells characterized by high plasticity and proliferative capacity. Additionally, employing emerging bioengineering techniques can enhance the efficiency and *in vivo* circulation duration of EVs, facilitating the delivery of therapeutic doses to specific tissues.

With the synergistic development of all related industries, the clinical translatability of EV therapies will be accelerated in the future. Overall, this study summarized the research progress of dental stem cell-derived EVs in oral tissue regeneration and discussed the current strategies for loading and modifying the functional cargo of engineered EVs. Furthermore, it has also addressed the progress and prospects of engineered EVs in tissue engineering and regenerative medicine. The primary goal of this study is to provide a strong basis for developing EV-based strategies for clinical applications.

Author contributions

WW: Data curation, Investigation, Validation, Visualization, Writing–original draft, Writing–review and editing. ZX: Data curation, Investigation, Validation, Visualization, Writing–review and editing. ML: Investigation, Validation, Writing–review and editing. XL: Conceptualization, Funding acquisition, Investigation, Methodology, Validation, Writing–review and editing.

Funding

The author(s) declare financial support was received for the research, authorship, and/or publication of this article. This study was funded by the National Natural Science Foundation of China (82201001), the Natural Science Foundation Projects of Guangdong (2021A1515010882), the Science and Technology Projects in Guangzhou (202102010040), the Clinical Frontier Technology Program of the First Affiliated Hospital of Jinan University, China (a01210), the Science and Technology Projects in Guangzhou (2023A03J1030).

Acknowledgments

Throughout the writing of this dissertation I have received a great deal of support and assistance. I would particularly like to acknowledge my tutors, XL, for their wonderful collaboration and patient support.

Conflict of interest

The authors declare that the research was conducted in the absence of any commercial or financial relationships that could be construed as a potential conflict of interest.

Publisher's note

References

Aheget, H., Mazini, L., Martin, F., Belqat, B., Marchal, J. A., and Benabdellah, K. (2020). Exosomes: their role in pathogenesis, diagnosis and treatment of diseases. *Cancers* 13 (1), 84. doi:10.3390/cancers13010084

Akbari, A., Nazari-Khanamiri, F., Ahmadi, M., Shoaran, M., and Rezaie, J. (2022). Engineered exosomes for tumor-targeted drug delivery: a focus on genetic and chemical functionalization. *Pharmaceutics* 15 (1), 66. doi:10.3390/pharmaceutics15010066

Alvarez-Erviti, L., Seow, Y., Yin, H., Betts, C., Lakhal, S., and Wood, M. J. A. (2011). Delivery of siRNA to the mouse brain by systemic injection of targeted exosomes. *Nat. Biotechnol.* 29 (4), 341–345. doi:10.1038/nbt.1807

Antes, T. J., Middleton, R. C., Luther, K. M., Ijichi, T., Peck, K. A., Liu, W. J., et al. (2018). Targeting extracellular vesicles to injured tissue using membrane cloaking and surface display. *J. Nanobiotechnology* 16 (1), 61. doi:10.1186/s12951-018-0388-4

Armstrong, J. P., Holme, M. N., and Stevens, M. M. (2017). Re-engineering extracellular vesicles as smart nanoscale therapeutics. *ACS Nano* 11 (1), 69–83. doi:10.1021/acsnano.6b07607

Asplund, M., Nilsson, M., Jacobsson, A., and von Holst, H. (2009). Incidence of traumatic peripheral nerve injuries and amputations in Sweden between 1998 and 2006. *Neuroepidemiology* 32 (3), 217–228. doi:10.1159/000197900

Bahmani, L., and Ullah, M. (2022). Different sourced extracellular vesicles and their potential applications in clinical treatments. *Cells* 11 (13), 1989. doi:10.3390/cells11131989

Baker, S. L., Kaupbayeva, B., Lathwal, S., Das, S. R., Russell, A. J., and Matyjaszewski, K. (2019). Atom transfer radical polymerization for biorelated hybrid materials. *Biomacromolecules* 20 (12), 4272–4298. doi:10.1021/acs.biomac.9b01271

Bakkar, M., Liu, Y., Fang, D., Stegen, C., Su, X., Ramamoorthi, M., et al. (2017). A simplified and systematic method to isolate, culture, and characterize multiple types of human dental stem cells from a single tooth. *Methods Mol. Biol. Clift. N.J.)* 1553, 191–207. doi:10.1007/978-1-4939-6756-8_15

Bala, S., Csak, T., Momen-Heravi, F., Lippai, D., Kodys, K., Catalano, D., et al. (2015). Biodistribution and function of extracellular miRNA-155 in mice. *Sci. Rep.* 5, 10721. doi:10.1038/srep10721

Baraniak, P. R., and McDevitt, T. C. (2010). Stem cell paracrine actions and tissue regeneration. *Regen. Med.* 5 (1), 121–143. doi:10.2217/rme.09.74

Bashyal, S., Thapa, C., and Lee, S. (2022). Recent progresses in exosome-based systems for targeted drug delivery to the brain. *J. Control. Release* 348, 723–744. doi:10.1016/j.jconrel.2022.06.011

Belhadj, Z., He, B., Deng, H., Song, S., Zhang, H., Wang, X., et al. (2020). A combined "eat me/don't eat me" strategy based on extracellular vesicles for anticancer nanomedicine. *J. Extracell. Vesicles* 9 (1), 1806444. doi:10.1080/20013078.2020.1806444

Beyer Nardi, N., and da Silva Meirelles, L. (2006). Mesenchymal stem cells: isolation, *in vitro* expansion and characterization. *Handb. Exp. Pharmacol.* 174, 249–282.

Buatois, V., Johnson, Z., Salgado-Pires, S., Papaioannou, A., Hatterer, E., Chauchet, X., et al. (2018). Preclinical development of a bispecific antibody that safely and effectively targets CD19 and CD47 for the treatment of B-cell lymphoma and leukemia. *Mol. Cancer Ther.* 17 (8), 1739–1751. doi:10.1158/1535-7163.MCT-17-1095

Caplan, H., Olson, S. D., Kumar, A., George, M., Prabhakara, K. S., Wenzel, P., et al. (2019). Mesenchymal stromal cell therapeutic delivery: translational challenges to clinical application. *Front. Immunol.* 10, 1645. doi:10.3389/fimmu.2019.01645

Cataldi, M., Vigliotti, C., Mosca, T., Cammarota, M., and Capone, D. (2017). Emerging role of the spleen in the pharmacokinetics of monoclonal antibodies, nanoparticles and exosomes. *Int. J. Mol. Sci.* 18 (6), 1249. doi:10.3390/ijms18061249

Čebatariūnienė, A., Kriaučiūnaitė, K., Prunskaitė, J., Tunaitis, V., and Pivoriūnas, A. (2019). Extracellular vesicles suppress basal and lipopolysaccharide-induced NFκB activity in human periodontal ligament stem cells. *Stem Cells Dev.* 28 (15), 1037–1049. doi:10.1089/scd.2019.0021

Chen, G., Huang, A. C., Zhang, W., Zhang, G., Wu, M., Xu, W., et al. (2018). Exosomal PD-L1 contributes to immunosuppression and is associated with anti-PD-1 response. *Nature* 560 (7718), 382–386. doi:10.1038/s41586-018-0392-8

Chen, K., Xiong, H., Huang, Y., and Liu, C. (2013a). Comparative analysis of *in vitro* periodontal characteristics of stem cells from apical papilla (SCAP) and periodontal ligament stem cells (PDLSCs). *Arch. Oral Biol.* 58 (8), 997–1006. doi:10.1016/j.archoralbio.2013.02.010

Chen, W. C., May, J. P., and Li, S. D. (2013b). Immune responses of therapeutic lipid nanoparticles. *Nanotechnol. Rev.* 2 (2), 201–213. doi:10.1515/ntrev-2012-0040

Cheng, L., and Hill, A. F. (2022). Therapeutically harnessing extracellular vesicles. *Nat. Rev. Drug Discov.* 21 (5), 379–399. doi:10.1038/s41573-022-00410-w

Choi, E. S., Song, J., Kang, Y. Y., and Mok, H. (2019). Mannose-modified serum exosomes for the elevated uptake to murine dendritic cells and lymphatic accumulation. *Macromol. Biosci.* 19 (7), e1900042. doi:10.1002/mabi.201900042

Corso, G., Heusermann, W., Trojer, D., Görgens, A., Steib, E., Voshol, J., et al. (2019). Systematic characterization of extracellular vesicle sorting domains and quantification at the single molecule - single vesicle level by fluorescence correlation spectroscopy and single particle imaging. *J. Extracell. Vesicles* 8 (1), 1663043. doi:10.1080/20013078.2019.1663043

Cordeiro, M. M., Dong, Z., Kaneko, T., Zhang, Z., Miyazawa, M., Shi, S., et al. (2008). Dental pulp tissue engineering with stem cells from exfoliated deciduous teeth. *J. Endod.* 34 (8), 962–969. doi:10.1016/j.joen.2008.04.009

Cvek, M. (1992). Prognosis of luxated non-vital maxillary incisors treated with calcium hydroxide and filled with gutta-percha. A retrospective clinical study. *Endod. Dent. Traumatology* 8 (2), 45–55. doi:10.1111/j.1600-9657.1992.tb00228.x

Dai, J., Su, Y., Zhong, S., Cong, L., Liu, B., Yang, J., et al. (2020). Exosomes: key players in cancer and potential therapeutic strategy. *Signal Transduct. Target. Ther.* 5 (1), 145. doi:10.1038/s41392-020-00261-0

de Carvalho, J. V., de Castro, R. O., da Silva, E. Z. M., Silveira, P. P., da Silva-Januário, M. E., Arruda, E., et al. (2014). Nef neutralizes the ability of exosomes from CD4+ T cells to act as decoys during HIV-1 infection. *PloS One* 9 (11), e113691. doi:10.1371/journal.pone.0113691

Diomede, F., D'Aurora, M., Gugliandolo, A., Merciaro, I., Ettorre, V., Bramanti, A., et al. (2018a). A novel role in skeletal segment regeneration of extracellular vesicles released from periodontal-ligament stem cells. *Int. J. Nanomedicine* 13, 3805–3825. doi:10.2147/IJN.S162836

Diomede, F., Gugliandolo, A., Cardelli, P., Merciaro, I., Ettorre, V., Traini, T., et al. (2018b). Three-dimensional printed PLA scaffold and human gingival stem cell-derived extracellular vesicles: a new tool for bone defect repair. *Stem Cell Res. Ther.* 9 (1), 104. doi:10.1186/s13287-018-0850-0

Donoso-Quezada, J., Ayala-Mar, S., and González-Valdez, J. (2020). State-of-the-art exosome loading and functionalization techniques for enhanced therapeutics: a review. *Crit. Rev. Biotechnol.* 40 (6), 804–820. doi:10.1080/07388551.2020.1785385

Elashiry, M., Morandini, A. C., Cornelius Timothius, C. J., Ghaly, M., and Cutler, C. W. (2021). Selective antimicrobial therapies for periodontitis: win the "battle and the war. *Int. J. Mol. Sci.* 22 (12), 6459. doi:10.3390/ijms22126459

Elsharkasy, O. M., Nordin, J. Z., Hagey, D. W., de Jong, O. G., Schiffelers, R. M., Andaloussi, S. E., et al. (2020). Extracellular vesicles as drug delivery systems: why and how? *Adv. Drug Deliv. Rev.* 159, 332–343. doi:10.1016/j.addr.2020.04.004

Farges, J.-C., Alliot-Licht, B., Renard, E., Ducret, M., Gaudin, A., Smith, A. J., et al. (2015). Dental pulp defence and repair mechanisms in dental caries. *Mediat. Inflamm.* 2015, 230251–230316. doi:10.1155/2015/230251

Fletcher, S., Honeyman, K., Fall, A. M., Harding, P. L., Johnsen, R. D., Steinhaus, J. P., et al. (2007). Morpholino oligomer-mediated exon skipping averts the onset of dystrophic pathology in the mdx mouse. *Mol. Ther.* 15 (9), 1587–1592. doi:10.1038/sj.mt.6300245

French, K. C., Antonyak, M. A., and Cerione, R. A. (2017). Extracellular vesicle docking at the cellular port: extracellular vesicle binding and uptake. *Semin. Cell Dev. Biol.* 67, 48–55. doi:10.1016/j.semcdb.2017.01.002

Fuhrmann, G., Serio, A., Mazo, M., Nair, R., and Stevens, M. M. (2015). Active loading into extracellular vesicles significantly improves the cellular uptake and photodynamic effect of porphyrins. *J. Control. Release* 205, 35–44. doi:10.1016/j.jconrel.2014.11.029

Fukuta, T., Nishikawa, A., and Kogure, K. (2020). Low level electricity increases the secretion of extracellular vesicles from cultured cells. *Biochem. Biophysics Rep.* 21, 100713. doi:10.1016/j.bbrep.2019.100713

Gao, X., Ran, N., Dong, X., Zuo, B., Yang, R., Zhou, Q., et al. (2018). Anchor peptide captures, targets, and loads exosomes of diverse origins for diagnostics and therapy. *Sci. Transl. Med.* 10 (444), eaat0195. doi:10.1126/scitranslmed.aat0195

Ge, S., Mrozik, K. M., Menicanin, D., Gronthos, S., and Bartold, P. M. (2012). Isolation and characterization of mesenchymal stem cell-like cells from healthy and inflamed gingival tissue: potential use for clinical therapy. *Regen. Med.* 7 (6), 819–832. doi:10.2217/rme.12.61

Ghiroldi, A., Piccoli, M., Cirillo, F., Monasky, M. M., Ciconte, G., Pappone, C., et al. (2018). Cell-based therapies for cardiac regeneration: a comprehensive review of past and ongoing strategies. *Int. J. Mol. Sci.* 19 (10), 3194. doi:10.3390/ijms19103194

Gnecchi, M., He, H., Liang, O. D., Melo, L. G., Morello, F., Mu, H., et al. (2005). Paracrine action accounts for marked protection of ischemic heart by Akt-modified mesenchymal stem cells. *Nat. Med.* 11 (4), 367–368. doi:10.1038/nm0405-367

Guo, S., Li, K., Hu, B., Li, C., Zhang, M., Hussain, A., et al. (2021). Membrane-destabilizing ionizable lipid empowered imaging-guided siRNA delivery and cancer treatment. *Explor. (Beijing)* 1 (1), 35–49. doi:10.1002/exp.20210008

Gupta, D., Wiklander, O. P. B., Görgens, A., Conceição, M., Corso, G., Liang, X., et al. (2021). Amelioration of systemic inflammation via the display of two different decoy protein receptors on extracellular vesicles. *Nat. Biomed. Eng.* 5 (9), 1084–1098. doi:10.1038/s41551-021-00792-z

Haney, M. J., Klyachko, N. L., Zhao, Y., Gupta, R., Plotnikova, E. G., He, Z., et al. (2021). Corrigendum to "Exosomes as drug delivery vehicles for Parkinson's disease therapy" [Journal of Controlled Release 207, (2015) 18-30]. *J. Control. Release* 339, 232–234. doi:10.1016/j.jconrel.2021.09.027

Haney, M. J., Klyachko, N. L., Zhao, Y., Gupta, R., Plotnikova, E. G., He, Z., et al. (2015). Exosomes as drug delivery vehicles for Parkinson's disease therapy. *J. Control. Release* 207, 18–30. doi:10.1016/j.jconrel.2015.03.033

Hao, D., Lu, L., Song, H., Duan, Y., Chen, J., Carney, R., et al. (2022). Engineered extracellular vesicles with high collagen-binding affinity present superior *in situ* retention and therapeutic efficacy in tissue repair. *Theranostics* 12 (13), 6021–6037. doi:10.7150/thno.70448

Hao, D., Swindell, H. S., Ramasubramanian, L., Liu, R., Lam, K. S., Farmer, D. L., et al. (2020). Extracellular matrix mimicking nanofibrous scaffolds modified with mesenchymal stem cell-derived extracellular vesicles for improved vascularization. *Front. Bioeng. Biotechnol.* 8, 633. doi:10.3389/fbioe.2020.00633

He, C., Zheng, S., Luo, Y., and Wang, B. (2018). Exosome theranostics: biology and translational medicine. *Theranostics* 8 (1), 237–255. doi:10.7150/thno.21945

Hettich, B. F., Bader, J. J., and Leroux, J.-C. (2022). Encapsulation of hydrophilic compounds in small extracellular vesicles: loading capacity and impact on vesicle functions. *Adv. Healthc. Mater.* 11 (5), e2100047. doi:10.1002/adhm.202100047

Hood, J. L. (2016). Post isolation modification of exosomes for nanomedicine applications. *Nanomedicine Lond. Engl.* 11 (13), 1745–1756. doi:10.2217/nnm-2016-0102

Hoshino, A., Costa-Silva, B., Shen, T.-L., Rodrigues, G., Hashimoto, A., Tesic Mark, M., et al. (2015). Tumour exosome integrins determine organotropic metastasis. *Nature* 527 (7578), 329–335. doi:10.1038/nature15756

Hu, X., Zhong, Y., Kong, Y., Chen, Y., Feng, J., and Zheng, J. (2019). Lineage-specific exosomes promote the odontogenic differentiation of human dental pulp stem cells (DPSCs) through TGFβ1/smads signaling pathway via transfer of microRNAs. *Stem Cell Res. Ther.* 10 (1), 170. doi:10.1186/s13287-019-1278-x

Hu, Y., Wang, Z., Fan, C., Gao, P., Wang, W., Xie, Y., et al. (2023). Human gingival mesenchymal stem cell-derived exosomes cross-regulate the Wnt/β-catenin and NF-κB signalling pathways in the periodontal inflammation microenvironment. *J. Clin. Periodontology* 50, 796–806. doi:10.1111/jcpe.13798

Huang, C.-C., Narayanan, R., Alapati, S., and Ravindran, S. (2016). Exosomes as biomimetic tools for stem cell differentiation: applications in dental pulp tissue regeneration. *Biomaterials* 111, 103–115. doi:10.1016/j.biomaterials.2016.09.029

Huang, X., Qiu, W., Pan, Y., Li, J., Chen, Z., Zhang, K., et al. (2021). Exosomes from LPS-stimulated hDPSCs activated the angiogenic potential of HUVECs *in vitro*. *Stem Cells Int.* 2021, 1–15. doi:10.1155/2021/6685307

Hwang, D. W., Choi, H., Jang, S. C., Yoo, M. Y., Park, J. Y., Choi, N. E., et al. (2015). Noninvasive imaging of radiolabeled exosome-mimetic nanovesicle using (99m)Tc-HMPAO. *Sci. Rep.* 5, 15636. doi:10.1038/srep15636

Imai, T., Takahashi, Y., Nishikawa, M., Kato, K., Morishita, M., Yamashita, T., et al. (2015). Macrophage-dependent clearance of systemically administered B16BL6-derived exosomes from the blood circulation in mice. *J. Extracell. Vesicles* 4, 26238. doi:10.3402/jev.v4.26238

Iohara, K., Zheng, L., Ito, M., Tomokiyo, A., Matsushita, K., and Nakashima, M. (2006). Side population cells isolated from porcine dental pulp tissue with self-renewal and multipotency for dentinogenesis, chondrogenesis, adipogenesis, and neurogenesis. *Stem Cells* 24 (11), 2493–2503. doi:10.1634/stemcells.2006-0161

Ivica, A., Ghayor, C., Zehnder, M., Valdec, S., and Weber, F. E. (2020). Pulp-derived exosomes in a fibrin-based regenerative root filling material. *J. Clin. Med.* 9 (2), 491. doi:10.3390/jcm9020491

Jarmalavičiūtė, A., Tunaitis, V., Pivoraitė, U., Venalis, A., and Pivoriūnas, A. (2015). Exosomes from dental pulp stem cells rescue human dopaminergic neurons from 6-hydroxy-dopamine-induced apoptosis. *Cytotherapy* 17 (7), 932–939. doi:10.1016/j.jcyt.2014.07.013

Jia, G., Han, Y., An, Y., Ding, Y., He, C., Wang, X., et al. (2018). NRP-1 targeted and cargo-loaded exosomes facilitate simultaneous imaging and therapy of glioma *in vitro* and *in vivo*. *Biomaterials* 178, 302–316. doi:10.1016/j.biomaterials.2018.06.029

Johnsen, K. B., Gudbergsson, J. M., Skov, M. N., Christiansen, G., Gurevich, L., Moos, T., et al. (2016). Evaluation of electroporation-induced adverse effects on adipose-derived stem cell exosomes. *Cytotechnology* 68 (5), 2125–2138. doi:10.1007/s10616-016-9952-7

Kamerkar, S., LeBleu, V. S., Sugimoto, H., Yang, S., Ruivo, C. F., Melo, S. A., et al. (2017). Exosomes facilitate therapeutic targeting of oncogenic KRAS in pancreatic cancer. *Nature* 546 (7659), 498–503. doi:10.1038/nature22341

Kanchanapally, R., Deshmukh, S. K., Chavva, S. R., Tyagi, N., Srivastava, S. K., Patel, G. K., et al. (2019). Drug-loaded exosomal preparations from different cell types exhibit distinctive loading capability, yield, and antitumor efficacies: a comparative analysis. *Int. J. Nanomedicine* 14, 531–541. doi:10.2147/IJN.S191313

Kaukua, N., Shahidi, M. K., Konstantinidou, C., Dyachuk, V., Kaucka, M., Furlan, A., et al. (2014). Glial origin of mesenchymal stem cells in a tooth model system. *Nature* 513 (7519), 551–554. doi:10.1038/nature13536

Keller, M. D., Ching, K. L., Liang, F.-X., Dhabaria, A., Tam, K., Ueberheide, B. M., et al. (2020). Decoy exosomes provide protection against bacterial toxins. *Nature* 579 (7798), 260–264. doi:10.1038/s41586-020-2066-6

Kim, M. S., Haney, M. J., Zhao, Y., Mahajan, V., Deygen, I., Klyachko, N. L., et al. (2016). Development of exosome-encapsulated paclitaxel to overcome MDR in cancer cells. *Nanomedicine Nanotechnol. Biol. Med.* 12 (3), 655–664. doi:10.1016/j.nano.2015.10.012

Kim, S., Kang, J. H., Nguyen Cao, T. G., Kang, S. J., Jeong, K., Kang, H. C., et al. (2022). Extracellular vesicles with high dual drug loading for safe and efficient combination chemo-phototherapy. *Biomaterials Sci.* 10 (11), 2817–2830. doi:10.1039/d1bm02005f

Kojima, R., Bojar, D., Rizzi, G., Hamri, G.C.-E., El-Baba, M. D., Saxena, P., et al. (2018). Designer exosomes produced by implanted cells intracerebrally deliver therapeutic cargo for Parkinson's disease treatment. *Nat. Commun.* 9 (1), 1305. doi:10.1038/s41467-018-03733-8

Kolar, M. K., Itte, V. N., Kingham, P. J., Novikov, L. N., Wiberg, M., and Kelk, P. (2017). The neurotrophic effects of different human dental mesenchymal stem cells. *Sci. Rep.* 7 (1), 12605. doi:10.1038/s41598-017-12969-1

Kooijmans, S. A. A., Aleza, C. G., Roffler, S. R., van Solinge, W. W., Vader, P., and Schiffelers, R. M. (2016a). Display of GPI-anchored anti-EGFR nanobodies on extracellular vesicles promotes tumour cell targeting. *J. Extracell. Vesicles* 5, 31053. doi:10.3402/jev.v5.31053

Kooijmans, S. a.A., Fliervoet, L. a.L., van der Meel, R., Fens, M. H. a.M., Heijnen, H. F. G., van Bergen En Henegouwen, P. M. P., et al. (2016b). PEGylated and targeted extracellular vesicles display enhanced cell specificity and circulation time. *J. Control. Release* 224, 77–85. doi:10.1016/j.jconrel.2016.01.009

Kooijmans, S. A. A., Gitz-Francois, J. J. J. M., Schiffelers, R. M., and Vader, P. (2018). Recombinant phosphatidylserine-binding nanobodies for targeting of extracellular vesicles to tumor cells: a plug-and-play approach. *Nanoscale* 10 (5), 2413–2426. doi:10.1039/c7nr06966a

Kooijmans, S. A. A., Vader, P., van Dommelen, S. M., van Solinge, W. W., and Schiffelers, R. M. (2012). Exosome mimetics: a novel class of drug delivery systems. *Int. J. Nanomedicine* 7, 1525–1541. doi:10.2147/IJN.S29661

Kugeratski, F. G., McAndrews, K. M., and Kalluri, R. (2021). Multifunctional applications of engineered extracellular vesicles in the treatment of cancer. *Endocrinology* 162 (3), bqaa250. doi:10.1210/endocr/bqaa250

Lai, C. P., Mardini, O., Ericsson, M., Prabhakar, S., Maguire, C., Chen, J. W., et al. (2014). Dynamic biodistribution of extracellular vesicles *in vivo* using a multimodal imaging reporter. *ACS Nano* 8 (1), 483–494. doi:10.1021/nn404945r

Lässer, C., Jang, S. C., and Lötvall, J. (2018). Subpopulations of extracellular vesicles and their therapeutic potential. *Mol. Aspects Med.* 60, 1–14. doi:10.1016/j.mam.2018.02.002

Lathwal, S., Yerneni, S. S., Boye, S., Muza, U. L., Takahashi, S., Sugimoto, N., et al. (2021). Engineering exosome polymer hybrids by atom transfer radical polymerization. *Proc. Natl. Acad. Sci. U. S. A.* 118 (2), e2020241118. doi:10.1073/pnas.2020241118

Lazar, S., Mor, S., Chen, J., Hao, D., and Wang, A. (2021). Bioengineered extracellular vesicle-loaded bioscaffolds for therapeutic applications in regenerative medicine. *Extracell. Vesicles Circ. Nucl. Acids* 2, 175–178. doi:10.20517/evcna.2021.10

Lazar, S. V., Mor, S., Wang, D., Goldbloom-Helzner, L., Clark, K., Hao, D., et al. (2022). Engineering extracellular vesicles for Alzheimer's disease: an emerging cell-free approach for earlier diagnosis and treatment. *WIREs Mech. Dis.* 14 (2), e1541. doi:10.1002/wsbm.1541

Lener, T., Gimona, M., Aigner, L., Börger, V., Buzas, E., Camussi, G., et al. (2015). Applying extracellular vesicles based therapeutics in clinical trials - an ISEV position paper. *J. Extracell. Vesicles* 4, 30087. doi:10.3402/jev.v4.30087

Liang, Y., Duan, L., Lu, J., and Xia, J. (2021). Engineering exosomes for targeted drug delivery. *Theranostics* 11 (7), 3183–3195. doi:10.7150/thno.52570

Li, J., Ju, Y., Liu, S., Fu, Y., and Zhao, S. (2021). Exosomes derived from lipopolysaccharide-preconditioned human dental pulp stem cells regulate Schwann cell migration and differentiation. *Connect. Tissue Res.* 62 (3), 277–286. doi:10.1080/03008207.2019.1694010

Li, R., Li, Y., Wu, Y., Zhao, Y., Chen, H., Yuan, Y., et al. (2018). Heparin-poloxamer thermosensitive hydrogel loaded with bFGF and NGF enhances peripheral nerve regeneration in diabetic rats. *Biomaterials* 168, 24–37. doi:10.1016/j.biomaterials.2018.03.044

Li, Y., Yang, Y.-Y., Ren, J.-L., Xu, F., Chen, F.-M., and Li, A. (2017). Exosomes secreted by stem cells from human exfoliated deciduous teeth contribute to functional recovery after traumatic brain injury by shifting microglia M1/M2 polarization in rats. *Stem Cell Res. Ther.* 8 (1), 198. doi:10.1186/s13287-017-0648-5

Liang, X., Niu, Z., Galli, V., Howe, N., Zhao, Y., Wiklander, O. P. B., et al. (2022). Extracellular vesicles engineered to bind albumin demonstrate extended circulation time and lymph node accumulation in mouse models. *J. Extracell. Vesicles* 11 (7), e12248. doi:10.1002/jev2.12248

Liang, Y., Xu, X., Li, X., Xiong, J., Li, B., Duan, L., et al. (2020). Chondrocyte-targeted MicroRNA delivery by engineered exosomes toward a cell-free osteoarthritis therapy. *ACS Appl. Mater. interfaces* 12 (33), 36938–36947. doi:10.1021/acsami.0c10458

Liao, W., Du, Y., Zhang, C., Pan, F., Yao, Y., Zhang, T., et al. (2019). Exosomes: the next generation of endogenous nanomaterials for advanced drug delivery and therapy. *Acta Biomater.* 86, 1–14. doi:10.1016/j.actbio.2018.12.045

Lim, G. T., You, D. G., Han, H. S., Lee, H., Shin, S., Oh, B. H., et al. (2021). Bioorthogonally surface-edited extracellular vesicles based on metabolic glycoengineering for CD44-mediated targeting of inflammatory diseases. *J. Extracell. Vesicles* 10 (5), e12077. doi:10.1002/jev2.12077

Lin, Y., Wu, J., Gu, W., Huang, Y., Tong, Z., Huang, L., et al. (2018). Exosome-liposome hybrid nanoparticles deliver CRISPR/Cas9 system in MSCs. *Adv. Sci. (Weinheim, Baden-Wurttemberg, Ger.* 5 (4), 1700611. doi:10.1002/advs.201700611

Liu, C., and Su, C. (2019). Design strategies and application progress of therapeutic exosomes. *Theranostics* 9 (4), 1015–1028. doi:10.7150/thno.30853

Liu, J., Ruan, J., Weir, M. D., Ren, K., Schneider, A., Wang, P., et al. (2019). Periodontal bone-ligament-cementum regeneration via scaffolds and stem cells. *Cells* 8 (6), 537. doi:10.3390/cells8060537

Liu, Y., Zhuang, X., Yu, S., Yang, N., Zeng, J., Liu, X., et al. (2021). Exosomes derived from stem cells from apical papilla promote craniofacial soft tissue regeneration by enhancing Cdc42-mediated vascularization. *Stem Cell Res. Ther.* 12 (1), 76. doi:10.1186/s13287-021-02151-w

Longatti, A., Schindler, C., Collinson, A., Jenkinson, L., Matthews, C., Fitzpatrick, L., et al. (2018). High affinity single-chain variable fragments are specific and versatile targeting motifs for extracellular vesicles. *Nanoscale* 10 (29), 14230–14244. doi:10.1039/c8nr03970d

Ma, S., Wu, J., Hu, H., Mu, Y., Zhang, L., Zhao, Y., et al. (2022). Novel fusion peptides deliver exosomes to modify injectable thermo-sensitive hydrogels for bone regeneration. *Mater. Today Bio* 13, 100195. doi:10.1016/j.mtbio.2021.100195

Mai, Z., Chen, H., Ye, Y., Hu, Z., Sun, W., Cui, L., et al. (2021). Translational and clinical applications of dental stem cell-derived exosomes. *Front. Genet.* 12, 750990. doi:10.3389/fgene.2021.750990

Mantesso, A., and Sharpe, P. (2009). Dental stem cells for tooth regeneration and repair. *Expert Opin. Biol. Ther.* 9 (9), 1143–1154. doi:10.1517/14712590903103795

Mao, Q., Nguyen, P. D., Shanti, R. M., Shi, S., Shakoori, P., Zhang, Q., et al. (2019). Gingiva-derived mesenchymal stem cell-extracellular vesicles activate Schwann cell repair phenotype and promote nerve regeneration. *Tissue Eng. Part A* 25 (11-12), 887–900. doi:10.1089/ten.TEA.2018.0176

Matsumoto, A., Takahashi, Y., Chang, H.-Y., Wu, Y.-W., Yamamoto, A., Ishihama, Y., et al. (2020). Blood concentrations of small extracellular vesicles are determined by a balance between abundant secretion and rapid clearance. *J. Extracell. Vesicles* 9 (1), 1696517. doi:10.1080/20013078.2019.1696517

Matsumura, S., Minamisawa, T., Suga, K., Kishita, H., Akagi, T., Ichiki, T., et al. (2019). Subtypes of tumour cell-derived small extracellular vesicles having differently externalized phosphatidylserine. *J. Extracell. Vesicles* 8 (1), 1579541. doi:10.1080/20013078.2019.1579541

Maugeri, M., Nawaz, M., Papadimitriou, A., Angerfors, A., Camponeschi, A., Na, M., et al. (2019). Linkage between endosomal escape of LNP-mRNA and loading into EVs for transport to other cells. *Nat. Commun.* 10 (1), 4333. doi:10.1038/s41467-019-12275-6

Mayo, V., Sawatari, Y., Huang, C.-Y. C., and Garcia-Godoy, F. (2014). Neural crest-derived dental stem cells--where we are and where we are going. *J. Dent.* 42 (9), 1043–1051. doi:10.1016/j.jdent.2014.04.007

Mendt, M., Kamerkar, S., Sugimoto, H., McAndrews, K. M., Wu, C.-C., Gagea, M., et al. (2018). Generation and testing of clinical-grade exosomes for pancreatic cancer. *JCI insight* 3 (8), e99263. doi:10.1172/jci.insight.99263

Mentkowski, K. I., Snitzer, J. D., Rusnak, S., and Lang, J. K. (2018). Therapeutic potential of engineered extracellular vesicles. *Aaps J.* 20 (3), 50. doi:10.1208/s12248-018-0211-z

Meyer, C., Losacco, J., Stickney, Z., Li, L., Marriott, G., and Lu, B. (2017). Pseudotyping exosomes for enhanced protein delivery in mammalian cells. *Int. J. Nanomedicine* 12, 3153–3170. doi:10.2147/IJN.S133430

Montagna, C., Petris, G., Casini, A., Maule, G., Franceschini, G. M., Zanella, I., et al. (2018). VSV-G-Enveloped vesicles for traceless delivery of CRISPR-cas9. *Mol. Ther. Nucleic Acids* 12, 453–462. doi:10.1016/j.omtn.2018.05.010

Morishita, M., Takahashi, Y., Nishikawa, M., Sano, K., Kato, K., Yamashita, T., et al. (2015). Quantitative analysis of tissue distribution of the B16BL6-derived exosomes using a streptavidin-lactadherin fusion protein and iodine-125-labeled biotin derivative after intravenous injection in mice. *J. Pharm. Sci.* 104 (2), 705–713. doi:10.1002/jps.24251

Morishita, M., Takahashi, Y., Nishikawa, M., and Takakura, Y. (2017). Pharmacokinetics of exosomes-an important factor for elucidating the biological roles of exosomes and for the development of exosome-based therapeutics. *J. Pharm. Sci.* 106 (9), 2265–2269. doi:10.1016/j.xphs.2017.02.030

Morsczeck, C., Götz, W., Schierholz, J., Zeilhofer, F., Kühn, U., Möhl, C., et al. (2005). Isolation of precursor cells (PCs) from human dental follicle of wisdom teeth. *Matrix Biol.* 24 (2), 155–165. doi:10.1016/j.matbio.2004.12.004

Nagelkerke, A., Ojansivu, M., van der Koog, L., Whittaker, T. E., Cunnane, E. M., Silva, A. M., et al. (2021). Extracellular vesicles for tissue repair and regeneration: evidence, challenges and opportunities. *Adv. Drug Deliv. Rev.* 175, 113775. doi:10.1016/j.addr.2021.04.013

Nakao, Y., Fukuda, T., Zhang, Q., Sanui, T., Shinjo, T., Kou, X., et al. (2021). Exosomes from TNF-α-treated human gingiva-derived MSCs enhance M2 macrophage polarization and inhibit periodontal bone loss. *Acta Biomater.* 122, 306–324. doi:10.1016/j.actbio.2020.12.046

Nakase, I., and Futaki, S. (2015). Combined treatment with a pH-sensitive fusogenic peptide and cationic lipids achieves enhanced cytosolic delivery of exosomes. *Sci. Rep.* 5, 10112. doi:10.1038/srep10112

Narbute, K., Piļipenko, V., Pupure, J., Dzirkale, Z., Jonavičė, U., Tunaitis, V., et al. (2019). Intranasal administration of extracellular vesicles derived from human teeth stem cells improves motor symptoms and normalizes tyrosine hydroxylase expression in the substantia nigra and striatum of the 6-hydroxydopamine-treated rats. *Stem Cells Transl. Med.* 8 (5), 490–499. doi:10.1002/sctm.18-0162

Nasirishargh, A., Kumar, P., Ramasubramanian, L., Clark, K., Hao, D., Lazar, S. V., et al. (2021). Exosomal microRNAs from mesenchymal stem/stromal cells: biology and applications in neuroprotection. *World J. Stem Cells* 13 (7), 776–794. doi:10.4252/wjsc.v13.i7.776

Ohno, S.-i., Takanashi, M., Sudo, K., Ueda, S., Ishikawa, A., Matsuyama, N., et al. (2013). Systemically injected exosomes targeted to EGFR deliver antitumor microRNA to breast cancer cells. *Mol. Ther.* 21 (1), 185–191. doi:10.1038/mt.2012.180

Oude Blenke, E., Klaasse, G., Merten, H., Plückthun, A., Mastrobattista, E., and Martin, N. I. (2015). Liposome functionalization with copper-free "click chemistry. *J. Control. Release* 202, 14–20. doi:10.1016/j.jconrel.2015.01.027

Parada, N., Romero-Trujillo, A., Georges, N., and Alcayaga-Miranda, F. (2021). Camouflage strategies for therapeutic exosomes evasion from phagocytosis. *J. Adv. Res.* 31, 61–74. doi:10.1016/j.jare.2021.01.001

Pham, T. C., Jayasinghe, M. K., Pham, T. T., Yang, Y., Wei, L., Usman, W. M., et al. (2021). Covalent conjugation of extracellular vesicles with peptides and nanobodies for targeted therapeutic delivery. *J. Extracell. Vesicles* 10 (4), e12057. doi:10.1002/jev2.12057

Phan, J., Kumar, P., Hao, D., Gao, K., Farmer, D., and Wang, A. (2018). Engineering mesenchymal stem cells to improve their exosome efficacy and yield for cell-free therapy. *J. Extracell. Vesicles* 7 (1), 1522236. doi:10.1080/20013078.2018.1522236

Phinney, D. G., and Pittenger, M. F. (2017). Concise review: MSC-derived exosomes for cell-free therapy. *Stem Cells Dayt. Ohio)* 35 (4), 851–858. doi:10.1002/stem.2575

Piffoux, M., Silva, A. K. A., Wilhelm, C., Gazeau, F., and Tareste, D. (2018). Modification of extracellular vesicles by fusion with liposomes for the design of personalized biogenic drug delivery systems. *ACS Nano* 12 (7), 6830–6842. doi:10.1021/acsnano.8b02053

Pittenger, M. F., Le Blanc, K., Phinney, D. G., and Chan, J. K. Y. (2015). MSCs: scientific support for multiple therapies. *Stem Cells Int.* 2015, 1–2. doi:10.1155/2015/280572

Pizzicannella, J., Gugliandolo, A., Orsini, T., Fontana, A., Ventrella, A., Mazzon, E., et al. (2019). Engineered extracellular vesicles from human periodontal-ligament stem cells increase VEGF/VEGFR2 expression during bone regeneration. *Front. Physiology* 10, 512. doi:10.3389/fphys.2019.00512

Podolak, I., Galanty, A., and Sobolewska, D. (2010). Saponins as cytotoxic agents: a review. *Phytochem. Rev.* 9 (3), 425–474. doi:10.1007/s11101-010-9183-z

Poggio, M., Hu, T., Pai, C.-C., Chu, B., Belair, C. D., Chang, A., et al. (2019). Suppression of exosomal PD-L1 induces systemic anti-tumor immunity and memory. *Cell* 177 (2), 414–427.e13. doi:10.1016/j.cell.2019.02.016

Qi, H., Liu, C., Long, L., Ren, Y., Zhang, S., Chang, X., et al. (2016). Blood exosomes endowed with magnetic and targeting properties for cancer therapy. *ACS Nano* 10 (3), 3323–3333. doi:10.1021/acsnano.5b06939

Qin, Y., Sun, R., Wu, C., Wang, L., and Zhang, C. (2016). Exosome: a novel approach to stimulate bone regeneration through regulation of osteogenesis and angiogenesis. *Int. J. Mol. Sci.* 17 (5), 712. doi:10.3390/ijms17050712

Qiu, G., Zheng, G., Ge, M., Wang, J., Huang, R., Shu, Q., et al. (2019). Functional proteins of mesenchymal stem cell-derived extracellular vesicles. *Stem Cell Res. Ther.* 10 (1), 359. doi:10.1186/s13287-019-1484-6

Rädler, J., Gupta, D., Zickler, A., and Andaloussi, S. E. (2023). Exploiting the biogenesis of extracellular vesicles for bioengineering and therapeutic cargo loading. *Mol. Ther.* 31 (5), 1231–1250. doi:10.1016/j.ymthe.2023.02.013

Ramasubramanian, L., Du, S., Gidda, S., Bahatyrevich, N., Hao, D., Kumar, P., et al. (2022). Bioengineering extracellular vesicles for the treatment of cardiovascular diseases. *Adv. Biol. (Weinh)* 6 (10), e2200087. doi:10.1002/adbi.202200087

Rana, S., Yue, S., Stadel, D., and Zöller, M. (2012). Toward tailored exosomes: the exosomal tetraspanin web contributes to target cell selection. *Int. J. Biochem. Cell Biol.* 44 (9), 1574–1584. doi:10.1016/j.biocel.2012.06.018

Rozier, P., Maria, A., Goulabchand, R., Jorgensen, C., Guilpain, P., and Noel, D. (2018). Mesenchymal stem cells in systemic sclerosis: allogenic or autologous approaches for therapeutic use? *Front. Immunol.* 9, 2938. doi:10.3389/fimmu.2018.02938

Sato, Y. T., Umezaki, K., Sawada, S., Mukai, S.-a., Sasaki, Y., Harada, N., et al. (2016). Engineering hybrid exosomes by membrane fusion with liposomes. *Sci. Rep.* 6, 21933. doi:10.1038/srep21933

Sawada, S.-I., Sato, Y. T., Kawasaki, R., Yasuoka, J.-I., Mizuta, R., Sasaki, Y., et al. (2020). Nanogel hybrid assembly for exosome intracellular delivery: effects on endocytosis and fusion by exosome surface polymer engineering. *Biomaterials Sci.* 8 (2), 619–630. doi:10.1039/c9bm01232j

Segawa, K., and Nagata, S. (2015). An apoptotic 'eat me' signal: phosphatidylserine exposure. *Trends Cell Biol.* 25 (11), 639–650. doi:10.1016/j.tcb.2015.08.003

Seo, B. M., Miura, M., Gronthos, S., Bartold, P. M., Batouli, S., Brahim, J., et al. (2004). Investigation of multipotent postnatal stem cells from human periodontal ligament. *Lancet* 364 (9429), 149–155. doi:10.1016/s0140-6736(04)16627-0

Shabbir, A., Cox, A., Rodriguez-Menocal, L., Salgado, M., and Van Badiavas, E. (2015). Mesenchymal stem cell exosomes induce proliferation and migration of normal and chronic wound fibroblasts, and enhance angiogenesis *in vitro*. *Stem Cells Dev.* 24 (14), 1635–1647. doi:10.1089/scd.2014.0316

Sharif, S., Ghahremani, M. H., and Soleimani, M. (2018). Delivery of exogenous miR-124 to glioblastoma multiform cells by wharton's jelly mesenchymal stem cells decreases cell proliferation and migration, and confers chemosensitivity. *Stem Cell Rev. Rep.* 14 (2), 236–246. doi:10.1007/s12015-017-9788-3

Shen, Z., Kuang, S., Zhang, Y., Yang, M., Qin, W., Shi, X., et al. (2020). Chitosan hydrogel incorporated with dental pulp stem cell-derived exosomes alleviates periodontitis in mice via a macrophage-dependent mechanism. *Bioact. Mater.* 5 (4), 1113–1126. doi:10.1016/j.bioactmat.2020.07.002

Shi, W., Guo, S., Liu, L., Liu, Q., Huo, F., Ding, Y., et al. (2020). Small extracellular vesicles from lipopolysaccharide-preconditioned dental follicle cells promote periodontal regeneration in an inflammatory microenvironment. *ACS biomaterials Sci. Eng.* 6 (10), 5797–5810. doi:10.1021/acsbiomaterials.0c00882

Shiraishi, K., and Yokoyama, M. (2019). Toxicity and immunogenicity concerns related to PEGylated-micelle carrier systems: a review. *Sci. Technol. Adv. Mater.* 20 (1), 324–336. doi:10.1080/14686996.2019.1590126

Smyth, T., Kullberg, M., Malik, N., Smith-Jones, P., Graner, M. W., and Anchordoquy, T. J. (2015). Biodistribution and delivery efficiency of unmodified tumor-derived exosomes. *J. Control. Release* 199, 145–155. doi:10.1016/j.jconrel.2014.12.013

Smyth, T., Petrova, K., Payton, N. M., Persaud, I., Redzic, J. S., Graner, M. W., et al. (2014). Surface functionalization of exosomes using click chemistry. *Bioconjugate Chem.* 25 (10), 1777–1784. doi:10.1021/bc500291r

Subra, C., Laulagnier, K., Perret, B., and Record, M. (2007). Exosome lipidomics unravels lipid sorting at the level of multivesicular bodies. *Biochimie* 89 (2), 205–212. doi:10.1016/j.biochi.2006.10.014

Suk, J. S., Xu, Q., Kim, N., Hanes, J., and Ensign, L. M. (2016). PEGylation as a strategy for improving nanoparticle-based drug and gene delivery. *Adv. Drug Deliv. Rev.* 99, 28–51. doi:10.1016/j.addr.2015.09.012

Sun, D., Zhuang, X., Xiang, X., Liu, Y., Zhang, S., Liu, C., et al. (2010). A novel nanoparticle drug delivery system: the anti-inflammatory activity of curcumin is enhanced when encapsulated in exosomes. *Mol. Ther.* 18 (9), 1606–1614. doi:10.1038/mt.2010.105

Swanson, W. B., Gong, T., Zhang, Z., Eberle, M., Niemann, D., Dong, R., et al. (2020). Controlled release of odontogenic exosomes from a biodegradable vehicle mediates dentinogenesis as a novel biomimetic pulp capping therapy. *J. Control. Release* 324, 679–694. doi:10.1016/j.jconrel.2020.06.006

Takahashi, Y., Nishikawa, M., Shinotsuka, H., Matsui, Y., Ohara, S., Imai, T., et al. (2013). Visualization and *in vivo* tracking of the exosomes of murine melanoma B16-BL6 cells in mice after intravenous injection. *J. Biotechnol.* 165 (2), 77–84. doi:10.1016/j.jbiotec.2013.03.013

Tamura, R., Uemoto, S., and Tabata, Y. (2017). Augmented liver targeting of exosomes by surface modification with cationized pullulan. *Acta Biomater.* 57, 274–284. doi:10.1016/j.actbio.2017.05.013

Tang, M., Chen, Y., Li, B., Sugimoto, H., Yang, S., Yang, C., et al. (2021). Therapeutic targeting of STAT3 with small interference RNAs and antisense oligonucleotides embedded exosomes in liver fibrosis. *FASEB J.* 35 (5), e21557. doi:10.1096/fj.202002777RR

Tatullo, M., Marrelli, M., and Paduano, F. (2015). The regenerative medicine in oral and maxillofacial surgery: the most important innovations in the clinical application of mesenchymal stem cells. *Int. J. Med. Sci.* 12 (1), 72–77. doi:10.7150/ijms.10706

Tatullo, M. (2019). Science is not a social opinion. *Dent. J. (Basel)* 7 (2), 34. doi:10.3390/dj7020034

Taylor, C. A., Braza, D., Rice, J. B., and Dillingham, T. (2008). The incidence of peripheral nerve injury in extremity trauma. *Am. J. Phys. Med. Rehabilitation* 87 (5), 381–385. doi:10.1097/PHM.0b013e31815e6370

Théry, C., Witwer, K. W., Aikawa, E., Alcaraz, M. J., Anderson, J. D., Andriantsitohaina, R., et al. (2018). Minimal information for studies of extracellular vesicles 2018 (MISEV2018): a position statement of the International Society for Extracellular Vesicles and update of the MISEV2014 guidelines. *J. Extracell. Vesicles* 7 (1), 1535750. doi:10.1080/20013078.2018.1535750

Tian, T., Zhang, H.-X., He, C.-P., Fan, S., Zhu, Y.-L., Qi, C., et al. (2018). Surface functionalized exosomes as targeted drug delivery vehicles for cerebral ischemia therapy. *Biomaterials* 150, 137–149. doi:10.1016/j.biomaterials.2017.10.012

Tomar, G. B., Srivastava, R. K., Gupta, N., Barhanpurkar, A. P., Pote, S. T., Jhaveri, H. M., et al. (2010). Human gingiva-derived mesenchymal stem cells are superior to bone marrow-derived mesenchymal stem cells for cell therapy in regenerative medicine. *Biochem. Biophys. Res. Commun.* 393 (3), 377–383. doi:10.1016/j.bbrc.2010.01.126

Valadi, H., Ekström, K., Bossios, A., Sjöstrand, M., Lee, J. J., and Lötvall, J. O. (2007). Exosome-mediated transfer of mRNAs and microRNAs is a novel mechanism of genetic exchange between cells. *Nat. Cell Biol.* 9 (6), 654–659. doi:10.1038/ncb1596

Wang, D., Wang, Y., Tian, W., and Pan, J. (2019). Advances of tooth-derived stem cells in neural diseases treatments and nerve tissue regeneration. *Cell Prolif.* 52 (3), e12572. doi:10.1111/cpr.12572

Wang, J., Li, W., Lu, Z., Zhang, L., Hu, Y., Li, Q., et al. (2017). The use of RGD-engineered exosomes for enhanced targeting ability and synergistic therapy toward angiogenesis. *Nanoscale* 9 (40), 15598–15605. doi:10.1039/c7nr04425a

Wang, M., Li, J., Ye, Y., He, S., and Song, J. (2020). SHED-derived conditioned exosomes enhance the osteogenic differentiation of PDLSCs via Wnt and BMP signaling *in vitro*. *Differ. Res. Biol. Divers.* 111, 1–11. doi:10.1016/j.diff.2019.10.003

Wang, Q., Yu, J., Kadungure, T., Beyene, J., Zhang, H., and Lu, Q. (2018). ARMMs as a versatile platform for intracellular delivery of macromolecules. *Nat. Commun.* 9 (1), 960. doi:10.1038/s41467-018-03390-x

Watson, D. C., Bayik, D., Srivatsan, A., Bergamaschi, C., Valentin, A., Niu, G., et al. (2016). Efficient production and enhanced tumor delivery of engineered extracellular vesicles. *Biomaterials* 105, 195–205. doi:10.1016/j.biomaterials.2016.07.003

Wei, H., Chen, J., Wang, S., Fu, F., Zhu, X., Wu, C., et al. (2019). A nanodrug consisting of doxorubicin and exosome derived from mesenchymal stem cells for osteosarcoma treatment *in vitro*. *Int. J. Nanomedicine* 14, 8603–8610. doi:10.2147/IJN.S218988

Wei, J., Song, Y., Du, Z., Yu, F., Zhang, Y., Jiang, N., et al. (2020). Exosomes derived from human exfoliated deciduous teeth ameliorate adult bone loss in mice through promoting osteogenesis. *J. Mol. Histology* 51 (4), 455–466. doi:10.1007/s10735-020-09896-3

Whitney, M. A., Crisp, J. L., Nguyen, L. T., Friedman, B., Gross, L. A., Steinbach, P., et al. (2011). Fluorescent peptides highlight peripheral nerves during surgery in mice. *Nat. Biotechnol.* 29 (4), 352–356. doi:10.1038/nbt.1764

Wiklander, O. P. B., Nordin, J. Z., O'Loughlin, A., Gustafsson, Y., Corso, G., Mäger, I., et al. (2015). Extracellular vesicle *in vivo* biodistribution is determined by cell source, route of administration and targeting. *J. Extracell. Vesicles* 4, 26316. doi:10.3402/jev.v4.26316

Wiklander, O. P. B., Brennan, M. Á., Lötvall, J., Breakefield, X. O., and El Andaloussi, S. (2019). Advances in therapeutic applications of extracellular vesicles. *Sci. Transl. Med.* 11 (492), eaav8521. doi:10.1126/scitranslmed.aav8521

Wu, J., Chen, L., Wang, R., Song, Z., Shen, Z., Zhao, Y., et al. (2019). Exosomes secreted by stem cells from human exfoliated deciduous teeth promote alveolar bone defect repair through the regulation of angiogenesis and osteogenesis. *ACS Biomater. Sci. Eng.* 5 (7), 3561–3571. doi:10.1021/acsbiomaterials.9b00607

Wu, M., Liu, X., Li, Z., Huang, X., Guo, H., Guo, X., et al. (2021a). SHED aggregate exosomes shuttled miR-26a promote angiogenesis in pulp regeneration via TGF-β/SMAD2/3 signalling. *Cell Prolif.* 54 (7), e13074. doi:10.1111/cpr.13074

Wu, P., Zhang, B., Ocansey, D. K. W., Xu, W., and Qian, H. (2021b). Extracellular vesicles: a bright star of nanomedicine. *Biomaterials* 269, 120467. doi:10.1016/j.biomaterials.2020.120467

Xian, X., Gong, Q., Li, C., Guo, B., and Jiang, H. (2018). Exosomes with highly angiogenic potential for possible use in pulp regeneration. *J. Endod.* 44 (5), 751–758. doi:10.1016/j.joen.2017.12.024

Xiao, C., Song, F., Zheng, Y. L., Lv, J., Wang, Q. F., and Xu, N. (2019). Exosomes in head and neck squamous cell carcinoma. *Front. Oncol.* 9, 894. doi:10.3389/fonc.2019.00894

Xie, L., Chen, J., Ren, X., Zhang, M., Thuaksuban, N., Nuntanaranont, T., et al. (2021). Alteration of circRNA and lncRNA expression profile in exosomes derived from periodontal ligament stem cells undergoing osteogenic differentiation. *Archives Oral Biol.* 121, 104984. doi:10.1016/j.archoralbio.2020.104984

Xie, X., Wu, H., Li, M., Chen, X., Xu, X., Ni, W., et al. (2019). Progress in the application of exosomes as therapeutic vectors in tumor-targeted therapy. *Cytotherapy* 21 (5), 509–524. doi:10.1016/j.jcyt.2019.01.001

Yáñez-Mó, M., Siljander, P. R., Andreu, Z., Zavec, A. B., Borràs, F. E., Buzas, E. I., et al. (2015). Biological properties of extracellular vesicles and their physiological functions. *J. Extracell. Vesicles* 4, 27066. doi:10.3402/jev.v4.27066

Yang, B., Qiu, Y., Zhou, N., Ouyang, H., Ding, J., Cheng, B., et al. (2017a). Application of stem cells in oral disease therapy: progresses and perspectives. *Front. Physiol.* 8, 197. doi:10.3389/fphys.2017.00197

Yang, Y., Hong, Y., Nam, G. H., Chung, J. H., Koh, E., and Kim, I. S. (2017b). Virus-Mimetic fusogenic exosomes for direct delivery of integral membrane proteins to target cell membranes. *Adv. Mater* 29 (13), 1605604. doi:10.1002/adma.201605604

Ye, Z., Zhang, T., He, W., Jin, H., Liu, C., Yang, Z., et al. (2018). Methotrexate-loaded extracellular vesicles functionalized with therapeutic and targeted peptides for the treatment of glioblastoma multiforme. *ACS Appl. Mater. interfaces* 10 (15), 12341–12350. doi:10.1021/acsami.7b18135

Yerneni, S. S., Lathwal, S., Shrestha, P., Shirwan, H., Matyjaszewski, K., Weiss, L., et al. (2019). Rapid on-demand extracellular vesicle augmentation with versatile oligonucleotide tethers. *ACS Nano* 13 (9), 10555–10565. doi:10.1021/acsnano.9b04651

Yin, L., Liu, X., Shi, Y., Ocansey, D. K. W., Hu, Y., Li, X., et al. (2020). Therapeutic advances of stem cell-derived extracellular vesicles in regenerative medicine. *Cells* 9 (3), 707. doi:10.3390/cells9030707

You, D. G., Lim, G. T., Kwon, S., Um, W., Oh, B. H., Song, S. H., et al. (2021). Metabolically engineered stem cell-derived exosomes to regulate macrophage heterogeneity in rheumatoid arthritis. *Sci. Adv.* 7 (23), eabe0083. doi:10.1126/sciadv.abe0083

Yuan, Q., Li, X.-D., Zhang, S.-M., Wang, H.-W., and Wang, Y.-L. (2021). Extracellular vesicles in neurodegenerative diseases: insights and new perspectives. *Genes & Dis.* 8 (2), 124–132. doi:10.1016/j.gendis.2019.12.001

Zha, Y., Li, Y., Lin, T., Chen, J., Zhang, S., and Wang, J. (2021). Progenitor cell-derived exosomes endowed with VEGF plasmids enhance osteogenic induction and vascular remodeling in large segmental bone defects. *Theranostics* 11 (1), 397–409. doi:10.7150/thno.50741

Zhang, Z., Dombroski, J. A., and King, M. R. (2020a). Engineering of exosomes to target cancer metastasis. *Cell. Mol. Bioeng.* 13 (1), 1–16. doi:10.1007/s12195-019-00607-x

Zhang, Z., Shuai, Y., Zhou, F., Yin, J., Hu, J., Guo, S., et al. (2020b). PDLSCs regulate angiogenesis of periodontal ligaments via VEGF transferred by exosomes in periodontitis. *Int. J. Med. Sci.* 17 (5), 558–567. doi:10.7150/ijms.40918

Zhou, H., Li, X., Yin, Y., He, X.-T., An, Y., Tian, B.-M., et al. (2020). The proangiogenic effects of extracellular vesicles secreted by dental pulp stem cells derived from periodontally compromised teeth. *Stem Cell Res. Ther.* 11 (1), 110. doi:10.1186/s13287-020-01614-w

Zhu, Q., Ling, X., Yang, Y., Zhang, J., Li, Q., Niu, X., et al. (2019). Embryonic stem cells-derived exosomes endowed with targeting properties as chemotherapeutics delivery vehicles for glioblastoma therapy. *Adv. Sci. (Weinheim, Baden-Wurttemberg, Ger.* 6 (6), 1801899. doi:10.1002/advs.201801899

Zhuang, X., Ji, L., Jiang, H., Liu, Y., Liu, X., Bi, J., et al. (2020). Exosomes derived from stem cells from the apical papilla promote dentine-pulp complex regeneration by inducing specific dentinogenesis. *Stem Cells Int.* 2020, 1–10. doi:10.1155/2020/5816723

Zickler, A. M., and El Andaloussi, S. (2020). Functional extracellular vesicles aplenty. *Nat. Biomed. Eng.* 4 (1), 9–11. doi:10.1038/s41551-019-0507-z

Zipkin, M. (2020). Big pharma buys into exosomes for drug delivery. *Nat. Biotechnol.* 38 (11), 1226–1228. doi:10.1038/s41587-020-0725-7

Zipkin, M. (2019). Exosome redux. *Nat. Biotechnol.* 37 (12), 1395–1400. doi:10.1038/s41587-019-0326-5

Glossary

Extracellular vesicle (EV)	membranous, lipid-bilayer enclosed vesicle released by cells that may contain full-length transmembrane proteins, soluble proteins in the vesicular lumen, as well as RNA and DNA, depending on vesicle type.
Mesenchymal stem cells (MSCs)	multipotent stromal cells that can differentiate into a variety of cell types, including osteoblasts (bone cells), chondrocytes (cartilage cells), myocytes (muscle cells) and adipocytes (fat cells which give rise to marrow adipose tissue).
Human bone marrow (hBM)	a semi-solid tissue found within the cancellous portions of bones. It is composed of hematopoietic cells, marrow adipose tissue, and supportive stromal cells.
Dental pulp stem cells (DPSCs)	DPSCs are a mesenchymal type of stem cells inside dental pulp. DPSCs have osteogenic and chondrogenic potential in vitro and can differentiate into dentin, in vivo and also differentiate into dentin-pulp-like complex.
Icrovesicle	type of small to large 150–1000-nm ectosome derived by direct outward budding of the plasma membrane followed by pinching off of the vesicle.
Stem cells from exfoliated deciduous teeth (SHEDs)	exfoliated human deciduous tooth contains multipotent stem cells.
Periodontal ligament stem cells (PDLSCs)	It is an adult stem cell derived from periodontal ligament tissue and has the basic characteristics of an adult stem cell.
Stem cells from apical papilla (SCAPs)	residing in the apical papilla of immature permanent teeth represent a novel population of dental MSCs that possess the properties of high proliferative potential, the self-renewal ability, and low immunogenicity.
Gingival MSCs (GMSCs)	It is an undifferentiated cell present in human gingival mesenchymal tissue with the ability of self-renewal, multidirectional differentiation and immune regulation.
Dentin sialophosphoprotein (DSPP)	It is a non-collagenous protein of dentin, mainly expressed by dentin cells, and is currently recognized as a tooth-specific protein.
Dentin matrix acidic phosphoprotein 1 (DMP1)	It is an extracellular matrix protein and a member of the small integrin-binding ligand N-linked glycoprotein family.
miRNA	small noncoding RNA that exerts post-transcriptional regulation of gene expression through RNA silencing.
Glycosylphosphatidylinositol (GPI)	a phosphoglyceride that can be attached to the C-terminus of a protein during posttranslational modification. The resulting GPI-anchored proteins play key roles in a wide variety of biological processes.
Indocyanine green(ICG)	a medical dye used in tests to help determine the cardiac (heart) output, liver function, and blood flow in the liver.
Azide (N3)	Azide anion is a pseudohalide anion. It has a role as a mitochondrial respiratory-chain inhibitor. It is a conjugate base of a hydrogen azide.
Rabies virus glycoprotein (RVG)	It is the only structural protein exposed outside the rabies virus membrane.
Blood–brain barrier (BBB)	It refers to the barriers between plasma and brain cells formed by the walls of brain capillaries and neuroglia and between plasma and cerebrospinal fluid formed by the choroid plexus, which prevent certain substances, mostly harmful, from entering the brain tissue from the bloodstream.
Lysosome-associated membrane protein 2b (Lamp2b)	It is a member of the lysosome-associated membrane protein (LAMP) family, which is mainly localized in lysosomes and endosomes, with a small amount on the cell surface, and is also abundantly expressed on the surface of exosomes.
Chondrocyte-affinity peptide (CAP)	It belongs to a kind of bioactive peptide, which consists of specific amino acid sequences, and can be used for affinity effect on some key factors of cartilage tissue engineering through identification and screening to improve the effectiveness of cartilage tissue engineering repair.
Phosphatidylserine (PS)	It is a component of the cell membrane of neuronal cells and activates protein kinase C .
Scavenger Receptor Class A family (SR-A)	Based on the structure and origin of scavenger receptor molecules, they have been categorized into eight subfamilies from A-H, with class A scavenger receptors being one of these classes.
Polyethylene glycol (PEG)	It is a polymerization of polyethylene oxide and water.
Exosome(EXO)	type of small 30–150-nm EV derived from the release of ILVs upon fusion of an MVE or amphisome with the plasma membrane.
Intraluminal vesicle (ILV)	small vesicle that buds from the limiting membrane into the endosomal lumen of developing MVEs.
Apoptotic extracellular vesicle	class of EVs ranging in size from 200 to 1000 nm apoptotic vesicles to 1 to 5-μm apoptotic bodies; generated when cells undergo programmed cell death (apoptosis).
Major histocompatibility complex (MHC)	group of genes that code for proteins found on the surfaces of cells that help the immune system recognize foreign substances.
single-chain Fragment Variable (scFV)	small-sized artificial constructs composed of the immunoglobulin heavy and light chain variable regions connected by a peptide linker

frontiers | Frontiers in Bioengineering and Biotechnology

TYPE Original Research
PUBLISHED 17 November 2023
DOI 10.3389/fbioe.2023.1282128

OPEN ACCESS

EDITED BY
Junxi Wu,
University of Strathclyde, United Kingdom

REVIEWED BY
Giovanni Solitro,
Louisiana State University Health Shreveport, United States
Jan Kubicek,
VSB-Technical University of Ostrava, Czechia

*CORRESPONDENCE
Changjun Yun,
✉ yunchangjun@sina.com

RECEIVED 23 August 2023
ACCEPTED 08 November 2023
PUBLISHED 17 November 2023

CITATION
Yun C, Qian W, Zhang J, Zhang W and Lv J (2023), Biomechanics of PHILOS plates in Vancouver B1 periprosthetic femoral fracture.
Front. Bioeng. Biotechnol. 11:1282128.
doi: 10.3389/fbioe.2023.1282128

Biomechanics of PHILOS plates in Vancouver B1 periprosthetic femoral fracture

Changjun Yun[1,2]*, Wenjie Qian[1,2], Jie Zhang[1,2], Wen Zhang[3] and Jinpeng Lv[4]

[1]Departmeut of Orthopaedics, The Affiliated Wujin Hospital of Jiangsu University, Changzhou, China, [2]The Wujin Clinical College of Xuzhou Medical University, Changzhou, China, [3]Orthopedic Institute, Soochow University, Suzhou, China, [4]School of Pharmacy, Changzhou University, Changzhou, China

Objective: To investigate the clinical efficacy of PHILOS plates in the treatment of Vancouver B1 periprosthetic femoral fracture (PFF) and to validate its biomechanical reliability via finite element analysis and mechanical testing on the Synbone femoral models.

Methods: Ten males and eight females with Vancouver B1 PFF who underwent PHILOS plate fixation between September 2017 and January 2022 were selected. The average age was 72.61 ± 8.19 years, with a range of 57–86 years old. X-ray films were taken to assess the fracture healing situation around the femoral prosthesis as well as the position of the PHILOS plates and femoral prosthesis. Two different plates (the PHILOS plate and the Cable GTR plate) were used for fixation, and the differences in biomechanical stability of the two fixation methods were compared using finite element analysis and mechanical testing on the Synbone femoral models to validate the biomechanical dependability of the PHILOS plate.

Results: All 18 cases were followed for at least 1 year, as a result. The average period of follow-up was 17 months, ranging from 12 to 36 months. At the most recent follow-up, Harris scores for the hip joints of patients ranged from 82 to 89, with an average score of 86. The X-rays revealed that all fractures surrounding the femoral prosthesis had healed and that there was no looseness in the femoral prosthesis. None of the PHILOS license plates had expired. All patients were able to perform full-load walking, and pain and claudication in affected limbs were significantly reduced. Finite element analysis and mechanical testing of the Synbone femoral model revealed that the fixation effect of the PHILOS group was superior to that of the Cable group; consequently, PHILOS plates can be used to effectively fix fractures around the proximal femoral prosthesis.

Conclusion: PHILOS plates are initially used in the treatment of Vancouver B1 PFF, which may be a good choice due to their simpler operation, lower medical costs, and satisfactory clinical efficacy.

KEYWORDS

femur, periprosthetic fracture, PHILOS plate, internal fixation, finite element analysis, biomechanics

Introduction

In China's society, the incidence of myeloid joint diseases and fractures has increased as the aging process has accelerated. Artificial joint replacement is an effective treatment (Bhattacharyya et al., 2007; Bulatović et al., 2017; Gitajn et al., 2017), and periprosthetic femoral fracture (PFF) is one of the most severe complications following hip replacement (Caruso et al., 2018). Consequently, the Vancouver B1 fracture is the most prevalent type of PFF (Sah et al., 2010; Wähnert et al., 2017), accounting for approximately 75% of all PFF cases (O'Connell et al., 2018), with a nonunion rate of 42% after conservative treatment (Moloney et al., 2016; Stoffel et al., 2020). The subsequent treatment of the aforementioned complications is difficult and ineffective. Increasing evidence demonstrates that early surgery, early rehabilitation, and early weight-bearing exercise can effectively reduce patient mortality (Caruso et al., 2018; Agostini et al., 2022). Currently, it is believed that surgery is the best treatment for the aforementioned complications, but there is no clear consensus regarding the optimal treatment strategy for them.

Common surgical treatments for Vancouver B1 fractures include locking plate internal fixation, cable (steel wire) internal fixation, and locking plate and cable internal fixation (Graham et al., 2015; Khan et al., 2017; Min et al., 2018). Otherwise, some investigators have used hook plates (Lenz et al., 2016) and distal femoral locking plates (Takahashi et al., 2021) to fixate Vancouver B1 fractures, but the results have been unsatisfactory. Since September 2017, the Department of Orthopaedics at Wujin Hospital, affiliated with Jiangsu University, has creatively applied PHILOS plates to the treatment of Vancouver B1 PFF, achieving excellent clinical efficacy and social benefits.

The mechanical stability of PHILOS plates in Vancouver B1 fractures is unknown. We used the three-dimensional finite element method and the mechanical test of the Synbone femoral model, the mechanical stability of PHILOS and the Cable Ready GTR titanium cable hook plate system was compared in the treatment of Vancouver B1 PFF, thereby providing a mechanical theoretical basis for the use of PHILOS in the treatment of Vancouver B1 PFF.

Data and methods

Clinical data

In this study, there were 18 cases (18 hips), including 10 males and 8 females. Their average age was 72.61 ± 8.19 years, with a range of 57–86 years old. There were 11 cases of left hip arthroplasty and 7 cases of right hip arthroplasty among the 18 cases, and all hips were Vancouver B1. All 18 cases had PFF following hip arthroplasty. The initial hip replacement was performed due to a femoral neck fracture, and the DePuy total biological hip system with a Corail stem was utilized. In terms of the causes of the injuries, three cases were the result of automobile accidents, while the remaining cases were the result of falls. From 5 months to 14 years and 2 months had passed since the last hip replacement surgery, with a mean of 62.34 ± 58.28 months. Before the injury, none of the patients exhibited obvious limitations in hip joint mobility and were capable of caring for themselves. 3 cases were simultaneously complicated by diabetes, hypertension, and renal insufficiency; 4 cases were simultaneously complicated by diabetes and hypertension; and 10 cases were simultaneously complicated by hypertension. The hospital's ethics committee approved the study, and all patients signed informed consent forms. All of the surgical procedures on the patients were performed by the same surgeon and team. The operation was performed under general anesthesia, and the patients were in a healthy lateral position. The modified Harding approach from the initial incision was utilized to expose the fractured end around the PFF, and the hip joint was extracted to evaluate the stability of the femoral prosthesis. As with the Vancouver B1 PFF, the fracture end was exposed and repositioned, and periosteal peeling should be kept to a minimum. 1-2 double-strand M650 steel wires were used for binding and fixing, and a PHILOS plate (Chuangsheng, Changzhou, China) of the proper length was then placed (Figure 1).

Data scanning and modeling

A 34-year-old male volunteer with a height of 173 cm and a weight of 65 kg was chosen to undergo continuous thin-layer spiral CT scanning from the hip joint to the middle tibia. The voltage was set at 120 kV, the current was 150 mA, and the scanning layer thickness was 0.625 mm. The femoral model was reconstructed using the threshold segmentation, regional growth, and 3D reconstruction functions of Mimics21.0 software (Belgium Materialise Company), while the cancellous bone model was created using the 3-matic software (Belgium Materialise Company). The solid model of the femur was created using the software Geomagic 12.0 (Raindrop, United States). The Medical Ethics Committee of Wujin Hospital, affiliated with Jiangsu University, has approved this study (No. 2021-SR-002). The participants have signed the informed consent form.

Fixed system modeling

The femur model was imported into Creo Parametric 5.0 (PTC, United States) software. In Creo software, the PHILOS and Cable Ready GTR titanium cable hook plate systems and the femoral stem prosthesis model were created, and the internal fixation was assembled with the femoral model to complete the grouping model of fixation after Vancouver B1 PFF (Figure 2).

Processing of grid model

The assembled model was imported into the Hypermesh software, and a component was created for each model component. The Vancouver B1 PFF was simulated at the middle and upper positions of the femoral shaft, and the femoral shaft was then cut with a fracture line gap of approximately 0.2 mm to complete the finite element model of two fixation methods after Vancouver B1 PFF, namely, PHILOS fixation (PHILOS group) and Cable plate fixation (Cable group). Contacts were defined between all interfaces using contact element. Plate and bone were considered as "No separation condition" and all the other interfaces were set as "Bonded condition" (Raja et al., 2020).

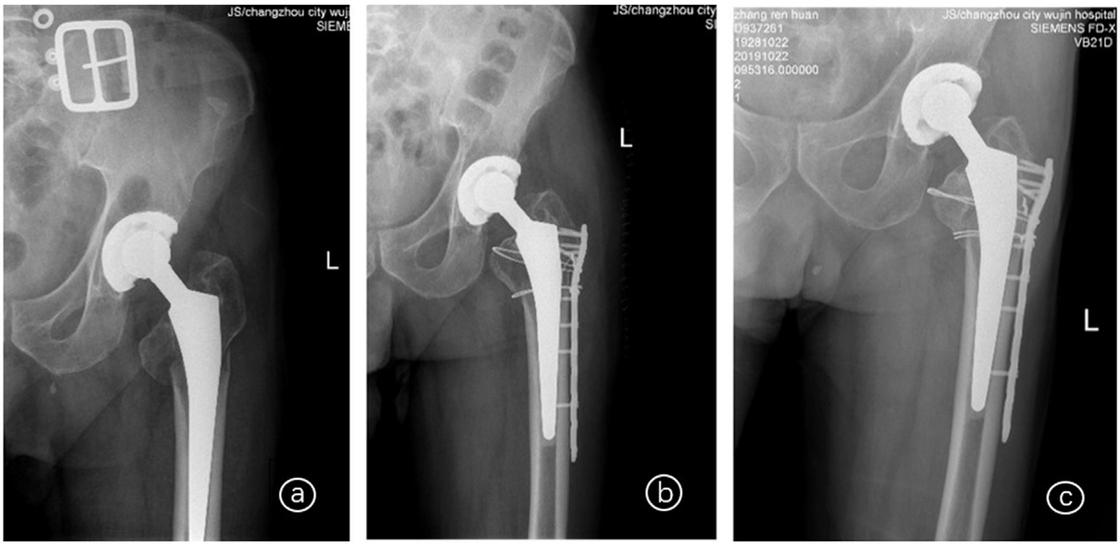

FIGURE 1
X-rays of an 86-year-old female patient with Vancouver B1 PFF who underwent left hip arthroplasty 14 years and 2 months ago; ⓐ Before surgery; ⓑ 5 days after surgery; ⓒ 1 year and 9 months after surgery.

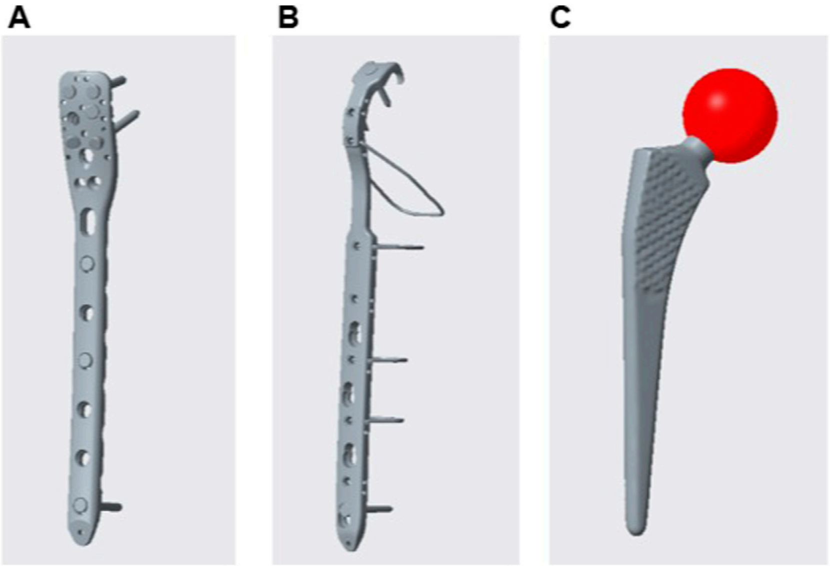

FIGURE 2
Internal fixation model: PHILOS **(A)**; Cable steel plate **(B)**; Femoral stem **(C)**; PHILOS is a proximal humeral locking plate.

The femoral model is divided into the cortical and cancellous bone by the requirements of the literature. The volume mesh was divided using tetrahedron Solid 187 element mesh after the necessary editing and processing for each part. Figure 3 depicts that the PHILOS group had 1649969 nodes and 1034123 elements, whereas the Cable group had 1977961 nodes and 1236660 elements.

Material property assignment

The corresponding material proper tie were assigned to each component of the model in Hypermesh software (Table 1), based on the literatures (Ma et al., 2014; Mei et al., 2014; Liang et al., 2017; Tianye et al., 2019; Cui et al., 2020).

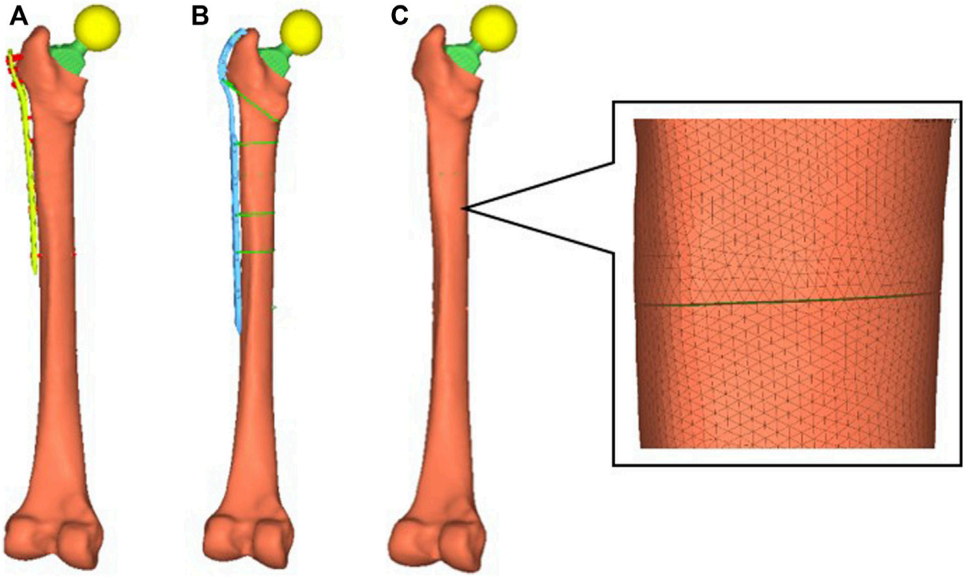

FIGURE 3
Model grouping. In PFF, the femoral shaft was situated at the end of the femoral stem. Two groups of models fractured at the same location, and PHILOS fixation and cable fixation, respectively, were performed. PHILOS group **(A)**; Cable group **(B)**; fracture position of the model **(C)**; Cable Ready GTR is a titanium cable hook plate system; PHILOS is a proximal humeral locking plate.

TABLE 1 Elastic modulus and poisson's ratio of each material.

Material	Elastic modulus (MPa)	Poisson's ratio
Cortical bone	16,800.0	0.3
Cancellous bone	840.0	0.3
Femoral head	110,000.0	0.3
Femoral stem	110,000.0	0.3
Bone plate	110,000.0	0.3
Titanium cable	110,000.0	0.3

Boundary conditions and loads

The femoral stress states are extremely complex. Under normal movement conditions, such as normal gait, the maximum load through the hip joint is approximately 2.6–4.1 times (Chang et al., 2015) an individual's body weight. The load on the hip joint increases with an increase in step speed, step length, or body weight. Furthermore, the muscle force on the femur is extremely complex. Taylor et al. (1996). Believed that the muscle loading of the femur model was subject to numerous uncertainties, including the selection of muscle quantities, gravity, and the direction of the muscle force loading. Particularly, it is nearly impossible to simulate the load accurately and completely under dynamic conditions. To simplify the analysis and highlight the fixation effect of the two groups of models, the femoral prosthesis head was used to simulate the cases of a human standing on two legs, standing on one leg, and ascending stairs, with vertical forces of 700, 1,400, and 2,100 N, respectively (Cui et al., 2020; Wang et al., 2020). All distal lymph nodes below the femoral condyle were fully constrained.

Effectiveness validation

To verify the efficacy of the model, a complete femoral model was constructed initially. Material properties were assigned based on research (Papini et al., 2007). The model's lower end is fully constrained, and a vertical load of 1,500 N was applied to the femoral head. The model was analyzed using Ansys19.0 software (ANSYS Company, United States), and the results were compared to those in the literature.

Biomechanical evaluation of a synthetic bone model

Six Type 2,200 femur models from Synbone were purchased. The femoral trochanter was modeled with a Vancouver B1 fracture and then divided into two groups that were fixed with PHILOS and Cable hook plates, respectively (Figure 4). According to the cited sources, a new set of femoral test fixtures was created. The distal end of the femur was placed in a custom fixture to simulate the contact force vector during the single-leg standing phase, and the lower end was embedded in dental support powder with an abducted femur and an 8° force line. The upper end of the femoral stem was embedded with bone cement, preventing the femur from moving in all directions during the loading process. Utilizing an Instron E10000 tensile torsional biaxial universal material mechanics testing machine, the test was conducted. The software for static testing was Bluehill 2.0, and the software for dynamic testing was WaveMatrix.

Adjustments were made to the distance between the upper and lower indenters so that the femur was perfectly vertical, with an 11° angle between the femoral shaft and the force line. The cycle test

FIGURE 4
Synbone femoral model with PHILOS and Cable GTR plates implanted for fixation, respectively.

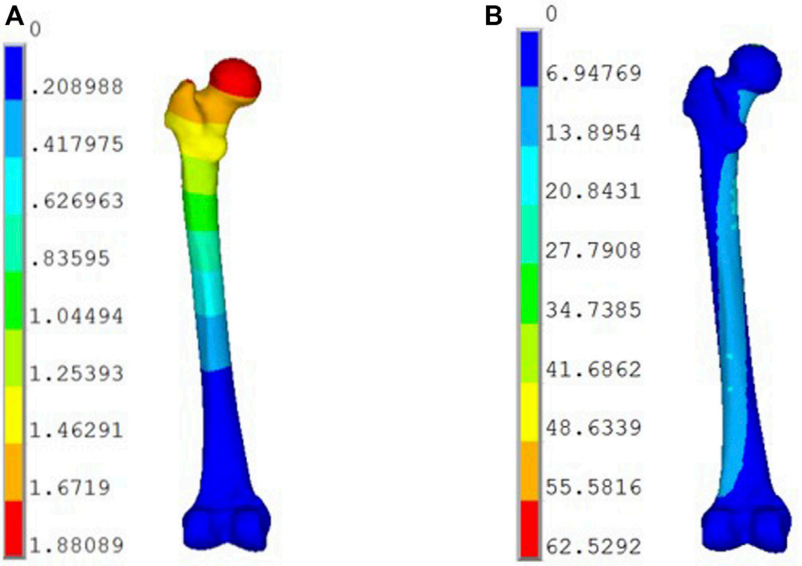

FIGURE 5
Displacement and stress distribution of the femur under physiological conditions: **(A)** Displacement Distribution (mm); **(B)** Stress Distribution (MPa).

was conducted initially with 0–500 N, 2 Hz, and 2,000 cycles (Pletka et al., 2011; Kemker et al., 2017). After the fatigue test, the load-displacement curve was recorded, and the dislocation displacement of the fracture line was measured. The displacement changes of the femur before and after the test cycle were analyzed statistically. The primary objective of this step was to eliminate the space between the femur and the fixture, as well as the displacement of the femoral neck fracture slip. After the cycle was completed, compression loads of 700 N, 1,400 N, and 2,100 N were applied at a rate of 3 mm/min until the model was damaged or the compression load reached 2,100 N (approximately three times the weight of a 70 kg adult). The load-displacement curve was recorded, and the fixation effect of each group's models was compared by calculating stiffness.

Evaluation indexes

After surgery, patients were followed up on as outpatients in the first, third, sixth, and 12th months, and then every 6 months. At each follow-up, X-rays were taken to determine if the fracture had healed, if the internal fixation had failed, and if the femoral prosthesis was loose. Each follow-up's Harris score was recorded. The total Harris score is 100 points, with 44 points assigned to pain, 47 to function, 4 to deformity, and 5 to mobility. ≥ 90 indicates Excellent, 80–89 indicates Good, 70–79 indicates Acceptable, and <70 indicates Poor.

Ansys 19.0 simulation software was used to observe the distribution of the Von Mises maximum stress and the maximum deformation in models of the two groups subjected to 700 N, 1,400 N, and 2,100 N load conditions. Perioperative data were recorded. The Harris score of the

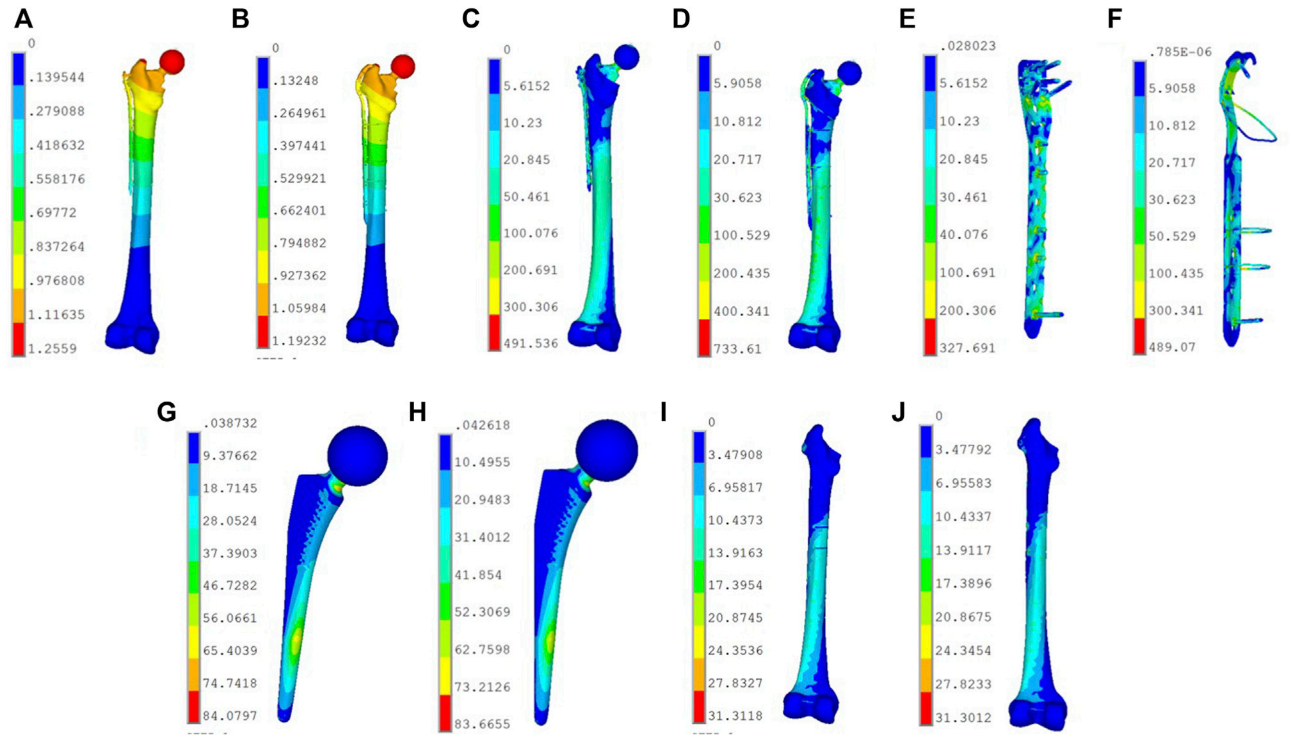

FIGURE 6
Displacement and stress distribution of PHILOS group and Cable group models. **(A)** Deformation distribution of PHILOS group (mm). **(B)** Deformation distribution of Cable group (mm). The maximum deformation of this two models in the Cable group under 700 N load. **(C)** Stress distribution of PHILOS group (MPa). **(D)** Stress distribution of Cable group (MPa). Stress distribution distribution of the overall model in the two groups under 2,100 N load. **(E)** Stress distribution of the plate in PHILOS group (MPa). Stress distribution distribution of fixed steel plate in the PHILOS group under 1,400 N load, with the maximum stress peak value of 327.69 Mpa, which is distributed on the fixed screw. **(F)** Stress distribution of the plate in Cable group (MPa). Stress distribution distribution of fixed steel plate in Cable group under 1,400 N load, with the maximum stress peak value of 489.07 Mpa, which is distributed on the second titanium wire under the fracture. **(G)** Stress distribution of femoral stem in PHILOS group (MPa). Stress distribution distribution of the femoral stem in the PHILOS group under 700 N load, with the maximum stress peak value of 83.45 Mpa, which is distributed at the neck of the femoral shaft. **(H)** Stress distribution of femoral stem in Cable group (MPa). Stress distribution distribution of the femoral stem in the Cable group under 700 N load, with the maximum stress peak value of 84.08 MPa, which is distributed at the neck of the femoral shaft. **(I)** Stress distribution of the bone model in PHILOS group (MPa). Stress distribution distribution of the femoral shaft in the PHILOS group under 700 N load, with the maximum stress peak value of 31.31 Mpa, which is distributed on the inner side of the femoral shaft below the fracture line. **(J)** Stress distribution of the bone model in Cable group (MPa). Stress distribution distribution of the femoral shaft in the Cable group under 700 N load, with the maximum stress peak value of 31.31 Mpa, which is distributed on the inner side of the femoral shaft below the fracture line.

hip joint was used to evaluate clinical outcomes and imaging tests were performed routinely. It was determined if the fracture had healed, if the internal fixation had failed, and if the femoral prosthesis was loose.

Statistical analysis

The SPSS 13.0 program was utilized for statistical data analysis. The measurement information was represented as ($\bar{x}\pm s$). One-way ANOVA was used to examine Harris scores at various follow-up periods. $p < 0.05$ indicates a statistically significant difference.

Results

Clinical results

In this study, 18 patients successfully underwent surgery; the duration of the operation ranged from 65 to 130 min, with an average of 105.00 ± 25.52 min; and intraoperative bleeding ranged from 150 to 650 mL, with an average of 303.39 ± 120.80 mL. There was no intraoperative blood transfusion. After surgery, there were no serious complications such as infection or deep vein thrombosis. All patients were monitored for a period of 12–36 months, with a mean of 17.29 ± 3.86 months. The difference is statistically significant (P0.001) from 1 month after surgery (54.33 ± 5.50 points) to 3 months after surgery (67.67 ± 5.32 points) to 6 months after surgery (78.67 ± 3.33 points) to 12 months after surgery (84.67 ± 3.08 points) to the last follow-up (86.00 ± 2.28 points); the difference is statistically significant ($p < 0.001$). At the most recent follow-up, 15 patients were able to walk without assistance, while 3 patients required a walker for full-load walking. In terms of imaging examination, successive callus was observed at the end of the PFF 3 months after surgery, and the PFF attained the bone healing standard 6 months after surgery without invalidation of the PHILOS plate and looseness of the femoral prosthesis.

TABLE 2 Stress value (MPa) of the femur and femoral stem in models of PHILOS group and cable group under 700 N, 1400 N, and 2100 N loads.

Load (N) stress on the femur			Stress on the femoral stem	
	PHILOS group	Cable group	PHILOS group	Cable group
700	31.30	31.31	83.67	84.08
1,400	62.62	62.62	166.91	168.16
2,100	93.90	93.94	250.36	252.24

Results of validation

The compression stiffness of the complete model under 1,500 N of pure compression was 0.798 kN/mm (Figure 5), which was very close to the compression stiffness [(0.76 ± 0.26) kN/mm] of the mechanical test reported in the literature (Papini et al., 2007). Taking into account the unique characteristics of each model, the models developed in this experiment were effective.

Maximum deformation of the model

Consistent with the location of load application, the maximum deformation of the models in both groups occurred on the prosthesis ball head. Since the material properties assigned to the femur, prosthesis, and internal fixation system were isotropic, the results demonstrated a linear relationship between the load and the deformation of the models in the two groups. The maximum deformation of the PHILOS group was 3.77 mm when the compression load was 2,100 N, which is greater than that of the Cable group (3.58 mm) (Figures 6A, B). Under a 1,400 N load, the PHILOS group and the Cable group deformed by 2.51 mm and 2.38 mm, respectively. When the load was 700 N, the difference in deformation between the models in the two groups was the greatest, and the maximum deformation in the PHILOS group was 5.8% greater than that in the Cable group (1.19 mm). However, there was no difference in the distribution of deformations on the fixed steel plate between the two groups of 1.05 mm models. It can be concluded that the two model groups possess comparable mechanical stability.

Stress distribution of the models

With an increase in compression load, the model's maximum stress also increased. Under a 2,100 N load, the PHILOS group's maximum peak stress was 491.54 MPa, while the Cable group's was 733.61 MPa (Figures 6C–J). Under three types of loads, the PHILOS group experienced approximately 49.2% less stress than the Cable group. Consequently, the maximum stress peak in the PHILOS group was predominantly distributed at the fourth and fifth fixed ends of the plate, whereas the maximum stress peak in the Cable group was predominantly distributed on the second titanium cable below the fracture line, while the stress on the other titanium cables was lower. According to the analysis of the stress nephogram distribution or stress peak, the stress distribution on the cortical bone, cancellous bone, and femoral shaft of the two groups of models was extremely similar. Nonetheless, the stress distribution on the prosthesis in the Cable group was slightly higher than that in the PHILOS group (Table 2), indicating that the analysis model was primarily scientific.

Biomechanical test of the artificial bone model

After the fatigue test with 0–500 N was completed, the results from the scale plates on both sides of the fracture line indicated that the fracture line displacements in the two groups of specimens were as follows: 1.06 ± 0.47 mm for the PHILOS group and 1.63 ± 0.90 mm for the Cable group (p = 0.615). As determined by the displacement sensors on the indenters, the overall deformations of the specimens were as follows: 1.77 ± 0.55 mm for PHILOS and 1.49 ± 0.53 mm for Cable (p = 0.253).

Following the fatigue test, static compression tests were conducted to apply compression loads of 700 N, 1,400 N, and 2,200 N to the specimens, thereby obtaining the static compression deformation. The compression rigidity was computed. Each group of specimens was examined three times, and the average values were then determined. Following are the values for compression stiffness under 700 N compression: 294.50 ± 89.07 N/mm for the PHILOS group and 275.16 ± 74.87 N/mm for the Cable group (p = 0.716); 233.14 ± 67.08 N/mm for the PHILOS group and 299.97 ± 25.69 N/mm for the Cable group (p = 0.200); 195.76 ± 34.49 N/mm for the PHILOS group and 180.51 ± 65.12 N/mm for the Cable group (p = 0.070).

Discussion

Since 1993, the incidence of periprosthetic fractures after hip arthroplasty has increased from 0.1% to 2.1% (Bulatović et al., 2017). The majority of these fractures occur in elderly patients, who frequently suffer from a variety of chronic diseases and osteoporosis. The Vancouver classification of PFF has treatment implications (Caruso et al., 2018; Agostini et al., 2022). Incision, reduction, and internal fixation are the treatment tenets for type B fractures. However, due to the complexity of the operation and the occurrence of numerous complications, there is no gold standard for the selection of internal fixation, and the surgical effect is debatable. Internal fixation options currently include primarily dynamic compression plate, memory alloy embracing device, steel cable encircling, and locking plate. Tsiridis et al. (2005) utilized a DCP plate to treat 18 cases of Vancouver B PFF, 11 of which were healed at the final follow-up after an average of 13 months. Nonunion was observed in 4 cases, and 3 patients died without observed fracture healing. Bulatović et al. (2017) found that the average hospital stay for patients with Vancouver B PFF was lengthy, and the modified Merle d'Aubigne score was low after surgery. Graham et al. (2015) reported that in biomechanics, the combination of locking nails and steel cable was more advantageous.

Chatziagorou et al. (2019) believed that the reoperation rate of Vancouver B PFF patients treated with conventional plating or locking plating after surgery was identical. Sah et al. (2010) reported that the efficacy of a single locking plate in the treatment of Vancouver B PFF was satisfactory, but they emphasized the importance of soft tissue cuff protection and adequate cortical bone screw fixation. Min et al. (2018) suggested a minimally invasive method for implanting a locking plate to treat Vancouver B1 PFF. This technique resulted in fewer intraoperative complications, and its postoperative imaging examination and clinical efficacy was comparable to those of incision reduction and internal fixation.

Due to the presence of the femoral stem prosthesis in the proximal femoral medullary cavity, implanting crews, particularly bicortical screws, is difficult. These patients are frequently afflicted with osteoporosis, which makes the control of screws extremely difficult. Lunebourg et al. (2015) created a non-locking arc plate with eccentric holes to avoid intramedullary femoral stem prosthesis and achieve bicortical screw fixation, thereby enhancing the fracture end's stability. However, the placement position of the plate was challenging, and the fracture end fixation was not reliable, necessitating customization. Wahnert et al. (2017) demonstrated that the application of double plates in the Vancouver B1 PFF could significantly enhance the structural strength of internal fixation and fracture end stability. Similar clinical research results were reported by O'Connell et al. (2018), but the internal fixation with a double plate has the disadvantages of larger surgical trauma, more bleeding, greater irritation of local soft tissue, and higher medical costs. The biomechanical study by O'Connell et al. (2018) confirmed that Vancouver B1 PFF with osteoporosis was fixed with bicortical screws at the proximal end of the femur, permitting early weight-bearing even without the reinforcement of an allograft bone plate. Stoffel et al. (2020) and Moloney et al. (2016) found that the clinical efficacy of a locking plate combined with an allograft bone plate in the treatment of Vancouver B1 PFF was adequate, but there was a high risk of infection and infectious disease transmission.

The anatomical outline of the lateral side of the proximal femur was quite similar to that of the lateral side of the proximal humerus, as determined by careful examination of the proximal femur's structure. Therefore, we applied the PHILOS plate creatively to Vancouver B1 and BFF PFF. At the proximal end of the PHILOS plate, there are A, B, C, D, and E holes, with a total of 8 locking holes, 1 LCP bonding hole, and 10 suture holes. When a femoral stem prosthesis occupies the proximal femoral medullary cavity, the implantation of sufficient and long locking nails is still possible, and even some locking nails are permitted to be implanted in the bicortical cortex, due to the presence of nine locking holes in different directions at the proximal end of PHILOS. Therefore, even in osteoporosis patients, it can still offer a high pull-out resistance. The presence of the suture hole permits suturing and fixing the fracture piece with blood supply around the fracture end, or transplanting iliac allograft to promote fracture healing, as well as providing auxiliary steel wire perforation fixation to prevent steel wire slip failure and suturing the surrounding muscles and tendons to neutralize muscle force. Multiple long and short locks at the proximal end of the PHILOS plate were staggered on seven patients in this study to fix the fracture end around the femoral prosthesis. Because the fracture end was reliably fixed and the blood supply to the fracture end was safeguarded as much as possible, patients were permitted to descend to the ground shortly after surgery, without serious complications or fracture nonunion. In addition, the Harris scores for postoperative follow-up indicated that the application of the PHILOS plate in Vancouver B1 PFF contributed to a speedy recovery. The patient's hip joint function stabilized 12 months after surgery and could be further enhanced with time extension. PHILOS is a single-locking steel plate with a small implant volume and minimal soft tissue irritation; therefore, double plate fixation, allograft bone plate strengthening fixation, and special steel cable encirclement were not required. Thus, it has clear benefits for controlling medical costs.

The fracture around the proximal femoral prosthesis was simulated using the finite element model of the femur obtained from the two-dimensional continuous CT data of volunteers and medical engineering software such as Mimics, Geomagic, Hypermesh, etc. There were two distinct surgical fixations utilized. Three-dimensional finite element models of two groups of internal fixation were given the same load and constraint conditions to simulate the single-leg standing condition of adult men. In conclusion, the biomechanical properties of various fixation techniques were compared and analyzed. Using the Ansys19.0 software, simulation calculations were performed to observe the maximum stress distribution and maximum deformation of the models in two groups under various load conditions.

Under various loads, the deformation value of the femur-cab group was less than that of the femur-philos group, which indicated that the mechanical stability provided by the femur-cab group was slightly better than that of the femur-philos group. Under various loads, the stress values on the femoral stem and femur of the two groups of models were comparable, indicating that both groups could provide adequate mechanical stability. Regarding the model's stress distribution, the stress of the femur-cab group was significantly higher than that of the femur-philos group, with the majority of the stress being distributed on the second titanium alloy binding wire. The overall conclusion is that the fixation effect of the femur-philos group is superior to that of the femur-cab group, making it a more effective method for PFF. In the range of 0–700 N load, the Philos group demonstrated superior mechanical properties compared to the Cable group; in the range of 700–1,400 N load, the Cable group demonstrated superior mechanical properties compared to the Philos group; and in the range of 1,400–2,100 N load, the Philos group demonstrated superior mechanical properties compared to the Cable group. Thus, under normal body exercise loads, the PHILOS plate's fixation effect is more reliable.

There are still some inadequacies of this study. As the biomechanical test conditions are limited, we cannot take into account the muscle forces around the femur (Amirouche et al., 2016) in the loading process during the biomechanical test and finite element analysis. Bone remodeling is an important clinical parameter in fracture healing and also is one of the major concerns of surgeons. Unfortunately, we have not studied the relationship between fracture healing and the different number of screws on the plate and the position of the screws. Simultaneous simplified methods of screw placement and threading were used for plate fixation, without the consideration of torque and extrusion forces that increase fracture fixation strength (Bronsnick et al., 2015; Mejia et al., 2018; Addevico et al., 2020; Addevico et al., 2021). In recent years, with the development of mechanical and biomechanical techniques (Travascio et al., 2021), the use of coated screws has increased the osteogenic effect, particularly in patients with osteoporosis (Patel et al., 2015), while increasing the screw-to-bone friction, which is critical for implant fixation and implant stability (Bronsnick et al., 2015).

In conclusion, our preliminary study demonstrates that the PHILOS plate can provide stable fixation for the treatment of Vancouver B1 PFF, with the benefits of good fracture healing, simpler operation, lower medical costs, and satisfactory clinical effect. Due to the small number of cases in this study and the brief follow-up durations, the definitive treatment effect must be confirmed on a larger scale.

Data availability statement

The original contributions presented in the study are included in the article/Supplementary material, further inquiries can be directed to the corresponding author.

Ethics statement

The studies involving humans were approved by the Medical Ethics Committee of Wujin Hospital. The studies were conducted in accordance with the local legislation and institutional requirements. The participants provided their written informed consent to participate in this study.

Author contributions

CY: Conceptualization, Funding acquisition, Investigation, Project administration, Supervision, Writing–original draft, Writing–review and editing. WQ: Data curation, Formal Analysis, Methodology, Software, Validation, Writing–original draft. JZ: Resources, Visualization, Writing–original draft. WZ: Methodology, Resources, Software, Supervision, Writing–original draft. JL: Writing–review and editing, Investigation.

Funding

The author(s) declare financial support was received for the research, authorship, and/or publication of this article. This study was sponsored by the Changzhou Science and Technology Program (Grant No. CJ20220011) to CY.

Conflict of interest

The authors declare that the research was conducted in the absence of any commercial or financial relationships that could be construed as a potential conflict of interest.

The author(s) declared that they were an editorial board member of Frontiers, at the time of submission. This had no impact on the peer review process and the final decision.

Publisher's note

References

Addevico, F., Morandi, M., Scaglione, M., and Solitro, G. F. (2020). Screw insertion torque as parameter to judge the fixation. Assessment of torque and pull-out strength in different bone densities and screw-pitches. *Clin. Biomech. (Bristol, Avon)* 72, 130–135. doi:10.1016/j.clinbiomech.2019.12.004

Addevico, F., Solitro, G. F., and Morandi, M. M. (2021). Salvaging pull-out strength in a previously stripped screw site: a comparison of three rescue techniques. *J. Funct. Morphol. Kinesiol* 6 (3), 71. doi:10.3390/jfmk6030071

Agostini, G., Angelini, I., Citarelli, C., Andreani, L., Carmassi, F., Scaglione, M., et al. (2022). Clinical and radiographical outcome after surgical treatment of periprosthetic type B proximal femur fractures: a retrospective study. *Musculoskelet. Surg.* 106 (1), 83–87. doi:10.1007/s12306-020-00676-6

Amirouche, F., Solitro, G., and Walia, A. (2016). No effect of femoral offset on bone implant micromotion in an experimental model. *Orthop. Traumatol. Surg. Res.* 102 (3), 379–385. doi:10.1016/j.otsr.2016.01.010

Bhattacharyya, T., Chang, D., Meigs, J. B., Estok, D. M., and Malchau, H. (2007). Mortality after periprosthetic fracture of the femur. *J. bone Jt. Surg.* 89 (12), 2658–2662. doi:10.2106/jbjs.f.01538

Bronsnick, D., Harold, R. E., Youderian, A., Solitro, G., Amirouche, F., and Goldberg, B. (2015). Can high-friction intraannular material increase screw pullout strength in osteoporotic bone? *Clin. Orthop. Relat. Res.* 473 (3), 1150–1154. doi:10.1007/s11999-014-3975-1

Bulatović, N., Kezunović, M., Vučetić, Č., Abdić, N., Benčić, I., and Čengić, T. (2017). Treatment of periprosthetic femoral fractures after total hip arthroplasty vancouver type B. *Acta Clin. Croat.* 56 (3), 536–543. doi:10.20471/acc.2017.56.03.21

Caruso, G., Milani, L., Marko, T., Lorusso, V., Andreotti, M., and Massari, L. (2018). Surgical treatment of periprosthetic femoral fractures: a retrospective study with functional and radiological outcomes from 2010 to 2016. *Eur. J. Orthop. Surg. traumatology Orthop. traumatologie* 28 (5), 931–938. doi:10.1007/s00590-017-2082-x

Chang, C.-W., Chen, Y. N., and Peng, Y. T. (2015). Role of the compression screw in the dynamic hip–screw system: a finite-element study. *Med. Eng. Phys.* 37 (12), 1174–1179. doi:10.1016/j.medengphy.2015.10.001

Chatziagorou, G., Lindahl, H., and Kärrholm, J. (2019). Surgical treatment of Vancouver type B periprosthetic femoral fractures: patient characteristics and outcomes of 1381 fractures treated in Sweden between 2001 and 2011. *bone & Jt. J.* 101-B (11), 1447–1458. doi:10.1302/0301-620x.101b11.bjj-2019-0480.r2

Cui, Y., Xing, W., Pan, Z., Kong, Z., Sun, L., Sun, L., et al. (2020). Characterization of novel intramedullary nailing method for treating femoral shaft fracture through finite element analysis. *Exp. Ther. Med.* 20 (2), 748–753. doi:10.3892/etm.2020.8763

Gitajn, I. L., Heng, M., Weaver, M. J., Casemyr, N., May, C., Vrahas, M. S., et al. (2017). Mortality following surgical management of vancouver B periprosthetic fractures. *J. Orthop. Trauma* 31 (1), 9–14. doi:10.1097/bot.0000000000000711

Graham, S. M., Mak, J. H., Moazen, M., Leonidou, A., Jones, A. C., Wilcox, R. K., et al. (2015). Periprosthetic femoral fracture fixation: a biomechanical comparison between proximal locking screws and cables. *J. Orthop. Sci.* 20 (5), 875–880. doi:10.1007/s00776-015-0735-3

Kemker, B., Magone, K., Owen, J., Atkinson, P., Martin, S., and Atkinson, T. (2017). A sliding hip screw augmented with 2 screws is biomechanically similar to an inverted triad of cannulated screws in repair of a Pauwels type-III fracture. *Injury* 48 (8), 1743–1748. doi:10.1016/j.injury.2017.05.013

Khan, T., Grindlay, D., Ollivere, B. J., Scammell, B. E., Manktelow, A. R. J., and Pearson, R. G. (2017). A systematic review of Vancouver B2 and B3 periprosthetic femoral fractures. *bone & Jt. J.* 99-B (4), 17–25. doi:10.1302/0301-620x.99b4.bjj-2016-1311.r1

Lenz, M., Stoffel, K., Kielstein, H., Mayo, K., Hofmann, G. O., and Gueorguiev, B. (2016). Plate fixation in periprosthetic femur fractures Vancouver type

B1—trochanteric hook plate or subtrochanterical bicortical locking? *Injury* 47 (12), 2800–2804. doi:10.1016/j.injury.2016.09.037

Liang, C., Peng, R., Jiang, N., Xie, G., Wang, L., and Yu, B. (2017). Intertrochanteric fracture: association between the coronal position of the lag screw and stress distribution. *Asian J. Surg.* 41, 241–249. doi:10.1016/j.asjsur.2017.02.003

Lunebourg, A., Mouhsine, E., Cherix, S., Ollivier, M., Chevalley, F., and Wettstein, M. (2015). Treatment of type B periprosthetic femur fractures with curved non-loc king plate with eccentric holes: retrospective study of 43 patients wi th minimum 1-year follow-up. *Orthop. traumatology, Surg. Res. OTSR* 101 (3), 277–282. doi:10.1016/j.otsr.2015.01.015

Ma, L., Zhou, Y., Zhang, Y., Zhou, X., Yao, Z., Huang, W., et al. (2014). Biomechanical evaluation with finite element analysis of the reconstruction of femoral tumor defects by using a double-barrel free vascularized fibular graft combined with a locking plate. *Int. J. Clin. Exp. Med.* 7 (9), 2425–2434.

Mei, J., Liu, S., Jia, G., Cui, X., Jiang, C., and Ou, Y. (2014). Finite element analysis of the effect of cannulated screw placement and drilling frequency on femoral neck fracture fixation. *Injury* 45 (12), 2045–2050. doi:10.1016/j.injury.2014.07.014

Mejia, A., Solitro, G., Gonzalez, E., Parekh, A., Gonzalez, M., and Amirouche, F. (2018). Pullout strength after multiple reinsertions in radial bone fixation. *Hand* 15 (3), 393–398. doi:10.1177/1558944718795510

Min, B.-W., Cho, C. H., Son, E. S., Lee, K. J., Lee, S. W., and Min, K. K. (2018). Minimally invasive plate osteosynthesis with locking compression plate in patients with Vancouver type B1 periprosthetic femoral fractures. *Injury* 49 (7), 1336–1340. doi:10.1016/j.injury.2018.05.020

Moloney, G. B., Toro, J. B., Helfet, D. L., and Wellman, D. S. (2016). Proximal periprosthetic femur fractures: strategies for internal fixat ion. *Am. J. Orthop. (Belle Mead, N.J.)* 45 (4), 213–218.

O'Connell, R. S., Owen, J. R., Hansen, E. J., Bashir, A. S., Wayne, J. S., Satpathy, J., et al. (2018). Biomechanical evaluation of osteoporotic proximal periprosthetic femur fractures with proximal bicortical fixation and allograft struts. *J. Orthop. Trauma* 32 (10), 508–514. doi:10.1097/bot.0000000000001261

Papini, M., Zdero, R., Schemitsch, E. H., and Zalzal, P. (2007). The biomechanics of human femurs in axial and torsional loading: comparison of finite element analysis, human cadaveric femurs, and synthetic femurs. *J. Biomechanics Eng* 129 (1), 12–19. doi:10.1115/1.2401178

Patel, S., Solitro, G. F., Sukotjo, C., Takoudis, C., Mathew, M. T., Amirouche, F., et al. (2015). Nanotopography and surface stress analysis of Ti6Al4V bioimplant: an alternative design for stability. *Jom* 67 (11), 2518–2533. doi:10.1007/s11837-015-1341-8

Pletka, J. D., Marsland, D., Belkoff, S. M., Mears, S. C., and Kates, S. L. (2011). Biomechanical comparison of 2 different locking plate fixation methods in vancouver b1 periprosthetic femur fractures. *Geriatr. Orthop. Surg. Rehabil.* 2 (2), 51–55. doi:10.1177/2151458510397609

Raja, D., Roy, S., Patil, S., and Datta, S. (2020). Analysis of carbon fibre bone plate for "B1" type periprosthetic femoral fracture. *IOP Conf. Ser. Mater. Sci. Eng.* 912, 022041. doi:10.1088/1757-899x/912/2/022041

Sah, A. P., Marshall, A., Virkus, W. V., Estok, D. M., and Della Valle, C. J. (2010). Interprosthetic fractures of the femur: treatment with a single-locked plate. *J. arthroplasty* 25 (2), 280–286. doi:10.1016/j.arth.2008.10.008

Stoffel, K., Horn, T., Zagra, L., Mueller, M., Perka, C., and Eckardt, H. (2020). Periprosthetic fractures of the proximal femur: beyond the Vancouver c lassification. *EFORT open Rev.* 5 (7), 449–456. doi:10.1302/2058-5241.5.190086

Takahashi, D., Noyama, Y., Asano, T., Shimizu, T., Irie, T., Terkawi, M. A., et al. (2021). Finite element analysis of double-plate fixation using reversed locking compression-distal femoral plates for Vancouver B1 periprosthetic femoral fractures. *BMC Musculoskelet. Disord.* 22 (1), 276. doi:10.1186/s12891-021-04152-5

Taylor, M. E., Tanner, K., Freeman, M., and Yettram, A. (1996). Stress and strain distribution within the intact femur: compression or bending? *Med. Eng. Phys.* 18 (2), 122–131. doi:10.1016/1350-4533(95)00031-3

Tianye, L., Peng, Y., Jingli, X., QiuShi, W., GuangQuan, Z., Wei, H., et al. (2019). Finite element analysis of different internal fixation methods for the treatment of Pauwels type III femoral neck fracture. *Biomed. Pharmacother.* 112, 108658. doi:10.1016/j.biopha.2019.108658

Travascio, F., Buller, L. T., Milne, E., and Latta, L. (2021). Mechanical performance and implications on bone healing of different screw configurations for plate fixation of diaphyseal tibia fractures: a computational study. *Eur. J. Orthop. Surg. Traumatol.* 31 (1), 121–130. doi:10.1007/s00590-020-02749-5

Tsiridis, E., Narvani, A. A., Timperley, J. A., and Gie, G. A. (2005). Dynamic compression plates for Vancouver type B periprosthetic femoral fractures: a 3-year follow-up of 18 cases. *Acta Orthop.* 76 (4), 531–537. doi:10.1080/17453670510041529

Wähnert, D., Grüneweller, N., Gehweiler, D., Brunn, B., Raschke, M. J., and Stange, R. (2017). Double plating in Vancouver type B1 periprosthetic proximal femur frac tures: a biomechanical study. *J. Orthop. Res.* 35 (2), 234–239. doi:10.1002/jor.23259

Wang, J., Ma, J. X., Lu, B., Bai, H. H., and Wang, Y. (2020). Comparative finite element analysis of three implants fixing stable and unstable subtrochanteric femoral fractures: proximal femoral nail antirotation (PFNA), proximal femoral locking plate (PFLP), and reverse less invasive stabilization system (LISS). *Orthop. Traumatol. Surg. Res.* 106 (1), 95–101. doi:10.1016/j.otsr.2019.04.027

frontiers | Frontiers in Bioengineering and Biotechnology

TYPE Review
PUBLISHED 19 January 2024
DOI 10.3389/fbioe.2023.1291969

OPEN ACCESS

EDITED BY
Junxi Wu,
University of Strathclyde, United Kingdom

REVIEWED BY
Ayan Samanta,
Uppsala University, Sweden
Jaydee Cabral,
University of Otago, New Zealand

*CORRESPONDENCE
Zhonglai Qian,
qzldoctor@163.com
Xuzhu Gao,
alexgwan@163.com
Mingming Liu,
drliumingming@163.com

†These authors have contributed equally to this work

RECEIVED 10 September 2023
ACCEPTED 06 December 2023
PUBLISHED 19 January 2024

CITATION
Lv N, Zhou Z, Hou M, Hong L, Li H, Qian Z, Gao X and Liu M (2024), Research progress of vascularization strategies of tissue-engineered bone.
Front. Bioeng. Biotechnol. 11:1291969.
doi: 10.3389/fbioe.2023.1291969

Research progress of vascularization strategies of tissue-engineered bone

Nanning Lv[1,2,3,4†], Zhangzhe Zhou[1†], Mingzhuang Hou[1†], Lihui Hong[2,3,4], Hongye Li[2,3,4], Zhonglai Qian[1*], Xuzhu Gao[2,3,4*] and Mingming Liu[2,3,4*]

[1]Department of Orthopedic Surgery, The First Affiliated Hospital of Soochow University, Suzhou, Jiangsu, China, [2]Department of Orthopedic Surgery, The Second People's Hospital of Lianyungang Affiliated to Kangda College of Nanjing Medical University, Lianyungang, Jiangsu, China, [3]Department of Orthopedic Surgery, The Affiliated Lianyungang Clinical College of Xuzhou Medical University, Lianyungang, Jiangsu, China, [4]Department of Orthopedic Surgery, The Affiliated Lianyungang Clinical College of Jiangsu University, Lianyungang, Jiangsu, China

The bone defect caused by fracture, bone tumor, infection, and other causes is not only a problematic point in clinical treatment but also one of the hot issues in current research. The development of bone tissue engineering provides a new way to repair bone defects. Many animal experimental and rising clinical application studies have shown their excellent application prospects. The construction of rapid vascularization of tissue-engineered bone is the main bottleneck and critical factor in repairing bone defects. The rapid establishment of vascular networks early after biomaterial implantation can provide sufficient nutrients and transport metabolites. If the slow formation of the local vascular network results in a lack of blood supply, the osteogenesis process will be delayed or even unable to form new bone. The researchers modified the scaffold material by changing the physical and chemical properties of the scaffold material, loading the growth factor sustained release system, and combining it with trace elements so that it can promote early angiogenesis in the process of induced bone regeneration, which is beneficial to the whole process of bone regeneration. This article reviews the local vascular microenvironment in the process of bone defect repair and the current methods of improving scaffold materials and promoting vascularization.

KEYWORDS

osteogenesis, bone tissue engineering, bone defect, biological materials, angiogenesis

1 Introduction

The increasing incidence of bone defects due to trauma, inflammation, tumor resection, pathological fractures, impaired blood supply, and congenital deformities with increasing population aging has dramatically increased demand for bone substitute materials (Yin et al., 2018; Chen et al., 2021). Although autologous bone transplantation is the gold standard for clinical treatment of bone defects, it has serious disadvantages, such as limited sources, many complications, and postoperative pain in the donor site (Cheng et al., 2020). In addition, allogeneic bone transplantation is also an effective way to treat bone defects. It can avoid the shortcomings of lack of bone source and secondary damage to the material obtained, but it still faces problems such as immune rejection and disease transmission (Juhl et al., 2019).

TABLE 1 Strategies of scaffold functionalization techniques for vascular bone tissue engineering.

Strategies	Type	Characteristic	Ref
Optimize physical and chemical properties	Surface morphology, porosity and pore size, pore structure	Recruit macrophage/monocyte and induce angiogenesis	Brydone et al. (2010), Chen et al. (2018), Liu et al. (2020), Huang et al. (2021), Jin et al. (2021)
		Reduce inflammation, promoting angiogenesis, and driving adhesion and osteogenesis of MSCs. Cell-material interaction promotion and MSC paracrine function modulation effects	
Loaded cytokine	VEGF, Deferoxamine, Angiopoietin 2	A sustained release	Yin et al. (2018), Keroured an et al. (2019b), Wu et al. (2020)
		Mimicked the microenvironment of extracellular matrix	
		Promoted angiogenesis and improved repair of bone defects	
Loaded trace elements	Magnesium, Strontium, Cobalt, Copper	Improve surface bioactivity and lead to better osteogenesis and angiogenesis	Son et al. (2019), Lee et al. (2020), Ma et al. (2020), Sun et al. (2021a)
		Alter physicochemical properties of cells, enhance the osteogenesis and angiogenesis of bioceramic scaffolds	
		Accelerated host angiogenesis and immune responses	
		Improve mechanical strength and handling properties, improve both biological and physicochemical properties	

Therefore, designing and constructing safe and efficient bone repair biomaterials for treating bone defects has become one of the hotspots in bone regenerative medicine.

In bone repair, bone regeneration and angiogenesis are closely linked. As an indispensable source of nutrients for bone tissue, blood vessels transport minerals and growth factors to promote calcium deposition in bones and release paracrine signals to regulate the growth, differentiation, and regeneration of different types of cells (Filipowska et al., 2017; Zheng et al., 2021). Bone repair materials with good biological activity should promote angiogenesis in and around the bone defect and promote the osteogenic differentiation of bone precursor cells, ultimately beneficial to bone defect healing and new bone formation. Although significant progress has been made in the application of tissue-engineered bone in treating bone defects, it still faces slow or absent vascularization obstacles. This makes it difficult for tissue-engineered bone to form an effective vascular network in a short period of time, resulting in the death of seed cells due to lack of nutrients, oxygen and excessive accumulation of metabolites (Quinlan et al., 2017).

For a long time, many researchers have been exploring the ideal artificial bone defect repair materials. The biomimetic porous structure functions as a natural matrix, supporting cell adhesion, growth, differentiation, and proliferation and positively impacting bone tissue integration and revascularization (Huang et al., 2021). Tissue growth and bone tissue reconstruction are promoted by adjusting the microstructure, including pore size, shape, porosity, and interconnected pore structure (Hayashi et al., 2020; Geng et al., 2021). Some researchers combine growth factors with biomaterials, trying to endow biomaterials with new functions. A number of growth factors promote angiogenesis, including vascular endothelial growth factor (VEGF) (Wu et al., 2020) and essential fibroblast growth factor (bFGF) (Zhao et al., 2020). Furthermore, bioactive ions can also be doped into bone repair materials to modify their properties. By ion doping modification, bone biomaterials' original physical, chemical, and biological properties can be improved or enhanced (Lai et al., 2019; Luo et al., 2021). Doping an appropriate amount of metal ions enhances the original related properties of bone repair materials and provides necessary trace elements for the metabolism of bone tissue. Table 1 showed the strategies of scaffold functionalization techniques for vascular bone tissue engineering.

In recent years, tissue engineering technology has become a hot research topic due to the development of materials science and molecular biology. However, inadequate vascularization after biological scaffold implantation remains a significant hurdle in bone tissue engineering research. How to ensure that the scaffold material can be rapidly vascularized after transplantation into the body and how to establish a vascular network to provide sufficient nutrition for subsequent new bone formation is an urgent problem that needs to be solved. This article reviews the local microenvironment in the process of bone defect repair and the current progress of bone tissue engineering to improve and promote vascularization.

2 Mechanisms that link bone tissue vascularization and osteogenesis

There are four stages in the process of bone defect repair: hematoma formation, fibrous callus formation, and bone remodeling (Zhang et al., 2020). Many studies have indicated that the initiation of bone regeneration relies on the inflammatory reaction and the formation of new blood vessels. Vascularization and bone regeneration are two fundamental components in the process of bone healing (Lu et al., 2022). Bone is a highly vascularized hard tissue. Bone remodeling and metabolism depend on the interaction of the vascular-bone microenvironment built between osteoblasts, osteocytes, osteoclasts, osteogenic differentiation, blood vessels, and angiogenesis. Osteogenic differentiation and angiogenesis are coupled through particular forms and related pathways. Therefore, the close temporal and spatial connection between bone formation and angiogenesis is called "osteogenic differentiation-angiogenesis coupling" (Gallardo-Calero et al., 2019). Bone remodeling and metabolism depend on vascular interactions. Blood vessels maintain the callus' high metabolic

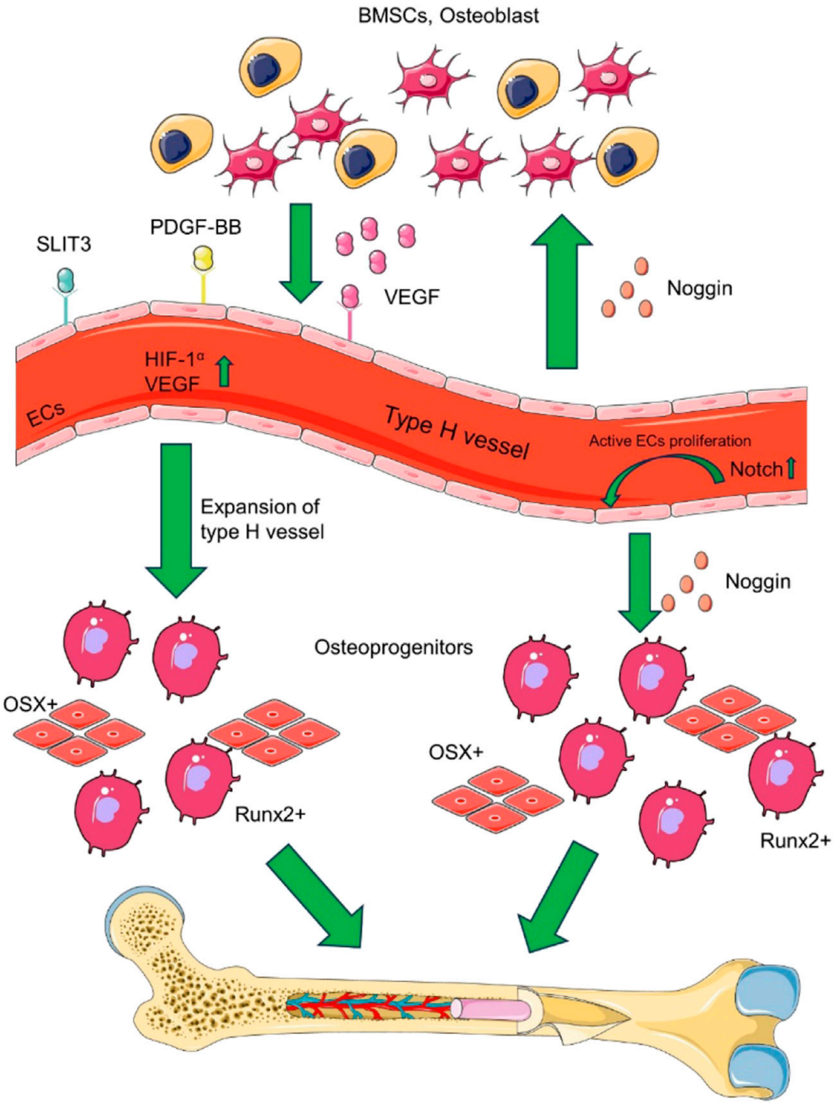

FIGURE 1
The coupling of type H vessel formation and osteogenesis in the bone marrow microenvironment involves multiple signalling factors. Various cell lineages, such as osteoblast lineage cells, vascular endothelial cells (ECs), and osteoclasts, contribute to the formation of type H vessels by secreting VEGF, SLIT3, and PDGF-BB. Additionally, type H vascular ECs secrete RANKL, which supports vessel-associated osteoclasts through a RANKL-RANK signalling mechanism, thereby facilitating bone regeneration. Based on (Zhang et al., 2020).

demand for oxygen and nutrients and provide pathways for inflammatory cells, osteoblast/osteoclast progenitors, and fibroblasts to enter the defect (Sivan et al., 2019). Factors that promote angiogenesis include VEGF, hypoxia-inducible factor-1α (HIF-1α), bone morphogenetic protein (BMP), FGF, transforming growth factor (TGF), and platelet-derived growth factor (PDGF-BB) are involved in initiating angiogenesis during bone formation and regulating bone formation (Peng et al., 2020).

2.1 H-type blood vessels promote osteogenic differentiation

A particular vascular endothelial cell exists between osteoblasts and osteoclasts to promote angiogenesis, called H-type vascular endothelial cells, which can actively guide bone formation by producing inducible factors (Zhang et al., 2020). H-type blood vessels regulate the growth of skeletal vasculature and the function of osteoblasts, which are essential regulators of bone regeneration (Peng et al., 2020). H-type vascular endothelial cells are surrounded by osteoprogenitor cells expressing osteoblast-specific transcription factors (Wang et al., 2017). These include osteoprogenitor cells expressing Runt-related transcription factor (Runx2), osteogenesis-related transcription factor, and osteoblasts expressing type I collagen (Yang et al., 2017). Osterix promotes bone formation effectively, Runx2 is an essential transcription factor for osteoblast differentiation, and type I collagen is involved in the stages of osteocyte proliferation, differentiation, and mineralization. In addition, H-type vascular endothelial cells promote the survival, proliferation, and differentiation of bone progenitor cells by secreting growth factors, such as PDGF, TGF-β1, TGF-β3, and FGF-1, etc., (Zhao and Xie, 2020). Osteoprogenitor cells are close to H-type blood vessels, which provide osteoblast resources for osteogenesis, while oxygen offers the necessary nutrients to support osteogenesis' metabolic demands. Therefore, H-type vascular endothelium regulates osteoblasts and osteoclasts and is an essential regulator of bone regeneration (Li et al., 2019). By combining signaling pathways and cytokines, H-type blood vessels play a vital role for bone formation and blood vessel growth. Figure 1 illustrates that the multiple signalling factors are involved in coupling of type H vessel formation and osteogenesis in the bone marrow microenvironment.

2.2 Osteogenic differentiation promotes angiogenesis

The H-type blood vessels is also regulated by a number of cell-derived cytokines. Various cytokines are secreted into the bone marrow microenvironment to induce endothelial cell proliferation, vascular assembly, and stabilization, providing sufficient guarantee for forming H-type blood vessels (Xu et al., 2018). HIF-1α, Notch, and VEGF can promote vascular assembly stabilization and bone formation (Zhu et al., 2020). VEGF is one of the most effective cytokines for inducing angiogenesis and is secreted by cells involved in bone development and repair, including endothelial cells, osteoblasts, and hypertrophic chondrocytes (Dreyer et al., 2020). VEGF mainly acts on endothelial cells, stimulates the formation of new blood vessels, and brings osteoprogenitor cells into the callus site to promote bone formation. Notch signaling is the key linking angiogenesis, vascular secretion signaling, and osteogenesis and is also a critical pathway for regulating the sprouting of new blood vessels in bone (AlMuraikhi et al., 2019; Guo et al., 2020). Under the condition of hypoxia or hypoxia, HIF-1α produced by osteoblasts promotes angiogenesis and the expression of VEGF-A (Hu and Olsen, 2016a). At the same time, an increase in HIF-1α expression in cells led to a significant expansion of H-type vascular endothelial cells, Osterix, and Runx2 osteoprogenitor cells (Hu and Olsen, 2016b). Slit homologous protein 3 (SLIT3) and PDGF-BB can bind to the corresponding endothelial cell receptors to further enhance VEGF secretion and stimulate blood vessel growth (Xu et al., 2018; Gao et al., 2019). In addition, miRNAs can also regulate H-type angiogenesis through various signaling pathways related to bone metabolism (Chen et al., 2020; Wang et al., 2020).

3 Effects of physicochemical properties of bone bioscaffolds on angiogenesis

Bone tissue engineering technology typically comprises three fundamental components: a biomaterial scaffold, bioactive factors, and graft cells. Among these, the biomaterial scaffold plays a central role in offering mechanical stability to the bone defect site, while also serving as a carrier for the bioactive factors and graft cells. The biomaterial scaffold is also crucial for achieving spatio-temporal regulation of the bioactive factors and effectively influencing the regeneration of blood vessels. The structural parameters and surface properties of bone grafts are closely related to cellular responses and angiogenesis and ultimately affect bone formation, including surface properties, pore shape, porosity, and fiber orientation (Bobbert and Zadpoor, 2017; Ortiz et al., 2018; Bank, 2019; Hayashi et al., 2020). Understanding the effect of bone substitute structure on angiogenesis is essential for optimizing the design of porous biomaterials targeting bone regeneration. By optimizing the parameters of biomimetic materials to enhance the synergistic interaction among scaffolding materials, bioactive factors, and cells within a biological milieu, these biomaterials facilitate the enhancement of bone regeneration and angiogenesis, thereby directing the process of new bone formation (Table 2).

3.1 Surface topography

The interaction between biomaterials and the host is crucial for successful regeneration during bone tissue engineering. The biomaterial's surface interacts with the host tissue fluid and cells, directly determining its mechanical binding and biological response to the host tissue (Bank, 2019). Optimizing the surface properties of biomaterials is a promising strategy to control various responses of cells involved in tissue repair processes, such as cell migration, adhesion, and ECM secretion (Denchai et al., 2018; Ortiz et al., 2018; Conserva et al., 2019; Huang et al., 2019; Richbourg et al., 2019). By comparing three different surface microstructures of electrospinning fiber membrane effect on blood vessels and osteogenesis, Jin et al. found that the reticular structure of fiber membrane promotes angiogenesis, macrophage recruitment, and osteogenesis, indicating that the reticular formation of the fiber surface can be used to regenerate bone as a surface design biomaterial (Jin et al., 2021). Nanotopological surfaces have been shown to modulate cell behaviors, such as initial adhesion, spreading, and differentiation. The application of nanomaterials to tailor the surface of polymer scaffolds can regulate and enhance biological responses with cells and enable tissue repair processes. For example, carbon nanotubes (CNTs) are used to modify the surface of biopolymer nanofibers to create unique bimodal nanoscale topography (500 nm nanofibers and 25 nm nanotubes), which can reduce inflammation, promote angiogenesis, and drive the adhesion of MSCs. It effectively promotes tissue healing and bone regeneration (Patel et al., 2020). Additionally, microgrooves added to the surface of composite scaffolds also aided in angiogenesis and bone regeneration. The micro-grooved structure helps guide human umbilical vascular endothelial cells (HUVECs) assembly into well-arranged tubular structures, promoting rapid angiogenesis (Chen et al., 2018).

3.2 Porosity and pore size

Pores in bone tissue biomaterials allow bone tissue to grow and blood vessels to form, which plays an important role in bone regeneration. It is crucial that the implant has a functional vascular network that delivers oxygen, nutrients, and signaling molecules, as well as removes metabolic waste and carbon dioxide (Bobbert and Zadpoor, 2017). Angiogenesis is also closely related to the pore structure in the scaffold (Yilgor et al., 2013; Vezenkova and Locs, 2022) and ultimately affects bone formation. Relevant parameters of pore structure in the scaffold include pore size (Freitas et al., 2022), orientation (Yilgor et al., 2013), uniformity

TABLE 2 Effects of physical and chemical properties of materials on bone angiogenesis.

Type	Characteristic	Effect	Ref
Surface morphology	PFCH fibrous membranes with random, aligned and latticed topography	Recruit macrophage/monocyte and induce angiogenesis	Jin et al. (2021)
	Surface of biopolymer nanofibers with CNTs to create a unique bi-modal nanoscale topography (500 nm CNTs with 25 nm CNTs)	Reduce inflammation, promoting angiogenesis, and driving adhesion and osteogenesis of MSCs	Patel et al. (2020)
	Dexamethasone-loaded biphasic calcium phosphate nanoparticles/collagen composite scaffolds with several types of concave microgrooves	facilitated angiogenesis and stimulated new bone formation	Chen et al. (2018)
	A sponge-like scaffold with hierarchical and interconnected pores	cell-material interaction promotion and MSC paracrine function modulation effects	Liu et al. (2020)
Porosity and pore size	A highly porous and elastic aerogel made from ultralong HAP nanowires with ultrahigh porosity (B98.5%), excellent elasticity and suitable porous structure	ingrowth of new bone and blood vessels	Huang et al. (2021)
	The architecture of larger pores at the periphery of graded scaffold	Enhance angiogenesis and osteogenesis	Yang et al. (2015)
Pore structure	Multi-level pores into the biocompatible scaffolds	promote angiogenesis and bone regeneration	Liu et al. (2020)
	Scaffolds with irregular pore sizes	be more conducive to bone tissue ingrowth and blood vessel formation	Wang et al. (2021)
Other	The 3R02 bivalent aptamer specific to VEGF was grafted to the HA surface	promotes bone regeneration and angiogenesis	Brydone et al. (2010)

PFCH., Poly (lactate-co-glycolate)/fish collagen/nano-hydroxyapatite.
CNTs. Carbon nanotubes.
HAP., hydroxyapatite.

(Wang et al., 2014; Vissers et al., 2015), interconnectivity (Vissers et al., 2015), and porosity (Ahn et al., 2018; Dou et al., 2021). These parameters are interrelated and coordinately influence the effect of bone regeneration. The effective threshold of aperture for bone regeneration was 100 μm (Bobbert and Zadpoor, 2017). Generally, when the pore size is less than 100 μm, the cell distribution and angiogenesis of the whole scaffold are limited, cell viability is reduced, cell proliferation and differentiation are delayed, and fibrous tissue is formed within the pores instead of bone (Bobbert and Zadpoor, 2017). Therefore, most studies have developed scaffolds with pore sizes exceeding 100 μm. Research reports vary on the importance of macropore size thresholds: some claim that macropores need to be larger than 400 μm for new bone to develop (Sicchieri et al., 2012). The threshold for pore size is closely related to the porosity, pore geometry, uniformity, orientation, interconnectivity, and chemical composition of different materials (Hayashi et al., 2020). The high-porosity scaffold facilitates osteoblasts' adhesion, proliferation, and migration and promotes angiogenesis and new bone formation in the defect area (Wang et al., 2021). For example, ultralong hydroxyapatite nanowires are assembled into cancellous bone-like aerogels by freeze-drying method, which has ultra-high porosity and multi-scale pores, providing a good environment for cell adhesion, proliferation, migration, and bone growth, and promoting osteogenesis and angiogenesis both *in vitro* and *in vivo* (Huang et al., 2021).

3.3 Pore structure

Evidence shows graded porous scaffolds are more effective at regenerating bone than scaffolds with uniform pore sizes (Yang et al., 2015; Liu et al., 2020). These gradient structures can promote cell migration, spreading, signaling, proliferation, and differentiation. Yang et al. fabricated a gradient porous scaffold (large central pores between 600 and 800 μm, tiny peripheral pores between 350 and 500 μm) and a scaffold with uniform pore sizes by template casting (Yang et al., 2015). The volume of newly formed bone in the gradient porous scaffold was significantly more prominent than in the scaffold with uniform pores *in vivo*. A gradient porous structure, which promotes angiogenesis and bone regeneration, is therefore a promising approach. The gradient porous scaffolds with large central and peripheral tiny pores can encourage tissue bone formation more than the uniform pore scaffolds. However, the macroporous structure around the gradient scaffold can promote angiogenesis and osteogenesis more than the small pore structure around the gradient scaffold (Li et al., 2020a). In addition, a 3D sponge scaffold with layered and interconnected pores promotes cell-material interactions, regulates the paracrine function of MSCs, and significantly supports vascularized bone regeneration (Lian et al., 2021).

3.4 3D printing promotes vascularized osteogenesis

3D bioprinting is a technology that combines 3D printing, tissue engineering, developmental biology and regenerative medicine to build bionic tissues (Vijayavenkataraman et al., 2018). 3D bioprinting allows spatially controlled and layer-by-layer deposition of specific biomaterials, cells and biomolecules to create complex vascularized tissues and intricate 3D structures (Pati and Cho, 2017). Compared with traditional methods, 3D bioprinting technology, which allows precise control of complex three-dimensional structures, multiple compositions, and spatial distributions (Vijayavenkataraman et al., 2018), has unparalleled advantages and is gradually gaining widespread attention. Kerouredan et al. (Kerouredan et al., 2019a) precisely printed high-density endothelial cells onto hydrogels containing mesenchymal stem cells to generate microvascular networks with specific structures. Piard et al. (Piard et al., 2019) developed an innovative fibrin-polycaprolactone composite scaffold, incorporating HUVECs, BMSCs, and fibronectin, through the utilization of extrusion 3D bioprinting. The resulting scaffold exhibited mechanical properties akin to bone, and subsequent *in vitro* and *in vivo* investigations demonstrated its commendable vascularization potential. Anada et al. (Anada et al., 2019) employed digital light processing to fabricate a dual 3D hydrogel structure, comprising an outer ring of gelatin methacrylate embedded with octacalcium phosphate and an inner ring of gelatin methacrylate containing HUVECs. This construct successfully facilitated the differentiation of BMSCs into osteoblasts and promoted the formation of blood vessels, thereby mimicking the process of bone formation in the human body. To simulate the vascularization of bone tissue, Shahabipour et al. (Shahabipour et al., 2022) used coaxial microextrusion to load HUVECs and osteoblasts (MC3T3) into the core and shell of bioink containing angiogenic and osteogenic factors, respectively, to form core-shell structures and indirect co-culture, and the scaffolds prepared demonstrated that the coaxial bioprinting technology and the indirect co-culture system can be used to construct bioreactive tissues with higher efficiency.

The angiogenesis of larger implants may be too slow, resulting in cell death or loss of function in the central region of the implant. To address this issue, prefabricated scaffolds or engineered tissues with a capillary-like network prior to implantation is a viable approach (Sharma et al., 2019). Such engineered vascular networks have been shown to anastomose with the host vascular system after implantation (Zhu et al., 2017). Kerouredan et al. (Kerouredan et al., 2019b) used laser-assisted bioprinting to implant labeled endothelial cells and collagen containing BMSCs and VEGF into cranial bone defects in mice to promote bone regeneration *in vivo* and to increase angiogenesis in bone defects. Nulty et al. (Nulty et al., 2021) co-cultured HUVECs, hBMSCs cells and 3D bioprinted them with different bioinks. *In vitro* 3D bioprinting of pre-designed sizes and shapes of implants and applying them to bone defects demonstrated that pre-vascularized bone tissues enhanced blood vessel formation in critical bone defects.

3.5 Microfluidics promotes vascularized osteogenesis

Microfluidics is a technology that precisely manipulates fluids in the micron scale, and the volume of the manipulated fluid can be as small as $10^{-9} \sim 10^{-18}$ L (Long et al., 2009). Injectable fillers have been found to be applicable in minimally invasive procedures and are also deemed suitable for bone defects with intricate shapes (Brydone et al., 2010). Moreover, injectable fillers can serve as drug delivery systems and, owing to their resemblance to the extracellular matrix (ECM), they can facilitate the proliferation and adhesion of MSCs while acting as osteogenic supports (Liu et al., 2017; Yousefi, 2019). Hydrogel microspheres, as a representative material of injectable fillers, have been widely studied in bone tissue engineering and tissue regeneration (Li et al., 2021; Sun et al., 2022). Cheng et al. (Cheng et al., 2023) prepared nanohydroxyapatite/chitosan (nHA/CS) composite hydrogel microspheres with uniform particle size distribution by microfluidic technology. The composite hydrogel was demonstrated by *in vivo* and thus *in vitro* experiments to promote osteogenic differentiation of mesenchymal stem cells and vascularization of endothelial cells by controlling the release of strontium ions, thus accelerating the repair of bone defects. Yang et al. (Yang et al., 2023) developed VEGF-loaded pearl powder hybrid hydrogel scaffolds for bone regeneration using microfluidics combined with 3D printing technology. In this process, microfluidics combined with 3D printing technology can precisely shape the scaffolds for different application purposes. The composite hydrogel promotes revascularization of the damaged area by loading and releasing VEGF, which improves the delivery of oxygen and nutrients in the early stage of bone repair.

4 The effect of cytokine-loaded bone bioscaffolds on angiogenesis

Growth factors directly or indirectly regulate endothelial cell migration, proliferation, and aggregation, so they play a crucial role in the formation of vascularization (Sun et al., 2021). Currently, known angiogenic growth factors can be divided into the following categories. 1) Only endothelial cells are targeted cells that promote angiogenesis and generation, including VEGF and angiopoietin. The former acts on the early stage of vascularization and promotes the formation of the original vascular network. The latter acts on the subsequent vascular remodeling and shaping and promotes the maturation of the vascular network. 2) It acts on various endothelial cells and directly affects vascularization, including growth factors and chemokines. A typical representative is FGF, which can promote endothelial cell division and chemotactic endothelial cells and strongly promotes angiogenesis. 3) It indirectly affects vascularization, mainly inducing the release of the above two types of factors to stimulate angiogenesis, including TGF-β and platelet-derived factors. The primary function of the former is to maintain the integrity of the vascular wall. At the same time, the latter promotes the division of vascular smooth muscle cells to promote vascular maturation and maintain vascular stability. Table 3 shows several cytokines loaded with bone biomaterials that promote angiogenesis and osteogenesis. Among all these factors, VEGF is the most commonly used in bone tissue engineering (Li et al., 2020b; Kauffmann et al., 2021).

There are mainly two different ways for growth factors to be applied in tissue engineering bone construction: one is to compound growth factors directly on the scaffold or to combine with it after the scaffold is constructed (Li et al., 2016; Yin et al., 2018; Cheng et al., 2020; Zheng et al., 2021). The other is to simultaneously transplant cells that can secrete growth factors on the scaffold. These cells can secrete growth factors in the natural state (Kang et al., 2014) or be modified by genetic engineering (Li et al., 2016; Li et al., 2017). However, as a dynamic and comprehensive process, bone regeneration requires the precise release of a certain dose of growth factors and signaling molecules at specific stages.

TABLE 3 Effect of cytokine-loaded materials on bone angiogenesis.

Factor	Carrier	Effect	Ref
VEGF	Polydopamine-Coated Poly (l-lactide) Nanofibers	Promote angiogenesis and osteogenesis	Li et al. (2020a)
	Hierarchical micro/nanofibrous membranes	A sustained release	Wu et al. (2020)
		Mimicked the microenvironment of extracellular matrix	
	Chemotactic Functional Scaffold	Stimulate mobilization and homing of MSCs to sites of bone loss	Brydone et al. (2010)
		A novel nucleotide aptamer-functionalized fibrin hydrogel (AFH)	
		Aptamer functionalization improve the release kinetics of VEGF from AFH.	
	Microbubbles	Combination with ultrasound-targeted microbubble destruction (UTMD)	Sharma et al. (2019)
Deferoxamine	Poly (lactic-co-glycolic acid)	Activate the HIF-1a signaling pathway stimulating production of VEGF and other downstream angiogenic factors	Kerouredan et al. (2019b)
	3D bioglass-nanoclay scaffolds	Sustained DFO release and inhibited DFO degradation	Zheng et al. (2021)
	Hydrogel	Multiple osteoinduction cues including organic–inorganic compositions, and angiogenic/osteoinductive factors	Pati and Cho (2017)
Angiopoietin 2	A hydroxyapatite/collagen scaffold	Promoted angiogenesis and improved repair of bone defects by inducing autophagy	Yin et al. (2018)

PA., peptide amphiphile.
SNF., silk nanofibers.
HA., hydroxyapatite nanoparticles.

Therefore, the simulation is not only about releasing growth factors from the drug delivery or presentation system *in vivo*. Since drugs' rapid or continuous release cannot ensure accurate coordination with the dynamic environment *in vivo*, it is essential to coordinate multi-dimensional factors such as time and dose in bone tissue regeneration and repair strategies.

Since growth factors lack stability and are readily inactivated, they decompose too quickly to be effective alone. Most reports use growth factors in combination with appropriate scaffold materials at specific target sites to achieve effective delivery and controllable release of growth factors (Jia et al., 2016; Wu et al., 2020). For example, a burst-release microbubble system loaded with VEGF can be developed to achieve the directional and concentrated release of VEGF through targeted microbubble destruction by ultrasound, which can significantly enhance the growth of blood vessels and new bone formation in bone defects (Gong et al., 2019). At present, the therapeutic methods of angiogenesis emphasize the local concentration and continuous use of growth factors rather than local and single rapid intravenous injection, and many natural, synthetic, and composite materials have been used as the release vectors of angiogenic growth factors. For example, some scholars have developed a sequential growth factor slow-release double-freezing hydrogel system. The outer layer is gelatin/chitosan frozen gel wrapped with VEGF, and the inner layer is gelatin/heparin frozen gel containing bone morphogenetic protein-4 (BMP-4). It promotes angiogenesis and osteogenesis through early release of VEGF and sustained release of BMP-4 (Lee et al., 2020). Of course, grafting the 3R02 bivalent nucleic acid aptamer specific to VEGF is also a good choice onto the surface of hydroxyapatite (HA). This aptamer-conjugated hydroxyapatite (Apt-HA) shows higher VEGF protein capture ability and faster growth of HUVEC (Son et al., 2019).

In addition, VEGF and various cytokines can exert synergistic effects and play a vital role in the interaction between osteoblasts and endothelial cells (Dohle et al., 2018; Simunovic et al., 2019). Wang et al. introduced BMP-2 and VEGF into silk fibroin microspheres and then incorporated these microspheres into nano-hydroxyapatite scaffolds to provide controlled release. The results showed that this scaffold's sustained-release extremely low-dose BMP-2 and VEGF synergistically affected vascularized bone regeneration. Compared with other systems, this controlled release system can significantly reduce the use of BMP-2 (Wang et al., 2017). The chemotactic effect of VEGF in angiogenesis was utilized to promote the recruitment and differentiation of osteoprogenitor cells into osteoblasts by activating specific receptors and to guide the migration of MSCs to bone defects. Based on this, some scholars have used amphiphilic polypeptide (PA) nanofiber gel to wrap vascular endothelial growth factor to form a chemotactic functional scaffold. It can guide stem cells to migrate to the defect area and induce differentiation by controlling the release of VEGF to promote angiogenesis and osteogenesis (Bakshi et al., 2021).

Although the engineering biomaterials combined with growth factors have achieved good results in inducing bone repair and angiogenesis, the clinical application of growth factors is limited by their short half-life, easy inactivation, and therapeutic effect exceeding the physiological dose. The transmission of growth factor genes rather than simple growth factors has been proven to be an effective way to maintain biological activity to treat bone defects and diseases (Chen et al., 2011). Viral vector has become a promising transmission tool for tissue regeneration because of its high expression efficiency. The gene fragment with growth factor is transfected into seed cells by

TABLE 4 Effect of materials loaded with trace elements on bone angiogenesis.

Metal	Carrier	Effect	Ref
Mg	3D printed porous tantalum scaffolds	Improve surface bioactivity and lead to better osteogenesis and angiogenesis	Lee et al. (2020)
	3D printed Mg-doped TCP scaffolds	Alter physicochemical properties of cells, enhance the osteogenesis and angiogenesis of bioceramic scaffolds	Sun et al. (2021a)
	Dual-crosslinked hydrogel	Promote cell adhesion, osteogenesis and vascularization	Li et al. (2020b)
	Microfluidic Hydrogel Microspheres	Capture Magnesium, sustained release performance, bone-targeting properties	Li et al. (2017)
strontium	Hybrid cement	Improve mechanical strength and handling properties, improve both biological and physicochemical properties	Son et al. (2019)
	Microspheres	Biomineralized, injectable and biodegradable	Bakshi et al. (2021)
		Induce bone regeneration and kill bacteria	
	3D printed porous scaffolds	Manipulates favorable macrophages activation to facilitate osteogenesis/angiogenesis	Wang et al. (2017b)
	Ceramics	Release of exosomal miR-146a, promote osteogenesis and angiogenesis	de Laia et al. (2021)
Cobalt	Bioceramics	Appropriate Co promote osteogenesis, excessive Co suppressed bone formation	Kristina et al. (2018)
	Metal–Organic Framework Hydrogel Nanocomposites	A powerful proangiogenic/osteogenic agent, tunable and Controlled Release of Cobalt Ions	Lai et al. (2019)
	Bioceramic scafolds	Enhance osteogenic and angiogenic properties	Nabiyouni et al. (2018)
Copper	Bioactive glass composite scaffolds	Activate the HIF-1α and TNF-α pathway of hUVECs	Nabiyouni et al. (2018)
	Mesoporous bioactive glass	Accelerated host angiogenesis and immune responses	Ma et al. (2020)

vector virus; seed cells can express the growth factor stably and continuously. After implantation at the target location, the cell will have a more vital ability to promote vascularization. Releasing the transfection vector that can express the growth factor gene from the scaffold effectively improves bone regeneration. For this purpose, viral vectors are commonly used due to their high efficiency and stability in delivering genes (Chang et al., 2009).

With drug-controlled release and non-viral vector technology development, Superparamagnetic gene microspheres with biodegradable and controlled gene release have emerged as the most promising carriers for cellular functions in scaffolds. This can generate revolutionary innovation in bone tissue engineering research. A non-invasive oscillating and static magnetic field was used to drive the micromotion of magnetic gene-loaded microspheres in the bone biomaterials to promote the release of plasmid genes. It has been shown that plasmids are released and enriched locally in VEGF magnetic microspheres under oscillating and static magnetic fields. It was also observed to promote vascularization and osteogenesis of artificial bone *in vivo* (Luo et al., 2018).

5 Effect of trace elements on angiogenesis of bone biological scaffold

Bones comprise about 20% collagen and 70% minerals, while other organic materials such as proteins, polysaccharides, and lipids account for only a tiny portion of bones (Lin et al., 2019). Bone minerals contain many trace elements, such as magnesium, calcium, zinc, and strontium, which are involved in many processes related to bone regeneration (Kristina et al., 2018). Therefore, combining these natural bioactive ions with scaffolds can provide a safer alternative strategy for bone regeneration (Table 4). Recently, it has been reported that ions such as magnesium, silicon, and copper can stimulate angiogenesis and promote new bone formation (Lai et al., 2019). Compared with growth factors, incorporating bioactive ions into bone substitutes is a simpler and safer method to encourage bone regeneration, and the cost is relatively low.

5.1 Magnesium

A vital component of bone development and maturation, magnesium occupies the second most abundant position in natural bones after calcium (Gu et al., 2019). Magnesium ion regulates many enzymes and cell functions and significantly impacts cell homeostasis (Lai et al., 2019). In addition, magnesium ions can improve cell adhesion and differentiation (Zhang et al., 2021) and regulate local bone formation by promoting angiogenesis (Yu et al., 2017).

Several attempts have been made in recent years to stimulate vascularized bone repair by adding bioactive magnesium ions to bone substitutes. For example, a magnesium-rich microsphere was made to simulate the bone microenvironment, thus inducing vascularized bone formation (Lin et al., 2019). Yu et al. reported a composite carrier containing Mg2+, which showed excellent angiogenic ability. Zhang et al. developed a double-crosslinked hydrogel containing magnesium ions to repair bone defects by promoting cell adhesion, angiogenesis, and osteogenesis (Zhang et al., 2021). Furthermore, magnesium surface biological coatings and magnesium-based bone cement also effectively promote angiogenesis (Nabiyouni et al., 2018; Ma et al., 2020).

There is, however, a problem with most magnesium-based bone biomaterials due to their passive mixing with metal magnesium, which has a defect of fast release rate. The rapid release will cause excessive magnesium hydroxide, forming a "high magnesium microenvironment" around the implant, destroying calcium-related physiological processes in surrounding cells and tissues and even causing toxic damage (Kuśnierczyk and Basista, 2016). Inspired by the attraction of metals by magnets, Zhao et al. developed bisphosphonate functionalized injectable hydrogel microspheres by using the coordination reaction of metal ion ligands, which can promote cancellous bone reconstruction in osteoporotic bone defects by capturing Mg^{2+}. The experimental results show that Mg^{2+} trapping composite microspheres excited by magnets can stimulate the function of osteoblasts and endothelial cells' function and inhibit osteoclasts' activation, which is beneficial to angiogenesis and osteogenesis and effectively promotes bone regeneration (Zhao et al., 2021).

5.2 Strontium

Strontium (sr) is an essential trace element in the human body and a regular component of bones. Many studies have shown that strontium can promote osteoblast generation, stimulate bone development and growth, inhibit the process of bone resorption, and maintain the normal physiological function of the human body (Pilmane et al., 2017). Strontium ranelate (SrR) has been proven effective in treating osteoporosis in postmenopausal women (Lin et al., 2021). In addition, Sr or SrR has also been shown to promote angiogenesis (Bakshi et al., 2021) effectively. For example, SrR can promote angiogenesis and differentiation of OVX-BMSCs and HUVECs, increase the mRNA levels of VEGF and Ang-1 in osteoporotic BMSCs, and increase the mRNA level of VEGF in HUVECs (Guo et al., 2016).

There is great potential in treating bone defects with strontium-doped bone tissue biomaterials with dual osteogenesis and angiogenesis effects. For example, to improve the physicochemical and biological properties of calcium phosphate mixed cement (CPHC), a strontium-reinforced CPC (Sr-CPHC) was developed. It was found that Sr-CPHC significantly promoted the endothelial cell migration and tube formation of HUVECs *in vitro* and upregulated the expression of VEGF and angiopoietin-1 (Ang-1) (Wu et al., 2021). Experiments *in vivo* and *in vitro* showed good osteogenic function.

In addition, the design of new composite bone biomaterials aimed at combining the complementary biological effects of various beneficial elements has also achieved good results (Baba et al., 2017; Ratnayake et al., 2017). For example, Sr2+/Fe3+ co-substituted nano-hydroxyapatite directly promoted the function of MC3T3 osteoblasts and HUVECs and greatly facilitated the activation of M2 macrophages to promote osteogenesis and angiogenesis. The results of subcutaneous implantation *in vivo* and repair of skull defects further confirmed the excellent ability of Sr2+/Fe3+ in immune regulation, angiogenesis, and bone regeneration *in situ* (Yang et al., 2021).

5.3 Cobalt

Cobalt (Co) plays a crucial role in the human body, which protects HIF-1a from degradation by inhibiting proline hydroxylase (PHD), simulates hypoxia, activates HIF-1a signal pathway, and then upregulates the expression of targeted genes to promote angiogenesis (Pacary et al., 2006). In addition, cobalt ions can modulate the expression of nuclear factor κB (NFkB), triggering the transcriptional activation of HIF-1α (Kulanthaivel et al., 2016). HIF-1 α can upregulate the expression of angiogenic genes (VEGF, bFGF, and SDF-1) related to bone regeneration (Hu et al., 2008; Zou et al., 2012).

Cobalt's angiogenic properties are widely used in tissue engineering, such as cobalt-containing bioactive glass stimulates angiogenesis and gene expression of HIF-1 α and VEGF (de Laia et al., 2021). The vascularization of the bone is vital for the repair of defects. Insufficient or abnormal vascularization can lead to cell death or poor bone formation due to deficient nutrient and oxygen supply. The dose effect of vascularization on bone formation was studied by tricalcium phosphate (TCP) scaffolds doped with different concentrations of cobalt. The study also found that TCP doped with Co positively influenced osteogenesis, but excessive Co inhibited differentiation of osteoblasts and bone formation (Zheng et al., 2019).

There is excellent potential for bone repair with cobalt ions as they simulate hypoxia to stimulate angiogenesis (Li et al., 2021). However, the release curve of cobalt ions is the key to better use of cobalt ions to repair bone defects. Sun et al. prepared in-situ photocrosslinked nanocomposite hydrogel as a controlled release system for regulating Co ions, which can maintain the continuous release of Co ions for 21 days, which matches the early angiogenesis in the process of bone formation. Experiments *In vivo* and *in vitro* showed good ability for bone formation and new blood vessel formation (Sun et al., 2021).

5.4 Copper

In the body, copper (Cu) is an essential micronutrient that participates in many biological processes and maintains many enzymes' homeostasis and physiological function (Shi et al., 2016; Dong et al., 2020). Cu can stimulate human endothelial cell proliferation and VEGF secretion, thus promoting angiogenesis (Rau et al., 2019). Copper ion is closely related to fibroblast growth factor, and they synergistically stimulate angiogenesis. VEGF activates endothelial cells by regulating the proliferation and migration of endothelial cells in surrounding tissues and finally forming tubular structures. Copper ions can also promote endothelial cells' recruitment, differentiation, and angiogenesis by increasing the expression of HIF 1α and inhibiting the degradation of hypoxia-inducible factor 1 α (Magri et al., 2017). At the same time, the activation of HIF-1α can promote the transcription of VEGF expression.

The characteristics of copper ion angiogenesis to promote bone repair are widely used in bone biomaterial engineering. In one study, copper-added Cu-CPS ceramics [Cu-Ca5 (PO4) 2SiO4] showed better angiogenic and osteogenic properties than pure CPS ceramics. It was found that Cu played an essential role in promoting angiogenesis in the early stage, and the synergistic effect of silicon and copper promoted osteogenesis and angiogenesis in the later stage (Wu et al., 2021). In addition, adding Cu can enhance the biological activity of cells in the bioactive glass field because Cu has osteogenic and angiogenic properties (Zhou et al., 2018; Dai et al., 2021).

5.5 Silicon

As one of the necessary trace elements for the growth and development of organisms, silicon can promote angiogenesis and the formation of functional vascular networks, participate in the regulation of bone formation and calcification, and play an essential role in bone metabolism (Khandmaa et al., 2017a; Yan et al., 2018). Silicon ions promote angiogenesis by inhibiting the expression of prolyl hydroxylase-2 and upregulating the HIF-1 α signal pathway (Khandmaa et al., 2017b).

It has been found that doping silicon-coated implants can promote angiogenesis by promoting adhesion, migration, proliferation, tube formation, and angiogenesis-related gene expression of HUVEC (Fu et al., 2020; Monte et al., 2020). Cell-cell interaction can promote silicon-mediated angiogenesis through a paracrine pathway. In one study, it was found that silicon ions did not promote the expression of the VEGF gene in individual cultured human dermal fibroblasts (human dermal fibroblast, HDF) and did not upregulate the expression of vascular endothelial cadherin (VE-cad) cad in cultured HUVEC cells alone. However, silicon ions greatly enhanced the expression of the VEGF gene in HDF cells co-cultured with HDF and HUVEC and then upregulated the expression of the KDR receptor in the co-cultured HUVEC through the paracrine pathway, which activate the expression of VEGF/KDR/eNOS/NO axis and VE-cad gene to promote functional angiogenesis (Li and Chang, 2013). In addition, It was found that strontium-substituted calcium silicate ceramics can stimulate BMSCs to release exosomal miR-146a to regulate osteogenesis and angiogenesis (Liu et al., 2021).

6 Conclusion

In conclusion, there is a close relationship between blood vessels and bone in bone growth and development and maintaining bone mass balance. The angiogenic-osteogenic coupling involves many growth factors, cells, and regulatory effects. The success of bone regeneration induced by biomaterials depends on the early promotion of angiogenesis and the regulation of critical links in bone healing. By optimizing the scaffold material and improving the parameters of the scaffold material, a scaffold with a specific structure suitable for vascular growth can indeed be made. However, the scaffold with optimized structure still needs vascular growth of the body after implantation, so it is limited to increasing the vascularization of tissue engineering bone only by optimizing the scaffold material. The effect of promoting vascular growth factor is positive, but this method still has difficulties in growth factor dose control and sustained release technology. Insufficient local release concentration and short duration can not achieve a good effect of inducing regeneration. Too high a release concentration can even produce cytotoxicity. Gene transfection technology no longer has the problem of controlled release of growth factors. Still, the characteristics and function of seed cells transfected with genes may be affected and face the risk of carcinogenesis. Trace elements and biomaterials were combined to modify bone repair materials to make them have good angiogenic properties. Trace elements can quickly pass through the cell membrane, regulate multiple cell physiological processes, improve the osteogenic microenvironment, and promote angiogenesis. However, most experiments lack research on the related mechanism, and relatively high concentrations of metal ions may have non-specific side effects on multiple systems and organs. Therefore, determining the optimal concentration of trace elements to promote angiogenesis and osteogenesis, controlling their release from scaffold materials, and elucidating their release kinetic basis *in vivo* and related immune regulatory mechanisms may be the issues that need to be addressed by future researchers.

Author contributions

NL: Investigation, Software, Writing–original draft, Project administration, Supervision, Validation. ZZ: Data curation, Investigation, Software, Supervision, Writing–original draft. MH: Conceptualization, Investigation, Software, Writing–original draft. LH: Conceptualization, Investigation, Software, Writing–original draft. HL: Data curation, Software, Writing–original draft. ZQ: Project administration, Supervision, Validation, Writing–review and editing. XG: Conceptualization, Formal Analysis, Investigation, Writing–review and editing. ML: Conceptualization, Investigation, Project administration, Supervision, Writing–review and editing.

Funding

The author(s) declare financial support was received for the research, authorship, and/or publication of this article. This work was supported by the National Natural Science Foundation of China (No. 82274558), Lianyungang Traditional Chinese Medicine Technology Development Plan Project (ZD202210), Lianyungang Key Science and Technology Research and Development Plan (No. SF2206), and Research Foundation of Kangda College of Nanjing Medical University (No. KD2022KYJJZD035).

Conflict of interest

The authors declare that the research was conducted in the absence of any commercial or financial relationships that could be construed as a potential conflict of interest.

Publisher's note

References

Ahn, H., Patel, R. R., Hoyt, A. J., Lin, A., Torstrick, F. B., Guldberg, R. E., et al. (2018). Biological evaluation and finite-element modeling of porous poly(para-phenylene) for orthopaedic implants. *Acta Biomater.* 72, 352–361. doi:10.1016/j.actbio.2018.03.025

AlMuraikhi, N., Ali, D., Vishnubalaji, R., Manikandan, M., Atteya, M., Siyal, A., et al. (2019). Notch signaling inhibition by LY411575 attenuates osteoblast differentiation and decreased ectopic bone formation capacity of human skeletal (mesenchymal) stem cells. *Stem Cells Int.* 2019, 1–12. doi:10.1155/2019/3041262

Anada, T., Pan, C. C., Stahl, A. M., Mori, S., Fukuda, J., Suzuki, O., et al. (2019). Vascularized bone-mimetic hydrogel constructs by 3D bioprinting to promote osteogenesis and angiogenesis. *Int. J. Mol. Sci.* 20, 1096. doi:10.3390/ijms20051096

Baba, I. Y., Wimpenny, I., Bretcanu, O., Dalgarno, K., and El, H. A. (2017). Development of multisubstituted hydroxyapatite nanopowders as biomedical materials for bone tissue engineering applications. *J. Biomed. Mater Res. A* 105, 1775–1785. doi:10.1002/jbm.a.36038

Bakshi, R., Hokugo, A., Khalil, D., Wang, L., Shibuya, Y., Zhou, S., et al. (2021). A chemotactic functional scaffold with VEGF-releasing peptide amphiphiles facilitates bone regeneration by BMP-2 in a large-scale rodent cranial defect model. *Plast. Reconstr. Surg.* 147, 386–397. doi:10.1097/prs.0000000000007551

Bank, R. A. (2019). Limiting biomaterial fibrosis. *Nat. Mater* 18, 781. doi:10.1038/s41563-019-0428-y

Bobbert, F., and Zadpoor, A. A. (2017). Effects of bone substitute architecture and surface properties on cell response, angiogenesis, and structure of new bone. *J. Mater Chem. B* 5, 6175–6192. doi:10.1039/c7tb00741h

Brydone, A. S., Meek, D., and Maclaine, S. (2010). Bone grafting, orthopaedic biomaterials, and the clinical need for bone engineering. *Proc. Inst. Mech. Eng. H.* 224, 1329–1343. doi:10.1243/09544119jeim770

Chang, P. C., Cirelli, J. A., Jin, Q., Seol, Y. J., Sugai, J. V., D'Silva, N. J., et al. (2009). Adenovirus encoding human platelet-derived growth factor-B delivered to alveolar bone defects exhibits safety and biodistribution profiles favorable for clinical use. *Hum. GENE Ther.* 20, 486–496. doi:10.1089/hum.2008.114

Chen, F. M., An, Y., Zhang, R., and Zhang, M. (2011). New insights into and novel applications of release technology for periodontal reconstructive therapies. *J. Control Release* 149, 92–110. doi:10.1016/j.jconrel.2010.10.021

Chen, K., Liao, S., Li, Y., Jiang, H., Liu, Y., Wang, C., et al. (2021). Osteoblast-derived EGFL6 couples angiogenesis to osteogenesis during bone repair. *Theranostics* 11, 9738–9751. doi:10.7150/thno.60902

Chen, Y., Chen, S., Kawazoe, N., and Chen, G. (2018). Promoted angiogenesis and osteogenesis by dexamethasone-loaded calcium phosphate nanoparticles/collagen composite scaffolds with microgroove networks. *Sci. Rep.* 8, 14143. doi:10.1038/s41598-018-32495-y

Chen, Y., Yu, H., Zhu, D., Liu, P., Yin, J., Liu, D., et al. (2020). miR-136-3p targets PTEN to regulate vascularization and bone formation and ameliorates alcohol-induced osteopenia. *FASEB J.* 34, 5348–5362. doi:10.1096/fj.201902463rr

Cheng, D., Ding, R., Jin, X., Lu, Y., Bao, W., Zhao, Y., et al. (2023). Strontium ion-functionalized nano-hydroxyapatite/chitosan composite microspheres promote osteogenesis and angiogenesis for bone regeneration. *ACS Appl. Mater Interfaces* 15, 19951–19965. doi:10.1021/acsami.3c00655

Cheng, W., Ding, Z., Zheng, X., Lu, Q., Kong, X., Zhou, X., et al. (2020). Injectable hydrogel systems with multiple biophysical and biochemical cues for bone regeneration. *Biomater. Sci.* 8, 2537–2548. doi:10.1039/d0bm00104j

Conserva, E., Pisciotta, A., Borghi, F., Nasi, M., Pecorini, S., Bertoni, L., et al. (2019). Titanium surface properties influence the biological activity and FasL expression of craniofacial stromal cells. *Stem Cells Int.* 2019, 1–11. doi:10.1155/2019/4670560

Dai, Q., Li, Q., Gao, H., Yao, L., Lin, Z., Li, D., et al. (2021). 3D printing of Cu-doped bioactive glass composite scaffolds promotes bone regeneration through activating the HIF-1α and TNF-α pathway of hUVECs. *Biomater.* 9, 5519–5532. doi:10.1039/D1BM00870F

de Laia, A., Valverde, T. M., Barrioni, B. R., Cunha, P., de Goes, A. M., de Miranda, M. C., et al. (2021). Cobalt-containing bioactive glass mimics vascular endothelial growth factor A and hypoxia inducible factor 1 function. *J. Biomed. Mater Res. A* 109, 1051–1064. doi:10.1002/jbm.a.37095

Denchai, A., Tartarini, D., and Mele, E. (2018). Cellular response to surface morphology: electrospinning and computational modeling. *Front. Bioeng. Biotechnol.* 6, 155. doi:10.3389/fbioe.2018.00155

Dohle, E., El, B. K., Sader, R., Choukroun, J., James, K. C., and Ghanaati, S. (2018). Platelet-rich fibrin-based matrices to improve angiogenesis in an *in vitro* co-culture model for bone tissue engineering. *J. Tissue Eng. Regen. M.* 12, 598–610. doi:10.1002/term.2475

Dong, C., Feng, W., Xu, W., Yu, L., Xiang, H., Chen, Y., et al. (2020). The coppery age: copper (Cu)-Involved nanotheranostics. *Adv. Sci.* 7, 2001549. doi:10.1002/advs.202001549

Dou, Y., Huang, J., Xia, X., Wei, J., Zou, Q., Zuo, Y., et al. (2021). A hierarchical scaffold with a highly pore-interconnective 3D printed PLGA/n-HA framework and an extracellular matrix like gelatin network filler for bone regeneration. *J. Mater. Chem. B* 9, 4488–4501. doi:10.1039/D1TB00662B

Dreyer, C. H., Kjaergaard, K., Ding, M., and Qin, L. (2020). Vascular endothelial growth factor for *in vivo* bone formation: a systematic review. *J. Orthop. Transl.* 24, 46–57. doi:10.1016/j.jot.2020.05.005

Filipowska, J., Tomaszewski, K. A., Niedzwiedzki, L., Walocha, J. A., and Niedzwiedzki, T. (2017). The role of vasculature in bone development, regeneration and proper systemic functioning. *Angiogenesis* 20, 291–302. doi:10.1007/s10456-017-9541-1

Freitas, P., Kishida, R., Hayashi, K., Tsuchiya, A., Shimabukuro, M., and Ishikawa, K. (2022). Fabrication and histological evaluation of porous carbonate apatite blocks using disodium hydrogen phosphate crystals as a porogen and phosphatization accelerator. *J. Biomed. MATER Res. A* 110, 1278–1290. doi:10.1002/jbm.a.37374

Fu, X., Liu, P., Zhao, D., Yuan, B., Xiao, Z., Zhou, Y., et al. (2020). Effects of nanotopography regulation and silicon doping on angiogenic and osteogenic activities of hydroxyapatite coating on titanium implant. *Int. J. Nanomedicine* 15, 4171–4189. doi:10.2147/ijn.s252936

Gallardo-Calero, I., Barrera-Ochoa, S., Manzanares, M. C., Sallent, A., Vicente, M., Lopez-Fernandez, A., et al. (2019). Vascularized periosteal flaps accelerate osteointegration and revascularization of allografts in rats. *Clin. Orthop. Relat. Res.* 477, 741–755. doi:10.1097/corr.0000000000000400

Gao, B., Deng, R., Chai, Y., Chen, H., Hu, B., Wang, X., et al. (2019). Macrophage-lineage TRAP+ cells recruit periosteum-derived cells for periosteal osteogenesis and regeneration. *J. Clin. Invest.* 129, 2578–2594. doi:10.1172/jci98857

Geng, M., Zhang, Q., Gu, J., Yang, J., Du, H., Jia, Y., et al. (2021). Construction of a nanofiber network within 3D printed scaffolds for vascularized bone regeneration. *Biomater. Sci.* 9, 2631–2646. doi:10.1039/d0bm02058c

Gong, Y., Li, S., Zeng, W., Yu, J., Chen, Y., and Yu, B. (2019). Controlled *in vivo* bone formation and vascularization using ultrasound-triggered release of recombinant vascular endothelial growth factor from poly(D,L-lactic-co-glycolicacid) microbubbles. *Front. Pharmacol.* 10, 413. doi:10.3389/fphar.2019.00413

Gu, Y., Zhang, J., Zhang, X., Liang, G., Xu, T., and Niu, W. (2019). Three-dimensional printed Mg-doped β-TCP bone tissue engineering scaffolds: effects of magnesium ion concentration on osteogenesis and angiogenesis *in vitro*. *Tissue Eng. Regen. Med.* 16, 415–429. doi:10.1007/s13770-019-00192-0

Guo, X., Jiang, H., Zong, X., Du, L., Zhao, J., Zhang, D., et al. (2020). The implication of the notch signaling pathway in biphasic calcium phosphate ceramic-induced ectopic bone formation: a preliminary experiment. *J. Biomed. Mater Res. A* 108, 1035–1044. doi:10.1002/jbm.a.36878

Guo, X., Wei, S., Lu, M., Shao, Z., Lu, J., Xia, L., et al. (2016). Dose-dependent effects of strontium ranelate on ovariectomy rat bone marrow mesenchymal stem cells and human umbilical vein endothelial cells. *Int. J. Biol. Sci.* 12, 1511–1522. doi:10.7150/ijbs.16499

Hayashi, K., Munar, M. L., and Ishikawa, K. (2020). Effects of macropore size in carbonate apatite honeycomb scaffolds on bone regeneration. *Mater Sci. Eng. C Mater Biol. Appl.* 111, 110848. doi:10.1016/j.msec.2020.110848

Hu, K., and Olsen, B. R. (2016a). The roles of vascular endothelial growth factor in bone repair and regeneration. *BONE* 91, 30–38. doi:10.1016/j.bone.2016.06.013

Hu, K., and Olsen, B. R. (2016b). Osteoblast-derived VEGF regulates osteoblast differentiation and bone formation during bone repair. *J. Clin. Invest.* 126, 509–526. doi:10.1172/jci82585

Hu, X., Yu, S. P., Fraser, J. L., Lu, Z., Ogle, M. E., Wang, J. A., et al. (2008). Transplantation of hypoxia-preconditioned mesenchymal stem cells improves infarcted heart function via enhanced survival of implanted cells and angiogenesis. *J. Thorac. Cardiovasc Surg.* 135, 799–808. doi:10.1016/j.jtcvs.2007.07.071

Huang, G. J., Yu, H. P., Wang, X. L., Ning, B. B., Gao, J., Shi, Y. Q., et al. (2021). Highly porous and elastic aerogel based on ultralong hydroxyapatite nanowires for high-performance bone regeneration and neovascularization. *J. Mater Chem. B* 9, 1277–1287. doi:10.1039/d0tb02288h

Huang, J., Chen, Y., Tang, C., Fei, Y., Wu, H., Ruan, D., et al. (2019). The relationship between substrate topography and stem cell differentiation in the musculoskeletal system. *Cell Mol. Life Sci.* 76, 505–521. doi:10.1007/s00018-018-2945-2

Jia, P., Chen, H., Kang, H., Qi, J., Zhao, P., Jiang, M., et al. (2016). Deferoxamine released from poly(lactic-co-glycolic acid) promotes healing of osteoporotic bone defect via enhanced angiogenesis and osteogenesis. *J. Biomed. MATER Res. A* 104, 2515–2527. doi:10.1002/jbm.a.35793

Jin, S., Yang, R., Chu, C., Hu, C., Zou, Q., Li, Y., et al. (2021). Topological structure of electrospun membrane regulates immune response, angiogenesis and bone regeneration. *ACTA Biomater.* 129, 148–158. doi:10.1016/j.actbio.2021.05.042

Juhl, O. T., Zhao, N., Merife, A. B., Cohen, D., Friedman, M., Zhang, Y., et al. (2019). Aptamer-functionalized fibrin hydrogel improves vascular endothelial growth factor release kinetics and enhances angiogenesis and osteogenesis in critically sized cranial defects. *ACS Biomater. Sci. Eng.* 5, 6152–6160. doi:10.1021/acsbiomaterials.9b01175

Kang, Y., Ren, L., and Yang, Y. (2014). Engineering vascularized bone grafts by integrating a biomimetic periosteum and beta-TCP scaffold. *ACS Appl. Mater Interfaces* 6, 9622–9633. doi:10.1021/am502056q

Kauffmann, P., Raschke, D., Troltzsch, M., Santander, P., Brockmeyer, P., and Schliephake, H. (2021). The use of rhBMP2 for augmentation of established horizontal/vertical defects may require additional use of rhVEGF to achieve significant bone regeneration: an *in vivo* experimental study. *Clin. Oral Implants Res.* 32, 1228–1240. doi:10.1111/clr.13820

Kerouredan, O., Bourget, J. M., Remy, M., Crauste-Manciet, S., Kalisky, J., Catros, S., et al. (2019a). Micropatterning of endothelial cells to create a capillary-like network with defined architecture by laser-assisted bioprinting. *J. Mater Sci. Mater Med.* 30, 28. doi:10.1007/s10856-019-6230-1

Kerouredan, O., Hakobyan, D., Remy, M., Ziane, S., Dusserre, N., Fricain, J. C., et al. (2019b). *In situ* prevascularization designed by laser-assisted bioprinting: effect on bone regeneration. *Biofabrication* 11, 045002. doi:10.1088/1758-5090/ab2620

Khandmaa, D., Ahmed, E., Jennifer, O. B., Roman, A. P., Jonathan, C. K., and Hae-Won, K. (2017a). A mini review focused on the proangiogenic role of silicate ions released from silicon-containing biomaterials. *J. Tissue Eng.* 8, 204173141770733. doi:10.1177/2041731417707339

Khandmaa, D., Guang-Zhen, J., Joong-Hyun, K., Roman, P., Jun-Hyeog, J., and Hae-Won, K. (2017b). Promoting angiogenesis with mesoporous microcarriers through a synergistic action of delivered silicon ion and VEGF. *Biomaterials* 116, 145–157. doi:10.1016/j.biomaterials.2016.11.053

Kristina, G., Phil, D., Alexander, K., Nada, M., Patrick, R., Sven, R., et al. (2018). Applications of metals for bone regeneration. *Int. J. Mol. Sci.* 19, 826. doi:10.3390/ijms19030826

Kulanthaivel, S., Roy, B., Agarwal, T., Giri, S., Pramanik, K., Pal, K., et al. (2016). Cobalt doped proangiogenic hydroxyapatite for bone tissue engineering application. *Mater Sci. Eng. C Mater Biol. Appl.* 58, 648–658. doi:10.1016/j.msec.2015.08.052

Kuśnierczyk, K., and Basista, M. (2016). Recent advances in research on magnesium alloys and magnesium-calcium phosphate composites as biodegradable implant materials. *J. Biomater. Appl.* 31, 878–900. doi:10.1177/0885328216657271

Lai, Y., Li, Y., Cao, H., Long, J., Wang, X., Li, L., et al. (2019). Osteogenic magnesium incorporated into PLGA/TCP porous scaffold by 3D printing for repairing challenging bone defect. *Biomaterials* 197, 207–219. doi:10.1016/j.biomaterials.2019.01.013

Lee, S. S., Kim, J. H., Jeong, J., Kim, S., Koh, R. H., Kim, I., et al. (2020). Sequential growth factor releasing double cryogel system for enhanced bone regeneration. *Biomaterials* 257, 120223. doi:10.1016/j.biomaterials.2020.120223

Li, D., Deng, L., Xie, X., Yang, Z., and Kang, P. (2016a). Evaluation of the osteogenesis and angiogenesis effects of erythropoietin and the efficacy of deproteinized bovine bone/recombinant human erythropoietin scaffold on bone defect repair. *J. Mater Sci. Mater Med.* 27, 101. doi:10.1007/s10856-016-5714-5

Li, H., and Chang, J. (2013). Bioactive silicate materials stimulate angiogenesis in fibroblast and endothelial cell co-culture system through paracrine effect. *Acta Biomater.* 9, 6981–6991. doi:10.1016/j.actbio.2013.02.014

Li, J., Jahr, H., Zheng, W., and Ren, P. G. (2017). Visualizing angiogenesis by multiphoton microscopy *in vivo* in genetically modified 3D-PLGA/nHAp scaffold for calvarial critical bone defect repair. *J. Vis. Exp.* 2017, 55381. doi:10.3791/55381

Li, J., Li, Z., Wang, C., Li, Z., Xu, H., Hu, Y., et al. (2020b). The regulatory effect of VEGF-ax on rat bone marrow mesenchymal stem cells' angioblastic differentiation and its proangiogenic ability. *Stem Cell Dev.* 29, 667–677. doi:10.1089/scd.2019.0198

Li, J., Xu, Q., Teng, B., Yu, C., Li, J., Song, L., et al. (2016b). Investigation of angiogenesis in bioactive 3-dimensional poly(d,l-lactide-co-glycolide)/nano-hydroxyapatite scaffolds by *in vivo* multiphoton microscopy in murine calvarial critical bone defect. *Acta Biomater.* 42, 389–399. doi:10.1016/j.actbio.2016.06.024

Li, J., Xu, T., Hou, W., Liu, F., Qing, W., Huang, L., et al. (2020a). The response of host blood vessels to graded distribution of macro-pores size in the process of ectopic osteogenesis. *Mater Sci. Eng. C Mater Biol. Appl.* 109, 110641. doi:10.1016/j.msec.2020.110641

Li, J., Zhao, C., Liu, C., Wang, Z., Ling, Z., Lin, B., et al. (2021b). Cobalt-doped bioceramic scaffolds fabricated by 3D printing show enhanced osteogenic and angiogenic properties for bone repair. *Biomed. Eng. ONLINE* 20, 70. doi:10.1186/s12938-021-00907-2

Li, L., Yu, M., Li, Y., Li, Q., Yang, H., Zheng, M., et al. (2021a). Synergistic anti-inflammatory and osteogenic n-HA/resveratrol/chitosan composite microspheres for osteoporotic bone regeneration. *Bioact. Mater* 6, 1255–1266. doi:10.1016/j.bioactmat.2020.10.018

Li, S., Song, C., Yang, S., Yu, W., Zhang, W., Zhang, G., et al. (2019). Supercritical CO2 foamed composite scaffolds incorporating bioactive lipids promote vascularized bone regeneration via Hif-1α upregulation and enhanced type H vessel formation. *Acta Biomater.* 94, 253–267. doi:10.1016/j.actbio.2019.05.066

Lian, M., Sun, B., Han, Y., Yu, B., Xin, W., Xu, R., et al. (2021). A low-temperature-printed hierarchical porous sponge-like scaffold that promotes cell-material interaction and modulates paracrine activity of MSCs for vascularized bone regeneration. *Biomaterials* 274, 120841. doi:10.1016/j.biomaterials.2021.120841

Lin, S., Yang, G., Jiang, F., Zhou, M., Yin, S., Tang, Y., et al. (2019b). A magnesium-enriched 3D culture system that mimics the bone development microenvironment for vascularized bone regeneration. *Adv. Sci. (Weinh)* 6, 1900209. doi:10.1002/advs.201900209

Lin, S. H., Zhang, W. J., and Jiang, X. Q. (2019a). Applications of bioactive ions in bone regeneration. *Chin. J. Dent. Res.* 22, 93–104. doi:10.3290/j.cjdr.a42513

Lin, S. Y., Hung, M. C., Chang, S. F., Tsuang, F. Y., Chang, J. Z., and Sun, J. S. (2021). Efficacy and safety of postmenopausal osteoporosis treatments: a systematic review and network meta-analysis of randomized controlled trials. *J. Clin. Med.* 10, 3043. doi:10.3390/jcm10143043

Liu, L., Yu, F., Li, L., Zhou, L., Zhou, T., Xu, Y., et al. (2021). Bone marrow stromal cells stimulated by strontium-substituted calcium silicate ceramics: release of exosomal miR-146a regulates osteogenesis and angiogenesis. *Acta BiomateR.* 119, 444–457. doi:10.1016/j.actbio.2020.10.038

Liu, M., Zeng, X., Ma, C., Yi, H., Ali, Z., Mou, X., et al. (2017). Injectable hydrogels for cartilage and bone tissue engineering. *Bone Res.* 5, 17014. doi:10.1038/boneres.2017.14

Liu, Y., Yang, S., Cao, L., Zhang, X., Wang, J., and Liu, C. (2020). Facilitated vascularization and enhanced bone regeneration by manipulation hierarchical pore structure of scaffolds. *Mater Sci. Eng. C Mater Biol. Appl.* 110, 110622. doi:10.1016/j.msec.2019.110622

Long, Z., Shetty, A. M., Solomon, M. J., and Larson, R. G. (2009). Fundamentals of magnet-actuated droplet manipulation on an open hydrophobic surface. *Lab. CHIP* 9, 1567–1575. doi:10.1039/b819818g

Lu, W., Zhou, C., Ma, Y., Li, J., Jiang, J., Chen, Y., et al. (2022). Improved osseointegration of strontium-modified titanium implants by regulating angiogenesis and macrophage polarization. *Biomater. Sci.* 10, 2198–2214. doi:10.1039/d1bm01488a

Luo, C., Yang, X., Li, M., Huang, H., Kang, Q., Zhang, X., et al. (2018). A novel strategy for *in vivo* angiogenesis and osteogenesis: magnetic micro-movement in a bone scaffold. *Artif. Cells Nanomed Biotechnol.* 46, 636–645. doi:10.1080/21691401.2018.1465947

Luo, R., Huang, Y., Yuan, X., Yuan, Z., Zhang, L., Han, J., et al. (2021). Controlled co-delivery system of magnesium and lanthanum ions for vascularized bone regeneration. *Biomed. Mater* 16, 065024. doi:10.1088/1748-605x/ac2886

Ma, L., Cheng, S., Ji, X., Zhou, Y., Zhang, Y., Li, Q., et al. (2020). Immobilizing magnesium ions on 3D printed porous tantalum scaffolds with polydopamine for improved vascularization and osteogenesis. *Mater Sci. Eng. C Mater Biol. Appl.* 117, 111303. doi:10.1016/j.msec.2020.111303

Magri, A., Tabbi, G., Breglia, R., De Gioia, L., Fantucci, P., Bruschi, M., et al. (2017). Copper ion interaction with the RNase catalytic site fragment of the angiogenin protein: an experimental and theoretical investigation. *Dalton Trans.* 46, 8524–8538. doi:10.1039/c7dt01209h

Monte, F., Awad, K. R., Ahuja, N., Kim, H., Aswath, P., Brotto, M., et al. (2020). Amorphous silicon oxynitrophosphide-coated implants boost angiogenic activity of endothelial cells. *Tissue Eng. Part A* 26, 15–27. doi:10.1089/ten.tea.2019.0051

Nabiyouni, M., Bruckner, T., Zhou, H., Gbureck, U., and Bhaduri, S. B. (2018). Magnesium-based bioceramics in orthopedic applications. *Acta Biomater.* 66, 23–43. doi:10.1016/j.actbio.2017.11.033

Nulty, J., Freeman, F. E., Browe, D. C., Burdis, R., Ahern, D. P., Pitacco, P., et al. (2021). 3D bioprinting of prevascularised implants for the repair of critically-sized bone defects. *Acta Biomater.* 126, 154–169. doi:10.1016/j.actbio.2021.03.003

Ortiz, R., Aurrekoetxea-Rodriguez, I., Rommel, M., Quintana, I., Vivanco, M. D., and Toca-Herrera, J. L. (2018). Laser surface microstructuring of a bio-resorbable polymer to anchor stem cells, control adipocyte morphology, and promote osteogenesis. *Polym. (Basel)* 10, 1337. doi:10.3390/polym10121337

Pacary, E., Legros, H., Valable, S., Duchatelle, P., Lecocq, M., Petit, E., et al. (2006). Synergistic effects of CoCl(2) and ROCK inhibition on mesenchymal stem cell differentiation into neuron-like cells. *J. Cell Sci.* 119, 2667–2678. doi:10.1242/jcs.03004

Patel, K. D., Kim, T. H., Mandakhbayar, N., Singh, R. K., Jang, J. H., Lee, J. H., et al. (2020). Coating biopolymer nanofibers with carbon nanotubes accelerates tissue healing and bone regeneration through orchestrated cell- and tissue-regulatory responses. *Acta Biomater.* 108, 97–110. doi:10.1016/j.actbio.2020.03.012

Pati, F., and Cho, D. W. (2017). Bioprinting of 3D tissue models using decellularized extracellular matrix bioink. *Methods Mol. Biol.* 1612, 381–390. doi:10.1007/978-1-4939-7021-6_27

Peng, Y., Wu, S., Li, Y., and Crane, J. L. (2020). Type H blood vessels in bone modeling and remodeling. *Theranostics* 10, 426–436. doi:10.7150/thno.34126

Piard, C., Baker, H., Kamalitdinov, T., and Fisher, J. (2019). Bioprinted osteon-like scaffolds enhance *in vivo* neovascularization. *Biofabrication* 11, 025013. doi:10.1088/1758-5090/ab078a

Pilmane, M., Salma-Ancane, K., Loca, D., Locs, J., and Berzina-Cimdina, L. (2017). Strontium and strontium ranelate: historical review of some of their functions. *Mater Sci. Eng. C Mater Biol. Appl.* 78, 1222–1230. doi:10.1016/j.msec.2017.05.042

Quinlan, E., Lopez-Noriega, A., Thompson, E. M., Hibbitts, A., Cryan, S. A., and O'Brien, F. J. (2017). Controlled release of vascular endothelial growth factor from spray-dried alginate microparticles in collagen-hydroxyapatite scaffolds for promoting vascularization and bone repair. *J. Tissue Eng. Regen. Med.* 11, 1097–1109. doi:10.1002/term.2013

Ratnayake, J. T. B., Mucalo, M., and Dias, G. J. (2017). Substituted hydroxyapatites for bone regeneration: a review of current trends. *J. Biomed. Mater. Res.* 105, 1285–1299. doi:10.1002/jbm.b.33651

Rau, J. V., Curcio, M., Raucci, M. G., Barbaro, K., Fasolino, I., Teghil, R., et al. (2019). Cu-releasing bioactive glass coatings and their *in vitro* properties. *ACS Appl. Mater Inter* 11, 5812–5820. doi:10.1021/acsami.8b19082

Richbourg, N. R., Peppas, N. A., and Sikavitsas, V. I. (2019). Tuning the biomimetic behavior of scaffolds for regenerative medicine through surface modifications. *J. Tissue Eng. Regen. Med.* 13, 1275–1293. doi:10.1002/term.2859

Shahabipour, F., Tavafoghi, M., Aninwene, G. N., Bonakdar, S., Oskuee, R. K., Shokrgozar, M. A., et al. (2022). Coaxial 3D bioprinting of tri-polymer scaffolds to improve the osteogenic and vasculogenic potential of cells in co-culture models. *J. Biomed. Mater Res. A* 110, 1077–1089. doi:10.1002/jbm.a.37354

Sharma, D., Ross, D., Wang, G., Jia, W., Kirkpatrick, S. J., and Zhao, F. (2019). Upgrading prevascularization in tissue engineering: a review of strategies for promoting highly organized microvascular network formation. *Acta Biomater.* 95, 112–130. doi:10.1016/j.actbio.2019.03.016

Shi, M., Chen, Z., Farnaghi, S., Friis, T., Mao, X., Xiao, Y., et al. (2016). Copper-doped mesoporous silica nanospheres, a promising immunomodulatory agent for inducing osteogenesis. *Acta Biomater.* 30, 334–344. doi:10.1016/j.actbio.2015.11.033

Sicchieri, L. G., Crippa, G. E., de Oliveira, P. T., Beloti, M. M., and Rosa, A. L. (2012). Pore size regulates cell and tissue interactions with PLGA-CaP scaffolds used for bone engineering. *J. Tissue Eng. Regen. Med.* 6, 155–162. doi:10.1002/term.422

Simunovic, F., Winninger, O., Strassburg, S., Koch, H. G., Finkenzeller, G., Stark, G. B., et al. (2019). Increased differentiation and production of extracellular matrix components of primary human osteoblasts after cocultivation with endothelial cells: a quantitative proteomics approach. *J. Cell Biochem.* 120, 396–404. doi:10.1002/jcb.27394

Sivan, U., De Angelis, J., and Kusumbe, A. P. (2019). Role of angiocrine signals in bone development, homeostasis and disease. *Open Biol.* 9, 190144. doi:10.1098/rsob.190144

Son, J., Kim, J., Lee, K., Hwang, J., Choi, Y., Seo, Y., et al. (2019). DNA aptamer immobilized hydroxyapatite for enhancing angiogenesis and bone regeneration. *Acta Biomater.* 99, 469–478. doi:10.1016/j.actbio.2019.08.047

Sun, H., Dong, J., Wang, Y., Shen, S., Shi, Y., Zhang, L., et al. (2021a). Polydopamine-coated poly(l-lactide) nanofibers with controlled release of VEGF and BMP-2 as a regenerative periosteum. *ACS Biomater. Sci. Eng.* 7, 4883–4897. doi:10.1021/acsbiomaterials.1c00246

Sun, H., Guo, Q., Shi, C., McWilliam, R. H., Chen, J., Zhu, C., et al. (2022). CD271 antibody-functionalized microspheres capable of selective recruitment of reparative endogenous stem cells for *in situ* bone regeneration. *Biomaterials* 280, 121243. doi:10.1016/j.biomaterials.2021.121243

Sun, Y., Liu, X., Zhu, Y., Han, Y., Shen, J., Bao, B., et al. (2021b). Tunable and controlled release of cobalt ions from metal-organic framework hydrogel nanocomposites enhances bone regeneration. *ACS Appl. Mater Interfaces* 13, 59051–59066. doi:10.1021/acsami.1c16300

Vezenkova, A., and Locs, J. (2022). Sudoku of porous, injectable calcium phosphate cements - path to osteoinductivity. *Bioact. Mater* 17, 109–124. doi:10.1016/j.bioactmat.2022.01.001

Vijayavenkataraman, S., Yan, W. C., Lu, W. F., Wang, C. H., and Fuh, J. (2018). 3D bioprinting of tissues and organs for regenerative medicine. *Adv. Drug Deliv. Rev.* 132, 296–332. doi:10.1016/j.addr.2018.07.004

Vissers, C. A. B., Harvestine, J. N., and Leach, J. K. (2015). Pore size regulates mesenchymal stem cell response to Bioglass-loaded composite scaffolds. *J. Mater. Chem.* 3, 8650–8658. doi:10.1039/c5tb00947b

Wang, C., Xu, D., Lin, L., Li, S., Hou, W., He, Y., et al. (2021). Large-pore-size Ti6Al4V scaffolds with different pore structures for vascularized bone regeneration. *Mater Sci. Eng. C Mater Biol. Appl.* 131, 112499. doi:10.1016/j.msec.2021.112499

Wang, J., Yang, M., Zhu, Y., Wang, L., Tomsia, A. P., and Mao, C. (2014). Phage nanofibers induce vascularized osteogenesis in 3D printed bone scaffolds. *Adv. Mater. Deerf. Beach, Fla.)* 26, 4961–4966. doi:10.1002/adma.201400154

Wang, L., Zhou, F., Zhang, P., Wang, H., Qu, Z., Jia, P., et al. (2017a). Human type H vessels are a sensitive biomarker of bone mass. *Cell Death Dis.* 8, e2760. doi:10.1038/cddis.2017.36

Wang, Q., Zhang, Y., Li, B., and Chen, L. (2017b). Controlled dual delivery of low doses of BMP-2 and VEGF in a silk fibroin-nanohydroxyapatite scaffold for vascularized bone regeneration. *J. Mater. Chem.* 5, 6963–6972. doi:10.1039/c7tb00949f

Wang, R., Zhang, H., Ding, W., Fan, Z., Ji, B., Ding, C., et al. (2020). miR-143 promotes angiogenesis and osteoblast differentiation by targeting HDAC7. *Cell Death Dis.* 11, 179. doi:10.1038/s41419-020-2377-4

Wu, L., Gu, Y., Liu, L., Tang, J., Mao, J., Xi, K., et al. (2020). Hierarchical micro/nanofibrous membranes of sustained releasing VEGF for periosteal regeneration. *Biomaterials* 227, 119555. doi:10.1016/j.biomaterials.2019.119555

Wu, Q., Xu, S., Wang, X., Jia, B., Han, Y., Zhuang, Y., et al. (2021b). Complementary and synergistic effects on osteogenic and angiogenic properties of copper-incorporated silicocarnotite bioceramic: *in vitro* and *in vivo* studies. *Biomaterials* 268, 120553. doi:10.1016/j.biomaterials.2020.120553

Wu, X., Tang, Z., Wu, K., Bai, Y., Lin, X., Yang, H., et al. (2021a). Strontium-calcium phosphate hybrid cement with enhanced osteogenic and angiogenic properties for vascularised bone regeneration. *J. Mater Chem. B* 9, 5982–5997. doi:10.1039/d1tb00439e

Xu, R., Yallowitz, A., Qin, A., Wu, Z., Shin, D. Y., Kim, J. M., et al. (2018). Targeting skeletal endothelium to ameliorate bone loss. *Nat. Med.* 24, 823–833. doi:10.1038/s41591-018-0020-z

Yan, H., Chengtie, W., Xiaoling, Z., Jiang, C., and Kerong, D. (2018). Regulation of immune response by bioactive ions released from silicate bioceramics for bone regeneration. *Acta Biomater.* 66, 81–92. doi:10.1016/j.actbio.2017.08.044

Yang, J., Kang, Y., Browne, C., Jiang, T., and Yang, Y. (2015). Graded porous beta-tricalcium phosphate scaffolds enhance bone regeneration in mandible augmentation. *J. Craniofac Surg.* 26, e148–e153. doi:10.1097/scs.0000000000001383

Yang, L., Fan, L., Lin, X., Yu, Y., and Zhao, Y. (2023). Pearl powder hybrid bioactive scaffolds from microfluidic 3D printing for bone regeneration. *Adv. Sci. (Weinh)* 2023, e2304190. doi:10.1002/advs.202304190

Yang, L., Ullah, I., Yu, K., Zhang, W., Zhou, J., Sun, T., et al. (2021). Bioactive Sr(2+)/Fe(3+)co-substituted hydroxyapatite in cryogenically 3D printed porous scaffolds for bone tissue engineering. *Biofabrication* 13, 035007. doi:10.1088/1758-5090/abcf8d

Yang, M., Li, C. J., Sun, X., Guo, Q., Xiao, Y., Su, T., et al. (2017). MiR-497~195 cluster regulates angiogenesis during coupling with osteogenesis by maintaining endothelial Notch and HIF-1α activity. *Nat. Commun.* 8, 16003. doi:10.1038/ncomms16003

Yilgor, P., Yilmaz, G., Onal, M. B., Solmaz, I., Gundogdu, S., Keskil, S., et al. (2013). An *in vivo* study on the effect of scaffold geometry and growth factor release on the healing of bone defects. *J. TISSUE Eng. Regen. M.* 7, 687–696. doi:10.1002/term.1456

Yin, J., Gong, G., Sun, C., Yin, Z., Zhu, C., Wang, B., et al. (2018). Angiopoietin 2 promotes angiogenesis in tissue-engineered bone and improves repair of bone defects by inducing autophagy. *Biomed. Pharmacother.* 105, 932–939. doi:10.1016/j.biopha.2018.06.078

Yousefi, A. M. (2019). A review of calcium phosphate cements and acrylic bone cements as injectable materials for bone repair and implant fixation. *J. Appl. Biomater. Funct. Mater* 17, 228080001987259. doi:10.1177/2280800019872594

Yu, Y., Jin, G., Xue, Y., Wang, D., Liu, X., and Sun, J. (2017). Multifunctions of dual Zn/Mg ion co-implanted titanium on osteogenesis, angiogenesis and bacteria inhibition for dental implants. *Acta Biomater.* 49, 590–603. doi:10.1016/j.actbio.2016.11.067

Zhang, J., Pan, J., and Jing, W. (2020). Motivating role of type H vessels in bone regeneration. *Cell Prolif.* 53, e12874. doi:10.1111/cpr.12874

Zhang, X., Huang, P., Jiang, G., Zhang, M., Yu, F., Dong, X., et al. (2021). A novel magnesium ion-incorporating dual-crosslinked hydrogel to improve bone scaffold-mediated osteogenesis and angiogenesis. *Mater. Sci. Eng. C* 121, 111868. doi:10.1016/j.msec.2021.111868

Zhao, W., Li, Y., Zhou, A., Chen, X., Li, K., Chen, S., et al. (2020). Controlled release of basic fibroblast growth factor from a peptide biomaterial for bone regeneration. *R. Soc. Open Sci.* 7, 191830. doi:10.1098/rsos.191830

Zhao, Y., and Xie, L. (2020). Unique bone marrow blood vessels couple angiogenesis and osteogenesis in bone homeostasis and diseases. *Ann. N. Y. Acad. Sci.* 1474, 5–14. doi:10.1111/nyas.14348

Zhao, Z., Li, G., Ruan, H., Chen, K., Cai, Z., Lu, G., et al. (2021). Capturing magnesium ions via microfluidic hydrogel microspheres for promoting cancellous bone regeneration. *ACS Nano* 15, 13041–13054. doi:10.1021/acsnano.1c02147

Zheng, X., Zhang, X., Wang, Y., Liu, Y., Pan, Y., Li, Y., et al. (2021). Hypoxia-mimicking 3D bioglass-nanoclay scaffolds promote endogenous bone regeneration. *Bioact. Mater* 6, 3485–3495. doi:10.1016/j.bioactmat.2021.03.011

Zheng, Y., Yang, Y., and Deng, Y. (2019). Dual therapeutic cobalt-incorporated bioceramics accelerate bone tissue regeneration. *Mater Sci. Eng. C Mater Biol. Appl.* 99, 770–782. doi:10.1016/j.msec.2019.02.020

Zhou, Y., Han, S., Xiao, L., Han, P., Wang, S., He, J., et al. (2018). Accelerated host angiogenesis and immune responses by ion release from mesoporous bioactive glass. *J. Mater. Chem. B* 6, 3274–3284. doi:10.1039/c8tb00683k

Zhu, S., Bennett, S., Kuek, V., Xiang, C., Xu, H., Rosen, V., et al. (2020). Endothelial cells produce angiocrine factors to regulate bone and cartilage via versatile mechanisms. *Theranostics* 10, 5957–5965. doi:10.7150/thno.45422

Zhu, W., Qu, X., Zhu, J., Ma, X., Patel, S., Liu, J., et al. (2017). Direct 3D bioprinting of prevascularized tissue constructs with complex microarchitecture. *Biomaterials* 124, 106–115. doi:10.1016/j.biomaterials.2017.01.042

Zou, D., Zhang, Z., He, J., Zhang, K., Ye, D., Han, W., et al. (2012). Blood vessel formation in the tissue-engineered bone with the constitutively active form of HIF-1α mediated BMSCs. *Biomaterials* 33, 2097–2108. doi:10.1016/j.biomaterials.2011.11.053

frontiers | Frontiers in Bioengineering and Biotechnology

TYPE Original Research
PUBLISHED 03 April 2024
DOI 10.3389/fbioe.2024.1275709

Collagen molecular organization preservation in human fascia lata and periosteum after tissue engineering

Julia Vettese[1,2*†], Julie Manon[1,2*†], Antoine Chretien[2], Robin Evrard[1], Lies Fievé[2], Thomas Schubert[1,3,4], Benoît G. Lengelé[2,5], Catherine Behets[2‡] and Olivier Cornu[1,3,4‡]

[1]Neuromusculoskeletal Lab (NMSK), Institut de Recherche Expérimentale et Clinique (IREC), UCLouvain, Brussels, Belgium, [2]Morphology Lab (MORF), IREC, UCLouvain, Brussels, Belgium, [3]Centre de Thérapie Cellulaire et Tissulaire Locomoteur, Cliniques Universitaires Saint-Luc, Brussels, Belgium, [4]Department of Orthopaedic and Trauma Surgery, Cliniques Universitaires Saint-Luc, Brussels, Belgium, [5]Department of Plastic and Reconstructive Surgery, Cliniques Universitaires Saint-Luc, UCLouvain, Brussels, Belgium

Large bone defect regeneration remains a major challenge for orthopedic surgeons. Tissue engineering approaches are therefore emerging in order to overcome this limitation. However, these processes can alter some of essential native tissue properties such as intermolecular crosslinks of collagen triple helices, which are known for their essential role in tissue structure and function. We assessed the persistence of extracellular matrix (ECM) properties in human fascia lata (HFL) and periosteum (HP) after tissue engineering processes such as decellularization and sterilization. Harvested from cadaveric donors (N = 3), samples from each HFL and HP were decellularized following five different chemical protocols with and without detergents (D1-D4 and D5, respectively). D1 to D4 consisted of different combinations of Triton, Sodium dodecyl sulfate and Deoxyribonuclease, while D5 is routinely used in the institutional tissue bank. Decellularized HFL tissues were further gamma-irradiated (minimum 25 kGy) in order to study the impact of sterilization on the ECM. Polarized light microscopy (PLM) was used to estimate the thickness and density of collagen fibers. Tissue hydration and content of hydroxyproline, enzymatic crosslinks, and non-enzymatic crosslinks (pentosidine) were semi-quantified with Raman spectroscopy. ELISA was also used to analyze the maintenance of the decorin (DCN), an important small leucine rich proteoglycan for fibrillogenesis. Among the decellularization protocols, detergent-free treatments tended to further disorganize HFL samples, as more thin fibers (+53.7%) and less thick ones (–32.6%) were recorded, as well as less collagen enzymatic crosslinks (–25.2%, p = 0.19) and a significant decrease of DCN (p = 0.036). GAG content was significantly reduced in both tissue types after all decellularization protocols. On the other hand, HP samples were more sensitive to the D1 detergent-based treatments, with more disrupted collagen organization and greater, though not significant loss of enzymatic crosslinks (–37.4%, p = 0.137). Irradiation of D5 HFL samples, led to a further and significant loss in the content of enzymatic crosslinks (–29.4%, p = 0.037) than what was observed with the decellularization process.

OPEN ACCESS

EDITED BY
Junxi Wu,
University of Strathclyde, United Kingdom

REVIEWED BY
Gwendolen Clair Reilly,
The University of Sheffield, United Kingdom
Jaroslava Halper,
University of Georgia, United States

*CORRESPONDENCE
Julia Vettese,
✉ julia.vettese@uclouvain.be
Julie Manon,
✉ julie.manon@uclouvain.be

†These authors have contributed equally to this work and share senior authorship

‡These authors have contributed equally to this work and share last authorship

RECEIVED 10 August 2023
ACCEPTED 08 March 2024
PUBLISHED 03 April 2024

CITATION
Vettese J, Manon J, Chretien A, Evrard R, Fievé L, Schubert T, Lengelé BG, Behets C and Cornu O (2024), Collagen molecular organization preservation in human fascia lata and periosteum after tissue engineering.
Front. Bioeng. Biotechnol. 12:1275709.
doi: 10.3389/fbioe.2024.1275709

Overall, the results suggest that the decellularization processes did not significantly alter the matrix. However, the addition of a gamma-irradiation is deleterious to the collagen structural integrity of the tissue.

KEYWORDS

extracellular matrix, collagen, crosslinks, decellularization, sterilization

1 Introduction

Bone regeneration is a well-regulated process requiring the recruitment of skeletal stem/progenitor cells (SSPCs) from adjacent tissues. Among them periosteum is a connective tissue that surrounds the external surface of bones and has been widely described as physiologically essential for bone development and healing (Duchamp de Lageneste and Colnot, 2019; Julien et al., 2022; Perrin and Colnot, 2022). This membrane consists of a fibrous outer layer composed of type I collagen and a highly cellular inner layer composed of fibroblasts, osteoprogenitor cells and mesenchymal stem cells (Squier, Ghoneim, and Kremenak, 1990; Dwek, 2010). However, in case of critical bone defect after a massive trauma, a tumoral resection or an osteomyelitis, the surrounding soft tissues, such as periosteum, are usually damaged and the normal physiological healing capacity is insufficient (Vidal et al., 2020).

Current strategies for the reconstruction of large bone defects exploit surgical approaches such as Ilizarov's (Aktuglu, Erol, and Vahabi, 2019) or Masquelet's induced-membrane (Masquelet and Begue, 2010) techniques. However, these methods require lengthy and tedious processing. Bone repair therefore remains a major concern for orthopedic surgeons (Evans, Chang, and Knothe Tate, 2013; Delloye et al., 2014; Dalisson et al., 2021) which has led to the emergence of a series of alternative tissue engineering approaches in recent decades (Chen et al., 2015; Lou et al., 2021; Manon et al., 2023). Among these, Manon et al. recently showed the suitability of using human fascia lata matrices as a periosteal-like scaffold for bone regeneration, mainly through their collagen type I composition and appropriate mechanical properties (Manon et al., 2022; Manon et al., 2023). The human fascia lata (HFL) is a dense connective tissue made up of three layers of collagen fiber bundles with little cellularity (Pancheri et al., 2014; Blottner et al., 2019).

Along with bone marrow and muscle, the periosteum is an important source of skeletal stem/progenitor cells (SSPCs) with a high potential for bone regeneration (Zhang et al., 2005; Duchamp de Lageneste et al., 2018). These progenitors reside in a rich environment formed by the periosteal extracellular matrix, where cellular and molecular crosstalk is crucial to achieve bone regeneration (Julien et al., 2022). This three-dimensional scaffold therefore not only provides a structural and mechanical support (Costa-Almeida et al., 2015; Hussey, Dziki, and Badylak, 2018; Sainio and Järveläinen, 2020) but is also a modulator of tissue homeostasis (Theocharis et al., 2016). Consequently, any alteration of this structure can lead to the disruption of tissue function (Theocharis et al., 2016). Collagen constitutes the major ECM component (Shoulders and Raines, 2009; Yamauchi and Sricholpech, 2012) and plays a key role in maintaining biological and architectural integrity of tissues as well as providing physical support (Dong and Lv, 2016). Lin et al. (2018) further emphasized this point by revealing that cell-free collagen scaffold of decellularized periosteum alone efficiently promotes orthotopic remodeling of skeletal defects *in vivo* (Lin et al., 2018).

Fibril forming collagen type I, the most prevalent one, provides tensile strength to tissues (Theocharis et al., 2016) through its complex hierarchical structure. Encoded by the *COL1A1* and *COL1A2* genes, collagen precursors undergo series of post-translational modifications (PTMs) to form mature molecules (Gjaltema and Bank, 2017; Rappu et al., 2019), which are stabilized by two main types of intermolecular crosslinks important for their assembly and for collagen functions (Yamauchi and Sricholpech, 2012). First, enzymatic crosslinks, considered a post-translational modification of lysine residues, are mediated by the lysyl hydroxylases and lysyl oxidases through a highly controlled mechanism. Initially formed as immature divalent crosslinking (e.g., dehydrodihydroxylysinonorleucine), some are converted into mature trivalent crosslinks (e.g., pyridinoline) (Thorpe, 2010; Yamauchi and Sricholpech, 2012; Saito and Marumo, 2015; Kamml et al., 2023). Secondly, non-enzymatic crosslinks result from a glycation process forming advanced glycation end products (AGEs), among which pentosidine is the most frequently characterized (Paul and Bailey, 1996; Pritchard and Willett, 2017). All AGEs are formed by a Lysine-Arginine or Lysine-Lysine interaction and predominantly accumulate in collagen because of its low turnover. Their emergence leads to an increase in connective tissue rigidity and insolubility (Paul and Bailey, 1996; Gautieri et al., 2014). Finally, interfibrillar bridges also result from the interactions of non-collagenous components between glycosaminoglycans (GAG)-decorin (DCN) complexes of adjacent fibrils (Scott, 2003; Thorpe, 2010; Costa-Almeida et al., 2015). DCN is a member of class 1 small leucine-rich proteoglycans (SLRPs) essential for the regulation of various tissular processes (Halper, 2014; Gubbiotti et al., 2016) but most notably studied for its involvement in collagen fibrillogenesis and matrix stability. This protein also acts as a reservoir of growth factors and cytokines (Gubbiotti et al., 2016; Zhang et al., 2018).

In the present study harvested human periosteum (HP) and HFL samples were treated with several protocols of decellularization (Manon et al., 2023) as well as by irradiation. Whereas the general microstructure, composition, and biosafety of the ECM-derived scaffold had received considerable attention, a special analysis of collagen *per se* is required as the main component contributing to matrix-cell crosstalks and, hence, to the global integrity of the periosteum. Therefore, since decellularization and sterilization processes can have a negative impact on the ECM, the aim of the present study was to characterize the collagen scaffold obtained after these engineering processes. Here, we hypothesized and sought to confirm the global persistence of important ECM components of HP and HFL samples after chemical decellularization and sterilization, and therefore a persistence of their functional and structural

TABLE 1 Decellularization protocols (D), from D1 to D5.

	Decellularization protocols
D1	12 h SDS 4 h Triton 12 h DNase
D2	12 h Triton 4 h SDS 12 h DNase
D3	24 h SDS 4 h Triton 12 h DNase
D4	24 h Triton 4 h SDS 12 h DNase
D5	Acetone, Ether, ethanol, NaCl (7%), NaOH, H_2O_2

SDS, sodium dodecyl sulfate; DNase, deoxyribonuclease.

properties. The ultimate goal of this study is to confirm the maintenance of HFL matrices properties in order to consider their future use as periosteal scaffold substitutes to promote bone regeneration.

2 Materials and methods

2.1 Sample collection and processing

HFL and HP were harvested from deceased donors (3 donors of average 86.81 ± 3.7 years) of the Human Anatomy Department of UCLouvain (Body donation service, IRB00008535, Brussels, Belgium) following the same procedure as previously described (Manon et al., 2022) and were subjected to five chemical decellularization (D) protocols (Table 1) performed under continuous agitation (N = 3 donors x 2 tissues x 5 protocols = 30 analyzes). The soap-based detergent protocols, D1 to D4, consisted of different combinations of Triton, Sodium dodecyl sulfate (SDS) and Deoxyribonuclease (DNase). Triton is a non-ionic detergent that disturbs the lipid-lipid and protein-DNA interactions. SDS is an ionic detergent that denatures protein structure and solubilizes nuclear and cellular membranes. DNase treatment is employed to cleave internucleotide bonds and eliminate undesirable cellular waste. In protocol D1, tissues were maintained for 12 h in SDS, followed by 4 h in Triton. The sequence was reversed for D2, with 12 h in Triton and by 4 h in SDS. For protocols D3 and D4, the sequence was the same as for D1 and D2, respectively, with an increase in the duration of the first treatment step maintained for 24 h instead of 12 h (SDS and Triton, respectively). Each protocol ended with a 12 h DNase treatment. D5 protocol is the one routinely used in the institutional tissue bank (van Steenberghe et al., 2017; Manon et al., 2023). In brief, it includes sequential immersion in pure acetone to degrease, ether to neutralize the previous compounds and 70° ethanol to further degrease. Following a washing step, sample are immersed in a hypertonic solution of NaCl (7%) and NaOH to finally been placed in H_2O_2 (7.5%). Quality controls were performed to confirm the full decellularization and to measure the pH and traces of H_2O_2 and acetone. To assess the efficacy of decellularization protocols, microscopic analyses were performed on DAPI and Hematoxylin and Eosin (HE) stained slices first. Then, 3 random samples of 25 mg were harvested from native and decellularized tissues of all protocols, and freeze-dried. The DNA content was measured using the Quant-iT PicoGreen DNA assay kit (ThermoFisher, Waltham, MA, United States) just after being extracted using the DNeasy® Blood & Tissue kit (Qiagen, Hilden, Germany). The very precise steps are previously described (Manon et al., 2022; Manon et al., 2023). Samples were then stored at −80°C.

Samples of decellularized HFL (D1-D5) were then frozen and sterilized by gamma(γ)-irradiation (HFLi, HFL irradiated) under dry ice using a minimal exposure dose of 25 kGy (IBA Mediris, Fleurus, Belgium), the recommended standard sterilization method for clinical applications (Dziedzic-Goclawska et al., 2005; Seto, Gatt, and Dunn, 2008; Harrell et al., 2018).

To perform the various analyses, samples were randomly taken from the entire decellularized scaffold to consider the whole tissue heterogeneity.

2.2 Polarized light microscopy

After paraffin histology processing, sirius red (SR) staining, an acidic hydrophilic stain, was used to highlight and evaluate qualitative modification in collagen organization ($n_{(HFL)}$ = 4 samples/protocol, $n_{(HP)}$ = 3 samples/protocol, with 3 sections per native samples and 1 per decellularization protocol). Deparaffinized and rehydrated sections were immersed in 1% Phosphomolybdic acid and then in 0.1% Sirius Red solution for 2 h. Sections were then incubated in hydrochloric acid before washing and mounting steps, then imaged under polarized light. Parallelly bound to collagen fibrils, this dye intensifies the birefringence of the samples which is manifested by shades of color under polarized light, each associated with properties of fiber organization. Thin fibers (diameter ≤0.8 μm) with a more scattered histoarchitecture are characterized by a weak birefringence and are detected in green/yellow while thick (diameter between 1.6–2.4 μm) organized ones appeared as shades of red and orange (Dayan et al., 1989). These parameters are quantified in order to highlight a possible alteration in collagen organization.

SR-stained sections were first imaged using the Axioplan microscope (ZEISS) with a 10-fold magnification. Linear polarization of light was obtained by using two filters that allow light to pass only in one direction of vibration: the polarizer and the analyzer, placed perpendicularly (Rittié, 2017). All slides were examined at the same time to ensure consistency of the experiment and were digitalized using the Nikon Digital sight DS SMC camera with NIS-Element BR 3.0 software. The average of five different acquisitions was assessed for each HFL section to cover the whole tissue surface, and three for HP, the surface of the sections being smaller. Collagen organization was then estimated with ImageJ software (Schneider, Rasband, and Eliceiri 2012) as a surface percentage of each color with a constructed macro (IREC imaging platform, 2IP). The analysis displayed green, yellow, orange, and red polarization colors.

To further validate our findings, whole slide images were then acquired with the ZEISS Axio Scan.Z1 Slide scanner under polarized light in order to approximate the proportion of each fiber type. These acquisitions were analyzed with QuPath (Bankhead et al., 2017) calibrated to detect the different shades of colors. With this approach, unlike with the previous one, only green, orange, and red colors are detected.

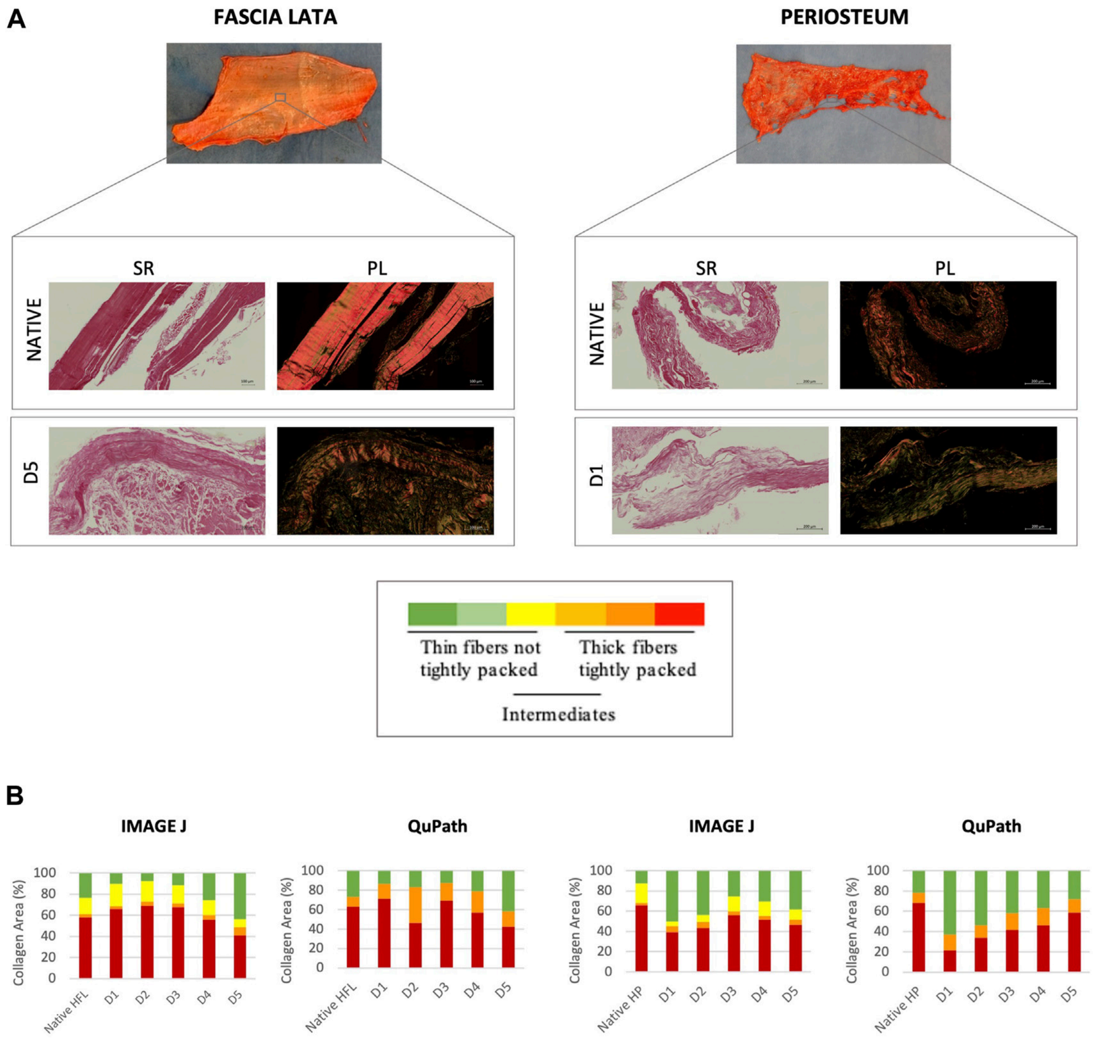

FIGURE 1
Qualitative **(A)** and quantitative **(B)** evaluations of the collagen organization of sections through native (*n* = 12) and decellularized HFL (*n* = 4) and HP (*n* = 3). **(A)** Sirius Red staining under bright field (SR, left) and polarized light (PL, right) obtained with ZEISS Axio Scan.Z1 Slide. Same analyses were carried out with polarized light microscope but are not shown. Variation in the polarization of collagen fibers under polarized light reflects differences in fiber thickness, density and packing: from green (thin, ≤0.8 µm, and loosely packed) to red (thick, 1.6–2.4 µm, and tightly packed) (Dayan et al., 1989). **(B)** Quantitative analyses were performed using ImageJ for the microscopic images and Qupath for scanner images. The quantitative analysis confirmed the qualitative assumptions: D5 and D1 protocols affected the most the HFL and HP samples respectively, with a higher average of thin fibers and lower of thick ones assessed by both ImageJ (microscope) and QuPath (scanner), despite remaining not significant.

2.3 Raman spectroscopy

2.3.1 Spectra acquisition

Molecular composition of fresh frozen and processed HFL, HFLi and HP samples (*n* = 3/protocol for each type of samples) was investigated using Raman spectroscopy (Renishaw confocal Raman inVia Quontor). Spectra of each sample were obtained as the average of 3 consecutive spectra randomly distributed over the sample surface. Each spectrum was collected using a 785 nm monochromatic laser beam with a power of 50 mW, a 50-fold magnification and the Renishaw Centrus 21KP95 detector. Two types of spectra ranges were recorded.

Acquisitions were first performed with a static mode in a wavelength range of 700–1800 cm^{-1} with an integration time of 10 s and 15 accumulations. The presence of non-enzymatic crosslinks (pentosidine, 1345 cm^{-1}) and hydroxyproline (872 cm^{-1}) was normalized to the amount of tissue using the proline peak (920 cm^{-1}). Enzymatic crosslink level is assessed by the ratio of mature to immature crosslinks (pyridinoline/dehydrodihydroxylysinonorleucine, 1670/1690 cm^{-1}). A 1657 cm^{-1} supplementary band was added for the Amide-I peak-fit model of HP. This lipid vibration band was used to correct its potential interference on the measure of enzymatic crosslinks (Mandair et al., 2020).

To estimate the collagen-bound water content, a second wavelength range of 2700–3800 cm^{-1} was recorded with extended mode, 10 s integration time, and 6 accumulations. Three parameters were considered: organic matrix-related water (3243 cm^{-1}), amine (NH) groups beside organic matrix-related water (3333 cm^{-1}) and hydroxide (OH) groups of

TABLE 2 Raman spectroscopy data of Human Fascia Lata matrices after decellularization with 5 different protocols (D1-D5) ($n = 3$/protocol and native). AGEs: Advanced Glycation End Products, NH: amine group, OH: hydroxide. Results are expressed as Mean ± SEM (Kruskal-Wallis).

		Native	*D1*	*D2*	*D3*	*D4*	*D5*	Kruskal-Wallis
								p-value
700–1800 cm^{-1}	Hydroxyproline *875/920*	0.601 ± 0.031	0.600 ± 0.031	0.610 ± 0.045	0.530 ± 0.035	0.637 ± 0.092	0.589 ± 0.080	0.861
	Pentosidine (AGEs) *1342/920*	0.391 ± 0.068	0.365 ± 0.005	0.378 ± 0.039	0.384 ± 0.024	0.322 ± 0.033	0.338 ± 0.015	0.560
	Enzymatic Cross-links *1666/1686*	4.191 ± 0.430	3.435 ± 0.299	3.183 ± 0.142	3.210 ± 0.118	4.490 ± 0.737	3.136 ± 0.172	0.121
2700–3800 cm^{-1}	Organic matrix related water *3220/2943*	0.062 ± 0.016	0.285 ± 0.020	0.252 ± 0.085	0.446 ± 0.083	0.270 ± 0.052	0.377 ± 0.041	0.061
	NH groups beside organic matrix related water *3333/2943*	0.078 ± 0.005	0.141 ± 0.007	0.155 ± 0.027	0.194 ± 0.027	0.131 ± 0.028	0.196 ± 0.016	0.052
	OH groups of hydroxyproline next to collagen-related water *3457/2943*	0.005 ± 0.001	0.054 ± 0.004	0.039 ± 0.020	0.086 ± 0.017	0.055 ± 0.011	0.078 ± 0.008	0.054

hydroxyproline beside collagen-related water (3457 cm^{-1}). Each of these parameters was normalized to the amount of organic matrix (mainly collagen) assessed at a wavelength of 2940 cm^{-1} (Unal and Akkus, 2015).

2.3.2 Spectra processing

Raman spectra were processed using two different softwares: the Windows®-based Raman Environment (WiRE 3.5, Renishaw) and MATLAB PLS toolbox (PLS_Toolbox 9.0 (23592) Eigenvector Research, Inc., Manson, WA United States 98831). WiRE software was used for peak deconvolution, applying a baseline correction. The latter was used to deconvolve the Amide I subpeaks (1605, 1635, (1657), 1666, 1686 cm^{-1}) and those present in the 2700–3800 cm^{-1} spectra (2943, 3220, 3333, 3457 cm^{-1}). Models were built by measuring the average centers (intensity wavelength), width and Gaussian percentage of each subpeak derived from the deconvolution. The PLS toolbox automates the measurement of height and area of each peak of interest with a local baseline correction, after the manual creation of a model, according to the mean values of the peaks of interest from all spectra.

2.4 Protein extraction and enzyme-linked immunosorbent assay

Decorin (DCN) content was evaluated using the enzyme-linked immunosorbent assay (ELISA). For this purpose, the protein extraction was performed as previously described (Manon et al., 2022). Samples of each HFL and HP were weighted, cut and lysed with the buffer solution containing the radioimmunoprecipitation assay (RIPA, ThermoFisher Scientific, 89900), the protease inhibitor cocktail (Sigma-Aldrich, P8340-1 ML), and phosphatase inhibitors (PhosSTOP™, Roche, Basel, Switzerland). The samples were subjected to four cycles in the Precellys homogenizer (Bertin Technologies SAS, France) at 7,200 rpm. The protein concentration in the supernatant was determined with the Pierce™ BCA Protein assay kit (ThermoFisher Scientific, 23227) and normalized to the sample weight.

Subsequently, DCN content was evaluated using the RayBio® Human Decorin ELISA kit (RayBiotech, ELH-Decorin-1,13485) following an adaptation of the manufacturer's instructions. Briefly, since the protein concentration was low, larger volumes were used to achieve the required concentration per well. Therefore, 145 µL of tissue homogenates and standards were incubated in the pre-coated 96 well microplate at room temperature for 2.5 h. Following the washing steps, biotinylated antibody was added for 1 h. The subsequent washing step removed unbound antibodies before the addition of streptavidin conjugated horseradish peroxidase (HRP) solution. 5′-Tetramethylbenzidine (TMB) substrate was added after four washes and incubated protected from light. After 30 min, the reaction was stopped (Stop solution of 0.2 M sulfuric acid) and the plate was red at 450 nm. Standard curve was obtained using Sigmaplot 13 software (version 20, SPSS, Inc., Chicago, IL, United States) and results were expressed as pg of DCN per mg of total protein (pg/mg).

TABLE 3 Raman spectroscopy data of Human Periosteum matrices after decellularization with 5 different protocols (D1-D5) (n = 3/protocol and native). AGEs: Advanced Glycation End Products, NH: amine group, OH: hydroxide. Results are expressed as Mean ± SEM (Kruskal-Wallis).

		Native	*D1*	*D2*	*D3*	*D4*	*D5*	Kruskal-Wallis
								p-value
700–1800 cm^{-1}	Hydroxyproline 875/920	0.922 ± 0.140	0.632 ± 0.043	0.599 ± 0.093	0.663 ± 0.038	0.626 ± 0.058	0.634 ± 0.042	0.544
	Pentosidine (AGEs) 1342/920	0.610 ± 0.111	0.325 ± 0.101	0.381 ± 0.055	0.417 ± 0 .115	0.399 ± 0.071	0.375 ± 0.016	0.460
	Enzymatic Cross-links 1666/1686	3.621 ± 0.099	2.269 ± 0.201	2.465 ± 0.220	2.328 ± 0.250	2.545 ± 0.061	2.346 ± 0.109	0.250
2700–3800 cm^{-1}	Organic matrix related water 3220/2943	0.152 ± 0.094	0.414 ± 0.065	0.456 ± 0.217	0.927 ± 0.355	0.455 ± 0.179	0.463 ± 0.102	0.267
	NH groups beside organic matrix related water 3333/2943	0.171 ± 0.050	0.234 ± 0.034	0.176 ± 0.058	0.370 ± 0.150	0.185 ± 0.059	0.223 ± 0.041	0.698
	OH groups of hydroxyproline next to collagen-related water 3457/2943	0.006 ± 0.004	0.072 ± 0.020	0.084 ± 0.041	0.163 ± 0.054	0.087 ± 0.036	0.093 ± 0.021	0.100

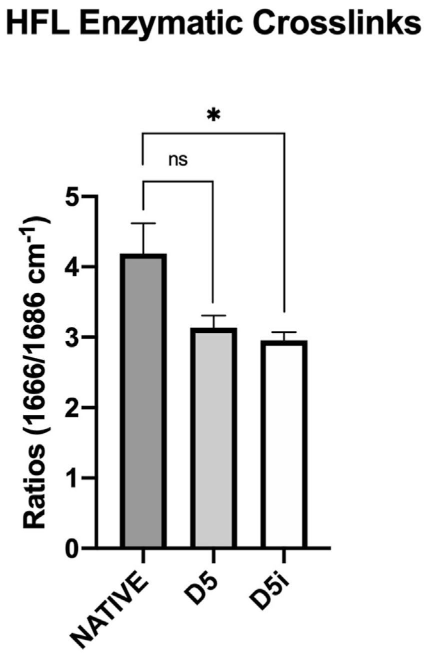

FIGURE 2
Measurement of enzymatic crosslinks by Raman spectroscopy in samples of native HFL and HFL decellularized according to the fifth protocol, followed (D5i) or not (D5) by gamma irradiation. The decellularization chemical treatment impaired the amount of enzymatic crosslinks but without significance (−25.2%, *p* = 0.195). However, after sterilization, the amount of enzymatic crosslink was further reduced and this reduction became significant (−29.4%, *p* = 0.037) compared to native.

2.5 GAG quantification

The content of sulfated glycosaminoglycans (GAGs) was quantified in native and decellularized HP and HFL samples (*n* = 3) using the Blyscan Sulfated Glycosaminoglycan Assay (Biocolor LTD., Carrickfergus, Northern Ireland) and following the manufacturer's protocol. Sulfated GAGs include chondroitin sulfate, dermatan sulfate, heparan sulfate and keratan sulfate. Three samples of 25 mg of each tissue were harvested. Samples were then first freeze-dried and dry-weighted. Before the quantitative measurement, each sample was placed in a Papain reagent (50 mL Na_2HPO_4/NaH_2PO_4 0.2 M pH 6.4, 400 mg sodium acetate, 200 mg EDTA and 40 mg cysteine HCL, 250 µL papain) overnight at 65°C for GAG extraction. Following centrifugation (10 min, 10,000 rpm), 100 µL of each sample were taken and 1 mL of Dye Reagent was added for 30 min. The Eppendorfs were centrifuged again at 12,000 rpm for 10 min and the supernatant discarded. Dissociation reagent (500 µL) was added for 10 min and, after a final centrifugation (5 min, 12,000 rpm), 200 µL of each sample were transferred to a 96-well plate. Standards were also prepared according to the manufacturer's protocol. The plate was read at 630 nm three times and the average of the three readings was used for final quantification. The concentration of GAGs was expressed in µg/mg dry weight.

TABLE 4 Raman spectroscopy data of Human Fascia Lata matrix after decellularization with 5 different protocols followed by irradiation (D1i-D5i) ($n = 3$/protocol and native). AGEs: Advanced Glycation End Products, NH: amine group, OH: hydroxide. Results are expressed as Mean ± SEM (Kruskal-Wallis) and significant values are in bold-italic.

		Native	*D1i*	*D2i*	*D3i*	*D4i*	*D5i*	Kruskal-Wallis
								p-value
700–1800 cm^{-1}	Hydroxyproline 875/920	0.601 ± 0.031	0.670 ± 0.086	0.586 ± 0.018	0.598 ± 0.036	0.607 ± 0.037	0.581 ± 0.077	0.942
	Pentosidine (AGEs) 1342/920	0.391 ± 0.068	0.384 ± 0.036	0.326 ± 0.015	0.320 ± 0.013	0.356 ± 0.024	0.345 ± 0.013	0.666
	Enzymatic Cross-links 1666/1686	4.191 ± 0.430	3.136 ± 0.162	3.134 ± 0.120	3.062 ± 0.090	3.273 ± 0.264	2.957 ± 0.116	0.161
2700–3800 cm^{-1}	Organic matrix related water 3220/2943	0.062 ± 0.016	0.115 ± 0.006	0.102 ± 0.005	0.185 ± 0.065	0.119 ± 0.017	0.279 ± 0.037	0.058
	NH groups beside organic matrix related water 3333/2943	0.078 ± 0.005	0.084 ± 0.004	0.086 ± 0.003	0.104 ± 0.022	0.086 ± 0.004	0.151 ± 0.023	0.145
	OH groups of hydroxyproline next to collagen-related water *3457/2943*	0.005 ± 0.001	0.020 ± 0.003	0.014 ± 0.0004	0.030 ± 0.013	0.020 ± 0.0006	0.048 ± 0.006	***0.034***

2.6 Statistics

Statistical analyses were carried out using GraphPad Prism (Version 8.4.0, Inc., San Diego, CA, United States) and SPSS software (Version 27, IBM SPSS, Inc., Chicago, IL, United States). Data were expressed as the mean ± standard error of mean (SEM) and compared with the non-parametric Mann-Whitney or Kruskal-Wallis test because of the small dataset and the subsequent non-respect of normality (tested by Shapiro-Wilk test). Pairwise comparisons were performed using the Dunn's test. All tests were two-tailed. The significance level was considered at a p-value < 0.05.

3 Results

All the decellularization protocols successfully achieved the Crapo's criteria (Crapo et al., 2011). These standards include an absence of nuclei visible by histological analysis (DAPI, HE staining), a DNA quantity of less than 50 ng/mg dry weight and a length of less than 200 bp for persistent DNA fragments after treatment. In all the samples, DNA concentration felt below the critical threshold of 50 ng/mg of dry weight and no cellular traces were visible on microscopic analyses.

3.1 Weak alteration of collagen structure

HFL samples appeared to be more disorganized after protocol D5 treatment than the other subgroups, as highlighted by a decrease, although not significant, of thick (1.6–2.4 μm) red hue fibers (ImageJ: −29%; QuPath: −32.6%) and an increase in thin (≤0.8 μm) green ones (ImageJ: +87.9%; QuPath: +53.7%) (Figure 1). HP samples seemed to be more affected by protocol D1. Although not significant, the D1-treated tissues presented the lowest proportion of red fibers (ImageJ: −33.8%; QuPath: −68.3%) and the highest of green ones (ImageJ: +300%, QuPath: +189%) compared to natives. No significant differences in the amount of intermediate fibers (yellow/orange) were recorded.

3.2 Weak difference in the matrix molecular composition in native tissues

Raman spectroscopy revealed no statistical differences between the molecular composition of native HFL and HP. Both tissues presented similar amounts of hydroxyproline and collagen-bound water, although HFL samples showed a slightly higher proportion of enzymatic crosslinks (+13.6%, $p > 0.05$) and a slightly lower amount of non-enzymatic crosslinks (−55.8%, $p > 0.05$) than native HP.

3.3 Weak alteration of the matrix molecular composition in decellularized tissues

3.3.1 Human fascia lata

Increase in tissue hydration was the most marked modification after HFL decellularization (Table 2), at the limit of significance for

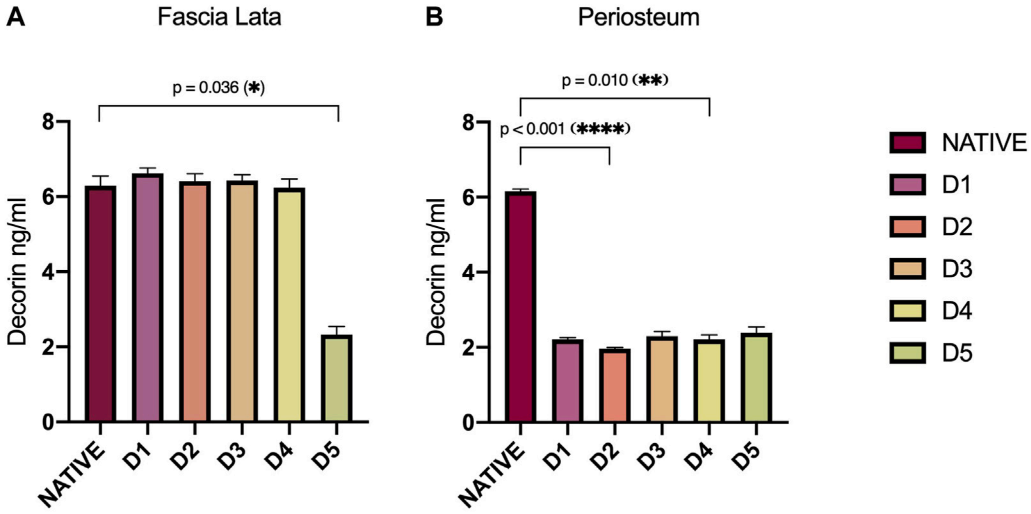

FIGURE 3
Decorin (DCN) levels (ng/mL) assessed by ELISA in HFL **(A)** and HP **(B)** protein extracts according to sample treatments (D1-D5). DCN in HFLs was significantly disrupted by tissue engineering processes in D5-treated tissue (p = 0.036). Concerning HP, DCN level was reduced with all decellularization protocols, but most importantly in D2 (p < 0.001) and D4 (p = 0.010)-treated tissues. Error bars represent the SEM. D: Decellularization protocol.

all three biomarkers of collagen-related water for all D-protocols: the hydroxyproline OH groups beside water bound to collagen (IR 3457/2943, $p = 0.054$), the NH groups beside organic matrix related water (IR 3333/2943, $p = 0.052$) and the organic matrix related water parameter (IR 3220/2943, $p = 0.061$). These increases were then confirmed, by a pairwise Dunn's comparison, for the three biomarkers in protocols D3 (IR 3220/2943, $p = 0.030$; IR 3333/2943 $p = 0.047$ and IR 3457/2943, $p = 0.037$) and D5 ($p = 0.030$, $p = 0.023$ and $p = 0.037$ respectively) when compared to native tissues. An average loss of 25.2% ($p = 0.195$) in the amount of enzymatic crosslinks was also observed after the D5 treatment, which was the largest, though not significant, loss among all protocols. Hydroxyproline and pentosidine content were not significantly affected by the chemical treatments as well.

3.3.2 Human periosteum

HP samples hydration also increased with all decellularization protocols (Table 3) but in a less important way than HFL. D1-HP presented the lowest average of enzymatic crosslinks (−37.4%, $p = 0.137$) and pentosidine (−46.7%, $p = 0.332$) among the different decellularization protocols. Once again, the content of hydroxyproline did not significantly vary according to the treatment.

3.3.3 Irradiated human fascia lata

By multiple comparison analyses, we highlighted a further loss in the proportion of enzymatic crosslinks in D5i sterilized samples, leading to a significant difference with natives (−29.4%, $p = 0.037$) (Figure 2). However, hydroxyproline and pentosidine levels were similar to that of native tissues (Table 4). Moreover, while hydration increased after decellularization (D1 to D5) of both tissues (HFL and HP), this proportion decreased after sterilization processes for HFL (D1i to D5i), without returning to basal levels of natives; the data obtained with protocol D5i remained the most different.

3.4 Interfibrillar bridges of decorin

ELISA analyses of protein extracts from HP and HFL samples provide a deeper insight into the effect of chemical treatments on interfibrillar bridges (Figure 3). The DCN levels in HFL were approximately 6.40 ng/mL (±0.23) for all subgroups except D5-tissues, which averaged 2.3 ng/mL (±0.33) ($p = 0.036$). HP samples of all D-protocols presented a homogenous alteration of DCN levels compared with the native subgroup, with a mean of 2.2 ng/mL (±0.15) *versus* 6.2 ng/mL (±0.04) for natives. DCN levels in protocol D2 were the lowest, exhibiting a significant decrease compared to natives ($p < 0.001$), followed by protocol D4 ($p = 0.010$).

Since interfibrillar bridges are formed by an association between DCN and sulfated GAG, we wanted to identify a relationship in their persistence within the tissue-engineered samples. In both tissue types, total sulfated GAG levels were similarly and significantly decreased after all D-protocols (Figure 4A). HFL decellularized samples contained average levels of 0.24 µg of GAG per mg of dry weight (±0.20), while native sample levels averaged 3.32 µg/mg (±0.38). For HP samples, a similar ratio was found, with an average of 0.66 µg/mg (±0.19) for decellularized tissues and 3.06 µg/mg (±0.79) for native tissues. No correlation was observed between GAG and DCN levels for both HFL ($R^2 = 0.022$) and HP ($R^2 = 0.784$) samples (Figure 4B). Changes in DCN and GAG level, resulting from chemical treatments were not related.

4 Discussion

None of the five decellularization protocols (D1 to D5, Table 1) significantly altered collagen arrangement. Detergent-free treatment (D5) disorganized HFL samples to a greater extent, significantly reducing DCN and GAGs, and non-significantly reducing collagen cross-links. HP samples, treated with detergent-based treatment D1,

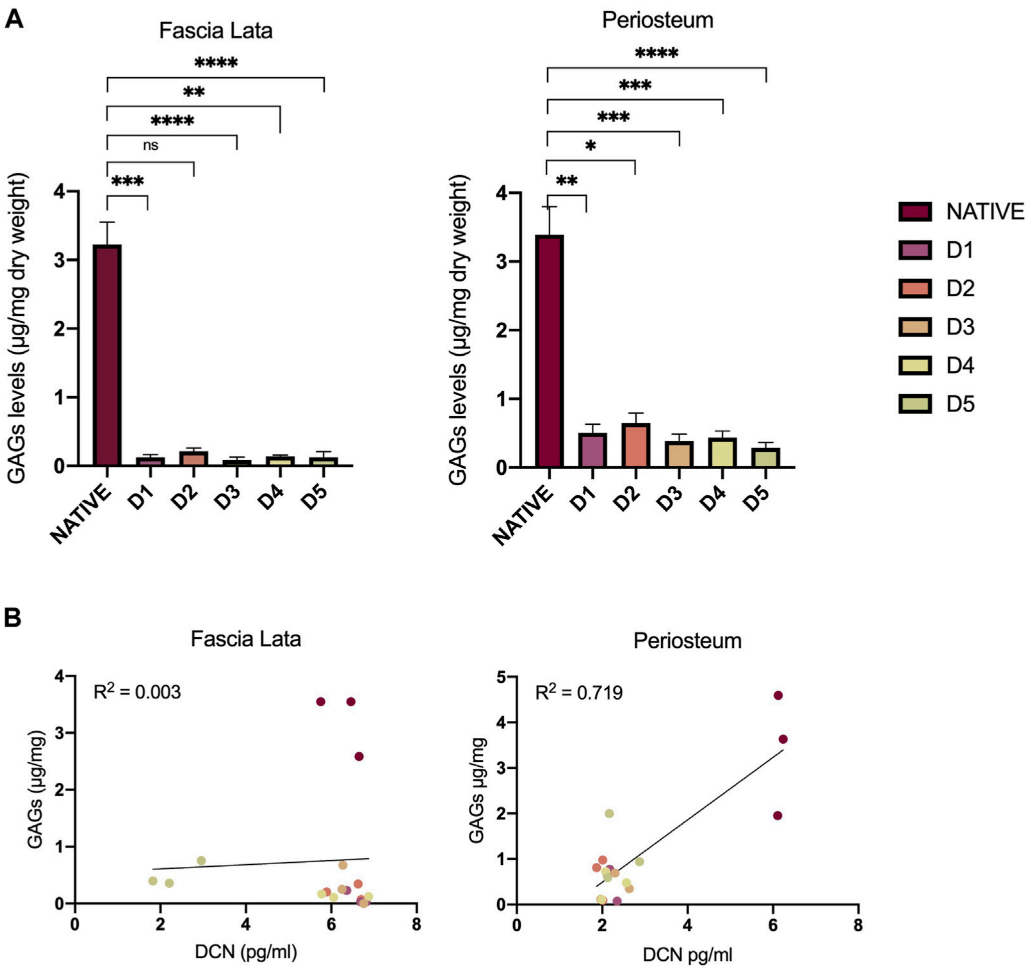

FIGURE 4
Impact of decellularization approaches on GAGs and DCN. **(A)** Quantitative analyses of GAG content in HFL and HP samples. The levels significantly decreased after all chemical treatments for both HFL (D1 (p = 0.0004), D2 (p = 0.024), D3 (p < 0.0001), D4 (p = 0.012), D5 (p < 0.0001)) and HP (D1 (p = 0.0002), D2 (p = 0.007), D3 (p < 0.0001), D4 (p < 0.0001), D5 (p = 0.007)) samples. **(B)** Variation of DCN and GAGs resulting from the chemical treatments are not related for both HFL (R^2 = 0.022) and HP (R^2 = 0.784). However, all decellurazed samples present similar profiles clearly distinguishable from native tissues. Error bars represent the standard error of the mean (SEM). GAGs: Glycosaminoglycans, D: Decellularization protocol, DCN: decorin.

showed collagen disorganization, and a reduction in enzymatic cross-links. Overall, decellularization had minimal impact on the matrix, while the addition of gamma irradiation impact leads to a significant negative effect on the integrity of collagen cross-links.

Structural modifications were therefore most pronounced in HFL when treated with the D5 protocol and in HP with the D1 protocol. This was first observed with the assessment of collagen bundle birefringence using PLM to understand the impact of the engineered treatments on the architectural arrangement (Dayan et al., 1989; Ribeiro et al., 2013; Rittié, 2017). The robustness of the results is confirmed by the convergence of birefringence measurements between various analysis tools. Interestingly, each of these subgroups, HFL-D5 and HP-D1, also showed the lowest levels of enzymatic crosslinks as measured by Raman spectroscopy. In the literature, optical density measures under polarized light were already used as indicator of crosslinked collagen organization (Kirby, Heuerman, and Yellon, 2018; Lien, Chen, and Phan, 2022).

Previous studies confirmed collagen persistence in decellularized scaffolds (Duisit et al., 2017; Manon et al., 2023). Being the major ECM component, collagen biological and architectural functions have already been well characterized (Snedeker and Gautieri, 2014; Dong and Lv, 2016). Ensuring the persistence of enzymatic crosslinks in decellularized collagen scaffolds is therefore crucial for maintaining the functional properties of native matrices, contributing to fibril stability and improving tissue biomechanical competence. Therefore, physical and chemical methods are nowadays used to achieve intermolecular collagen crosslinking in engineered scaffolds (Dong and Lv, 2016).

In addition to collagen enzymatic crosslinks, its overall molecular composition has an impact on its structure and biomechanical properties. Indeed, AGEs are known to alter the mechanical strength of tissues (Saito and Marumo, 2010). In addition, as Unal and Akkus (2015) have shown, the hydration level of bones also plays a role in their mechanical properties. Moreover, it is also known that physical training has an impact on collagen crimps, which can be analyzed by measuring birefringence (Mazon et al., 2018). Therefore, by taking all collagen parameters into account, we could in future investigate a relationship between the structural data of our scaffolds and their mechanical properties.

It is important to note, however, that the samples were taken from old subjects, which may also have an impact on the results. Since the rate of crosslinks is age-related, the slight decrease in enzymatic crosslinks after the engineering protocols could be explained by an age-related decrease, itself associated with a decrease in the mechanical capacity of the tissue. These decreases could therefore possibly be significant in tissues from younger subjects, which should be verified in the future. Moreover, it should be noted that these analyses were carried out on a small number of samples randomly taken from the entire decellularized scaffold, allowing potential tissue heterogeneity to be taken into account.

Raman spectra of the HFL samples differed slightly from those of the periosteal ones, particularly in the amide I region (1670/1690 cm^{-1}). We suspected interference from tissues other than periosteum, adding some background in the spectra. The samples were harvested from old subjects and, despite efforts to remove muscle and fat, some residues remained due to the thinness of the HP. Indeed, anomalies in the spectra were observed for all protocols, including native tissue, with the exception of protocol D5, the only one to include a degreasing step. Therefore, in line with the literature, an additional peak (1657 cm^{-1}) was added for deconvolution of this amide region, known to correct for potential interference from lipid vibrations (Mandair et al., 2020). In addition, we observed increased hydration in samples after decellularization, probably because decellularization disrupts the natural barriers regulating hydration. This leads to increased water uptake during abundant rinsing steps. Irradiation, however, leads to a partial loss of this increased hydration, without returning to baseline levels.

Since these decellularized tissues are intended to regenerate *in vivo* damaged structures, sterilization processes are required to prevent pathogen transmission (Dziedzic-Goclawska et al., 2005; Seto, Gatt, and Dunn, 2008; Harrell et al., 2018). Althoug gamma irradiation is commonly used in bone banks for sterilization, it causes radiolysis of water molecules, releasing free radicals (Nguyen et al., 2007) that damage collagen (Seto, Gatt, and Dunn, 2008; Harrell et al., 2018). Previous studies on bones showed a negative synergic effect on mechanical resistance when irradiation was added to freeze-dried samples (Cornu et al., 2000; Cornu et al., 2011), attributed to a significant reduction in enzymatic crosslinks density (Cornu, 2012). This is consistent with our results revealing a more pronounced alteration of crosslinks post-irradiation. Future studies should explore decellularization procedures under totally sterile conditions to avoid the detrimental effects of subsequent irradiation on tissue properties.

We did not investigate irradiated periosteum since the priority, for the creation of the new regenerative membrane, was the use of irradiated decellularized HFL (Manon et al., 2023).

DCN-GAG complexes are essential for the ECM organization, especially in collagen fibrillogenesis, as evidenced by the alteration of the latter in DCN-deficient mice (Gubbiotti et al., 2016; Zhang et al., 2018). This PG is also involved in stress transfer between collagen fibrils (Thorpe, 2010) and in the bioavailability of growth factors such as TGF-β (Gubbiotti et al., 2016; Zhang et al., 2018). Alteration in decorin content vary according to the tissue type, with HFL samples globally maintaining their DCN concentration after decellularization, except for D5, while HP samples show a decrease in all D-protocols.

Furthermore, it has already been demonstrated that detergent-based decellularization affects the GAG composition of ECM (Duisit et al., 2017; Liguori et al., 2020; Uhl et al., 2020), as confirmed by our quantitative measurements, with potential dysfunction of persistent GAGs (Uhl et al., 2020). However, the maintenance of functional GAGs is necessary. Abundantly distributed on cell surface and in the ECM, they modulate various physiological processes. They provide biochemical and mechanical support in the ECM and influence cell behavior (adhesion, proliferation, differentiation) (Salbach et al., 2012; Menezes et al., 2022).

Despite the lower proportions of DCN and GAG in decellularized samples compared to native ones, no correlation could be demonstrated in their alteration after chemical treatments. Since GAGs are ubiquitous on the cell surface, their removal by the decellularization protocol is expected. Therefore, proportionally, the loss of GAGs could be greater than that of DCN.

The present study confronts different decellularization approaches. Protocols D1 to D4 are based on the use of Triton, SDS and DNase and ensure cell membrane lysis, protein solubilization and residual DNA elimination. Triton and SDS are known for their efficiency in decellularization, but also for altering the structure of the ECM (Crapo et al., 2011). Protocol D5 consists of a succession of solvent- and detergent-based baths, which has also already demonstrated its decellularization potential (Manon et al., 2023), including the monitoring of Crapo's criteria (Crapo et al., 2011). In this protocol, solvents such as ethanol and acetone are used for cell lysis and lipid removal but are both also known as altering the ECM ultrastructure. The additional advantage of this protocol is that it also neutralizes prions, which the other protocols do not allow.

As qualitatively shown in the Figure 1 on the SR stained sections, more undulating collagen structure are observed in decellularized tissues than in native tissues. The crosslink alteration could modifiy the fibers alignment. In the future, analysis of the collagen distribution could support the observations made in this study. Approaches such as transmission electron microscopy (Adeoye et al., 2022), histology and contrast-enhanced microCT (Maes et al., 2022) could be used and be gathered in order to precisely cartograph the entire HFL structure.

In conclusion, a relationship was observed between the ECM structure and its molecular composition. The decellularization approaches demonstrated no significant alteration of the matrices, which justifies, along with the analysis of other parameters, the future clinical use of these processed matrices for bone regeneration. However, the combination of D5 treatment with subsequent irradiation appears the most deleterious for tissue properties. In the future, an analysis of the entire sample surface would provide more accurate information about potential sample heterogeneity, and precise quantitative analyses of the crosslink content could further validate our results. It would also be interesting to correlate all the observations of this study with the mechanical properties of the tissues.

Data availability statement

The original contributions presented in the study are included in the article/Supplementary material, further inquiries can be directed to the corresponding authors.

Ethics statement

The studies involving humans were approved by the Human Anatomy Department of UCLouvain (Body donation service, IRB00008535, Brussels, Belgium. The studies were conducted in accordance with the local legislation and institutional requirements. The participants provided their written informed consent to participate in this study.

Author contributions

JV: Writing–original draft, Software, Methodology, Investigation, Data curation. JM: Writing–review and editing, Writing–original draft, Supervision, Resources, Methodology, Investigation, Funding acquisition, Data curation, Conceptualization. AC: Writing–review and editing, Software, Data curation. RE: Writing–review and editing. LF: Writing–review and editing, Methodology, Investigation, Data curation. TS: Writing–review and editing. BL: Conceptualization, Writing–review and editing, Supervision. CB: Conceptualization, Writing–review and editing, Supervision. OC: Supervision, Writing–review and editing, Conceptualization.

Funding

The author(s) declare financial support was received for the research, authorship, and/or publication of this article. This work was supported by the F.S.R. Fund (Fonds Spécial pour la Recherche, Belgium) and F.N.R.S. Aspirant Fund granted to JM (Fonds National de la Recherche Scientifique, Application ID 40004991, Belgium), and FRIA grant awarded to JV (Fonds pour la Formation à la Recherche dans l'Industrie et dans l'Agriculture, Application ID 40021733, Belgium).

Acknowledgments

The authors would like to express their sincere gratitude to all the colleagues for their contribution to this work, including Xavier Merny, Olivier Goffin, Laurence Lekeux, Dimitri Roman, Angélique Arts, Shalaw Fawzi, Andreia Teixeira da Cunha, Dimitri Pinto de Carvalho, Anthony Marais, Paulo Ferreira Gomes and all the members of the institutional tissue bank, Guillaume Falgayrac, Caroline Bouzin and the 2IP platform, Christine de Ville de Goyet, Bernard Caelen, Nicolas Charles-Pirlot, Michelle Cougnon, Walter Hudders, Grégoire André. The authors would like to extend special gratitude to the donors used in this study, along with their families.

Conflict of interest

The authors declare that the research was conducted in the absence of any commercial or financial relationships that could be construed as a potential conflict of interest.

Publisher's note

References

Adeoye, A. O., Mukasheva, F., Smatov, S., Khumyrzakh, B., Kadyr, S., Shulgau, Z., et al. (2022). A biomimetic synthetic nanofiber-based model for anterior cruciate ligament regeneration. *Front. Bioeng. Biotechnol.* 10, 969282. doi:10.3389/fbioe.2022.969282

Aktuglu, K., Erol, K., and Vahabi, A. (2019). 'Ilizarov bone transport and treatment of critical-sized tibial bone defects: a narrative review. *J. Orthop. Traumatol.* 20, 22. doi:10.1186/s10195-019-0527-1

Blottner, D., Huang, Y., Trautmann, G., and Sun, L. (2019). The fascia: continuum linking bone and myofascial bag for global and local body movement control on Earth and in Space. A scoping review. *REACH* 14-15, 100030. doi:10.1016/j.reach.2019.100030

Chen, K., Lin, X., Zhang, Q., Ni, J., Li, J., Xiao, J., et al. (2015). 'Decellularized periosteum as a potential biologic scaffold for bone tissue engineering. *Acta Biomater.* 19, 46–55. doi:10.1016/j.actbio.2015.02.020

Cornu, O. (2012). "Influence of freeze-drying and irradiation on mechanical properties of human cancellous bone: application to impaction bone grafting," in *Bone grafting*. Editor Dr Alessandro Zorzi (Croatia: InTech), 41–58. Chapter 3.

Cornu, O., Banse, X., Docquier, P. L., Luyckx, S., and Delloye, C. (2000). 'Effect of freeze-drying and gamma irradiation on the mechanical properties of human cancellous bone. *J. Orthop. Res.* 18, 426–431. doi:10.1002/jor.1100180314

Cornu, O., Boquet, J., Nonclercq, O., Docquier, P. L., Van Tomme, J., Delloye, C., et al. (2011). 'Synergetic effect of freeze-drying and gamma irradiation on the mechanical properties of human cancellous bone. *Cell Tissue Bank.* 12, 281–288. doi:10.1007/s10561-010-9209-1

Costa-Almeida, R., Gonçalves, A., Gershovich, P., Rodrigues, M., Reis, R. L., and Gomes, M. (2015). *Tendon stem cell niche*.

Crapo, P. M., Gilbert, T. W., and Badylak, S. F. (2011). An overview of tissue and whole organ decellularization processes. *Biomaterials* 32, 3233–3243. doi:10.1016/j.biomaterials.2011.01.057

Dalisson, B., Charbonnier, B., Ahmed, A., Gilardino, M., Harvey, E., Makhoul, N., et al. (2021). 'Skeletal regeneration for segmental bone loss: vascularised grafts, analogues and surrogates. *Acta Biomater.* 136, 37–55. doi:10.1016/j.actbio.2021.09.053

Dayan, D., Hiss, Y., Hirshberg, A., Bubis, J. J., and Wolman, M. (1989). Are the polarization colors of picrosirius red-stained collagen determined only by the diameter of the fibers? *Histochemistry* 93, 27–29. doi:10.1007/bf00266843

Delloye, C., van Cauter, M., Dufrane, D., Francq, B. G., Docquier, P. L., and Cornu, O. (2014). Local complications of massive bone allografts: an appraisal of their prevalence in 128 patients. *Acta Orthop. Belg* 80 (2), 196–204.

Dong, C., and Lv, Y. (2016). Application of collagen scaffold in tissue engineering: recent advances and new perspectives. *Polym. (Basel)* 8, 42. doi:10.3390/polym8020042

Duchamp de Lageneste, O., and Colnot, C. (2019). Periostin in bone regeneration. *Adv. Exp. Med. Biol.* 1132, 49–61. doi:10.1007/978-981-13-6657-4_6

Duchamp de Lageneste, O., Julien, A., Abou-Khalil, R., Frangi, G., Carvalho, C., Cagnard, N., et al. (2018). 'Periosteum contains skeletal stem cells with high bone regenerative potential controlled by Periostin. *Nat. Commun.* 9, 773. doi:10.1038/s41467-018-03124-z

Duisit, J., Maistriaux, L., Taddeo, A., Orlando, G., Joris, V., Coche, E., et al. (2017). ’Bioengineering a human face graft: the matrix of identity. *Ann. Surg.* 266, 754–764. doi:10.1097/sla.0000000000002396

Dwek, J. R. (2010). The periosteum: what is it, where is it, and what mimics it in its absence? *Skelet. Radiol.* 39, 319–323. doi:10.1007/s00256-009-0849-9

Dziedzic-Goclawska, A., Kaminski, A., Uhrynowska-Tyszkiewicz, I., and Stachowicz, W. (2005). ’Irradiation as a safety procedure in tissue banking. *Cell Tissue Bank.* 6, 201–219. doi:10.1007/s10561-005-0338-x

Evans, S. F., Chang, H., and Knothe Tate, M. L. (2013). Elucidating multiscale periosteal mechanobiology: a key to unlocking the smart properties and regenerative capacity of the periosteum? *Tissue Eng. Part B Rev.* 19, 147–159. doi:10.1089/ten.teb.2012.0216

Gautieri, A., Redaelli, A., Buehler, M. J., and Vesentini, S. (2014). ’Age- and diabetes-related nonenzymatic crosslinks in collagen fibrils: candidate amino acids involved in Advanced Glycation End-products. *Matrix Biol.* 34, 89–95. doi:10.1016/j.matbio.2013.09.004

Gjaltema, R. A., and Bank, R. A. (2017). ’Molecular insights into prolyl and lysyl hydroxylation of fibrillar collagens in health and disease. *Crit. Rev. Biochem. Mol. Biol.* 52, 74–95. doi:10.1080/10409238.2016.1269716

Gubbiotti, M. A., Vallet, S. D., Ricard-Blum, S., and Iozzo, R. V. (2016). ’Decorin interacting network: a comprehensive analysis of decorin-binding partners and their versatile functions. *Matrix Biol.* 55, 7–21. doi:10.1016/j.matbio.2016.09.009

Halper, J. (2014). “Proteoglycans and diseases of soft tissues,” in *Progress in heritable soft connective tissue diseases*. Editor J. Halper (Dordrecht: Springer Netherlands).

Harrell, C. R., Djonov, V., Fellabaum, C., and Volarevic, V. (2018). ’Risks of using sterilization by gamma radiation: the other side of the coin. *Int. J. Med. Sci.* 15, 274–279. doi:10.7150/ijms.22644

Hussey, G. S., Dziki, J. L., and Badylak, S. F. (2018). Extracellular matrix-based materials for regenerative medicine. *Nat. Rev. Mater.* 3, 159–173. doi:10.1038/s41578-018-0023-x

Julien, A., Perrin, S., Martínez-Sarrà, E., Kanagalingam, A., Carvalho, C., Luka, M., et al. (2022). ’Skeletal stem/progenitor cells in periosteum and skeletal muscle share a common molecular response to bone injury. *J. bone mineral Res. official J. Am. Soc. Bone Mineral Res.* 37, 1545–1561. doi:10.1002/jbmr.4616

Kamml, J., Ke, C. Y., Acevedo, C., and Kammer, D. S. (2023). The influence of AGEs and enzymatic cross-links on the mechanical properties of collagen fibrils. *J. Mech. Behav. Biomed. Mater* 43, 105870.

Kirby, M. A., Heuerman, A. C., and Yellon, S. M. (2018). ’Utility of optical density of picrosirius red birefringence for analysis of cross-linked collagen in remodeling of the peripartum cervix for parturition. *Integr. Gynecol. Obstet. J.* 1. doi:10.31038/IGOJ.2018107

Lien, C. H., Chen, Z. H., and Phan, Q. H. (2022). ’Birefringence effect studies of collagen formed by nonenzymatic glycation using dual-retarder Mueller polarimetry. *J. Biomed. Opt.* 27, 087001. doi:10.1117/1.jbo.27.8.087001

Liguori, G. R., Liguori, T. T. A., de Moraes, S. R., Sinkunas, V., Terlizzi, V., van Dongen, J. A., et al. (2020). ’Molecular and biomechanical clues from cardiac tissue decellularized extracellular matrix drive stromal cell plasticity. *Front. Bioeng. Biotechnol.* 8, 520. doi:10.3389/fbioe.2020.00520

Lin, X., Zhao, C., Zhu, P., Chen, J., Yu, H., Cai, Y., et al. (2018). ’Periosteum extracellular-matrix-mediated acellular mineralization during bone formation. *Adv. Healthc. Mater* 7. doi:10.1002/adhm.201700660

Lou, Y., Wang, H., Ye, G., Li, Y., Liu, C., Yu, M., et al. (2021). ’Periosteal tissue engineering: current developments and perspectives. *Adv. Healthc. Mater* 10, e2100215. doi:10.1002/adhm.202100215

Maes, A., Pestiaux, C., Marino, A., Balcaen, T., Leyssens, L., Vangrunderbeeck, S., et al. (2022). Cryogenic contrast-enhanced microCT enables nondestructive 3D quantitative histopathology of soft biological tissues. *Nat. Commun.* 13 (1), 6207. doi:10.1038/s41467-022-34048-4

Mandair, G. S., Oest, M. E., Mann, K. A., Morris, M. D., Damron, T. A., and Kohn, D. H. (2020). Radiation-induced changes to bone composition extend beyond periosteal bone. *Bone Rep.* 12, 100262. doi:10.1016/j.bonr.2020.100262

Manon, J., Evrard, R., Fievé, L., Bouzin, C., Magnin, D., Xhema, D., et al. (2023). ’A new osteogenic membrane to enhance bone healing: at the crossroads between the periosteum, the induced membrane, and the diamond concept. *Bioengineering* 10, 143. doi:10.3390/bioengineering10020143

Manon, J., Evrard, R., Maistriaux, L., Fievé, L., Heller, U., Magnin, D., et al. (2022). Periosteum and fascia lata: are they so different? *Front. Bioeng. Biotechnol.* 10, 944828. doi:10.3389/fbioe.2022.944828

Masquelet, A. C., and Begue, T. (2010). ’The concept of induced membrane for reconstruction of long bone defects. *Orthop. Clin. North Am.* 41, 27–37. doi:10.1016/j.ocl.2009.07.011

Mazon, J., de Aro, A. A., Simões, P. W., and Pimentel, E. R. (2018). ’Effect of different resistance-training protocols on the extracellular matrix of the calcaneal tendon of rats. *Ann. Anat.* 216, 75–81. doi:10.1016/j.aanat.2017.11.002

Menezes, R., Vincent, R., Osorno, L., Hu, P., and Treena Livingston Arinzeh (2022). Biomaterials and tissue engineering approaches using glycosaminoglycans for tissue repair: lessons learned from the native extracellular matrix. *Acta Biomater.* 163, 210–227. doi:10.1016/j.actbio.2022.09.064

Nguyen, H., Morgan, D. A., and Forwood, M. R. (2007). Sterilization of allograft bone: effects of gamma irradiation on allograft biology and biomechanics. *Cell Tissue Bank* 8 (2), 93–105. doi:10.1007/s10561-006-9020-1

Pancheri, F. Q., Eng, C. M., Lieberman, D. E., Biewener, A. A., and Dorfmann, L. (2014). ’A constitutive description of the anisotropic response of the fascia lata. *J. Mech. Behav. Biomed. Mater.* 30, 306–323. doi:10.1016/j.jmbbm.2013.12.002

Paul, R. G., and Bailey, A. J. (1996). ’Glycation of collagen: the basis of its central role in the late complications of ageing and diabetes. *Int. J. Biochem. Cell Biol.* 28, 1297–1310. doi:10.1016/s1357-2725(96)00079-9

Perrin, S., and Colnot, C. (2022). ’Periosteal skeletal stem and progenitor cells in bone regeneration. *Curr. Osteoporos. Rep.* 20, 334–343. doi:10.1007/s11914-022-00737-8

Pritchard, J. M., and Willett, T. L. (2017). “Pentosidine as a biomarker for poor bone quality and elevated fracture risk,” in *Biomarkers in bone disease*. Editors V. B. Patel and V. R. Preedy (Dordrecht: Springer Netherlands).

Rappu, P., M Salo, A., Myllyharju, J., and Heino, J. (2019). Role of prolyl hydroxylation in the molecular interactions of collagens. *Essays Biochem.* 63, 325–335. doi:10.1042/ebc20180053

Ribeiro, J. F., dos Anjos, E. H., Mello, M. L., and de Campos Vidal, B. (2013). ’Skin collagen fiber molecular order: a pattern of distributional fiber orientation as assessed by optical anisotropy and image analysis. *PLoS One* 8, e54724. doi:10.1371/journal.pone.0054724

Rittié, L. (2017). ’Method for picrosirius red-polarization detection of collagen fibers in tissue sections. *Methods Mol. Biol.* 1627, 395–407. doi:10.1007/978-1-4939-7113-8_26

Sainio, A., and Järveläinen, H. (2020). Extracellular matrix-cell interactions: focus on therapeutic applications. *Cell. Signal.* 66, 109487. doi:10.1016/j.cellsig.2019.109487

Saito, M., and Marumo, K. (2010). ’Collagen cross-links as a determinant of bone quality: a possible explanation for bone fragility in aging, osteoporosis, and diabetes mellitus. *Osteoporos. Int.* 21, 195–214. doi:10.1007/s00198-009-1066-z

Saito, M., and Marumo, K. (2015). ’Effects of collagen crosslinking on bone material properties in health and disease. *Calcif. Tissue Int.* 97, 242–261. doi:10.1007/s00223-015-9985-5

Salbach, J., TilmanRachner, D. M. R., Ute Hempel, U. A., Sandra Franz, J.-C. S., Lorenz, C. H., Franz, S., et al. (2012). Regenerative potential of glycosaminoglycans for skin and bone. *J. Mol. Med.* 90, 625–635. doi:10.1007/s00109-011-0843-2

Scott, J. E. (2003). Elasticity in extracellular matrix shape modules of tendon, cartilage etc A sliding proteoglycan-filament model. *J. physiology* 553, 335–343. doi:10.1113/jphysiol.2003.050179

Seto, A., Gatt, C. J., Jr., and Dunn, M. G. (2008). ’Radioprotection of tendon tissue via crosslinking and free radical scavenging. *Clin. Orthop. Relat. Res.* 466, 1788–1795. doi:10.1007/s11999-008-0301-9

Shoulders, M. D., and Raines, R. T. (2009). ’Collagen structure and stability. *Annu. Rev. Biochem.* 78, 929–958. doi:10.1146/annurev.biochem.77.032207.120833

Snedeker, J. G., and Gautieri., A. (2014). The role of collagen crosslinks in ageing and diabetes - the good, the bad, and the ugly. *Muscles, ligaments tendons J.* 4, 303–308. doi:10.32098/mltj.03.2014.07

Squier, C. A., Ghoneim, S., and Kremenak, C. R. (1990). ’Ultrastructure of the periosteum from membrane bone. *J. Anat.* 171, 233–239.

Theocharis, A. D., Skandalis, S. S., Gialeli, C., and Karamanos, N. K. (2016). Extracellular matrix structure. *Adv. Drug Deliv. Rev.* 97, 4–27. doi:10.1016/j.addr.2015.11.001

Thorpe, C. T. (2010). *Extracellular matrix synthesis and degradation in functionally distinct tendons.* University College London.

Uhl, F. E., Zhang, F., Pouliot, R. A., Uriarte, J. J., Rolandsson Enes, S., Han, X., et al. (2020). ’Functional role of glycosaminoglycans in decellularized lung extracellular matrix. *Acta Biomater.* 102, 231–246. doi:10.1016/j.actbio.2019.11.029

Unal, M., and Akkus, O. (2015). ’Raman spectral classification of mineral- and collagen-bound water’s associations to elastic and post-yield mechanical properties of cortical bone. *Bone* 81, 315–326. doi:10.1016/j.bone.2015.07.024

van Steenberghe, M., Schubert, T., Guiot, Y., Bouzin, C., Bollen, X., and Gianello, P. (2017). ’Enhanced vascular biocompatibility of decellularized xeno-/allogeneic matrices in a rodent model. *Cell Tissue Bank.* 18, 249–262. doi:10.1007/s10561-017-9610-0

Vidal, L., Kampleitner, C., Brennan, M. Á., Hoornaert, A., and Layrolle, P. (2020). Reconstruction of large skeletal defects: current clinical therapeutic strategies and future directions using 3D printing. *Front. Bioeng. Biotechnol.* 8, 61. doi:10.3389/fbioe.2020.00061

Yamauchi, M., and Sricholpech, M. (2012). ’Lysine post-translational modifications of collagen. *Essays Biochem.* 52, 113–133. doi:10.1042/bse0520113

Zhang, W., Ge, Y., Cheng, Q., Zhang, Q., Fang, L., and Zheng, J. (2018). Decorin is a pivotal effector in the extracellular matrix and tumour microenvironment. *Oncotarget* 9, 5480–5491. doi:10.18632/oncotarget.23869

Zhang, X., Xie, C., Lin, A. S., Ito, H., Awad, H., Lieberman, J. R., et al. (2005). ’Periosteal progenitor cell fate in segmental cortical bone graft transplantations: implications for functional tissue engineering. *J. bone mineral Res. official J. Am. Soc. Bone Mineral Res.* 20, 2124–2137. doi:10.1359/jbmr.050806

Frontiers in Bioengineering and Biotechnology

Accelerates the development of therapies, devices, and technologies to improve our lives

A multidisciplinary journal that accelerates the development of biological therapies, devices, processes and technologies to improve our lives by bridging the gap between discoveries and their application.

Discover the latest Research Topics

See more →

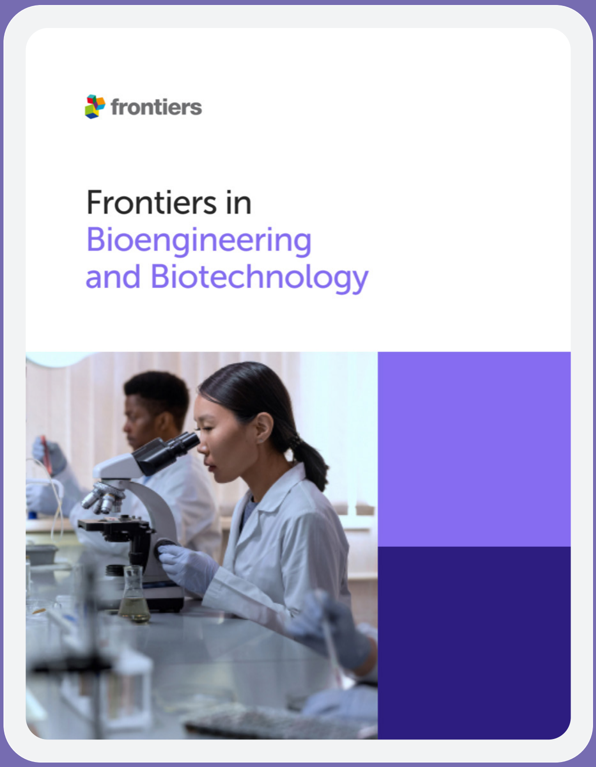

frontiers

Frontiers in Bioengineering and Biotechnology

Frontiers

Avenue du Tribunal-Fédéral 34
1005 Lausanne, Switzerland
frontiersin.org

Contact us

+41 (0)21 510 17 00
frontiersin.org/about/contact